Quantum Chemical Studies on Bonding and Reactivity at Hybrid Organic-Inorganic Interfaces

Dissertation
(kumulativ)

zur Erlangung des Grades
Doktor der Naturwissenschaften
(Dr. rer. nat.)
des Fachbereichs Chemie der Philipps-Universität Marburg

vorgelegt von
Jan-Niclas Luy, M.Sc.
aus Neuhof (bei Fulda)

Marburg, 2021

Die vorliegende Dissertation wurde von Juli 2017 bis März 2021 am Fachbereich Chemie unter Leitung von Prof. Dr. Ralf Tonner angefertigt.

Vom Fachbereich Chemie der Philipps-Universität Marburg
(Hochschulkennziffer 1180) als Dissertation angenommen am: 19.5.2021

Erstgutachter: Prof. Dr. Ralf Tonner
Zweitgutachter: Prof. Dr. Michael Gottfried

Tag der Disputation: 26.5.2021

Erklärung

Ich erkläre, dass eine Promotion noch an keiner anderen Hochschule als der Philipps-Universität Marburg, Fachbereich Chemie, versucht wurde.

Hiermit versichere ich, dass ich die vorliegende Dissertation

Quantum Chemical Studies on Bonding and Reactivity at Hybrid Organic-Inorganic Interfaces

selbstständig, ohne unerlaubte Hilfe Dritter angefertigt und andere als die in der Dissertation angegebenen Hilfsmittel nicht benutzt habe. Alle Stellen, die wörtlich oder sinngemäß aus veröffentlichten oder unveröffentlichten Schriften entnommen sind, habe ich als solche kenntlich gemacht. Dritte waren an der inhaltlich-materiellen Erstellung der Dissertation nicht beteiligt; insbesondere habe ich hierfür nicht die Hilfe eines Promotionsberaters in Anspruch genommen. Kein Teil dieser Arbeit ist in einem anderen Promotions- oder Habilitationsverfahren verwendet worden. Mit dem Einsatz von Software zur Erkennung von Plagiaten bin ich einverstanden.

_____ _____

Ort/Datum Unterschrift (Vor- und Nachname)

Contents

Publications

Publications and conference contributions made since acceptance into the doctoral program at the Philipps University of Marburg are listed below in chronological order beginning with the most recent. Not all publications are considered as parts of this dissertation.

Articles and Book Chapters

Jan-Niclas Luy, Ralf Tonner, *Organic functionalization at the Si(001) dimer vacancy defect – structure, bonding and reactivity*, *J. Phys. Chem. C* **2021**, *125*, 5635-5646.

Jan-Niclas Luy, Mahlet Molla, Lisa Pecher, Ralf Tonner, *Efficient hierarchical models for reactivity of organic layers on semiconductor surfaces*, *J. Comput. Chem.* **2021**, *42*, 827-839.

Timo Glaser, Jannick Meinecke, Lukas Freund, Christian Länger, **Jan-Niclas Luy**, Ralf Tonner, Ulrich Koert, Michael Dürr, *Click chemistry in ultra-high vacuum - tetrazine coupling with methyl enol ether covalently linked to Si(001)*, *Chem. Eur. J.* **2021**, *27*, 8082-8087.

Timo Glaser, Jannick Meinecke, Christian Länger, **Jan-Niclas Luy**, Ralf Tonner, Ulrich Koert, Michael Dürr, *Combined XPS and DFT investigation of the adsorption modes of methyl enol ether functionalized cyclooctyne on Si(001)*, *ChemPhysChem* **2021**, *22*, 404-409.

Natalie Dehnhardt, **Jan-Niclas Luy**, Philip Klement, Luca Schipplick, Sangam Chatterjee, Ralf Tonner, Johanna Heine, *Mixed group 14-15 metalates as model compounds for doped lead halide perovskites*, *Angew. Chem. Int. Ed.* **2020**, *60*, 3906.

Jan-Niclas Luy, Ralf Tonner, *Complementary base lowers the barrier in SuFEx click chemistry for primary amine nucleophiles*, *ACS Omega* **2020**, *5*, 31432-31439.

Jan Herritsch, **Jan-Niclas Luy**, Sebastian Rohlf, Manuel Gruber, Benedikt P. Klein, Matthias Kalläne, Peter Schweyen, Martin Bröring, Kai Rossnagel, Ralf Tonner, J. Michael Gottfried, *Influence of ring contraction on the electronic structure of nickel tetrapyrrole complexes: corrole versus porphyrin*, *ECS J. Solid State Sci. Technol.* **2020**, *9*, 061005.

Malte Zugermeier, Jan Herritsch, **Jan-Niclas Luy**, Min Chen, Benedikt P. Klein, Falk Niefind, Peter Schweyen, Martin Bröring, Martin Schmid, Ralf Tonner, J. Michael Gottfried, *On-surface formation of a transient corrole radical and aromaticity-driven interfacial electron transfer*, *J. Phys. Chem. C* **2020**, *124*, 13825–13836.

Julian Heep, **Jan-Niclas Luy**, Christian Länger, Jannick Meinecke, Ulrich Koert, Ralf Tonner, Michael Dürr, *Adsorption of methyl-substituted benzylazide on Si(001): reaction channels and final configurations*, *J. Phys. Chem. C* **2020**, *124*, 9940–9946.

Natalie Dehnhardt, **Jan-Niclas Luy**, Marvin Szabo, Mirco Wende, Ralf Tonner, Johanna Heine, *Synthesis of a two-dimensional organic–inorganic bismuth iodide metalate through in situ formation of iminium cations*, *Chem. Commun.* **2019**, *55*, 14725-14728.

Qitang Fan, **Jan-Niclas Luy**, Martin Liebold, Katharina Greulich, Malte Zugermeier, Jörg Sundermeyer, Ralf Tonner, J. Michael Gottfried, *Template-controlled on-surface synthesis of a lanthanide supernaphthalocyanine and its open-chain polycyanine counterpart*, *Nat. Commun.* **2019**, *10*, 5049.

Fabian Pieck, Lisa Pecher, **Jan-Niclas Luy**, Ralf Tonner, *Inorganic and organic functionalisation of silicon studied by density functional theory*, in *High Performance Computing in Science and Engineering ' 18*, Eds. Wolfgang E. Nagel, Michael M. Resch, Dietmar H. Kröner, Springer International Publishing **2019**, 153-166.

Theodor Peez, **Jan-Niclas Luy**, Klaus Harms, Ralf Tonner, Ulrich Koert, *From acenaphthenes to (+)-Delavatine A: visible-light-induced ring closure of methyl (a-naphthyl) acrylates*, *Chem. Eur. J.* **2018**, *24*, 1-6.

Oral Presentations

Jan-Niclas Luy, Ralf Tonner, *Introduction to DFT and some applications*, SFB 1083 Winter School (Kleinwalsertal, Austria), **2019**.

Jan-Niclas Luy, Ralf Tonner, *VASP - applications in surface chemistry*, VASP on HPC user meeting (Gießen, Germany), **2018**.

Jan-Niclas Luy, Ralf Tonner, *Computational insights into inorganic/organic interfaces*, GRK 1782 & SFB 1083 2nd Joint Seminar (Kloster Volkenroda, Germany), **2018**.

Poster Presentations

Jan-Niclas Luy, Benedikt P. Klein, J. Michael Gottfried, Ralf Tonner, *Application of periodic energy decomposition analysis to metallic systems*, DPG Spring Meeting of the Surface Science Division (virtual), **2021**.

Jan-Niclas Luy, Benedikt P. Klein, J. Michael Gottfried, Ralf Tonner, *Application of periodic energy decomposition analysis to metallic systems*, ASE Workshop: Software Development for Atomic Scale Modeling (Gothenburg, Sweden), **2019**.

Jan-Niclas Luy, Benedikt P. Klein, J. Michael Gottfried, Ralf Tonner, *Application of periodic energy decomposition analysis to metallic systems*, 55th Symposium on Theoretical Chemistry (Rostock, Germany), **2019**.

Jan-Niclas Luy, Ralf Tonner, *In silico modelling of hybrid organic-inorganic interfaces*, Bunsentagung 2019 - 118th General Assembly of the German Bunsen Society for Physical Chemistry (Jena, Germany), **2019**.

Jan-Niclas Luy, Ralf Tonner, *Si(001) defects and their impact on surface reactivity*, 54th Symposium on Theoretical Chemistry (Halle an der Saale, Germany), **2018**.

Jan-Niclas Luy, Jan Herritsch, J. Michael Gottfried, Ralf Tonner, *Density functional studies of metal organic interfaces - Corroles on Ag(111)*, European Conference On Surface Science (Aarhus, Denmark), **2018**.

Jan-Niclas Luy, Jan Herritsch, J. Michael Gottfried, Ralf Tonner, *Density functional studies of metal organic interfaces - Corroles on Ag(111)*, Materials Science Day Mittelhessen (Marburg, Germany), **2018**.

Jan-Niclas Luy, Ralf Tonner, *Computational chemistry at interfaces*, Fachbereichstag Chemie (Marburg, Germany), **2017**.

Jan-Niclas Luy, J. Michael Gottfried, Ralf Tonner, *Density functional studies of tetrapyrroles on Ag(111)*, 11th Triennial Congress of the World Association of Theoretical and Computational Chemists (Munich, Germany), **2017**.

Jan-Niclas Luy, J. Michael Gottfried, Ralf Tonner, *Density functional studies of tetrapyrroles on Ag(111)*, Hands-on Workshop Density-Functional Theory and Beyond: Accuracy, Efficiency and Reproducibility in Computational Materials Science (Berlin, Germany), **2017**.

1 Motivation

Microelectronic devices are ubiquitous in modern everyday life. Displays and communication equipment based on diodes provide almost instant access to information for anyone. Transistors supply storage and computing capabilities enabling the development of artificial intelligence. Sensors can save lives by detecting toxic substances or diagnosing diseases.[1] In short, the significance of micro- and nano-technology for society cannot be overstated. However, technology must keep improving in order to tackle some of the most pressing challenges now and for the coming decades: rising energy demand and resource exhaustion.

In the past, miniaturization of electronic devices has proven to be the most effective way of simultaneously improving performance and energy efficiency.[2] This is achieved mainly through an increase of contact area at solid-solid interfaces where desired properties originate.[3] Over time, miniaturization has advanced to the scale of individual atoms and molecules which represents a physical limit. This limit poses significant challenges to the design of devices which are now increasingly subjected to quantum mechanical effects such as tunneling or quantum confinement.[4] Controlling and potentially harnessing quantum effects in order to enable continuous improvements requires precise control over composition and structure of functional interfaces. Since feature sizes of classical top-down photolithographic approaches are fundamentally constrained by the used wavelength[5], alternative bottom-up approaches where the device is self-assembled from precursor molecules are increasingly investigated.[6,7] Here, benefits gained from more precise manufacturing can be combined with novel material classes offering advantages over established semiconductors.

Organic building blocks are versatile and therefore particularly well suited for bottom-up assembly of solid-solid hybrid interfaces.[8,9] In this dissertation two interface types between organic molecules and either an inorganic semiconductor (**A**) or a metal (**B**) are investigated. The organic building blocks must be carefully selected for their ability to react in a unique, well defined manner at the interface as any side reaction can have a detrimental impact on uniformity and thus device performance. Therefore, detailed understanding of surface and molecular reactivity

as well as resulting bonding patterns is of great importance. In the collected publications constituting this cumulative dissertation the focus is therefore placed on the elucidation of reaction mechanisms and bonding analysis at interfaces. For this task, *ab initio* quantum chemical methods are uniquely qualified due to their ability to explain experimental observations and make predictions about suitable material systems.

1.1 Interface A: Organic / Inorganic Semiconductor

Organic layers have a multitude of possible applications when covalently attached to inorganic semiconductors. They shield the inorganic substrate from oxidizing environments like air or moisture and molecules with low polarizabilities can reduce electrical interference between device parts.[10] In addition, organic materials tend to have a higher mechanical flexibility compared to their inorganic counterparts, enabling the creation of flexible circuits.[11] Furthermore, bioorganic molecules can be used to integrate electronic devices with living tissue which is an important prerequisite for medical applications.[12]

1.2 Interface B: Organic / Metal

In many areas silicon based semiconductors are already being replaced with other materials possessing superior properties.[13] One particularly promising class of materials due to their functional versatility are organic semiconductors. Organic semiconductors are prominently used for applications in optoelectronic devices such as solar cells and organic light emitting diodes but also in organic thin-film transistors.[14] However, in order to harness the properties of molecules for organic electronics, an interface to metallic conductors must be formed.[3] Here, not only the reactivity at the interface but also the modifications to the electronic structure of the organic layer by the metal are of interest.[15]

2 Introduction

2.1 Bonding at Interfaces

Reaction mechanisms involving surfaces and interfaces are qualitatively different from those found in the gas or liquid phase. Firstly, the underlying substrate not only acts as a reaction partner for molecular building blocks but also defines the chemical environment. It provides a structural template for attaching molecules by restricting access for reactions from one hemisphere and confinement to two dimensions. Secondly, the internal energy of impinging molecules is equilibrated with the substrate upon adsorption. Therefore, reaction barriers and energies at the interface must not be calculated from the reference level (set to zero) of isolated reactants, as would be the case in the gas phase, but from an initial intermediate as shown in Figure 2.1.1.

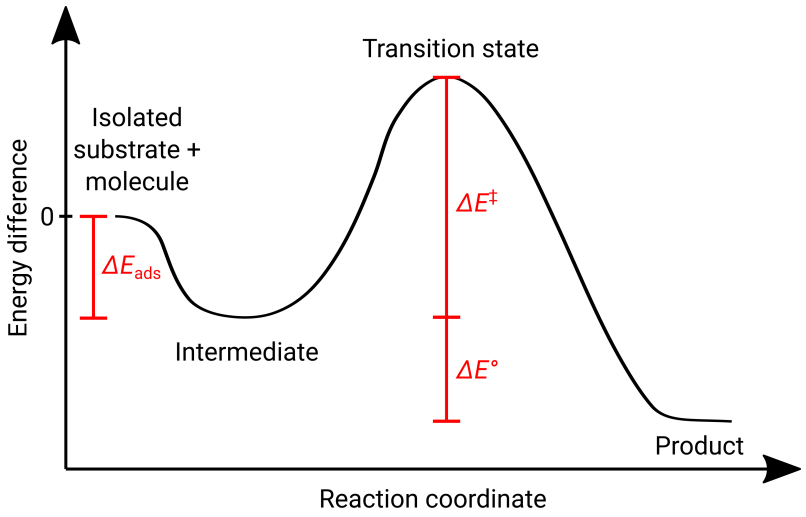

Figure 2.1.1: Energy diagram of a surface or interface reaction. The initial adsorption is direct and has a negative energy ΔE_{ads}. The intermediate can be physisorbed or chemisorbed. Further reaction through a transition state (TS) requires an activation energy $\Delta E^{\ddagger}$. The reaction energy ΔE° is calculated as the difference between intermediate and product.

The intermediate can be either physisorbed or chemisorbed. In the latter case the adsorption is said to be direct. From there, a series of interface reactions is possible,

however, in contrast to heterogeneous catalysis, formed interface bonds are ideally strong and not meant to be fully cleaved again. Physisorption, dominated by van der Waals interactions, is comparatively weak and leaves the electronic structure of the bonding partners largely undisturbed. Under the term chemisorption stronger bonding interactions are collected, which includes ionic bonds dominated by electrostatics and covalent bonds dominated by orbital interactions. Depending on the origin of the involved electrons, covalent bonds can be further classified into shared-electron bonds with roughly equal contributions and dative bonds with unidirectional donor-acceptor character.[16] This distinction is less useful for molecules adsorbed on metal surfaces due to the strong delocalization of metal valence electrons and the absence of an energy gap. The implications of this 'metallic' bonding are discussed in more detail in Sections 2.3.1 and 4.9.2. These intuitive yet highly predictive concepts are however challenging to quantify without theoretical aid. Here, bonding analysis is a valuable tool for categorizing and understanding chemical characteristics and bond formation mechanisms. Any bonding analysis method being applied to solid-solid interfaces must be able to describe local bonds and strongly delocalized bands on equal footing. One such method is the quantum theory of atoms in molecules[17,18] since it relies only on a rigorous topological analysis of the electron density. In the solid state, bonding is sometimes more conveniently interpreted based on the density of states (DOS) as shown below in Figure 2.3.1. With projection schemes, the contributions of certain elements and angular momenta (s, p, d, f) to a feature can be quantified.[19,20] Thus, comparing the energetic position and shape of DOS components before and after a reaction can already reveal many details about the bonds formed in the course of a reaction. These concepts have been further advanced in the crystal orbital Hamilton population method[21] which takes bonding as well as anti-bonding interactions into account. A more nuanced picture of the chemical nature of interfaces can be painted by additionally considering natural bonding orbitals (NBO). The NBO method has been recently made available for periodic descriptions using a plane wave basis set[22] by projecting crystal orbitals onto a localized orbital basis (see Section 4.9.1). As a result, lone pairs and shared electron bonds spanning multiple atomic centers[23] can be identified. However, the primarily used bonding analysis scheme in this dissertation is the energy decomposition analysis (EDA)[24,25] and its periodic implementation (pEDA)[26]. The strength of the pEDA for surface science applications lies in its ability to distinguish between the different physical driving forces of bond formation and relate them to the concepts of physisorption and chemisorption. Here, the total bond energy is dissected into contributions from quasiclassical electrostatics, orbital interactions, Pauli re-

pulsion and preparation energies of the chosen fragments. The orbital interaction might be even further decomposed with the natural orbitals for chemical valence (NOCV) extension[27]. In the NOCV, the flow of electrons between the fragments is quantified in terms of orbital specific deformation densities which aids visual characterization of the bond. For a discussion of the underlying theoretical details the reader is referred to Section 4.9.2. In the past, the pEDA was already successfully used to characterize bonds of organic molecules with inorganic semiconductors[28], in molecular solids[29,30] and at transition metal surfaces[26,31].

2.2 Interface A: Organic / Inorganic Semiconductor

2.2.1 The Silicon (001) Surface

Silicon is often the first semiconductor investigated regarding compatibility with novel materials and manufacturing approaches due to several decades of experience.[32] Therefore, the technologically most significant Si(001) facet, shown in Figure 2.2.1c, which forms a stable native oxide (SiO_2) interface is also used as a model for the attachment of organic layers in this dissertation.

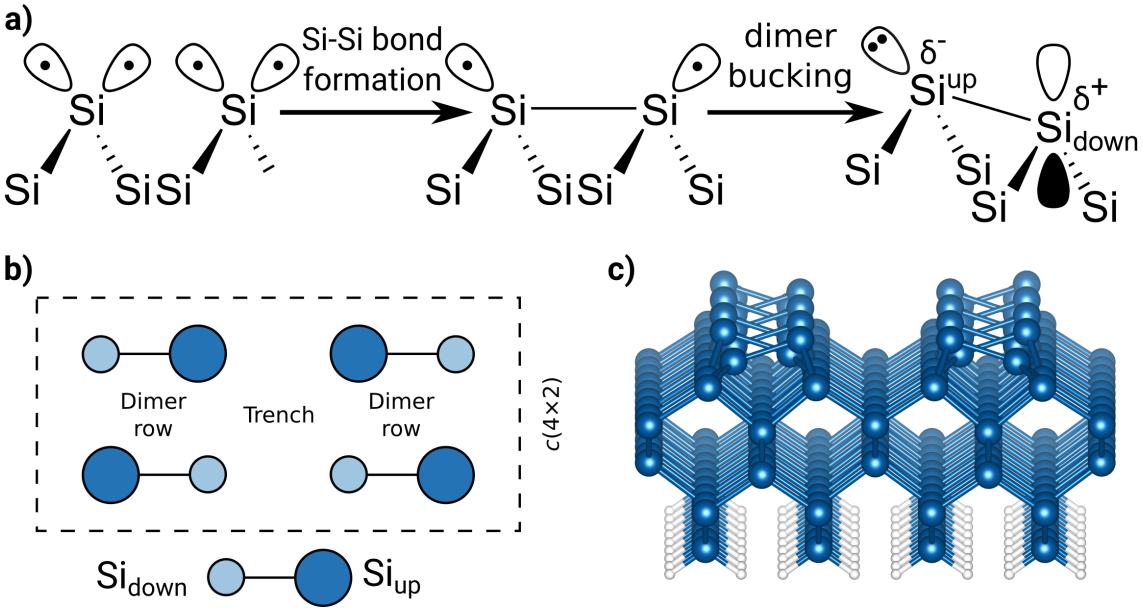
a)
Si-Si bond formation
dimer bucking
δ-
δ+
Si
Si
Si

relaxes by forming single bonds between two neighboring Si atoms thus reducing the number of unpaired electrons (Figure 2.2.1a). In addition, the surface reconstructs into buckled Si-dimers[33,34] where one unpaired electron is transferred from the Si_{down} atom to the p-orbital of the Si_{up} atom. In the most stable $c(4\times2)$[35] superlattice dimers are alternatingly buckled along rows and trenches (Figure 2.2.1b). At elevated temperatures the Si dimers perform a flipping motion which makes Si_{down} and Si_{up} atoms exchange orientations and introduces disorder.[36] However, despite these significant structural and electronic relaxation mechanisms, the Si(001) surface remains highly electrophilic and nucleophilic at Si_{down} and Si_{up} respectively.[35]

2.2.2 Attachment of the First Organic Layer

Due to the zwitterionic nature of the surface dimer, attachment of the first organic layer on Si(001) is challenging and adsorbate molecules have to be carefully designed in order to react selectively towards a single product. Over time, several avenues based on different functional groups have been pursued as shown in Figure 2.2.2. For instance, amines and alcohols (1) preferably form dative bonds with a Si_{down} atom from where they are cleaved by the Si_{up} atom at the same dimer.[37] Ethers on the other hand dissociate across the dimer trench (2).[38] Another class of reactions of organic molecules with Si dimers are cycloadditions. In the 1,3-dipolar variant (3) the Si dimer takes on the role of the diene albeit not formally possessing a double bond. Commonly used 1,3-dipoles are azides (N_3-R), diazoalkanes (N_2-R) or nitrile oxides ($ON-R$).[39] After the initial adsorption, further rearrangement reactions can take place where leaving groups such as N_2 are eliminated. In the case of azides, a three-membered Si–N–Si ring is created which strongly stabilizes the product[40]. An alternative cycloaddition, which does not undergo rearrangements, is the nonconcerted [2+2] cycloaddition (4) between a Si dimer and unsaturated hydrocarbons. In contrast to the reaction between two alkenes this variant is not symmetry-forbidden due to the buckling of the dimer.[41]

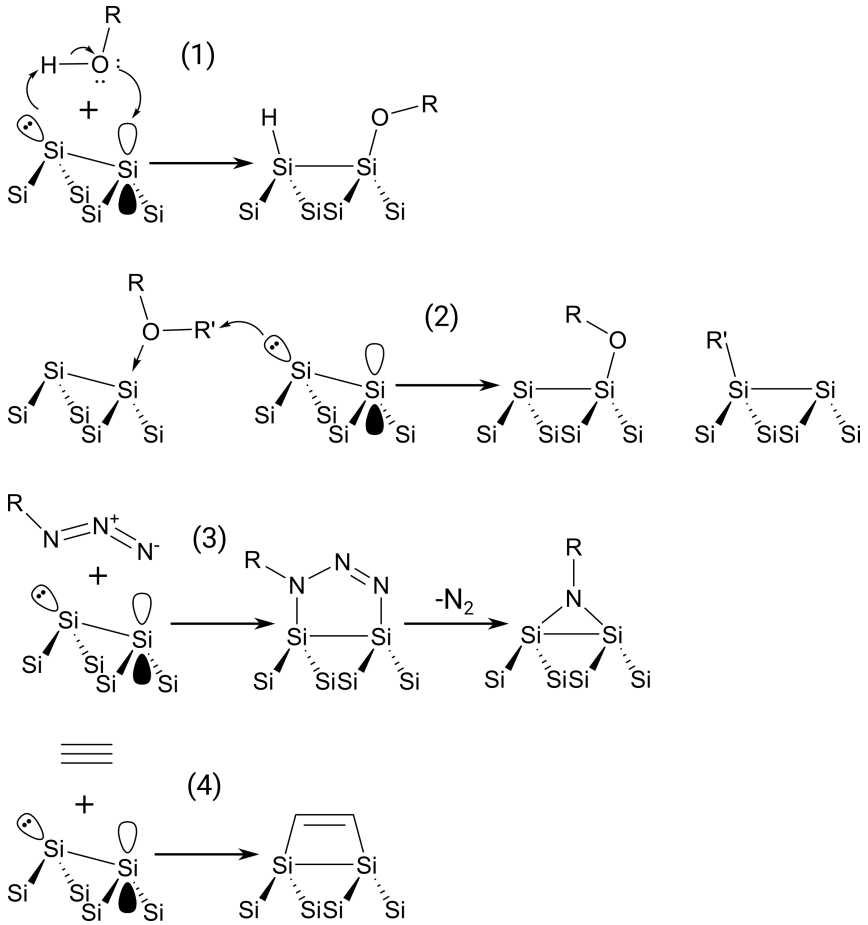

Figure 2.2.2: Four common synthetic routes towards the attachment of organic molecules to silicon dimers. (1) Cleavage of alcohols. (2) Nucleophilic substitution of ethers. (3) 1,3-dipolar cycloaddition of azides coupled with an elimination. (4) [2+2] cycloaddition of acetylene.

So far, none of the introduced attachment reactions is sufficiently selective with respect to other functional groups which might be present in bifunctional molecules. However, this selectivity is necessary in order to retain an intact second functional group for the attachment of subsequent layers. A notable selectivity improvement could be demonstrated with strained alkynes rather than linear ones. The simplest proponent of this class of molecules is cyclooctyne which releases its ring strain energy upon chemisorption via the triple bond.[42,43] As a result, it is able to selectively adsorb on a dimer while exhibiting good tolerance towards other functional groups.[44] Furthermore, the attachment self-limits to a well ordered monolayer on Si(001).[45] Therefore, all molecular building blocks for attachment on Si(001) investigated in this dissertation are based on the cyclooctyne platform.

An additional constraint is put on the design of organic building blocks when they are required to be non-destructively vaporizable[8] for gas phase deposition[7]. This is

not the case for liquid phase approaches where the term layer-by-layer[46] deposition is used.

2.3 Interface B: Organic / Metal

2.3.1 Metal Surface Reactivity

The reactivity of metal surfaces is markedly different from inorganic semiconductors. While adsorption on the latter is dominated by local covalent bonds, there are additional metallic contributions on the former. The characteristics of a metallic bond are delocalization and the absence of an energy gap between occupied and unoccupied crystal orbitals (bands). Its main bonding mechanism is the establishment of a common chemical potential (Fermi level) between the electron reservoir of the metal and the adsorbate. Empty adsorbate orbitals below the Fermi energy (E_F) get filled while occupied orbitals above get depleted. This phenomenon is referred to as energy level alignment in the context of solid-state physics.[47] As a result, interfacial charge transfer occurs which leads to a change of the work function.[48] In response to the charge transfer, the electronic structure of the molecule is furthermore reorganized manifesting in polarization. It is therefore beneficial to discuss bonding on metals also in terms of charge transfer and polarization in addition to shared-electron and donor-acceptor bonds.[49] Besides the quantitative bonding analysis methods introduced above in Section 2.1, the reactivity of transition metals can be qualitatively described with the d-band center model.[50] While the occupation of s- and p-orbitals is here assumed to be constant, the band of d-orbitals is shifted downwards in energy as it is successively filled. For the coinage metals copper, silver, and gold, the d-subshell is completely filled and located largely below E_F (see Figure 2.3.1) making it mostly unavailable for bonding.[51]

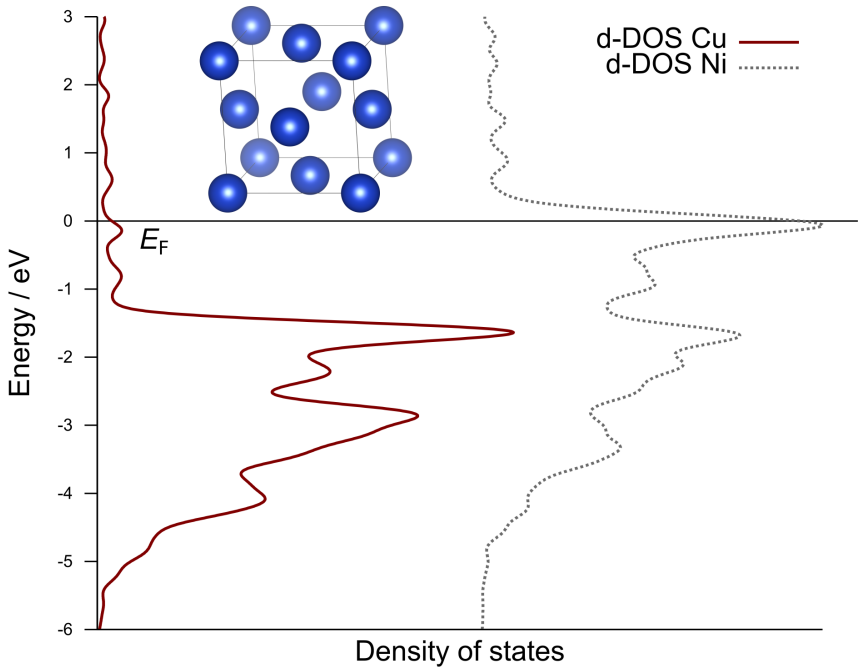

Figure 2.3.1: Density of states (DOS) of the d-band of bulk Cu and Ni. While Ni has a high DOS around E_F, the Cu d-band is mostly found below. The DOS has been calculated with the experimental lattice constants[52] and a Γ-centered k-mesh of 10 points per lattice vector in the cubic unit cell (inset). More details concerning the computational setup are given in Chapter 5.

Furthermore, the d-band is narrower than the s- and p-bands due to a smaller orbital radius. As a result, electrons at the Fermi level of coinage metals move freely through the broad sp-band explaining their excellent conductivity. Additionally, delocalized electrons are very flexible when interacting with the molecular orbitals of an adsorbate and formed bonds exhibit low directionality. Therefore, adsorbates are generally more mobile on coinage metals than on early transition metals which bond also via their localized, partially filled d-bands.[53,54]

Another simple but useful predictor for metal surface reactivity is its 'openness' or number of next neighbors in the first coordination sphere. The most closely packed surface is also the most stable and least reactive. For the coinage metals which crystallize in the close packed face centered cubic (FCC) lattice, those are the low Miller index facets ((111) < (100) < (110))[55] shown in Figure 2.3.2.

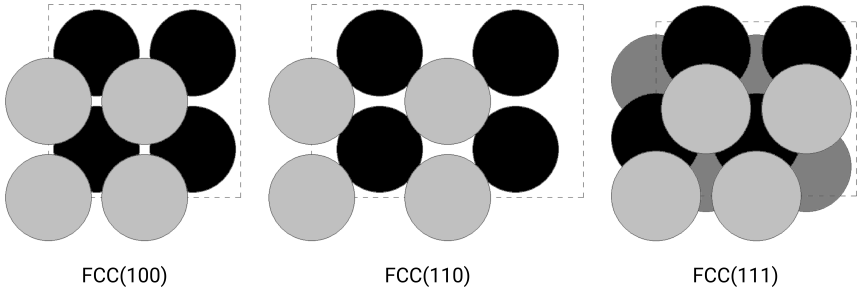

Figure 2.3.2: Low index 2×2 surface cells of FCC crystals. The topmost layer is colored in light gray while the second and third layer are black and dark gray respectively.

Overall, the low reactivity of the coinage metal surfaces makes them ideal substrates for the study of organic semiconductors under well controlled conditions. However, despite their relatively inert nature, coinage metals are not chemically inactive. Under the right conditions, they enable the on-surface synthesis of complex functional molecules with unique properties through catalysis and stabilization of intermediates.[56]

2.3.2 The Tunable Electronic Structure of Cyclic Tetrapyrroles

In most naturally occurring organic semiconductors, desired properties originate from conjugated π-systems which interact strongly with light. These pigments perform a variety of different functions such as photosynthesis (chlorophyll) or photoreception (phytochrome) in addition to gas transport (heme). Therefore, research into technical applications of organic semiconductors is often inspired by biological systems.[57] In particular, molecules derived from cyclic tetrapyrroles and related compounds have received much attention in surface science.[58] A shared feature of these macrocycles is the 18 π-electron aromatic system cross-conjugated with two peripheral double bonds (Figure 2.3.3a). The basic building block is pyrrole, a five-membered, heterocyclic aromatic compound. Assembly of four pyrrole units bridged by methine ($-$CH=) yields the parent tetrapyrrole porphine. As shown in Figure 2.3.3b, many possible modifications can be made to porphine.

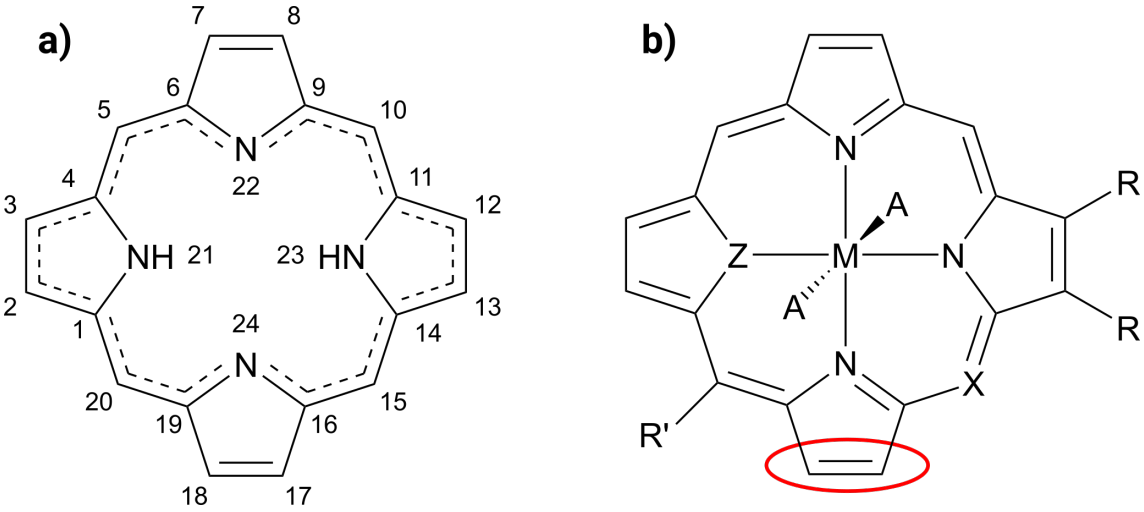

Figure 2.3.3: a) Porphine macrocylce comprised of twenty C and four N atoms with a conjugated 18-electron π-system (dashed line) b) Possible substitution patterns as discussed in the text. Red oval: peripheral double bond.

Through deprotonation at the pyrrolic nitrogens (−NH−), tetrapyrroles become anionic ligands which can form complexes with most elements (M) of the periodic table. The central atom M can have additional axial ligands (A), one of which is the substrate at an interface.[59] The coordinating nitrogen atoms might be replaced with other heteroatoms (Z). When all bridges (X) are replaced with nitrogen, a porphyrazine molecule is formed which can be benzannulated to form phthalocyanine. Further modifications of the electronic structure of the complex are also possible through substituting atoms and functional groups at the periphery (R) or the bridge (R'). These groups can either exert mesomeric or inductive effects on the π-system or control lateral interactions as linkers or spacers. Peripheral double bonds (red oval) may also be hydrogenated to form a chlorin. This versatility makes tetrapyrroles ideal candidates for the tuning of interface properties of different electronic devices.

3 Scope of Investigations

3.1 Interface A: Organic / Inorganic Semiconductor

3.1.1 Investigation of Promising Interface-Building Reactions

In order to attach additional organic layers on the first, suitable building blocks must contain two functional groups. Since cyclooctyne has been identified as the ideal platform molecule, the second functional group has to be inert with respect to the strained triple bond. The mechanisms used to couple between layers are thus said to be 'orthogonal'.[60] However, the requirement of a seamless integration of organic layer synthesis into existing semiconductor manufacturing processes puts further constraints on proposed reaction schemes. They must be highly selective, fast, and produce excellent yields in order to be scalable to large production volumes. In addition, the reactions should also be relatively robust with respect to varying synthetic conditions and chemical environments such as high temperature and solvents. Fulfillment of these requirements enables a simple, single step ('click') connection of molecular building blocks. Initially developed for use in biological systems, click reactions[61] (Figure 3.1.1) also show great promise for functional materials synthesis[62]. The reaction schemes considered in this thesis are the azide-alkyne cycloaddition (AAC, 6)[63], the first prototypical click reaction described in the literature, the inverse electron demand Diels-Alder (IEDDA, 7) reaction[64], the acyl chloride mediated esterification[65] (ACE, 8) and the recently rediscovered sulfur (VI) fluoride exchange (SuFEx, 5)[66]. In the latter, the F^- atom of the RSO_2F moiety is replaced by a nucleophile. It is compatible with Diels-Alder type reactions and has been experimentally demonstrated to work particularly well with primary amines at surfaces.[67]

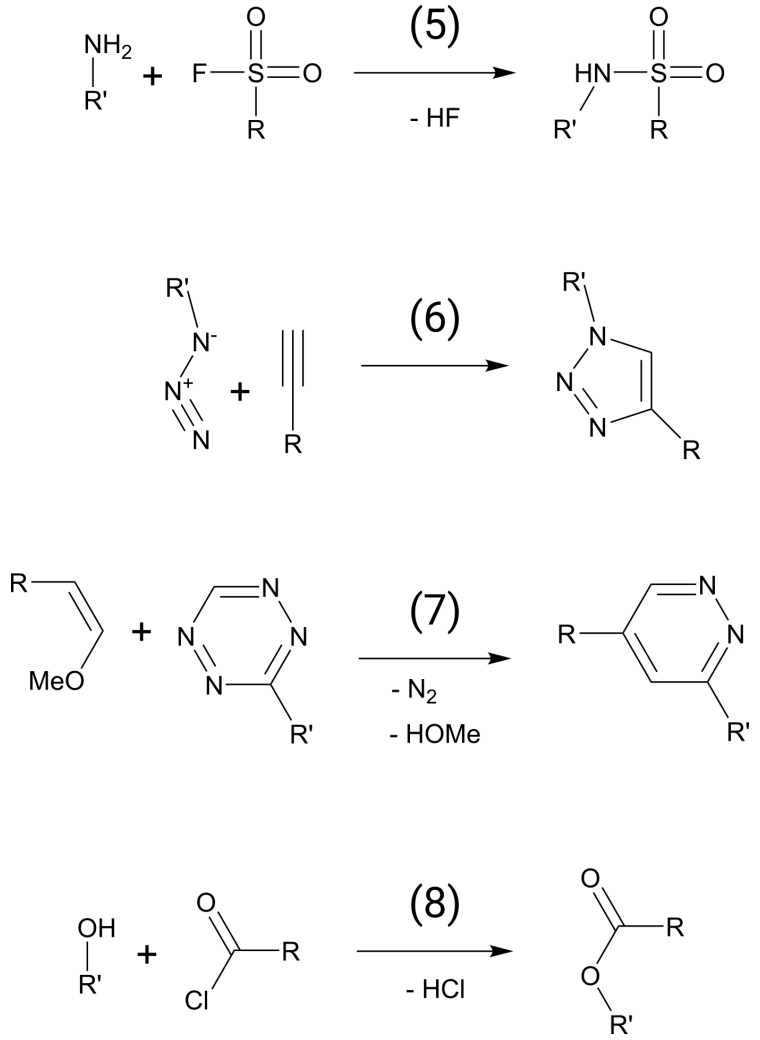

Figure 3.1.1: Four examples of click-like reactions for connecting organic building blocks. (5) Sulfur (VI) fluoride exchange (SuFEx) with a primary amine nucleophile. (6) Azide-alkyne coupling (AAC) via a [3+2] cycloaddition. (7) Inverse electron demand Diels-Alder (IEDDA) reaction via a retro [4+2] cycloaddition. (8) Acyl chloride mediated esterification (ACE).

In order to validate the applicability of a reaction scheme to the bottom-up creation of organic-inorganic interfaces, three steps have to be performed which are shown in Figure 3.1.2. In a first step, the selectivity of the bifunctional cyclooctyne adsorbing on the surface has to be investigated. As mentioned above, selectivity is the primary concern and the conditions promoting side reactions have to be well understood (see Publication A.2). However, before proceeding to the attachment of the next layer, also side reactions of the second building block with the surface must be investigated, as some molecules might be able to bypass the initial layer

(see Publication A.1). Finally, in the last step the performance of the click reaction is probed at the interface (see Publication A.3).

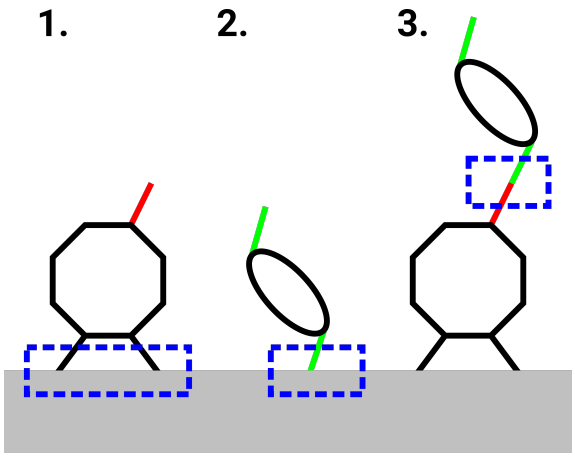

Figure 3.1.2: Three necessary steps for the validation of interface building schemes. Newly formed bonds are highlighted in blue boxes. 1. Probing the selectivity of the first building block reacting with the surface. 2. Determining possible side reactions of the second building block with the surface. 3. Investigation of second layer attachment characteristics.

In practice, the measured growth rate of organic layers often appears to decrease with the number of growth cycles. Several reasons for this decrease are discussed in the literature such as termination of two reactive sites by homobifunctional precursors[68], tilting of molecular chains and steric hindrance of bulky groups.[7] This open question serves as motivation for one part of Publication A.5 in which the tendency towards termination reactions of modified building blocks is investigated.

3.1.2 Towards Realistic Interface Models

In past work on hybrid organic-inorganic interface formation, the broad applicability of quantum chemical methods has been successfully demonstrated.[69,70] Building on these experiences, a step towards more realistic models with increased predictive power is taken in the work presented here. The majority of theoretical models relies on an idealized version of the investigated interface in order to reduce complexity and computational demand. However, no real crystal is ever totally devoid of defects since they increase the configurational entropy of the system. In the case of Si(001), vacancies are more stable at the surface than in the bulk.[71] Here, a bonded dimer vacancy (DV) shown in Figure 3.1.3 is energetically preferred over a single atom vacancy[72] and can reach concentrations of up to 9 %[73].

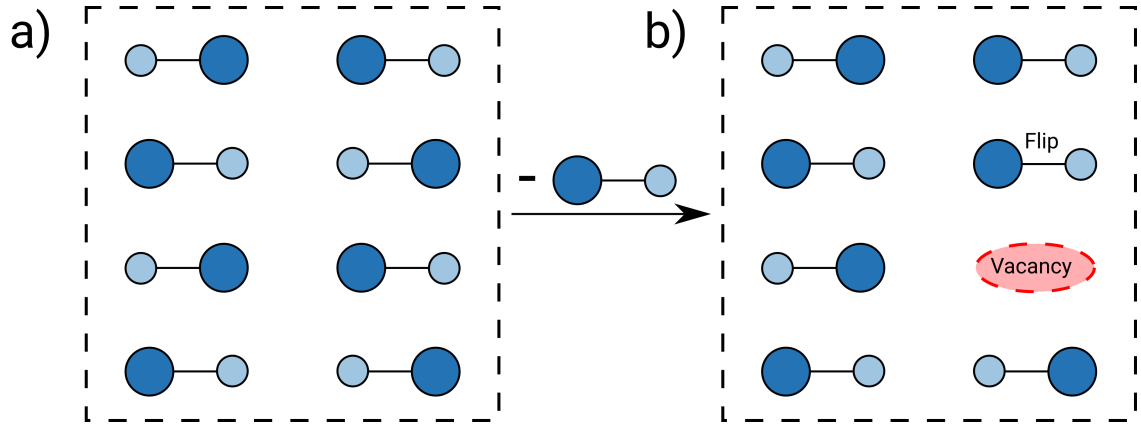

Figure 3.1.3: a) Schematic representation of surface dimers in a 4×4 supercell. b) Same supercell after removal of a dimer. One dimer next to the vacancy (red) is flipped. Figure adapted from Publication A.6.

Due to the aforementioned challenges, research into the adsorption behavior of molecules at or close to vacancies has not been a priority up to now. Therefore it is currently unknown how the presence of even a few DVs influences the growth of organic layers. For this reason, a first step towards the inclusion of defects into interface models is taken with this dissertation (see Publication A.6).
Another source of mismatch between theory and experiment is the neglect of the chemical environment which can influence reaction energies and barriers. In particular, interfaces which are synthesized under wet-chemical conditions exhibit different kinetic and thermodynamic signatures than vacuum processed ones.[74] In this dissertation, two conceptually different approaches to solvent corrections for interfaces are explored. For non-coordinating solvents implicit treatments, such as the conductor-like screening model[75] and polarizable continuum model (PCM)[76], that only capture the electrostatic response of the solvent to the surface charges of the solute, are usually sufficient (see Publication A.5). Coordinating solvents like water on the other hand require explicit calculation of bonding interactions. Since the number of solvent molecules treated explicitly is severely limited by current computational resources, a microsolvation approach of a few molecules is chosen for Publication A.4 that nonetheless includes the most important interactions of the first solvent shell. Furthermore, thermodynamic effects are routinely calculated in order to improve the agreement between calculated and measured Gibbs free energies.

3.1.3 Improving Computational Efficiency

The higher degree of realism aimed for in this dissertation consequently leads to more complex systems to be computed. The challenge lies therefore in the construction of

theoretical models that reduce complexity in accord with available computational resources while capturing the essential features of a real interface. The main method for reaching this goal relies on the local nature of covalent bonds formed at organic-inorganic interfaces. Under the assumption that reactions at the interface are not significantly influenced by distant regions of the system, parts of the interface can be removed. This approach results in a series of hierarchical model systems, shown in Figure 3.1.4, with successively smaller sizes while allowing for the estimation of errors (see Publication A.5).

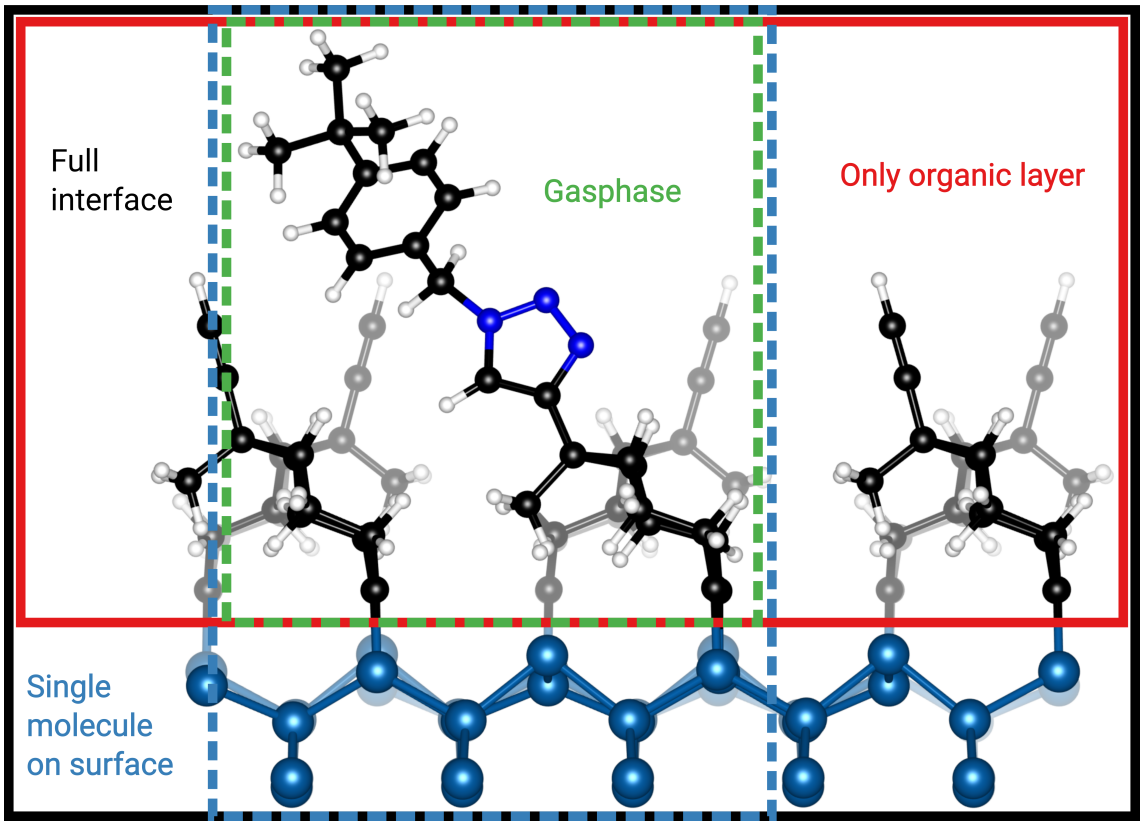

Figure 3.1.4: Hierarchical model systems for an organic-inorganic hybrid interface. Black box: System containing the full interface. Red box: Removal of the substrate. Dashed blue box: Slab model of a single adsorbed molecule. Dashed green box: Both the substrate and neighboring molecules are removed resulting in a gasphase model. Figure adapted from Publication A.5.

Calculation of thermodynamic effects based on the vibrational partition function (see Equation 4.7) becomes prohibitively demanding for realistic interfaces due to the large number of atomic degrees of freedom. In practice, the partition function is determined numerically by displacing every atom (N) in the positive and negative direction along all three Cartesian axes. Thus, $6N$ total energy calculations have to be performed in order to assemble the Hessian matrix of second derivatives with

respect to atomic positions (see Equation 4.6.6). However, as is shown in Publication A.6, the number of necessary calculations can be dramatically reduced by considering only those degrees of freedom which change significantly during a reaction.
The complexity of hybrid interfaces also strongly depends on the properties of the organic building blocks. In contrast to most inorganic crystals, molecules retain many of their internal degrees of freedom upon adsorption. In the absence of cross-links within layers, this leads to flexible, amorphous materials with a large number of energetically similar conformations. In order to sample this conformational space and identify likely minimum structures, the potential energy surfaces (PES) is sampled with simulated annealing molecular dynamics[77] (see Publication A.5). Through sampling at higher temperatures the system is able to escape from local PES minima. However, solving the electronic structure problem self-consistently for every atomic displacement using *ab initio* methods quickly becomes a computational bottleneck. Instead, one may resort to more approximate, semi-empirical methods such as density functional tight binding[78]. Here, considerable speed-up is achieved by replacing parts of the Hamiltonian with precomputed parameters.

3.2 Interface B: Organic / Metal

Modifications of cyclic tetrapyrroles as shown in the introduction (Figure 2.3.3), were limited to the exchange of functional groups. With the organic semiconductors investigated in this dissertation a different route is pursued by focusing on the structure of the backbone itself. Removal of a bridging carbon atom from porphine and linking two pyrrole units directly transforms it into a corrole which has a contracted macrocycle and is a triprotic acid.[79] The altered reactivity of corroles when forming interfaces with Ag(111) is investigated in Publication B.3 as well as their ability to complexate the late transition metal nickel in Publication B.2. Even more drastic structural changes, such as a five-membered supernaphthalocyanine and an open chain polycyanine, are studied in Publication B.1. Due to the large size of these organic molecules, the experimentally observed surface cell cannot be easily transferred into a computational model. Instead, single adsorbate models of the low coverage limit are utilized. This approach is validated by calculating the adsorption energy at different surface sites. With insights gained about the electronic structure of a single adsorbate through bonding analysis and calculated spectra, the groundwork for investigation of mutilayered interfaces is laid.[80]

4 Theoretical Background

A short introduction to the theoretical background of this dissertation is given based on selected publications and established textbooks in the respective fields.[81,82,83,84,85]

4.1 Basics of Quantum Chemistry

Quantum chemistry is a discipline revolving around the application of quantum mechanical laws, to problems pertaining the electronic structure of chemical systems. The development of quantum mechanics became necessary due to the failure of classical mechanics to accurately describe the observed, discrete interactions of small particles like electrons and protons. Perhaps the most notable feature of the theory is the wave-particle duality[86] which explains physical observations such as the photoelectric effect and black-body radiation. In order to reconcile quantum descriptions with the probabilistic nature of measurements, the mathematical framework of wave mechanics was put forward in the Schrödinger equation[87] $\hat{H}\Psi = E\Psi$. Possible solutions of this eigenvalue equation are the wave functions Ψ which contain all information about the state of the system. Applying the Hamilton operator $\hat{H}$ to the wave function yields its corresponding energy eigenvalue E. Among many other successes, this approach is able to predict the energy levels of electrons in hydrogen-like atoms and establish a system of quantum numbers. For larger systems, such as molecules, the Hamilton operator is comprised of kinetic T and potential V energy contributions of the nuclei n and electrons e (in atomic units):

$$\hat{H} = \hat{T}_\mathrm{n} + \hat{T}_\mathrm{e} + \hat{V}_\mathrm{ne} + \hat{V}_\mathrm{ee} + \hat{V}_\mathrm{nn} \tag{4.1.1}$$

$$= -\sum_a \frac{1}{2M_a}\nabla_a^2 - \sum_i \frac{1}{2}\nabla_i^2 \tag{4.1.2}$$

$$- \sum_{a,i} \frac{Z_a}{|R_a - r_i|} + \sum_i \sum_{j>i} \frac{1}{|r_i - r_j|} + \sum_a \sum_{b>a} \frac{Z_a Z_b}{|R_a - R_b|}.$$

Here, the index a (b) runs over all nuclei of mass M_a and atomic number Z_a at position R_a while the index i (j) runs over all electrons at position r_i.

Since the lightest nucleus, a single proton, is already over 1836 times heavier than an electron, electronic motion is mostly independent of nuclear motion and can therefore be separated. This approximation proposed by Born and Oppenheimer simplifies the Schrödinger equation significantly by setting $\hat{T}_\mathrm{n}$ to zero and including $\hat{V}_\mathrm{nn}$ as a constant which enters the solution only parametrically.[88] This separation of electronic and nuclear coordinates is not only useful for calculating electronic properties but also for applications where the positions of nuclei are propagated in time according to Newton's laws of motion.
As stated before, solving the Schrödinger equation in principle provides the wave functions of a system along with its energy spectrum. However, no analytic solution exists for systems of more than two particles. Methods which nonetheless yield approximate solutions are discussed in the following.
With the variational method an approximation to the ground state energy E_0 can be obtained by choosing a trial function $\tilde{\Psi}$ that is physically meaningful. The expectation value of the Hamilton operator then gives an upper bound to the ground state energy.

$$\frac{\left\langle \tilde{\Psi} \middle| \hat{H} \middle| \tilde{\Psi} \right\rangle}{\left\langle \tilde{\Psi} \middle| \tilde{\Psi} \right\rangle} = \tilde{E} \geq E_0 \tag{4.1.3}$$

A common approach for minimizing $\tilde{E}$ is the Hartree-Fock (HF) method.

4.2 Hartree-Fock Method

The HF method employs a product ansatz for its many-electron (N) wave function called the Slater determinant (SD)

$$\tilde{\Psi}_\mathrm{SD} = \frac{1}{\sqrt{N!}} \begin{vmatrix} \phi_1(1) & \phi_2(1) & \cdots & \phi_N(1) \\ \phi_1(2) & \phi_2(2) & \cdots & \phi_N(2) \\ \vdots & \vdots & \ddots & \vdots \\ \phi_1(N) & \phi_2(N) & \cdots & \phi_N(N) \end{vmatrix} \tag{4.2.1}$$

with orthonormal single-particle functions:

$$\langle \phi_i | \phi_j \rangle = \delta_{ij} = \begin{cases} 0 & \text{if } i \neq j, \\ 1 & \text{if } i = j. \end{cases} \tag{4.2.2}$$

In this form, the wave function is antisymmetrized with respect to the exchange of two electrons and therefore obeys the Pauli principle. Rewriting the energy operator of Equation 4.1.1 in terms of a one-electron ($\hat{h}_i$) and two-electron ($\hat{g}_{ij}$) part yields:

$$\begin{aligned}\hat{H}_{ij} &= -\sum_i \frac{1}{2}\nabla_i^2 - \sum_{a,i}\frac{Z_a}{|R_a - r_i|} + \sum_i \sum_{j>i} \frac{1}{|r_i - r_j|} + \hat{V}_{\mathrm{nn}}. \\ &= \sum_i \hat{h}_i + \sum_i \sum_{j>i} \hat{g}_{ij} + \hat{V}_{\mathrm{nn}}\end{aligned} \tag{4.2.3}$$

Application of $\hat{h}_i$ to the SD then results in the one-electron energy t_i.

$$t_i = \langle \tilde{\Psi}_{\mathrm{SD}} | \hat{h}_i | \tilde{\Psi}_{\mathrm{SD}} \rangle \tag{4.2.4}$$

Due to the use of a single SD the complicated two-electron term is approximated by the Coulomb integral J_{ij} and the exchange integral K_{ij} for which no classical equivalent exists.

$$\langle \tilde{\Psi}_{SD} | \hat{g}_{ij} | \tilde{\Psi}_{SD} \rangle = \langle \phi_i \phi_j | \hat{g}_{ij} | \phi_i \phi_j \rangle - \langle \phi_i \phi_j | \hat{g}_{ij} | \phi_j \phi_i \rangle = J_{ij} - K_{ij} \tag{4.2.5}$$

The HF method is a mean-field theory since the influence of all other electrons j on i is averaged and the total electronic energy is:

$$E = \sum_i t_i + \sum_i \sum_{j>i} (J_{ij} - K_{ij}) + \hat{V}_{\mathrm{nn}}. \tag{4.2.6}$$

The energy is then minimized under the orthogonality condition by variation with regards to orbitals ϕ_m utilizing the Lagrange method. It follows a set of one-electron Hartree-Fock equations with the Fock operator $\hat{F}_i$ yielding energies for molecular orbitals ϵ_m.

$$\hat{F}_i \phi_m = \left(\hat{h}_i + \sum_j \left[2\hat{J}_{ij} - \hat{K}_{ij} \right] \right) \phi_m = \epsilon_m \phi_m \tag{4.2.7}$$

In the closed-shell case orbitals are doubly occupied leading to a factor two for the Coulomb operator. Since those equations depend on their own solutions, presenting a pseudo-eigenvalue problem, an iterative procedure must be employed until self-consistency is reached.

4.3 Coupled-Cluster Theory

Due to the HF method utilizing a mean-field approximation to the many-body Schrödinger equation, only correlation effects between electrons of parallel spin (Fermi correlation) are correctly described. In order to recover the remaining correlation energy caused by Coulomb repulsion, different 'post-HF' methods that improve upon the HF reference wave function $|\Psi_0\rangle$ have been developed. Since HF relies on a single SD, post-HF methods also fail when the single SD is qualitatively wrong.
One frequently used method to reach the accuracy required to model chemical reactions by including Coulomb correlation is coupled cluster (CC). Its advantage over other post-HF methods such as configuration interaction is size consistency. Here, the total energy of two quantum chemical systems at infinite separation is identical to the sum of the systems being calculated individually. In CC the correlation energy is determined by transforming $|\Psi_0\rangle$ into a combination of excited determinants using an exponential ansatz:

$$|\Psi_{\mathrm{CC}}\rangle = \mathrm{e}^{\hat{T}} |\Psi_0\rangle \,. \tag{4.3.1}$$

The cluster operator $\hat{T}$ is a sum over all single excitations $\hat{T}_1$, double excitations $\hat{T}_2$ and so forth.

$$\hat{T} = \hat{T}_1 + \hat{T}_2 + \hat{T}_3 + \dots \tag{4.3.2}$$

$$\hat{T}_1 = \sum_i \sum_a t_a^i \hat{a}_a^\dagger \hat{a}_i \tag{4.3.3}$$

$$\hat{T}_2 = \frac{1}{4} \sum_{i,j} \sum_{a,b} t_{a,b}^{i,j} \hat{a}_a^\dagger \hat{a}_b^\dagger \hat{a}_j \hat{a}_i \tag{4.3.4}$$

In the second quantization formalism $\hat{a}^\dagger$ are creation and $\hat{a}$ annihilation operators of virtual orbitals $i, j, \dots$ and occupied orbitals $a, b, \dots$ respectively. The CC equation is then solved for the coefficients t. Due to the exponential ansatz, a CC wave function including only single and double excitations (CCSD) already contains contributions of higher order.

$$\mathrm{e}^{\hat{T}} = 1 + \hat{T} + \frac{1}{2}\hat{T}^2 + \dots \tag{4.3.5}$$

$$= 1 + \hat{T}_1 + \hat{T}_2 + \frac{1}{2}\hat{T}_1^2 + \frac{1}{2}\hat{T}_1\hat{T}_2 + \frac{1}{2}\hat{T}_2\hat{T}_1 + \frac{1}{2}\hat{T}_2^2 + \cdots \tag{4.3.6}$$

However the number of excitations grows very quickly with the number of orbitals, rendering CC unfeasible for larger systems. Fortunately the strength of correlation

decreases rapidly with the distance between electrons. Based on this observation, reduced scaling CC-methods have been developed which transform the occupied HF orbitals into localized molecular orbitals (LMOs) through orbital rotations. As a result, the number of two-electron integrals being evaluated in double excitations is reduced and only virtual orbitals spatially close to an LMO pair contribute to the correlation energy. In the hybrid orbital-specific virtual (OSV) pair natural orbital (PNO) approach[89] an intermediate OSV basis is determined by contracting the virtual molecular orbitals with respect to each LMO. This step is performed prior to further contraction into a PNO basis depending on two LMOs, thus combining the advantages of efficient transformation of OSVs and compact PNOs. In order to match the accuracy of the canonical quantum chemical "gold standard" method CCSD(T) which includes triplets perturbatively, triple natural orbitals are constructed from OSVs of three LMOs.[90]

4.4 Density Functional Theory

As outlined above, wave function based approaches can achieve high accuracy for atomic and molecular observables. However, the electronic structure problem depends on 3 spatial and one spin coordinate of N electrons. Unfavorable scaling of formally N^4 (for HF) severely limits the system size to which the methods can be applied. In order to remedy this problem density functional theory (DFT) was developed on the premise that the simpler electron density ρ, which depends on just three spatial coordinates in total, can be used in place of the wavefunction.

$$\rho\left(r\right) \equiv N \int \cdots \int \left|\Psi(r, r_2, ..., r_N)\right|^2 \mathrm{d}r_2 ... \mathrm{d}r_N. \tag{4.4.1}$$

In two theorems, Hohenberg and Kohn showed that an electron density is uniquely connected to the underlying external potential and that the ground state density ρ_0 leads to the energy minimum.[91] Therefore, all information about a system is encoded in the electron density and the energy can be obtained variationally.

$$E_0\left[\rho_0\right] \leq E\left[\rho\right] \tag{4.4.2}$$

The general expression of the energy as a functional of the density in the Born-Oppenheimer approximation is given by:

$$E\left[\rho\right] = T_\mathrm{e}\left[\rho\right] + V_\mathrm{ee}\left[\rho\right] + V_\mathrm{ne}\left[\rho\right]. \tag{4.4.3}$$

$V_{\mathrm{ee}}[\rho]$ can be separated into the classical Coulomb interaction $J[\rho]$ and a non-classical exchange-correlation part $E_{\mathrm{ncl}}[\rho]$. Thus, the Schrödinger equation can in principle be solved exactly using the density. However, no exact expression is known for either $T_{\mathrm{e}}[\rho]$ or $E_{\mathrm{ncl}}[\rho]$. The most commonly applied approximation today was proposed by Kohn and Sham (KS).[92] It expresses the total density as a sum of non-interacting single-electron densities moving in an effective external potential v_{eff}. For this purpose, orbitals are re-introduced to calculate the kinetic energy similar to the HF method.

$$T_{\mathrm{S}} = -\frac{1}{2}\sum_{i}\left\langle \phi_i \,\middle|\, \nabla^2 \,\middle|\, \phi_i \right\rangle \tag{4.4.4}$$

The kinetic energy of the non-interacting system T_{S} is not equal to T_{e} and a correction term recovering electron correlation is introduced.

$$T_{\mathrm{C}}[\rho] \equiv T_{\mathrm{e}}[\rho] - T_{\mathrm{S}}[\rho] \tag{4.4.5}$$

Together with the non-classical part, the exchange-correlation energy is defined.

$$\begin{aligned} E_{\mathrm{XC}}[\rho] &= T_{\mathrm{C}}[\rho] + E_{\mathrm{ncl}}[\rho] \\ &\equiv (T_{\mathrm{e}}[\rho] - T_{\mathrm{S}}[\rho]) + (V_{\mathrm{ee}}[\rho] - J[\rho]) \end{aligned} \tag{4.4.6}$$

Collecting all terms only depending on the electronic coordinates yields the Kohn-Sham functional with the external potential of the interacting system v_{ext}:

$$E^{\mathrm{KS}}[\rho] = T_{\mathrm{S}}[\rho] + J[\rho] + E_{\mathrm{XC}}[\rho] + \int v_{\mathrm{ext}}\rho \mathrm{d}r. \tag{4.4.7}$$

In analogy to the HF-equations a set of KS-equations must be solved self-consistently (with the KS-operator $\hat{F}^{\mathrm{KS}}$):

$$\begin{aligned} \hat{F}^{\mathrm{KS}}\phi_m^{\mathrm{KS}} &= \\ \left(-\frac{1}{2}\nabla^2 + \int \frac{\rho(r_j)}{r_{ij}}\mathrm{d}r_j + v_{\mathrm{XC}} + v_{\mathrm{ext}}\right)\phi_m^{\mathrm{KS}} &= \\ \left(-\frac{1}{2}\nabla^2 + v_{\mathrm{eff}}\right)\phi_m^{\mathrm{KS}} &= \epsilon_m\phi_m^{\mathrm{KS}}. \end{aligned} \tag{4.4.8}$$

The only unknown term left is the exchange-correlation potential and its corresponding energy.

$$v_{\mathrm{XC}} \equiv \frac{\partial E_{\mathrm{XC}}}{\partial \rho}. \tag{4.4.9}$$

The development of approximate XC-functionals is a major area of DFT research and some examples are given in the following section.

4.4.1 Exchange-Correlation Functionals

A simple approach to approximate E_{XC} is to use the XC energy of the homogeneous electron gas. In this case the energy is only dependent on the density at a given point. Therefore the method is known as the local-density approximation (LDA).

$$E_{\mathrm{XC}}^{\mathrm{LDA}}[\rho] = \int \rho(r)\, \epsilon_{\mathrm{XC}}[\rho]\, \mathrm{d}r, \tag{4.4.10}$$

ϵ_{XC} is the exchange-correlation energy per particle. However, the LDA performs poorly for chemical applications where rapid changes of the electron density are of interest. Improvements can be achieved by considering also the gradient of the density yielding the generalized-gradient approximation (GGA).

$$E_{\mathrm{XC}}^{\mathrm{GGA}}[\rho] = \int \rho(r)\, \epsilon_{\mathrm{XC}}[\rho, \nabla\rho]\, \mathrm{d}r, \tag{4.4.11}$$

Frequently, the exchange and correlation terms are separated linearly to find individual solutions. This allows, in principle, to freely combine XC-functionals.

$$E_{\mathrm{XC}} = E_{\mathrm{X}} + E_{\mathrm{C}} \tag{4.4.12}$$

Another philosophy for calculating the exchange-correlation energy is through hybrid functionals. Here, the exact exchange energy obtained from HF theory is mixed with the approximate exchange functional. The degree of mixing a is subject to debate and varies from functional to functional.

$$E_{\mathrm{XC}}^{\mathrm{hybrid}} = E_{\mathrm{XC}}^{\mathrm{DFT}} + a(E_{\mathrm{X}}^{\mathrm{HF}} - E_{\mathrm{X}}^{\mathrm{DFT}}) \tag{4.4.13}$$

Furthermore a can itself be a function of interatomic distance giving rise to the class of range-separated hybrid functionals.

4.4.2 Dispersion Correction

A well-known shortcoming of DFT is the neglect of dispersion interactions due to the long-range correlation of electron movement. DFT cannot adequately capture these effects since it is a local theory. There exist several approaches to include dispersion

into DFT of which the most efficient one relies on an empirical correction applied *a posteriori*.

$$E_{\mathrm{DFT}}^{\mathrm{disp}} = E_{\mathrm{DFT}} + E_{\mathrm{disp}} \tag{4.4.14}$$

In the D3 formulation by Grimme *et al.*[93] the dispersion energy is given by a sum of pairwise atomic interactions. To ensure correct physical behavior at small distances the Becke-Johnson type (BJ) damping function[94] (parenthesis in the denominator) is applied.

$$E_{\mathrm{disp}}^{\mathrm{D3BJ}} = -\frac{1}{2}\sum_{A\neq B}\sum_{n=6,8} s_n \frac{C_n^{AB}}{R_{AB}^n + (\alpha_1 R_{AB}^0 + \alpha_2)^n} \tag{4.4.15}$$

The equation includes the atomic distance R_{AB}, two scaling factors ($n = 6, 8$) s_n and dispersion coefficients C_n^{AB} determined from calculated atomic polarizabilities. In the damping function the cut-off radius R_{AB}^0 and two fitted parameters α_1 and α_2 are employed.

4.4.3 Extended Systems

In contrast to commonly less accurate cluster models cut out of the bulk structure, surfaces and interfaces of solids, are best described in a slab model.[95,96] Here, exploitation of translation symmetry can make computations more efficient. Furthermore, finite size effects are reduced due to the application of Born-von Karman periodic boundary conditions (PBC) in two dimensions.

$$V(r) = V(r + \vec{T}) \tag{4.4.16}$$

In PBC the potential V created by the nuclei at a point r must be identical to the potential after translation by a vector $\vec{T}$ obeying the symmetry of the given Bravais lattice. $\vec{T}$ can be any integer multiple of the basis vectors $\vec{a}_i$ (here given for three dimensions).

$$\vec{T} = n_1\vec{a_1} + n_2\vec{a_2} + n_3\vec{a_3} \tag{4.4.17}$$

The unit cell spanned by the basis vectors contains all information about a crystal structure. The same holds true for a unit cell expressed in reciprocal coordinates, the first Brillouin zone (BZ). Transformations between real and reciprocal space are frequently performed since some crystal properties are more conveniently visualized

in the latter. The reciprocal basis vectors $\vec{b}$ are constructed from the real ones obeying the orthogonality condition $\vec{a}_i \cdot \vec{b}_j = 2\pi\delta_{ij}$.

$$\vec{b_1} = 2\pi \frac{\vec{a_2} \times \vec{a_3}}{\vec{a}_1 \cdot (\vec{a}_2 \times \vec{a}_3)} \tag{4.4.18}$$

$$\vec{b_2} = 2\pi \frac{\vec{a_3} \times \vec{a_1}}{\vec{a}_1 \cdot (\vec{a}_2 \times \vec{a}_3)} \tag{4.4.19}$$

$$\vec{b_3} = 2\pi \frac{\vec{a_1} \times \vec{a_2}}{\vec{a}_1 \cdot (\vec{a}_2 \times \vec{a}_3)} \tag{4.4.20}$$

Under PBC the wave function $\Psi_k(r)$ depends not only on the electronic coordinates r but also on a wave vector $\vec{k}$ encoding the phase. Additionally, translated wavefunctions may only differ by a factor $\mathrm{e}^{\mathrm{i}\vec{k}\vec{T}}$.

$$\Psi_k(r + \vec{T}) = \mathrm{e}^{\mathrm{i}\vec{k}\vec{T}} \Psi_k(r) \tag{4.4.21}$$

Possible solutions to the Schrödinger equation in a periodic potential are given by the periodic function modulated by a plane wave $\mathrm{e}^{\mathrm{i}\vec{k}r}$ as stated in Bloch's theorem.[97]

$$\Psi_k(r) = \mathrm{e}^{\mathrm{i}\vec{k}\vec{r}} \cdot u_k(\vec{r}) \tag{4.4.22}$$

In principle, $\vec{k}$ can be continuously varied leading to the replacement of discrete orbitals by energy bands. However, the computation of arbitrary k-values is practically intractable and one usually limits the evaluation to discrete values within the 1. BZ ($0 \leq \vec{k}_i \leq \frac{\pi}{|a_i|}$). All other values are then obtained by interpolation within the 1. BZ. The density of the k-mesh is a quality criterion of a periodic calculation that must be converged carefully.

4.4.4 Relativistic Corrections

The Schrödinger equation and its approximations generally work well for light elements. However, relativistic effects become increasingly important for heavier elements proportional to the square of the nuclear charge. In order to counterbalance the stronger attractive potential of heavy cores, electrons move with at a considerable fraction of the speed of light c. According to Einstein's theory of special relativity[98], this leads to the mass m of an electron increasing with respect to its mass at rest m_0.

$$m = m_0 \cdot \left(\sqrt{1 - \frac{v^2}{c^2}} \right)^{-1} \tag{4.4.23}$$

As a result, the orbital radius of a hydrogen-like atom decreases (according to the Bohr model).

$$r = \frac{\hbar}{Zm_e c\alpha} \tag{4.4.24}$$

Here, α is the fine structure constant. This also impacts chemical reactivity of heavy elements as s- and p-orbitals close to the core are contracted. In turn, the now screened effective nuclear potential makes d- and f-orbitals more diffuse. The first successful combination of quantum mechanics with special relativity was achieved by Dirac through the introduction of a four-component wavefunction.[99] In the form given here (again using atomic units), the components are grouped into the large ϕ and small component χ multiplied by the 2×2 Pauli vector $\vec{\sigma}$.

$$\begin{pmatrix} V^{\mathrm{KS}} & c\vec{\sigma}\cdot\vec{p} \\ c\vec{\sigma}\cdot\vec{p} & (V^{\mathrm{KS}} - 2c^2) \end{pmatrix} \begin{pmatrix} \phi \\ \chi \end{pmatrix} = E \begin{pmatrix} \phi \\ \chi \end{pmatrix} \tag{4.4.25}$$

V^{KS} is the Kohn-Sham potential and $\vec{p}$ is the momentum operator. The small component can be eliminated (ESC) by expressing it in terms of the large component using the bottom equation.

$$\chi = \frac{1}{2c^2 + E - V^{\mathrm{KS}}} c\vec{\sigma}\cdot\vec{p}\phi = \frac{1}{2c}\left(1 + \frac{E - V^{\mathrm{KS}}}{2c^2}\right)^{-1} \vec{\sigma}\cdot\vec{p}\phi \tag{4.4.26}$$

Substituting back into the upper equation yields the ESC-Hamiltonian.

$$\hat{H}_{\mathrm{ESC}} \equiv V^{\mathrm{KS}} + \frac{1}{2}\vec{\sigma}\cdot\vec{p}\left(1 + \frac{E - V^{\mathrm{KS}}}{2c^2}\right)^{-1} \vec{\sigma}\cdot\vec{p} \tag{4.4.27}$$

In the next step the Hamiltonian is rearranged and expanded in a series of the factor $E/(2c^2 - V)$. Truncating this series after the zeroth order results in the zeroth order regular approximation (ZORA)[100] of the Dirac equation which is also used in this dissertation.

$$\hat{H}_{\mathrm{ZORA}} = V^{\mathrm{KS}} + \vec{\sigma}\cdot\vec{p}\frac{c^2}{2c^2 - V^{\mathrm{KS}}}\vec{\sigma}\cdot\vec{p} \tag{4.4.28}$$

ZORA includes spin-orbit effects, however the scalar relativistic energy can be obtained by eliminating all spin-dependent terms which reduces computational demand.

4.5 Basis Sets

Since the one electron wave functions described in Sections 4.2 and 4.4 are generally not known exactly, approximations have to be employed. In chemistry, the most common approach is the linear combination of atomic orbitals. The atomic orbitals χ act as a basis set whose coefficients c_α are subsequently optimized in the course of the self-consistent field (SCF) cycle.

$$\phi_i = \sum_\alpha c_{\alpha i} \cdot \chi_\alpha \tag{4.5.1}$$

A larger number of basis functions increases the flexibility and therefore the quality of the approximation, but computational complexity increases also. Thus, the choice of basis is generally a compromise between accuracy and computational demand. In this dissertation three different types of basis functions, Gaussian-type-orbitals (GTOs), Slater-type orbitals (STOs), and plane waves (PW) have been employed. The latter is, for historical reasons, primarily used for solid state systems within PBC. Each type of basis function has unique advantages which are discussed in the following.

4.5.1 Gaussian- and Slater Type Orbitals

GTOs and STOs are both local, atom centered, natural exponential functions multiplied by a spherical harmonic $Y_{l,m}(\theta, \varphi)$ and the normalization constant N.

$$\chi^{\mathrm{GTO}}_{\zeta,n,l,m}(r,\theta,\varphi) = N Y_l^m(\theta,\varphi) r^{2n-2-l} \mathrm{e}^{-\zeta r^2} \tag{4.5.2}$$

$$\chi^{\mathrm{STO}}_{\zeta,n,l,m}(r,\theta,\varphi) = N Y_l^m(\theta,\varphi) r^{n-1} \mathrm{e}^{-\zeta r} \tag{4.5.3}$$

The indices n, l, and m stand for the main quantum number, angular quantum number, and magnetic quantum number respectively. In spherical coordinates the position is given by the radial distance r and the angles θ, φ. The diffuseness of the basis function is controlled by the orbital exponent ζ. However, STOs and GTOs differ in their r dependence. GTOs decrease too quickly at large distances due to their $-r^2$-exponent. In addition, GTOs do not satisfy the cusp condition at the position of the core. In order to approximate the cusp, a linear combination of several GTOs is used for each basis function, which increases computational demand. Despite these shortcomings, GTOs are frequently used as basis functions due to their simple analytical evaluation; A product of GTOs is itself a GTO.
STOs on the other hand correctly recover the asymptotic behavior and the cusp,

decreasing the number of basis functions needed to achieve the same accuracy as comparable GTOs significantly. However, this efficiency advantage is offset by complicated analytic expressions of two-electron integrals, making numerical integration necessary.
The overall quality of an atom centered basis set is described by the number of basis functions per electron. In the simplest case, a primitive basis, every electron is described by just one basis function. Twice the number of functions constitutes a double-ζ valence basis, three times a triple-ζ and so forth. In many cases, additional polarization functions of higher angular momentum are used to improve the description of bonds. Usually, core orbitals require less flexibility and are described with fewer functions than the valence region giving rise to split-valence basis sets.
Linear combinations of GTOs or STOs transform the Schrödinger equation into matrix form.

$$\boldsymbol{FC} = \boldsymbol{SC}\boldsymbol{\epsilon} \tag{4.5.4}$$

$\boldsymbol{S}$ is the overlap matrix and $\boldsymbol{C}$ the coefficient matrix of the basis functions. In the spin-restricted case these equations are called Roothaan-Hall equations.

4.5.2 Plane Waves

A popular non-local basis set choice for electrons in a periodic potential are plane waves due to their own inherent periodicity. Here, the number of oscillations of the wavefunction within a unit cell of volume V_{cell} is determined by the wave vector $\vec{k}$.

$$\chi_k(r) = \frac{1}{\sqrt{V_{\text{cell}}}} \mathrm{e}^{\mathrm{i}\vec{k}r} \tag{4.5.5}$$

In a PW basis set the number of basis function can be conveniently controlled through setting an upper limit for the kinetic energy $E_{\text{kin}}^{\text{cutoff}}$ of electrons. In addition, only plane waves that have the same periodicity as the lattice are considered.

$$\frac{1}{2} \cdot |\vec{k} + \vec{G}|^2 \leq E_{\text{kin}}^{\text{cutoff}} \tag{4.5.6}$$

This description is rather efficient for quasi free electrons in metals but requires a large number of basis functions to model the nodal structure of core electrons as well as bonds in molecules and insulators. This problem is addressed by pseudopotentials (PP, also known as effective core potentials). Within a PP the Coulomb potential of the nuclear charge and core electrons are combined resulting in considerable computational speedup. This approach is well motivated for chemical processes such as

bond formation and cleavage since those pertain mostly to valence electrons. For heavier elements of the periodic table, usually PPs of different sizes exist, giving some flexibility to the researcher depending on the investigated system.
The projector augmented wave method[101] (PAW) combines PPs for core electrons with a real space projection scheme replacing a KS orbital with a pseudo wave function $\tilde{\phi}$.

$$|\phi\rangle = \sum_i c_i |\chi\rangle_i = |\tilde{\phi}\rangle + \sum_i (|\chi\rangle_i - |\tilde{\chi}_i\rangle) \langle\tilde{p}_i|\tilde{\phi}\rangle \tag{4.5.7}$$

In the valence region, $\tilde{\phi}$ is identical to the KS orbital and constructed from a linear combination of pseudo partial waves $\tilde{\chi}_i$ with fewer oscillations than the more accurate χ_i. In the core region, $\tilde{\chi}_i$ are transformed into χ_i using projection functions $\tilde{p}_i$. Those are orthogonal to the pseudo partial waves $\langle\tilde{p}_i|\tilde{\chi}_j\rangle = \delta_{ij}$ and ensure a smooth transition at the region boundary. The PAW method is very efficient due to the possibility of calculating certain terms in reciprocal space utilizing fast Fourier transforms. However, for gas phase calculations a large vacuum region must be included. Due to PWs not decaying, empty space is treated with the same accuracy as atoms, thus wasting resources.
From a quantum chemist's perspective the use of plane waves has another disadvantage which is due to the fact that many bonding and charge analysis techniques rely on atom centered basis functions by design. Therefore, an additional projection step from PWs to GTOs or STOs has to be performed. Besides increasing the demand for computational resources, these projections introduce an additional source for numerical errors.

4.6 Structure Optimization

For the calculation of many chemical properties, detailed knowledge of the PES is a prerequisite. In particular, local minima and transition states (TS) are of interest for thermodynamic and kinetic evaluation of reactions. However, the exact atomic arrangement at these high-interest points is rarely known in advance. Therefore, methods for optimizing the total energy as a function of the $3N$ atomic coordinates $E(R)$ are employed in this dissertation. Since an analytical expression for $E(R)$ is generally not available, iterative numerical methods are required to find roots and derivatives. These algorithms are then applied until a predefined convergence criterion for the energy or its first derivative, the forces $\vec{F}$ acting on nuclei, is fulfilled.

4.6.1 Finding Local Minima

The simplest approach to finding a local minimum is to follow the negative gradient vector of $E(R)$ as obtained by the Hellmann-Feynman theorem for variational wave functions.[102]

$$-\vec{g} = -\nabla E(R) = -\langle\Psi|\nabla\hat{H}|\Psi\rangle = \vec{F} \tag{4.6.1}$$

This gradient descent method is simple to implement and execute but not guaranteed to arrive at a minimum due to oscillations. Furthermore, the rate of convergence slows down the closer it gets to the minimum. The oscillatory behavior can be reduced by including not only the gradient of the current step but also the previous search vector $\vec{d}$.

$$\vec{d}_i = -\vec{g}_i + \beta_i\vec{d}_{i-1} \tag{4.6.2}$$

The directions $\vec{d}_i$ and $\vec{d}_{i-1}$ are conjugate, giving the method its name; conjugate gradient.

$$\vec{d}_{i-1} = \vec{d}_i^{-1}\vec{d}_{i-1}\vec{d}_i \tag{4.6.3}$$

For the scaling factor β several different representations exist. In the vicinity of the minimum, the PES is usually well approximated by a harmonic potential. This fact is used in Newton's method to accelerate convergence by considering also the matrix of second derivatives $\boldsymbol{H}$ (Hessian). The gradient is here determined as:

$$\vec{g}_{i+1} \approx \vec{g}_i + \boldsymbol{H}_i \cdot (R_{i+1} - R_i). \tag{4.6.4}$$

At a stationary point the gradient is zero and above equation can be rearranged to yield R_{i+1}.

$$R_{i+1} = R_i - \boldsymbol{H}_i^{-1}\vec{g}_i \tag{4.6.5}$$

However, an inversion of $\boldsymbol{H}$ must be performed. This operation becomes prohibitively demanding for large systems and the inverse Hessian matrix is instead approximated by an initial guess which is refined with data from previous steps. Methods that use approximate $\boldsymbol{H}^{-1}$, are called Quasi-Newton methods.
In order to ensure that one has indeed found a minimum, all eigenvalues of the Hessian have to be positive. When no analytic expression for the Hessian is available it can be numerically approximated by the method of finite differences. Here, every atomic coordinate is displaced individually by a small amount h and the resulting forces are calculated. The more displacements are performed per coordinate, the more accurate the approximation of the local PES becomes. In most cases it is suffi-

cient to calculate one positive and one negative displacement per coordinate, known as 'central-differences'.

$$\boldsymbol{H}_{\mu,\nu} = \frac{\vec{F}_\mu(R_\nu - h) - \vec{F}_\mu(R_\nu + h)}{2h} \tag{4.6.6}$$

4.6.2 Finding Transition States

Transition states are first-order saddle points of the PES which means they are minima with respect to all directions except one. Hence, the Hessian has exactly one negative eigenvalue with a corresponding eigenvector (mode) which leads back to the closest minimum. When the initial guess of the TS is good, the optimization methods described above can be modified to follow the negative mode 'uphill' while simultaneously optimizing all others. This local approach can however only be successful when the followed eigenvalue corresponds to the reaction coordinate of interest. Usually, initial guesses are far from the TS or not provided at all, requiring non-local methods that sample a larger part of the PES. Two of these methods are outlined in the following.

Climbing-Image Nudged Elastic Band

The Nudged Elastic Band method (NEB)[103] is a chain-of-state method that utilizes known minima of products and reactants to calculate the reaction path. This is achieved by generating linearly interpolated points, called images, between the reactants and products. These images are optimized individually under the constraint of maintaining equidistant spacing between them. This approach is taken to avoid optimization of the images back into the initial minima. To satisfy the constraint, an NEB-force on each image i is constructed from two parts.

$$\vec{F}_i^{\,\mathrm{NEB}} = \vec{F}_i^{\,\perp} + \vec{F}_i^{\,k\parallel} \tag{4.6.7}$$

The first part is obtained by projecting the total force acting on an image $\vec{F}_i$ onto the unit vector $\vec{\tau}$ pointing in the direction of the next image. This is equivalent to subtracting the parallel component from $\vec{F}_i$ to obtain the perpendicular component $\vec{F}_i^{\,\perp}$.

$$\vec{F}_i^{\,\perp} = \vec{F}_i - \vec{F}_i^{\,\parallel} = -\nabla E(R_i) + \vec{\tau}_i \left[\vec{\tau}_i \cdot \nabla E(R_i)\right] \tag{4.6.8}$$

The second (nudging) component $\vec{F}_i^{\,k\parallel}$ is defined by a force constant k scaled by the Euclidean distances of image R_i with its neighbors and also projected onto $\vec{\tau}_i$.

$$\vec{F}_i^{\,k\parallel} = k\left[(|R_{i+1} - R_i| - |R_i - R_{i-1}|) \cdot \vec{\tau}_i\right]\vec{\tau}_i \tag{4.6.9}$$

Choice of the force constant is arbitrary since it does not interfere with the optimization of the path but only controls the distribution of images on it. With the NEB method, usually a very rough estimate of the TS is obtained. Thus, the method has to be modified in order to push the highest image on the reaction path towards the saddle point. In the climbing-image (CI-NEB) extension[104], spring forces are switched off for the highest image and the parallel force is inverted (compare Equation 4.6.7). In the CI-NEB the distances of images before and after the TS are not identical any more.

$$\vec{F}_{\max}^{\mathrm{CI}} = \vec{F}_{\max} - 2\vec{F}_{\max}^{\parallel} \tag{4.6.10}$$

The approximation of the TS is improved in this method, however, accurate activation energies require well converged structures. Since chain-of-state methods optimize several images simultaneously computational resources are wasted if one is just interested in the TS. Therefore, it is customary to refine TS further with a more efficient method such as the dimer method which requires only two images.

Dimer Method

The dimer method is conceptually related to local mode-following methods. However, it determines the minimum mode without calculating the Hessian, making it superior in terms of efficiency. Instead, two images $R_{1,2}$ (the dimer) are generated within equal distance ΔR from the initial guess R.

$$R_{1,2} = R \pm \Delta R \cdot \vec{\tau} \tag{4.6.11}$$

The orientation of the dimer is determined by a unit vector $\vec{\tau}$ that can be calculated from two points such as the reactants, products or a guessed TS. Without prior knowledge, $\vec{\tau}$ is randomly generated. In order to advance R towards the saddle point, the lowest curvature mode of the dimer potential C must be found. Using the finite difference formula yields an expression for C which only depends on the energies and forces of the dimer images.

$$C = \frac{(\vec{F}_2 - \vec{F}_1) \cdot \vec{\tau}}{2\Delta R} = \frac{E - 2E_0}{(\Delta R)^2} \tag{4.6.12}$$

$$E = E_1 + E_2 \tag{4.6.13}$$

The dimer energy E is optimized by rotating $\vec{\tau}$ along $\vec{F}^{\perp} = \vec{F}_1^{\perp} - \vec{F}_2^{\perp}$. Since ΔR and the approximate energy at the central point E_0 stay constant, minimizing E

also minimizes C. The direction of translation is obtained by reversing the parallel component of the dimer force $\vec{F}_R = (\vec{F}_1 + \vec{F}_2)/2$.

$$\vec{F}^{\dagger} = \vec{F}_R - 2\vec{F}^{\parallel} \tag{4.6.14}$$

For every translation step usually several rotation steps are performed.

4.7 Thermodynamic Corrections

The methods presented in Sections 4.2 and 4.4 approximate the electronic energy E in a perfect vacuum and at absolute zero (0 K). However, chemical processes take place at finite temperature T and pressure p. In order to correctly predict if a process is spontaneous, i.e. exergonic, thermodynamic corrections must be considered. One method to calculate these corrections is the theory of statistical thermodynamics. Under experimental conditions customary in chemistry, T and p are constant. Thus, the relevant quantity to be evaluated is not E but the Gibbs free energy G. In addition, thermally excited electronic states are considered to be inaccessible. Therefore, G consists of just two terms, the enthalpy H and the entropy S multiplied by the temperature.

$$G(T,p) = H(T) - TS(T,p) \tag{4.7.1}$$

The enthalpy is obtained as the sum of E, the zero point energy E_{ZPE} and the temperature integral over the constant-pressure heat capacity C_p.

$$H(T) = E + E_{\mathrm{ZPE}} + \int_0^T C_p \mathrm{d}T \tag{4.7.2}$$

$$E_{\mathrm{ZPE}} = \sum_i \frac{\hbar\omega_i}{2} \tag{4.7.3}$$

$$\int_0^T C_p \mathrm{d}T = \int_0^T \left(k_{\mathrm{B}} + C_V\right) \mathrm{d}T = \int_0^T \left(k_{\mathrm{B}} + C_{V,\mathrm{trans}} + C_{V,\mathrm{rot}} + C_{V,\mathrm{vib}}\right) \mathrm{d}T \tag{4.7.4}$$

In the ideal gas, rigid-rotor approximation the translational and rotational terms are both 3/2 k_{B} (for a nonlinear molecule). The vibrational heat capacity is given by the sum over frequencies scaled by a Boltzmann factor. Here, the frequencies are obtained in the harmonic approximation as the square roots of the eigenvalues of the mass-weighted Hessian (compare Equation 4.6.6).

$$\int_0^T C_{V,\mathrm{vib}} \mathrm{d}T = \sum_i \frac{\hbar\omega_i}{\mathrm{e}^{\hbar\omega_i/k_{\mathrm{B}}T} - 1} \tag{4.7.5}$$

For the entropy a similar separation of terms is performed.

$$S(T,p) = S_{\text{trans}} + S_{\text{rot}} + S_{\text{vib}} + S_{\text{elec}} \tag{4.7.6}$$

$$S_{\text{trans}} = k_{\text{B}} \left\{ \ln \left[\left(\frac{2\pi m k_{\text{B}} T}{h^2} \right)^{3/2} \frac{k_{\text{B}} T}{p} \right] + \frac{5}{2} \right\} \tag{4.7.7}$$

$$S_{\text{rot}} = k_{\text{B}} \left\{ \ln \left[\frac{\sqrt{\pi I_{\text{A}} I_{\text{B}} I_{\text{C}}}}{\sigma} \left(\frac{8\pi^2 k_{\text{B}} T}{h^2} \right)^{3/2} \right] + \frac{3}{2} \right\} \tag{4.7.8}$$

$$S_{\text{vib}} = k_{\text{B}} \sum_i \left[\frac{\hbar\omega_i}{k_{\text{B}} T \left(e^{\hbar\omega_i / k_{\text{B}} T} - 1 \right)} - \ln \left(1 - \mathrm{e}^{-\hbar\omega_i / k_{\text{B}} T} \right) \right] \tag{4.7.9}$$

$$S_{\text{elec}} = k_{\text{B}} \ln \left(2s + 1 \right) \tag{4.7.10}$$

Here, m is the molecular mass, $I_{\text{A,B,C}}$ are the moments of inertia, σ is the symmetry number, and s is the total spin of the system. The sensitivity of the entropy on a change of p is much smaller than a change of T due to a logarithmic dependence.

$$S(T,p_1) = S(T,p) - k_{\text{B}} \ln \frac{p_1}{p} \tag{4.7.11}$$

4.8 Implicit Solvent Corrections

A large part of chemical reactions are performed in solution. However, like the thermodynamic effects discussed in Section 4.7, the solvent environment is usually not included in standard quantum chemical calculations. A combination of both leads to a realistic description of the liquid phase but requires PBC in order to capture the desired temperature, pressure and particle density. Even though solvent molecules and other additives can be explicitly calculated together with the reactants and products, significant challenges arise from this approach. With every additional solvent molecule, the computational effort for electronic convergence increases dramatically. Furthermore, the space of possible conformations grows and finding minimum structures becomes a daunting task. Therefore, properties of the total solute-solvent system are only available as ensemble averages through sampling sufficiently long molecular dynamics trajectories.

In cases where most of the solute-solvent interactions can be isolated to the first few solvent shells, the explicit treatment can be simplified to small, molecular clusters. This approach, referred to as microsolvation, can be combined with charge-embedding and quantum-classical hybrid methods. It furthermore provides a middle ground between a completely explicit treatment and implicit methods which aim to parametrize solvent properties into a continuum model.[105] The continuum enables

an efficient computation of electrostatic interactions between solute and dielectric medium which is one of the main contributions to the solvation energy ΔE_{sol}. This is achieved through the approximation of the electrostatic interaction by a single parameter, the permittivity ϵ of the continuum. It corresponds to the amount of screening the solute charge density experiences relative to the vacuum. Hence, the KS-energy expression of the solute in vacuum $E_{\mathrm{vac}}^{\mathrm{solute}}$ can be extended with a polarization term E_{pol}.

$$E_{\mathrm{tot}} = E_{\mathrm{vac}}^{\mathrm{solute}} + E_{\mathrm{pol}} \tag{4.8.1}$$

In the polarizable continuum model[76] E_{pol} is given by the integral over the polarization charge density ρ_{pol} in the potential of the solute charge density ϕ^{solute}.

$$E_{\mathrm{pol}} = \frac{1}{2}\int \rho_{\mathrm{pol}}(r)\phi^{\mathrm{solute}}(r)\mathrm{d}r \tag{4.8.2}$$

Introduction of the polarization charge density enables the evaluation of the electrostatic interaction in a localized fashion at the solvent-solute interface.

$$\rho_{\mathrm{pol}}(r) = \frac{1}{4\pi}\nabla \ln\epsilon(r) \cdot \nabla\phi_{\mathrm{tot}}(r) - \frac{\epsilon(r)-1}{\epsilon(r)}\rho^{\mathrm{solute}}(r) \tag{4.8.3}$$

$$\phi_{\mathrm{tot}}(r) = \phi^{\mathrm{solute}}(r) + \phi_{\mathrm{pol}}(r) \tag{4.8.4}$$

In continuum models it is customary to put the solute into a cavity into which the solvent does not penetrate. While, some approaches evaluate the polarization charge density on surface segments of the cavity, the revised self-consistent continuum solvation model[106], developed for PW basis sets and based on the polarizable continuum model, introduces a dependency of the dielectric function $\epsilon(r)$ on the electron density $\epsilon(\rho(r))$. Here, $\epsilon(\rho(r))$ is equal to 1 in the solute volume and smoothly transitions to the permittivity of the solvent ϵ outside of it. In addition to the electronic contribution E_{pol} to ΔE_{sol}, a cavitation term, which is usually destabilizing, can be considered.

$$\Delta E_{\mathrm{sol}} = E_{\mathrm{pol}} + E_{\mathrm{cav}} \tag{4.8.5}$$

$$E_{\mathrm{cav}} = \gamma S \tag{4.8.6}$$

Here, γ is the surface tension of the solvent and S the solute surface area. Aside from the PCM model, the conductor-like screening model[75] enjoys significant popularity in the quantum chemistry community. Its implementation is more efficient and reduces errors caused by charge density spilling out from the cavity. Furthermore, the continuum is treated as a perfect conductor ($\epsilon = \infty$) which leads to the cancellation of the electric potential at the surface and ideal solute polarization charge densities.

With finite ϵ, this approach is still a good approximation and the ideal polarization charge densities $\rho_{\text{pol}}(r)$ are scaled by a factor f

$$f = \frac{\epsilon - 1}{\epsilon + x} \tag{4.8.7}$$

where $x = 0.5$ for neutral solutes and $x = 0$ for ions. However, the accuracy of different continuum models is rather similar and deviations are usually much smaller than errors with respect to experimental results. All implicit solvent corrections suffer from the same shortcomings which is the neglect of all non-electrostatic interactions between solute and solvent. Hydrogen bonds, for example, are well known to be insufficiently described since local charge density changes cannot be modeled by global parameters such as ϵ.

4.9 Electronic Structure Analysis

4.9.1 Charge Analysis

Chemical reactions are characterized by the reorganization of electron density during the transformation of reactants into products. Furthermore, chemists rely on concepts such as partial charges and oxidation numbers to explain experimentally observed reactivities. Since the early development of quantum chemistry, theoreticians have devised charge partitioning schemes in order to make empirical concepts quantifiable. While the total charge density is an observable, the partitioning between atoms or functional groups is not and therefore somewhat arbitrary. The natural population analysis (NPA)[107] approaches this problem by utilizing a set of orthogonal natural atomic orbitals (NAOs) that are localized as much as possible on a single atomic center (A, B, ...).

$$\boldsymbol{P} = \begin{pmatrix} \boldsymbol{P}^{AA} & \boldsymbol{P}^{AB} & \boldsymbol{P}^{AC} & \vdots \\ \boldsymbol{P}^{AB} & \boldsymbol{P}^{BB} & \boldsymbol{P}^{BC} & \vdots \\ \boldsymbol{P}^{AC} & \boldsymbol{P}^{BC} & \boldsymbol{P}^{CC} & \vdots \\ \dots & \dots & \dots & \ddots \end{pmatrix} \tag{4.9.1}$$

The NAOs are constructed in two steps by diagonalizing the one-center blocks (e.g. $\boldsymbol{P}^{AA}$) of the density matrix ($\boldsymbol{P}_{ij} = \boldsymbol{C}_{ij}\chi_i\chi_j^*$) and removing interatomic overlap ($\boldsymbol{S}_{ij} = \chi_i^*\chi_j$). After the first step, a set of pre-NAOs are obtained which are orthogonal only for their respective center and can be divided into strongly occupied and weakly occupied (Rydberg) orbitals. In the second step all pre-NAOs

are orthogonalized with respect to each other. In order to preserve the structure of the pre-NAOs as much as possible a symmetric orthogonalization procedure weighted by the occupation number is chosen. The Rydberg orbitals are then Schmidt-orthogonalized with respect to the strongly occupied orbitals and a second time in the weighted fashion among themselves. This is done to avoid over-counting of occupation. The final NAOs (ϕ^{NAO}) and their occupations are then obtained as eigenfunctions and eigenvalues of the one-center blocks. The atomic charge is calculated by summation over the occupation number at the corresponding center.

NPA theory can also be applied to periodic systems by calculating the density matrix independently for every k-point. Since the NPA assumes an atom centered basis set $\chi_\mu(k)$, an extension to planewaves $\psi(k)$ requires a projection scheme from one basis to another[22]. The projected band a is then defined as

$$|X_a(k)\rangle = \sum_\mu c_{a,\mu} |\chi_\mu(k)\rangle = \hat{P}(k) |\psi_a(k)\rangle . \tag{4.9.2}$$

with the projection operator $\hat{P}(k)$:

$$\hat{P}(k) = \sum_\mu |\chi_\mu(k)\rangle \langle\chi^\mu(k)| . \tag{4.9.3}$$

A superscript signifies here the orthogonal dual such that:

$$\langle\chi_\mu(k)\rangle |\chi^\nu(k) = \delta_{\mu\nu}. \tag{4.9.4}$$

The projection quality can be determined from a spillage parameter Y that quantifies the lost density by summation over the total number of k-points N_k and bands N_a.

$$Y = \frac{1}{N_k N_a} \sum_k^{N_k} \sum_a^{N_a} \langle\psi_a(k)|(1 - \boldsymbol{P}(k))|\psi_a(k)\rangle \tag{4.9.5}$$

4.9.2 Energy Decomposition Analysis

Another observable quantity of interest to chemists is the bond energy ΔE_{bond} between two molecular fragments (A-B). By definition it is the negative of the bond dissociation energy D_0. For a better understanding of the driving forces behind the formation and breaking of bonds, theoreticians have developed energy decomposition analyses that aim to quantify the terms comprising ΔE_{bond}. Similarly to the different charge decomposition schemes, the energy decomposition is arbitrary

since the individual terms are not experimentally obtainable and researchers have suggested various energy decomposition analysis (EDA) schemes motivated by addressing different chemical questions. In the EDA of Morokuma[24] and Ziegler[25] the first decomposition step divides the bond energy into an intrinsic interaction energy ΔE_{int} and the preparation energy ΔE_{prep} required to bring the fragments from their ground state structure E^{GS} into the structure they have in the combined system. In case the fragments are electronically excited to generate a reasonable reference state, the excitation energy also enters ΔE_{prep}.

$$-D_0 = \Delta E_{\text{bond}} = \Delta E_{\text{int}} + \Delta E_{\text{prep}} \tag{4.9.6}$$

$$\Delta E_{\text{int}} = E_{\text{AB}} - E_{\text{A}} - E_{\text{B}} \tag{4.9.7}$$

$$\Delta E_{\text{prep}} = E_{\text{A}} - E_{\text{A}}^{\text{GS}} + E_{\text{B}} - E_{\text{B}}^{\text{GS}} \tag{4.9.8}$$

The contributions to ΔE_{int} are calculated in three steps starting from the normalized product wave function of the fragments $\{\Psi_{\text{A}}\Psi_{\text{B}}\}$ with energy E_{AB}^0 in the equilibrium geometry of molecule AB. The quasiclassical Coulomb interaction ΔE_{elstat} between the nuclei and fragment densities is then calculated as:

$$\Delta E_{\text{elstat}} = \sum_{\alpha\in\text{A}}\sum_{\beta\in\text{B}} \frac{Z_\alpha Z_\beta}{R_{\alpha\beta}} + \int V_{\text{B}}(r)\rho_{\text{A}}(r)\mathrm{d}r + \int V_{\text{A}}(r)\rho_{\text{B}}(r)\mathrm{d}r \tag{4.9.9}$$

$$+ \int\int \frac{\rho_{\text{A}}(r_1)\rho_{\text{B}}(r_2)}{r_{12}}\mathrm{d}r_1\mathrm{d}r_2. \tag{4.9.10}$$

In the second step $\{\Psi_{\text{A}}\Psi_{\text{B}}\}$ is antisymmetrized by the operator $\hat{A}$ to satisfy the Pauli principle.

$$\Psi^0 = N\hat{A}\{\Psi_{\text{A}}\Psi_{\text{B}}\} \tag{4.9.11}$$

The difference between the corresponding energy E^0 and E_{AB}^0 is the Pauli energy which is always repulsive.

$$\Delta E_{\text{Pauli}} = E^0 - E_{\text{AB}}^0 \tag{4.9.12}$$

In the third step, the intermediate wave function Ψ^0 is relaxed to yield the final state Ψ_{AB}. The energy difference results from the mixing of fragment orbitals.

$$\Delta E_{\text{orb}} = E_{\text{AB}} - E^0 \tag{4.9.13}$$

If a dispersion correction is calculated *a posteriori* its contribution $\Delta E_{\text{int}}(\text{disp})$ is added as a fourth term to the interaction energy. As an optional extension to the EDA, ΔE_{orb} can be further decomposed with the natural orbitals for chemical va-

lence (NOCV) method.[27] Here, the total deformation density $\Delta\rho^{\text{orb}}$ is expressed by the deformation density matrix $\Delta\boldsymbol{P}^{\text{orb}}$ in a basis of fragment orbitals λ.

$$\Delta\rho^{\text{orb}} = \rho_{\text{AB}} - \rho^0 = \sum_m^N \sum_n^N \Delta P_{mn}^{\text{orb}} \lambda_m \lambda_n \tag{4.9.14}$$

The NOCVs ψ_i are the eigenvectors obtained through diagonalization of $\Delta\boldsymbol{P}^{\text{orb}}$. The corresponding eigenvalues ν_i quantify the amount of charge transferred through a NOCV. There is always a pair of eigenvalues with opposite sign but identical absolute value which form a deformation density $\Delta\rho_i$. The sum of all $\Delta\rho_i$ is also called charge density difference.

$$\Delta\rho^{\text{orb}} = \sum_i^{N/2} \Delta\rho_i = \sum_i^{N/2} \nu_i \left[-|\psi_{-i}|^2 + |\psi_i|^2 \right] \tag{4.9.15}$$

Under PBC the same procedure can be applied, however the total density is now a sum of densities at different k-points. The weight due to symmetry is contained in the occupation number of the bands at that k-point.

$$\rho = \sum_k \rho(k) \tag{4.9.16}$$

It is not possible to decompose the EDA terms by k since the exchange-correlation energy depends non-linearly on the density. Furthermore, the NOCV extension can currently only be applied to calculations at the Γ-point. Interpretation of the pEDA becomes more challenging for metallic systems due to partially filled bands. Additionally, occupation numbers change depending on the placement of a k-point within or outside the Fermi surface (or path in 2D).[108] The Fermi surface separates occupied and unoccupied states in reciprocal space. At the boundary, electrons have an energy of E_{Fermi}. The Fermi surface is only defined for zero temperature and unique to metals since E_{Fermi} lies in the bandgap for semiconductors and insulators.

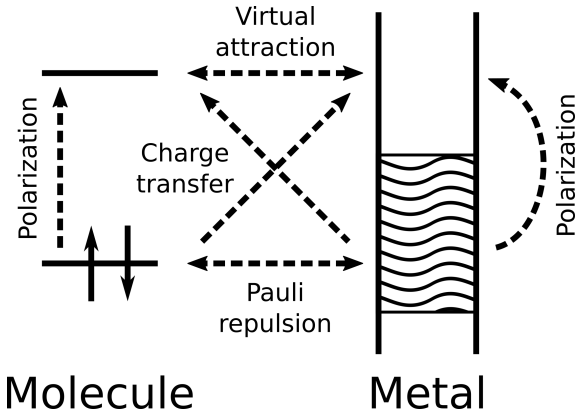

Figure 4.9.1: A generalized energy diagram detailing the possible interactions of a partially filled metal band with occupied and virtual molecular orbitals. A discussion of the terms can be found in the main text. Figure adapted from Reference 108. The method presented therein precedes the pEDA used in this dissertation.

The main bonding interactions for metals shown in Figure 4.9.1 differ somewhat from the localized orbital picture of molecules and non-metallic solids. Covalent interactions are partially replaced by delocalized bidirectional charge transfer from occupied orbitals at one fragment to unoccupied orbitals at the other. Polarization corresponds to the promotion of electrons from occupied to unoccupied orbitals within the same fragment. This effect is particularly strong at the metal fragment which possesses many energetically close states at E_{Fermi}. For the same reason Pauli repulsion is reduced for metals with a high DOS at the surface, such as palladium [26], since electrons can easily evade each other without a large energetic penalty. When bonding combinations of formerly virtual orbitals fall below the Fermi energy, they become occupied leading to virtual attraction.

4.9.3 Scanning Tunneling Microscopy

The experimental scanning tunneling microscopy (STM) technique creates images of surfaces by measuring the tunneling current I of electrons between a probe and the surface. The theoretical framework of STM was initially developed by Tersoff and Hamann [109] as a first order perturbation and is shortly described in the following.

$$I = \frac{2\pi \mathrm{e}^2}{\hbar} \sum_{\mu,\nu} f(E_\mu)[1 - f(E_\nu + eU)] \times |M_{\mu\nu}|^2 \delta(E_\mu - E_\nu) \tag{4.9.17}$$

Here, f is the Fermi function, U the applied voltage, and δ the density of states delta distribution. The tunneling matrix element between the electronic state of the probe Ψ_μ and the surface Ψ_ν is given by $M_{\mu\nu}$.

$$M_{\mu\nu} = \frac{\hbar^2}{2m_e} \int (\Psi_\mu^* \nabla \Psi_\nu - \Psi_\nu \nabla \Psi_\mu^*) \mathrm{d}S \tag{4.9.18}$$

The integration is performed over any surface lying entirely in the vacuum region between probe and surface. Generally, STM measurements are performed at low temperatures where the Fermi function becomes a step function. Furthermore, the small bias voltage limit is applied since sample and probe are conducting. Thus, equation 4.9.17 at E_F simplifies to:

$$I = \frac{2\pi \mathrm{e}^2}{\hbar} U \sum_{\mu,\nu} |M_{\mu\nu}|^2 \delta(E_\nu - E_\mathrm{F}) \delta(E_\mu - E_\mathrm{F}). \tag{4.9.19}$$

When the probe is considered to be point-like, elements of M become independent of the probe state Ψ_μ. The tunneling current is then proportional to the local density of states (LDOS) of the surface at a given energy (here E_F).

$$I \propto \sum_{\nu} |\Psi_\nu(r_0)|^2 \delta(E_\nu - E_\mathrm{F}) \tag{4.9.20}$$

By scanning the probe through different positions r_0 a contour plot of the LDOS is generated which is often in good agreement with experiment. Application of a negative bias plots a sum of all occupied surface states in the interval between the voltage multiplied by the elementary charge and the Fermi energy $[E_F, eU]$, while a positive bias plots unoccupied states.

5 Computational Details

During the preparation of this dissertation various methods and program packages were employed. The details are given in the computational- and method sections of the individual publications constituting Chapter 8. In addition, a summary of the most used program versions and common settings are given in the following.
The majority of calculations were performed with the PBE[110] (Perdew-Burke-Ernzerhof) density functional due to its computational efficiency and applicability as a general purpose functional for a host of different material classes such as organic molecules, inorganic semiconductors and bulk metals. Missing dispersion interactions were included with the semi-empirical D3 correction[93] using an improved damping function[94].
Calculations of periodic systems were performed with the Vienna Ab initio Simulation Package[111,112,113] (VASP) version 5.4.4 including the transitions state tools[114] version 1.73. The kinetic energy cutoff for the plane wave basis set was set to 400 eV for all systems and the most recent pseudopotentials (PBE5.4) were utilized. The SCF procedure was converged to at least 10^{-5} eV while structure optimizations had to satisfy a force criterion smaller than 10^{-2} eV Å^{-1}. For metallic systems, the occupation of electronic states was smeared out by 0.2 eV to speed up convergence. Bonding analysis with the pEDA[26] method was performed with the Amsterdam modeling suite[115] (AMS) BAND program adopting various versions (2017.107, 2017.108, 2019.301). The TZ2P[116] (triple-zeta with two polarization functions) basis set was used whenever the available computational resources allowed it, in conjunction with an SCF convergence of 10^{-6} eV.
Molecules and clusters were treated mostly with TURBOMOLE[117] 7.2 and 7.3 using the def2-TZVPP[118] (valence triple-zeta with two sets of polarization functions) basis. The SCF procedure was converged to 10^{-8} E_h and the force to 10^{-3} $E_h a_0^{-1}$. Again, the EDA[24,25,27] analysis was carried out with the non-periodic code AMS-ADF 2019.301 using the TZ2P basis.

Molecular structures were created and drawn primarily with the editors Avogadro[119] and Chemcraft[120] as well as the Atomic Simulation Environment[121] (ASE). Post-processing of data calculated with VASP was done with python scripts based on ASE and p4vasp[122]. Graphs were plotted either with gnuplot[123] or QtiPlot[124] while orbitals and densities were visualized with VESTA[125] and ADFview in case of calculations with AMS programs. Figures were put together in Inkscape[126]. Finally, this document is set with LaTeX[127].

6 Summary

In this cumulative dissertation organic-inorganic hybrid interfaces with relevance for nanoelectronic applications are investigated with theoretical methods. An emphasis is put on the elucidation of interface reaction mechanisms and the employment of bonding analysis to better inform synthetic design choices. Furthermore, electronic structure related properties are calculated in order to explain experimental observations. The dissertation is organized in two parts. In the first part, the covalent attachment of organic layers on the (001) facet of the inorganic semiconductor silicon is studied. The second part is concerned with the creation of interface models for organic semiconductors on Ag(111).

In the past it was shown that cyclooctyne is a particularly suitable platform molecule for the purpose of creating a contact layer with Si(001) due to its highly selective adsoption. Building on this prior work, the focus of this dissertation is hence the growth of a second layer on the contact layer. For this purpose, promising reactions schemes with 'click'-characteristics (fast, excellent yield, solvent tolerant) are studied. These are the azide-alkyne cycloaddition (AAC), the enolether-tetrazine inverse electron demand Diels-Alder reaction (IEDDA) as well as the nucleophilic substitutions of an acid chloride mediated esterification (ACE) and the sulfonylfluoride exchange (SuFEx).
In the AAC variant, an alkyne functionalized cyclooctyne molecule is used as the first layer building block while a *para*-substituted methyl-benzylazide is chosen for the second layer. However, the azide can itself react in various ways with the silicon surface if gaps in the cyclooctyne layer exist. In order to better understand these side reactions, different adsorption modes are investigated. In agreement with earlier studies, the azide is confirmed to initially react with a surface dimer through a 1,3-dipolar cycloaddition generating a five-membered ring. At elevated temperatures, N_2 is eliminated forming the more stable –Si–N–Si– three-membered ring. However, the slab model used in this dissertation also shows that in addition to the azide, the benzyl group can simultaneously bind to the surface in reversible fashion.

In the alternative IEDDA scheme the azide is replaced by a tetrazine with additional electron withdrawing groups resulting in the inversion of the electron demand. As the diene, an enolether is used, which can eliminate methanol to restore the π-system later on. However, the adsorption behavior of the cyclooctyne-enolether on the surface is examined first since this combination of functional groups has not been investigated before. As expected, the [2+2] cycloaddition of the C≡C bond at a silicon dimer is the preferred adsorption path. Due to the presence of two more functional groups, the ether and the C=C bond, various single- and multi-adsorption modes are found. The most stable product is formed when the O–C bond is cleaved in addition to the attachment of the triple bond. However, this reaction path is kinetically hindered at low temperatures due to the presence of a barrier. Thus, the computational result explains the low intensity of O–Si and O=C signals in experimental X-ray photoelectron spectra.
Thereby, the groundwork for the attachment of tetrazine molecules in the second layer is laid. The free energy barrier of the IEDDA is predicted to be 100 kJ/mol at room temperature which can therefore only be overcome at temperatures well above ambient. Indeed, desorption of molecules is experimentally found to be favored over a reaction if the substrate is slowly heated, whereas a coverage of 20% is reached if the reaction is performed at 380 K.
The SuFEx scheme is another promising method for linking molecular building blocks. In particular, primary amine nucleophiles are well suited for interface reactions due to simple, one-step synthetic routes. Since gaps exist in the understanding of this SuFEx variant, the mechanism is studied in this dissertation with bonding analysis and reaction path calculations. It is shown that reaction barriers can be lowered irrespective of solvent by added base molecules which improve the nucleophilicity of the amine. Furthermore, the side product HF is scavenged by the base, increasing the thermodynamic driving force. The latter insight also provides an explanation for the experimental finding that base must be added in excess in order to achieve high yields. These results suggest that the SuFEx reaction is more suited for a solution based synthesis than for gas phase deposition of organic layers.
In order to obtain a realistic interaction model of molecules within a layer, larger simulation cells are required. Since these calculations can quickly surpass contemporary computational resources, approximations have to be introduced. For research questions concerning chemical reactivity, a possible solution is presented by exploiting the local nature of covalent bonds and neglecting distant interface parts. Thus system sizes are reduced in this dissertation by systematically removing interface regions in the explicit description of reactions. For this purpose, a hierarchical

model is created that neglects either the substrate, neighboring molecules within a layer or both. The validity of this approach is confirmed through a comparison of several density functionals with coupled cluster results and evaluation of the model error with respect to the complete interface. The best compromise between accuracy and computational demand is found for a model in which the substrate is not a part of the calculation but its templating effect is considered. This is achieved by adhering to the lattice constant given by the dimer reconstruction of Si(001) and excluding the approach of reactants from the substrate-blocked hemisphere.
Realistic surfaces contain defects. The most common point defect of Si(001) is the bonded dimer vacancy (DV). In its vicinity the reactivity changes significantly, which could potentially lead to uneven growth of organic layers. This finding is of importance for future studies and therefore investigated through the adsorption of the unsaturated hydrocarbons acetylene, ethylene and cyclooctyne at the defect. While the adsorption of these molecules at the pristine surface is direct or via a short-lived intermediate, a barrier has to be overcome at the DV. However, the most stable products of reactions with the defect are significantly more favorable than compared to adsorption at an intact dimer for acetylene and ethylene, while the larger cyclooctyne experiences steric repulsion in the defect cavity. This initially disadvantageous differentiation of surface reactivity can open up possibilities for patterning through selective adsorption.

The second main topic of this dissertation is the chemical interplay of the Ag(111) surface with nature inspired organic semiconductors based on pyrrole units. In comparison to silicon, the coinage metal surface has a comparatively low reactivity. This property is crucial for keeping the π-systems of the organic semiconductors intact after interface formation. Still, various bonding patterns can emerge at the interface. Besides van der Waals interactions, an exchange of electron density between the surface and the organic π-system is observed. The strength of this interaction is determined primarily by the frontier orbitals of the molecule.
Investigations include metalated as well as free base variants of different organic semiconductors. Here, it becomes evident that metal atoms not only alter the electronic structure of the molecule but can also serve as structural motifs during on-surface synthesis. For instance, Gd has a larger ionic radius than the transition metal Fe and provides a template for the formation of a macrocycle comprised of five pyrrole-derived units instead of the more common four. This results in a reduction of the HOMO-LUMO excitation energy by about 0.3 eV. Furthermore, an open chain polycyanine with an unusual atomic and electronic structure is found

when the surface alone is used as a structural template. The resulting polymer backbone is constituted alternately of carbon and nitrogen making it electron deficient. Therefore, the chain must be stabilized trough electron transfer from the surface. Additionally, conjugation between the π-system and orthogonally positioned N-lonepairs leads to a disruption of the polymer's planarity.
The size of the central cavity is however not only determined by the number of pyrrole units but also depends on the presence of bridging atoms. In corroles, a sub-class of tetrapyrroles, exactly one of these bridging atoms is missing which leads to ring contraction. For this reason, corroles are particularly suitable for complexating late transition metals with small ionic radii such as nickel. Although corroles are formally trianionic ligands, the spin state of Ni is unaltered with respect to porphyrines and the resulting radical character of the complex is instead delocalized over the whole molecule. However, due to the tighter coordination environment the overlap of the antibonding combination of Ni-d and N-p atomic orbitals increases. As a consequence, the lowest unoccupied molecular orbital is shifted to higher energy by about 1 eV.
It is known that free base corroles can easily be deprotonated in solution. This property is also present in a similar fashion on Ag(111), which catalytically supports hydrogen abstraction. The calculated and experimentally determined barrier are in very good agreement. However, in contrast to the solution reaction, atomic H is formed instead of a proton and a corrole radical with weakened aromaticity remains. As was the case for the polycyanine mentioned above, a stabilization of this state is achieved trough charge transfer from the surface into the molecule which quenches the radical and reinstates aromaticity. Furthermore, each of the two iminic (–N=) nitrogens is coordinated to one surface atom which decreases the molecule-surface distance by almost 0.2 Å.

In summary, the collected work of this dissertation shows that quantum chemical methods are a valuable tool for better understanding the chemistry and electronic structure of hybrid interfaces. Insights gained from theory not only explain experimental observations but can also be used to guide synthetic efforts even though, different terminologies and concepts exist for metal and semiconductor surfaces. Furthermore, the studies presented here highlight that various types of interfaces can be described efficiently within an *ab inito* framework.

7 Zusammenfassung

In dieser kumulativen Dissertation werden organisch-anorganische Hybridgrenzflächen mit Relevanz für nanoelektronische Anwendungen mittels theoretischer Methoden untersucht. Der Schwerpunkt liegt dabei auf der Aufklärung von Grenzflächenreaktionsmechanismen und der Bindungsanalyse, um synthetische Designentscheidungen besser zu begründen. Weiterhin werden von der elektronischen Struktur abgeleitete Eigenschaften berechnet, um experimentelle Beobachtungen zu erklären. Die vorliegende Arbeit besteht aus zwei Teilen. Im ersten Teil wird die kovalente Bindung von organischen Lagen an die (001) Oberfläche des anorganischen Halbleiters Silizium untersucht. Der zweite Teil befasst sich mit der Erstellung von Grenzflächenmodellen für organische Halbleiter auf Ag(111).

In der Vergangenheit konnte gezeigt werden, dass Cyclooctin aufgrund seiner hochselektiven Adsorption eine ideale Plattform für die Ausbildung einer Kontaktlage auf Si(001) ist. Aufbauend auf diesen früheren Arbeiten liegt der Fokus dieser Dissertation nun auf dem Aufbau einer zweiten Lage auf der Kontaktlage. In diesem Rahmen werden vier vielversprechende Reaktionen mit „click“-Eigenschaften (schnell, exzellente Ausbeute, lösemitteltolerant) untersucht. Dabei handelt es sich um die Azid-Alkin Cycloaddition (AAC), die Enolether-Tetrazin inverse Diels-Alder Reaktion (IEDDA), sowie nukleophile Substitutionen bei der Veresterung eines Säurechlorids (ACE) und der Fluoridaustausch an einem Sulfonylfluorid (SuFEx). Bei der AAC Variante wird ein Alkin-funktionalisiertes Cyclooctinmolekül als Baustein für die erste Lage und ein in *para*-Position Methyl-substituiertes Benzylazid für die zweite Lage verwendet. Allerdings kann auch das Azid selbst auf verschiedene Weisen mit der Siliziumoberfläche reagieren, wenn Lücken in der Cyclooctinlage bestehen. Um diese Nebenreaktionen besser zu verstehen, werden verschiedene Adsorptionsmodi untersucht. In Übereinstimmung mit früheren Studien bestätigt sich, dass das Azid zunächst über eine 1,3-dipolare Cycloaddition mit einem Oberflächendimer reagiert, wodurch sich ein Fünfring bildet. Bei höheren Temperaturen entsteht daraus unter N_2-Abspaltung ein stabilerer –Si–N–Si– Dreiring. Zusätzlich zeigt das in dieser Dissertation verwendete Slabmodell, dass gleichzeitig zur Azid-

auch die Benzylgruppe an die Oberfläche binden kann. Diese Reaktion ist jedoch reversibel.
Im alternativen IEDDA Ansatz wird das Azid durch eine Tetrazinfunktion mit elektronenziehenden Gruppen ersetzt, wodurch es zu einer Umkehr des Elektronenbedarfs kommt. Als Dien wird hier ein Enolether verwendet, welcher später Methanol eliminieren kann, um das π-System wiederherzustellen. Zunächst wird allerdings das Adsorptionsverhalten des Cyclooctin-Enolethers auf dem Substrat untersucht, da dies bisher nicht geschehen ist. Wie bereits zu erwarten war, ist eine [2+2] Cycloaddition der C≡C Bindung an ein Siliziumdimer der bevorzugte Adsorptionspfad. Da mit dem Ether und der C=C Bindung zwei weitere funktionelle Gruppen vorhanden sind, werden verschiedene Einzel- und Mehrfachadsorptionsmodi gefunden. Das stabilste Produkt entsteht, wenn zusätzlich zur Reaktion der Dreifachbindung auch eine Spaltung der O–C Bindungen stattfindet. Dieser Reaktionspfad geht jedoch mit einer Barriere einher und ist damit bei niedrigen Temperaturen kinetisch gehindert. Das Ergebnis der Berechnungen erklärt somit die niedrige Intensität von O–Si und C=O Signalen in experimentellen Röntgen-Photoelektronenspektren.
Damit ist die Grundlage für das Anknüpfen von Tetrazinmolekülen in zweiter Lage geschaffen. Bei Raumtemperatur wird eine freie Energiebarriere von 100 kJ/mol für die IEDDA vorhergesagt, weshalb deutlich höhere Temperaturen für ihre Überwindung nötig sind. In der Tat ist die Desorption der Moleküle im Experiment gegenüber einer Reaktion bevorzugt, wenn das Substrat langsam erwärmt wird. Wird die Reaktion hingegen bei 380 K durchgeführt, liegt die Bedeckung anschließend bei etwa 20%.
Die SuFEx Reaktion ist eine weitere vielversprechende Methode für die Verknüpfung zweier molekularer Bausteine. Insbesondere primäre Amine sind gut als Nukleophile für Grenzflächenreaktionen geeignet, da mit ihnen Synthesen in einem Schritt gelingen. Die SuFEx Reaktion gilt als noch nicht vollständig verstanden und wird daher in dieser Dissertation mittels Bindungsanalyse und der Berechnung von Reaktionspfaden untersucht. Dabei kann gezeigt werden, dass zugesetzte Basemoleküle unabhängig vom Lösemittel die Reaktionsbarriere herabsetzen indem sie die Nukleophilie des Amins verstärken. Zusätzlich wird das Nebenprodukt HF von der Base abgefangen, was die thermodynamische Triebkraft erhöht. Damit wird zugleich eine Erklärung für den experimentellen Befund geliefert, dass Base im Überschuss verwendet werden sollte um hohe Umsätze zu erzielen. Diese Resultate legen nahe, dass die SuFEx Reaktion eher für lösemittelbasierte Methoden als für Gasphasenabscheidung von organischen Lagen geeignet ist.

Um ein realistischeres Wechselwirkungsmodell von Molekülen innerhalb einer Lage zu erhalten, werden größere Simulationszellen benötigt. Da deren Berechnung allerdings schnell die aktuell zur Verfügung stehenden Computerressourcen übersteigen kann, müssen Näherungen eingeführt werden. Dabei ist ein naheliegender Ansatz bei Fragestellungen, die vor allem die chemische Reaktivität betreffen, die Lokalisierung von Bindungen auszunutzen und weit entfernte Grenzflächenregionen zu vernachlässigen. Daher werden in dieser Dissertation Systemgrößen reduziert, indem systematisch Teile der Grenzfläche aus der expliziten Berechnung von Reaktionen entfernt werden. Für diesen Zweck wird ein hierarchisches Modell erzeugt indem entweder das Substrat, benachbarte Moleküle einer Lage oder beide vernachlässigt werden. Die Validität dieses Vorgehens wird über einen Vergleich mehrerer Dichtefunktionale mit Coupled Cluster Resultaten und der Berechnung von Modellfehlern gegenüber der vollständigen Grenzfläche bestätigt. Der beste Kompromiss zwischen Genauigkeit und benötigter Rechenzeit ergibt sich für ein Modell, in dem das Substrat zwar nicht Teil der Berechnung ist, aber seine Wirkung als Templat berücksichtigt wird. Dies wird erreicht, indem die durch Oberflächenrekonstruktion vorgegebenen Gitterkonstanten von Si(001) eingehalten und Annäherung von Edukten aus dem vom Substrat belegten Halbraum ausgeschlossen werden.
Reale Oberflächen enthalten Defekte. Im Fall von Si(001) ist der am häufigsten auftretende Punktdefekt die gebundene Dimerfehlstelle (DV). In ihrer Umgebung verändert sich die Reaktivität, was potentiell zu unregelmäßigem Wachstum von organischen Lagen führen kann. Dieser für zukünftige Studien wichtige Befund wird mittels Adsorption der ungesättigten Kohlenwasserstoffe Acetylen, Ethen und Cyclooctin am Defekt untersucht. Während die Adsorption dieser Moleküle auf der defektfreien Oberfläche üblicherweise direkt oder über kurzlebige Zwischenstufen verläuft, ist an der DV eine Barriere zu überwinden. Gleichzeitig ist aber das stabilste Produkt von Reaktionen des Defekts mit Acetylen und Ethen deutlich gegenüber Adsorption am intakten Dimer bevorzugt. Das größere Cyclooctin ist hingegen in der Defektlücke sterisch eingeschränkt. Aus dieser zunächst nachteiligen Differenzierung der Oberfläche kann allerdings auch die Möglichkeit erwachsen über selektive Adsorption ein „Patterning“ vorzunehmen.

Im zweiten Kernthema dieser Dissertation wird das chemische Zusammenspiel der Ag(111) Oberfläche mit, von der Natur inspirierten, organischen Halbleitern auf Pyrrolbasis untersucht. Im Vergleich zu Silizium zeichnet sich die Münzmetalloberfläche durch eine vergleichsweise geringe Reaktivität aus. Dies ist entscheidend, damit die π-Systeme der organischen Halbleiter nach Ausbildung

einer Grenzfläche intakt bleiben. Trotzdem treten vielfältige Bindungsmuster an der Grenzfläche auf. Neben van der Waals Wechselwirkungen lässt sich ein Austausch von Elektronendichte zwischen Oberfläche und dem organischen π-System beobachten. Die Stärke dieser Interaktion wird vor allem von den Grenzorbitalen des Moleküls bestimmt.
Die Untersuchungen umfassen metallierte, als auch die freien Basen verschiedener organischer Halbleiter. Dabei zeigt sich, dass die Metallatome nicht nur die elektronische Struktur des Moleküls verändern, sondern auch als strukturgebendes Motiv dienen. Gd zum Beispiel besitzt einen größeren Ionenradius als das Übergangsmetall Fe und ist daher ein Templat für die Bildung von Makrozyklen mit fünf pyrrolähnlichen Baueinheiten statt der häufiger auftretenden vier. Daraus resultiert eine Verringerung der HOMO-LUMO Anregungsenergie um etwa 0,3 eV. Wenn lediglich die Oberfläche selbst als Templat verwendet wird, wird ein offenkettiges Polycyanin mit ungewöhnlicher atomarer und elektronischer Struktur erhalten. Das abwechselnd aus Kohlenstoff und Stickstoff aufgebaute Rückgrat des Polymers ist elektronendefizitär und wird durch Ladungsdichtetransfer von der Oberfläche stabilisiert. Zusätzlich tritt Konjugation zwischen dem π-System der Kette und orthogonal dazu liegenden freien N-Elektronenpaaren auf, was zur Aufhebung der Planarität des Polymers führt.
Der Durchmesser der Zentralkavität ist allerdings nicht nur durch die Zahl der Pyrroleinheiten gegeben, sondern hängt auch von der Menge vorhandener Brückenatome zwischen diesen ab. Bei Corrolen, einer Unterfamilie der Tetrapyrrole, fehlt genau eines dieser Brückenatome was zu einer Ringverengung führt. Daher sind Corrole besonders geeignet um späte Übergangsmetalle mit kleinen Ionenradien, wie Nickel, zu komplexieren. Obwohl Corrole formal trianionische Liganden sind, ändert sich der Spinzustand des Ni im Vergleich zu Porphyrinen nicht und der resultierende radikalische Charakter des Komplexes ist stattdessen über das gesamte Molekül delokalisiert. Allerdings steigt durch die verengte Koordinationsumgebung der Überlapp der antibindende Kombination aus Ni-d und N-p Atomorbitalen. Als Konsequenz ist das niedrigste unbesetzte Molekülorbital um etwa 1 eV zu höherer Energie verschoben.
Es ist bekannt, dass freie Corrole in Lösung leicht deprotoniert werden können. Eine ähnliche Beobachtung wird auch bei einer Adsorption auf der Ag(111) Oberfläche gemacht, welche die Wasserstoffabstraktion katalytisch unterstützt. Die berechnete und experimentell bestimmte Barriere stimmen sehr gut überein. Es entsteht jedoch, im Gegensatz zur Reaktion in Lösung, atomarer Wasserstoff und ein Corrolradikal mit geschwächter Aromatizität bleibt zurück. Ebenso wie

im zuvor genannten Fall des Polycyanin wird eine Stabilisierung dieses Zustandes durch Elektronentransfer von der Oberfläche ins Molekül erreicht, wodurch das Radikal gequencht und die Aromatizität wiederhergestellt wird. Dabei koordinieren die beiden iminischen (–N=) Stickstoffe jeweils zu einem Oberflächenatom. Insgesamt verringert sich so der Abstand des Corrolmoleküls zur Oberfläche um fast 0,2 Å.

Zusammenfassend zeigen die gesammelten Arbeiten dieser Dissertation, das quantenchemische Methoden ein wertvolles Werkzeug sind, um die Chemie und elektronische Struktur von Hybridgrenzflächen besser zu verstehen. Durch Theorie erhaltene Erkenntnisse erklären nicht nur experimentelle Beobachtungen, sondern können auch genutzt werden, um Synthesestrategien abzuleiten, obwohl verschiedene Konzepte und Terminologien für Halbleiter- und Metalloberflächen existieren. Zudem heben die hier präsentierten Studien hervor, dass unterschiedliche Grenzflächen effizient mit *ab initio*-Methoden beschrieben werden können.

8 Results and Discussion

Abstracts of the publications constituting the main body of this dissertation are given in the following alongside author contributions. Reprints of the complete articles and their supporting information can be found in the appendix.

8.1 Interface A: Organic / Inorganic Semiconductor

8.1.1 Adsorption of methyl-substituted benzylazide on Si(001): reaction channels and final configurations

Julian Heep, **Jan-Niclas Luy**, Christian Länger, Jannick Meinecke, Ulrich Koert, Ralf Tonner, Michael Dürr, *J. Phys. Chem. C* **2020**, *124*, 9940–9946.

Abstract

The reaction of a methyl-substituted benzylazide on the silicon (001) surface was investigated by means of X-ray photoelectron spectroscopy (XPS), scanning tunneling microscopy (STM), and density functional theory (DFT)-based computations. It was found that the reaction takes place via an intermediate state, which could be experimentally observed at low temperatures. XPS analysis showed that at temperatures of 150 K and above, the azide further reacts on the silicon surface via abstraction of N_2. The final state sees the remaining nitrogen atom of the adsorbate binding covalently to the surface. In the STM images, this final state is associated with two different adsorption configurations. In comparison with DFT calculations, these two configurations are assigned to the molecule being bound via the nitrogen atom only and to a configuration with the molecule bound to the substrate via the nitrogen atom and carbon ring simultaneously.

Contributions

The author conducted all computational work related to the elucidation of the reaction mechanism and simulated STM images in agreement with experimental data. For this purpose suitable adsorbate structures were proposed by the author based

on experimental results and previously published results. The choice of computational methods was made in collaboration with the supervisor. In the course of the work, a Python script interfacing ASE with VASP was written by the author to extract thermodynamic corrections. Interpretation of the computational results was compiled in the form of figures and tables by the author who also wrote the first draft of the theory section which was subsequently refined by the supervisor. The project outline was initially proposed by the experimental collaborators who also performed all measurements and edited the final manuscript.

8.1.2 Combined XPS and DFT investigation of the adsorption modes of methyl enol ether functionalized cyclooctyne on Si(001)

Timo Glaser, Jannick Meinecke, Christian Länger, **Jan-Niclas Luy**, Ralf Tonner, Ulrich Koert, Michael Dürr, *ChemPhysChem* **2021**, *22*, 404-409.

Abstract

The reaction of methyl enol ether functionalized cyclooctyne on the silicon (001) surface was investigated by means of X-ray photoelectron spectroscopy (XPS) and density functional theory (DFT). Three different groups of final states were identified; all of them bind on Si(001) via the strained triple bond of cyclooctyne but they differ in the configuration of the methyl enol ether group. The majority of molecules adsorbs without additional reaction of the enol ether group; the relative contribution of this configuration to the total coverage depends on substrate temperature and coverage. Further configurations include enol ether groups which reacted on the silicon surface either via ether cleavage or enol ether groups which transformed on the surface into a carbonyl group.

Contributions

The author conducted all computational work regarding the adsorption paths of methyl enol ether functionalized cyclooctyne on Si(001). Suitable adsorbate structures were proposed by the author based on experimental results and previously published results. The choice of computational methods was made after discussion with the supervisor. Interpretation of the computational results was compiled in the form of figures by the author who also wrote the computational methods section. The computational results section was written by the supervisor and subsequently refined collaboratively with the author. The project outline was initially proposed

by the experimental collaborators who also performed all measurements and edited the final manuscript.

8.1.3 Click chemistry in ultra-high vacuum - tetrazine coupling with methyl enol ether covalently linked to Si(001)

Timo Glaser, Jannick Meinecke, Lukas Freund, Christian Länger, **Jan-Niclas Luy**, Ralf Tonner, Ulrich Koert, Michael Dürr, *Chem. Eur. J.* **2021**, *27*, 8082-8087.

Abstract

The additive-free tetrazine/enol ether click reaction was performed in ultra-high vacuum (UHV) with an enol ether group covalently linked to a silicon surface: Dimethyl 1,2,4,5-tetrazine-3,6-dicarboxylate molecules were coupled to the enol ether group of a functionalized cyclooctyne which was adsorbed on the silicon (001) surface via the strained triple bond of cyclooctyne. The reaction was observed at a substrate temperature of 380 K by means of X-ray photoelectron spectroscopy (XPS). A moderate energy barrier was deduced for this click reaction in vacuum by means of density functional theory based calculations, in good agreement with the experimental results. This UHV-compatible click reaction thus opens a new, flexible route for synthesizing covalently bound organic architectures.

Contributions

The author conducted all computational work regarding the reaction of the tetrazine with methyl enol ether functionalized cyclooctyne adsorbed on Si(001). Suitable structures of stationary points were proposed by the author based on literature data for closely related compounds. The choice of computational methods was made after discussion with the supervisor. Interpretation of the computational results was compiled in the form of figures by the author who also wrote the computational methods section. The computational results section was written by the supervisor and subsequently refined collaboratively with the author. The project outline was initially proposed by the experimental collaborators who also performed all measurements and edited the final manuscript.

8.1.4 Complementary base lowers the barrier in SuFEx click chemistry for primary amine nucleophiles

Jan-Niclas Luy, Ralf Tonner *ACS Omega* **2020**, *5*, 31432-31439.

Abstract

The sulfur(VI) fluoride exchange (SuFEx) reaction is an emerging scheme for connecting molecular building blocks. Due to its broad functional group tolerance and rather stable resulting linkage, it is seeing rapid adoption in various fields of chemistry. Still, to date the reaction mechanism is poorly understood, which hampers further development. Here, we show that the mechanism of the SuFEx reaction for the prototypical example of methanesulfonyl fluoride reacting with methylamine can be understood as an S_N2-type reaction. By analyzing the reaction path with the help of density functional theory *in vacuo* and under consideration of solvent and co-reactant influence, we identify the often used complementary base as a crucial ingredient to lower the reaction barrier significantly by increasing the nucleophilicity of the primary amine. With the help of energy decomposition analysis at the transition state structures, we quantify the underlying stereoelectronic effects and propose new avenues for experimental exploration of the potential of SuFEx chemistry.

Contributions

The study was motivated by discussions with Prof. Ulrich Koert and Jannick Meinecke. The employed computational methods were selected by the author and the supervisor. All calculations were performed and analyzed by the author who also drafted a first version of the manuscript which was subsequently refined in collaboration with the supervisor.

8.1.5 Efficient hierarchical models for reactivity of organic layers on semiconductor surfaces

Jan-Niclas Luy, Mahlet Molla, Lisa Pecher, Ralf Tonner, *J. Comput. Chem.* **2021**, *42*, 827-839.

Abstract

Computational modeling of organic interface formation on semiconductors poses a challenge to a density functional theory-based description due to structural and chemical complexity. A hierarchical approach is presented, where parts of the interface are successively removed in order to increase computational efficiency while maintaining the necessary accuracy. First, a benchmark is performed to probe the validity of this approach for three model reactions and five dispersion corrected density functionals. Reaction energies are generally well reproduced by generalized

gradient approximation-type functionals but accurate reaction barriers require the use of hybrid functionals. Best performance is found for the model system that does not explicitly consider the substrate but includes its templating effects. Finally, this efficient model is used to provide coverage dependent reaction energies and suggest synthetic principles for the prevention of unwanted growth termination reactions for organic layers on semiconductor surfaces.

Contributions

The project was conceptualized in collaboration with the supervisor. Parts of the functional benchmark were performed by Mahlet Molla during an internship supervised by the author. The most stable monolayer configuration of bifunctional cyclooctyne molecules on Si(001) was determined by Lisa Pecher. All other calculations were performed by the author who also analyzed the results and wrote a first draft of the manuscript. The final manuscript was then collaboratively refined with the supervisor following suggestions from the co-authors.

8.1.6 Organic functionalization at the Si(001) dimer vacancy defect – structure, bonding and reactivity

Jan-Niclas Luy, Ralf Tonner, *J. Phys. Chem. C* **2021**, *125*, 5635-5646.

Abstract

In this density functional theory study, the influence of the bonded dimer vacancy (DV) on the reactivity of the Si(001) surface is investigated. To this end, electronic and structural properties of the defect are analyzed. Band structure calculations reveal a higher-lying valence band which would suggest increased reactivity. However, the opposite is found when organic molecules for interface formation (acetylene, ethylene, and cyclooctyne) are adsorbed at the defect. Significant reaction barriers have to be overcome in order to form bonds with defect atoms, while adsorption on the pristine surface is mostly direct. This suggests the presence of a rather weak Si–Si bond across the defect which must be dissociated before organic adsorbates can react. A rich adsorption and reaction network is found in addition to the structures known from the pristine surface. All three investigated adsorbates show different bonding characteristics. For acetylene and ethylene, the preferred thermodynamic sink is the insertion into the defect, with the latter molecule even dissociating. Bulky cyclooctyne on the other hand avoids reaction with the defect due to steric demands

imposed by the small defect cavity. The DV has no effect on the reactivity of neighboring dimers. A combination of defect creation and hydrogen-precoverage could be a promising approach for selective surface functionalization. We thus show the influence of a nonideal surface on organic functionalization and interface build-up reactions for a prototypical interface.

Contributions

The project was conceptualized in collaboration with the supervisor. All calculations were performed and analyzed by the author who also drafted a first version of the manuscript which was subsequently refined together with the supervisor.

8.2 Interface B: Organic / Metal

8.2.1 Template-controlled on-surface synthesis of a lanthanide supernaphthalocyanine and its open-chain polycyanine counterpart

Qitang Fan, **Jan-Niclas Luy**, Martin Liebold, Katharina Greulich, Malte Zugermeier, Jörg Sundermeyer, Ralf Tonner, J. Michael Gottfried, *Nat. Commun.* **2019**, *10*, 5049.

Abstract

Phthalocyanines possess unique optical and electronic properties and thus are widely used in (opto)electronic devices, coatings, photodynamic therapy, etc. Extension of their π-electron systems could produce molecular materials with red-shifted absorption for a broader range of applications. However, access to expanded phthalocyanine analogues with more than four isoindoline units is challenging due to the limited synthetic possibilities. Here, we report the controlled on-surface synthesis of a gadolinium-supernaphthalocyanine macrocycle and its open-chain counterpart poly(benzodiiminoisoindoline) on a silver surface from a naphthalene dicarbonitrile precursor. Their formation is controlled by the on-surface high-dilution principle and steered by different metal templates, i.e., gadolinium atoms and the bare silver surface, which also act as oligomerization catalysts. By using scanning tunneling microscopy, photoemission spectroscopy, and density functional theory calculations, the chemical structures along with the mechanical and electronic properties of these phthalocyanine analogues with extended π-conjugation are investigated in detail.

Contributions

The author conducted all computational work related to the determination of the atomic and electronic structure of the molecular species synthesized by the collaborators. In particular, the origin of the unusual in-plane deformation of the open-chain polymer was revealed by the author utilizing periodic, as well as molecular models and a range of theoretical methods (discussed in the supporting information). Additionally the author simulated STM images in agreement with experimental data. The choice of computational methods was made in collaboration with the supervisor. Interpretation of the computational results was compiled in the form of figures, tables and written paragraphs by the author. The results were subsequently discussed and refined in an iterative fashion through project meetings with the supervisor and the collaborators. The project outline was initially proposed by the experimental collaborators who also performed all measurements and edited the final manuscript.

8.2.2 Influence of ring contraction on the electronic structure of nickel tetrapyrrole complexes: corrole versus porphyrin

Jan Herritsch, **Jan-Niclas Luy**, Sebastian Rohlf, Manuel Gruber, Benedikt P. Klein, Matthias Kalläne, Peter Schweyen, Martin Bröring, Kai Rossnagel, Ralf Tonner, J. Michael Gottfried, *ECS J. Solid State Sci. Technol.* **2020**, *9*, 061005.

Abstract

The influence of the contracted corrole macrocycle, in comparison to the larger porphyrin macrocycle, on the electronic structure of nickel was studied with X-ray and ultraviolet photoelectron spectroscopy (XPS, UPS) and near-edge X-ray absorption fine structure (NEXAFS) spectroscopy. Synthesis and in situ characterization of the Ni complexes of octaethylporphyrin (NiOEP) and hexaethyldimethylcorrole (NiHEDMC) were performed in ultra-high vacuum. XPS and NEXAFS spectra reveal a +2 oxidation state and a low-spin d^8 electron configuration of Ni in both complexes, despite the formal trianionic nature of the corrole ligand. UPS, in combination with density functional theory (DFT) calculations, support the electronic structure of a Ni(II) corrole with a π-radical character of the ligand. The NEXAFS spectra also reveal differences in the valence electronic structure, which are attributed to the size mismatch between the small Ni(II) center and the larger central cavity of NiOEP. Analysis of the gas-phase structures shows that the Ni–N bonds in NiOEP are 4%–6% longer than those in NiHEDMC, even when NiOEP adopts a ruffled conformation. The individual interactions that constitute the Ni–ligand bond are

altogether stronger in the corrole complex, according to bonding analysis within the energy decomposition analysis and the natural orbitals for chemical valence theory (EDA-NOCV).

Contributions

The author proposed the method for simulating the NEXAFS spectra and performed these calculation independently. For better comparison of calculated delta-peaks to the experimental spectra, the author wrote a GNU Octave script applying Gaussian broadening. All other calculations were performed by the co-author Jan Herritsch. The results were subsequently discussed and refined in an iterative fashion through project meetings with the supervisor and the collaborators. The project outline was initially proposed by the experimental collaborators who also performed all measurements, wrote and edited the final manuscript.

8.2.3 On-surface formation of a transient corrole radical and aromaticity-driven interfacial electron transfer

Malte Zugermeier, Jan Herritsch, **Jan-Niclas Luy**, Min Chen, Benedikt P. Klein, Falk Niefind, Peter Schweyen, Martin Bröring, Martin Schmid, Ralf Tonner, J. Michael Gottfried, *J. Phys. Chem. C* **2020**, *124*, 13825–13836.

Abstract

Corroles on metal surfaces show substantial reactivity and aromaticity-driven interfacial electron transfer of their transient σ/π-radicals. These effects are much more pronounced than for the closely related porphyrins, as has been demonstrated by using an octaalkylcorrole (2,3,8,12,17,18-hexaethyl-7,13-dimethylcorrole, 3H-HEDMC) and its singly N–H dehydrogenated product 2H-HEDMC on a Ag(111) surface through a combination of experimental and theoretical methods. 3H-HEDMC assumes a nonplanar adsorption geometry caused by intramolecular steric repulsion between the three N–H hydrogen atoms. One of the N–H bonds is tilted far out of the molecular plane and points toward the surface. This N–H bond undergoes surface-catalyzed and entropy-driven homolytic scission already below 230 K, resulting in the formation of planar, strain-relieved 2H-HEDMC as a formal π-radical with a 17π-electron conjugation path. The experimental N–H bond scission barrier of 74 kJ/mol agrees well with theory. 2H-HEDMC engages in transfer of electron density from the surface to the molecule. The additional electron density quenches the radical spin and leads to aromatic stabilization because it influences the electronic structure

toward an aromatic 18π-electron conjugation path. Our study demonstrates that aromaticity considerations are useful to rationalize and predict interfacial electron transfer effects, which play an important role in organic electronics, electrocatalysis, and sensors.

Contributions

The author conducted all computational work related to the determination of the atomic and electronic structure of the HEDMC molecule in the gas phase and adsorbed on Ag(111). Calculations concerning the smaller, parent corrole molecule were performed by co-author Jan Herritsch. The choice of computational methods was made together with the supervisor. Interpretation of the computational results on HEDMC was compiled in the form of figures and tables by the author who also wrote the computational methods section. The computational results section was written by the supervisor and subsequently refined collaboratively with the author. The final manuscript was edited by the collaborators and refined in an iterative fashion with all co-authors. The project outline was initially proposed by the experimental collaborators who also performed all measurements.

Bibliography

[1] Cavalcanti, A.; Shirinzadeh, B.; Zhang, M.; Kretly, L. C. Nanorobot hardware architecture for medical defense. *Sensors* **2008**, *8*, 2932–2958.

[2] Radamson, H. H.; He, X.; Zhang, Q.; Liu, J.; Cui, H.; Xiang, J.; Kong, Z.; Xiong, W.; Li, J.; Gao, J.; Yang, H.; Gu, S.; Zhao, X.; Du, Y.; Yu, J.; Wang, G. Miniaturization of CMOS. *Micromachines* **2019**, *10*, 293.

[3] Koch, N. Organic electronic devices and their functional interfaces. *ChemPhysChem* **2007**, *8*, 1438–1455.

[4] Fairus, A.; Arora, V. Quantum engineering of nanoelectronic devices: the role of quantum confinement on mobility degradation. *Microelectron. J.* **2001**, *32*, 679 – 686.

[5] Okazaki, S. Resolution limits of optical lithography. *J. Vac. Sci. Technol. B* **1991**, *9*, 2829–2833.

[6] Lu, W.; Lieber, C. M. Nanoelectronics from the bottom up. *Nat. Mater.* **2007**, *6*, 841–850.

[7] Sundberg, P.; Karppinen, M. Organic and inorganic-organic thin film structures by molecular layer deposition: a review. *Beilstein J. Nanotechnol.* **2014**, *5*, 1104–1136.

[8] George, S. M.; Yoon, B.; Dameron, A. A. Surface chemistry for molecular layer deposition of organic and hybrid organic–inorganic polymers. *Acc. Chem. Res.* **2009**, *42*, 498–508.

[9] Ma, Z.; Zaera, F. Organic chemistry on solid surfaces. *Surf. Sci. Rep.* **2006**, *61*, 229–281.

[10] Morgen, M.; Zhao, J.-H.; Hu, C.; Cho, T.; Ho, P. S.; Todd, E. Low dielectric constant materials for advanced interconnects. *JOM* **1999**, *51*, 37–40.

[11] Root, S. E.; Savagatrup, S.; Printz, A. D.; Rodriquez, D.; Lipomi, D. J. Mechanical properties of organic semiconductors for stretchable, highly flexible, and mechanically robust electronics. *Chem. Rev.* **2017**, *117*, 6467–6499.

[12] Rotenberg, M. Y.; Tian, B. Talking to cells: semiconductor nanomaterials at the cellular interface. *Adv. Biosyst.* **2018**, *2*, 1700242.

[13] Hills, G.; Lau, C.; Wright, A.; Fuller, S.; Bishop, M. D.; Srimani, T.; Kanhaiya, P.; Ho, R.; Amer, A.; Stein, Y.; Murphy, D.; Arvind,; Chandrakasan, A.; Shulaker, M. M. Modern microprocessor built from complementary carbon nanotube transistors. *Nature* **2019**, *572*, 595–602.

[14] Forrest, S. R.; Thompson, M. E. Introduction: organic electronics and optoelectronics. *Chem. Rev.* **2007**, *107*, 923–925.

[15] Jakob, P.; Zaitsev, N. L.; Namgalies, A.; Tonner, R.; Nechaev, I. A.; Tautz, F. S.; Höfer, U.; Sánchez-Portal, D. Adsorption geometry and interface states: relaxed and compressed phases of NTCDA/Ag(111). *Phys. Rev. B* **2016**, *94*, 125436.

[16] Zhao, L.; Hermann, M.; Schwarz, W. H. E.; Frenking, G. The lewis electron-pair bonding model: modern energy decomposition analysis. *Nat. Rev. Chem.* **2019**, *3*, 48–63.

[17] Bader, R. F. W. A quantum theory of molecular structure and its applications. *Chem. Rev.* **1991**, *91*, 893–928.

[18] Henkelman, G.; Arnaldsson, A.; Jónsson, H. A fast and robust algorithm for Bader decomposition of charge density. *Comput. Mater. Sci.* **2006**, *36*, 354–360.

[19] Sánchez-Portal, D.; Artacho, E.; Soler, J. M. Projection of plane-wave calculations into atomic orbitals. *Solid State Commun.* **1995**, *95*, 685–690.

[20] Sánchez-Portal, D.; Artacho, E.; Soler, J. M. Analysis of atomic orbital basis sets from the projection of plane-wave results. *J. Phys. Condens. Matter* **1996**, *8*, 3859–3880.

[21] Dronskowski, R.; Bloechl, P. E. Crystal orbital hamilton populations (COHP): energy-resolved visualization of chemical bonding in solids based on density-functional calculations. *J. Phys. Chem.* **1993**, *97*, 8617–8624.

[22] Dunnington, B. D.; Schmidt, J. R. Generalization of natural bond orbital analysis to periodic systems: applications to solids and surfaces via plane-wave density functional theory. *J. Chem. Theory Comput.* **2012**, *8*, 1902–1911.

[23] Galeev, T. R.; Dunnington, B. D.; Schmidt, J. R.; Boldyrev, A. I. Solid state adaptive natural density partitioning: a tool for deciphering multi-center bonding in periodic systems. *Phys. Chem. Chem. Phys.* **2013**, *15*, 5022–5029.

[24] Kitaura, K.; Morokuma, K. A new energy decomposition scheme for molecular interactions within the Hartree-Fock approximation. *Int. J. Quantum Chem* **1976**, *10*, 325–340.

[25] Ziegler, T.; Rauk, A. On the calculation of bonding energies by the Hartree Fock Slater method. *Theoret. Chim. Acta* **1977**, *46*, 1–10.

[26] Raupach, M.; Tonner, R. A periodic energy decomposition analysis method for the investigation of chemical bonding in extended systems. *J. Chem. Phys.* **2015**, *142*, 194105.

[27] Mitoraj, M. P.; Michalak, A.; Ziegler, T. On the nature of the agostic bond between metal centers and β-hydrogen atoms in alkyl complexes. An analysis based on the extended transition state method and the natural orbitals for chemical valence scheme (ETS-NOCV). *Organometallics* **2009**, *28*, 3727–3733.

[28] Pecher, L.; Tonner, R. Precursor states of organic adsorbates on semiconductor surfaces are chemisorbed and immobile. *ChemPhysChem* **2017**, *18*, 34–38.

[29] Dehnhardt, N.; Luy, J.-N.; Szabo, M.; Wende, M.; Tonner, R.; Heine, J. Synthesis of a two-dimensional organic–inorganic bismuth iodide metalate through in situ formation of iminium cations. *Chem. Commun.* **2019**, *55*, 14725–14728.

[30] Winkler, C.; Jeindl, A.; Mayer, F.; Hofmann, O. T.; Tonner, R.; Zojer, E. Understanding the correlation between electronic coupling and energetic stability of molecular crystal polymorphs: the instructive case of quinacridone. *Chem. Mater.* **2019**, *31*, 7054–7069.

[31] Kachel, S. R.; Klein, B. P.; Morbec, J. M.; Schöniger, M.; Hutter, M.; Schmid, M.; Kratzer, P.; Meyer, B.; Tonner, R.; Gottfried, J. M. Chemisorption and physisorption at the metal/organic interface: bond energies of naphthalene and azulene on coinage metal surfaces. *J. Phys. Chem. C* **2020**, *124*, 8257–8268.

[32] Wolkow, R. A. Controlled molecular adsorption on silicon: laying a foundation for molecular devices. *Annu. Rev. Phys. Chem.* **1999**, *50*, 413–441.

[33] Schlier, R. E.; Farnsworth, H. E. Structure and adsorption characteristics of clean surfaces of germanium and silicon. *J. Chem. Phys.* **1959**, *30*, 917–926.

[34] Chadi, D. J. Atomic and electronic structures of reconstructed Si(100) surfaces. *Phys. Rev. Lett.* **1979**, *43*, 43–47.

[35] Yoshinobu, J. Physical properties and chemical reactivity of the buckled dimer on Si(100). *Prog. Surf. Sci.* **2004**, *77*, 37 – 70.

[36] Murata, Y.; Kubota, M. Order-disorder transition on Si(001). *Phase Transit.* **1995**, *53*, 125–141.

[37] Mui, C.; Wang, G. T.; Bent, S. F.; Musgrave, C. B. Reactions of methylamines at the Si(100)-2×1 surface. *J. Chem. Phys.* **2001**, *114*, 10170–10180.

[38] Pecher, L.; Laref, S.; Raupach, M.; Tonner, R. Ethers on Si(001): a prime example for the common ground between surface science and molecular organic chemistry. *Angew. Chem. Int. Ed.* **2017**, *56*, 15150–15154.

[39] Barriocanal, J. A.; Doren, D. J. 1,3-dipolar cycloadditions on Si(100)-2×1: theoretical studies of novel attachment chemistry for organic monolayers. *J. Vac. Sci. Technol.* **2000**, *18*, 1959–1964.

[40] Leftwich, T. R.; Teplyakov, A. V. Cycloaddition reactions of phenylazide and benzylazide on a Si(100)-2 × 1 surface. *J. Phys. Chem. C* **2008**, *112*, 4297–4303.

[41] Fan, X. L.; Zhang, Y. F.; Lau, W. M.; Liu, Z. F. Violation of the symmetry rule for the [2 + 2] addition in the chemisorption of C_2H_4 on Si(100). *Phys. Rev. B* **2005**, *72*, 165305.

[42] Mette, G.; Dürr, M.; Bartholomäus, R.; Koert, U.; Höfer, U. Real-space adsorption studies of cyclooctyne on Si(001). *Chem. Phys. Lett.* **2013**, *556*, 70 – 76.

[43] Pecher, L.; Schober, C.; Tonner, R. Chemisorption of a strained but flexible molecule: cyclooctyne on Si(001). *Chem. Eur. J.* **2017**, *23*, 5459–5466.

[44] Reutzel, M.; Münster, N.; Lipponer, M. A.; Länger, C.; Höfer, U.; Koert, U.; Dürr, M. Chemoselective reactivity of bifunctional cyclooctynes on Si(001). *J. Phys. Chem. C* **2016**, *120*, 26284–26289.

[45] Länger, C.; Heep, J.; Nikodemiak, P.; Bohamud, T.; Kirsten, P.; Höfer, U.; Koert, U.; Dürr, M. Formation of Si/organic interfaces using alkyne-functionalized cyclooctynes—precursor-mediated adsorption of linear alkynes versus direct adsorption of cyclooctyne on Si(001). *J. Phys.: Condens. Matter* **2018**, *31*, 034001.

[46] Decher, G.; Hong, J.-D. Buildup of ultrathin multilayer films by a self-assembly process, 1 consecutive adsorption of anionic and cationic bipolar amphiphiles on charged surfaces. *Makromol. Chem., Macromol. Symp.* **1991**, *46*, 321–327.

[47] Willenbockel, M.; Lüftner, D.; Stadtmüller, B.; Koller, G.; Kumpf, C.; Soubatch, S.; Puschnig, P.; Ramsey, M. G.; Tautz, F. S. The interplay between interface structure, energy level alignment and chemical bonding strength at organic–metal interfaces. *Phys. Chem. Chem. Phys.* **2015**, *17*, 1530–1548.

[48] Klein, B. P.; Morbec, J. M.; Franke, M.; Greulich, K. K.; Sachs, M.; Parhizkar, S.; Bocquet, F. C.; Schmid, M.; Hall, S. J.; Maurer, R. J.; Meyer, B.; Tonner, R.; Kumpf, C.; Kratzer, P.; Gottfried, J. M. Molecule–metal bond of alternant versus nonalternant aromatic systems on coinage metal surfaces: naphthalene versus azulene on Ag(111) and Cu(111). *J. Phys. Chem. C* **2019**, *123*, 29219–29230.

[49] Staub, R.; Iannuzzi, M.; Khaliullin, R. Z.; Steinmann, S. N. Energy decomposition analysis for metal surface–adsorbate interactions by block localized

wave functions. *J. Chem. Theory Comput.* **2019**, *15*, 265–275.

[50] Hammer, B.; Nørskov, J. Electronic factors determining the reactivity of metal surfaces. *Surf. Sci.* **1995**, *343*, 211 – 220.

[51] Jerabek, P.; Roesky, H. W.; Bertrand, G.; Frenking, G. Coinage metals binding as main group elements: structure and bonding of the carbene complexes [TM(cAAC)2] and [TM(cAAC)2]+ (TM = Cu, Ag, Au). *J. Am. Chem. Soc.* **2014**, *136*, 17123–17135.

[52] Davey, W. P. Precision measurements of the lattice constants of twelve common metals. *Phys. Rev.* **1925**, *25*, 753–761.

[53] Ruban, A.; Hammer, B.; Stoltze, P.; Skriver, H.; Nørskov, J. Surface electronic structure and reactivity of transition and noble metals. *J. Mol. Catal. A: Chem.* **1997**, *115*, 421 – 429.

[54] Klein, B. P.; Harman, S. E.; Ruppenthal, L.; Ruehl, G. M.; Hall, S. J.; Carey, S. J.; Herritsch, J.; Schmid, M.; Maurer, R. J.; Tonner, R.; Campbell, C. T.; Gottfried, J. M. Enhanced bonding of pentagon–heptagon defects in graphene to metal surfaces: insights from the adsorption of azulene and naphthalene to Pt(111). *Chem. Mater.* **2020**, *32*, 1041–1053.

[55] Galanakis, I.; Papanikolaou, N.; Dederichs, P. Applicability of the broken-bond rule to the surface energy of the FCC metals. *Surf. Sci.* **2002**, *511*, 1 – 12.

[56] Fan, Q.; Gottfried, J. M.; Zhu, J. Surface-catalyzed C–C covalent coupling strategies toward the synthesis of low-dimensional carbon-based nanostructures. *Acc. Chem. Res.* **2015**, *48*, 2484–2494.

[57] Senge, M. O. Exercises in molecular gymnastics—bending, stretching and twisting porphyrins. *Chem. Commun.* **2006**, 243–256.

[58] Gottfried, J. M. Surface chemistry of porphyrins and phthalocyanines. *Surf. Sci. Rep.* **2015**, *70*, 259 – 379.

[59] Hieringer, W.; Flechtner, K.; Kretschmann, A.; Seufert, K.; Auwärter, W.; Barth, J. V.; Görling, A.; Steinrück, H.-P.; Gottfried, J. M. The surface trans effect: influence of axial ligands on the surface chemical bonds of adsorbed metalloporphyrins. *J. Am. Chem. Soc.* **2011**, *133*, 6206–6222.

[60] Wong, C.-H.; Zimmerman, S. C. Orthogonality in organic, polymer, and supramolecular chemistry: from Merrifield to click chemistry. *Chem. Commun.* **2013**, *49*, 1679–1695.

[61] Kolb, H. C.; Finn, M. G.; Sharpless, K. B. Click chemistry: diverse chemical function from a few good reactions. *Angew. Chem. Int. Ed.* **2001**, *40*, 2004–2021.

[62] Escorihuela, J.; Marcelis, A. T. M.; Zuilhof, H. Metal-free click chemistry reactions on surfaces. *Adv. Mater. Interfaces* **2015**, *2*, 1500135.

[63] Rostovtsev, V. V.; Green, L. G.; Fokin, V. V.; Sharpless, K. B. A stepwise Huisgen cycloaddition process: copper(I)-catalyzed regioselective "ligation" of azides and terminal alkynes. *Angew. Chem. Int. Ed.* **2002**, *41*, 2596–2599.

[64] Thalhammer, F.; Wallfahrer, U.; Sauer, J. Reaktivität einfacher offenkettiger und cyclischer Dienophile bei Diels-Alder-Reaktionen mit inversem Elektronenbedarf. *Tetrahedron Lett.* **1990**, *31*, 6851 – 6854.

[65] Ruff, F.; Farkas, Ö. Concerted SN2 mechanism for the hydrolysis of acid chlorides: comparisons of reactivities calculated by the density functional theory with experimental data. *J. Phys. Org. Chem.* **2011**, *24*, 480–491.

[66] Dong, J.; Krasnova, L.; Finn, M. G.; Sharpless, K. B. Sulfur(VI) fluoride exchange (SuFEx): another good reaction for click chemistry. *Angew. Chem. Int. Ed.* **2014**, *53*, 9430–9448.

[67] Gahtory, D.; Sen, R.; Pujari, S.; Li, S.; Zheng, Q.; Moses, J. E.; Sharpless, K. B.; Zuilhof, H. Quantitative and orthogonal formation and reactivity of SuFEx platforms. *Chem. Eur. J.* **2018**, *24*, 10550–10556.

[68] Bergsman, D. S.; Closser, R. G.; Bent, S. F. Mechanistic studies of chain termination and monomer absorption in molecular layer deposition. *Chem. Mater.* **2018**, *30*, 5087–5097.

[69] Raupach, M. Quantenchemische Untersuchungen zur chemischen Bindung an Oberflächen. Ph.D. thesis, Philipps Universität Marburg, 2015.

[70] Pecher, L. Adsorption dynamics and bonding analysis of organic molecules on silicon(001) surfaces. Ph.D. thesis, Philipps Universität Marburg, 2017.

[71] Sueoka, K.; Kamiyama, E.; Śpiewak, P.; Vanhellemont, J. Review—Properties of intrinsic point defects in Si and Ge assessed by density functional theory. *ECS J. Solid State Sci. Technol.* **2016**, *5*, P3176–P3195.

[72] Roberts, N.; Needs, R. J. Total energy calculations of missing dimer reconstructions on the silicon (001) surface. *J. Phys.: Condens. Matter* **1989**, *1*, 3139–3143.

[73] Wang, J.; Arias, T. A.; Joannopoulos, J. D. Dimer vacancies and dimer-vacancy complexes on the Si(100) surface. *Phys. Rev. B* **1993**, *47*, 10497–10508.

[74] Glaser, T.; Meinecke, J.; Länger, C.; Heep, J.; Koert, U.; Dürr, M. Solution-based alkyne–azide coupling on functionalized Si(001) prepared under UHV conditions. *J. Phys. Chem. C* DOI: 10.1021/acs.jpcc.0c11353.

[75] Klamt, A.; Schüürmann, G. COSMO: a new approach to dielectric screening in solvents with explicit expressions for the screening energy and its gradient. *J. Chem. Soc., Perkin Trans. 2* **1993**, 799–805.

[76] Cancès, E.; Mennucci, B. New applications of integral equations methods for solvation continuum models: ionic solutions and liquid crystals. *J. Math. Chem.* **1998**, *23*, 309–326.

[77] Biswas, R.; Hamann, D. R. Simulated annealing of silicon atom clusters in Langevin molecular dynamics. *Phys. Rev. B* **1986**, *34*, 895–901.

[78] Gaus, M.; Cui, Q.; Elstner, M. DFTB3: extension of the self-consistent-charge density-functional tight-binding method (SCC-DFTB). *J. Chem. Theory Comput.* **2011**, *7*, 931–948.

[79] Aviv-Harel, I.; Gross, Z. Aura of corroles. *Chem. Eur. J.* **2009**, *15*, 8382–8394.

[80] Zaitsev, N. L.; Jakob, P.; Tonner, R. Structure and vibrational properties of the PTCDA/Ag(1 1 1) interface: bilayer versus monolayer. *J. Phys.: Condens. Matter* **2018**, *30*, 354001.

[81] Jensen, F. *Introduction to computational chemistry*, 2nd ed.; Wiley-VCH, 2007.

[82] Koch, W.; Holthausen, M. C. *A chemist's guide to density functional theory*; Wiley-VCH, 2001.

[83] Szabo, A.; Ostlund, N. S. *Modern quantum chemistry*; Dover Publications, 1996.

[84] Ashcroft, N. W.; Mermin, N. D. *Solid state physics*, 1st ed.; Brooks Cole, 1976.

[85] Cramer, C. J. *Essentials of computational chemistry*, 2nd ed.; Wiley, 2004.

[86] de Broglie, L. Recherches sur la théorie des quanta. *Ann. Phys.* **1925**, *10*, 22–128.

[87] Schrödinger, E. An undulatory theory of the mechanics of atoms and molecules. *Phys. Rev.* **1926**, *28*, 1049–1070.

[88] Born, M.; Oppenheimer, R. Zur Quantentheorie der Molekeln. *Ann. Phys.* **1927**, *389*, 457–484.

[89] Hättig, C.; Tew, D. P.; Helmich, B. Local explicitly correlated second- and third-order Møller–Plesset perturbation theory with pair natural orbitals. *J. Chem. Phys.* **2012**, *136*, 204105.

[90] Schmitz, G.; Hättig, C. Perturbative triples correction for local pair natural orbital based explicitly correlated CCSD(F12*) using Laplace transformation techniques. *J. Chem. Phys.* **2016**, *145*, 234107.

[91] Hohenberg, P.; Kohn, W. Inhomogeneous electron gas. *Phys. Rev.* **1964**, *136*, B864–B871.

[92] Kohn, W.; Sham, L. J. Self-consistent equations including exchange and correlation effects. *Phys. Rev.* **1965**, *140*, A1133–A1138.

[93] Grimme, S.; Antony, J.; Ehrlich, S.; Krieg, H. A consistent and accurate ab initio parametrization of density functional dispersion correction (DFT-D) for the 94 elements H-Pu. *J. Chem. Phys.* **2010**, *132*, 154104.

[94] Grimme, S.; Ehrlich, S.; Goerigk, L. Effect of the damping function in dispersion corrected density functional theory. *J. Comput. Chem.* **2011**, *32*, 1456–1465.

[95] Banerjee, J.; Behnle, S.; Galbraith, M. C. E.; Settels, V.; Engels, B.; Tonner, R.; Fink, R. F. Comparison of the periodic slab approach with the finite cluster description of metal–organic interfaces at the example of PTCDA on Ag(110). *J. Comput. Chem.* **2018**, *39*, 844–852.

[96] Tracey, D. F.; Delley, B.; McKenzie, D. R.; Warschkow, O. Molecular adsorption on silicon (001): a systematic evaluation of size effects in slab and cluster models. *AIP Adv.* **2013**, *3*, 042117.

[97] Bloch, F. Über die Quantenmechanik der Elektronen in Kristallgittern. *Z. Phys.* **1929**, *52*, 555–600.

[98] Einstein, A. Zur Elektrodynamik bewegter Körper. *Ann. Phys.* **1905**, *322*, 891–921.

[99] Dirac, P. A. M.; Fowler, R. H. The quantum theory of the electron. *Proc. R. Soc. A* **1928**, *117*, 610–624.

[100] van Lenthe, E.; Baerends, E. J.; Snijders, J. G. Relativistic regular two-component Hamiltonians. *J. Chem. Phys.* **1993**, *99*, 4597–4610.

[101] Blöchl, P. E. Projector augmented-wave method. *Phys. Rev. B* **1994**, *50*, 17953–17979.

[102] Feynman, R. P. Forces in molecules. *Phys. Rev.* **1939**, *56*, 340–343.

[103] Sheppard, D.; Xiao, P.; Chemelewski, W.; Johnson, D. D.; Henkelman, G. A generalized solid-state nudged elastic band method. *J. Chem. Phys.* **2012**, *136*, 074103.

[104] Henkelman, G.; Uberuaga, B. P.; Jónsson, H. A climbing image nudged elastic band method for finding saddle points and minimum energy paths. *J. Chem. Phys.* **2000**, *113*, 9901–9904.

[105] Tomasi, J.; Mennucci, B.; Cammi, R. Quantum mechanical continuum solvation models. *Chem. Rev.* **2005**, *105*, 2999–3094.

[106] Andreussi, O.; Dabo, I.; Marzari, N. Revised self-consistent continuum solvation in electronic-structure calculations. *J. Chem. Phys.* **2012**, *136*, 064102.

[107] Reed, A. E.; Weinstock, R. B.; Weinhold, F. Natural population analysis. *J. Chem. Phys.* **1985**, *83*, 735–746.

[108] Philipsen, P. H. T.; Baerends, E. J. Role of the Fermi surface in adsorbate–metal interactions: an energy decomposition analysis. *J. Phys. Chem. B* **2006**, *110*, 12470–12479.

[109] Tersoff, J.; Hamann, D. R. Theory of the scanning tunneling microscope. *Phys. Rev. B* **1985**, *31*, 805–813.

[110] Perdew, J. P.; Burke, K.; Ernzerhof, M. Generalized gradient approximation made simple. *Phys. Rev. Lett.* **1996**, *77*, 3865–3868.

[111] Kresse, G.; Hafner, J. Ab initio molecular dynamics for liquid metals. *Phys. Rev. B* **1993**, *47*, 558.

[112] Kresse, G.; Furthmüller, J. Efficiency of ab-initio total energy calculations for metals and semiconductors using a plane-wave basis set. *Comput. Mater. Sci.* **1996**, *6*, 15.

[113] Kresse, G.; Furthmüller, J. Efficient iterative schemes for ab initio total-energy calculations using a plane-wave basis set. *Phys. Rev. B* **1996**, *54*, 11169–11186.

[114] Transition State Tools for VASP, Henkelman group, university of texas at austin, http://theory.cm.utexas.edu/vtsttools/index.html, retrieved 26.01.2021.

[115] AMS2019, SCM Theoretical Chemistry, Vrije Universiteit, Amsterdam, The Netherlands, http://www.scm.com, retrieved 26.01.2021.

[116] van Lenthe, E.; Baerends, E. J. Optimized Slater-type basis sets for the elements 1–118. *J. Comput. Chem.* **2003**, *24*, 1142–1156.

[117] Furche, F.; Ahlrichs, R.; Hättig, C.; Klopper, W.; Sierka, M.; Weigend, F. Turbomole. *Wiley Interdiscip. Rev. Comput. Mol. Sci.* **2014**, *4*, 91–100.

[118] Weigend, F.; Ahlrichs, R. Balanced basis sets of split valence, triple zeta valence and quadruple zeta valence quality for H to Rn: design and assessment of accuracy. *Phys. Chem. Chem. Phys.* **2005**, *7*, 3297–3305.

[119] Hanwell, M. D.; Curtis, D. E.; Lonie, D. C.; Vandermeersch, T.; Zurek, E.; Hutchison, G. R. Avogadro: an advanced semantic chemical editor, visualization, and analysis platform. *J. Cheminf.* **2012**, *4*, 17.

[120] Chemcraft - graphical software for visualization of quantum chemistry computations, https://www.chemcraftprog.com, retrieved 26.01.2021.

[121] Larsen, A. H.; Mortensen, J. J.; Blomqvist, J.; Castelli, I. E.; Christensen, R.; Dułak, M.; Friis, J.; Groves, M. N.; Hammer, B.; Hargus, C.; Hermes, E. D.; Jennings, P. C.; Jensen, P. B.; Kermode, J.; Kitchin, J. R.; Kolsbjerg, E. L.; Kubal, J.; Kaasbjerg, K.; Lysgaard, S.; Maronsson, J. B.; Maxson, T.;

Olsen, T.; Pastewka, L.; Peterson, A.; Rostgaard, C.; Schiøtz, J.; Schütt, O.; Strange, M.; Thygesen, K. S.; Vegge, T.; Vilhelmsen, L.; Walter, M.; Zeng, Z.; Jacobsen, K. W. The atomic simulation environment-a python library for working with atoms. *J. Phys. Condens. Matter.* **2017**, *29*, 273002.

[122] p4vasp, the VASP Visualization Tool, http://www.p4vasp.at, retrieved 26.01.2021.

[123] Gnuplot, http://www.gnuplot.info/, retrieved 26.01.2021.

[124] QtiPlot - Data Analysis and Scientific Visualisation, https://www.qtiplot.com/, retrieved 26.01.2021.

[125] Momma, K.; Izumi, F. *VESTA3* for three-dimensional visualization of crystal, volumetric and morphology data. *J. Appl. Crystallogr.* **2011**, *44*, 1272–1276.

[126] Inkscape, https://inkscape.org/, retrieved 26.01.2021.

[127] LaTeX – A document preparation system, https://www.latex-project.org/, retrieved 26.01.2021.

[128] Ghiringhelli, L. M.; Carbogno, C.; Levchenko, S.; Mohamed, F.; Huhs, G.; Lüders, M.; Oliveira, M.; Scheffler, M. Towards efficient data exchange and sharing for big-data driven materials science: metadata and data formats. *npj Comput. Mater.* **2017**, *3*, 46.

Alphabetical List of Abbreviations

AAC	Azide-alkyne coupling
ACE	Acyl chloride mediated esterification
ADF	Amsterdam density functional
AMS	Amsterdam modeling suite
ASE	Atomic simulation environment
BJ	Becke-Johnson damping
BZ	Brillouin zone
CC	Coupled cluster
CCSD	Coupled cluster singles and doubles
CCSD(T)	Coupled cluster singles and doubles plus perturbative triples
CI-NEB	Climbing-image nudged elastic band
D3	Grimme dispersion version 3
DFT	Density functional theory
DOS	Density of states
DV	Bonded dimer vacancy
EDA	Energy decomposition analysis
ESC	Eliminated small component
FCC	Face centered cubic
GGA	Generalized gradient approximation
GTO	Gaussian type orbital
HF	Hartree-Fock
IEDDA	Inverse electron demand Diels-Alder
KS	Kohn-Sham
LDA	Local density approximation
LDOS	Local density of states
LMO	Localized molecular orbital
NAO	Natural atomic orbital
NBO	Natural bonding orbital
NEB	Nudged elastic band
NOCV	Natural orbitals for chemical valence

NPA	Natural population analysis
OSV	Orbital-specific virtual
PAW	Projector augmented wave
PBC	Periodic boundary conditions
PCM	Polarizable continuum model
pEDA	Periodic energy decomposition analysis
PES	Potential energy surface
PNO	Pair natural orbital
PP	Pseudopotential
PW	Plane wave
SCF	Self-consistent field
SD	Slater determinant
STM	Scanning tunneling microscopy
STO	Slater type orbital
SuFEx	Sulfur (VI) fluoride exchange
TS	Transition state
VASP	Vienna ab initio simulation package
ZORA	Zeroth order regular approximation

Acknowledgments - Danksagungen

Zunächst möchte ich Prof. Ralf Tonner für die Auswahl dieses spannenden Themas und für die Betreuung meiner Doktorarbeit danken. Ralf war es auch, der mir im Rahmen der Wahlpflichtvorlesung im fünften Semester ersten Einblicke in die theoretische Chemie gewährte. Mein Interesse war geweckt und es sollte sowohl eine Bachelor- als auch eine Masterarbeit in seiner noch jungen Arbeitsgruppe in Marburg folgen. Dass diese Zusammenarbeit nun in einer Promotion gipfeln konnte verdanke ich insbesondere Ralfs engagiertem Einsatz als Mentor, bei gleichzeitiger Bereitschaft mir wissenschaftliche Freiheiten einzuräumen. Ich habe die Zeit während der Promotion auf akademischer und persönlicher Ebene sehr genossen. Die Betreuung war auch neben der fleißigen Arbeit an der eigenen Karriere immer erstklassig. Drei Rufe innerhalb eines Jahres sprechen für sich und so darf ich nun mit Recht behaupten an drei verschiedenen Universitäten promoviert zu haben. Einen besseren Doktorvater hätte ich mir nicht wünschen können!

Auch gilt mein Dank dem Sonderforschungsbereich 1083 “Struktur und Dynamik innerer Grenzflächen” der nicht nur die Finanzierung, sondern auch den Rahmen für wissenschaftlichen Austausch bereitstellte. Aus diesem kollaborativen Umfeld entstanden einige fruchtbare Kooperationen. Hier sind insbesondere Prof. Michael Gottfried, der auch bereit war das Zweitgutachten dieser Arbeit zu übernehmen, sowie die weiteren Mitglieder der Prüfungskommission Prof. Michael Dürr und Prof. Ulrich Koert zu nennen.

Das Arbeitsumfeld in den Arbeitsgruppen der theoretischen Chemie in Marburg war sehr angenehm und ich danke allen Kollegen für die wissenschaftlich anregenden Diskussionen sowie die geselligen Runden bei Kaffee und Kuchen oder unterwegs auf Konferenzen. Weiterhin sei meinen Forschungspraktikanten für ihre Mitarbeit an Projekten und für das entgegengebrachte Vertrauen gedankt. Danken möchte ich auch allen Korrekturlesern dieser Arbeit für ihre wertvollen Ratschläge. Nicht zuletzt wäre diese Arbeit ohne die technische Unterstützung von Thomas “Reuti” Reuter sicherlich weniger umfangreich ausgefallen. Danke für die geduldige Hilfe beim installieren von Programmen auf den Hochleistungsrechnern und dem Beheben von allerlei Problemen! Weitere Rechnerinfrastruktur und Hilfestellung wurde vom

Höchstleistungsrechenzentrum Stuttgart, Center for Scientific Computing Frankfurt und den Universitätsrechenzentren in Marburg und Regensburg bereitgestellt.
Auch außerhalb der Universität haben mich einige Menschen begleitet, für deren Unterstützung ich mich an dieser Stelle herzlich bedanken möchte. Der größte Anteil gebührt meinen Eltern und meiner Schwester, die mir immer das Gefühl gegeben haben ein Zuhause zu haben. Dass dies nicht nur eine leere Floskel ist durfte ich während der virusbedingten Wirrungen im Jahr 2020 erfahren, als ich wegen verhängter Ausgangssperren kurzfristig "obdachlos" wurde. Danke Mama, dass du mich für einige Wochen wieder bei dir aufgenommen hast. Danke Papa, dass du mich bei den zahlreichen Umzügen in Marburg, Regensburg und zuletzt Leipzig tatkräftig unterstützt hast.
Natürlich kann der Mensch nicht nur arbeiten, auch wenn es Wissenschaftlern manchmal schwer fallen mag sich loszureißen. Meiner Wohngemeinschaft in der Bahnhofstraße danke ich für die Zerstreuung mit Spiele- und Serienabenden sowie den anderen gemeinsamen Unternehmungen. Ebenso blicke ich gerne auf diverse Unisport-Kurse zurück. Die Tournierfahrten zur Deutschen Bouncerball-Meisterschaft waren immer wieder ein tolles Erlebnis, welches ich in Zukunft sehr vermissen werde. Zu guter Letzt möchte ich mich noch bei den Organisatoren der Promovierendenwochenenden und -Stammtische in Marburg bedanken. Der überfachliche Austausch zu den Herausforderungen der Promotion mit "Leidensgenossen" war äußerst wertvoll.

Appendix A

Manuscripts: Organic / Inorganic Semiconductor

Permissions to reprint full-text publications have been obtained from the right holders where necessary.

Adsorption of methyl-substituted benzylazide on Si(001): reaction channels and final configurations: Copyright (2020) American Chemical Society.

Combined XPS and DFT investigation of the adsorption modes of methyl enol ether functionalized cyclooctyne on Si(001): Copyright (2020) The Authors. ChemPhysChem published by Wiley-VCH GmbH.

Click chemistry in ultra-high vacuum - tetrazine coupling with methyl enol ether covalently linked to Si(001): Copyright (2021) The Authors. Published by Wiley-VCH GmbH.

Complementary base lowers the barrier in SuFEx click chemistry for primary amine nucleophiles: Copyright (2020) American Chemical Society. ACS Author Choice.

Efficient hierarchical models for reactivity of organic layers on semiconductor surfaces: Copyright (2021) The Authors. Journal of Computational Chemistry published by Wiley Periodicals LLC.

Organic functionalization at the Si(001) dimer vacancy defect – structure, bonding and reactivity: Copyright (2021) The Authors. Published by American Chemical Society.

THE JOURNAL OF PHYSICAL CHEMISTRY C

pubs.acs.org/JPCC Article

Adsorption of Methyl-Substituted Benzylazide on Si(001): Reaction Channels and Final Configurations

Julian Heep, Jan-Niclas Luy, Christian Länger, Jannick Meinecke, Ulrich Koert, Ralf Tonner,* and Michael Dürr*

Cite This: J. Phys. Chem. C 2020, 124, 9940–9946

Read Online

ACCESS | Metrics & More | Article Recommendations | Supporting Information

ABSTRACT: The reaction of a methyl-substituted benzylazide on the silicon (001) surface was investigated by means of X-ray photoelectron spectroscopy (XPS), scanning tunneling microscopy (STM), and density functional theory (DFT)-based computations. It was found that the reaction takes place via an intermediate state, which could be experimentally observed at low temperatures. XPS analysis showed that at temperatures of 150 K and above, the azide further reacts on the silicon surface via abstraction of N_2. The final state sees the remaining nitrogen atom of the adsorbate binding covalently to the surface. In the STM images, this final state is associated with two different adsorption configurations. In comparison with DFT calculations, these two configurations are assigned to the molecule being bound via the nitrogen atom only and to a configuration with the molecule bound to the substrate via the nitrogen atom and carbon ring simultaneously.

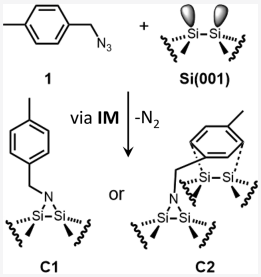

INTRODUCTION

The preparation of well-defined organic structures on semiconductor surfaces can play an important role in various fields of applications such as microelectronics or biosensor technology.[1] Azides are of interest as building blocks for this kind of organic surface functionalization, in particular, because of reactions such as alkyne−azide coupling used in click chemistry.[2] The latter might be also employed for the formation of well-ordered organic multilayers on semiconductor surfaces, in particular on Si(001), the technologically most important semiconductor surface.[3−6] It is thus important to investigate the reaction of azides on Si(001). Earlier experiments and calculations for unsubstituted benzylazide on Si(001) showed that the reaction proceeds via an intermediate involving the intact molecule. N_2 elimination leads then to the final state with the molecule attached to the silicon via the remaining nitrogen atom.[7,8]

In this work, we show by means of X-ray photoelectron spectroscopy (XPS), scanning tunneling microscopy (STM), and density functional theory (DFT)-based computations that the reaction of a methyl-substituted benzylazide (1-(azidomethyl)-4-methylbenzene (**1**), $C_8H_9N_3$, see Figure 1) on Si(001) is more complex than these earlier findings suggest. In particular, in the STM images of the final configurations, we observed two very different features; from XPS analysis, we found that both configurations are the result of a reaction via N_2 elimination. DFT calculations revealed the associated reaction pathways and adsorption configurations; in particular, two final configurations were identified. Both configurations are covalently bound to the substrate via the remaining nitrogen atom of the adsorbate, but one configuration shows additional interaction between the benzyl ring and silicon surface.

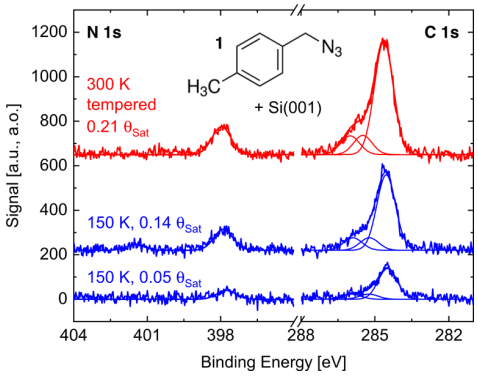

Figure 1. N 1s and C 1s spectra of **1** on Si(001) after adsorption at 150 K. Blue: measurement at 150 K for two different coverages. Red: sample tempered to 300 K and measured at 150 K. The ratio between the sensitivity-corrected N 1s and C 1s signals is 1:8 for all measurements. The three profiles fitted in each C 1s signal show a ratio of 1:1:6.

Received: February 5, 2020
Revised: April 8, 2020
Published: April 17, 2020

EXPERIMENTAL AND COMPUTATIONAL METHODS

The XPS and STM experiments were performed in the same UHV chamber; thus, both methods could be used on one and the same sample without additional transfer between two chambers. Base pressure was $<1 \times 10^{-10}$ mbar. Silicon samples (n-doped, 1×10 mm^2, covered by native oxide) were degassed at 700 K and heated by repeated direct current heating cycles to temperatures >1450 K.[9,10] The well-ordered 2×1 reconstruction of the Si(001) surface was achieved by cooling the sample with low rates ≤ 1 K s^{-1}. For XPS measurements, an Al K_α X-ray source with a monochromator (Omicron XM1000) and hemispherical analyzer (Omicron EA125) were used. All spectra were referenced to the Si $2p_{3/2}$ peak with a binding energy of 99.4 eV.[11] All spectra were fitted using superpositions of single Voigt profiles with a FWHM of 0.9 eV, which was obtained as a typical linewidth for such systems in this setup.[5,12] For STM measurements, a variable temperature STM was used (Omicron VT-STM); all data shown are representative for at least two sets of data taken, e.g., with two different tips. Adsorption was performed, and STM images were taken at both room temperature and 50 K. Following a general procedure, compound **1** was prepared from the corresponding benzyl bromide by nucleophilic substitution with sodium azide.[13,14] It was dosed from the vapor phase in a test tube via a leak valve into the UHV chamber. Gas doses indicated for the different measurements refer to uncorrected ion gauge measurements.

DFT-based calculations were performed with the Vienna ab initio simulation package (VASP 5.4.4)[15−17] using the PBE[18] exchange correlation functional and setting the plane wave energy cutoff to 400 eV. A total energy difference of at least 10^{-5} eV and "accurate" precision are used for SCF convergence. For structural optimization, the force convergence criterion has been set to 10^{-2} eV Å^{-1}. Standard PAW-pseudopotentials[19] PBE.54 with a large core configuration are used to speed up the calculations. A Γ-centered $2 \times 2 \times 1$ *k*-mesh was chosen together with a setup of Si(001) slabs (six layers, two bottom layers frozen and terminated with hydrogen atoms) as determined in previous work.[20] All structures were optimized at the PBE level, while dispersion effects were considered via the DFT-D3 scheme including an improved damping function.[21] Transition-state structures were first approximated by the climbing image nudged elastic band approach[22,23] and subsequently optimized with the dimer method. Thermodynamic corrections were obtained by calculating the vibrational partition function in the harmonic oscillator, rigid rotor, and ideal gas approximations.[20] A script interfacing VASP with the atomic simulation environment (ASE)[24] to derive Gibbs energies is given in the Supporting Information. Energies presented are Gibbs energies based on structural optimization and thermodynamic partition functions with PBE-D3 on top of electronic energies determined with the more accurate range-separated hybrid functional HSE06, also including DFT-D3 correction.[25] STM simulations were carried out using the Tersoff−Hamann approximation[26] with HSE06.

RESULTS AND DISCUSSION

Figure 1 shows the XPS data of the methyl-substituted benzylazide **1** on Si(001) adsorbed at 150 K. Both the N 1s and C 1s spectra are depicted. The two spectra at the bottom (blue) show the measurements at 150 K for coverages of 5 and 14% of the saturation coverage (Θ_{Sat}), and the topmost spectrum (red) was acquired after tempering the sample to room temperature (measurement at 150 K). Qualitatively, all three measurements show the same behavior, thus indicating no intermediate state at temperatures of 150 K or higher. Comparing the cross section-corrected signal intensities of N 1s and C 1s, a ratio of approximately 1:8 is obtained, indicating the loss of two nitrogen atoms as the intact molecule consists of eight carbon and three nitrogen atoms. This is in accordance with the literature reporting the reaction of unsubstituted benzylazide on Si(001) via N_2 elimination.[7]

The N 1s spectra show one main peak at 398 eV, which we attribute to nitrogen bound to the silicon surface. The small peak at 401 eV (only at 150 K, 0.14 Θ_{Sat} and higher coverages) is attributed to the formation of physically bound aggregates at higher coverage eventually leading to multilayers. The C 1s signal is more complex. It shows a main peak at 284.6 eV and a shoulder to higher binding energies. Two additional profiles can be fitted in this area at 285.5 and 286.0 eV. The ratio of the intensity associated with these two components compared to the main peak is 1:1:6. They are attributed to the C atom of the methyl group and the one closest to the N atom, respectively. The spectra do not change with coverage up to saturation. Figure 2 shows the signal intensity of the C 1s and N 1s lines as a function of coverage when adsorption and measurement were performed at room temperature. After cross section correction, the C 1s signal was divided by 8 to visualize the ratio of 1:8, which was obtained for all coverages up to saturation within the accuracy of the measurement. The inset of Figure 2 shows a C 1s spectrum with a fit to the data, which includes an additional component at a binding energy associated with a carbon atom bound to the silicon surface (284.2 eV), indicating the possibility of a reaction of the carbon ring with the surface.

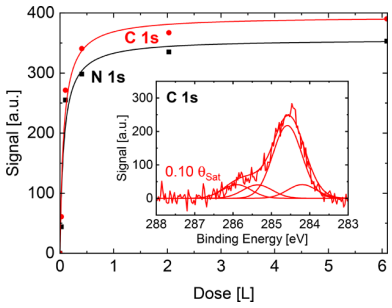

Figure 2. XPS intensity of the C 1s and N 1s spectra of **1** on Si(001) as a function of dose. The N 1s signal was cross section-corrected. The C 1s signal was divided by 8 for better comparison of the intensities. The signal saturates for higher doses. Inset: C 1s spectrum of a low dose with an additionally fitted profile at 284.2 eV. For details, see main text.

In addition to the XPS analysis, STM images were taken at room temperature and 50 K after adsorption at these temperatures. Figure 3a,b shows room-temperature STM images of the same region taken at sample bias values of +1 V (a) and −2 V (b). In Figure 3a, two kinds of features, a dark one and a bright one, are labeled with red and blue circles, respectively. These circles were copied from Figure 3b where two kinds of features could be detected as well. In this filled state image, the features labeled in blue appear in average less bright, whereas the features labeled in red are brighter. To quantify this brightness difference, the features were analyzed via line profiles. The deduced heights are shown in Figure 3c as a histogram. It clearly shows a bimodal distribution. In Figure 3c, we

https://dx.doi.org/10.1021/acs.jpcc.0c01009
J. Phys. Chem. C 2020, 124, 9940−9946

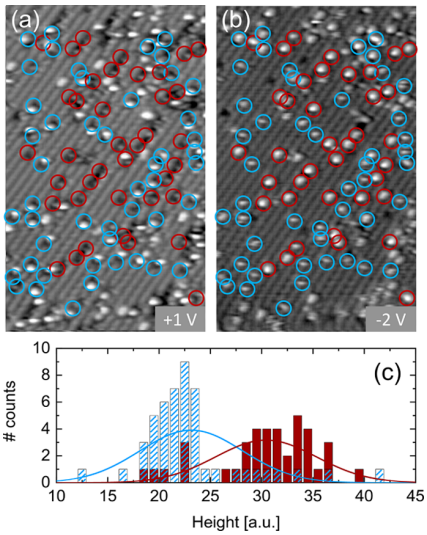

Figure 3. (a, b) Room-temperature STM images (28×18 nm^2, I_t = 0.5 nA) taken at +1 and −2 V after adsorption of **1** on Si(001), respectively. Labeled with red circles: dark features at positive sample bias. Labeled with blue circles: bright features at positive sample bias. (c) Histogram of the height distribution of the features at −2 V. Color assignment according to the STM image taken at positive sample bias. The two different species observed in (a) clearly show different height distributions in (b).

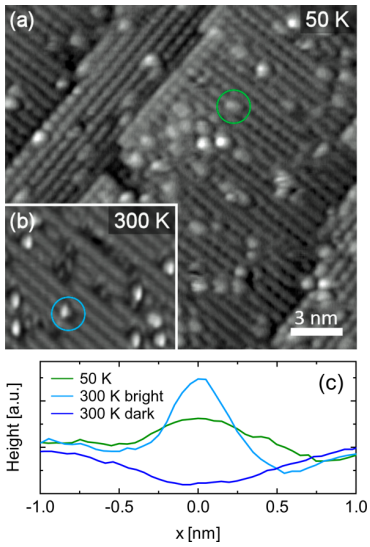

Figure 4. (a) STM image of 0.18 ML of **1** on Si(001). Adsorption and measurement were performed at 50 K (U_t = +1 V, I_t = 0.5 nA). Only bright features were detected. Scale bar applies for (a) and (b). (b) STM image for which adsorption and measurement were performed at room temperature (U_t = +1 V, I_t = 0.5 nA). Bright and dark features are observable. For better comparison, two representative bright features are labeled in (a) and (b) with green and blue circles, respectively. (c) Line scans through these features as well as through a dark feature (300 K) along the dimer rows are compared. The bright features observed at 50 K exhibit a smaller height when compared to the 300 K features (compare also Figure S1 in the Supporting Information). Additionally, bright 300 K features always show a small depression close to the protrusion (on the right side in the line scan shown). We can exclude a tip artefact as the depression is seen either on one or the other side of the bright feature.

additionally labeled if the respective feature was a dark one (red) or a bright one (blue) at positive sample bias. A good correlation between the different heights obtained from (b) and the appearance of the signatures as observed in (a) was found. The observation of these two kinds of features indicates a reaction of **1** to the silicon surface into two different final configurations. Both of them take place via N_2 elimination as the XPS results exclude that half of the products still contain three N atoms.

Figure 4a shows a representative STM image taken at a sample bias of +1 V at 50 K with 0.04 Θ_{Sat} of **1** adsorbed at the same temperature. In contrast to the images taken at room temperature (Figure 3a,b), there are only bright features visible. These features are also in clear difference to the bright features in Figures 3a and 4b as the latter ones always show a combination of bright and dark parts (compare labeled configurations in Figure 4a,b and line scans in Figure 4c). Furthermore, quantitative comparison of the height distributions of the features observed in the images taken at 50 and at 300 K shows two clearly separated distributions (Figure S1 in the Supporting Information). The signatures observed at 50 K are thus different to all features observed at 300 K. We therefore conclude that the reaction path contains an intermediate state, which is stable at 50 K and imaged in Figure 4a.

The variety of features experimentally observed for **1** on Si(001) as outlined above motivated our investigation of the surface adsorption and reactivity by DFT-based computations using a slab model that takes into account the full periodicity of the surface.[20] The surface was represented in the $c(4 \times 2)$ reconstruction, exhibiting buckled surface dimers of silicon.

The reaction path of **1** on Si(001) is shown in Figure 5, displaying the most important ground- and transition-state structures with their Gibbs energies relative to the separated molecule and surface. We discuss the more accurate HSE06-D3 data here, and electronic energy differences ΔE for the widely used PBE-D3 are given in Table S1 of the Supporting Information. Initially, **1** adsorbs barrierless into a very stable ($\Delta G = -263$ kJ mol^{-1}) [3 + 2] cycloaddition product, showing a five-membered ring with nearly symmetric Si−N bonds. This intermediate state (**IM**) can further decompose via N−N bond cleavage and a rather high barrier associated with the first transition-state structure (**TS1**) of $\Delta G^{\ddagger} = 142$ kJ mol^{-1} toward thermodynamically stable ($\Delta G = -346$ kJ mol^{-1}) first adsorption configuration (**C1**), showing a three-membered Si−N−Si ring and loss of N_2. A second adsorption configuration (**C2**) is accessible via a low-lying transition-state structure (**TS2**, $\Delta G^{\ddagger} = 29$ kJ mol^{-1}) and more stable by 50 kJ mol^{-1} compared to **C1**. This higher stability stems from an additional interaction of the benzyl moiety with the silicon dimer row, similar to the butterfly structure observed for benzene on Si(001).[27,28] Notably, this structure cannot be found using one-dimer cluster models of the Si(001) surface.

In light of these computational results, we can now understand the single feature observed in experiments at low temperatures to be **IM**, which is underlined by the similarity in the experimental and simulated STM images as shown in Figure 6.

Upon heating, two structures are observed in the experiment, which can be matched to the two adsorption configurations **C1** and **C2** in the computational investigations. If we compare the computed STM images of these two configurations with the experimental findings, we see brighter and darker features for positive sample bias voltage (Figure 7, top) stemming from **C1** and **C2**, respectively. For negative sample bias voltage, both

https://dx.doi.org/10.1021/acs.jpcc.0c01009
J. Phys. Chem. C 2020, 124, 9940−9946

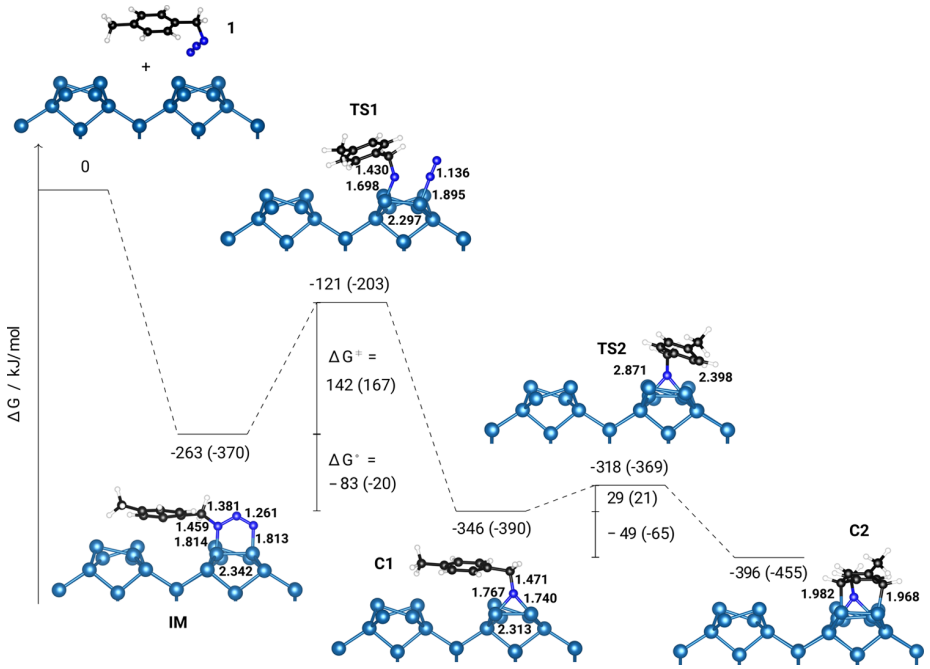

Figure 5. Computed adsorption and reaction profile of **1** on Si(001) $c(4 \times 2)$. Changes in Gibbs energy ΔG (electronic energies ΔE in parentheses) are given relative to the free molecule and surface. Energies computed with HSE06-D3 and thermodynamic correction terms using PBE-D3.

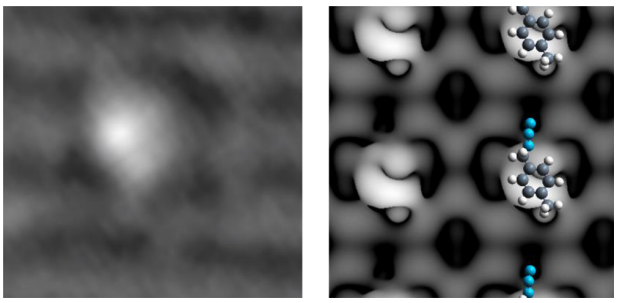

Figure 6. Comparison of the experimental low-temperature STM image (left, U = +1 V, I_t = 0.5 nA) and the computed image for **IM** (right, U = +1 V). The adsorbate structure is shown for clarity.

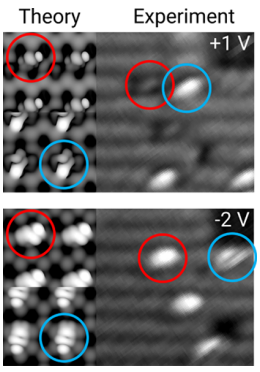

Figure 7. Comparison of STM measurement (right panels, I_t = 0.5 nA) and computed STM images (left panels) taken at RT at positive sample bias (top) and negative sample bias (bottom). The computed STM images show **C1** (blue circles, lower left subpanels) and **C2** (red circles, upper left subpanels).

configurations appear as oval-shaped bright spots in the simulation and experiment. **C1** and **C2** agree with the observed 8:1 C/N ratio in the XPS spectra. As shown in the inset of Figure 2, the C 1s spectrum is also compatible with an additional profile at lower binding energy, indicating the interaction of two carbon atoms (with reference to half of the number of the adsorbed molecules) with the silicon substrate (typical binding energy of 284.2 eV).[29,30] Based on the relatively small barrier between **C1** and **C2**, one might expect that the two configurations can convert from one into the other at room temperature. Indeed, in subsequent STM scans, we observe a small fraction of **C1** configurations to convert into **C2** configurations and vice versa.

In the following paragraphs, we discuss possible alternative reaction pathways and evaluate them in light of the experimental and computational data presented. Previous investigations of parent benzylazide also found the [3 + 2] cycloaddition of the azide moiety to the Si(001) surface.[7,31] In addition, a competing [1 + 2] cycloaddition reaction channel was found via a transient intermediate where the N–N bond is already broken. While both reactions were deemed possible, the [1 + 2] cycloaddition was proposed to be the dominant pathway based on spectroscopic signatures.[8,32] If we compare these results based on a cluster approach to surface modeling with our slab approach (electronic energies ΔE at the PBE-D3 level), we are able to locate the additional intermediate **IM2** with a single N atom bound to the electrophilic surface silicon atom (see Figure 8). However, a simple, barrierless rotation around the N–Si bond leads to another intermediate (**IM3** in Figure 8), which is less stable than **IM** by 125 kJ mol^{-1} on the same level of computation. The transition-state structure **TS3** found in the cluster approach is not a stationary point on the potential energy surface with the slab approach. The reaction with a low barrier ($\Delta E^{\ddagger}$ = 10 kJ mol^{-1}) toward adsorption configuration **C1** means that this pathway cannot completely be excluded. However, the configurations observed in the STM images taken after

https://dx.doi.org/10.1021/acs.jpcc.0c01009
J. Phys. Chem. C 2020, 124, 9940–9946

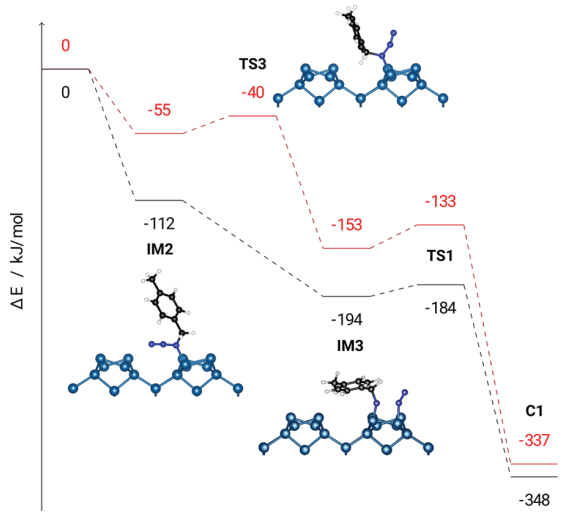

Figure 8. Alternative reaction pathways of **1** on Si(001) $c(4 \times 2)$ following the investigation by Bocharov et al. Red: cluster model data calculated with B3LYP/6-311+G(d,p), taken from ref 7. Black: slab model (this work) calculated with PBE-D3. Shown are electronic energy differences (ΔE). We like to note that the energies for **C1** in this figure and Table S1 differ slightly. We consider the final state to be reached when the product N_2 has left the reaction, while Bocharov et al. consider a weakly bound post-complex. To make the numbers comparable, we also give this value here for our slab approach (black curve).

adsorption at 50 K indicate a stable intermediate, neither in line with **IM2** nor with **IM3**.

Considering the higher stability of **C2**, it is surprising that both final configurations (**C1** and **C2**) are observed in the experiment. Thus, we searched for alternative reaction pathways, and indeed, a third final configuration (**C3**) is accessible from **C1**, showing a Si_{dimer}−N−$Si_{subsurface}$ ring (see Figure S2). Structures **C1** and **C3** are nearly isoenergetic, which could explain the observed two features in the STM measurement. However, the barrier toward **C3** is very high (**TS4**, $\Delta G^{\ddagger} = 203$ kJ mol^{-1}), and we thus conclude that although this structure would show very similar STM features compared to **C2** (see Figure S3), it is probably not accessible at the experimental conditions. An intermediate state bound only via the tolyl ring is another possibility we investigated since it is known that this state is accessible without a barrier.[33] The resulting structure, resembling the tight-bridge mode of benzene, is 185 kJ mol^{-1} less stable than **IM** (see Figure S4a). This structure would lead to different XPS features than observed experimentally, and the azide moiety cannot easily react any further. It can thus also be excluded. Similar considerations hold for the structure resembling the butterfly mode of benzene (see Figure S4b), which is 171 kJ mol^{-1} less stable than **IM**.

The adsorption configurations **C1** and **C2** could also be stabilized by additional dissociative adsorption of the methyl group on the neighboring surface dimers, which is a well-known reaction route for methyl-substituted aromatic compounds.[34] We evaluated these pathways and found activation energies of $\Delta G^{\ddagger} = 166$ kJ mol^{-1} for **C1** leading to **C1′** (Figure S5a) and $\Delta G^{\ddagger} = 140$ kJ mol^{-1} for **C2** leading to **C2′** (Figure S5c) with the HSE06-D3 functional. The latter barrier is comparable in size to the barrier found before for toluene (135 kJ mol^{-1}), although the methodology is not directly comparable (no dispersion effects considered).[34] Thus, for the dissociative adsorption of the methyl group across the dimer rows leading to **C1′**, the barrier is significantly higher compared to the reaction of **IM** to **C1** (see Figure 5), and resulting simulated STM images do not fit the experimental findings (dark features at positive sample bias, see Figure S5b in contrast to bright features for **C1**). For the dissociative adsorption along the dimer row leading to **C2′**, the barrier is very similar to the pathway from **IM** to **C1**; also, the simulated STM image is in reasonable agreement with experiments (Figure S5d). However, we can largely exclude this structure based on several experimental indications: While the fit of the XPS spectra is good when assuming two final configurations (Figure 2), all attempts to fit the spectrum with three species considerably worsened the agreement. Furthermore, the STM images clearly show two different species and not three. Lastly, the experimentally observed interconversion of configurations is not compatible with the large barrier for the back reaction of **C2′** to **C2** of $\Delta G^{\ddagger} = 258$ kJ mol^{-1}. Thus, we have considerable evidence to exclude the possibility of the further reaction of **C1** or **C2** via C−H activation of the methyl group. The results for **1** are thus comparable to the previous investigation of parent benzylazide.

From the DFT investigations, we thus conclude that the [3 + 2] cycloaddition product **IM** is the most likely species observed at low temperatures, which converts to adsorption configurations **C1** and **C2** at higher temperatures, exhibiting three-membered Si−N−Si rings (Figure 9).

CONCLUSIONS

Our combined approach has shown that both with respect to theory and experiment, a detailed analysis of the reaction of organic molecules on silicon can give further insight into the reaction mechanisms and the resulting products. In particular, combining spectroscopy such as XPS and microscopy on the molecular scale such as STM, the latter can give additional information on the products, which cannot be distinguished by means of spectroscopic methods. The two final states for the adsorption of methyl-substituted benzylazide on Si(001) were

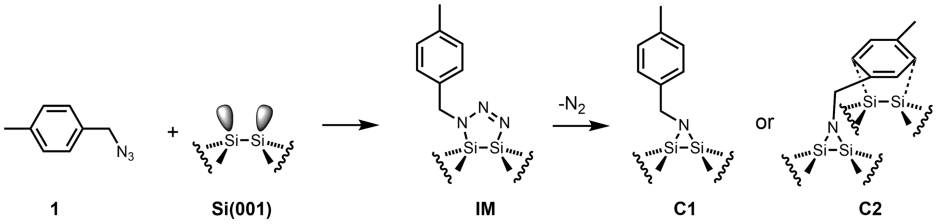

Figure 9. Schematic representation of the adsorption of **1** on Si(001) via intermediate **IM** into **C1** and **C2**. For easier inspection of the figure, the dimers are drawn in a symmetric configuration, and only the dimers involved in the reaction are shown.

https://dx.doi.org/10.1021/acs.jpcc.0c01009
J. Phys. Chem. C 2020, 124, 9940−9946

identified by means of DFT calculations using the slab approach, which can account for configurations beyond the adsorption on one single dimer. Several alternative pathways can be excluded by the combined insights from experiments and computations. In particular, with respect to the adsorption of multifunctional molecules and the synthesis of more complex molecular structures on the surface, such an approach as presented here will be of increased importance.

■ ASSOCIATED CONTENT

Supporting Information

The Supporting Information is available free of charge at https://pubs.acs.org/doi/10.1021/acs.jpcc.0c01009.

Detailed analysis of the STM data obtained at 50 K, calculated energies and configurations of alternative reaction pathways, information on the computational data repository, and python scripts interfacing VASP with ASE (PDF)

■ AUTHOR INFORMATION

Corresponding Authors

Ralf Tonner − *Fachbereich Chemie, Philipps-Universität Marburg, D-35032 Marburg, Germany;* orcid.org/0000-0002-6759-8559; Email: tonner@chemie.uni-marburg.de

Michael Dürr − *Institut für Angewandte Physik and Zentrum für Materialforschung, Justus-Liebig-Universität Giessen, D-35392 Giessen, Germany;* orcid.org/0000-0002-4676-8715; Email: michael.duerr@ap.physik.uni-giessen.de

Authors

Julian Heep − *Institut für Angewandte Physik and Zentrum für Materialforschung, Justus-Liebig-Universität Giessen, D-35392 Giessen, Germany*

Jan-Niclas Luy − *Fachbereich Chemie, Philipps-Universität Marburg, D-35032 Marburg, Germany*

Christian Länger − *Institut für Angewandte Physik and Zentrum für Materialforschung, Justus-Liebig-Universität Giessen, D-35392 Giessen, Germany*

Jannick Meinecke − *Fachbereich Chemie, Philipps-Universität Marburg, D-35032 Marburg, Germany*

Ulrich Koert − *Fachbereich Chemie, Philipps-Universität Marburg, D-35032 Marburg, Germany;* orcid.org/0000-0002-4776-8549

Complete contact information is available at: https://pubs.acs.org/10.1021/acs.jpcc.0c01009

Notes

The authors declare no competing financial interest.

■ ACKNOWLEDGMENTS

We acknowledge financial support by the Deutsche Forschungsgemeinschaft through SFB 1083, GRK 1782, and DU 1157/4-1. We thank HRZ Marburg, GOETHE-CSC Frankfurt, and HLR Stuttgart for computational resources.

■ REFERENCES

(1) Teplyakov, A. V.; Bent, S. F. Semiconductor surface functionalization for advances in electronics, energy conversion, and dynamic systems. *J. Vac. Sci. Technol., A* **2013**, *31*, No. 050810.

(2) Kolb, H. C.; Finn, M. G.; Sharpless, K. B. Click Chemistry: Diverse Chemical Function from a Few Good Reactions. *Angew. Chem., Int. Ed.* **2001**, *40*, 2004−2021.

(3) Münster, N.; Nikodemiak, P.; Koert, U. Chemoselective Layer-by-Layer Approach Utilizing Click Reactions with Ethynylcyclooctynes and Diazides. *Org. Lett.* **2016**, *18*, 4296−4299.

(4) Reutzel, M.; Münster, N.; Lipponer, M. A.; Länger, C.; Höfer, U.; Koert, U.; Dürr, M. Chemoselective Reactivity of Bifunctional Cyclooctynes on Si(001). *J. Phys. Chem. C* **2016**, *120*, 26284−26289.

(5) Länger, C.; Heep, J.; Nikodemiak, P.; Bohamud, T.; Kirsten, P.; Höfer, U.; Koert, U.; Dürr, M. Formation of Si/organic interfaces using alkyne-functionalized cyclooctynes—precursor-mediated adsorption of linear alkynes versus direct adsorption of cyclooctyne on Si(0 0 1). *J. Phys.: Condens. Matter* **2019**, *31*, No. 034001.

(6) Pecher, L.; Tonner, R. Computational analysis of the competitive bonding and reactivity pattern of a bifunctional cyclooctyne on Si(001). *Theor. Chem. Acc.* **2018**, *137*, 48.

(7) Bocharov, S.; Dmitrenko, O.; Mendéz de Leo, L. P.; Teplyakov, A. V. Azide Reactions for Controlling Clean Silicon Surface Chemistry: Benzylazide on Si(100)-2×1. *J. Am. Chem. Soc.* **2006**, *128*, 9300−9301.

(8) Leftwich, T. R.; Teplyakov, A. V. Cycloaddition Reactions of Phenylazide and Benzylazide on a Si(100)-2×1 Surface. *J. Phys. Chem. C* **2008**, *112*, 4297−4303.

(9) Schwalb, C. H.; Lawrenz, M.; Dürr, M.; Höfer, U. Real-space investigation of fast diffusion of hydrogen on Si(001) by a combination of nanosecond laser heating and STM. *Phys. Rev. B* **2007**, *75*, No. 085439.

(10) Mette, G.; Schwalb, C. H.; Dürr, M.; Höfer, U. Site-selective reactivity of ethylene on clean and hydrogen precovered Si(001). *Chem. Phys. Lett.* **2009**, *483*, 209−213.

(11) Reutzel, M.; Mette, G.; Stromberger, P.; Koert, U.; Dürr, M.; Höfer, U. Dissociative Adsorption of Diethyl Ether on Si(001) Studied by Means of Scanning Tunneling Microscopy and Photoelectron Spectroscopy. *J. Phys. Chem. C* **2015**, *119*, 6018−6023.

(12) Länger, C.; Bohamud, T.; Heep, J.; Glaser, T.; Reutzel, M.; Höfer, U.; Dürr, M. Adsorption of Methanol on Si(001): Reaction Channels and Energetics. *J. Phys. Chem. C* **2018**, *122*, 14756−14760.

(13) Song, W.; Zheng, N. Iridium-Catalyzed Highly Regioselective Azide-Ynamide Cycloaddition to Access 5-Amido Fully Substituted 1,2,3-Triazoles under Mild, Air, Aqueous, and Bioorthogonal Conditions. *Org. Lett.* **2017**, *19*, 6200−6203.

(14) Cilliers, P.; Seldon, R.; Smit, F. J.; Aucamp, J.; Jordaan, A.; Warner, D. F.; N'Da, D. D. Design, synthesis, and antimycobacterial activity of novel ciprofloxacin derivatives. *Chem. Biol. Drug Des.* **2019**, *94*, 1518−1536.

(15) Kresse, G.; Hafner, J. Ab initio molecular dynamics for liquid metals. *Phys. Rev. B* **1993**, *47*, 558−561.

(16) Kresse, G.; Furthmüller, J. Efficiency of ab-initio total energy calculations for metals and semiconductors using a plane-wave basis set. *Comput. Mater. Sci.* **1996**, *6*, 15−50.

(17) Kresse, G.; Furthmüller, J. Efficient iterative schemes for ab initio total-energy calculations using a plane-wave basis set. *Phys. Rev. B* **1996**, *54*, 11169−11186.

(18) Perdew, J. P.; Burke, K.; Ernzerhof, M. Generalized Gradient Approximation Made Simple. *Phys. Rev. Lett.* **1996**, *77*, 3865−3868.

(19) Kresse, G.; Joubert, D. From ultrasoft pseudopotentials to the projector augmented-wave method. *Phys. Rev. B* **1999**, *59*, 1758−1775.

(20) Pecher, J.; Tonner, R. Precursor States of Organic Adsorbates on Semiconductor Surfaces are Chemisorbed and Immobile. *ChemPhysChem* **2017**, *18*, 34−38.

(21) Grimme, S.; Ehrlich, S.; Goerigk, L. Effect of the damping function in dispersion corrected density functional theory. *Comput. Mater. Sci.* **2011**, *32*, 1456−1465.

(22) Henkelman, G.; Jónsson, H. Improved tangent estimate in the nudged elastic band method for finding minimum energy paths and saddle points. *J. Chem. Phys.* **2000**, *113*, 9978−9985.

(23) Henkelman, G.; Uberuaga, B. P.; Jónsson, H. A climbing image nudged elastic band method for finding saddle points and minimum energy paths. *J. Chem. Phys.* **2000**, *113*, 9901−9904.

(24) Larsen, A. H.; Mortensen, J. J.; Blomqvist, J.; Castelli, I. E.; Christensen, R.; Dułak, M.; Friis, J.; Groves, M. N.; Hammer, B.; Hargus, C.; et al. The atomic simulation environment − a Python

library for working with atoms. *J. Phys.: Condens. Matter* **2017**, *29*, 273002.
(25) Krukau, A. V.; Vydrov, O. A.; Izmaylov, A. F.; Scuseria, G. E. Influence of the exchange screening parameter on the performance of screened hybrid functionals. *J. Chem. Phys.* **2006**, *125*, 224106.
(26) Tersoff, J.; Hamann, D. R. Theory of the scanning tunneling microscope. *Phys. Rev. B* **1985**, *31*, 805−813.
(27) Self, K. W.; Pelzel, R. I.; Owen, J. H. G.; Yan, C.; Widdra, W.; Weinberg, W. H. Scanning tunneling microscopy study of benzene adsorption on Si(100)-(2×1). *J. Vac. Sci. Technol., A* **1998**, *16*, 1031−1036.
(28) Silvestrelli, P. L.; Ancilotto, F.; Toigo, F. Adsorption of benzene on Si(100) from first principles. *Phys. Rev. B* **2000**, *62*, 1596−1599.
(29) Mette, G.; Reutzel, M.; Bartholomäus, R.; Laref, S.; Tonner, R.; Dürr, M.; Koert, U.; Höfer, U. Complex Surface Chemistry of an Otherwise Inert Solvent Molecule: Tetrahydrofuran on Si(001). *ChemPhysChem* **2014**, *15*, 3725−3728.
(30) O'Donnell, K. M.; Byron, C.; Moore, G.; Thomsen, L.; Warschkow, O.; Teplyakov, A.; Schofield, S. R. Dissociation of CH3-O as a Driving Force for Methoxyacetophenone Adsorption on Si(001). *J. Phys. Chem. C* **2019**, *123*, 22239−22249.
(31) Barriocanal, J. A.; Doren, D. J. 1,3-dipolar cycloadditions on Si(100)-2×1: Theoretical studies of novel attachment chemistry for organic monolayers. *J. Vac. Sci. Technol., A* **2000**, *18*, 1959−1964.
(32) Leftwich, T. R.; Teplyakov, A. V. Chemical manipulation of multifunctional hydrocarbons on silicon surfaces. *Surf. Sci. Rep.* **2008**, *63*, 1−71.
(33) Jung, Y.; Gordon, M. S. Cycloaddition of Benzene on Si(100) and Its Surface Conversions. *J. Am. Chem. Soc.* **2005**, *127*, 3131−3139.
(34) Costanzo, F.; Sbraccia, C.; Silvestrelli, P. L.; Ancilotto, F. Proton-transfer reaction of toluene on Si(100) surface. *Surf. Sci.* **2004**, *566*, 971−976 10.1016/j.susc.2004.06.038..

https://dx.doi.org/10.1021/acs.jpcc.0c01009
J. Phys. Chem. C 2020, 124, 9940−9946

Supporting Information for:

Adsorption of Methyl-Substituted Benzylazide on Si(001) – Reaction Channels and Final Configurations

J. Heep[1], J.-N. Luy[2], C. Länger[1], J. Meinecke[2], U. Koert[2], R. Tonner[2] and M. Dürr[1]

[1]*Institut für Angewandte Physik and Zentrum für Materialforschung, Justus-Liebig-Universität Giessen, Heinrich-Buff-Ring 16, D-35392 Giessen*

[2]*Fachbereich Chemie, Philipps-Universität Marburg, Hans-Meerwein-Straße 4, D-35032 Marburg, Germany*

(Dated: April 7, 2020)

This Supporting Information includes

(I) Analysis of the STM data obtained at 50 K (Fig. S1)

(II) Calculated energies and configurations of alternative reaction pathways (Tab. S1; Figs. S2 – S5)

(III) Computational data repository

(IV) Python script interfacing VASP with ASE

I Analysis of the STM data obtained at 50 K

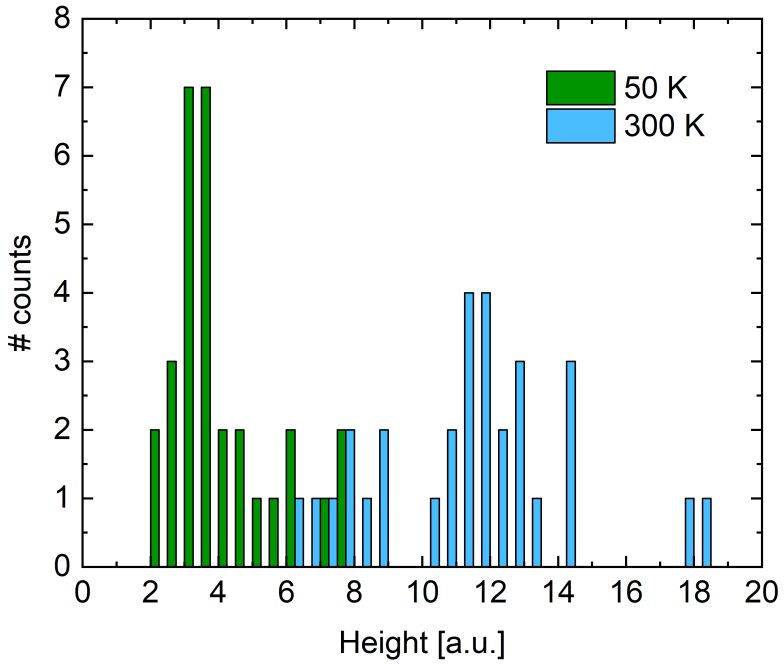

FIG. S1: Height distribution of the bright features observed at positive sample bias for measurements at 50 K and 300 K. Two clearly separated distributions are observed. For the few cases in the area where the distributions overlap, analysis of the single configurations shows that all configurations from the images taken at 300 K show the additional dip in the line scan close to the protrusion (compare Fig. 4(c) in the main paper) whereas the configurations from the images taken at 50 K do not show this additional dip. These brighter features observed at 50 K might be the result of two molecules adsorbed in direct neighborhood.

II Calculated energies and configurations of alternative reaction pathways

TAB. S1: Adsorption energies of the stationary points from Fig. 5 calculated with PBE-D3 (electronic energies, ΔE without thermodynamic corrections).

configuration	ΔE (kJmol^{-1})
1+slab	0
IM	-319
TS1	-184
C1	-335
TS2	-313
C2	-377

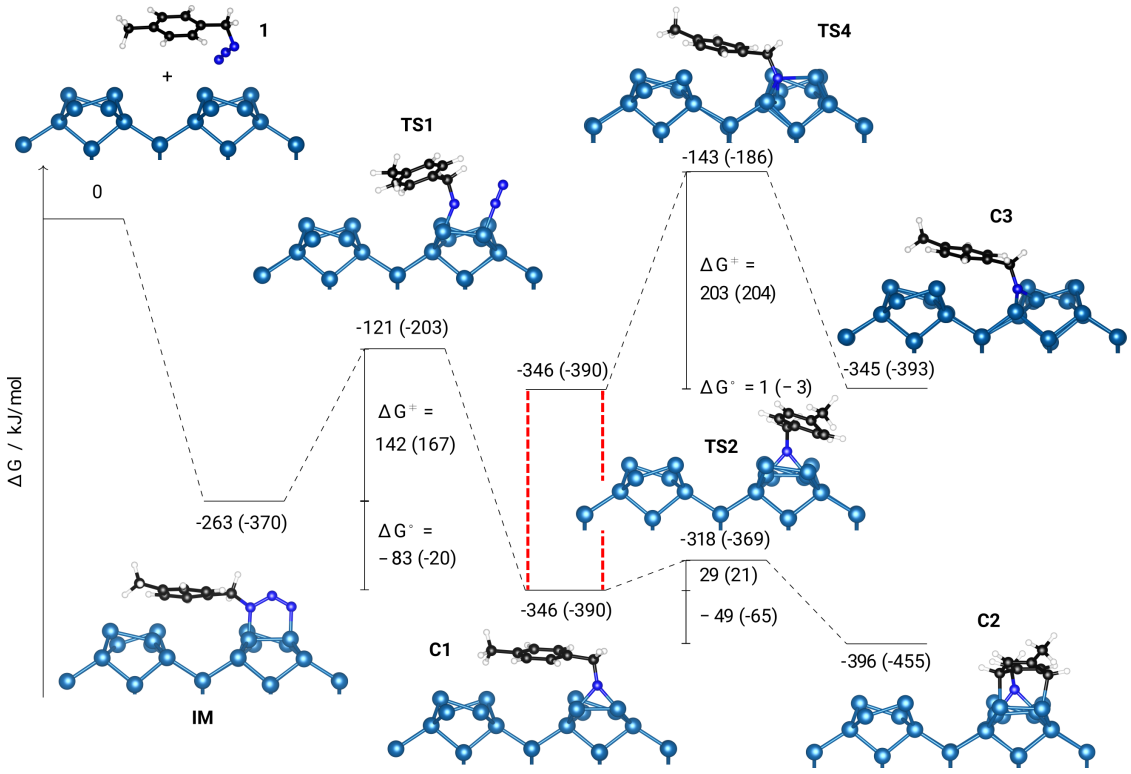

FIG. S2: Computed adsorption and reaction profile of **1** on Si(001)c(4x2) showing Gibbs energy differences ΔG including the pathway to subsurface structure **C3**.

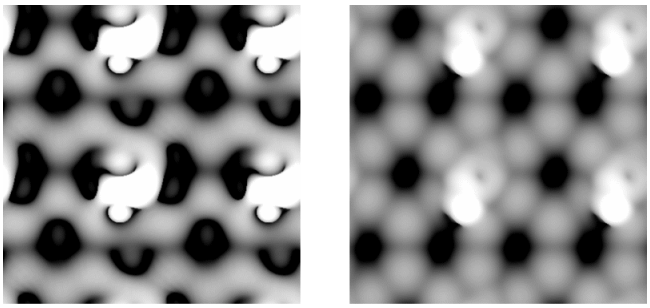

FIG. S3: STM simulation of **C3** at positive (left) and negative (right) bias voltage.

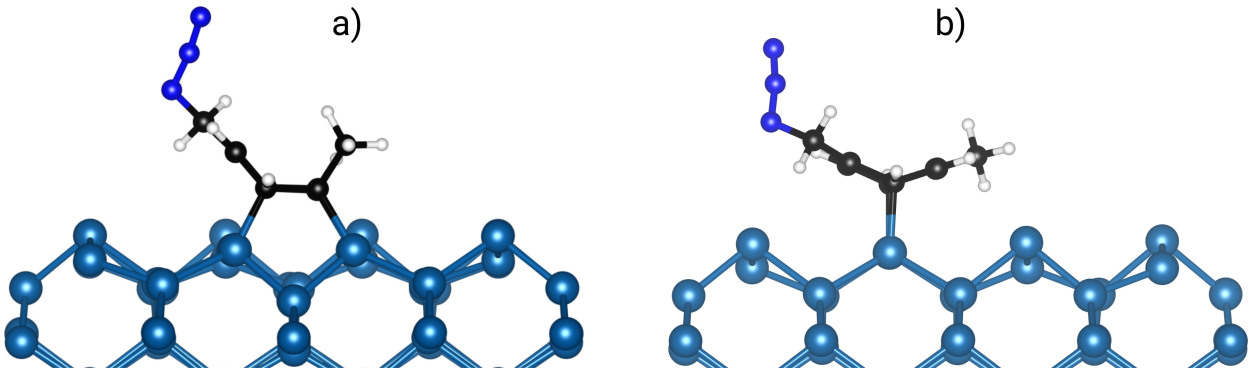

FIG. S4: Alternative adsorption structures to **IM**: a) Binding along the dimer-row similar to the tight-bridge mode for benzene, $\Delta E = -134$ kJ mol^{-1} and b) binding on one dimer similar to the butterfly-mode of benzene, $\Delta E = -148$ kJ mol^{-1}. Electronic energy differences on PBE-D3 level.

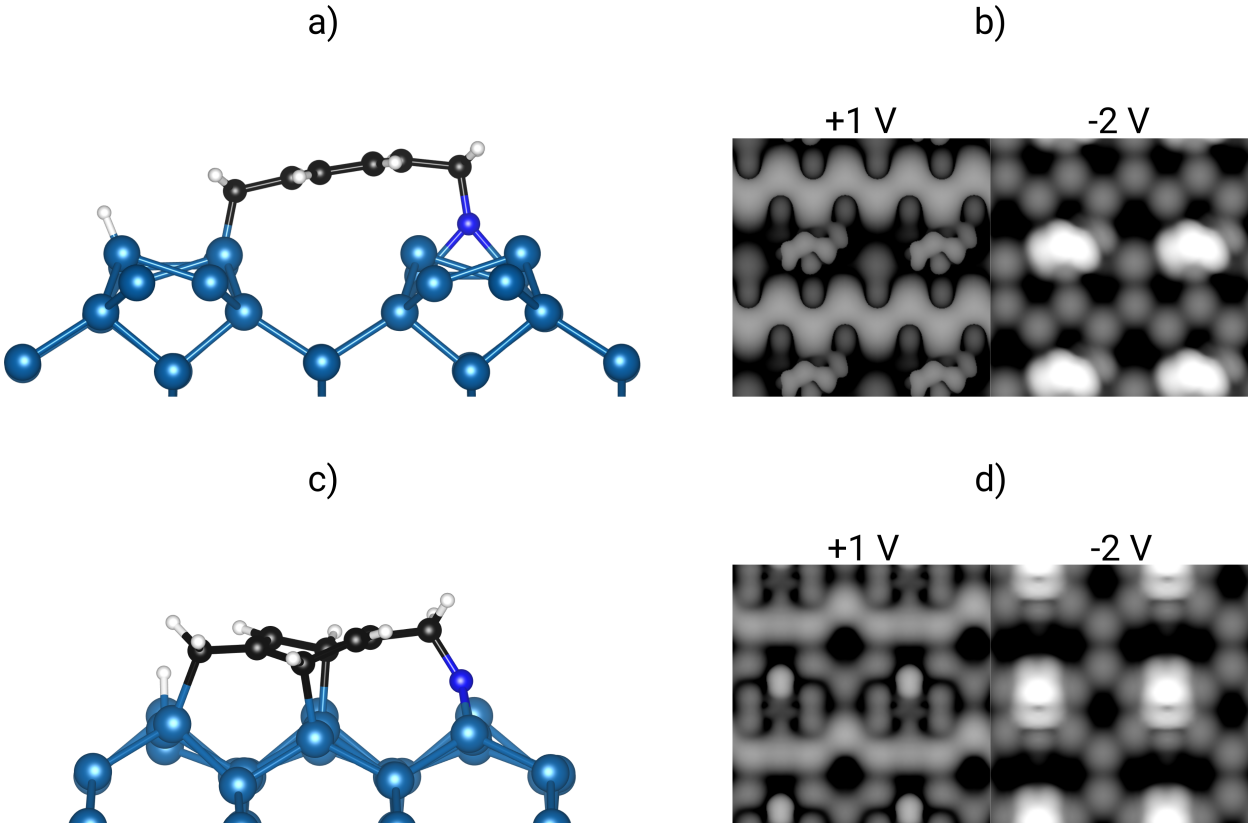

FIG. S5: Possible reactions of the methyl-substituent in the tolyl-moiety. a) Starting from structure **C1** leads to structure **C1'** via dissociative adsorption of one C-H bond on a neighboring Si-dimer across the row with a barrier of $\Delta G^{\ddagger} = 166$ (184 kJ mol^{-1} w.r.t **C1** and a thermodynamic stabilization of $\Delta G = -493$ (-545) kJ mol^{-1} w.r.t. the reactant). b) Simulated STM picture of **C1'** at positive and negative sample bias. c) Starting from structure **C2** leads to structure **C2'** via dissociative adsorption of one C-H bond on a neighboring Si-dimer along the row with a barrier of $\Delta G^{\ddagger} = 140$ (149 kJ mol^{-1} w.r.t **C2** and a thermodynamic stabilization of $\Delta G = -514$ (-577) kJ mol^{-1} w.r.t. the reactants. d) Simulated STM picture of **C2'** at positive and negative sample bias. Energies including thermodynamic corrections at HSE06-D3 (in brackets: PBE-D3) level.

III Computational data repository

Structures and other computational output can be accessed at the NOMAD repository.

DOI: https://dx.doi.org/10.17172/NOMAD/2019.12.12-1

DOI: https://dx.doi.org/10.17172/NOMAD/2020.04.03-1

IV Python script interfacing VASP with ASE

(a) Harmonic

```
import os
import sys
import numpy as np
from ase.io import write, read
from ase.calculators.vasp import vasp
from ase.thermochemistry import HarmonicThermo
#sys.stdout = open('thermo.txt', 'w') #output to file instead
potentialenergy = vasp.Vasp.read_energy('OUTCAR',all)[1][0]
print(potentialenergy)
#only real frequencies
energies = vasp.Vasp.read_vib_freq('OUTCAR')[0]
nfreq=int(len(energies)/2)
#scaling to eV and removing doubly counted frequencies
vib_energies = [i / 1000 for i in energies][0:nfreq]
print(vib_energies)
thermo = HarmonicThermo(vib_energies=vib_energies,
                        potentialenergy=potentialenergy
                        )
F = thermo.get_helmholtz_energy(temperature=300)
```

(b) Nonlinear ideal gas

```
import os
import sys
import numpy as np
from ase.io import write, read
from ase.calculators.vasp import vasp
from ase.thermochemistry import IdealGasThermo
#sys.stdout = open('thermo.txt', 'w') #output to file instead
atoms = read('OUTCAR')
natoms=len(atoms)
print(atoms)
dof=3*natoms-6 #Degrees of freedom
print(dof)
potentialenergy = vasp.Vasp.read_energy('OUTCAR',all)[1][0]
print(potentialenergy)
#only real frequencies
energies = vasp.Vasp.read_vib_freq('OUTCAR')[0]
#scaling to eV and removing lowest DOF
vib_energies = [i / 1000 for i in energies][0:dof]
print(vib_energies)
thermo = IdealGasThermo(vib_energies=vib_energies,
                        potentialenergy=potentialenergy,
                        atoms=atoms,
                        geometry='nonlinear', #'linear', 'monoatomic'
                        symmetrynumber=1, #rotational
                        spin=0, #S/2
                        natoms=natoms)
G = thermo.get_gibbs_energy(temperature=300, pressure=100000.)
```

Combined XPS and DFT investigation of the adsorption modes of methyl enol ether functionalized cyclooctyne on Si(001)

Timo Glaser,[a] Jannick Meinecke,[b] Christian Länger,[a] Jan-Niclas Luy,[b, c, d] Ralf Tonner,[b, c, d] Ulrich Koert,[b] and Michael Dürr*[a]

The reaction of methyl enol ether functionalized cyclooctyne on the silicon (001) surface was investigated by means of X-ray photoelectron spectroscopy (XPS) and density functional theory (DFT). Three different groups of final states were identified; all of them bind on Si(001) via the strained triple bond of cyclooctyne but they differ in the configuration of the methyl enol ether group. The majority of molecules adsorbs without additional reaction of the enol ether group; the relative contribution of this configuration to the total coverage depends on substrate temperature and coverage. Further configurations include enol ether groups which reacted on the silicon surface either via ether cleavage or enol ether groups which transformed on the surface into a carbonyl group.

1. Introduction

Well-defined structures of organic molecules on semiconductors, in particular on Si(001) as the technologically most important semiconductor surface, may open new possibilities in semiconductor technology with its wide range of applications.[1–7] One prerequisite for the formation of such well-defined organic structures is the chemoselective attachment of bifunctional molecules. However, due to the high reactivity of the dangling bonds, only a few bifunctional molecules have been shown to exhibit chemoselective reactivity on Si(001),[8–12] often restricted to a fixed combination of the two functional groups.

A more general concept is based on cyclooctynes, which are well known from click chemistry.[13,14] Previous investigations have shown that substituted cyclooctynes selectively react on Si(001) over the strained triple bond of the cyclooctyne ring.[15–17] The chemoselective reactivity of substituted cyclooctynes was traced back to the direct reaction pathway of cyclooctyne on Si(001),[15,18,19] in contrast to almost all other organic functional groups, which adsorb on Si(001) via an indirect reaction channel.[3,5] In consequence, the second functional group of the substituted cyclooctynes was found not to take part in the adsorption process[15–17] and thus can be used for further reactions.

In this context, methyl enol ether functionalized cylooctyne (MEECO, **1**, Figure 1) is a promising molecule to build the first organic layer on the silicon surface via the strained triple bond. The enol ether group could then be employed in click reactions with tetrazine derivatives,[20] which opens up a new way of building well-ordered multilayers on the silicon substrate. It is thus important to investigate the reaction of MEECO on Si(001), in particular with respect to the reaction of the enol ether group with the silicon surface.

Here we use X-ray photoelectron spectroscopy (XPS) and density functional theory (DFT) in order to investigate the

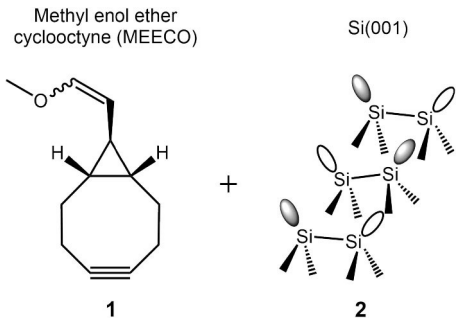

Figure 1. The adsorption of methyl enol ether functionalized cyclooctyne (MEECO, **1**) on the buckled dimers of Si(001) (**2**) is investigated. The latter are shown with filled dangling bonds (grey ellipses) and unfilled dangling bonds (white ellipses).[3,4]

[a] T. Glaser, Dr. C. Länger, Prof. Dr. M. Dürr
Institut für Angewandte Physik and Zentrum für Materialforschung, Justus-Liebig-Universität Giessen,
Heinrich-Buff-Ring 16, D-35392 Giessen, Germany
E-mail: michael.duerr@ap.physik.uni-giessen.de
[b] J. Meinecke, J.-N. Luy, Prof. Dr. R. Tonner, Prof. Dr. U. Koert
Fachbereich Chemie, Philipps-Universität Marburg, Hans-Meerwein-Straße 4, D-35032 Marburg, Germany
[c] J.-N. Luy, Prof. Dr. R. Tonner
Fakultät für Chemie und Pharmazie, Universität Regensburg, Universitätsstraße 31, D-93053 Regensburg, Germany
[d] J.-N. Luy, Prof. Dr. R. Tonner
Wilhelm-Ostwald-Institut für Physikalische und Theoretische Chemie, Universität Leipzig, Linnéstraße 2, D-04103 Leipzig, Germany

Supporting information for this article is available on the WWW under https://doi.org/10.1002/cphc.202000870

adsorption configurations of methyl enol ether functionalized cyclooctyne at different temperature and coverage.

Methods

The XPS experiments were performed in a UHV chamber with a base pressure $< 1 \times 10^{-10}$ mbar. Si(001) samples were prepared by degassing at 700 K and repeated direct current heating cycles to 1450 K. A well ordered 2×1 reconstruction was obtained by cooling with rates of about 1 K/s.[21,22]

The synthesis of MEECO was carried out via 8 linear steps leading into a yield of 32 %, consisting of a mixture of 64% E-isomer and 36% Z-isomer. The functionalization of the cyclooctyne ring was carried out using copper mediated cyclopropanation.[20] Methyl enol ether functionalized cyclooctyne was dosed via a leak valve from the vapor phase in a test tube. Pressures are given as uncorrected ion-gauge readings.

XPS measurements were performed using an Al K_α X-ray source with monochromator (Omicron XM1000) and a hemispherical energy analyzer (Omicron EA125). All XPS spectra were referenced to the Si $2p_{3/2}$ peak at 99.4 eV.[23] Voigt-profiles were used for fitting the data; they are composed of 90% Gaussian function and 10% Lorentzian function. Full width at half maximum (FWHM) of the single components was chosen between 0.9 and 1.1 eV, which are typical values for the measured line widths of such systems in this setup.[24]

DFT investigations were done with the Vienna ab initio simulation package (VASP 5.4.4)[25–27] using the HSE06[28] range-separated hybrid functional and standard PAW-pseudopotentials PBE.54[29] with a large core configuration while dispersion effects were considered via the DFT-D3 scheme including an improved damping function.[30,31] The plane wave energy cutoff was set to 400 eV and a total energy difference of at least 10^{-6} eV with "accurate" precision was used for SCF convergence. Prior structural optimization was performed with the PBE[32] generalized gradient approximation including DFT-D3 correction and a force convergence criterion of 10^{-2} eV. Transition-state structures were calculated with the dimer method[33] as implemented in the transition state tools (1.73) for VASP with tighter electronic convergence of 10^{-7} eV. A Γ -centered $2 \times 2 \times 1$ *k*-mesh was chosen together with a setup of Si(001) slabs (six layers, two bottom layers frozen and terminated with hydrogen atoms) as determined in previous work.[34] Thermodynamic corrections were determined in a constrained Hessian approach at the PBE-D3 level with only the adsorbate and the two topmost slab layers being considered for displacements in finite difference calculations. The free energy differences at 300 K and 1 bar were then added as a higher order correction to the HSE06-D3 energies. Scripts for extracting thermodynamic quantities form a VASP calculation have been published elsewhere.[23] We will discuss electronic energy differences and Gibbs energies of adsorption at the HSE06-D3 level of approximation unless otherwise noted. PBE-D3 values are found in the Supporting Information (Figures S2 and S3).

2. Results and Discussion

In Figure 2, XPS spectra measured directly after adsorption of MEECO (3.5×10^{-6} mbar×s) on Si(001) at 150 K as well as after a further temper cycle to 300 K are compared. Initial adsorption at 150 K led to the formation of a multilayer shown in light purple; the intensity is scaled by a factor of ≈0.5 for better

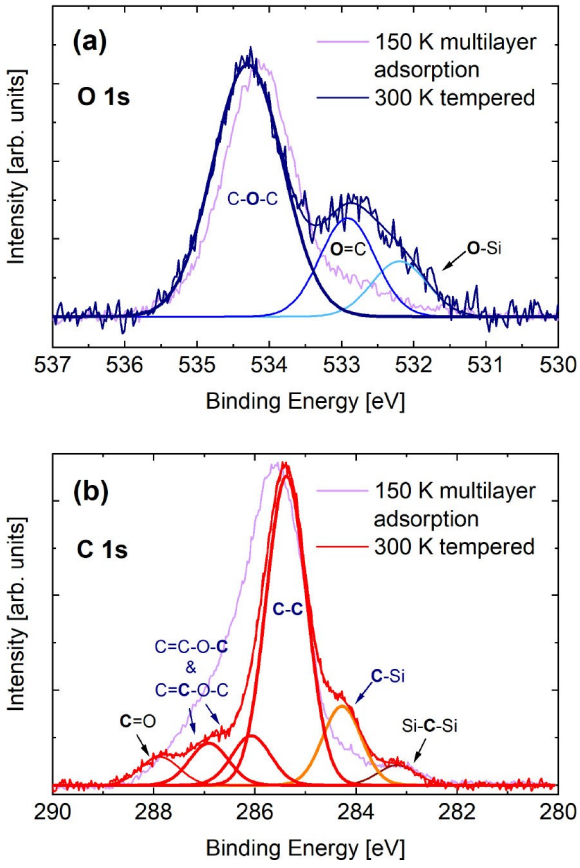

Figure 2. O 1s (a) and C 1s (b) core level spectra after adsorption of MEECO on Si(001) at 150 K. The light purple data were measured right after adsorption at 150 K. The O 1s and C 1s spectra in blue and red, respectively, were measured at 150 K after tempering the sample to 300 K within 30 minutes. The initial 150-K-spectra are higher in intensity indicating adsorption of a multilayer; they were scaled by a factor of ≈0.5 for better comparison with the spectra measured on the tempered sample. Fit components which are associated with the intact MEECO molecules attached via the strained triple bond are drawn with thick solid lines and are labelled dark blue. Further fit components are shown with thin solid lines. Decomposition of the multilayer spectra is shown in Figure S1 in the Supporting Information.

comparison with the data of the tempered sample, which are shown in blue (Figure 2 (a), O 1s) and red (Figure 2 (b), C 1s). The O 1s spectrum taken after the temper cycle (Figure 2 (a)) indicates three different peaks. The peak at the highest binding energy (534.3 eV, fit component shown in dark blue) can be assigned to the intact methyl enol ether group, as it coincides with the most dominant peak in the multilayer spectrum. In comparison with data reported in literature, the peak at 532.8 eV (azure fit component) can be assigned to a carbonyl group[35,36] and the third peak, indicated by the light blue component at a binding energy of 532.2 eV, can be assigned to an oxygen atom binding to the silicon surface.[24,37–39] This Si–O configuration indicates that an ether cleavage reaction took place on the surface.[39] The relative intensities of the O 1s components in the spectrum shows that the majority of the methyl enol ether groups stays intact when the molecule adsorbs on the Si(001) surface, while side reactions forming

C=O and Si–O bonds can take place. The intensity ratio of the three components is approx. 6:2:1.

The C 1s spectrum taken after the temper cycle shows six different peaks. The peak with the highest intensity at 285.4 eV can be assigned to C–C or C–H configurations, which are present in the main unit of the molecule.[15,17,36] The peak at a binding energy of 284.2 eV can be assigned to carbon atoms bonding via one covalent bond to the Si surface.[15,36,39] The fitted component is highlighted in orange in Figure 2. The intensity ratio of this component with respect to the total intensity of the carbon spectrum indicates that approximately 2 out of 12 carbon atoms are bonding in that mode on the Si surface.

The peaks at lowest and highest binding energy, 283.2 eV (dark red component) and 287.9 eV, are assigned to a C atom bound more strongly to the silicon substrate, e.g., via two Si dimer atoms as in disiliranes,[36,40] and a C atom in a carbonyl group,[35,36] respectively. The two remaining peaks at a binding energy of 286.0 eV and 286.9 eV are then assigned to the intact methyl enol ether group (C=**C**–O–C and C=C–O–**C**,[15]), in accordance with the O 1s spectrum, which also indicates a strong contribution of the intact enol ether group to the signal. Indeed, the relative intensity of each of these two peaks amounts to approx. 1/12 of the total intensity, indicating that the majority of the enol ether groups were not reacted.

When taking into account the different relative sensitivity factors for the O 1s and C 1s signals, an intensity ratio of 1.1:12 for I(O):I(C) was deduced for the spectra of the tempered sample, in accordance with the 1:12 ratio of the number of oxygen and carbon atoms in the MEECO molecule.

Furthermore, taking into account that most of the molecules bound to the surface exhibit an intact enol ether group as deduced from the O 1s and C 1s spectra, the ratio of 2:12 between the **C**-Si peak intensity and the total carbon intensity is a strong indication that most MEECO molecules bind via the strained triple bond of the cyclooctyne ring. However, the enol ether groups which react via ether cleavage also contribute to the Si–C peak intensity. It is thus possible that some of the MEECO molecules bind via the Si–O bond of the reacted enol ether group only; within the uncertainty of our measurements, we can neither exclude nor safely confirm such a bonding via the cleaved enol ether group only. On the other hand, a substantial contribution of molecules which additionally adsorb via the activated C=C bond of the enol ether group can be largely excluded as they would lead to a further increase of the intensity of the **C**–Si peak.

We thus propose three different groups of adsorption products as summarized in Figure 3: (a) MEECO bound to Si(001) solely via the strained triple bond of cyclooctyne, thus exhibiting an intact enol ether group. (b) MEECO bound via the strained triple bond of cyclooctyne and a further reaction via the ether group. One possible configuration for the respective product is sketched in Figure 3 (b) with the oxygen atom and an additional CH_3 group bound to the surface. C–O cleavage could also take place at the C–O bond next to the C=C double bond leading to an adsorbed methoxy group. As both configurations contribute in a similar way to the XPS spectra, we cannot distinguish the two modes experimentally. (c) MEECO bound via the strained triple bond of cyclooctyne and the enol ether group being reacted to a carbonyl group.

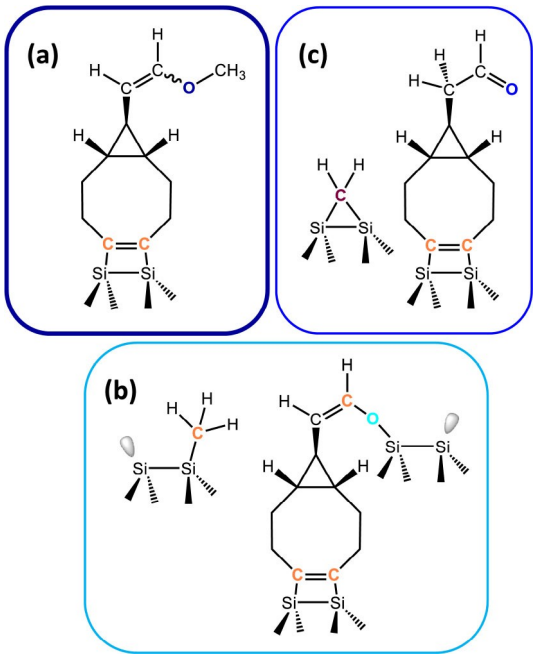

Figure 3. Three different adsorption configurations of MEECO on Si(001). (a) Adsorption via the cycloocytyne ring only. (b) Including an additional covalent Si–O bond due to ether cleavage. In the shown example, ether cleavage leads to a CH_3 group adsorbed on an additional Si dimer as observed for cyclooctyne ether.[15] (c) Including a carbonyl group in the former MEECO molecule and the resulting CH_2 fragment bound to two silicon atoms.

Two further XPS measurements are shown in Figure 4. The spectra shown in Figure 4 (a) represent a Si(001) surface saturated with MEECO at room temperature (coverage $\Theta = \Theta_{sat}$). The spectra shown in Figure 4 (b) were obtained at 150 K with a MEECO coverage below Θ_0, the coverage which we obtained when tempering a multilayer to 300 K after adsorption at 150 K (compare Figure 2). Θ_0 is $\approx$50% higher than the saturation coverage of MEECO molecules on the surface at $T_s =$ 300 K. All peaks observed in the measurements shown in Figure 2 are also observed in the spectra in Figure 4. At 150 K, an additional peak at 535.1 eV can be observed. It is assigned to a dative O-Si bond of the oxygen atom of the methyl enol ether group.[39] In this configuration, the enol ether group is still intact; if we combine the intensity of this component with the intensity of the component assigned to the free enol ether group, the majority of molecules adsorb with an intact enol ether group at low coverage, as well. However, compared to the measurement shown in Figure 2, the ratio is shifted towards molecules which reacted via ether cleavage or carbonyl formation. In particular, the relative intensity of the peak assigned to the carbonyl peak in the O 1s spectrum shows the highest intensity of all single peaks. At 300 K, the ratio of intact methyl enol ether groups compared to reacted groups is then favouring the reacted groups; the signal associated with oxygen

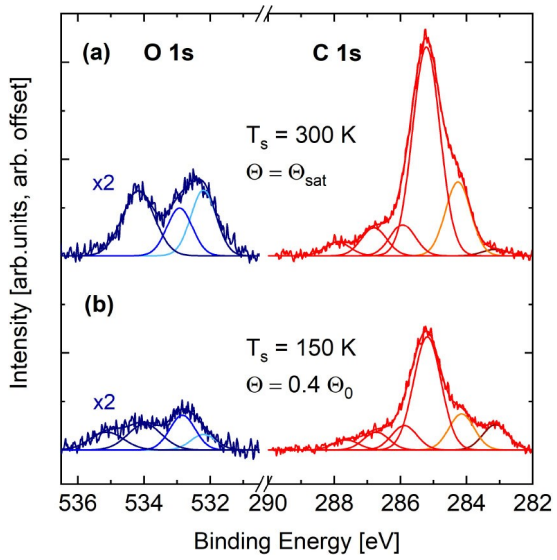

Figure 4. O 1s spectra shown in blue and C 1s spectra shown in red of methyl enol ether functionalized cyclooctyne on Si(001) after adsorption at 300 K (a) and 150 K (b). At 150 K, an additional peak at 535.1 eV can be observed when compared to Figure 1 (a), which is assigned to a dative O–Si bond of the methyl enol ether group to Si(001).[39] Further peak assignments are identical to Figure 1. The O 1s spectra are scaled by a factor 2 for better comparison.

bonding to the silicon surface (light blue) is slightly increased compared to the signal of the carbonyl group (azure).

The relative contribution of the different configurations as deduced from the intensity of the different oxygen species is summarized in Figure 5. The data include adsorption and measurement at 150 K (dashed box), adsorption and measurement at 300 K (dotted box), and measurements of a sample prepared at 150 K and further tempered to 300 K (also measured at 150 K, dot-dashed box). Oxygen atoms bonding

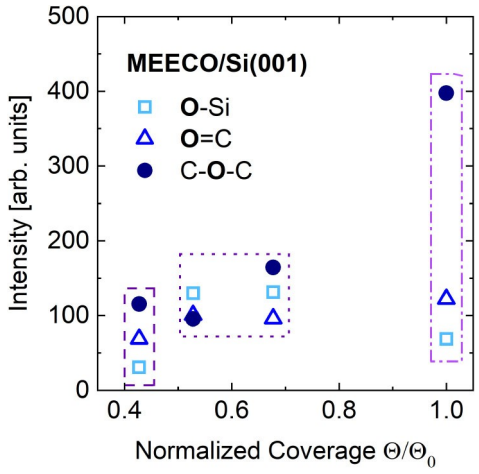

Figure 5. Intensity of the different oxygen species of the methyl enol ether group as measured for different surface coverage and adsorption/measurement temperature: adsorption and measurement at 150 K (dashed box), adsorption and measurement at 300 K (dotted box), adsorption at 150 K and further tempering to 300 K (also measured at 150 K, dot-dashed box).

covalently with the Si(001) surface and the carbonyl group are formed with high relative contribution at 300 K and low coverage on the surface, indicating a high probability for cleavage of the methyl enol ether group at these conditions. At high coverage and reduced temperature, the reaction of the enol ether group with the surface is suppressed. In particular, ether cleavage is suppressed at lower temperatures, in accordance with previous work on the reaction of ether-functionalized cyclooctynes on Si(001).[15,41] With the latter preparation scheme (multilayer adsorption at 150 K, tempering to 300 K), the highest contribution of intact MEECO molecules to the total coverage was obtained (approx. 70% as deduced from the O 1s spectra in Figure 2 (a)).

The three types of bonding configurations shown in Figures 3 (a) to (c) are deduced from the assignment of the single components found in the O 1s and C 1s spectra at different surface coverage and temperature. Although all three configurations seem to be plausible with respect to the adsorption of the single functional groups, i. e., strained triple bond and enol ether group, it is not clear if they can react in this way when combined in one single molecule. Furthermore, the relative contribution of the side reactions is dependent on both coverage and temperature. The latter might be caused either by kinetic or thermodynamic control. We thus performed DFT calculations to reveal more details about the possible adsorption modes.

The most stable adsorption modes found in the computational investigations are shown in Figures 6 (a) to (d). They reflect the configurations shown in Figure 3, explicitly taking into account two possibilities for O–C cleavage in combination with the formation of a Si–O bond. They show large adsorption energies throughout, indicating strong chemisorption, with

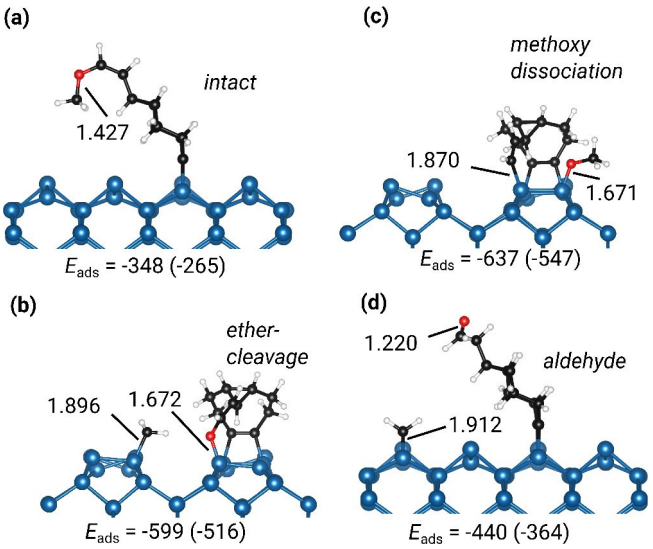

Figure 6. Results from DFT studies. (a) to (d): Most important adsorption modes with adsorption energies (HSE06-D3) given in kJ mol^{-1} (Gibbs free energy in brackets). Selected bond distances are given in Å. In (b) and (c), the silicon substrate is rotated by 90° with respect to the situation shown in (a) and (d). In Figure S4 in the Supporting Information, the rotated view of (a) is also shown.

rather constant contributions from enthalpic and entropic effects (Gibbs energies are given in brackets). Regarding the mix of stereoisomers used in the experimental study, we find that the *E*-isomer of free MEECO is more stable by 17 kJ mol^{-1} compared to the *Z*-isomer. We find the same adsorption modes for both isomers, however the *Z*-isomer binds more strongly to the surface and those structures are thus depicted in Figures 6 (a) and (b). The *E*-isomer is less strongly bound (*intact* mode: $\Delta E_{ads}^{PBE-D3} = +6$ kJ mol^{-1}, *ether-cleavage* mode: $\Delta E_{ads}^{PBE-D3} = +52$ kJ mol^{-1}) but it seems reasonable to assume that both isomers will react in the same manner with the surface. All adsorption energies are given with respect to the energy of the respective isomer.

The *intact* adsorption mode is very similar to the *on-top* structure for parent cyclooctyne which shows exactly the same adsorption energy at PBE level ($E_{ads}^{PBE-D3} = -308$ kJ mol^{-1},[42]). This supports the previous finding that the substitution of cyclooctyne in the backbone does not have an influence on the bonding to the substrate.[16] The adsorbate can further react via breaking the C–O bond at the ether group via the previously observed S_N2-type attack[43] of a silicon atom in the neighboring dimer row leading to the strongly bound adsorption mode *ether-cleavage*. Like in the previous investigation, breaking of the C–O bond proceeds via an intermediate state with the intact ether group being datively bonded to the surface dimer. The adsorption energy for the final state is comparable to the doubly-bonded configuration of an ether-functionalized cyclooctyne (5-ethoxymethyl-5-methylcyclooctyne, EMC) with the triple bond attached to the surface and the ether bond cleaved across the dimer rows (*ether-cleavage*: $E_{ads}^{PBE-D3} = -540$ kJ mol^{-1}, EMC: $E_{ads}^{PBE-D3} = -557$ kJ mol^{-1}[16]).

An alternative to the *ether-cleavage* reaction across dimer rows is O-C cleavage via the *methoxy dissociation* mode (Figure 6 (c)). Here, we also find a very stable structure with $E_{ads} = -637$ kJ mol^{-1}. This cleavage reaction is preferred on-top of the same dimer in contrast to the ether cleavage reaction across rows.

The fourth important structure found is the *aldehyde* mode (Figure 6 (d)), which shows an increased adsorption energy compared to *intact* due to the additional methylene group bonding to the surface. Here, a tautomeric enol-configuration can be envisioned which turns out to be less stable by $\Delta E = 25$ kJ mol^{-1}. In the XPS spectra, this tautomerism would lead to a lower intensity of the **C**=O signal when compared to the Si–**C**–Si signal, which is only observed in the low coverage measurement performed at 150 K (Figure 4 (b)). Indeed, the tautomeric enol-configuration might serve as an intermediate in the reaction towards the *aldehyde* mode. However, as the respective pathway is not obvious, a full computational description is beyond the scope of this investigation.

There are further possibilities for MEECO to react with Si(001) which have been investigated computationally. We find that the adsorption via the ether oxygen only (dative bond) shows adsorption energies of $E_{ads}^{PBE-D3} = -91/-86$ kJ mol^{-1} (Z/E) which is considerably lower compared to previously investigated ether dative bonds on Si(001) (tetrahydrofuran: $E_{ads}^{PBE-D3} = -132$ kJ mol^{-1}; diethylether: $E_{ads}^{PBE-D3} = -116$ kJ mol^{-1}[43]). Bonding analysis with an energy decomposition method for extended systems (pEDA)[44] indicates that this is due to reduced donation from the non-bonded electron pairs into the acceptor orbitals at the surface ($\Delta E_{orb}^{donation}$(PBE-D3) = 198 kJ mol^{-1} compared to $\Delta E_{orb}^{donation}$(PBE-D3) = 284 kJ mol^{-1} for diethylether[43]) due to increased conjugation with the double bond. As found for EMC before, this dative bond can thus be excluded as final state but plays a role as intermediate as outlined above.[15]

The third functional group in MEECO is the double bond. Adsorption via this double bond alone leads to a reasonably stable structure for the *E*-isomer ($E_{ads} = -231$ kJ mol^{-1}) which is nevertheless much less stable compared to the adsorption via the triple bond. Adsorption via both functional groups – double and triple bond – has also been tested and the most stable configuration (triple bond in bridge-configuration and double bond in on-top configuration on neighboring dimer row) results in $E_{ads} = -462$ kJ mol^{-1} (*Z*) and $E_{ads} = -454$ kJ mol^{-1} (*E*). It is thus comparable to the *intact* and *aldehyde* modes. Nevertheless, this mode can be excluded based on the XPS findings that a rather low ratio of signal intensity in the C 1s spectrum is associated with C–Si bonds.

Finally, we computed the energy barrier for the reaction from *intact* to *ether-cleavage* structure via the datively bonded intermediate (Figure 7) in analogy to previously investigated ether cleavage reactions on Si(001).[16,43] A moderate barrier of $\Delta E^{\ddagger} = 79$ kJ mol^{-1} was calculated. For the alternative reaction of methoxy cleavage, a higher barrier was found ($\Delta E^{\ddagger} = 102$ kJ mol^{-1}). These calculated barriers support the experimental observation that reduced reaction via ether cleavage is found in the low temperature measurements but MEECO reacts more readily via the enol ether group upon increasing the temperature. In addition, if at reduced temperature the reaction rate is low when compared to the flux of the incoming molecules, site blocking can further reduce the number of molecules additionally reacted via the enol ether group, in particular at high coverage.

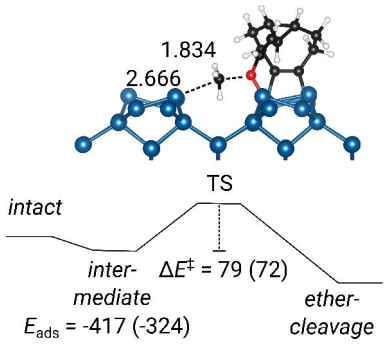

Figure 7. Reaction path of the MEECO molecule bound in the *intact* configuration to the *ether-cleavage* structure via the datively bonded *intermediate*. The transition state configuration is shown with barrier height ($\Delta E^{\ddagger}$, Gibbs energy in brackets). Selected bond distances are given in Å, energies in kJ mol^{-1}.

3. Conclusion

Preferential adsorption of MEECO molecules via the strained triple bond of cyclooctyne has been experimentally observed at 150 K. Increased substrate temperature leads to additional products via reaction of the enol ether group, i.e., ether cleavage leading to a Si-bound oxygen atom or the formation of a carbonyl group in the former MEECO molecule. DFT-based computational investigations support the bonding configurations proposed from XPS. They furthermore rationalize the experimental findings as they find a lower adsorption energy for the MEECO molecules bound solely via the strained triple bond when compared to multi-tethered molecules but, where calculated, a finite reaction barrier into these thermodynamically preferred configurations.

Supporting Information

The Supporting Information includes O 1s and C 1s spectra and their decomposition of a MEECO multilayer adsorbed at 150 K on Si(001) as well as additional results from DFT calculations and information on the computational raw data.

Acknowledgement

We acknowledge financial support by the Deutsche Forschungsgemeinschaft through SFB 1083 (project-ID 223848855) and DU 1157/4-1. We thank HRZ Marburg, GOETHE-CSC Frankfurt and HLR Stuttgart for computational resources. Open access funding enabled and organized by Projekt DEAL.

Conflict of Interest

The authors declare no conflict of interest.

Keywords: chemoselective adsorption · density functional calculations · organic molecules · silicon surface · X ray photoelectron spectroscopy

[1] J. T. Yates Jr., *Science* **1998**, *279*, 335–336.
[2] R. A. Wolkow, *Annu. Rev. Phys. Chem.* **1999**, *50*, 413–41.
[3] M. A. Filler, S. F. Bent, *Prog. Surf. Sci.* **2003**, *73*, 1–56.
[4] J. Yoshinobu, *Prog. Surf. Sci.* **2004**, *77*, 37–70.
[5] T. R. Leftwich, A. V. Teplyakov, *Surf. Sci. Rep.* **2008**, *63*, 1–71.
[6] F. F. Tao, Y. Zhu, S. L. Bernasek in *Functionalization of Semiconductor Surfaces*, John Wiley and Sons Inc., Hoboken, New Jersey, **2012**.
[7] A. V. Teplyakov, S. F. Bent, *J. Vac. Sci. Technol. A* **2013**, *31*, 050810.
[8] M. Hossain, Y. Yamashita, K. Mukai, J. Yoshinobu, *Chem. Phys. Lett.* **2004**, *388*, 27–30.
[9] Y. X. Shao, Y. H. Cai, D. Dong, S. Wang, S. G. Ang, G. Q. Xu, *Chem. Phys. Lett.* **2009**, *482*, 77–80.
[10] M. Ebrahimi, K. Leung, *Surf. Sci.* **2009**, *603*, 1203–1211.
[11] Y. P. Zhang, J. H. He, G. Q. Xu, E. S. Tok, *J. Phys. Chem. C* **2011**, *115*, 15496–15501.
[12] B. Shong, T. E. Sandoval, A. M. Crow, S. F. Bent, *J. Phys. Chem. Lett.* **2015**, *6*, 1037–1041.
[13] M. F. H. C. Kolb, K. B. Sharpless, *Angew. Chem. Int. Ed.* **2001**, *40*, 2004–2021; *Angew. Chem.* **2001**, *113*, 2056–2075.
[14] N. Münster, P. Nikodemiak, U. Koert, *Org. Lett.* **2016**, *18*, 4296–4299.
[15] M. Reutzel, N. Münster, M. A. Lipponer, C. Länger, U. Höfer, U. Koert, M. Dürr, *J. Phys. Chem. C* **2016**, *120*, 26284–26289.
[16] L. Pecher, R. Tonner, *Theor. Chem. Acc.* **2018**, *137*, 48.
[17] C. Länger, J. Heep, P. Nikodemiak, T. Bohamud, P. Kirsten, U. Höfer, U. Koert, M. Dürr, *J. Phys. Condens. Matter* **2019**, *31*, 034001.
[18] G. Mette, M. Dürr, R. Bartholomaus, U. Koert, U. Höfer, *Chem. Phys. Lett.* **2013**, *556*, 70–76.
[19] L. Pecher, S. Schmidt, R. Tonner, *J. Phys. Chem. C* **2017**, *121*, 26840–26850.
[20] J. Meinecke, U. Koert, *Org. Lett.* **2019**, *21*, 7609–7612.
[21] M. Dürr, Z. Hu, A. Biedermann, U. Höfer, T. F. Heinz, *Phys. Rev. B* **2001**, *63*, 121315.
[22] G. Mette, C. Schwalb, M. Dürr, U. Höfer, *Chem. Phys. Lett.* **2009**, *483*, 209–213.
[23] J. Heep, J.-N. Luy, C. Langer, J. Meinecke, U. Koert, R. Tonner, M. Dürr, *J. Phys. Chem. C* **2020**, *124*, 9940–9946.
[24] C. Länger, T. Bohamud, J. Heep, T. Glaser, M. Reutzel, U. Höfer, M. Dürr, *J. Phys. Chem. C* **2018**, *122*, 14756–14760.
[25] G. Kresse, J. Hafner, *Phys. Rev. B* **1993**, *47*, 558–561.
[26] G. Kresse, J. Furthmüller, *Comput. Mater. Sci.* **1996**, *6*, 15–50.
[27] G. Kresse, J. Furthmüller, *Phys. Rev. B* **1996**, *54*, 11169–11186.
[28] A. V. Krukau, O. A. Vydrov, A. F. Izmaylov, G. E. Scuseria, *J. Chem. Phys.* **2006**, *125*, 224106.
[29] G. Kresse, D. Joubert, *Phys. Rev. B* **1999**, *59*, 1758–1775.
[30] S. Grimme, J. Antony, S. Ehrlich, H. Krieg, *J. Chem. Phys.* **2010**, *132*, 154104.
[31] S. Grimme, S. Ehrlich, L. Goerigk, *Comput. Mater. Sci.* **2011**, *32*, 1456–1465.
[32] J. P. Perdew, K. Burke, M. Ernzerhof, *Phys. Rev. Lett.* **1996**, *77*, 3865–3868.
[33] G. Henkelman, H. Jonsson, *J. Chem. Phys.* **1999**, *111*, 7010–7022.
[34] J. Pecher, R. Tonner, *ChemPhysChem* **2017**, *18*, 34–38.
[35] J. L. Armstrong, J. M. White, M. Langell, *J. Vac. Sci. Technol. A* **1997**, *15*, 1146–1154.
[36] K. M. O'Donnell, C. Byron, G. Moore, L. Thomsen, O. Warschkow, A. Teplyakov, S. R. Schofield, *J. Phys. Chem. C* **2019**, *123*, 22239–22249.
[37] H.-N. Hwang, J. Y. Baik, K.-S. An, S. S. Lee, Y. Kim, *J. Phys. Chem. B* **2004**, *108*, 8379–8384.
[38] G. Mette, M. Reutzel, R. Bartholomäus, S. Laref, R. Tonner, M. Dürr, U. Koert, U. Höfer *ChemPhysChem* **2014**, *15*, 3725–3728.
[39] M. Reutzel, G. Mette, P. Stromberger, U. Koert, M. Dürr, U. Höfer, *J. Phys. Chem. C* **2015**, *119*, 6018–6023.
[40] F. Rochet, F. Jolly, F. Bournel, G. Dufour, F. Sirotti, J.-L. Cantin, *Phys. Rev. B* **1998**, *58*, 11029–11042.
[41] T. Glaser, C. Länger, J. Heep, J. Meinecke, M. G. Silly, U. Koert, M. Dürr, *J. Phys. Chem. C* **2020**, *124*, 22619–22624.
[42] J. Pecher, C. Schober, R. Tonner, *Chem. Eur. J.* **2017**, *23*, 5459–5466.
[43] L. Pecher, S. Laref, M. Raupach, R. Tonner, *Angew. Chem. Int. Ed.* **2017**, *56*, 15150–15154; *Angew. Chem.* **2017**, *129*, 15347–15351.
[44] M. Raupach, R. Tonner, *J. Chem. Phys.* **2015**, *142*, 194105.

Manuscript received: October 20, 2020
Revised manuscript received: November 25, 2020
Accepted manuscript online: December 1, 2020
Version of record online: January 21, 2021

I. O 1s and C 1s spectra of MEECO adsorbed at 150 K on Si(001)

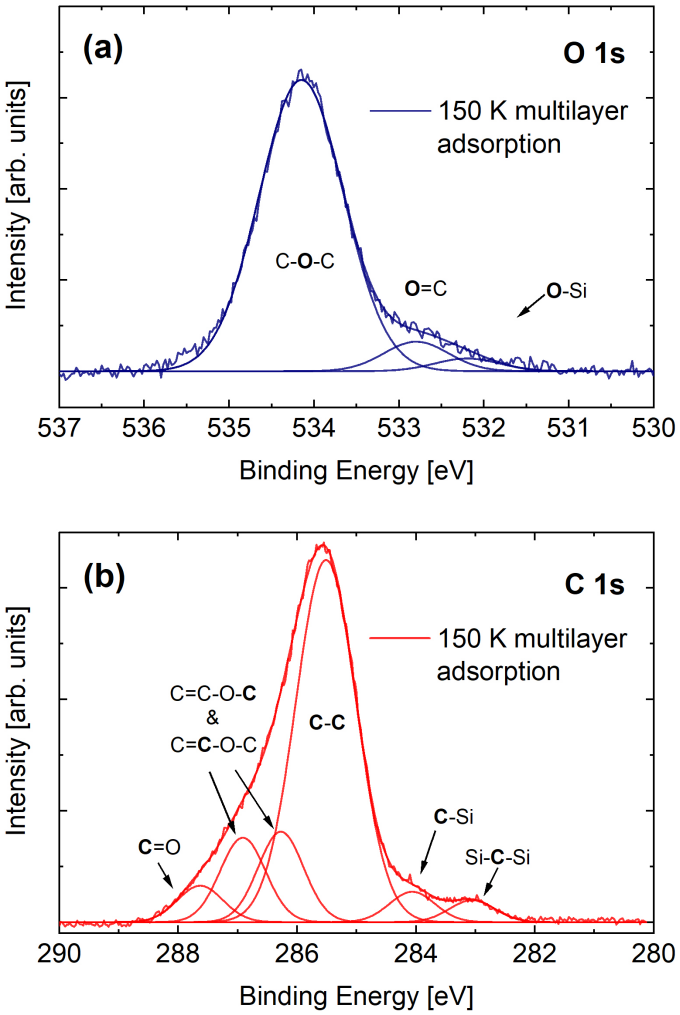

FIG. S1: O 1s (a) and C 1s (b) core level spectra after adsorption of MEECO on Si(001) at 150 K. Fit components are chosen as in Fig. 2 of the main paper. The single components have been shifted (< 0.15 eV in the case of O 1s and < 0.2 eV in the case of C 1s) with respect to the peak positions used in the main paper in order to properly account for the position of the main peaks.

II. Computational data with the PBE-D3 functional

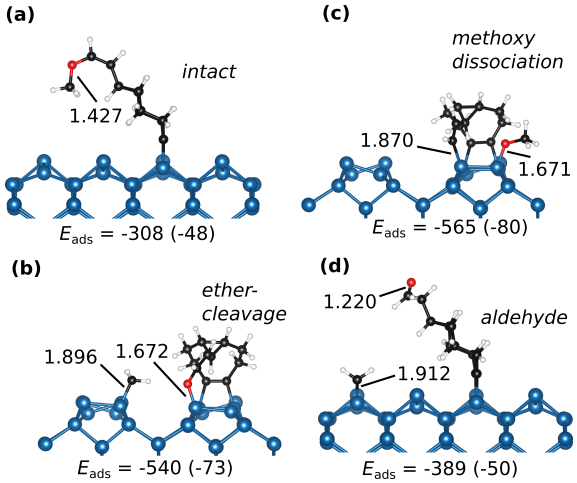

FIG. S2: Results from DFT studies. (a) to (d) Most important adsorption modes with adsorption energies (PBE-D3) given in kJ mol^{-1} (contributions from dispersion interactions in brackets). Selected bond distances are given in Å. In (b) and (c), the silicon substrate is rotated by 90° with respect to the situation shown in (a) and (d).

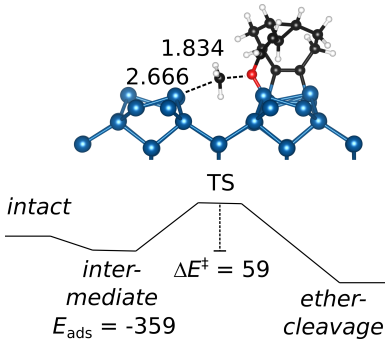

FIG. S3: Reaction path (PBE-D3 based calculations) of the MEECO molecule bound in the *intact* configuration to the *ether-cleavage* structure via the datively bonded *intermediate*. The transition state configuration is shown, it is associated with a barrier of $\Delta E^{\ddagger} = 59$ kJ mol^{-1}. Selected bond distances are given in Å, energies in kJ mol^{-1}.

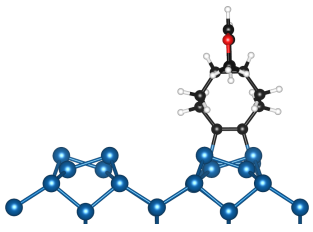

FIG. S4: Intact configuration as shown in Figs. 6(a) and S2(a) but rotated by 90° for better inspection of the cyclooctyne ring.

III. Computational raw data

Computational raw data is available at the NOMAD repository:
https://dx.doi.org/10.17172/NOMAD/2020.11.24-1

Chemistry Europe
European Chemical Societies Publishing

Click Chemistry in Ultra-high Vacuum – Tetrazine Coupling with Methyl Enol Ether Covalently Linked to Si(001)

Timo Glaser,[a] Jannick Meinecke,[b] Lukas Freund,[a] Christian Länger,[a] Jan-Niclas Luy+,[b, c] Ralf Tonner+,[b, c] Ulrich Koert,[b] and Michael Dürr*[a]

Abstract: The additive-free tetrazine/enol ether click reaction was performed in ultra-high vacuum (UHV) with an enol ether group covalently linked to a silicon surface: Dimethyl 1,2,4,5-tetrazine-3,6-dicarboxylate molecules were coupled to the enol ether group of a functionalized cyclooctyne which was adsorbed on the silicon (001) surface via the strained triple bond of cyclooctyne. The reaction was observed at a substrate temperature of 380 K by means of X-ray photoelectron spectroscopy (XPS). A moderate energy barrier was deduced for this click reaction in vacuum by means of density functional theory based calculations, in good agreement with the experimental results. This UHV-compatible click reaction thus opens a new, flexible route for synthesizing covalently bound organic architectures.

Click reactions[1,2] are employed in various fields of chemistry such as drug development[3] and material science.[4] The concept is well developed for reactions in solution, including heterosequences of click reactions using orthogonal reaction types (Figure 1(a)). No general strategy for vacuum-based click chemistry, in particular using orthogonal heterosequences, has been reported so far. This is mainly based on the fact that conventional click reactions are typically developed in solution and can require a catalyst; they are thus not compatible with a UHV-based approach. On the other hand, highly reactive semiconductor surfaces are typically prepared under UHV conditions and vacuum-based click chemistry could lead to predictable tailored layer-by-layer synthesis on such surfaces without the experimental challenge of transferring the samples from UHV to solution (and reverse).[5]

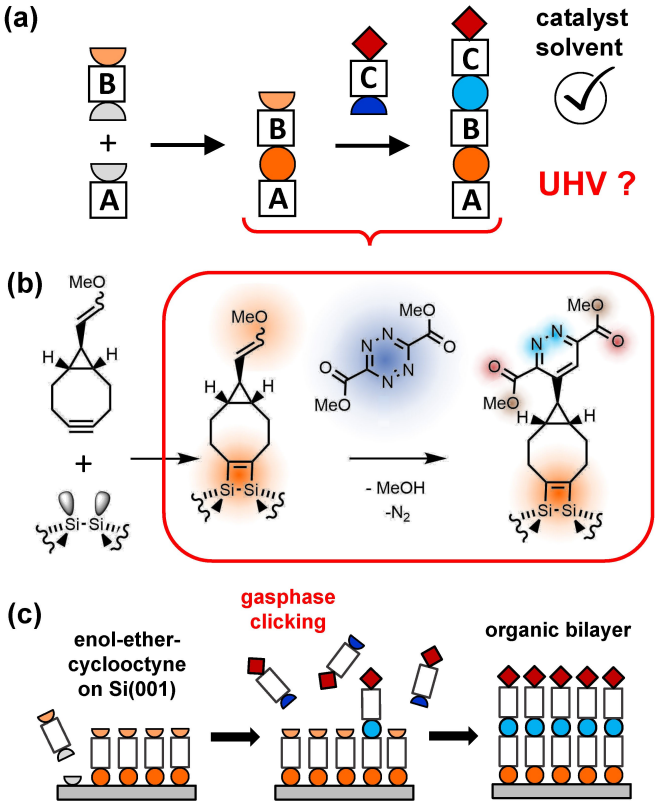

Figure 1. a) Heterosequences of orthogonal click reactions are well established in solution. b) The reaction of dimethyl 1,2,4,5-tetrazine-3,6-dicarboxylate with a methyl enol ether group attached to Si(001) via cyclooctyne was studied as part of such a heterosequence under ultra-high vacuum conditions. c) Chemoselective adsorption of methyl enol ether-substituted cyclooctyne (MEECO) on Si(001) is the first step of this heterosequence. Gas-phase clicking as the second step can then lead to a well-ordered organic bilayer.

A carefully tuned enolether/tetrazine cycloaddition has been shown to proceed in solution without catalyst.[6] It is thus a promising candidate for a vacuum-based click reaction (Figure 1(b)). Furthermore, it is orthogonal to the strain-promoted cycloaddition of cyclooctynes to azides.[7] Given the fact that substituted cyclooctynes can react in a chemoselective, strain promoted 2+2 cycloaddition on Si(001),[8–12] an orthogonal cycloaddition sequence under UHV-conditions could be

[a] T. Glaser, L. Freund, Dr. C. Länger, Prof. Dr. M. Dürr
Institut für Angewandte Physik and Zentrum für Materialforschung, Justus-Liebig-Universität Giessen, 35392 Giessen, Germany
E-mail: michael.duerr@ap.physik.uni-giessen.de

[b] J. Meinecke, J.-N. Luy,+ Prof. Dr. R. Tonner,+ Prof. Dr. U. Koert
Fachbereich Chemie, Philipps-Universität Marburg, 35032 Marburg, Germany

[c] J.-N. Luy+, Prof. Dr. R. Tonner+
Fakultät für Chemie und Pharmazie, Universität Regensburg, 93053 Regensburg, Germany

[+] Current address: Wilhelm-Ostwald-Institut für Physikalische und Theoretische Chemie, Universität Leipzig, 04103 Leipzig, Germany

Supporting information for this article is available on the WWW under https://doi.org/10.1002/chem.202005371

realized when combining both reaction schemes (Figures 1(b) and (c)).

Here we show experimentally by means of XPS that tetrazine/enol-ether coupling can be performed under ultra-high vacuum conditions at elevated substrate temperature. The results are backed by DFT calculations which find a moderate energy barrier for this reaction in the absence of solvent or catalyst. We employ this reaction for coupling a tetrazine molecule to an enol ether group which is covalently attached on a Si(001) surface via cyclooctyne as a linker (Figures 1(b) and (c)). In this context, UHV-based click chemistry can be employed for the synthesis of covalently bound, complex organic architectures on surfaces[13,14] (Figure 1(c)), with many applications, e.g., in surface functionalization or organic electronics.

In Figure 2, N 1s core level spectra of different adsorption experiments are compared. No nitrogen signal is obtained from the MEECO-covered surface (Figure 2(d)), which serves as the starting point of our experiment (compare Figure 1(b), left). When a multilayer of tetrazine molecules is physically adsorbed on the MEECO-covered Si surface at 150 K, a clear nitrogen peak is observed (Figure 2(a)). However, this peak completely vanishes when the sample is heated to 300 K (Supporting Information, Figure S1). Thus, all tetrazine molecules again desorbed from the surface, indicating that no covalent bonds were established under these conditions. In contrast, a clear peak is observed at 401.6 eV when tetrazine is reacted on the MEECO-covered Si surface at $T_S = 380$ K as shown in Figure 2(c).

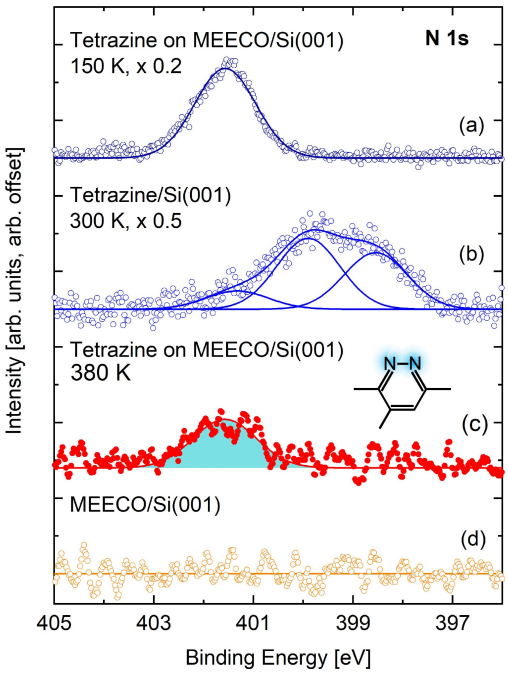

Figure 2. N 1s spectra measured under different experimental conditions. a) Multilayer of tetrazine molecules physically adsorbed on the MEECO covered Si surface at 150 K. Tetrazine was adsorbed b) on bare Si(001) at 300 K or c) on MEECO/Si(001) at 380 K. In (c), one single peak is observed that can be assigned to the product of the click reaction of tetrazine on MEECO. d) For reference, the nitrogen spectrum measured directly after MEECO adsorption is shown, no N signal is identified.

We interpret this peak as the result of the click reaction based on the following reasoning: first, we can exclude a direct binding of tetrazine via the nitrogen atoms to the silicon surface by comparison with Figure 2(b), which shows a measurement of tetrazine adsorbed on bare Si(001). In the latter case, two major peaks are observed at lower binding energy; the peak at 398.5 eV can be assigned to N atoms directly bound to silicon,[15] the peak at 400.0 eV is assigned to further nitrogen atoms in these molecules which are adsorbed on silicon via one or two nitrogen atoms. The small peak at 401.4 eV might be assigned to tetrazine molecules which do not bind via nitrogen atoms but solely via the ester groups to the silicon surface. Second, although the peak position is similar to the spectrum in Figure 2(a), we can exclude physisorbed tetrazine molecules to be the origin of the signal in Figure 2(c), as such physisorbed molecules were shown to desorb at temperature below room temperature. Thus the signal in Figure 2(c) indeed can be assigned to the tetrazine-MEECO coupling which proceeds at temperatures higher than room temperature only. The similar peak position in Figure 2(a) and Figure 2(c) can be explained by the fact that the chemical environment of the nitrogen atoms does not change significantly when tetrazine is reacted with MEECO.

Further evidence is obtained from the O 1s spectra shown in Figure 3, which were measured during the same experiments as the N 1s spectra shown in Figure 2. It has to be taken into account that the adsorbed MEECO on the Si(001) surface already accounts for three peaks in the O 1s spectra (Figure 3(d)), as discussed in detail in a previous work.[12] In brief, these components can be assigned to the intact ether group (534.1 eV),[16] oxygen from the ether group reacted on silicon (532 eV),[17] and a C=O group as a product of CH_2 abstraction (532.7 eV).[18] In Figure 3(c), the spectrum of the tetrazine/enol-ether coupling product is shown. Two additional peaks are observed, which are assigned to the C–O–C configuration (534.7 eV, brown) and the C=O configuration (533.2 eV, red) in the tetrazine molecule. Both of these configurations have been assigned in the spectrum of MEECO on silicon as well (Figure 3(d)), however, with a slightly different binding energy. This difference in binding energy results from two contributions: first, the two components are closely coupled in the ester group of the tetrazine derivative but there is always only one oxygen atom in the configurations related to MEECO on Si(001). Second, the total chemical environment is different: The reacted tetrazine molecule contains two nitrogen atoms, whereas no further heteroatom with an electronegativity higher than for carbon is present in the MEECO molecule. This assignment is further backed by the peak positions deduced from the DFT calculations shown in Figure 3(c).

The peak at 534.0 eV, which is assigned to the intact enol ether group of MEECO, shows a reduced intensity in Figure 3(c) when compared to Figure 3(d). This can be seen as a further indication for the click reaction, which reduces the number of intact enol ether groups on the surface.

The corresponding C 1s spectra are shown in Figure 4. All spectra are dominated by the peaks of MEECO adsorbed on silicon (compare Figure 4(d)). In Figure 4(a), when tetrazine is

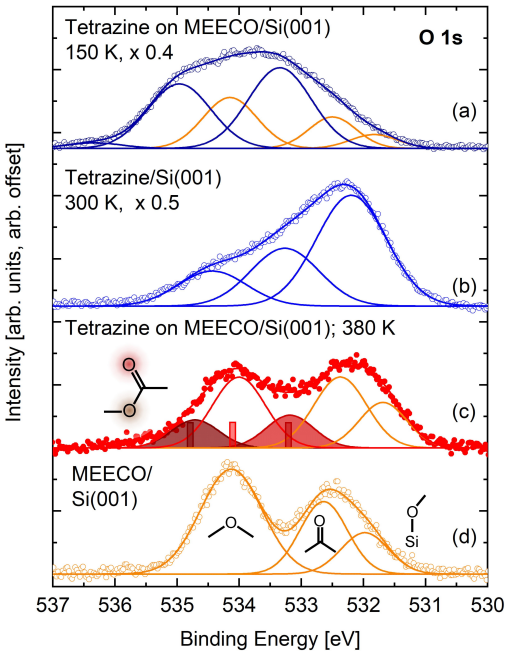

Figure 3. O 1s spectra measured under different experimental conditions. a) The spectrum of tetrazine on MEECO/Si(001) at 150 K. Most of the intensity (peaks at 533.3 and 535.0 eV, blue lines) can be assigned to the two oxygen species present in the tetrazine molecule. Additionally, the oxygen atoms from the adsorbed MEECO molecules contribute to the total intensity (orange components, cf (d), the O 1s spectrum after MEECO adsorption on Si(001)). b) The spectrum of tetrazine adsorbed on bare Si(001) at 300 K. The most intense peak at 532.2 eV can be assigned to O–Si, thus indicating that adsorption of tetrazine molecules on Si(001) involves on average more than one oxygen atom per tetrazine molecule. In combination with Figure 2(b), multi-tethered molecules, including the O and N atoms, can be deduced from these experiments. c) The spectrum after tetrazine reaction on MEECO/Si(001) at 380 K. The peak of the intact enol ether group decreases; two additional peaks (brown and red) can be assigned to the oxygen atoms in the tetrazine molecule (cf Figure 1(b)); they are in good agreement with the calculated peak positions indicated by bars drawn in the respective color.

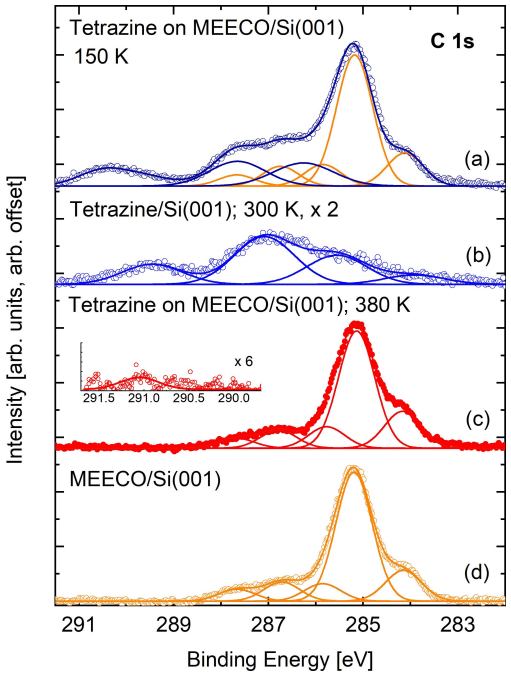

Figure 4. C 1s spectra measured under different conditions. a) Tetrazine adsorbed on MEECO/Si(001) at 150 K. Blue lines: components attributed to tetrazine (blue) and to MEECO on Si(001) (orange; cf (d)). b) Tetrazine adsorbed on Si(001) at 300 K. The components attributed in (a) to carbon atoms in tetrazine are shifted to lower binding energy due to adsorption of the molecule to silicon, thus increasing the electronic density also at the carbon atoms being in next neighborhood to the reacting N and O atoms. The spectrum measured after tetrazine reaction on MEECO/Si(001) at 380 K is shown in (c). The inset in (c) indicates a small signal at higher binding energy. In (d), the C 1s spectrum after the MEECO adsorption on Si(001) is shown for comparison.

adsorbed on MEECO/Si at 150 K, three further components at relatively high binding energy around 290 to 291 eV and between 286 and 288 eV can be measured. These peaks are assigned to the carbon atoms binding with the oxygen atoms (C–O; O–C=O) and nitrogen atoms in the intact tetrazine molecule. These three components are also present in the spectrum taken after tetrazine adsorption on Si(001) at 300 K (Figure 4(b)). The spectrum shown in Figure 4(c) was taken after reaction of tetrazine on a MEECO-covered surface at $T_S = 380$ K. The contribution of the carbon atoms of tetrazine coupled to MEECO to the total carbon signal is low, as the number of reacted MEECO accounts only for approximately one fifth of the MEECO coverage. Nonetheless, we observe a small peak at a binding energy of 291 eV as indicated in the inset of Figure 4(c) which can be assigned to the C atom in the intact ester group (O–C=O) of the tetrazine molecules coupled to MEECO on Si(001).

We carried out DFT calculations to shed light on the reaction of adsorbed MEECO with tetrazine with the main results summarized in Figure 5. We start from intact MEECO adsorbed on Si(001) as investigated before.[12] The reaction with tetrazine first leads to a physisorbed pre-complex **2**–**3** bound by 29 kJ mol^{-1} at room temperature (all energies refer to Gibbs free energies, $\triangle G$). The reaction then proceeds via a moderate reaction barrier of 100 kJ mol^{-1} towards the post-complex **4** which is already 75 kJ mol^{-1} more stable than the reactants. The final product **5** is then reached via loosing dinitrogen and methanol. Due to the very high thermodynamic driving force for this second reaction we did not investigate the reaction barrier. The transition state structure **TS** shows the early state of the formation of two C–C bonds that form the ring structure in the product. The bond lengths are still quite long (2.052 Å and 2.329 Å) in comparison to post-complex **4** which shows typical values for C–C single bonds. This explains the moderate barrier since the strong deformation in both molecules at the transition state structure is not counter-balanced by stabilization via bond formation processes. The barrier is nevertheless not too high to be overcome at room temperature and perfectly in line with the low reaction rates observed in experiment. For the higher reaction temperature of 380 K, we find the barrier only mildly increasing (+9 kJ mol^{-1}).

In experiment, the reaction is only observed at elevated temperature while it is not observed when heating the MEECO-covered surface which was prepared with a multilayer of physically bound tetrazine at 150 K (Figure S1, Supporting

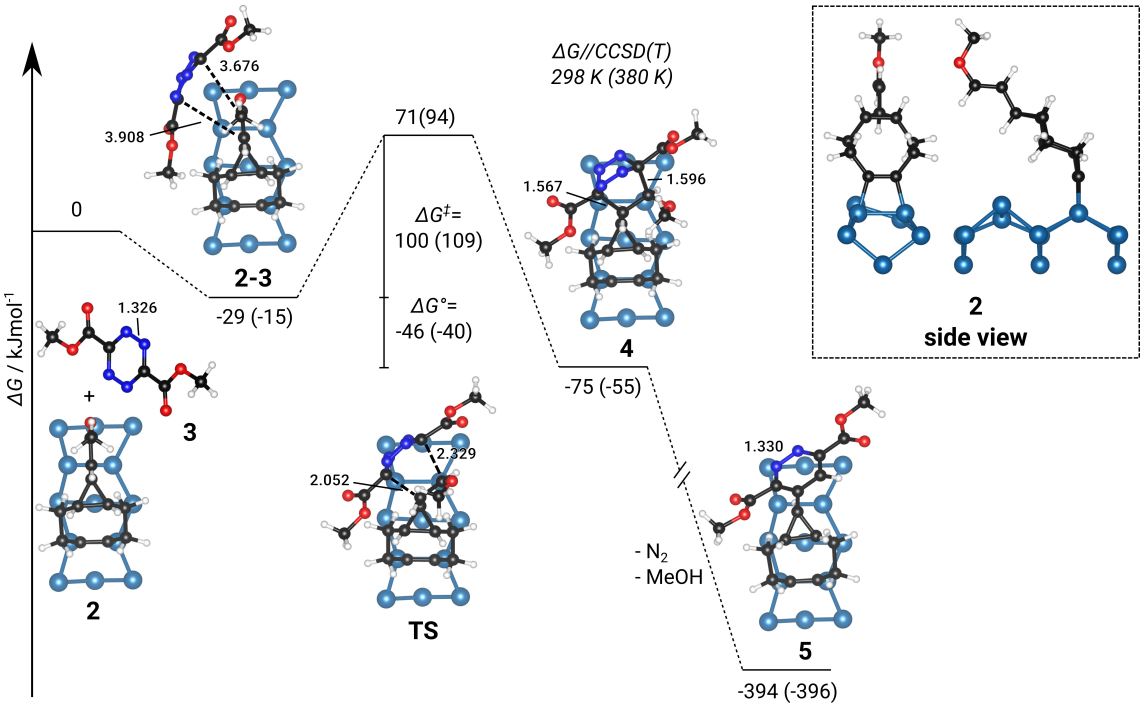

Figure 5. Computed reaction pathway (Gibbs free energy ΔG) of tetrazine with MEECO as adsorbed on Si(001). The reaction shows pre- (**2**–**3**) and post-complexes (**4**) connected via a transition state structure (**TS**) and ends in the product (**5**) after loosing dinitrogen and methanol. Reaction energies including thermodynamic corrections and high-level energy corrections are given at 298 and 380 K (in brackets) relative to the separated reactants. Selected bond lengths are given in Å.

Information). This observation is in agreement with the theoretical results which suggest a substantial conversion rate from **2**–**3** to **4** only at elevated temperatures. When slowly heating the tetrazine-covered surface, desorption via the rather low desorption barrier is favored over reaction via **TS** with its higher energy barrier.

At this point, we would like to note that, in the experiment, the MEECO-covered surface consists of several products and is thus not homogeneous as assumed in the calculations. This may alter the quantitative comparison between experiment and calculations but should have no influence on the qualitative interpretation of the data.

As summarized in Figure 6, coupling between a tetrazine derivative and an enol ether group, the latter being covalently attached on a Si(001) surface via cyclooctyne, has been experimentally observed under ultrahigh vacuum conditions, i.e., in the absence of solvent or catalyst. Even under these conditions, the reaction proceeds via a moderate energy barrier between the physisorbed molecule and **4**, as shown by means of DFT calculations. The further reaction towards the experimentally observed final product **5** then exhibits a strong

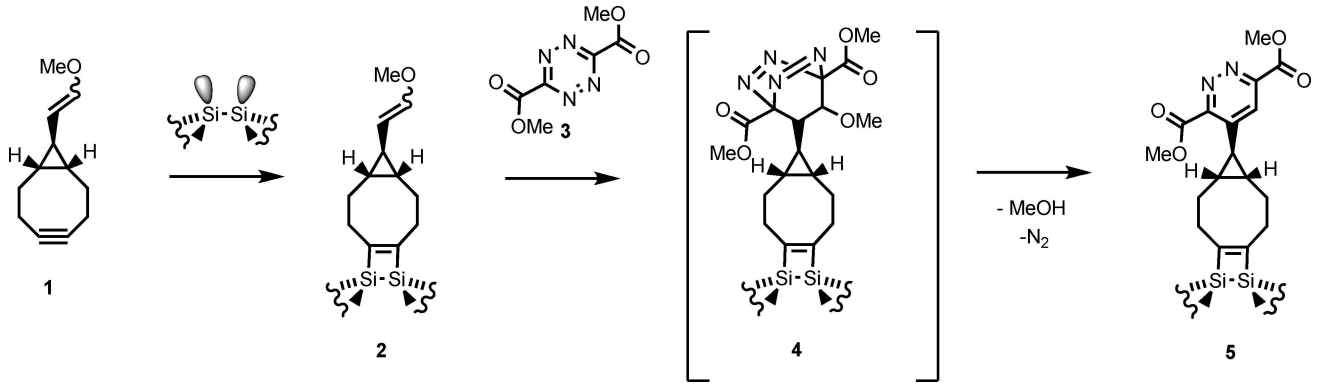

Figure 6. Summary of the reaction investigated: MEECO (**1**) reacts on the dimers of Si(001) via the strained triple bond of cyclooctyne forming **2**.[12] 1,2,4,5-Tetrazine-3,6-dicarboxylate (**3**) reacts with **2** via **4** to the final product **5** releasing N_2 and MeOH.

thermodynamic driving force. In conclusion, this click chemistry scheme in combination with the chemoselective reactivity of substituted cyclooctynes (**1**→**2** in Figure 6) allows for the synthesis of covalently bound molecular architectures in an UHV environment. As no catalyst is needed for the reaction investigated in this study, it can be applied on a substrate of choice, different to previously reported approaches, which were performed on the surfaces of Cu-containing materials,[19,20] the latter acting both as substrate and catalyst.

Methods

The XPS experiments were performed in a UHV chamber with a base pressure $< 1\times10^{-10}$ mbar. Si(001) samples were prepared by degassing at 700 K and repeated direct current heating cycles to 1450 K. A well ordered 2×1 reconstruction was obtained by cooling rates of about 1 K/s.[21,22] The preparation of methyl enol ether functionalized cyclooctyne (MEECO) on Si(001) was carried out according to Ref. [12]. MEECO adsorption on Si(001) preferentially takes place via the strained triple bond of the cyclooctyne ring; side reactions include ether cleavage and the formation of an aldehyde group.[12]

Synthesis of dimethyl 1,2,4,5-tetrazine-3,6dicarboxylate (short: tetrazine, Figure 1(b)) was carried out according to Ref. [6]. Tetrazine was dosed via a leak valve from the vapor phase in a test tube while the sample was kept at constant temperature using direct current heating of the sample and liquid nitrogen cooling of the sample holder. XPS measurements were performed using an Al K_α X-ray source with a monochromator (Omicron XM1000) and a hemispherical energy analyzer (Omicron EA125). All XPS spectra were referenced to the Si $2p_{3/2}$ peak at 99.4 eV.[23] Voigt-profiles were used for fitting the data; they are composed of 90% Gaußfunction and 10% Lorentzfunction. If not otherwise stated, full width at half maximum (FWHM) was approximately 0.9 eV in case of the single components of the C 1s and O 1s signals, and approximately 1.5 eV for the N 1s signals; these values are typical for XPS spectra measured in this setup.[15,24]

DFT investigations were done with the Vienna ab initio simulation package (VASP 5.4.4)[25–27] and standard PAW-pseudopotentials PBE.54[28] with a large core configuration while dispersion effects were considered via the DFT–D3 scheme including an improved damping function.[29,30] The plane wave energy cutoff was set to 400 eV and a total energy difference of at least 10^{-6} eV with "accurate" precision was used for SCF convergence. Structural optimizations were performed with the PBE-D3[31] exchange correlation functional with the force convergence criterion set to 10^{-2} eV/Å while more accurate energies were then derived using HSE06-D3[32] range-separated hybrid functional as single-point energies. For tetrazine, a planar structure has been used, PBE-D3 gives an unphysically buckled structure as minimum. Transition-state structures were calculated with the dimer method[33] as implemented in the transition state tools (1.73) for VASP with tighter electronic convergence of 10^{-7} eV. For the Si(001) slab calculations, a Γ-centered 2×2×1 *k*-mesh was chosen together with a setup of six layers (two bottom layers frozen and terminated with hydrogen atoms) as determined in previous work.[34] Thermodynamic corrections for the Gibbs energy were calculated at the PBE-D3 level in a pseudo gas phase model by replacing all Si–C bonds with capping hydrogens while keeping the C=C distance fixed. Thus a restricted Hessian calculation is performed except for free molecules (tetrazine, dinitrogen, and methanol) for which the full Hessian is used. Scripts to extract thermodynamic data from the VASP output have been published elsewhere.[15] In order to improve the energies obtained with HSE06-D3, OSV-PNO-CCSD(T)[35] calculations as implemented in TURBOMOLE 7.3[36] were performed for the same gas phase model that was used for the thermodynamic corrections. The higher order correction is then given as follows:

$$\begin{aligned}\Delta G_{slab}^{CCSD(T)} =& \Delta E_{slab}^{HSE06-D3} \\ &+ \Delta E_{gas}^{CCSD(T)} - \Delta E_{gas}^{HSE06-D3} \\ &+ \Delta G_{gas}^{PBE-D3}\end{aligned} \quad (1)$$

O 1s XPS peaks were determined in the initial state approximation from recalculation of the core orbital Kohn-Sham eigenvalues (VASP option: ICORELEVEL = 1) and shifted by + 25.7 eV.

Supporting Information

Supporting Information include XPS spectra on tetrazine adsorption on MEECO-covered Si(001) after adsorption at 150 K and heating to 300 K as well as information on computational raw data.

Acknowledgement

We acknowledge financial support by the Deutsche Forschungsgemeinschaft through SFB 1083 (project-ID 223848855). We thank HRZ Marburg, GOETHE-CSC Frankfurt and HLR Stuttgart for computational resources. Open access funding enabled and organized by Projekt DEAL.

Conflict of Interest

The authors declare no conflict of interest.

Keywords: click chemistry · density functional calculations · silicon · surface chemistry · X-ray photoelectron spectroscopy

[1] H. C. Kolb, M. G. Finn, K. B. Sharpless, *Angew. Chem. Int. Ed.* **2001**, *40*, 2004–2021; *Angew. Chem.* **2001**, *112*, 2056–2075.
[2] E. M. Sletten, C. R. Bertozzi, *Angew. Chem. Int. Ed.* **2009**, *48*, 6974–98; *Angew. Chem.* **2009**, *121*, 7108–7133.
[3] B. Peng, A.-G. Thorsell, T. Karlberg, H. Schüler, S. Q. Yao, *Angew. Chem. Int. Ed.* **2017**, *56*, 248–253; *Angew. Chem.* **2017**, *129*, 254–259.

[4] W. Xi, T. F. Scott, C. J. Kloxin, C. N. Bowman, *Adv. Funct. Mater.* **2014**, *24*, 2572–2590.
[5] T. Glaser, J. Meinecke, C. Langer, J. Heep, U. Koert, M. Dürr, *J. Phys. Chem. C* **2021**, *125*, 4021–4026.
[6] J. Meinecke, U. Koert, *Org. Lett.* **2019**, *21*, 7609–7612.
[7] N. Münster, P. Nikodemiak, U. Koert, *Org. Lett.* **2016**, *18*, 4296–4299.
[8] G. Mette, M. Dürr, R. Bartholomäus, U. Koert, U. Höfer, *Chem. Phys. Lett.* **2013**, *556*, 70–76.
[9] M. Reutzel, N. Münster, M. A. Lipponer, C. Länger, U. Höfer, U. Koert, M. Dürr, *J. Phys. Chem. C* **2016**, *120*, 26284–26289.
[10] L. Pecher, R. Tonner, *Theo. Chem. Acc.* **2018**, *137*, 48.
[11] C. Länger, J. Heep, P. Nikodemiak, T. Bohamud, P. Kirsten, U. Höfer, U. Koert, M. Dürr, *J. Phys.: Condens. Matter* **2019**, *31*, 034001.
[12] T. Glaser, J. Meinecke, C. Länger, J.-N. Luy, R. Tonner, U. Koert, M. Dürr, *ChemPhysChem* **2020**, *22*, 404–409.
[13] N. K. Devaraj, J. P. Collman, *QSAR Comb. Sci.* **2007**, *26*, 1253–1260.
[14] A. C. Gouget-Laemmel, J. Yang, M. A. Lodhi, A. Siriwardena, D. Aureau, R. Boukherroub, J.-N. Chazalviel, F. Ozanam, S. Szunerits, *J. Phys. Chem. C* **2013**, *117*, 368–375.
[15] J. Heep, J.-N. Luy, C. Länger, J. Meinecke, U. Koert, R. Tonner, M. Dürr, *J. Phys. Chem. C* **2020**, *124*, 9940–9946.
[16] T. Glaser, C. Länger, J. Heep, J. Meinecke, M. G. Silly, U. Koert, M. Dürr, *J. Phys. Chem. C* **2020**, *124*, 22619–22624.
[17] G. Mette, M. Reutzel, R. Bartholomäus, S. Laref, R. Tonner, M. Dürr, U. Koert, U. Höfer, *ChemPhysChem* **2014**, *15*, 3725–3728.
[18] K. M. O'Donnell, C. Byron, G. Moore, L. Thomsen, O. Warschkow, A. Teplyakov, S. R. Schofield, J. Phys, *Chem. C* **2019**, *123*, 22239–22249.
[19] F. Bebensee, C. Bombis, S.-R. Vadapoo, J. R. Cramer, F. Besenbacher, K. V. Gothelf, T. R. Linderoth, *J. Am. Chem. Soc.* **2013**, *135*, 2136–2139.
[20] C. He, R. Janzen, S. Bai, A. V. Teplyakov, *Chem. Mater.* **2019**, *31*, 2068–2077.
[21] C. H. Schwalb, M. Lawrenz, M. Dürr, U. Höfer, *Phys. Rev. B* **2007**, *75*, 085439.
[22] G. Mette, A. Adamkiewicz, M. Reutzel, U. Koert, M. Dürr, U. Höfer, *Angew. Chem. Int. Ed.* **2019**, *58*, 3417–3420; *Angew. Chem.* **2019**, *131*, 3455–3458.
[23] M. Reutzel, G. Mette, P. Stromberger, U. Koert, M. Dürr, U. Höfer, *J. Phys. Chem. C* **2015**, *119*, 6018–6023.
[24] C. Länger, T. Bohamud, J. Heep, T. Glaser, M. Reutzel, U. Höfer, M. Dürr, *J. Phys. Chem. C* **2018**, *122*, 14756–14760.
[25] G. Kresse, J. Hafner, *Phys. Rev. B* **1993**, *47*, 558–561.
[26] G. Kresse, J. Furthmüller, *Comput. Mater. Sci.* **1996**, *6*, 15–50.
[27] G. Kresse, J. Furthmüller, *Phys. Rev. B* **1996**, *54*, 11169–11186.
[28] G. Kresse, D. Joubert, *Phys. Rev. B* **1999**, 59, 1758–1775.
[29] S. Grimme, J. Antony, S. Ehrlich, H. Krieg, *J. Chem. Phys.* **2010**, *132*, 154104.
[30] S. Grimme, S. Ehrlich, L. Goerigk, *Comput. Mater. Sci.* **2011**, *32*, 1456–1465.
[31] J. P. Perdew, K. Burke, M. Ernzerhof, *Phys. Rev. Lett.* **1996**, *77*, 3865–3868.
[32] A. V. Krukau, O. A. Vydrov, A. F. Izmaylov, G. E. Scuseria, *J. Chem. Phys.* **2006**, *125*, 224106.
[33] G. Henkelman, H. Jonsson, *J. Chem. Phys.* **1999**, *111*, 7010–7022.
[34] J. Pecher, R. Tonner, *ChemPhysChem* **2017**, *18*, 34–38.
[35] G. Schmitz, C. Hättig, D. P. Tew, *Phys. Chem. Chem. Phys.* **2014**, *16*, 22167–22178.
[36] TURBOMOLE V7.2 **2017**, a development of University of Karlsruhe and Forschungszentrum Karlsruhe GmbH, 1989–2007, TURBOMOLE GmbH, since 2007; available from http://www.turbomole.com.

Manuscript received: December 16, 2020
Accepted manuscript online: April 13, 2021
Version of record online: May 7, 2021

Chemistry–A European Journal

Supporting Information

Click Chemistry in Ultra-high Vacuum – Tetrazine Coupling with Methyl Enol Ether Covalently Linked to Si(001)

Timo Glaser, Jannick Meinecke, Lukas Freund, Christian Länger, Jan-Niclas Luy[+], Ralf Tonner[+], Ulrich Koert, and Michael Dürr*

I. N 1s spectra of tetrazine adsorbed on MEECO-covered Si(001)

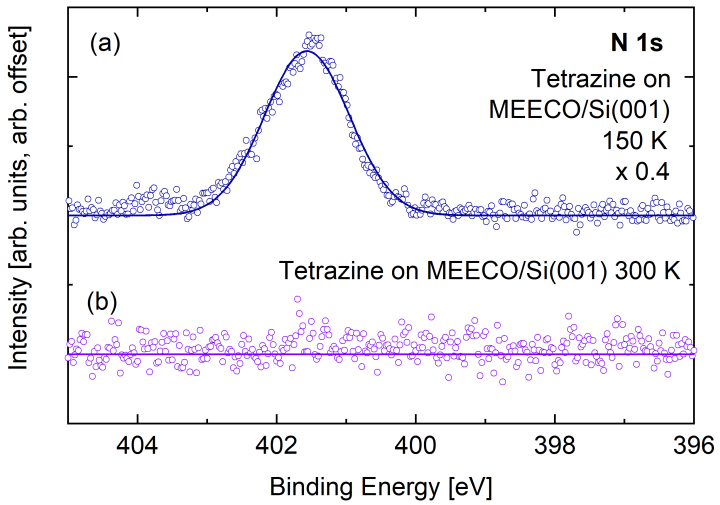

Figure S1: (a) N 1s spectra from a tetrazine multilayer adsorbed on a MEECO covered Si(001) surface at 150 K (same experiment as shown in Fig. 2(a) in the main paper). (b) After heating to 300 K (30 min), no N 1s signal is observed any more, all tetrazine molecules are desorbed. No reaction neither with the MEECO nor with the surface has taken place. The latter indicates sufficient passivation by the adsorption of MEECO with respect to direct adsorption of tetrazine on Si(001).

II. Computational raw data

Computational raw data is available at the NOMAD repository:
https://dx.doi.org/10.17172/NOMAD/2020.11.19-1

ACS OMEGA

http://pubs.acs.org/journal/acsodf

Article

Complementary Base Lowers the Barrier in SuFEx Click Chemistry for Primary Amine Nucleophiles

Jan-Niclas Luy and Ralf Tonner*

Cite This: *ACS Omega* 2020, 5, 31432−31439

Read Online

ACCESS | Metrics & More | Article Recommendations | Supporting Information

ABSTRACT: The sulfur(VI) fluoride exchange (SuFEx) reaction is an emerging scheme for connecting molecular building blocks. Due to its broad functional group tolerance and rather stable resulting linkage, it is seeing rapid adoption in various fields of chemistry. Still, to date the reaction mechanism is poorly understood, which hampers further development. Here, we show that the mechanism of the SuFEx reaction for the prototypical example of methanesulfonyl fluoride reacting with methylamine can be understood as an S_N2-type reaction. By analyzing the reaction path with the help of density functional theory *in vacuo* and under consideration of solvent and co-reactant influence, we identify the often used complementary base as a crucial ingredient to lower the reaction barrier significantly by increasing the nucleophilicity of the primary amine. With the help of energy decomposition analysis at the transition state structures, we quantify the underlying stereoelectronic effects and propose new avenues for experimental exploration of the potential of SuFEx chemistry.

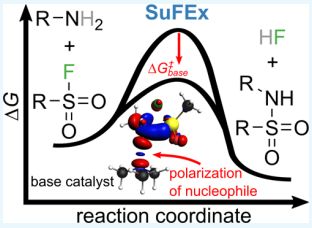

INTRODUCTION

The sulfur(VI) fluoride exchange reaction (SuFEx) was introduced as a new member of the "click chemistry" family[1] by Sharpless et al.,[2] thus significantly extending the previous work on organosulfur fluorides.[3,4] The method has recently seen a surge in research interest due to its excellent functional group tolerance, robustness, and reliability in diverse applications such as drug design,[5−7] polymer chemistry,[8,9] and materials science.[10−12] The SuFEx scheme is mainly used for linking molecular building blocks by substituting the fluoride atom of sulfonyl fluorides with a suitable nucleophile (see Scheme 1 for a typical example investigated here).

Scheme 1. Typical Example of SuFEx Chemistry Investigated in this Study Reaction of Methanesulfonyl Fluoride 1 with Nucleophile Methylamine 2 Yields Sulfonylamine 3 and Hydrogenfluoride

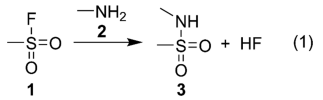

From the wealth of available nucleophiles, aryl silyl ethers have so far received most attention since they lead to high yields and show a broad substrate scope.[13] An alternative to aryl silyl ethers that promises simpler protocols and stronger (S−N) links while providing good yields are amine-based nucleophiles.[5,14] These characteristics explain the interest in SuFEx chemistry far beyond the realm of organic synthesis, e.g., in surface chemistry. But how can this reaction scheme lead to progress in these fields?

Controlled organic functionalization of semiconductor surfaces is a major research goal in materials science with applications ranging from sensors to molecular devices.[15] Functionalization can be carried out with solvent being present and also under ultrahigh vacuum (UHV) conditions more typical for surface science or even a combination of both.[16]

Our long-term goal in this research field is the identification of suitable reaction schemes for controlled functionalization in a layer-by-layer fashion from a computational perspective.[17,18] In this context, single-step reaction procedures like SuFEx are strongly preferred due to the synthetic constraints added by the surface.[19] Furthermore, optimization of reaction conditions in UHV chemistry is limited since variation of, e.g., solvent or pH values are not possible. Thus, a "click"-type reaction is sought for. Suitability of SuFEx for surface functionalization and the "click"-character under typical reaction conditions has been shown recently in several studies.[19−21] It has also been noted that for surface functionalization, amine-based nucleophiles (Scheme 1) are preferred over the standard SuFEx route since no prior installation of silyl ethers on the surface is necessary.[19] We thus set out to understand the reaction mechanism of SuFEx in vacuum as well as wet chemical conditions to test its feasibility for the scenarios of surface functionalization mentioned above.

Received: October 16, 2020
Accepted: October 27, 2020
Published: November 23, 2020

https://dx.doi.org/10.1021/acsomega.0c05049
ACS Omega 2020, 5, 31432−31439

The main factor limiting the potential of SuFEx chemistry is the lack of mechanistic insight, e.g., concerning the role of co-reactants and solvents.[22] The current understanding of the reaction mechanism based on experimental observations states that stabilization of the fluoride ion in intermediates and products is the determining factor in achieving high reaction rates.[2] There are also suggestions regarding the role of the base as either attacking the fluorosulfonate moiety to displace fluorine or act as a fluorine shuttle.[10,23] Overall, it is observed that strong bases and H_2F^- can act as catalysts for the reaction but the exact role is unclear up to now.[10,19,24,25]

We challenge and extend this understanding in the present study. Very recently, the mechanism of the Si-free SuFEx reaction with phenolate anions was investigated with the help of density functional theory (DFT), and an addition−elimination mechanism with very low barriers and early transition states was found while an S_N2-type reaction could not be excluded under experimental conditions.[26] The authors also concluded that the very high reactivity of the phenolate anion probably leads to a different mechanism compared to less strong nucleophiles, as investigated here.

As a suitable model system comprising all the essential elements of SuFEx chemistry suitable for surface functionalization, we chose the reaction of methanesulfonyl fluoride **1** with methylamine **2** (reaction (1), Scheme 1). The results should be transferable to other aliphatic amines and further nucleophiles, as shown below. The article is structured as follows: We start with an in-depth analysis of the gas phase reaction mechanism, including thermodynamic and kinetic aspects. Following this, the influence of solvent and co-reactant is investigated with the aid of implicit solvation modeling and microsolvation approaches.[27,28] Finally, the electronic structure of the product and transition state structure are analyzed with the help of energy decomposition analysis (EDA) to provide a rationale for the observations.

RESULTS AND DISCUSSION

First, we discuss gas phase reaction energies (ΔE°) and energy barriers ($\Delta E^\ddagger$) for the most plausible mechanism proposed in the literature: nucleophilic substitution at the sulfur atom (Figure 1).[2] Reaction (1) proceeds via a weakly-bound pre-complex **1-2** (dispersion interactions contribute ∼50% to the bonding energy) through a high-lying transition-state structure (**TS**) toward a post-complex with hydrogen-bonded HF (**3**-HF) that can dissociate in the final reaction step to yield product **3**. The total reaction is computed (PBE0-D3/def2-TZVPP//PBE-D3/def2-TZVPP) to be slightly exothermic (ΔE° = −8 kJ/mol), while the activation energy to the TS is high ($\Delta E^\ddagger$ = 159 kJ/mol). Considering thermodynamic and entropic corrections leads to a slight increase in barrier (ΔG° = −4 kJ/mol, $\Delta G^\ddagger$ = 170 kJ/mol). But these correction terms have a significant influence on pre- and post-complexes, which are significantly destabilized due to the unfavorable entropic term $T\Delta S$ for association reactions (loss of translational freedom). The reaction might indeed proceed without these pre- and post-complexes under typical lab conditions, similar to the difference in S_N2 reaction profiles between gas-phase and solution-phase chemistry.[29] This will be further discussed below when solvent effects are presented.

The high barriers computed are in line with the long reaction times and low yields reported in some studies for reactions at room temperature.[2,5,7] In comparison, the frequently utilized Cu-catalyzed azide−alkyne cycloaddition

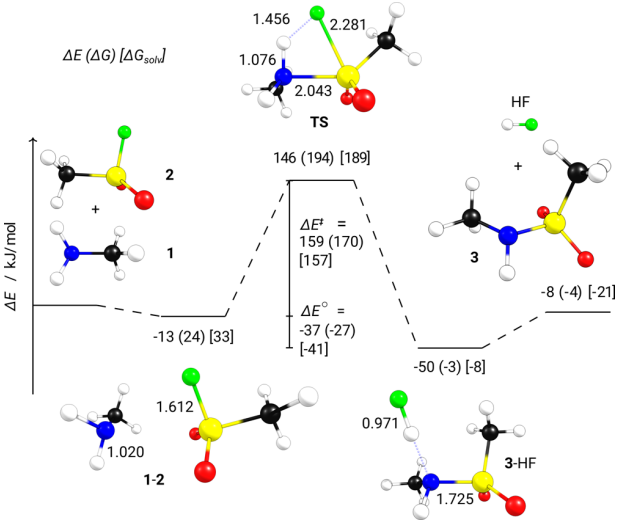

Figure 1. Reaction profile of **1** with **2** yielding **3** and HF. The reaction energy ΔE° (PBE0) is the difference between energies of pre-complex **1-2** and post-complex **3**-HF. The barrier $\Delta E^\ddagger$ (PBE0) is the difference between **1-2** and TS. Gibbs energies ΔG (PBE) are given in parentheses and the energies with implicit solvent correction for water ΔG_{solv} (PBE) in square brackets. All calculations with def2-TZVPP basis set.

"click" reaction shows much more favorable thermodynamic and kinetic signatures (ΔE° = −254 kJ/mol, $\Delta E^\ddagger$ = 62 kJ/mol[30]). The strain-promoted azide−alkyne cycloaddition shows an even lower reaction barrier of $\Delta E^\ddagger$ = 33 kJ/mol,[31] highlighting the need for further optimization of the amine SuFEx reaction scheme. We will outline some possibilities for this optimization in the following.

Next, we analyze the nature of the **TS** with the help of reaction force analysis of the potential energy surface (PES) from **1-2** to **3**-HF. This approach based on a fine-grained intrinsic reaction coordinate (IRC) calculation starting at the **TS** yields the reaction force (F, blue line in Figure 2) and the

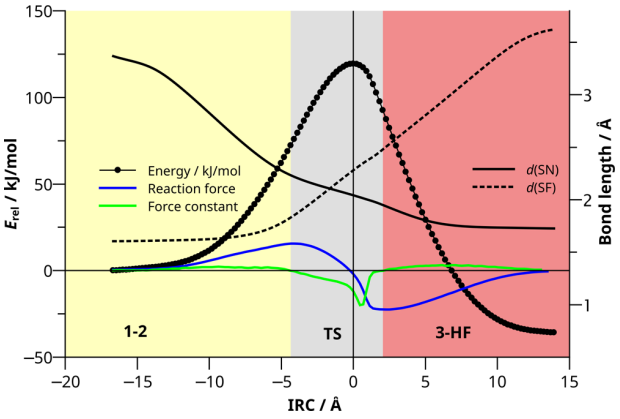

Figure 2. Result of reaction force analysis for reaction (1). The Euclidean distance between steps is tracked on the x axis and energy relative to **1-2** on the left axis. The reaction force, F (blue) and force constant, κ (green) are the first and second derivative of the energy with respect to atomic positions, respectively. Changes in the bond lengths d(SN) (solid) and d(SF) (dotted) are tracked on the right axis.

https://dx.doi.org/10.1021/acsomega.0c05049
ACS Omega 2020, 5, 31432−31439

force constant (κ, green line in Figure 2) along the IRC. The roots of κ separate the IRC path into regions resembling **TS** (gray), reactants (yellow), and products (red) whose shape and size characterize the phases of a reaction.[32,33] It thus allows to characterize the nature of transition states and provides a microscopic picture on the crucial changes in the molecule along the minimum energy path with the largest influence on the reaction barrier.[34]

The first finding is an asymmetric profile of the transition region (gray area). The **TS** is positioned rather close to the product, and the minimum of the force constant curve (green) does not coincide with the maximum of the energy (black circles). Those characteristics are indicative of a non-concerted reaction where bond-breaking and bond-making do not happen simultaneously along the reaction path as has been found before for the β-H elimination of group 15 alkyls.[34] An analysis of the bond lengths along the reaction path (Figure 2) confirms that the S−F bond is only slightly elongated at the beginning of the transition region (deviation from value in **2**, Δd(SF) = +0.227 Å) while the S−N bond is already close to its value at the **TS** (deviation from value at TS: Δd(SN) = +0.190 Å, see also the animated IRC in the Video S1). At the **TS**, the N−H bond is only moderately elongated (Δd(NH) = +0.056 Å, see Figure 1) and cannot be considered broken, yet. However, after the **TS**, cleavage of the N−H bond together with H−F bond formation proceeds fast and simultaneously. It becomes evident that around **TS**, the fluorine atom is already dissociated from S but not yet bound to H. As supported by partial charge analysis (natural population analysis, NPA), we have a nearly "naked" fluorine anion at the TS, which explains the high barrier (q(F): −0.47 (**1**); −0.70 (**TS**); −0.54 e (**3**-HF)). This seemingly supports the findings in the literature that stabilization of F^- should lead to a decreased barrier and in turn, an increase in the reaction rate. We will now show that the picture is more complex.

EFFECTS OF SOLVENT, SIDE PRODUCT, AND CO-REACTANT

After the examination of the gas-phase reaction, we now include solvent effects by means of (i) a continuum solvation model (conductor-like screening model, COSMO)[35] and (ii) microsolvation approaches. Initially, we look at the effect of H_2O since it is a typical solvent for the SuFEx reaction, e.g., for *in vivo* studies and biphasic solvent approaches.[2,7] Furthermore, we investigate the effects of the side product HF and of $N(CH_3)_3$ as a typical example for the base often used in SuFEx reactions as co-reactant.[2,5] The results are summarized in Table 1.

First, we investigate the influence of H_2O on thermodynamic and kinetic signatures of reaction (1) (Table 1). The stabilizing electrostatic effect of water due to its high dielectric constant (ε = 80) is already found with the COSMO approach (which is not able to capture hydrogen bonding effects), and the numbers are given in Figure 1 (ΔG_{solv} in square brackets). We discuss the values relative to the Gibbs energy reference (ΔG, in round brackets). Notably, the pre-complex **1**-**2** is destabilized ($\Delta\Delta G$ = +9 kJ/mol) while the post-complex **3**-HF is slightly stabilized ($\Delta\Delta G$ = −5 kJ/mol). The polar transition state is stabilized leading to a slightly lower barrier ($\Delta\Delta G^{\ddagger}$ = −13 kJ/mol, Table 1).

Next, we look at the effect of microsolvation by including one H_2O molecule explicitly in the calculation. The effect on the barrier is small ($\Delta\Delta G^{\ddagger}$ = −5 kJ/mol, Table 1), and the thermodynamic driving force is also less strong ($\Delta\Delta G^{\circ}$ = −5 kJ/mol) compared to the implicit solvent treatment ($\Delta\Delta G^{\circ}$ = −14 kJ/mol). Both methods show qualitatively the same trends, but for a quantitative answer a comprehensive modeling of several explicit solvation shells (possibly in addition to an implicit treatment) is needed, which is beyond the scope of this study. An improved estimate of the reaction barrier in water is given by combining implicit solvent modeling and three explicit water molecules in a trimer structure,[36] leading to a barrier of $\Delta E^{\ddagger}$ = 153 kJ/mol. This value is only 6 kJ/mol smaller compared to the gas-phase value (Table S2), supporting the notion of small solvent influence.

It is likely that the implicit solvation model overestimates the stabilization of **TS** and post-complex **3**-HF in aqueous solution when compared to the explicit treatment since structural changes induced by hydrogen bonds are not accounted for. Those structural changes can be large, as shown in Figure 3. Coordination of H_2O to the leaving group fluorine (Figure 3a) leads to longer F−H (+0.162 Å), S−N (+0.040 Å) distances and shorter N−H (−0.033 Å) and S−F bonds (−0.040 Å) with respect to the *in vacuo* values (Figure 1). This stabilization thus leads to an earlier transition state, in accordance with the Hammond−Leffler postulate and the slightly lower barrier.

Next, we consider the influence of side product HF taking part in the reaction, which is rather likely due to the stoichiometric amounts being formed in reaction (1). The reaction becomes considerably less favorable ($\Delta\Delta G^{\circ}$ = +25 kJ/mol, Table 1), and the barrier increases slightly ($\Delta\Delta G^{\ddagger}$ = +5 kJ/mol). The changes in bond lengths for the transition state structure are puzzling at first sight (Figure 3b). While the longer F−H (+0.276 Å) and S−N (+0.058 Å) bonds as well as the short N−H (−0.044 Å) bond indicate an even earlier transition state, the S−F distance is unchanged wrt the *in vacuo* calculation. This can be understood by the exceptionally high stability of the 4e3c bond (1.492 Å) in $[FHF]^-$, which leads to a stabilized and almost detached fluorine leaving group rather early on the IRC.[37] The apparent destabilization of **TS** comes as a result of choosing the pre-complex where HF is coordinated to the amine as the reference. When calculating the barrier with respect to the reactants, a stabilization of 24 kJ/mol is found compared to the gas-phase reaction. Ultimately, an HF dimer is formed, which has a weaker hydrogen bond compared to $[FHF]^-$.

Table 1. Reaction Free Energies and Barriers of the SuFEx Reaction Showing the Influence of Solvent (H_2O), Side Product (HF) and Base ($N(CH_3)_3$)[a]

solvent description	ΔG°	$(\Delta\Delta G^{\circ})$	$\Delta G^{\ddagger}$	$(\Delta\Delta G^{\ddagger})$
in vacuo	−27	(0)	170	(0)
+H_2O (implicit)	−41	(−14)	157	(−13)
+H_2O (explicit)	−32	(−5)	165	(−5)
+HF	−2	(+25)	175	(+5)
+$N(CH_3)_3$	−60	(−33)	143	(−27)
+HF and $N(CH_3)_3$	−33	(−6)	143	(−27)

[a]All energies in kJ/mol at PBE0/def2-TZVPP//PBE/def2-TZVPP. Solvent correction at PBE/def2-TZVPP. Gibbs free energies (ΔG°, $\Delta G^{\ddagger}$) are given with respect to the pre- and post-complexes with the shortest Euclidian distance to the TS (see Figure S2 in the Supporting Information for product structures) and changes w.r.t. the in vacuo value are given in parentheses ($\Delta\Delta G^{\circ}$, $\Delta\Delta G^{\ddagger}$). Electronic energies ($\Delta E$) are listed in the Supporting Information (Table S2) as well.

https://dx.doi.org/10.1021/acsomega.0c05049
ACS Omega 2020, 5, 31432−31439

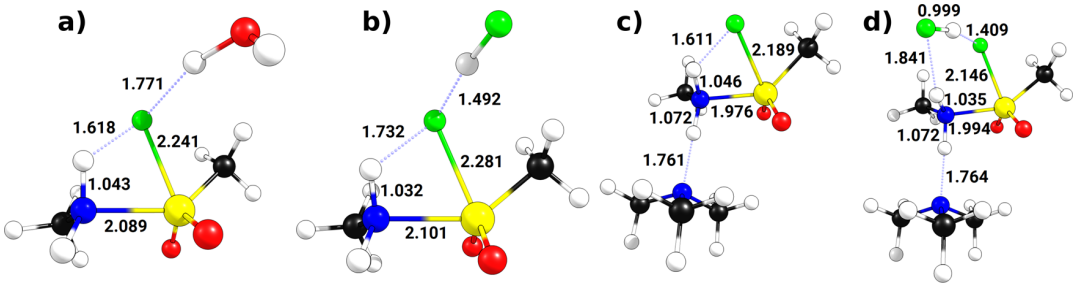

Figure 3. Optimized transition state structures with selected structural parameters under consideration of (a) explicit solvent (H_2O), (b) side product (HF), (c) base ($N(CH_3)_3$), and (d) side product and base combined (HF + $N(CH_3)_3$). Bond lengths are given in Å.

Common co-reactants in SuFEx chemistry are tertiary amine bases.[5] Thus, we consider next the reaction including $N(CH_3)_3$. The added base has the strongest influence on the reactivity among the additives considered here and leads to a stronger exergonic reaction ($\Delta\Delta G^\circ$ = −33 kJ/mol, Table 1) as well as a significantly lower reaction barrier ($\Delta\Delta G^{\ddagger}$ = −27 kJ/mol). The base coordinates to the nucleophile (Figure 3c) and leads to an unusual transition state structure where the S−F bond is rather short (−0.092 Å) and the F−H distance long (+0.155 Å), indicating an early transition state but the N−S bond is quite short already (−0.067 Å). This can be understood through the increased nucleophilicity of the attacking amine as evidenced by the HOMO being higher in energy with added base compared to the free nucleophile (ΔE_{HOMO} = +0.63 eV).

After traversal of the transition region, structural reorganization of the post-complex takes place (see Figure S2). The thermodynamic driving force of this reorganization is the formation of a HF/$N(CH_3)_3$ acid/base adduct. This reaction thus removes the base from the reaction mixture and helps to rationalize the experimental finding that the base is necessary in stoichiometric amounts to achieve good yields.[2,5]

Finally, we investigate the effect of side product HF and amine base being present at the same time. The barrier lowered by the base is not affected by HF being present ($\Delta\Delta G^{\ddagger}$ = −27 kJ/mol), and the transition state structure (Figure 3d) shows similar features compared to base alone (Figure 3c). The difference is found for two additional hydrogen bonds being formed by HF with fluorine and the amine group, respectively. The hydrogen bond between the fluorine atom and amine group present in all other transition state structures is thus broken but there is no net energetic penalty ($\Delta\Delta G^{\ddagger}$ is the same for the last two lines in Table 1). The final structure is less stable compared to the pure base adduct ($\Delta\Delta G^\circ$ = −6 kJ/mol) due to an extended H−bond network (see Figure S2 in the Supporting Information).

From these investigations, we conclude that the largest influence on the reaction barrier is found for the amine base increasing the nucleophilicity of CH_3NH_2. The stabilization of the leaving group fluorine has a much smaller effect on the reaction barrier. The solvent effect at the example of water is moderate and seems to be well captured by an implicit solvation model.

BONDING ANALYSIS

Concerning the reaction mechanism, two questions remain which cannot be answered by total energy calculations alone: What are the details of bond formation providing the driving force for the SuFEx reaction? Which (electronic) effect causes the added base to lower the barrier? The energy decomposition analysis (EDA) is an ideal tool to address both questions as it decomposes the interaction energy (ΔE_{int}) between two molecular fragments into quantities that can be correlated to chemical bonding concepts.[38−40] First, ΔE_{int} is decomposed into an electronic interaction term (ΔE_{int}(elec)) and a dispersion contribution (ΔE_{int}(disp)) that is derived by semiempirical approximations (DFT-D3).[41] The actual EDA procedure then breaks down ΔE_{int}(elec) into a quasiclassical electrostatic contribution (ΔE_{elstat}), orbital interaction comprising charge transfer and polarization (ΔE_{orb}), and Pauli repulsion (ΔE_{Pauli}).[40,42] After including the energy that is required to deform the fragments into the structure (and electronic state) they have in the molecule (ΔE_{prep}), the total bonding energy (ΔE_{bond}) can be written as

$$\Delta E_{bond} = \Delta E_{int} + \Delta E_{prep}$$

$$\Delta E_{int} = \Delta E_{int}(elec) + \Delta E_{int}(disp)$$

$$\Delta E_{int}(elec) = \Delta E_{elstat} + \Delta E_{orb} + \Delta E_{Pauli}.$$

The orbital interaction term (ΔE_{orb}) can be further decomposed with the help of natural orbitals for chemical valence (NOCV).[43] Here, the major orbital interactions can be visually identified and their energy contribution quantified.

Table 2 shows the EDA results of **3** and **TS** with and without base. First, we note that the best description of the newly formed S−N bond changes along the reaction path. This finding is in line with chemical intuition but can now be quantitatively supported by EDA. The **TS** is best described as a donor−acceptor complex between closed shell molecules. Here, the role of the donor is adopted by the nucleophile methylamine, and the electron poor sulfur atom of the sulfonylfluoride is the acceptor. Product **3** on the other hand shows a shared electron S−N bond, which is a consequence of cleaving the bond homolytically assigning one electron to each of the fragments. The EDA allows for different fragmentations favoring either a donor−acceptor or shared electron description. It is well established that the best description of a system is given by the EDA fragmentation with the lowest orbital energy value.[44] The EDA can thus help in deciding which bonding picture is more appropriate. As shown in Table S3 in the Supporting Information, the alternative fragmentation scheme for **3** as a donor−acceptor complex shows a significantly higher ΔE_{orb} value and is thus the less suitable description.

The shared electron S−N bond in **3** is strong (ΔE_{bond} = −293 kJ/mol) and shows only very small contributions from dispersion interaction; the interaction energy is governed by large EDA terms ΔE_{elstat}, ΔE_{orb}, and ΔE_{Pauli}. The major

https://dx.doi.org/10.1021/acsomega.0c05049
ACS Omega 2020, 5, 31432−31439

Table 2. Bonding Analysis (EDA) of 3 and TS with and without $N(CH_3)_3$[a]

bonding analysis (EDA)	3		TS		TS + $N(CH_3)_3$	
ΔE_{int}	−308		−152		−193	
ΔE_{int}(disp)[b]	−12	4%	−13	9%	−21	11%
ΔE_{int}(elec)[b]	−296	96%	−138	91%	−172	89%
ΔE_{Pauli}	1742		852		957	
ΔE_{elstat}[c]	−885	43%	−479	48%	−560	50%
ΔE_{orb}[c]	−1153	57%	−511	52%	−569	50%
ΔE_{orb}(S−N)[d]	−971	84%	−402	79%	−466	82%
ΔE_{orb}(NH--F)[d]			−55	11%	−34	6%
ΔE_{orb}(rest)[d]	−182	16%	−54	11%	−69	12%
ΔE_{prep}	15		260		266	
ΔE_{bond}	−293		108		72	

[a]All energies in kJ/mol at PBE/TZ2P. Fragments for **3** are generated from homolytic cleavage at N−S into neutral doublets. For the **TS**, the reactants are used as fragments in a neutral, singlet configuration. [b]Percentage values: Relative contributions of dispersion and electronic effects to the interaction energy ΔE_{int}. [c]Percentage values: Relative contributions between the attractive EDA terms ΔE_{elstat} and ΔE_{orb}. [d]Percentage values: Relative contributions to the orbital interaction ΔE_{orb}. The character of the orbital contribution as S−N bond or NH--F hydrogen bond is revealed by NOCV analysis, as shown below. Non-assignable contributions are summed in the "rest" term.

stabilizing term (57%) is the orbital interaction energy (ΔE_{orb}), which is typical for bonds with a strong covalent character found in orbital-driven reactions.[42] The ΔE_{orb} term is largely governed by contributions from the S−N bond (84% of ΔE_{orb}) as indicated by deformation densities ($\Delta\rho$) derived from the NOCV analysis (Figure 4). The unequal contributions from

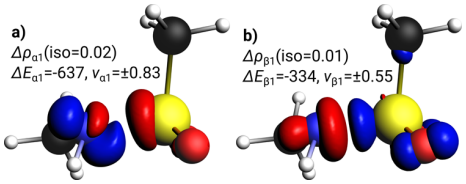

Figure 4. Deformation density $\Delta\rho_1$ shows charge flow between NOCVs of **3** and associated contributions to the total orbital energy (ΔE_1 in kJ/mol) for α- and β-electrons, respectively. Eigenvalues ν_1 quantify the amount of transferred electron density (red: charge depletion, blue: charge accumulation). Iso-values are chosen for visual clarity. Bonding character of $\Delta\rho 1$ is a polar shared-electron N−S bond with contributions from the (a) sulfonyl fragment and from the (b) amine fragment.

the sulfonyl group (Figure 4a; $\Delta\rho_{\alpha 1}$, $\Delta E_{\alpha 1}$ = −637 kJ/mol) and the amine group (Figure 4b; $\Delta\rho_{\beta 1}$, $\Delta E_{\beta 1}$ = −334 kJ/mol) together with the difference in eigenvalues ($\nu_{\alpha 1}$ = ±0.83, $\nu_{\beta 1}$ = ±0.55) are characteristics for a shared-electron bond polarized toward nitrogen, in line with the higher electronegativity of this element.

In contrast to the product, the S−N bond in the **TS** with and without base can be described as a donor−acceptor interaction (Table 2). Although, fluorine could in principle be described as being an independent fragment (leading to a three-fragment EDA), we chose to describe the former sulfonylfluoride as one fragment based on previous experience with transition state analysis in similar systems.[34] The interaction energy in the **TS** is much lower (ΔE_{int} = −152 kJ/mol) as expected for a state where the bond formation process is still ongoing. Again, the major bonding contributions are of covalent nature, and dispersion interactions play a minor role. The nearly equal contribution of electrostatic (48%) and orbital interaction (52%) to the attractive energy terms are typical for a donor−acceptor interaction.[45] The bonding energy is positive here due to a high preparation energy (ΔE_{prep} = +260 kJ/mol) in line with the high energy barrier described earlier. The major contribution to the orbital interaction (79%) is given by the charge donation of the non-bonded electron pair at nitrogen into the acceptor orbital at the sulfonyl fragment (ΔE_1 = −402 kJ/mol, Figure 5a). A

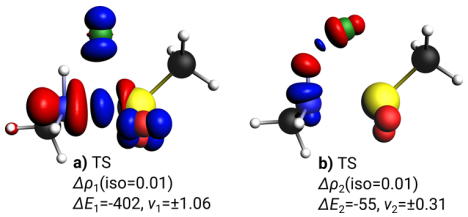

Figure 5. Selected deformation densities $\Delta\rho_i$ show charge flow between NOCVs of **TS** and associated contributions to the total orbital energy (ΔE_i in kJ/mol). Eigenvalues ν_i quantify the amount of transferred electron density (red: charge depletion, blue: charge accumulation). Iso-values are chosen for visual clarity. Bonding character of $\Delta\rho_i$ is (a) LP(N) → p*(S) donor−acceptor bond, (b) NH---F hydrogen bond.

further significant stabilization comes from the already forming hydrogen bond NH---F delivering a further 55 kJ/mol to the orbital energy term (Figure 5b). In line with the partial charge at the fluorine atom discussed above, we find charge flow in $\Delta\rho_1$ to F, which is not compensated by the reverse, much smaller, charge flow in $\Delta\rho_2$.

Adding the amine base changes the bonding picture only gradually (Table 2). But the value of the interaction energy increases significantly ($\Delta\Delta E_{int}$ = −41 kJ/mol), in line with the lowering of the barrier discussed above. The resulting shorter S−N distance in the transition state structure leads to all three EDA terms rising in total value. The resulting balance between orbital (50%) and electrostatic (50%) energy contributions indicates an increased significance of the latter term compared to **TS** without base. We can reveal the nature of the increased orbital interaction by NOCV analysis. The deformation densities are unaltered compared to **TS** without base and are thus shown in the Supporting Information (Figure S3). Significant change is found for the donor-acceptor bond, where the orbital contribution (ΔE_{orb}(S−N)) increases by 64 kJ/mol, and the NH---F hydrogen bond (ΔE_{orb}(NH--F)) is weakened by 21 kJ/mol.

Thus, it appears that the major effect of the added base is a strengthening of the dative S−N bond in the transition state structure by increasing the nucleophilicity of the amine base. This local effect should be found in other reactants as well since it depends only on a local bonding interaction.

■ CONCLUSIONS

Our computational investigations of the mechanism for the SuFEx reaction for a prototypical case of fluoride substitution by a primary amine at the density functional theory level revealed that the reaction shows a high energy barrier that can be lowered significantly by an added base. The reaction

https://dx.doi.org/10.1021/acsomega.0c05049
ACS Omega 2020, 5, 31432−31439

proceeds via a non-synchronous one-step mechanism with initial weakening of the S−F bond and slightly delayed nucleophilic attack of the amine. The major effect of the base is to increase the nucleophilicity of the amine. The influence of a typical solvent (water) and side product HF on the reaction barrier is small. But HF can decrease the reactivity by destabilizing the product and should therefore be scavenged. As an added side effect, scavenging might reduce the risk of racemization.[46]

The results indicate further possibility for experimentally improving the scope of SuFEx chemistry by adjusting the strengths and stoichiometry of the base added. Tertiary amine bases are favorable since they cannot act as nucleophiles in this reaction scheme themselves due to lack of acidic protons, thus avoiding side reactions. Possibly, steric effects of the added base have to be considered when the transition state structure becomes crowded. Polar solvents that stabilize the leaving group F^- are able to lower the reaction barrier further. This study gives some indication from a microsolvation approach but for a quantitative result, large-scale solvent-shell simulations are a possible next step.

Our hypothesis can be experimentally probed by kinetic measurements, testing a dependency of the reaction rate on the base concentration in SuFEx schemes. Since the main effect of the base is an increase in nucleophilicity while not changing the bonding at the transition state structure, this conclusion can be extended to other typical nucleophiles in SuFEx chemistry that probably follow the same mechanism (e.g., other amines, alcohols).

We show that electronic structure analysis of a prototypical system via energy decomposition analysis can reveal the determining factor for an important class of organic reactions.

Computational Methods. Structure optimizations were performed with TURBOMOLE 7.2[47] using the generalized gradient approximation (GGA)-based exchange−correlation density functional PBE,[48] including DFT-D3 dispersion correction with a Becke−Johnson (BJ) type damping function.[41,49] After careful benchmarking against high-precision wave function-based methods (see Table S1 in the Supporting Information), the hybrid functional PBE0-D3[50] was employed for total energy calculations. Throughout this work, the def2-TZVPP basis set[51] together with a fine integration grid (*m4*) was used and the self-consistent field (SCF) energy convergence criteria set to 10^{-8} E_h. All generated minima (transition states) were verified to have zero (one) imaginary frequency modes via analytic computation of the Hesse matrix.

Additionally, the implicit solvation model COSMO[35] was used to compare the response of the solute to the explicit "microsolvation" method. Default values were taken for cavity construction. Solvation energies are reported, including the outlying charge correction.

Gibbs free energies (ΔG) were calculated at the PBE-D3(BJ) level. For this purpose the interactive program "freeh" included in the TURBOMOLE suite was used. The partition sums were computed in the rigid rotor, harmonic oscillator, and ideal gas approximations. Vibrational energies were not scaled and imaginary vibrational modes (at transition states) were excluded from the analysis. Standard ambient temperature (298.15 K) and pressure (0.1 MPa) (SATP) values were chosen. Calculated chemical potentials were then added to the total electronic energy at the hybrid-DFT PBE0-D3 level to yield Gibbs free energies.

The reaction force $F(\zeta) = -\partial E/\partial\zeta$ and force constant[32,33] $\kappa(\zeta) = \partial E^2/\partial^2\zeta$ were calculated by numerical differentiation (centered finite differences) of a high-resolution intrinsic reaction coordinate (IRC) ζ with PBE-D3. The IRC connects stationary points on the potential energy surface (PES). Points of inflection along the IRC separate the reaction into reactant, product, and transition regions. A symmetrical transition region indicates a concerted mechanism. The IRC was generated with the Gaussian16 (A.03) program[52] (CalcAll, MaxPoints = 150, Tight). Settings used with Gaussian16 were set to resemble those of TURBOMOLE as close as possible. While the basis set and functional are identical to those used with TURBOMOLE, the numerical integration grid was set to "UltraFine", and the quadratically convergent SCF procedure was used.

The energy decomposition analysis (EDA)[53] was performed with the Amsterdam density functional (ADF 2019.301) package.[54−56] Again, the PBE-D3 functional was used in conjunction with the triple-zeta Slater-type basis set TZ2P[57] and the frozen core was set to "large". Scalar relativistic effects were treated with the zeroth order regular approximation.[58] Within the EDA scheme, the interaction energy between molecular fragments is decomposed into electrostatic contribution, Pauli repulsion, orbital relaxation, and dispersion. Together with the fragment preparation energy the bonding energy is derived as outlined in the manuscript.

The natural orbitals for chemical valence (NOCV)[43] scheme is an extension to this method. Here, the orbital relaxation is further separated into individual deformation densities $\Delta\rho$ and corresponding eigenvalues $\pm\nu$ that quantify the electron flow. This allows for the interpretation of interactions between fragments by visual inspection of the most important deformation densities.

■ ASSOCIATED CONTENT

Supporting Information

The Supporting Information is available free of charge at https://pubs.acs.org/doi/10.1021/acsomega.0c05049.

Additional structural data, energies, and computational raw data (PDF)

Video showing IRC animations (MP4)

■ AUTHOR INFORMATION

Corresponding Author

Ralf Tonner − *Institut für Physikalische und Theoretische Chemie, Fakultät für Chemie und Pharmazie, Universität Regensburg, 93053 Regensburg, Germany;* orcid.org/0000-0002-6759-8559; Email: ralf.tonner@chemie.uni-regensburg.de

Author

Jan-Niclas Luy − *Institut für Physikalische und Theoretische Chemie, Fakultät für Chemie und Pharmazie, Universität Regensburg, 93053 Regensburg, Germany;* orcid.org/0000-0002-0552-5223

Complete contact information is available at: https://pubs.acs.org/10.1021/acsomega.0c05049

Notes

The authors declare no competing financial interest.

https://dx.doi.org/10.1021/acsomega.0c05049
ACS Omega 2020, 5, 31432−31439

■ ACKNOWLEDGMENTS

The authors thank the German Research Foundation (DFG) for funding via SFB 1083 and also acknowledge computational resources provided by HRZ Marburg and CSC Frankfurt.

■ REFERENCES

(1) Kolb, H. C.; Finn, M. G.; Sharpless, K. B. Click Chemistry: Diverse Chemical Function from a Few Good Reactions. *Angew. Chem., Int. Ed.* **2001**, *40*, 2004−2021.
(2) Dong, J.; Krasnova, L.; Finn, M. G.; Sharpless, K. B. Sulfur (VI) fluoride exchange (SuFEx): another good reaction for click chemistry. *Angew. Chem. Int. Ed.* **2014**, *53*, 9430−9448.
(3) Steinkopf, W. Über Aromatische Sulfofluoride. *J. Prakt. Chem.* **1927**, *117*, 1−82.
(4) Krutak, J. J.; Burpitt, R. D.; Moore, W. H.; Hyatt, J. A. Chemistry of ethenesulfonyl fluoride. Fluorosulfonylethylation of organic compounds. *J. Org. Chem.* **1979**, *44*, 3847−3858.
(5) Bogolubsky, A. V.; Moroz, Y. S.; Mykhailiuk, P. K.; Pipko, S. E.; Konovets, A. I.; Sadkova, I. V.; Tolmachev, A. Sulfonyl Fluorides as Alternative to Sulfonyl Chlorides in Parallel Synthesis of Aliphatic Sulfonamides. *ACS Comb. Sci.* **2014**, *16*, 192−197.
(6) Liu, Z.; Li, J.; Li, S.; Li, G.; Sharpless, K. B.; Wu, P. SuFEx Click Chemistry Enabled Late-Stage Drug Functionalization. *J. Am. Chem. Soc.* **2018**, *140*, 2919−2925.
(7) Wang, N.; Yang, B.; Fu, C.; Zhu, H.; Zheng, F.; Kobayashi, T.; Liu, J.; Li, S.; Ma, C.; Wang, P. G.; Wang, Q.; Wang, L. Genetically Encoding Fluorosulfate-l-tyrosine To React with Lysine, Histidine, and Tyrosine via SuFEx in Proteins in Vivo. *J. Am. Chem. Soc.* **2018**, *140*, 4995−4999.
(8) Oakdale, J. S.; Kwisnek, L.; Fokin, V. V. Selective and Orthogonal Post-Polymerization Modification using Sulfur(VI) Fluoride Exchange (SuFEx) and Copper-Catalyzed Azide−Alkyne Cycloaddition (CuAAC) Reactions. *Macromolecules* **2016**, *49*, 4473−4479.
(9) Brendel, J. C.; Martin, L.; Zhang, J.; Perrier, S. SuFEx − a selectively triggered chemistry for fast, efficient and equimolar polymer−polymer coupling reactions. *Polym. Chem.* **2017**, *8*, 7475−7485.
(10) Brooks, K.; Yatvin, J.; Kovaliov, M.; Crane, G. H.; Horn, J.; Averick, S.; Locklin, J. SuFEx Postpolymerization Modification Kinetics and Reactivity in Polymer Brushes. *Macromolecules* **2018**, *51*, 297−305.
(11) Fan, H.; Ji, Y.; Xu, Q.; Zhou, F.; Wu, B.; Wang, L.; Li, Y.; Lu, J. Sulfur (VI) Fluoride Exchange Polymerization for Large Conjugate Chromophores and Functional Main-Chain Polysulfates with Non-volatile Memory Performance. *ChemPlusChem* **2018**, *83*, 407−413.
(12) Park, S.; Song, H.; Ko, N.; Kim, C.; Kim, K.; Lee, E. SuFEx in Metal−Organic Frameworks: Versatile Postsynthetic Modification Tool. *ACS Appl. Mater. Interfaces* **2018**, *10*, 33785−33789.
(13) Gao, B.; Zhang, L.; Zheng, Q.; Zhou, F.; Klivansky, L. M.; Lu, J.; Liu, Y.; Dong, J.; Wu, P.; Sharpless, K. B. Bifluoride-catalysed sulfur(VI) fluoride exchange reaction for the synthesis of polysulfates and polysulfonates. *Nat. Chem.* **2017**, *9*, 1083−1088.
(14) Li, C.; Zheng, Y.; Rakesh, K. P.; Qin, H.-L. But-3-ene-1,3-disulfonyl difluoride (BDF): a highly selective SuFEx clickable hub for the quick assembly of sultam-containing aliphatic sulfonyl fluorides. *Chem. Commun.* **2020**, *56*, 8075−8078.
(15) Wolkow, R. A. Controlled molecular adsorption on silicon: Laying a Foundation for Molecular Devices. *Annu. Rev. Phys. Chem.* **1999**, *50*, 413−441.
(16) He, C.; Abraham, B.; Fan, H.; Harmer, R.; Li, Z.; Galoppini, E.; Gundlach, L.; Teplyakov, A. V. Morphology-Preserving Sensitization of ZnO Nanorod Surfaces via Click-Chemistry. *J. Phys. Chem. Lett.* **2018**, *9*, 768−772.
(17) Pecher, L.; Schober, C.; Tonner, R. Chemisorption of a Strained but Flexible Molecule: Cyclooctyne on Si(001). *Chem. − Eur. J.* **2017**, *23*, 5459−5466.
(18) Pecher, L.; Tonner, R. Computational analysis of the competitive bonding and reactivity pattern of a bifunctional cyclooctyne on Si(001). *Theor. Chem. Acc.* **2018**, *137*, 48.
(19) Gahtory, D.; Sen, R.; Pujari, S.; Li, S.; Zheng, Q.; Moses, J. E.; Sharpless, K. B.; Zuilhof, H. Quantitative and Orthogonal Formation and Reactivity of SuFEx Platforms. *Chem. − Eur. J.* **2018**, *24*, 10550−10556.
(20) Liu, S.; Cao, Y.; Wu, Z.; Chen, H. Reactive films fabricated using click sulfur(vi)−fluoride exchange reactions via layer-by-layer assembly. *J. Mater. Chem. B* **2020**, *8*, 5529−5534.
(21) Randall, J. D.; Eyckens, D. J.; Stojcevski, F.; Francis, P. S.; Doeven, E. H.; Barlow, A. J.; Barrow, A. S.; Arnold, C. L.; Moses, J. E.; Henderson, L. C. Modification of Carbon Fibre Surfaces by Sulfur-Fluoride Exchange Click Chemistry. *ChemPhysChem* **2018**, *19*, 3176−3181.
(22) Barrow, A. S.; Smedley, C. J.; Zheng, Q.; Li, S.; Dong, J.; Moses, J. E. The growing applications of SuFEx click chemistry. *Chem. Soc. Rev.* **2019**, *48*, 4731−4758.
(23) Gembus, V.; Marsais, F.; Levacher, V. An Efficient Organo-catalyzed Interconversion of Silyl Ethers to Tosylates Using DBU and p-Toluenesulfonyl Fluoride. *Synlett* **2008**, *2008*, 1463−1466.
(24) Smedley, C. J.; Zheng, Q.; Gao, B.; Li, S.; Molino, A.; Duivenvoorden, H. M.; Parker, B. S.; Wilson, D. J. D.; Sharpless, K. B.; Moses, J. E. Bifluoride Ion Mediated SuFEx Trifluoromethylation of Sulfonyl Fluorides and Iminosulfur Oxydifluorides. *Angew. Chem., Int. Ed.* **2019**, *58*, 4552−4556.
(25) Mahapatra, S.; Woroch, C. P.; Butler, T. W.; Carneiro, S. N.; Kwan, S. C.; Khasnavis, S. R.; Gu, J.; Dutra, J. K.; Vetelino, B. C.; Bellenger, J.; am Ende, C. W.; Ball, N. D. SuFEx Activation with $Ca(NTf_2)_2$: A Unified Strategy to Access Sulfamides, Sulfamates, and Sulfonamides from S(VI) Fluorides. *Org. Lett.* **2020**, *22*, 4389−4394.
(26) Liang, D.-D.; Streefkerk, D. E.; Jordaan, D.; Wagemakers, J.; Baggerman, J.; Zuilhof, H. Silicon-Free SuFEx Reactions of Sulfonimidoyl Fluorides: Scope, Enantioselectivity, and Mechanism. *Angew. Chem., Int. Ed.* **2020**, *59*, 7494−7500.
(27) Bachrach, S. M. Microsolvation of Glycine: A DFT Study. *J. Phys. Chem. A* **2008**, *112*, 3722−3730.
(28) Flörez, E.; Acelas, N.; Ibargüen, C.; Mondal, S.; Cabellos, J. L.; Merino, G.; Restrepo, A. Microsolvation of NO^{3-}: structural exploration and bonding analysis. *RSC Adv.* **2016**, *6*, 71913.
(29) Vayner, G.; Houk, K. N.; Jorgensen, W. L.; Brauman, J. I. Steric Retardation of S_N2 Reactions in the Gas Phase and Solution. *J. Am. Chem. Soc.* **2004**, *126*, 9054−9058.
(30) Himo, F.; Lovell, T.; Hilgraf, R.; Rostovtsev, V. V.; Noodleman, L.; Sharpless, K. B.; Fokin, V. V. Copper(I)-Catalyzed Synthesis of Azoles. DFT Study Predicts Unprecedented Reactivity and Intermediates. *J. Am. Chem. Soc.* **2005**, *127*, 210−216.
(31) Ess, D. H.; Jones, G. O.; Houk, K. N. Transition States of Strain-Promoted Metal-Free Click Chemistry: 1,3-Dipolar Cycloadditions of Phenyl Azide and Cyclooctynes. *Org. Lett.* **2008**, *10*, 1633−1636.
(32) Politzer, P.; Toro-Labbé, A.; Gutiérrez-Oliva, S.; Herrera, B.; Jaque, P.; Concha, M. C.; Murray, J. S. The reaction force: Three key points along an intrinsic reaction coordinate. *J. Chem. Sci.* **2005**, *117*, 467−472.
(33) Inostroza-Rivera, R.; Herrera, B.; Toro-Labbé, A. Using the reaction force and the reaction electronic flux on the proton transfer of formamide derived systems. *Phys. Chem. Chem. Phys.* **2014**, *16*, 14489−14495.
(34) Stegmüller, A.; Tonner, R. β-Hydrogen elimination mechanism in the absence of low-lying acceptor orbitals in $EH_2(t\text{-}C_4H_9)$ (E = N−Bi). *Inorg.Chem.* **2015**, *54*, 6363−6372.
(35) Schäfer, A.; Klamt, A.; Sattel, D.; Lohrenz, J. C. W.; Eckert, F. COSMO Implementation in TURBOMOLE: Extension of an efficient quantum chemical code towards liquid systems. *Phys. Chem. Chem. Phys.* **2000**, *2*, 2187.
(36) Xantheas, S. S.; Dunning, T. H., Jr. The structure of the water trimer from ab initio calculations. *J. Chem. Phys.* **1993**, *98*, 8037−8040.

https://dx.doi.org/10.1021/acsomega.0c05049
ACS Omega 2020, 5, 31432−31439

(37) Wenthold, P. G.; Squires, R. R. Bond Dissociation Energies of F_2^- and HF_2^-. A Gas-Phase Experimental and G2 Theoretical Study. *J. Phys. Chem.* **1995**, *99*, 2002−2005.
(38) Ziegler, T.; Rauk, A. On the calculation of bonding energies by the Hartree Fock Slater method. *Theor. Chim. Acta* **1977**, *46*, 1−10.
(39) Kitaura, K.; Morokuma, K. A new energy decomposition scheme for molecular interactions within the Hartree-Fock approximation. *Int. J. Quantum Chem.* **1976**, *10*, 325−340.
(40) Bickelhaupt, F. M.; Nibbering, N. M. M.; Van Wezenbeek, E. M.; Baerends, E. J. Central bond in the three CN. indicating radical species NC-CN, CN-CN and CN-NC: electron pair bonding and Pauli repulsion effects. *J. Phys. Chem.* **1992**, *96*, 4864−4873.
(41) Grimme, S.; Antony, J.; Ehrlich, S.; Krieg, H. A consistent and accurate ab initio parametrization of density functional dispersion correction (DFT-D) for the 94 elements H-Pu. *J. Chem. Phys.* **2010**, *132*, 154104.
(42) von Hopffgarten, M.; Frenking, G. Energy decomposition analysis. *WIREs Comput. Mol. Sci.* **2011**, *2*, 43−62.
(43) Mitoraj, M. P.; Michalak, A.; Ziegler, T. On the nature of the agostic bond between metal centers and β-hydrogen atoms in alkyl complexes. An analysis based on the extended transition state method and the natural orbitals for chemical valence scheme (ETS-NOCV). *Organometallics* **2009**, *28*, 3727−3733.
(44) Frenking, G.; Matthias Bickelhaupt, F. *The Chemical Bond*; John Wiley & Sons, Ltd: 2014; Chapter 4, pp. 121−157.
(45) Pecher, L.; Laref, S.; Raupach, M.; Tonner, R. Ethers on Si(001): a prime example for the common ground between surface science and molecular organic chemistry. *Angew. Chem., Int. Ed.* **2017**, *56*, 15150−15154.
(46) Greed, S.; Briggs, E. L.; Idiris, F. I. M.; White, A. J. P.; Lücking, U.; Bull, J. A. Synthesis of highly enantioenriched sulfonimidoyl fluorides and sulfonimidamides by stereospecific sulfur−fluorine exchange (SuFEx) reaction. *Chem. − Eur. J.* **2020**, *26*, 12533−12538.
(47) *TURBOMOLE V7.2 2017*; a development of University of Karlsruhe and Forschungszentrum Karlsruhe GmbH, 1989−2007, TURBOMOLE GmbH, since 2007; available from http://www.turbomole.com, last accessed 21.08.2020.
(48) Perdew, J. P.; Burke, K.; Ernzerhof, M. Generalized Gradient Approximation Made Simple. *Phys. Rev. Lett.* **1996**, *77*, 3865.
(49) Grimme, S.; Ehrlich, S.; Goerigk, L. Effect of the damping function in dispersion corrected density functional theory. *J. Comput. Chem.* **2011**, *32*, 1456−1465.
(50) Ernzerhof, M.; Scuseria, G. E. Assessment of the Perdew−Burke−Ernzerhof exchange-correlation functional. *J. Chem. Phys.* **1999**, *110*, 5029−5036.
(51) Weigend, F.; Ahlrichs, R. CC2 excitation energy calculations on large molecules using the resolution of the identity approximation. *Phys. Chem. Chem. Phys.* **2000**, *7*, 3297−3305.
(52) Frisch, M. J.; Trucks, G. W.; Schlegel, H. B.; Scuseria, G. E.; Robb, M. A.; Cheeseman, J. R.; Scalmani, G.; Barone, V.; Petersson, G. A.; Nakatsuji, H.; Li, X.; Caricato, M.; Marenich, A. V.; Bloino, J.; Janesko, B. G.; Gomperts, R.; Mennucci, B.; Hratchian, H. P.; Ortiz, J. V.; Izmaylov, A. F.; Sonnenberg, J. L.; Williams-Young, D.; Ding, F.; Lipparini, F.; Egidi, F.; Goings, J.; Peng, B.; Petrone, A.; Henderson, T.; Ranasinghe, D.; Zakrzewski, V. G.; Gao, J.; Rega, N.; Zheng, G.; Liang, W.; Hada, M.; Ehara, M.; Toyota, K.; Fukuda, R.; Hasegawa, J.; Ishida, M.; Nakajima, T.; Honda, Y.; Kitao, O.; Nakai, H.; Vreven, T.; Throssell, K.; Montgomery, J. A., Jr.; Peralta, J. E.; Ogliaro, F.; Bearpark, M. J.; Heyd, J. J.; Brothers, E. N.; Kudin, K. N.; Staroverov, V. N.; Keith, T. A.; Kobayashi, R.; Normand, J.; Raghavachari, K.; Rendell, A. P.; Burant, J. C.; Iyengar, S. S.; Tomasi, J.; Cossi, M.; Millam, J. M.; Klene, M.; Adamo, C.; Cammi, R.; Ochterski, J. W.; Martin, R. L.; Morokuma, K.; Farkas, O.; Foresman, J. B.; Fox, D. J. *Gaussian 16*; Revision A.03, Gaussian, Inc.: Wallingford CT, 2016.
(53) Mitoraj, M. P.; Michalak, A.; Ziegler, T. A Combined Charge and Energy Decomposition Scheme for Bond Analysis. *J. Chem. Theory Comput.* **2009**, *5*, 962.
(54) te Velde, G.; Bickelhaupt, F. M.; Baerends, E. J.; Guerra, C. F.; van Gisbergen, S. J. A.; Snijders, J. G.; Ziegler, T. Chemistry with ADF. *J. Comput. Chem.* **2001**, *22*, 931.
(55) Guerra, C. F.; Snijders, J. G.; te Velde, G.; Baerends, E. J. Towards an order-N DFT method. *Theor. Chem. Acc.* **1998**, *99*, 391.
(56) *ADF2019, SCM Theoretical Chemistry*; Vrije Universiteit, Amsterdam, The Netherlands, http://www.scm.com, last accessed 21.08.2020.
(57) van Lenthe, E.; Baerends, E. J. Optimized Slater-type basis sets for the elements 1−118. *J. Comput. Chem.* **2003**, *24*, 1142.
(58) van Lenthe, E.; Baerends, E. J.; Snijders, J. G. Relativistic regular two-component Hamiltonians. *J. Chem. Phys.* **1993**, *99*, 4597−4610.

https://dx.doi.org/10.1021/acsomega.0c05049
ACS Omega 2020, 5, 31432−31439

Supporting Information

Complementary Base Lowers the Barrier in SuFEx Click Chemistry for Primary Amine Nucleophiles

Jan-Niclas Luy[1], Ralf Tonner[1]*

[1]Institut für Physikalische und Theoretische Chemie, Fakultät für Chemie und Pharmazie, Universität Regensburg, Universitätsstraße 31, 93053 Regensburg, Germany

*Corresponding author: ralf.tonner@chemie.uni-regensburg.de

Table of contents

1) Method benchmark

We benchmark the performance of several density functionals against advanced wave function-based approaches. The structures on which the benchmark was performed are not strictly identical to those reported in the main document.

Table S1. Stationary points on the SuFEx reaction path calculated with different density functionals and wave function-based methods using structures optimized by PBE-D3.

	PBE-D3	TPSS-D3[SS1]	PBE0-D3	B3LYP-D3[SS2]	M06 [SS3]	MP2 [SS4]	CCSD [SS4]	CCSD(T) [SS4]
∑(products)	1	10	-8	-5	-7	-18	-14	-14
pre-complex	-31	-28	-30	-30	-25	-28	-25	-27
TS	108	118	146	136	161	158	187	163
post-complex	-41	-29	-43	-40	-31	-49	-38	-43
MAE[b]	19.1	20.8	6.4	10.6	5.9	5.2	7.9	-
ΔE^o	-10	-1	-13	-10	-6	-22	-13	-16
$\Delta E^{\ddagger}$	139	146	176	166	186	180	211	190

[a] All calculations using def2-TZVPP basis set. Energies in kJ/mol.
[b] Mean absolute error (MAE) calculated with respect to the CCSD(T) energy of the three stationary points and the sum of products.

Within our small test set, the M06 functional agrees best with CCSD(T). PBE0-D3 is a close second and chosen over M06 as it contains fewer fit parameters.

2) Alternative base catalysed TS structure

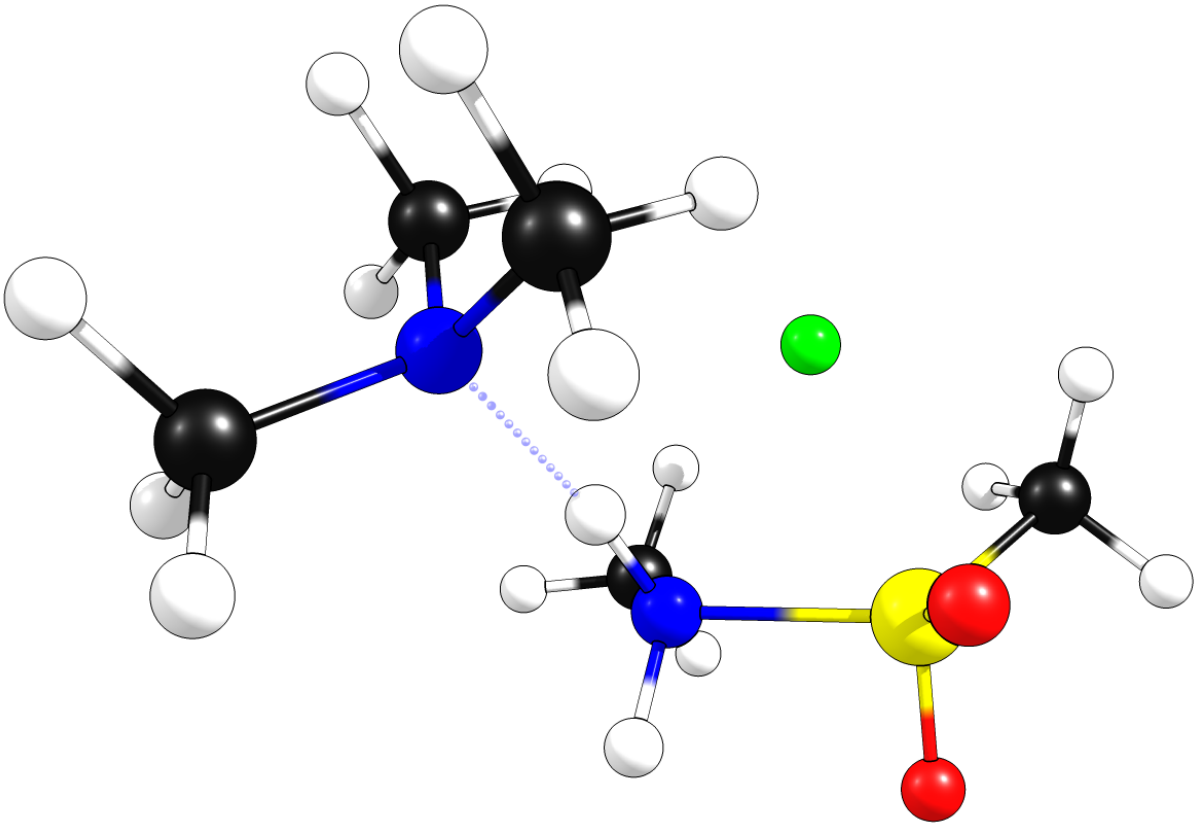

Figure S1. Alternative optimized (PBE-D3/def2-TZVPP) structure of the TS including $N(CH_3)_3$. This structure is less stable by 11 kJ/mol (ΔE) and 18 kJ/mol (ΔG) with respect to the structure given in the main manuscript.

3) Final structures

The endpoints of the reaction path calculations (IRC) are not the energetically optimal structures. Rearrangements of adducts can lead to more stable structures (lowest-energy minima). The reaction paths for these rearrangements have not been investigated, thus only thermodynamic data are given in Figure S2. Reaction energies in the main text (Table 2) are given with respect to the lowest-energy minima shown here.

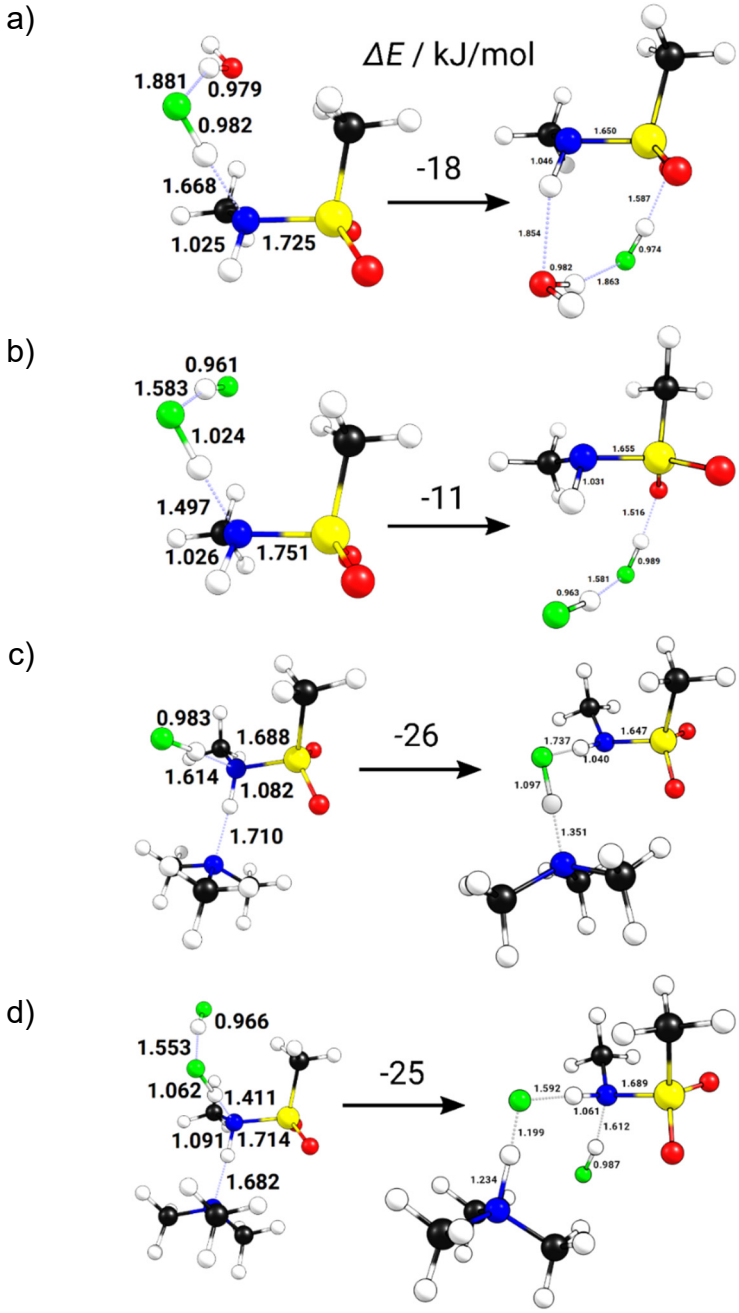

Figure S2. Optimized (PBE-D3/def2-TZVPP) structures of the IRC endpoints (left)and the most stable minima (right) found for post-complexes with additional **a)** H_2O, **b)** HF, **c)** $N(CH_3)_3$ and **d)** HF + $N(CH_3)_3$.

4) Electronic reaction energies

Table S2. Reaction energies (ΔE^0) and barriers ($\Delta E^{\ddagger}$) of the SuFEx reaction showing the influence of solvent (H_2O), side-product (HF) and base ($N(CH_3)_3$).

Solvent[a]	ΔE^o	$\Delta\Delta E^o$	$\Delta E^{\ddagger}$	$\Delta\Delta E^{\ddagger}$
in vacuo	-37	0	159	0
+H_2O (implicit)	-51	-14	145	-14
+H_2O (explicit)	-47	-10	147	-12
+HF	-12	25	169	10
+$N(CH_3)_3$	-72	-35	124	-35
+HF & $N(CH_3)_3$	-40	-3	125	-34

[a] All energies in kJ/mol at PBE0/def2-TZVPP//PBE/def2-TZVPP. Solvent correction at PBE/def2-TZVPP. Energies are given with respect to the pre- and post-complexes.

The S_N1 mechanism is not competitive due to a bond dissociation energy leading to fluorine anion of ΔE^o[+H_2O (implicit)] = 389 kJ/mol. Furthermore, a nucleophilic attack by $N(CH_3)_3$ with subsequent detachment of F^- is an endothermic process with a reaction energy of ΔE^o[+H_2O (implicit)] = 124 kJ/mol. This alternative pathway is therefore unfavorable when compared to the attack by **1**.

5) Structure & output repository

All structures computed and connected raw data can be accessed via the open-data repository NOMAD under the permanent link:

DOI: https://dx.doi.org/10.17172/NOMAD/2020.08.05-1

6) Energy decomposition analysis

Shown in Table S3 are EDA results for an alternative fragmentation scheme of **3** with a donor-acceptor picture of the S-N bond with an anionic amine fragment and a cationic sulfonyl fragment. The considerably higher orbital energy term (ΔE_{orb}) indicates that this fragmentation is a worse description of the bonding situation compared to the neutral fragmentation (electron-sharing bond) discussed in the main manuscript.

Table S3. EDA of **3** with ionic fragments.

	3	
	kJ/mol	%
ΔE_{int}	-1216	
ΔE_{Pauli}	1851	
ΔE_{elstat}	-1686	45
ΔE_{orb}	-1369	55

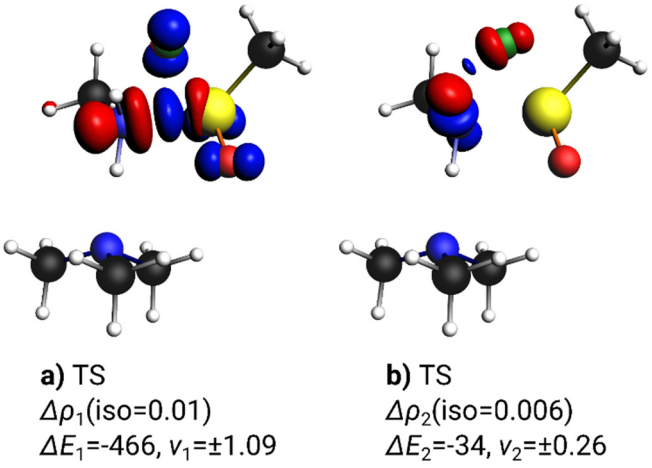

a) TS
$\Delta\rho_1$(iso=0.01)
ΔE_1=-466, v_1=±1.09

b) TS
$\Delta\rho_2$(iso=0.006)
ΔE_2=-34, v_2=±0.26

Figure S3. Selected deformation densities $\Delta\rho_i$ show charge flow between NOCVs of **TS** including $N(CH_3)_3$ and associated contributions to the total orbital energy (ΔE_i in kJ/mol). Eigenvalues v_i quantify the amount of transferred electron density (red: charge depletion, blue: charge accumulation). Iso-values are chosen for visual clarity. Bonding character of $\Delta\rho_i$ is a) LP(N) → p*(S) donor-acceptor bond, b) N-H---F hydrogen bond.

7) ADF sample input

```
Title Fragment-1
atoms
C       -1.09443      0.37015      1.37079
S        0.06532     -0.92532      0.96322
O        1.36096     -0.51978      1.48318
O       -0.52949     -2.20243      1.31729
H       -0.73518      1.31586      0.94975
H       -1.12288      0.43273      2.46469
H       -2.07542      0.10388      0.96595
end
symmetry NOSYM
Relativistic Scalar ZORA
SCF
 Mixing 0.2
 Iterations 300
End
 XC
  LDA LDA
  GGA PBE
  dispersion Grimme3 BJdamp
 END
 Basis
  Type TZ2P
  Core large
 End
NumericalQuality Good
UNRESTRICTED
IRREPOCCUPATIONS
   A 13 // 12
End

Title Fragment-2
atoms
C        1.11141     -0.08851     -1.37569
N        0.06724     -0.87545     -0.71265
H        2.13077     -0.40955     -1.11706
H        0.96131     -0.17303     -2.45911
H        1.00234      0.96903     -1.10396
H       -0.01551     -1.83698     -1.04366
end
symmetry NOSYM
Relativistic Scalar ZORA
SCF
 Mixing 0.2
 Iterations 300
End
 XC
  LDA LDA
  GGA PBE
  dispersion Grimme3 BJdamp
 END
 Basis
  Type TZ2P
  Core large
 End
NumericalQuality Good
UNRESTRICTED
IRREPOCCUPATIONS
   A 6 // 7
End

Title EDA-NOCV
atoms
C       -1.09443      0.37015      1.37079 f=f1
S        0.06532     -0.92532      0.96322 f=f1
O        1.36096     -0.51978      1.48318 f=f1
O       -0.52949     -2.20243      1.31729 f=f1
H       -0.73518      1.31586      0.94975 f=f1
H       -1.12288      0.43273      2.46469 f=f1
```

```
H       -2.07542       0.10388       0.96595 f=f1
C        1.11141      -0.08851      -1.37569 f=f2
N        0.06724      -0.87545      -0.71265 f=f2
H        2.13077      -0.40955      -1.11706 f=f2
H        0.96131      -0.17303      -2.45911 f=f2
H        1.00234       0.96903      -1.10396 f=f2
H       -0.01551      -1.83698      -1.04366 f=f2
end
charge 0
symmetry NOSYM
Relativistic Scalar ZORA
SCF
 Mixing 0.2
 Iterations 300
End
 XC
  LDA LDA
  GGA PBE
  dispersion Grimme3 BJdamp
 END
 Basis
  Type TZ2P
  Core large
 End
NumericalQuality Good
UNRESTRICTEDFRAGMENTS
UNRESTRICTED
fragments
f1 f1.t21
f2 f2.t21
end
ETSNOCV
End
PRINT ETSLOWDIN-Unrestricted
```

8) Animated IRC

The animated intrinsic reaction coordinate for the reaction of methylamine and sulfonylfluoride is found as animated gif in a separate file (SI.irc.gif).

9) Cartesian coordinates, total energies and number of imaginary frequencies

1

Energy = -95.77003465279 Eh, imaginary frequencies = 0

C	0.0516030	0.7048413	-0.0000000
N	0.0566021	-0.7615613	-0.0000000
H	-0.9476109	1.1815037	0.0000000
H	0.5951542	1.0679453	0.8834367
H	0.5951542	1.0679453	-0.8834367
H	-0.4470318	-1.1133916	-0.8151971
H	-0.4470318	-1.1133916	0.8151971

2

Energy = -688.0799266616 Eh, imaginary frequencies = 0

C	8.6683491	8.5879006	14.3196027
S	8.8238522	6.8426502	14.6113375
O	7.5414410	6.2004057	14.5073913
O	9.7250963	6.5958853	15.7043752
F	9.6300623	6.4661106	13.2640808
H	8.1012075	8.7378607	13.3956971
H	9.6713351	9.0214523	14.2570220
H	8.1235563	8.9959746	15.1786034

1-2

Energy = -783.854102 Eh, imaginary frequencies = 0

C	-1.208494	0.544828	2.140675
S	-0.380007	-0.103000	0.704385
O	1.043069	-0.007711	0.897141
O	-1.036987	-1.307870	0.275350
F	-0.810991	1.076336	-0.306644
H	-0.791181	1.530043	2.370834
H	-1.009470	-0.158770	2.956806
H	-2.281402	0.599283	1.931742
C	2.095733	0.266683	-2.161535
N	0.870408	-0.533561	-2.198707
H	2.665738	0.001670	-1.261708
H	2.762348	0.160456	-3.038651
H	1.828599	1.328861	-2.067045
H	1.088725	-1.529248	-2.232531
H	0.325162	-0.324208	-3.035009

TS

Energy = -783.8087896901 Eh, imaginary frequencies = 1

C	-1.2399847	0.5019112	1.9141760
S	-0.3244798	-0.5019132	0.7217433
O	1.0411018	-0.4682237	1.2390906
O	-1.0918601	-1.7269673	0.5453055
F	-1.3599833	1.1387748	-0.4781731
H	-0.7971118	1.4992398	1.9260735
H	-1.0875484	-0.0274446	2.8645997
H	-2.2818909	0.5279171	1.5956301
C	1.6040776	0.0172482	-1.4846806
N	0.2265130	-0.3850604	-1.2416100
H	2.2953680	-0.6360452	-0.9396991
H	1.8231204	-0.0277639	-2.5619706
H	1.7366690	1.0472985	-1.1369004
H	-0.0131188	-1.3217451	-1.5742280
H	-0.5320051	0.3629168	-1.3907929

3-HF

Energy = -783.8680749412 Eh, imaginary frequencies = 0

C	-0.6547039	0.7887153	1.3792012
S	0.0699190	-0.6224734	0.5716178
O	1.3970306	-0.8337002	1.1189684
O	-0.9027413	-1.6946145	0.5010035
F	-1.6016263	1.8153350	-1.5024361
H	0.0278305	1.6407573	1.2881810

H -0.7655750 0.5040836 2.4318314
H -1.6213014 1.0094036 0.9159737
C 1.4905364 0.5816704 -1.4059997
N 0.2051466 -0.0512683 -1.0500312
H 2.3498236 -0.0731302 -1.2141857
H 1.4483832 0.8508920 -2.4680988
H 1.6079591 1.5056516 -0.8278681
H 0.0004954 -0.8716159 -1.6292190
H -0.9811664 1.0809735 -1.3679584

3

Energy = -683.4558352012 Eh, imaginary frequencies = 0
C -1.0944306 0.3701538 1.3707924
S 0.0653164 -0.9253174 0.9632246
O 1.3609646 -0.5197811 1.4831754
O -0.5294902 -2.2024346 1.3172916
H -0.7351804 1.3158556 0.9497520
H -1.1228788 0.4327349 2.4646926
H -2.0754166 0.1038809 0.9659543
C 1.1114100 -0.0885077 -1.3756874
N 0.0672447 -0.8754451 -0.7126454
H 2.1307699 -0.4095533 -1.1170622
H 0.9613114 -0.1730274 -2.4591053
H 1.0023438 0.9690311 -1.1039578
H -0.0155142 -1.8369796 -1.0436648

HF

Energy = -100.3936173106 Eh, imaginary frequencies = 0
F -0.7369210 2.3513324 -0.8499349
H -0.3906690 1.4881976 -0.8542551

Precomplex benchmark

Energy = -783.8616672310 Eh, imaginary frequencies = 0
C 8.4172798 8.1182982 13.9396381
S 9.6805205 6.8878776 14.0845431
O 10.3652384 6.6788681 12.8366265
O 10.3983651 7.0427959 15.3259148
F 8.7204290 5.6001958 14.2890422
H 7.7752832 7.8553006 13.0928865
H 8.9374124 9.0648128 13.7497273
H 7.8800803 8.1449696 14.9046121
C 7.0051914 6.4384670 17.4030199
N 7.7199955 7.6814269 17.0830970
H 7.2252096 6.0185734 18.4011210
H 5.9224450 6.6139945 17.3407832
H 7.2586108 5.6763248 16.6541815
H 8.7290640 7.5224624 17.1231744
H 7.5116950 8.3976225 17.7798324

Postcomplex benchmark

Energy = -783.8654355793 Eh, imaginary frequencies = 0
C -1.3847573 0.1317828 1.4882784
S 0.1972966 -0.4894852 0.9530457
O 1.2611867 0.3492587 1.4632235
O 0.2325444 -1.9290973 1.1443379
F -0.7445286 2.3702996 -0.8498369
H -1.5044083 1.1609383 1.1316835
H -1.3582986 0.0930973 2.5834792
H -2.1721245 -0.5298264 1.1097333
C 1.3668743 -0.4050840 -1.4424320
N 0.0936900 -0.1304915 -0.7373326
H 1.6637246 -1.4612438 -1.3726393
H 1.2322023 -0.1287438 -2.4944020
H 2.1495757 0.2243142 -1.0069806
H -0.6510472 -0.7248077 -1.1172434
H -0.3830629 1.4692316 -0.8543517

1-2+H_2O

Energy = -860.2466089558 Eh, imaginary frequencies = 0
C -0.92308 0.41914 2.37017
S -0.02093 0.17772 0.86514
O 1.38204 -0.00497 1.11753

O	-0.74530	-0.72016	-0.00953
F	-0.20281	1.64731	0.24996
H	-0.44395	1.22751	2.93152
H	-0.85771	-0.52653	2.92083
H	-1.96306	0.64523	2.09907
C	2.69152	-0.45553	-2.21029
N	1.30984	-0.03358	-2.46288
H	2.86451	-0.47673	-1.12604
H	2.96965	-1.44627	-2.61881
H	3.38140	0.28728	-2.63543
H	0.65774	-0.70625	-2.05701
H	1.12249	-0.02149	-3.46616
O	-3.50656	0.23585	0.44312
H	-2.77068	-0.23323	0.00821
H	-3.77398	0.90895	-0.20047

TS+H_2O

Energy = -860.2058593847 Eh, imaginary frequencies = 1

C	-1.2138352	0.5133081	1.9036351
S	-0.4046711	-0.5446323	0.6822125
O	0.9495406	-0.6804556	1.2146411
O	-1.2715457	-1.6830113	0.4181375
F	-1.3977963	1.0559039	-0.5318598
H	-0.7435474	1.4978264	1.8578235
H	-0.9977738	0.0078983	2.8542489
H	-2.2805066	0.5531740	1.6584670
C	1.6331555	0.0907090	-1.4544274
N	0.2840021	-0.4315899	-1.2867948
H	2.3171963	-0.4406731	-0.7821464
H	1.9690323	-0.0302677	-2.4947915
H	1.6309335	1.1558968	-1.1992899
H	0.1560247	-1.3985436	-1.5929368
H	-0.4868718	0.2120557	-1.5688029
O	-3.9714773	0.4218734	0.1148322
H	-3.9255633	-0.5412967	0.0160406
H	-3.1189505	0.7283867	-0.2719648

3-HF+H_2O

Energy = -860.2644063825 Eh, imaginary frequencies = 0

C	-0.8839200	0.4974500	1.5999900
S	-0.1260300	-0.9314000	0.8561400
O	1.1933200	-1.1056400	1.4344100
O	-1.0834500	-2.0183000	0.8069900
F	-1.7943603	1.3987188	-1.3793739
H	-0.2036500	1.3513000	1.5085500
H	-1.0267900	0.2396900	2.6557800
H	-1.8370200	0.6981600	1.1007900
C	1.3105900	0.2257700	-1.1395400
N	0.0315100	-0.4198200	-0.7835500
H	2.1798000	-0.3931000	-0.8836700
H	1.2944200	0.4288000	-2.2169200
H	1.3869700	1.1861300	-0.6163700
H	-0.1433600	-1.2673100	-1.3327800
H	-1.1762900	0.6656300	-1.1666700
O	-0.0365236	3.1388469	-0.0641493
H	0.0749401	4.0491244	-0.3739740
H	-0.7588158	2.7678555	-0.6108532

Postcomplex+H_2O

Energy = -860.2699920221 Eh, imaginary frequencies = 0

C	7.9394756	8.5046288	14.0874823
S	9.0999897	7.4612966	14.9401213
O	9.0379403	6.1558631	14.2436450
O	10.3843683	8.1286720	15.0376590
F	10.1592238	4.3873945	15.7038503
H	6.9415677	8.0554599	14.1358884
H	8.2766704	8.5589445	13.0464045
H	7.9575080	9.4902373	14.5621338
C	7.3570413	6.4502531	16.6902727
N	8.4861174	7.3667195	16.4692651
H	7.0929585	6.5103468	17.7524400
H	6.4842809	6.7743697	16.1089145

H 7.5914549 5.4064213 16.4350443
H 9.3019237 7.1378709 17.0821530
H 9.7549435 5.0074364 15.0707733
O 10.8035380 6.2483551 17.7064858
H 11.5151648 6.7779780 17.3120288
H 10.7258330 5.4735725 17.1074577

H_2O
Energy = -860.2644063825 Eh, imaginary frequencies = 0
O -0.0365236 3.1388469 -0.0641493
H 0.0749401 4.0491244 -0.3739740
H -0.7588158 2.7678555 -0.6108532

1-2+HF
Energy = -884.2779825723 Eh, imaginary frequencies = 0
C -0.5958258 0.1114509 3.6488112
S -0.3843803 0.7426340 2.0030546
O 0.7784629 1.5856543 1.9351936
O -0.6113374 -0.3117352 1.0435811
F -1.6665074 1.6914371 1.9562628
H -0.5388792 0.9493275 4.3506547
H 0.2270499 -0.5923871 3.8178958
H -1.5614569 -0.4006926 3.7051219
C 1.8388498 1.2311224 -1.4439825
N 0.4199736 0.8964415 -1.6484930
H 1.9769489 1.5468439 -0.4031772
H 2.5260368 0.3956573 -1.6538575
H 2.1079501 2.0764168 -2.0896083
H 0.1322530 0.1470440 -1.0150564
H 0.2517866 0.5754769 -2.6021657
F -1.0623525 2.8655849 -0.9472542
H -0.5007522 2.1077435 -1.2619311

TS+HF
Energy = -884.2276478150 Eh, imaginary frequencies = 1
C -1.3133454 0.4366312 1.9492223
S -0.3394250 -0.4991832 0.7508587
O 1.0308061 -0.4005630 1.2335293
O -1.0632565 -1.7470628 0.5551151
F -1.1693673 1.2719986 -0.4223825
H -0.8799187 1.4349276 2.0266761
H -1.1837581 -0.1449811 2.8722807
H -2.3518463 0.4635409 1.6083262
C 1.5641364 0.0678927 -1.5225329
N 0.2301542 -0.4655162 -1.2709085
H 2.2973587 -0.4719827 -0.9136678
H 1.8229006 -0.0288135 -2.5874538
H 1.5699837 1.1264727 -1.2432806
H 0.0975237 -1.4441849 -1.5355665
H -0.5283295 0.1599870 -1.5854458
F -3.5953254 1.4241547 -0.0514110
H -2.6444156 1.4246603 -0.2612591

3-HF+HF
Energy = -884.2829952749 Eh, imaginary frequencies = 0
C -0.8845844 0.4942221 1.6452877
S -0.1586602 -0.9196493 0.8517054
O 1.1664528 -1.1385447 1.3951637
O -1.1306135 -1.9902557 0.7585009
F -1.6444640 1.4610870 -1.3578574
H -0.2545523 1.3750693 1.4729232
H -0.9215845 0.2420756 2.7115480
H -1.8897989 0.6469525 1.2398618
C 1.3203549 0.2409190 -1.1358148
N 0.0044894 -0.3537852 -0.7971891
H 2.1495664 -0.4174625 -0.8526466
H 1.3328786 0.4217295 -2.2173075
H 1.4155933 1.2063760 -0.6263198
H -0.1850992 -1.1951371 -1.3534154
H -1.0336295 0.6682507 -1.1412435
F -0.1604488 3.1126466 -0.1566600
H -0.7995002 2.6082963 -0.6677563

Postcomplex+HF

Energy = -884.2843517198 Eh, imaginary frequencies = 0

C	-0.9378910	0.7150071	1.6370515
S	-0.1762831	-0.8645731	1.3503287
O	1.1399373	-0.7821563	2.0314310
O	-1.0789709	-1.9336466	1.7149541
F	1.3955663	-3.4129648	-0.7078726
H	-0.3015330	1.5081528	1.2302675
H	-1.0242476	0.8232366	2.7239810
H	-1.9221502	0.7070298	1.1594123
C	1.1036085	-0.1311723	-0.8834624
N	-0.0013193	-0.9047860	-0.2949351
H	2.0933815	-0.4535224	-0.5306517
H	1.0499168	-0.2608706	-1.9701477
H	0.9719355	0.9356719	-0.6637665
H	0.0438486	-1.8990478	-0.5630563
H	1.9583167	-3.1840405	0.0386921
F	2.7302296	-2.5525023	1.2658090
H	2.1288542	-1.8621756	1.6407650

1-2+TMA

Energy = -958.1680364104 Eh, imaginary frequencies = 0

C	-1.1785223	1.2542235	3.3943009
S	-0.6683119	0.9408192	1.7180888
O	0.5932191	0.2476008	1.7242108
O	-1.7981705	0.4947712	0.9478292
F	-0.3752290	2.4666077	1.3106633
H	-0.3448963	1.7139794	3.9341717
H	-1.4293731	0.2796742	3.8280545
H	-2.0576240	1.9059149	3.3764781
C	1.9583377	1.5359622	-1.2152128
N	0.5477502	1.2164049	-1.4322274
H	2.3595859	0.8692493	-0.4386636
H	2.6118785	1.4481886	-2.1061687
H	2.0534484	2.5631866	-0.8331188
H	0.4546141	0.2590853	-1.7991325
H	0.1450682	1.8442047	-2.1285755
N	0.2409668	-1.8398715	-2.0042057
C	1.0584146	-2.2775037	-0.8794870
C	-1.1790432	-1.9785291	-1.7050943
C	0.5989756	-2.5446235	-3.2252214
H	0.9084226	-3.3539299	-0.6412371
H	-1.4696785	-3.0353117	-1.5136689
H	0.4271036	-3.6419176	-3.1525369
H	2.1212102	-2.1247084	-1.1137240
H	0.8132961	-1.6839415	0.0105935
H	-1.4318037	-1.3778708	-0.8219121
H	-1.7724157	-1.6101938	-2.5536317
H	0.0025634	-2.1617143	-4.0649799
H	1.6616741	-2.3806217	-3.4517597

TS+TMA

Energy = -958.1333799151 Eh, imaginary frequencies = 1

C	-1.0383741	0.3377151	1.9854745
S	-0.5851250	-0.7132275	0.5805362
O	0.7578258	-1.1544768	0.9842519
O	-1.6554909	-1.6813504	0.3742617
F	-1.5467339	1.0432625	-0.3035673
H	-0.3934741	1.2194109	1.9704772
H	-0.8318170	-0.2913821	2.8609231
H	-2.0866109	0.6127888	1.8729676
C	1.2452879	0.0943483	-1.5280639
N	-0.0825592	-0.4718187	-1.3149908
H	1.9800194	-0.4794794	-0.9508904
H	1.4997577	0.0475056	-2.5970924
H	1.2548260	1.1401301	-1.2001525
H	-0.1963287	-1.4497111	-1.7379569
H	-0.8546406	0.2105303	-1.4959112
N	-0.3320479	-3.0692240	-2.4154470
C	0.1973649	-3.9780451	-1.3946956
C	-1.7683268	-3.2825238	-2.6096075

C 0.3992534 -3.2043906 -3.6733087
H 0.1014362 -5.0387639 -1.7012572
H -1.9883609 -4.3102899 -2.9609668
H 0.3009178 -4.2200218 -4.1072297
H 1.2587958 -3.7583845 -1.2187211
H -0.3469924 -3.8232074 -0.4559049
H -2.2896352 -3.1050068 -1.6612636
H -2.1483006 -2.5725708 -3.3568917
H 0.0170817 -2.4799918 -4.4056287
H 1.4665417 -3.0054552 -3.5053942

3-HF+TMA

Energy = -958.1947460420 Eh, imaginary frequencies = 0

C -0.6537300 1.7528355 2.0602074
S 0.2608874 0.3063825 1.5565987
O 1.5146321 0.2830871 2.2920964
O -0.6360716 -0.8382549 1.5871997
F -1.4465627 1.8369173 -1.2018535
H -0.0218762 2.6380942 1.9269433
H -0.8894083 1.6142897 3.1214763
H -1.5627269 1.8228935 1.4538801
C 1.7966113 1.3291436 -0.3956462
N 0.5494470 0.6146253 -0.0776628
H 2.6811763 0.8336909 0.0258297
H 1.8820115 1.3717992 -1.4886226
H 1.7560804 2.3601854 -0.0208196
H 0.4518519 -0.3188759 -0.6151508
H -0.6983473 1.3814071 -0.7554757
N 0.1015620 -1.6800318 -1.5895383
C 0.6381487 -2.8761331 -0.9392678
C -1.3649875 -1.6986745 -1.6094085
C 0.6447178 -1.5072697 -2.9356535
H 0.3513753 -3.8026423 -1.4749795
H -1.7544037 -2.5438955 -2.2099571
H 0.3627740 -2.3409659 -3.6094670
H 1.7347085 -2.8187259 -0.9080457
H 0.2604922 -2.9267664 0.0896691
H -1.7363172 -1.7860655 -0.5811180
H -1.7374943 -0.7565087 -2.0324942
H 0.2643157 -0.5716068 -3.3672362
H 1.7412586 -1.4569815 -2.8903769

Postcomplex+TMA

Energy = -958.2037320924 Eh, imaginary frequencies = 0

C -0.7607754 -0.3342653 1.3834323
S -0.7296020 -0.4721504 -0.4046993
O 0.1295005 -1.5894253 -0.7533501
O -2.1196930 -0.4392803 -0.8442683
F -1.7311863 2.8792963 -0.0170773
H 0.2695100 -0.2946908 1.7552124
H -1.2690426 -1.2233177 1.7736576
H -1.3085288 0.5791892 1.6428419
C 1.4065048 1.0875307 -0.7749433
N -0.0331873 0.9114119 -0.9633055
H 1.9254070 0.1761801 -1.0916538
H 1.7360532 1.9155489 -1.4149723
H 1.6906059 1.3205635 0.2661742
H -0.6135356 1.7271418 -0.6817646
H -4.6357325 4.3121468 -0.4396571
H -4.8923724 2.0573501 0.3909395
C -4.4044842 3.9252009 -1.4395503
C -4.6684932 1.6556829 -0.6051959
H -5.3332547 3.8793928 -2.0335413
H -5.6138571 1.5107454 -1.1554272
H -3.6991744 4.6090610 -1.9270332
N -3.7853367 2.5970870 -1.3167128
H -2.6566895 2.7443100 -0.5896849
H -4.1488648 0.6967251 -0.5018952
C -3.3952570 2.0633715 -2.6353927
H -4.2772599 1.9470447 -3.2879246
H -2.6886507 2.7572429 -3.1072518
H -2.9065234 1.0926362 -2.4943764

TMA

Energy = -174.3028656920 Eh, imaginary frequencies = 0

N	-0.3198409	0.2028080	0.0000000
C	0.7935396	1.1370121	-0.0000000
C	-0.3193584	-0.6175753	1.1996803
C	-0.3193584	-0.6175753	-1.1996803
H	1.7855182	0.6289792	0.0000000
H	0.5911657	-1.2538421	1.2894009
H	0.5911657	-1.2538421	-1.2894009
H	0.7413716	1.7788329	-0.8905692
H	0.7413716	1.7788329	0.8905692
H	-0.3733092	0.0244888	2.0900339
H	-1.1966781	-1.2793040	1.1986526
H	-1.1966781	-1.2793040	-1.1986526
H	-0.3733092	0.0244888	-2.0900339

1-2+HF+TMA

Energy = -1058.594981171 Eh, imaginary frequencies = 0

C	-0.6962972	0.4563336	3.9861503
S	-0.7250993	0.4847401	2.2076807
O	0.6150339	0.6529420	1.7053510
O	-1.6001485	-0.5453661	1.7167894
F	-1.4759057	1.8843146	2.0322688
H	-0.1302769	1.3232437	4.3411183
H	-0.1974085	-0.4759620	4.2737039
H	-1.7279461	0.4703568	4.3514386
C	1.9785109	1.4585428	-1.4885049
N	0.7709799	0.9873408	-2.1829417
H	1.9428755	1.1139410	-0.4480339
H	2.9172929	1.1058550	-1.9472848
H	1.9915338	2.5562264	-1.4720399
H	0.7400116	-0.0524638	-2.2125621
H	0.7499606	1.3263302	-3.1454423
F	-1.3278412	1.5224798	-0.8897582
H	-0.4874260	1.3491675	-1.4328986
N	0.3153449	-1.9488898	-1.8802816
C	0.9767278	-2.2532931	-0.6144708
C	-1.1360009	-1.8748070	-1.7038557
C	0.6746484	-2.9196203	-2.9057103
H	0.6720671	-3.2424837	-0.2102860
H	-1.5589456	-2.8382129	-1.3491501
H	0.3547643	-3.9512554	-2.6432071
H	2.0664647	-2.2618909	-0.7579789
H	0.7260289	-1.4857471	0.1278519
H	-1.3863673	-1.0890195	-0.9803470
H	-1.6087422	-1.6228136	-2.6630057
H	0.1991745	-2.6479458	-3.8582935
H	1.7642688	-2.9262748	-3.0492874

TS+HF+TMA

Energy = -1058.558874895 Eh, imaginary frequencies = 1

C	-0.9580633	0.1347697	2.1222232
S	-0.5759257	-0.6345418	0.5217793
O	0.7684498	-1.1652319	0.7607470
O	-1.7554105	-1.4608366	0.2644889
F	-0.8579617	1.4446771	0.0711986
H	-0.1823268	0.8684068	2.3474084
H	-0.9357192	-0.7117304	2.8201883
H	-1.9454402	0.5933525	2.0577853
C	1.0393041	0.2376965	-1.7723692
N	-0.2280042	-0.4098174	-1.4292018
H	1.8476941	-0.2571838	-1.2224715
H	1.2202934	0.1399973	-2.8527313
H	0.9935265	1.2958411	-1.5000289
H	-0.2546041	-1.4314886	-1.7523202
H	-1.0357713	0.1157216	-1.8068320
F	-2.1032036	1.6075094	-1.9584617
H	-1.6569521	1.6693834	-1.0673358
N	-0.3200000	-3.0894287	-2.3504208
C	0.0921469	-3.9836079	-1.2652292
C	-1.7292717	-3.2957554	-2.6916508

C 0.5390071 -3.2531203 -3.5217723
H 0.0322832 -5.0483484 -1.5672742
H -1.9222583 -4.3275419 -3.0467499
H 0.4794918 -4.2765921 -3.9438812
H 1.1246067 -3.7559363 -0.9705748
H -0.5561966 -3.8209156 -0.3964123
H -2.3469810 -3.0990136 -1.8067827
H -2.0233581 -2.5959813 -3.4858127
H 0.2412675 -2.5414806 -4.3040984
H 1.5835060 -3.0555371 -3.2452942

3-HF+HF+TMA

Energy = -1058.610446129 Eh, imaginary frequencies = 0

C -0.6584753 1.3582240 2.1908335
S 0.1570258 -0.1100887 1.6048738
O 1.4201621 -0.2610411 2.3049689
O -0.8010854 -1.2027304 1.5648725
F -0.2983656 3.7151746 -0.0481594
H -0.0319331 2.2334940 1.9852820
H -0.7918635 1.2169871 3.2694667
H -1.6221726 1.4483581 1.6797237
C 1.7262029 0.9929645 -0.2999705
N 0.4635660 0.2666041 -0.0384622
H 2.5773443 0.5109426 0.1956521
H 1.8817979 0.9953746 -1.3859493
H 1.6378016 2.0346782 0.0317076
H 0.4242063 -0.6775486 -0.5828807
H -0.5931429 1.0171261 -0.5969864
F -1.3205495 1.6540716 -1.0374950
H -0.7702224 3.0028366 -0.4979987
N 0.2251409 -2.0532942 -1.5304808
C 0.7763981 -3.1930548 -0.7932650
C -1.2306717 -2.1655430 -1.6700318
C 0.8709507 -1.8919837 -2.8332858
H 0.6007482 -4.1496735 -1.3225189
H -1.5178638 -3.0548985 -2.2632842
H 0.6968758 -2.7636083 -3.4943879
H 1.8590765 -3.0594462 -0.6651400
H 0.3095707 -3.2408648 0.1983479
H -1.6828881 -2.2362672 -0.6733838
H -1.6216066 -1.2679106 -2.1675524
H 0.4762771 -0.9963229 -3.3317399
H 1.9543034 -1.7730933 -2.6976330

Postcomplex+HF+TMA

Energy = -1058.619941395 Eh, imaginary frequencies = 0

C -0.5477393 0.1650203 1.8389692
S -0.9428982 -0.6635273 0.3033335
O -0.1536314 -1.8762499 0.2026632
O -2.3888736 -0.6955091 0.1836367
F -1.6032896 2.6707308 -0.2198994
H 0.5402954 0.2542976 1.9317516
H -0.9455286 -0.4605674 2.6460141
H -1.0315256 1.1487667 1.8222932
C 1.0531695 0.4791621 -1.0871069
N -0.4038232 0.4058122 -0.8881817
H 1.4496082 -0.5281038 -1.2517631
H 1.2370276 1.0853019 -1.9824462
H 1.5759295 0.9430258 -0.2362001
H -1.1561555 0.1704208 -2.2939856
H -0.8303132 1.3504671 -0.6600973
H -4.7299626 3.4071679 0.1502184
H -4.4490207 1.0454470 -0.4342242
C -4.5178924 3.7050517 -0.8831047
C -4.3030313 1.3462019 -1.4770614
H -5.4645145 3.8140368 -1.4344183
H -5.2717284 1.3781842 -1.9996628
H -3.9852088 4.6632420 -0.8750542
N -3.6631764 2.6809381 -1.5129482
H -2.6206512 2.6489435 -0.8532740
H -3.6419786 0.6208435 -1.9622922
C -3.2908531 3.0568801 -2.8941847

H -4.1904126 3.1510756 -3.5218854
H -2.7595568 4.0157935 -2.8704425
H -2.6343604 2.2793027 -3.3020614
F -1.6044741 0.2114937 -3.1726157

$MeSO_2^+$
Energy = -587.9194567583 Eh, imaginary frequencies = 0
C 8.6530594 8.6264342 14.3349389
S 8.6962542 6.9135512 14.8214827
O 7.5866849 6.1297410 14.3855067
O 9.8216808 6.5333871 15.6117569
H 8.0892085 8.6747205 13.3938944
H 9.6956131 8.9656976 14.2747082
H 8.1123490 9.1385984 15.1517422

$MeSO_2^+$+TMA
Energy = -762.3381801520, imaginary frequencies = 0
C -0.7566991 -0.3103244 1.5644913
S -0.6424989 -0.8826264 -0.1147468
O 0.3429577 -1.9254645 -0.2307961
O -1.9445614 -0.9226524 -0.7272141
H 0.2448847 -0.1534248 1.9762778
H -1.2443728 -1.1482318 2.0841281
H -1.3949182 0.5770921 1.6158436
C 1.5735857 0.8479691 -0.4881612
N 0.2133674 0.6124535 -1.0494596
H 2.1310651 -0.0940076 -0.4944171
H 2.0836048 1.5873014 -1.1182357
H 1.4898397 1.2419008 0.5297135
C -0.6493109 1.8246163 -0.9608064
H -0.2239003 2.5985549 -1.6116637
H -0.6650006 2.1929187 0.0699395
H -1.6594677 1.5706575 -1.2972723
C 0.3019088 0.1291693 -2.4651944
H 0.7666326 0.9225073 -3.0624766
H -0.7064671 -0.0796143 -2.8361558
H 0.9168505 -0.7757247 -2.4972541

1-2+$(H2O)_3$
Energy = -1013.057253848, imaginary frequencies = 0
C -1.6068240 0.6198377 2.3667436
S -0.1635322 0.0398134 1.5304054
O 0.9189705 -0.2107551 2.4431912
O -0.5149102 -0.9098412 0.5021806
F 0.2243349 1.4087399 0.7463260
H -1.2918729 1.3739032 3.0955717
H -2.0289142 -0.2553265 2.8752827
H -2.3081929 1.0334651 1.6226671
C 0.9985353 0.1365811 -2.7140788
N -0.3373475 -0.4618759 -2.5745794
H 1.1302300 0.8978107 -1.9341836
H 1.8290910 -0.5842828 -2.6297716
H 1.0741309 0.6408451 -3.6863232
H -0.4235701 -0.9078522 -1.6582686
H -0.4795318 -1.1875252 -3.2779009
H -2.6651287 2.7436544 -0.1715147
O -3.3270915 2.0638058 0.1459523
O -1.4506412 3.5828530 -1.0692942
H -0.5752056 3.3925315 -0.6997696
H -4.1607216 2.5468369 0.2436961
H -1.5845793 2.8934548 -1.7894095
H -1.5773346 0.7822963 -2.6282692
H -2.8519418 1.3414017 -1.8942566
O -2.2300325 1.5507982 -2.6164670

TS+$(H2O)_3$
Energy = -1013.000779140, imaginary frequencies = 1
O 5.9975357 8.4600871 7.8918768
O 8.5406791 7.3130614 8.3551947
H 6.0515021 9.8458309 9.1895236
H 6.0068861 8.7684669 6.9740067
H 6.8361814 7.9617789 8.0056209

H	8.8061064	7.4158167	9.3027647
H	8.7915506	6.4128382	8.1008212
S	9.7728922	9.7104698	10.7311372
O	9.5686942	8.2464943	10.6785116
F	8.7948258	11.4773257	9.8106410
H	9.5854782	10.7567413	8.6184393
H	6.9782188	10.9948616	9.6915739
C	8.5284003	10.2084634	11.9372664
O	6.1687648	10.4920529	9.9177218
H	8.6872649	11.2664331	12.1476026
H	8.7395189	9.5514709	12.7913149
H	7.5385696	10.0257234	11.4945096
H	11.8469958	8.7408118	8.6086114
H	11.5731828	9.8780221	7.2517237
H	9.4786867	9.0579244	8.2948358
N	10.0452933	9.8207408	8.6929653
O	11.0582019	10.2573419	11.1245442
C	11.4567564	9.7281557	8.3352665
H	12.0162338	10.4993750	8.8735920

10) References

S1. Tao, J.; Perdew, J. P.; Staroverov, V. N.; Scuseria, G. E. Climbing the Density Functional Ladder: Nonempirical Meta-Generalized Gradient Approximation Designed for Molecules and Solids. *Phys. Rev. Lett.* **2003**, *91*, 146401.

S2. Stephens, P. J.; Devlin, F. J.; Chabalowski, C. F.; Frisch, M. J. Ab Initio Calculation of Vibrational Absorption and Circular Dichroism Spectra Using Density Functional Force Fields. *J. Phys. Chem*. **1994**, *98*, 11623–11627.

S3. Zhao, Y.; Truhlar, D. G. The M06 suite of density functionals for main group thermochemistry, thermochemical kinetics, noncovalent interactions, excited states, and transition elements: two new functionals and systematic testing of four M06-class functionals and 12 other functionals. *Theo. Chem. Acc.* **2008**, *120*, 215–241.

S4. Tew, D. P.; Klopper, W.; Neiss, C.; Hättig, C. Quintuple-ζ quality coupled-cluster correlation energies with triple-ζ basis sets. *Phys. Chem. Chem. Phys.* **2007**, *9*, 1921–1930.

Received: 14 December 2020 | Revised: 20 January 2021 | Accepted: 3 February 2021

DOI: 10.1002/jcc.26503

FULL PAPER

Journal of COMPUTATIONAL CHEMISTRY WILEY

Efficient hierarchical models for reactivity of organic layers on semiconductor surfaces

Jan-Niclas Luy[1,2] | Mahlet Molla[1] | Lisa Pecher[1] | Ralf Tonner[1,2]

[1]Fachbereich Chemie, Philipps-Universität Marburg, Marburg, Germany

[2]Wilhelm-Ostwald-Institut für Physikalische und Theoretische Chemie, Universität Leipzig, Linnéstraße 2, Leipzig, Germany

Correspondence
Ralf Tonner, Fachbereich Chemie, Philipps-Universität Marburg, Hans-Meerwein-Straße 4, D-04103 Leipzig, Germany.
Email: ralf.tonner@uni-leipzig.de

Funding information
German Research Foundation (DFG), Grant/Award Number: SFB 1083

Abstract

Computational modeling of organic interface formation on semiconductors poses a challenge to a density functional theory-based description due to structural and chemical complexity. A hierarchical approach is presented, where parts of the interface are successively removed in order to increase computational efficiency while maintaining the necessary accuracy. First, a benchmark is performed to probe the validity of this approach for three model reactions and five dispersion corrected density functionals. Reaction energies are generally well reproduced by generalized gradient approximation-type functionals but accurate reaction barriers require the use of hybrid functionals. Best performance is found for the model system that does not explicitly consider the substrate but includes its templating effects. Finally, this efficient model is used to provide coverage dependent reaction energies and suggest synthetic principles for the prevention of unwanted growth termination reactions for organic layers on semiconductor surfaces.

KEYWORDS
density functional theory, hybrid organic–inorganic materials, interfaces, model hierarchy, semiconductor functionalization

1 | INTRODUCTION

The creation of hybrid organic–inorganic interfaces is an important aspect of many technological applications. Some prominent examples include the combination of established silicon-based technology with the emerging approach of molecular electronics,[1–4] encapsulation of organic solar cells or organic light emitting diodes (OLED)[5,6] and (biomedical) sensing.[7] The goal of advancing miniaturization leads to a relative increase in size of the surface-area with respect to the bulk. This increases the importance of surface properties. To analyze and understand these properties, interfaces have to be uniform and defect free. Such quality requirements can only be fulfilled with molecular-scale control during synthesis while remaining compatible with established clean-room manufacturing techniques. One promising approach is the build-up of layered organic films on a solid inorganic semiconductor surface using well-tailored molecular building blocks.[8] Here, the most critical step is the attachment of the first layer since pristine semiconductor surfaces are generally highly reactive[9] resulting in low selectivity. In order to increase selectivity, attachment should be covalent which has the added benefit of being self-limiting to one layer once the substrate is fully covered. Subsequent deposition of a different building block on top of the first layer then offers fine control over thickness and composition of the organic material. This approach shares some ideas with molecular layer deposition[10,11] and layer-by-layer (LbL)[12] methods for polymer films.[13] However, the focus of this work is not on growth of bulk materials but the reactivity of the crucial interface region shown in Figure 1.

Commonly, interface formation on solid semiconducting substrates is studied in ultra-high vacuum (UHV).[14] However, synthetic routes toward organic layers are often first investigated and optimized in solution.[15] Computations can thus help to assess the question of transferability of wet-chemical schemes to UHV before performing time-consuming experiments. This can be done with modeling techniques that go beyond supplementing experimental research toward suggesting

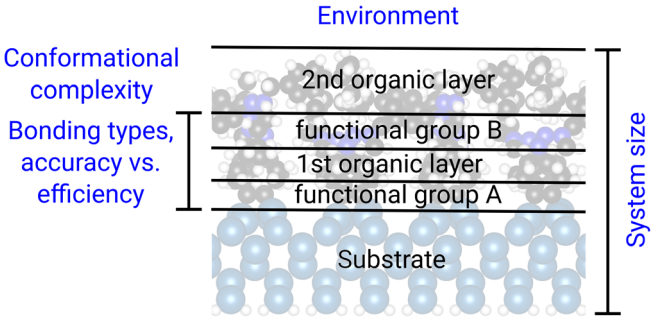

FIGURE 1 The interface model investigated in this work is comprised of a solid substrate in slab geometry and up to two layers of an organic material in contact to vacuum or a solvent. The organic layers are covalently linked to the substrate and each other by functional groups A and B. The computational challenges arising from this model are printed in blue

new avenues of investigation. Furthermore, interface characterization based on electronic structure methods can lead to a deeper understanding of the physicochemical origins of various material properties.

The computational challenges of interface modeling stem from the large system sizes often with large conformational freedom, the various types of bonding interactions involved and the chemical environment that needs to be considered while weighing accuracy against efficiency (Figure 1). We will use different density functionals (DFs), sampling via simulated annealing (SA)[16] and the semi-empirical density functional tight binding (DFTB)[17] method and solvent effects via a polarizable continuum model (PCM).[18]

We note in passing that additional synthetic challenges such as double adsorption of bifunctional molecules are still not fully overcome. These issues are also under investigation but not further discussed in this study.[19,20] However, attachment of molecules in the second organic layer could recently be demonstrated.[21]

With this work we are aiming at deriving an accurate yet efficient computational model based on density functional theory (DFT) for studying hybrid interfaces and their growth processes. The proposed model is then validated with three experimentally significant reaction schemes.

1.1 | The model reactions

We validate our computational protocol for organic layers by selecting a suitable test set. Common synthetic approaches for organic layers are derived from the concept of "click-chemistry."[22] Those were initially developed for biochemical applications but are also increasingly employed in material science.[23–25] Click reactions must be fast (i.e., low barriers) and produce excellent yields with high selectivity (i.e., highly negative reaction energies). In addition, reactions should proceed without a catalyst, produce as few side products as possible and be largely independent of solvent environments.[10] Application of click-chemistry in interface synthesis under UHV conditions constrains possible precursors further to be simultaneously volatile and thermally stable. The three reaction schemes chosen for investigation in this article are introduced briefly in the following (Figure 2).

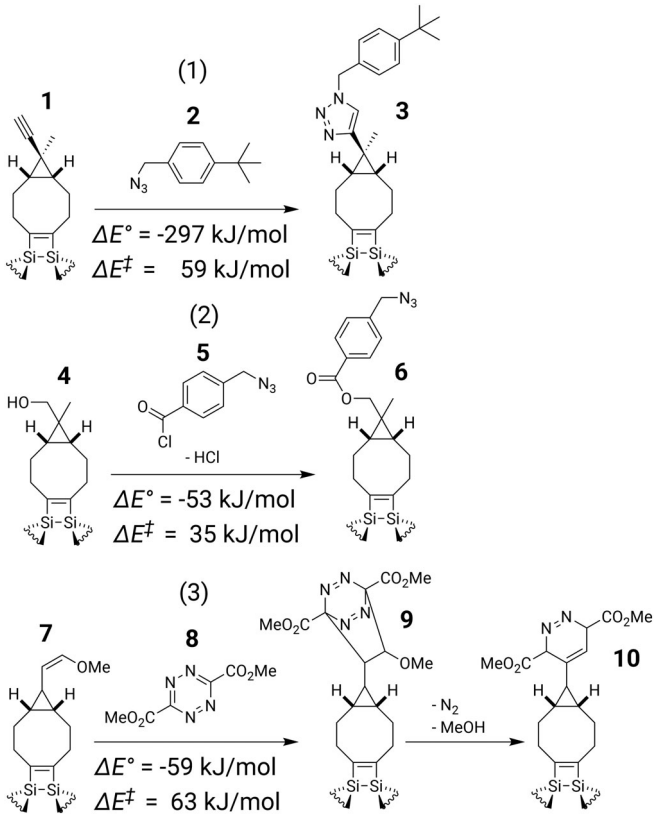

FIGURE 2 Selection of interface building schemes chosen as model systems in this work. (1) Cu-free azide-alkyne cycloaddition (AAC). The mono-functional variant of azide **2** is investigated here. The bi-functional form is discussed at the end of this article. (2) Acyl-chloride mediated esterification (ACE). The azide moiety indicates the possibility of attaching a third layer via AAC. (3) Inverse electron demand Diels–Alder (IEDDA) reaction. We focus on the first reaction step leading to **9** here. Reaction energies and energy barriers taken from Table 1 (PBE-D3)

The first reaction is a variant of the azide-alkyne 1,3-dipolar cycloaddition (AAC).[26] This reaction can be considered a prototypical click reaction and has shown excellent performance when combined with a Cu(I) catalyst in organic solvents.[27] However, the catalyst cannot be applied in UHV conditions and is thus not considered here. The second model reaction shown in Figure 2 is an acyl-chloride mediated esterification (ACE).[28] The reaction provides a low reaction barrier even in the gas phase and could therefore be an alternative to the AAC when concerns about precursor stability limit the use of elevated temperatures. As a side-note, the by-product HCl could initiate undesired side-reactions with the substrate or other precursor molecules—a problem we are not further investigating here. Finally, an inverse electron demand Diels–Alder (IEDDA) reaction utilizing a tetrazine derivative as the diene[15] has been recently proposed. As part of our test set, we limit our investigation to the rate-determining first synthetic step.[29] An advantage of this reaction is the tolerance of the strain promoted AAC (SPAAC)[30] variant which allows for sequential execution in an interface building approach.

2 | DEFINING THE SYSTEM

2.1 | The substrate

As a model for interface formation between a semiconductor surface and a layered organic material (Figure 1), silicon and its (001) facet are an obvious choice due to their technological prevalence and versatility in forming covalent bonds.[31] Even though novel materials such as III/V compound semiconductors or transition metal dichalcogenides are increasingly incorporated in devices, the "post-silicon" age is only just appearing at the horizon.[4] Si-based technology is very mature and will, for the foreseeable future, remain an important part of nanoelectronic devices. However, the methodology used in this study is built upon first principles and insights should therefore be transferable to other substrates. But other combinations of substrates and adsorbates might require a computation of the full system for an accurate description.

A model of the Si(001) surface is given in Figure 3. Upon cleavage from the single crystal, each surface atom has two unpaired electrons (dangling bonds). The surface energy is lowered by those atoms reconstructing into rows of tilted dimers which share a single bond. Furthermore, the Si_{down} atom transfers its remaining electron to Si_{up} resulting in an unoccupied *p*-orbital and a non-bonding electron pair respectively (Figure 3 inset). In order to reduce repulsion between lone pairs, dimers tilt alternatingly along a row. Between rows, trenches are formed across also tilting alternately. The resulting $c(4 \times 2)$ reconstruction is the most stable under UHV conditions at low temperatures.[31]

2.2 | The organic adsorbate

Cyclooctyne solves many questions of low selectivity at the Si(001) surface. Due to the release of about 80 kJ/mol of ring strain energy (Figure S1) the triple bond reacts barrierless with a single surface dimer via a 2 + 2 cycloaddition.[32] This markedly improves selectivity with respect to other functional groups.[33] Thus, cyclooctyne is an ideal platform molecule for interface build-up.[34] After some optimization of the molecular design, bicyclic derivatives of cyclooctyne (Figure 4) have emerged as preferred building block candidates due to increased rigidity, restriction of conformational space and limiting of side reactions.[34–36]

All organic layers investigated in this work and shown in Figure 2, are thus based on [(1R,8S)-bicyclo[6.1.0]non-4-yne] (CCO).[27] Apart from the strained triple bond, the molecule contains two additional substituents R (functional group) and R′ (aliphatic group or H). As a consequence of its specific molecular structure, group R is forced to point in the direction of growth where the next layer can be attached.

2.3 | The first layer

In previous work, parent cyclooctyne was shown to block two surface dimers due to tilting of the backbone.[36] The first adsorbed molecule steers the next one through dispersion attraction toward adjacent sites.[36] Hence, an ordered first layer is formed on Si(001)[14] with a maximum coverage of $\Theta = 0.5$ monolayers (ML) CCO with a complete ML being defined as one adsorbate per surface dimer.

Here, we model the experimental system by considering an idealized CCO/Si(001) interface that is uniform and defect free. During the creation of our interface model we took both the steric demand and the inherent symmetry of the molecule into consideration. Since CCO has two chiral centers, several possibilities exist for the adsorption of more than one adsorbate. Two neighboring molecules can either face the same direction or be positioned "back-to-back." Assuming a random distribution of *N* molecules, 2^N possible arrangements emerge. In order to calculate the relative energies of different arrangements, a 4×4 supercell containing eight dimers and four CCO derivatives **1** (R = —C≡CH and R′ = —CH_3) was chosen (see Figure 5).

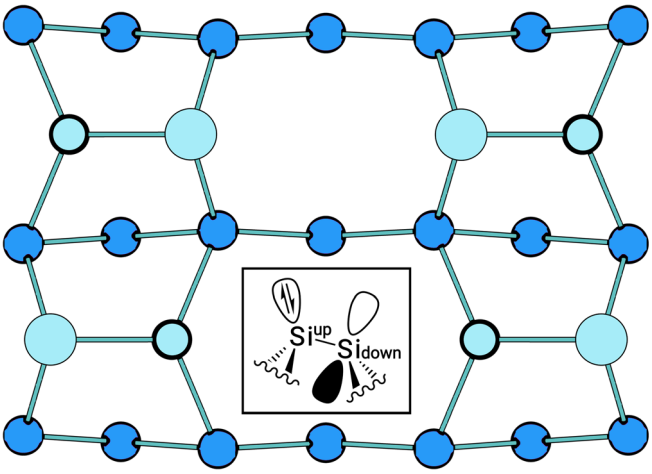

FIGURE 3 Top view of the $c(4 \times 2)$ reconstruction of the Si(001) surface. Dark blue: Sub-surface atoms. Light blue: Buckled surface dimers with Si_{down} (small circle) and Si_{up} atoms (large circle). Inset: Side view of a buckled dimer with simplified frontier orbital sketch

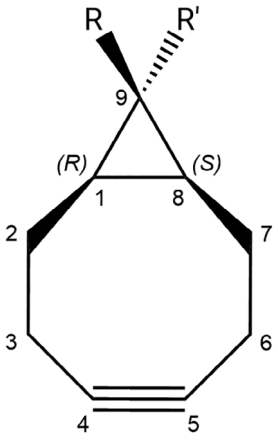

FIGURE 4 [(1R,8S)-bicyclo[6.1.0]non-4-yne] (CCO, R = R′ = H) platform molecule with chiral centers at C1 and C8. **1**: R = —C≡CH, R′ = —CH_3**4**: R = —CH_2—OH, R′ = —CH_3**7**: R = —CH = CH—OMe, R′ = H

Consequently, there exist 2^4 = 16 possible configurations of four CCO molecules in the 4 × 4 supercell. This number is doubled when a shift by one dimer is applied to every second row. Through the exploitation of symmetry operations, the number of unique structures is reduced to nine (see Figure S3). In this setup, the computational demand is still feasible while all possible nearest neighbor interactions between adsorbate molecules are sampled.

Relative energies of these nine structures are listed in Table S1. Evidently, even the least favorable configuration is only 7 kJ/mol less stable than the most favorable one depicted in Figure 5. Energy differences of this magnitude are smaller than the overall accuracy of DFT[37] and all configurations can therefore be considered isoenergetic. Thus, a random arrangement of molecules on the macroscopic scale appears likely.

2.4 | The computational models—A hierarchical approach

The central question of this study is how to create an accurate structural model of hybrid organic–inorganic interfaces that can be efficiently computed. Accurate reaction barriers and energies based on highly accurate approaches quickly become unattainable for such systems. Thus it is imperative to develop means to minimize computational complexity while maintaining acceptable accuracy for properties of interest.

We propose to reduce the complexity of an interface model based on the assumption that bond cleavage and formation are predominantly local phenomena. Thus, it stands to reason that only the immediate chemical environment exerts a noticeable influence on the shape of a potential energy surface. In the following, we test this hypothesis by comparing the energetic signatures of the reactions shown in Figure 2 with those obtained from structurally increasingly simplified model systems. For this purpose, a hierarchical system (Figure 6) is introduced and benchmarked with respect to the full interface model which is assigned rank 1 (see Figure S7 for structures). The computational speedup achieved by the hierarchical approach is shown for the AAC reaction in Figure S8 and approximately scales with the number of atoms in the model.

Rank 1. The full system contains the surface slab, which is constructed as described in Section 3, and the desired number of organic layers at complete coverage. No structural approximations besides the supercell size and slab thickness are made.

Rank 2. At the first rank of simplification, the substrate is removed. Whenever a covalent bond must be cut during system size reduction, dangling bonds are saturated with hydrogen atoms. Thus, rank 2 models explicitly capture intra-layer effects in the organic layer but disregard influence of the interface. However, template effects of the inorganic substrate are included by freezing positions of some

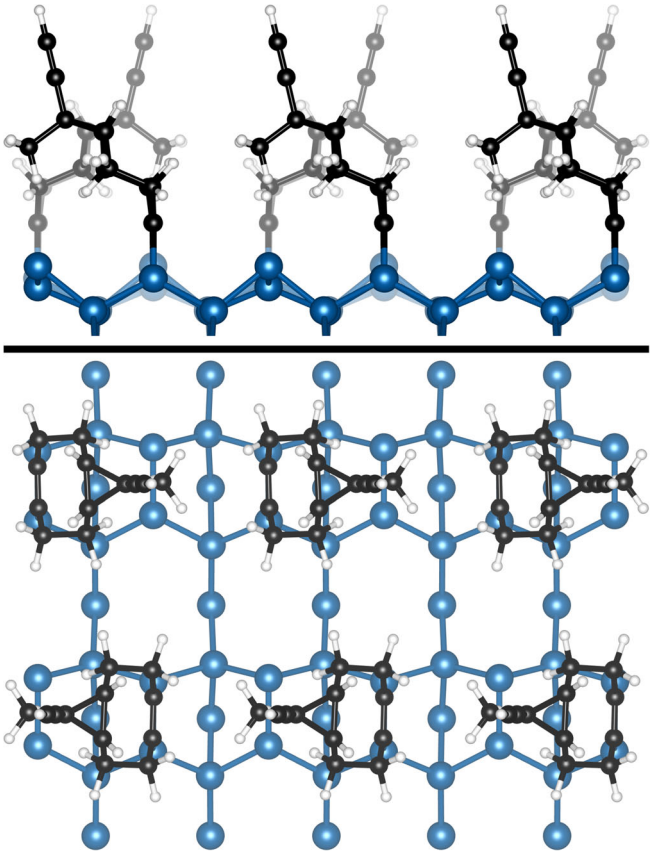

FIGURE 5 Structure of the most favorable arrangement of CCO **1** on Si(001)c(4 × 2) at full coverage. Molecules within a row point in the same direction while molecules in adjacent rows point in the opposing direction. Alternating rows are offset by one dimer (see Figure S2 for discussion of alternative configurations)

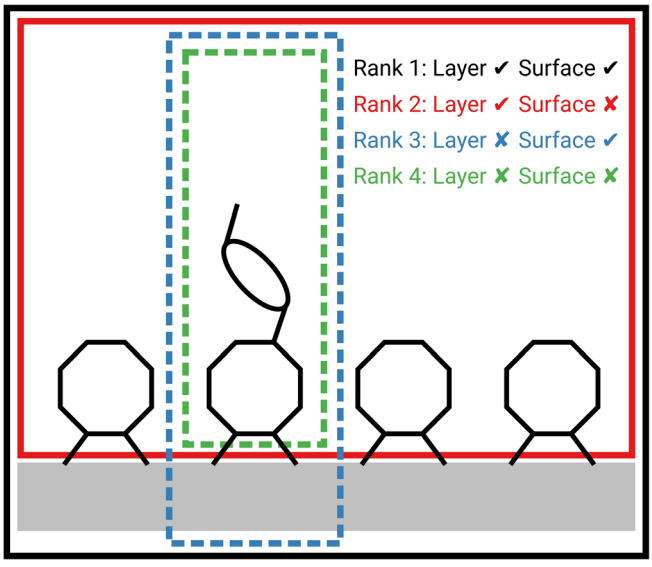

FIGURE 6 Hierarchically designed model systems of an interface between a semiconductor surface and an organic layer. Rank 1 (black): Full system containing the substrate and an organic layer. Rank 2 (red): The substrate is removed while the organic layer is structurally constrained to mimic the substrate template. Rank 3 (blue): Substrate same as rank 1 with a single adsorbed molecule. Rank 4 (green): A single molecule confined to surface-accessible geometry

atoms in the first organic layer. One advantage of rank 2 systems is the option of using cluster approaches instead of periodic boundary conditions (PBC) (see Section 3 for details). Speedup of factor 2–6 is achieved w.r.t. rank 1 for the AAC reaction.

Rank 3. The opposite route to rank 2 is taken with rank 3 approximations. Here, effects at the interface are explicitly included. A reduction in computational effort is achieved by diluting the surface coverage to a single adsorbate. Consequently, all coverage and intralayer effects cannot be captured with rank 3. Speedup of factor 1.5–2 is achieved.

Rank 4. The simplest possible system is just the individual molecule without surface. There are, however, two possible ways in which one can design this model. Without prior knowledge of the surface structure, all molecular degrees of freedom have to be explored in order to find the minimum energy path connecting reactants and products. This model is assigned the rank 4b. On the other hand, some degrees of freedom are constrained when one of the reactants is immobilized on the substrate. Here, the gas phase minimum energy path might be inaccessible. Some mechanism-altering effects of the surface are therefore already contained in a rank 4 model. For instance, the cycloaddition of the AAC reaction cannot be initiated from below when the alkyne is attached to the surface. Speedup of up to a factor of 50 is achieved.

3 | METHODS

Rank 1–4. Structure optimizations of all systems were performed with the Vienna Ab initio Simulation Package (VASP 5.4.4[38–40]) compiled with the transition state tools by Henkelman et al.[41,42] The conjugate gradient algorithm for structural optimization was considered converged with forces smaller than 10^{-2} eV/Å. For gas phase calculations, stationary points found were verified by calculation of the Hessian matrix. The generalized gradient approximation (GGA)-based exchange-correlation DF proposed by Perdew, Burke and Ernzerhof (PBE)[43] was used to calculate the electronic energy and forces.

The inclusion of dispersion interaction corrections is important for the performance of semi-local DFs.[44] Benchmarks for low-density solids show good accuracy for bond lengths, angles, volumes and lattice constants.[45] In this study, dispersion effects were captured with the DFT-D3 scheme including the improved Becke–Johnson damping function[46,47] for PBE and the rPBE[48] functional. Furthermore, the range-separated hybrid functional HSE06[49] which is based on PBE and includes 25% Hartree–Fock exchange at short distances was also paired with D3 in order to quantify improvements on reaction barriers. For comparison, the dispersion correction scheme by Tkatchenko and Scheffler (TS)[50] was applied to the PBE functional. With optB88[51] a third approach to capture dispersion effects was investigated.

The planewave energy cutoff was set to 400 eV for all calculations and "standard" pseudopotentials for all atoms (version PBE5.4)[52] were applied in conjunction with the projector-augmented wave (PAW) method. The precision tag was set to accurate and a total energy difference of at most 10^{-5} eV was applied for self-consistent field (SCF) convergence. The Si(001) surface was described with a six-layered slab-supercell model with PBC. The theoretically optimized lattice parameter (a = 5.418 Å) was determined previously.[35] The surface opposite to the organic layer was saturated with two hydrogen atoms per Si atom using the silane (SiH_4) bond length (1.480 Å)[53] while the bottom two layers were frozen at their bulk positions during relaxation. The thickness of the vacuum layer between periodically repeated units was at least 10 Å. Electronic levels around the Fermi-energy are smeared out by σ = 0.05 eV with Gaussian functions to accelerate SCF convergence. Momentum space was sampled by a 2×2 Γ-centered k-point mesh for calculations including the substrate and Γ-only otherwise. This computational setup has yielded accurate results for molecular adsorbates in the past.[35] Organic layers were constructed by removal of the Si slab from the optimized system. Cleaved Si—C bonds were capped with H atoms on relaxed atomic positions while keeping all other atoms fixed. In all subsequent optimizations, the capping H atoms and directly attached C atoms were frozen. In order to calculate reaction barriers, transition state structures were optimized with the dimer method[41] after pre-determination with the nudged elastic band (NEB)[42] method.

Effects of solvation were modeled by using VASPsol[54] that implements a PCM-like[55] model. Here, the electrostatic solute-solvent interaction can be efficiently described through a generalized Poisson equation. The only free parameter is the relative permittivity ε_r which is solvent-dependent and quantifies the rate at which a medium screens charges with respect to the vacuum (ε_r = 1 per definition). The dielectric constant is applied to the continuum region outside the solute cavity depending on an isodensity cutoff n_c. In order to prevent numerical instabilities due to a sharp change of the electrostatic potential around the cavity a diffuse region of width σ is introduced in which the relative permittivity is smoothly varied from 1 to ε. The solvation energy can be corrected for the destabilization due to cavitation by scaling the cavity shape function with the surface tension τ of the solvent. Default values for n_c and σ were applied with all other settings kept identical to the non-solvated case.

Due to repetition of the unit cell perpendicular to the slab plane, finite size effects caused by the presence of a net dipole moment can occur. The resulting errors to the energy and forces can be corrected by applying a linear potential counteracting the dipole moment.[56] In our test, using this dipole correction did not result in any total energy changes of a H-saturated, bare slab and was thus not applied to the interfaces investigated.

The SA molecular dynamics approach can be used to find minimum structures when the initial guess is poor. Calculations were performed with CP2K 5.1[57] and the solution to the electronic SCF was given by the semi-empirical SCC-DFTB method with the "mio-1-1" parameter set[58] for elements H, C, N. Dispersion interactions were here included with a simplified D3 correction. We employ a three-step procedure where the system is first equilibrated in an NVT ensemble at T = 1500 K using a Nosé–Hoover thermostat for 1.25 ps with a time step of 0.5 fs. The high temperature does not lead to bond cleavage in a tight binding approach but ensures that

the system explores a larger subsection of the configuration space. In the second step, the temperature is decreased slowly to 300 K with a cooling rate of 0.1% per step. Lastly, the structure found is crudely optimized (conjugate gradient algorithm, 10^{-3} E_h/a_0) to the closest local minimum before the final optimization is performed with VASP as described above.

Rank 2 and 4. Additional single-point and gas phase calculations with a cluster approach were performed with TURBOMOLE 7.2[59] using PBE-D3. The basis set def2-TZVPP[60] was used together with a fine integration grid (*m4*) and the SCF energy convergence criteria set to 10^{-8} E_h. Clusters are constructed by simply removing PBC from a rank 2 supercell leading to saturated clusters. The number of atoms is thereby retained.

For the benchmark of gas phase energies, the orbital-specific virtual pair natural orbital coupled-cluster (CC) method implemented in TURBOMOLE 7.3 was employed.[61] Here, the correlation-consistent cc-pVTZ basis set including auxiliary functions was used while the energetic convergence criterion was lowered to 10^{-7} E_h in order to speed up the calculation.

4 | RESULTS AND DISCUSSION

4.1 | Functional benchmark

Before quantifying the model error introduced by the ranking approach, it needs to be disentangled from the systematic error of the functional. In Table 1, we assess the performance of five DF including dispersion corrected by benchmarking against the wavefunction based "gold standard" CCSD(T).[61] However, due to the size of the investigated molecules and current unavailability of coupled cluster methods for periodic systems, only rank 4 is benchmarked. Due to the varying accuracy of DFs with respect to minimum structures and transition states, reaction energies ($\Delta E^0 = \Delta E_{prod} - \Delta E_{reac}$) and barriers ($\Delta E^\ddagger = \Delta E_{TS} - \Delta E_{reac}$) are discussed separately. All reported energies were determined from single point calculations on the PBE-D3 optimized structure.

Furthermore, the mean signed error (MSE) is calculated in addition to the mean absolute error (MAE) to evaluate systematic trends of over- and underestimation of energies.

We begin with the comparison of different dispersion corrected GGA functionals for ΔE^0. As shown in Table 1, all DFs give rather similar errors with optB88 showing the smallest MAE, followed closely by PBE-D3, PBE-TS and rPBE-D3. While the deviations between the DFs are small for the AAC reaction, larger deviations are found for ACE and IEDDA. For the barriers, $\Delta E^\ddagger$, MAE and MSE values are identical in absolute terms suggesting a systematic error of the chosen DFs. While for DFT and MP2 too small barriers are found (negative MSEs), CCSD overestimates them (positive MSE). The PBE-TS functional gives smaller errors than the other GGA functionals by 6–8 kJ/mol but errors are about two times larger than for the reaction energies.

Notably, range-separated hybrid DF HSE06-D3 shows the largest MAE for ΔE^0 which is probably caused by a failure to correctly describe the product of the AAC reaction. This behavior is a systematic error since similar reaction energies are also yielded for ranks 1–3 (see Table S6). A likely explanation is the overestimation of Hartree–Fock exchange for the triazole-ring as the similarly constructed PBE0-D3 functional yields a reaction energy of −336 kJ/mol (compared to the −334 kJ/mol of HSE06-D3). Concerning the barriers, HSE06-D3 shows the best agreement with the CCSD(T) reference value as is often found for hybrid functionals that typically suffer less from delocalization errors of stretched bonds.[62]

TABLE 1 Benchmark of several density functionals and wavefunction-based methods in comparison to CCSD(T) data

Rkt.	CCSD(T)[a]	CCSD[a]	MP2[a]	PBE-D3[b]	PBE-D3[c]	PBE-TS[c]	rPBE-D3[c]	HSE06-D3[c]	optB88[c]
ΔE^0(AAC)	−289	−291	−292	−291	−297	−293	−295	−334	−286
ΔE^0(ACE)	−88	−95	−80	−66	−65	−59	−75	−80	−63
ΔE^0(IEDDA)	−64	−66	−60	−48	−51	−54	−39	−59	−54
MAE(^{0})	/	3.6	4.9	13.4	14.8	14.3	14.9	19.2	13.0
MSE(^{0})	/	−3.6	3.1	12.4	9.6	12.2	11.0	−10.4	13.0
$\Delta E^\ddagger$(AAC)	96	117	72	65	63	69	60	83	61
$\Delta E^\ddagger$(ACE)	55	74	15	27	26	34	17	39	25
$\Delta E^\ddagger$(IEDDA)	99	112	86	71	69	73	73	90	66
MAE(‡)	/	17.7	26.0	28.9	30.5	24.8	33.2	13.0	32.8
MSE(‡)	/	17.7	−26.0	−28.9	−30.5	−24.8	−33.2	−13.0	−32.8

Note: Gas phase structures (rank 4) were optimized at the PBE-D3 level. Reaction energies for the three model reactions AAC, ACE and IEDDA are listed in the first part. From these three data points mean absolute errors (MAE) and mean signed errors (MSE) are calculated. In the second half of the table reaction barriers and their errors are listed. Energies and errors in kJ/mol.

Abbreviations: AAC, azide-alkyne cycloaddition; ACE, acyl chloride mediated esterification; IEDDA, inverse electron demand Diels–Alder.

[a]Basis set: cc-pVTZ.

[b]Basis set: def2-TZVPP.

[c]Planewave basis set (E_{cutoff} = 400 eV).

Thus, the conclusion drawn from this small benchmark fits the general notion that GGAs perform reasonably well for reaction energies while accurate reaction barriers require hybrid functionals. Overall, mean errors introduced by the choice of the DF are below 15 kJ/mol but larger deviations of more than 30 kJ/mol are found for some reactions. Notably, errors caused by the change from an atom-centered to a plane wave basis set together with the application of PBC are much smaller with at most 6 kJ/mol (compare PBE-D3 columns of Table 1). Unless noted otherwise, PBE-D3 is employed for all further calculations since it is the least parametrized functional while performing comparable to others and being computationally much more efficient than HSE06-D3.

4.2 | Geometry changes with respect to model ranks

Systematic reduction of the system size has some influence on the geometry of the organic molecules which in turn leads to energetic differences. Removal of the substrate in rank 2 causes the organic layer to be slightly compressed due to missing steric repulsion between it and the topmost silicon atoms (Figure S4). Steric repulsion is also present between molecules of the first and second organic layers.

Removal of all surrounding molecules in rank 3 causes the single azide molecule (**2**) to stick out less toward the vacuum. This effect is somewhat compensated by the absence of dispersion attraction between substrate and adsorbate. The single molecule therefore stands more upright than in rank 1 (see Figure S5). Lastly, comparison of optimized geometries of rank 3 and 4 leads to the same local minimum and reveals no discernible differences.

4.3 | Model error

Next, we investigate the influence of the ranking approach on barriers and reaction energies as well as on reaction paths. For this purpose, the dataset of the AAC reaction, found in Table 2 and plotted in Figure 7, is discussed in detail.

Afterwards, comparison to the other two reactions, ACE (Figure 8) and IEDDA (Figure 9), are made.

At rank 1, the reaction energy and barrier of the AAC reaction are found to be −297 and 59 kJ/mol respectively. These results are not significantly changed at rank 2 since the precomplex and product as well as the TS are shifted slightly downwards in energy with respect to the isolated reactants. Further analyzing the relative energies without dispersion correction (Table S13) reveals that purely electronic effects are captured with cluster models just as well as with slab models. Thus, cluster calculations can be used in cases where no PBC implementation of a method is available. For rank 3, relative energies of the stationary points are shifted upwards by 30–40 kJ/mol, resulting in a ΔE^0 of −304 kJ/mol. A similar shift upwards in relative energies is also determined for rank 4 which presents the surface-anchored structure. Here, the reaction energy agrees with rank 1. Relaxing all structural constraints imposed by the layer or substrate leads to additional angles of attack becoming available for the reaction at rank 4b. Thus, considering otherwise inaccessible interface structures in the gas phase model results in a less good agreement of rank 4b with the more elaborate models. We will thus not consider this approach further.

In conclusion, reaction energies and barriers are only moderately affected by the rank of the model system. However, this observation only holds true provided structural information is carried over from previous ranks. Otherwise, changes in mechanism are possible in the simplified models as shown in column "rank 4b" of Table 2. From the data at hand, two dominant structural effects can be identified. The

TABLE 2 Energies of stationary points on the AAC reaction path with respect to the isolated reactants as well as reaction energies and barriers

	Rank 1	Rank 2	Rank 3	Rank 4	Rank 4b
Precomplex	−39	−48	−7	−8	−32
TS	20	9	51	55	31
Product	−336	−340	−311	−306	−310
ΔE^0	−297	−292	−304	−297	−278
$\Delta E^{\ddagger}$	59	57	58	63	64

Note: PBE-D3 energies in kJ/mol. Model systems of ranks 1–4 are compared.
Abbreviations: AAC, azide-alkyne cycloaddition; TS, transition state.

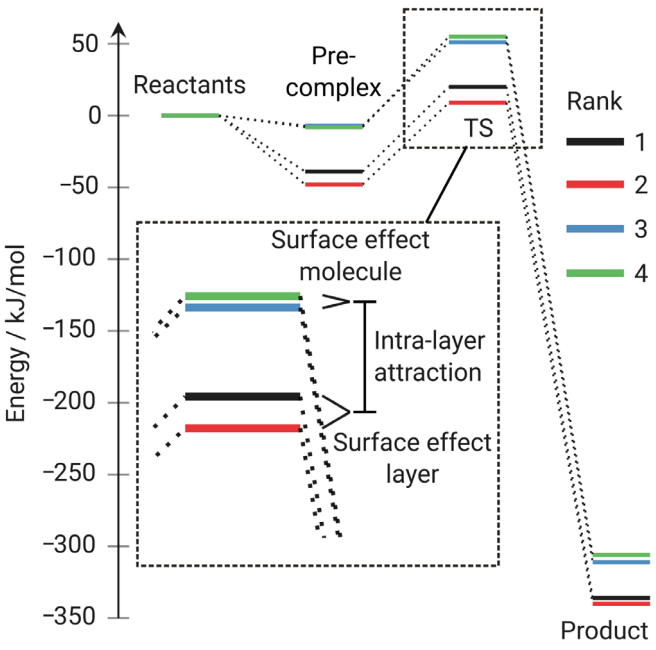

FIGURE 7 Energies (PBE-D3) of stationary points on the azide-alkyne cycloaddition (AAC) reaction path from Table 2. Inset: The model systems show clustering of ranks 1 & 2 and 3 & 4 due to intra-layer attraction. Further splitting of ranks is caused by surface effects on layer and molecule

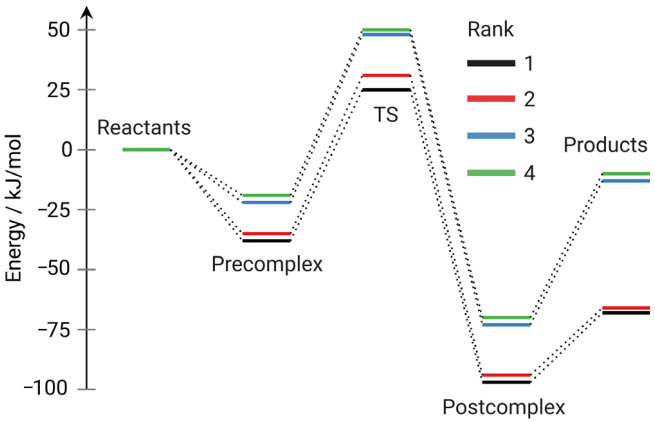

FIGURE 8 Energies of stationary points on the acyl chloride mediated esterification (ACE) reaction path from Table S3 at the PBE-D3 level

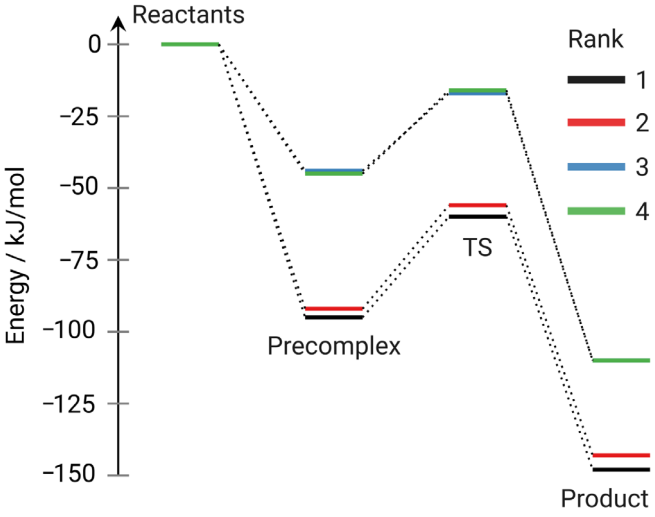

FIGURE 9 Energies of stationary points on the inverse electron demand Diels–Alder (IEDDA) reaction path from Table S4 at the PBE-D3 level

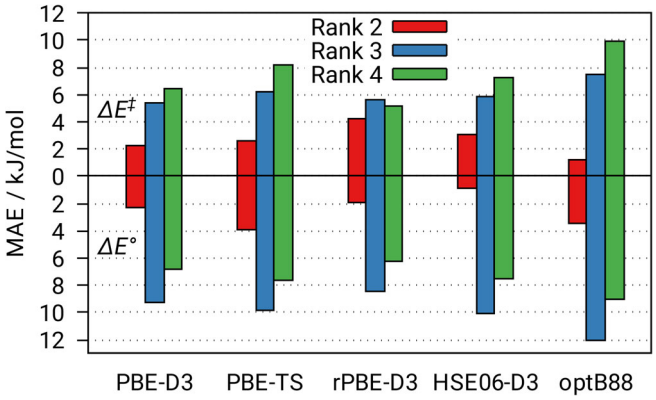

FIGURE 10 Model errors of different density functionals (DFs) with respect to the total system (rank 1). Mean absolute errors (MAE) of the barriers ($\Delta E^{\ddagger}$) are plotted in the upper part while reaction energy errors (ΔE^{0}) are shown in the bottom part

larger one, called intra-layer effect (Figure 7), causes a clustering of values for ranks 1 and 2 as well as 3 and 4. Due to the more crowded environment of the complete first organic layer, rank 1 and 2 structures are stabilized by dispersion interactions with respect to 3 and 4. The smaller surface effect (Figure 7) caused by restricting reaction possibilities through the surface as template is responsible for the remaining difference between ranks 1 and 2 and to a lesser extent between 3 and 4. Its influence can mostly be attributed to the presence of steric repulsion between the silicon surface and the first layer of molecules. This conclusion is supported by analyzing the energy diagrams of the ACE (Figure 8) and the IEDDA (Figure 9) reactions with respect to the clustering of ranks. However, the impact of the different ranks on ΔE^{0} and $\Delta E^{\ddagger}$ is not uniform, as shown in Table S5. While the reaction energy increases for ACE it decreases for IEDDA and stays approximately constant for AAC.

Quantifying the model error introduced as a consequence of increasing computational simplicity is an important guideline for the decision whether an approximation is acceptable. We therefore calculated the reaction energies and barriers of ranks 1–4 for all three reactions with the same five functionals benchmarked in Table 1. The full dataset is found in Tables S2–S9. In Figure 10, the model error of ranks 2–4 for reaction barriers and energies is plotted as the MAE with respect to rank 1.

Independently of functional, models of rank 2 (Figure 10, red bars) perform very well for reaction energies with mean errors relative to rank 1 consistently below 5 kJ/mol. In contrast, reaction energy MAEs for ranks 3 and 4 (Figure 10, blue and green bars) are found to be significantly larger even surpassing 10 kJ/mol for optB88. A similar trend is present for the reaction barriers where rank 2 significantly outperforms 3 and 4 with the exception of rPBE. Taking a closer look at the functionals investigated clearly shows differing responses to the reduction of model complexity. The performance of rPBE is somewhat erratic as the functional has the lowest MAEs for ranks 3 and 4 but the highest for the barrier of rank 2. In light of these findings the usefulness of rPBE for the ranking approach is put into question. In terms of the three investigated dispersion correction schemes, DFT-D3 is slightly superior to the DFT-TS scheme while optB88 shows the largest errors. Surprisingly, the hybrid functional HSE06-D3 does not lead to significant improvements w.r.t. PBE-D3.

However, in rank 2, HSE06 and optB88 show lower MAEs for reaction energies and barriers respectively.

We note that the statistical analysis performed here can only be understood as preliminary since a set of three reactions is subject to strong perturbance by outliers. An example is the low accuracy of rank 3 reaction energies over rank 4, which can be attributed to an outlier in the AAC reaction. Nonetheless we will discuss some implications in the following since the reactions are highly representative for interface chemistry.

4.4 | Interplay of XC and model error

Model errors for reaction energies are smaller than those caused by the choice of the electronic structure method. We thus prioritize identifying a dispersion-corrected functional that well describes the chemistry at hand across different models. When calculating reaction rates which depend exponentially on the barrier model rank 2 should be considered. Interestingly, HSE06-D3 performs best for the reaction energy at rank 2 while having the largest error for the same quantity in the functional benchmark. The same is true for the barrier calculated with optB88. At this point we are unable to determine if these findings are correlated or by chance.

On the other hand, when the property of interest is not exponentially dependent on the error, gas phase models (rank 4) are suitable alternatives to rank 2. Their performance is only slightly worse than that of single molecule adsorbates (rank 3), at drastically reduced computational demand. Here, PBE-D3 convinces with a good overall performance and consistent error statistics across different model ranks. It is necessary though to compute the complete interface at rank 1 before resorting to simplified models.

4.5 | Solvation effects

In the last part of this benchmark study, we use the PCM approach to investigate the influence of increasingly polar solvents on each model rank. The ACE reaction is discussed here since the observed effects are most pronounced for its polar groups.

Relative energies of TS, pre- and postcomplex at rank 1 are listed in Table 3. The cavitation correction is neglected for the comparison of solvents since we aim to decrease the number of parameters by ignoring surface tension ($\tau = 0$).

Inclusion of the solvent correction results in the destabilization of adsorbed structures with respect to the isolated reactants. This effect becomes stronger as solvent polarity increases. The postcomplex is destabilized more than the precomplex which is in turn less destabilized than the TS. However, the effect on reaction energies and barriers with varying polarity from 9.1 to 80.1 is small with energy changes of 3–7 kJ/mol.

Next, the behavior of implicit solvent modeling when applied to different model ranks is investigated (Table 4). For this part of the study the cavitation energy is included since its shape will be different for each rank. The cavitation energy is a destabilizing contribution to the solvation energy. Its effect is most pronounced for isolated reactants and products since the combined cavity volume is largest. Reduction of the volume upon formation of a precomplex has therefore a stabilizing effect on relative energies (Table S10).

The previously noted clustering of results for model ranks 1 and 2, as well as 3 and 4 is also found for the solvation correction. This suggests a rather weak influence of the substrate but strong influence of the organic layer. This behavior is expected since the organic layer reduces the solvent accessible surface by blocking the substrate-facing hemisphere. Thus, adsorbing molecules need to shed a larger part of their solvent sphere before being able to react, resulting in an energetic penalty. This observation is generalizable as shown in Tables S11 and S12.

We note that the accuracy of the PCM model for interfaces cannot be judged with great confidence at this point since experimental data is scarce. Some computational parameters, especially concerning cavity construction might need to be reevaluated in the future.

TABLE 4 Stabilization of the ACE reaction path by implicit solvation (H_2O)

	1	2	3	4
ΔE Precomplex	20	17	11	11
ΔE TS	16	13	−1	−1
ΔE Postcomplex	25	24	13	13
$\Delta E \sum$ Products[a]	10	10	−5	−6
$\Delta\Delta E^0$	5	7	2	2
$\Delta\Delta E^{\ddagger}$	−4	−4	−12	−11

Note: Model system ranks 1–4 are compared. Positive values indicate destabilization w.r.t. the computations without solvent. Energies in kJ/mol including the cavitation energy.
Abbreviations: ACE, acyl chloride mediated esterification; TS, transition state.
[a]Sum of the individual product energies after separation of the postcomplex.

TABLE 3 Stabilization of the ACE reaction path (rank 1) by different solvents

	DCM (9.1)	Acetone (20.7)	CH_3OH (32.7)	H_2O (80.1)
ΔE Precomplex	15	19	21	24
ΔE TS	11	15	17	21
ΔE Postcomplex	20	25	27	31
$\Delta E \sum$ Products[a]	9	11	12	13
$\Delta\Delta E^0$	5	6	6	7
$\Delta\Delta E^{\ddagger}$	−4	−4	−4	−3

Note: The solvation is treated implicitly (ε in brackets). Positive values indicate destabilization w.r.t. the computations without solvent. All values at rank 1. Energies in kJ/mol without the cavitation energy.
Abbreviations: ACE, acyl chloride mediated esterification; TS, transition state.
[a]Sum of the individual product energies after separation of the postcomplex.

5 | APPLYING THE MODEL

After having determined that a rank 2 model, containing just the organic layer, well reproduces the full interface system while significantly reducing computational demand, we now apply it to two typical questions in interface research (Figure 11).

The first question concerns the coverage dependence of reaction energies. With increasing coverage, attraction between adsorbates rises, thus increasing the reaction energy. This effect can also lead to a steering of subsequent molecules to adsorb close to those already present on the surface.[36] At higher coverages, the reaction energy falls again due to steric repulsion experienced in more crowded environments.[63] Knowledge of the reaction energy profile with respect to coverage is important to monitor the deposition progress.

The second question treated concerns unwanted termination reactions of bifunctional molecules which negatively impact growth rates and interface uniformity. Thus, identifying means to prevent terminations is of high interest for organic surface functionalization. In a termination reaction, a single molecule reacts twice with the previous layer, effectively decreasing the number of reactive sites by two.[64,65] After a certain number of deposition cycles no reactive sites remain and growth comes to a halt. This problem is primarily observed for molecules carrying two identical functional groups. However, those molecules are still preferred for LbL synthesis since only two steps per growth cycle are required there. Furthermore, every additional different functional group in a molecule increases the risk of side reactions. Therefore, an approach to increase the selectivity of bifunctional molecules proposed earlier[66] is computationally examined here. The idea is to increase the steric demand of one functional group by attaching bulky carbon moieties in its vicinity (i.e., linkers **11** and **15** in Figure 12). Extending this idea, we present additional functional groups to suppress these termination reactions.

Both of these research questions cannot be fully addressed with gas phase or single adsorbate models as they cannot capture coverage effects. Hence, they lend themselves as showcases for the periodic, organic layer model (rank 2).

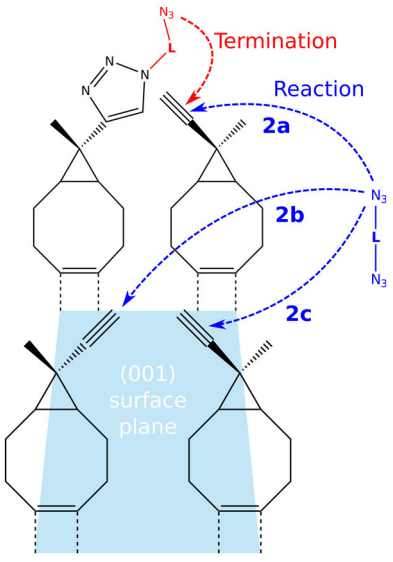

FIGURE 11 Lewis structure representation of the complete first organic layer after azide-alkyne cycloaddition (AAC) reaction with a single molecule attached in the second layer. This molecule can perform a termination reaction. In the 4 × 4 supercell, three possible reaction modes for a second molecule (N_3-L-N_3) exist (2a, 2b, 2c). **L** is a linker group (see Figure 12)

5.1 | Coverage dependent reaction energy

Based on the idealized interface model of one CCO molecule per two surface dimers as introduced above in Figure 5, the smallest unit cell allowing the study of coverage contains four reactive sites in the first organic layer. This cell can accommodate four possible coverages: Θ = 0.25, 0.5, 0.75, 1 ML. Representative structures were generated from SA molecular dynamics simulations as described in Section 3. The results are given in Table 5.

The reaction energy of the first molecule (0.25 ML, 340 kJ/mol) has been reported in column "rank 2" of Table 2. For a coverage of 0.5 ML, the average reaction energy per molecule falls off considerably (−313 to −319 kJ/mol) before rising again for values of 0.75 and 1 ML. When increasing the coverage from 0.25 to 0.5 ML three modes are possible (**2a**–**2c**, Figure 11). A molecule reacting at the neighboring position across the Si-dimer trench (**2a**) has a reaction

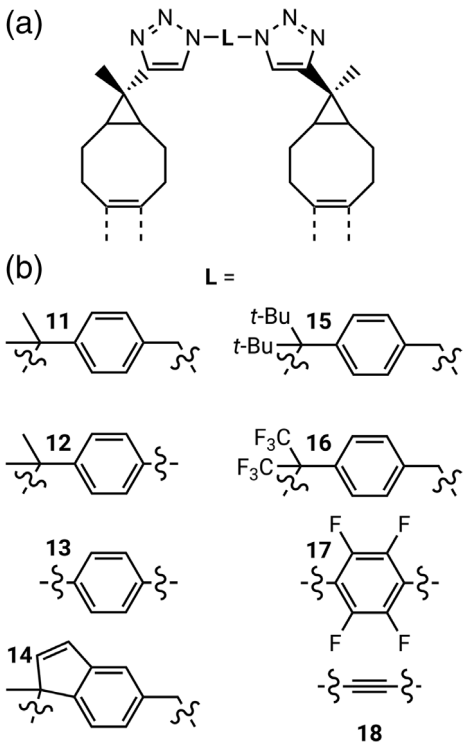

FIGURE 12 (A) Termination of two alkyne reactive sites by a bisazide molecule in the azide-alkyne cycloaddition (AAC) scheme. (B) Linker groups **L** altering the reactivity of the bisazide through steric demand, strain and electron withdrawing groups

energy of −286 kJ/mol. Within a dimer-row (**2b**) the reaction is slightly more favorable at −295 kJ/mol.

Notably, the dispersion contribution for case **2a** (−63 kJ/mol) is almost the same as for the first molecule (−64 kJ/mol), while it is less for the intra-row case **2b** (−26 kJ/mol). This is due to space constraints disfavoring relaxation into a flattened structure of two neighboring molecules within a row (see Figure S6). In the case of two molecules being attached along the diagonal (**2c**), a similar behavior to **2a** is found with a relatively high dispersion contribution to the reaction energy.

For the third incoming molecule (0.75 ML), only one unique configuration exists. Its reaction energy rises again to −334 kJ/mol (relative to **2c**) with dispersion attraction contributing strongly (30%).

The fourth molecule (1 ML) has the highest reaction energy (−348 kJ/mol). Here, the dispersion contribution amounts to 20%.

In summary, reactions with directly neighboring sites are electronically less favorable while dispersion attraction stabilizes higher coverages. Due to the small number of reactive sites per area in the second layer, additional molecules always react exothermically until full coverage is reached. In order to validate the performance of the rank 2 model, the value for the reaction of the fourth molecule is recalculated at rank 1. Here the reaction energy is on average −342 instead of −330 kJ/mol. Two thirds of this increase can be attributed to additional dispersion attraction of the substrate. An absolute error of 12 kJ/mol is acceptable for applications where correct trends are the primary concern.

5.2 | Prevention of terminating reactions

In the following we assess the success of different modifications to a molecular building block for reducing the thermodynamic driving force of a termination reaction shown in Figure 11. As a test case the AAC reaction is used where the two functional groups of the azide precursor are differentiated. In Figure 12A two neighboring CCO derived molecules are terminated by a bisazide molecule. Through variation of the linker group **L** the thermodynamic termination energy is calculated with respect to reaction at a single site ($\Delta E_{term} = \Delta E_{reac}(2) - \Delta E_{reac}(1)$) and listed in Table 6. We focus here on links across the trench, however, the same approach could also be applied to termination reactions within a row.

The modifications made to the bisazide are rationalized by one or more of the following design principles. Molecule **11** is structurally similar to reactant **2** of the AAC reaction but contains two azide moieties, one of which is sterically encumbered by methyl groups. In order to further reduce the termination energy, steric demand is increased by replacing both methyl groups with *tert*-butyl groups in linker **15**. An alternative to steric demand is strain engineering, with successively shorter linkers (**11** > **12** > **13** > **18**) or more rigid backbones (**14**). Lastly, the option of chemically tuning the linker through adding electron withdrawing groups on the dienophile is explored. This last approach might be combined with the other ideas by exchanging —CH_3 with —CF_3 groups (**16**) or fluorine substitutions at the benzene ring (**17**).

5.2.1 | Steric effect

The reaction energy of **11** with only the less sterically hindered azide group (−346 kJ/mol) is similar to that of **2** (−340 kJ/mol). Termination of a neighboring reactive site is energetically less favorable by 72 kJ/mol, however a thermodynamic driving force of −274 kJ/mol remains, indicating the insufficiency of two methyl groups to increase selectivity. Comparing this value at rank 2 to rank 1 (−280 kJ/mol) shows a small deviation of −6 kJ/mol.

The thermodynamic driving force is decreased by just 18 kJ/mol when using linker **15**. This suggests that steric demand can only slightly inhibit termination and other avenues should be pursued instead.

TABLE 5 Influence of pre-coverage on energies of AAC reaction of **1** and **2** leading to **3** (Figure 2)

Θ/ML	$\Delta E_{reac}(\Theta)$	$\Delta\Delta E_{reac}(\Theta)$	$\Delta\Delta E_{reac}$(disp)
0.25	−340	−340	−63
0.5[a]	−626 (−313)	−286	−64
0.5[b]	−635 (−317)	−295	−26
0.5[c]	−638 (−319)	−298	−55
0.75	−972 (−324)	−334	−101
1	−1320 (−330)	−348	−70

Note: PBE-D3 energies in kJ/mol for rank 2 models.
Abbreviations: AAC, azide-alkyne cycloaddition; Θ/ML, coverage (4 × 4 cell); $\Delta E_{reac}(\Theta)$, sum of reaction energies as a function of Θ, average energies per molecule in brackets; $\Delta\Delta E_{reac}(\Theta)$, reaction energy of the last attached molecule; $\Delta\Delta E_{reac}$(disp), dispersion contribution to the energies in column "$\Delta\Delta E_{ads}(\Theta)$."
[a]Configuration **2a** (Figure 11).
[b]Configuration **2b** (Figure 11).
[c]Configuration **2c** (Figure 11).

TABLE 6 Differences in growth termination reaction energies caused by the chemical modification of linker groups **L** in bisazide molecules

Linker (L)	ΔE_{term} (kJ/mol)	$\Delta\Delta E_{term}$ (kJ/mol)
11	−274	0
12	−263	10
13	−171	102
14	−275	−1
15	−256	18
16	−258	16
17	−167	107
18	−177	97

Note: Relative reaction energies $\Delta\Delta E_{term}$ are calculated with respect to linker **11**.

5.2.2 | Strain effect

Removal of a single -CH_2- unit leading to **12** has only a small effect of 10 kJ/mol while removal of two (**13**) results in a large destabilization of 102 kJ/mol. Replacing the phenyl ring with an alkyne **18** has a similar influence on the termination energy (97 kJ/mol). However, such a molecule is only a hypothetical option due to cross reactivity between the azide and alkyne moieties within the same molecule. Therefore, we conclude that the length of **L** is a successful indicator for the thermodynamic stability of termination products.

Simply increasing the rigidity by introducing a second ring (e.g., **14**) appears to not decrease reactivity, however higher growth rates per cycle can be expected.[64]

5.2.3 | Electronic effect

This effect is quantifiable but rather small with 6 kJ/mol for CF_3 groups in **16** and 5 kJ/mol decreased reactivity for **17**.

In summary, strain is the most promising approach for the prevention of termination reactions using thermodynamic control. This assessment can be expanded to low temperature kinetic control by invoking the Bell–Evans–Polany principle stating a linear correlation between reaction energy and barrier. The optimal length of linker groups is system-dependent due to templating effects of the underlying substrate. In the case of Si(001), inter- and intra-row dimers distances must therefore be taken into consideration. This is possible within the efficient rank 2 interface model.

6 | CONCLUSIONS

We investigated the modeling of organic layers on semiconductor surfaces with a hierarchy of structural models at the DFT level. The assumption that chemical reactions involving only localized bonds can be accurately described by a limited model that mimics structural constraints imposed by the substrate could be supported by a small benchmark set of three different reactions. It was furthermore shown that intra-layer interactions such as dispersion attraction and steric repulsion are crucial to obtain accurate barriers and reaction energies. For the latter case the least parametrized GGA functional PBE performs the most consistently while a hybrid functional description improves on barrier heights. We note however that due to the small size of our test set, statistical evaluation should be taken with caution. Additional calculations should be performed in the future to supplement existing data.

We have also expanded the theoretical description of attachment processes on organic layers to the wet-chemical domain. Here, implicit models like PCM offer an efficient means of including electrostatic solvent interactions. Again, models abandoning the substrate in favor of computational simplicity perform well since the shape of the solvent shell is mostly determined by the geometry of the previous organic layer.

TABLE 7 Recommendations for model systems addressing common research questions in the study of organic–inorganic interfaces

Model	Description	Research questions
Rank 1	Full system	Benchmarks, template effects, interface properties
Rank 2	Organic layer	Energies and barriers, layer effects, bonding analysis
Rank 3	Substrate + 1 molecule	Adsorption energies, adsorption modes
Rank 4	Gas phase	High level methods, quick screening

Application of the model was then showcased with two typical questions of interest for interface research. Both the variation of reaction energy in the second layer with coverage and the thermodynamics of termination reactions require a periodic model of the previous layer. For the latter question, a correlation between the length of the linker molecule and strain induced decrease of reaction energy was found. Steric demand and electronic effects seem to be inferior means of inhibiting termination.

Lastly, we offer recommendations for preferred use cases of the four introduced model ranks (summarized in Table 7). The full system of rank 1 originally shown in Figure 1 is best employed to generate reference data to benchmark the other models. Furthermore, it is used to determine template effects such as lattice spacings and coverages. Finally, one may be forced to include the substrate when actual interface properties are of interest. A rank 2 model should be considered as the main method to study the chemistry within the organic layers. The rank 3 model is a common choice to investigate adsorption energies and reactivity on the substrate. Finally, the gas phase model (rank 4) can be used for benchmarking against more accurate approaches or quickly screening molecular building blocks before employing rank 2.

It remains open for investigation how fast template effects decay with the number of layers. Disorder increases in the second layer as molecules become free to explore the configurational space. It is therefore highly likely that structural properties of a layered organic system change quickly from an ordered interface to an (amorphous) bulk. In that case computational tools developed for polymer research[67] including (semi-)classical force fields and potential of mean force approaches can be applied. This opens up an opportunity to implement a multi-scale approach where the inorganic semiconductor and the interface is treated with high level methods while very efficient semi-empirical methods are applied to the organic bulk. Hence, the computation of macroscopic properties such as the elastic modulus and thermal stability may become feasible.

ACKNOWLEDGMENTS

We thank Prof Ulrich Koert and Jannick Meinecke for the suggestion of model reactions and Fabian Pieck for sharing preliminary computational results on the adsorption behavior of CCO on Si(001). Financial support was given by the German Research Foundation (DFG) via SFB

1083. Computational resources provided by HRZ Marburg, RZ Regensburg, GOETHE-CSC Frankfurt and HLR Stuttgart are gratefully acknowledged. Open access funding enabled and organized by Projekt DEAL. WOA Institution: UNIVERSITAET LEIPZIG Blended DEAL: Projekt DEAL.

Open access funding enabled and organized by Projekt DEAL.

ORCID

Jan-Niclas Luy https://orcid.org/0000-0002-0552-5223
Lisa Pecher https://orcid.org/0000-0001-7130-0287
Ralf Tonner https://orcid.org/0000-0002-6759-8559

REFERENCES

[1] R. A. Wolkow, *Annu. Rev. Phys. Chem.* **1999**, *50*, 413.
[2] J. T. Yates, *Science* **1998**, *279*, 335.
[3] S. V. Aradhya, L. Venkataraman, *Nat. Nanotechnol.* **2013**, *8*, 399.
[4] G. Hills, C. Lau, A. Wright, S. Fuller, M. D. Bishop, T. Srimani, P. Kanhaiya, R. Ho, A. Amer, Y. Stein, D. Murphy, Arvind, A. Chandrakasan, M. M. Shulaker, *Nature* **2019**, *572*, 595.
[5] L. Miozzo, A. Yassar, G. Horowitz, *J. Mater. Chem.* **2010**, *20*, 2513.
[6] H. Zhou, S. F. Bent, *J. Vac. Sci. Technol.* **2013**, *31*, 040801.
[7] A. V. Teplyakov, S. F. Bent, *J. Vac. Sci. Technol.* **2013**, *31*, 050810.
[8] S. M. George, B. Yoon, A. A. Dameron, *Acc. Chem. Res.* **2009**, *42*, 498.
[9] J. T. Yates, *J. Phys. Condens. Matter* **1991**, *3*, S143.
[10] P. Sundberg, M. Karppinen, *Beilstein J. Nanotechnol.* **2014**, *5*, 1104.
[11] X. Meng, *J. Mater. Chem. A* **2017**, *5*, 18326.
[12] H. Zhou, S. F. Bent, *Appl. Mater. Interfaces* **2011**, *3*, 505.
[13] P. K. B. Palomaki, P. H. Dinolfo, *Langmuir* **2010**, *26*, 9677.
[14] C. Länger, J. Heep, P. Nikodemiak, T. Bohamud, P. Kirsten, U. Höfer, U. Koert, M. Dürr, *J. Phys. Condens. Matter* **2018**, *31*, 034001.
[15] J. Meinecke, U. Koert, *Org. Lett.* **2019**, *21*, 7609.
[16] R. Biswas, D. R. Hamann, *Phys. Rev. B* **1986**, *34*, 895.
[17] M. Gaus, Q. Cui, M. Elstner, *J. Chem. Theory Comput.* **2011**, *7*, 931.
[18] A. Klamt, C. Moya, J. Palomar, *J. Chem. Theory Comput.* **2015**, *11*, 4220.
[19] J. Heep, J.-N. Luy, C. Länger, J. Meinecke, U. Koert, R. Tonner, M. Dürr, *J. Phys. Chem. C* **2020**, *124*, 9940.
[20] T. Glaser, J. Meinecke, C. Länger, J.-N. Luy, R. Tonner, U. Koert, M. Dürr, unpublished.
[21] T. Glaser, J. Meinecke, L. Freund, C. Länger, J.-N. Luy, R. Tonner, U. Koert, M. Dürr, unpublished.
[22] H. C. Kolb, M. G. Finn, K. B. Sharpless, *Angew. Chem., Int. Ed.* **2001**, *40*, 2004.
[23] J. S. Oakdale, L. Kwisnek, V. V. Fokin, *Macromolecules* **2016**, *49*, 4473.
[24] H. Fan, Y. Ji, Q. Xu, F. Zhou, B. Wu, L. Wang, Y. Li, J. Lu, *ChemPlusChem* **2018**, *83*, 407.
[25] W. H. Binder, C. Kluger, *Curr. Org. Chem.* **2006**, *10*, 1791.
[26] V. V. Rostovtsev, L. G. Green, V. V. Fokin, K. B. Sharpless, *Angew. Chem., Int. Ed.* **2002**, *41*, 2596.
[27] N. Münster, P. Nikodemiak, U. Koert, *Org. Lett.* **2016**, *18*, 4296.
[28] F. Ruff, Ö. Farkas, *J. Phys. Org. Chem.* **2011**, *24*, 480.
[29] L. R. Domingo, M. T. Picher, J. A. Sáez, *J. Org. Chem.* **2009**, *74*, 2726.
[30] N. J. Agard, J. A. Prescher, C. R. Bertozzi, *J. Am. Chem. Soc.* **2004**, *126*, 15046.
[31] J. Yoshinobu, *Prog. Surf. Sci.* **2004**, *77*, 37.
[32] L. Pecher, S. Schmidt, R. Tonner, *J. Phys. Chem. C* **2017**, *121*, 26840.
[33] M. Reutzel, N. Münster, M. A. Lipponer, C. Länger, U. Höfer, U. Koert, M. Dürr, *J. Phys. Chem. C* **2016**, *120*, 26284.
[34] L. Pecher, R. Tonner, *Theor. Chem. Acc.* **2018**, *137*, 48.
[35] L. Pecher, C. Schober, R. Tonner, *Chem. – Eur. J.* **2017**, *23*, 5459.
[36] L. Pecher, S. Schmidt, R. Tonner, *Beilstein J. Org. Chem.* **2018**, *14*, 2715.
[37] M. D. Wodrich, C. Corminboeuf, P. R. Schreiner, A. A. Fokin, P. von Rague Schleyer, *Org. Lett* **2007**, *9*, 1851.
[38] G. Kresse, J. Hafner, *Phys. Rev. B* **1993**, *47*, 558.
[39] G. Kresse, J. Furthmüller, *Comput. Mater. Sci.* **1996**, *6*, 15.
[40] G. Kresse, J. Furthmüller, *Phys. Rev. B* **1996**, *54*, 11169.
[41] G. Henkelman, H. Jónsson, *J. Chem. Phys* **1999**, *111*, 7010.
[42] G. Henkelman, B. P. Uberuaga, H. Jónsson, *J. Chem. Phys* **2000**, *113*, 9901.
[43] J. P. Perdew, K. Burke, M. Ernzerhof, *Phys. Rev. Lett.* **1996**, *77*, 3865.
[44] N. Marom, A. Tkatchenko, M. Rossi, V. V. Gobre, O. Hod, M. Scheffler, L. Kronik, *J. Chem. Theory Comput.* **2011**, *7*, 3944.
[45] D. Nazarian, P. Ganesh, D. S. Sholl, *J. Mater. Chem. A* **2015**, *3*, 22432.
[46] S. Grimme, J. Antony, S. Ehrlich, H. Krieg, *J. Chem. Phys.* **2010**, *132*, 154104.
[47] S. Grimme, S. Ehrlich, L. Goerigk, *J. Comput. Chem.* **2011**, *32*, 1456.
[48] B. Hammer, L. B. Hansen, J. K. Nørskov, *Phys. Rev. B* **1999**, *59*, 7413.
[49] A. V. Krukau, O. A. Vydrov, A. F. Izmaylov, G. E. Scuseria, *J. Chem. Phys.* **2006**, *125*, 224106.
[50] A. Tkatchenko, M. Scheffler, *Phys. Rev. Lett.* **2009**, *102*, 073005.
[51] J. Klimeš, D. R. Bowler, A. Michaelides, *J. Phys. Condens. Matter.* **2009**, *22*, 022201.
[52] G. Kresse, D. Joubert, *Phys. Rev. B* **1999**, *59*, 1758.
[53] D. R. J. Boyd, *J. Chem. Phys* **1955**, *23*, 922.
[54] K. Mathew, R. Sundararaman, K. Letchworth-Weaver, T. A. Arias, R. G. Hennig, *J. Chem. Phys.* **2014**, *140*, 084106.
[55] D. Gunceler, K. Letchworth-Weaver, R. Sundararaman, K. A. Schwarz, T. A. Arias, *Model. Simul. Mat. Sci. Eng.* **2013**, *21*, 074005.
[56] J. Neugebauer, M. Scheffler, *Phys. Rev. B* **1992**, *46*, 16067.
[57] J. Hutter, M. Iannuzzi, F. Schiffmann, J. VandeVondele, *Wiley Interdiscip. Rev. Comput. Mol. Sci.* **2014**, *4*, 15.
[58] M. Elstner, D. Porezag, G. Jungnickel, J. Elsner, M. Haugk, T. Frauenheim, S. Suhai, G. Seifert, *Phys. Rev. B* **1998**, *58*, 7260.
[59] TURBOMOLE V7.2 2017, a development of University of Karlsruhe and Forschungszentrum Karlsruhe GmbH, 1989-2007, TURBOMOLE GmbH, since 2007, http://www.turbomole.com, (accessed 16 February 2021).
[60] F. Weigend, R. Ahlrichs, *Phys. Chem. Chem. Phys.* **2005**, *7*, 3297.
[61] G. Schmitz, C. Hättig, D. P. Tew, *Phys. Chem. Chem. Phys.* **2014**, *16*, 22167.
[62] J. Heyd, G. E. Scuseria, M. Ernzerhof, *J. Chem. Phys* **2003**, *118*, 8207.
[63] S. R. Kachel, B. P. Klein, J. M. Morbec, M. Schöniger, M. Hutter, M. Schmid, P. Kratzer, B. Meyer, R. Tonner, J. M. Gottfried, *J. Phys. Chem. C* **2020**, *124*, 8257.
[64] D. S. Bergsman, R. G. Closser, C. J. Tassone, B. M. Clemens, D. Nordlund, S. F. Bent, *Chem. Mater.* **2017**, *29*, 1192.
[65] D. S. Bergsman, R. G. Closser, S. F. Bent, *Chem. Mater.* **2018**, *30*, 5087.
[66] P. L. Golas, N. V. Tsarevsky, K. Matyjaszewski, *Macromol. Rapid Commun.* **2008**, *29*, 1167.
[67] L. J. Abbott, K. E. Hart, C. M. Colina, *Theor. Chem. Acc.* **2013**, *132*, 1334.

SUPPORTING INFORMATION

Additional supporting information may be found online in the Supporting Information section at the end of this article.

How to cite this article: Luy J-N, Molla M, Pecher L, Tonner R. Efficient hierarchical models for reactivity of organic layers on semiconductor surfaces. *J Comput Chem*. 2021;42:827–839. https://doi.org/10.1002/jcc.26503

Supporting Information for

Hierarchical computational models for organic interface formation on semiconductors

Jan-Niclas Luy[1], Mahlet Molla[1], Lisa Pecher[1], and Ralf Tonner[1]

[1]Fachbereich Chemie und Wissenschaftliches Zentrum für Materialwissenschaften, Hans-Meerwein-Straße, 35032 Marburg, Germany
Current address: Wilhelm-Ostwald-Institut für Physikalische und Theoretische Chemie, Universität Leipzig, D-04103 Leipzig, Germany
E-Mail: ralf.tonner@chemie.uni-leipzig.de

Table of contents

1. Ring strain of cyclooctyne

A novel method for calculating ring strain energies (SE) using periodic boundary conditions is proposed here and applied to the cyclooctyne molecule. In this method, an arbitrary bond of the cyclic molecule is cut and the ring unfolded into a linear chain. This chain is subsequently placed into periodic boundary conditions. This procedure ensures that the same number of atoms is present within the unit cell as in the original molecule. Optimization of the unit cell makes it possible to directly compare absolute energies of the chain and ring conformers. The method is straightforward and avoids errors introduced by calculating chemical potentials or balancing reaction equations as present in other approaches. For the twist conformer we calculate a SE of 80 kJ/mol and for the less stable chair conformer 92 kJ/mol which agrees with the 83 kJ/mol derived from -CH_2- equivalents (G3 method) [1].

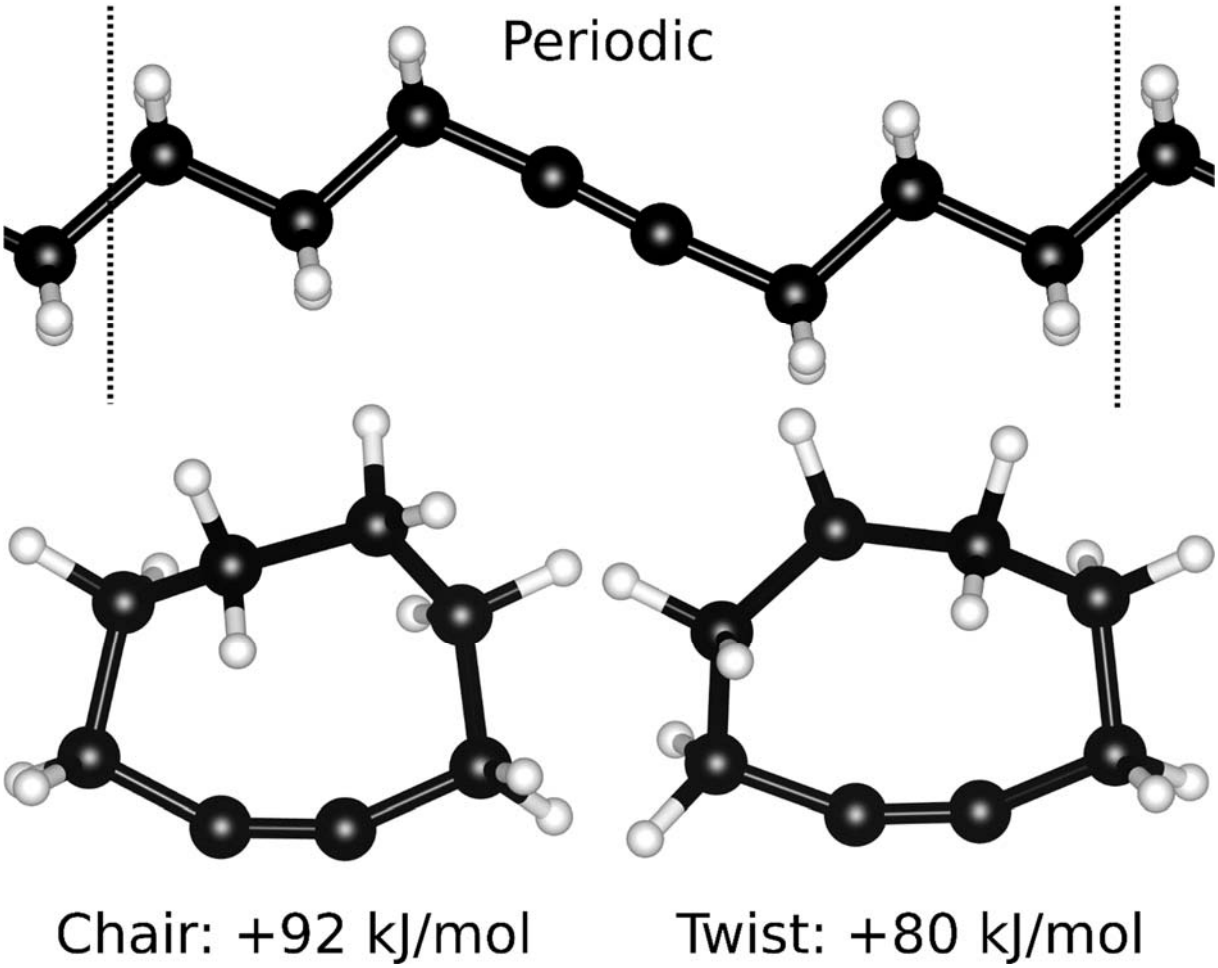

Figure S1. Top: The unfolded cyclooctyne ring placed in periodic boundary conditions. Bottom: Chair (left) and twist (right) conformers of cyclooctyne. The twist and chair conformers are optimized in the same periodic unit cell as the chain in order to ensure comparability of absolute energies.

2. First layer configurations

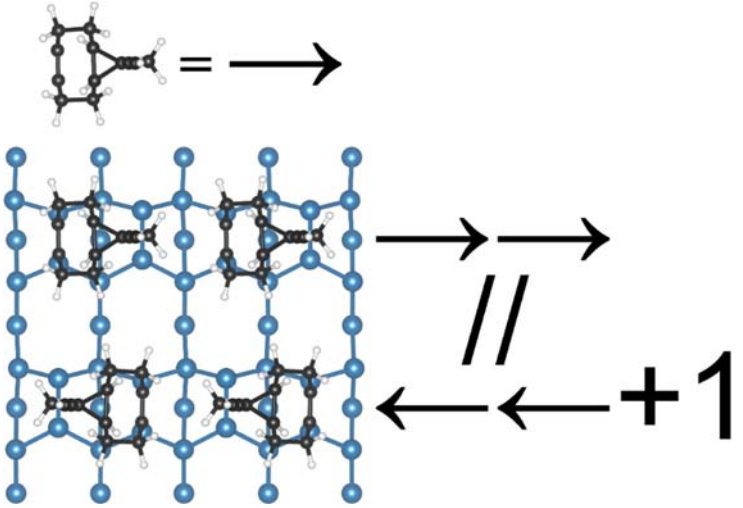

Figure S2. On the left side a 4×4 supercell with four adsorbed CCO molecules (R = -C≡CH, R’ = -CH3) is shown. In the schematic depiction of the supercell on the right, a molecule is abstracted by an arrow whose head points in the direction of the propyl ring’s apex atom. The trench between dimer rows is represented by two forward slashes. An offset of the lower row by one primitive unit vector in the x-direction (equal to the distance between two dimers) is indicated by an integer, here “+1”. Thus, the configuration of adsorbates can also be written horizontally in one line as shown in Figure S3.

→→//→→ = ←←//←← →→//→→+1 = ←←//←←+1

→→//←← = ←←//→→ →→//←←+1 = ←←//→→+1

←→//←→ = →←//→← ←→//←→+1 = →←//→←+1 =
←→//→←+1 = →←//←→+1 =

←→//→← = →←//←→ (←→//→←-1 = →←//←→-1)

→→//→← = →→//←→ = →→//→←+1 = →→//←→+1 =
←←//→← = ←←//←→ = ←←//→←+1 = ←←//←→+1 =
←→//←← = ←→//→→ = ←→//←←+1 = ←→//→→+1 =
→←//←← = →←//→→ →←//←←+1 = →←//→→+1

Figure S3. There are nine unique ways in which four arrows can be arranged on a 2×4 grid assuming periodic boundary conditions. The reduction from 32 configurations is achieved by exploiting translational- and mirror symmetries of the unit cell.

Table S1. List of the nine unique configurations of four cyclopropyl-cyclooctyne molecules in a *c*(4×2) supercell with energies calculated relative to the most stable one (R = -C≡CH and R’ = -CH_3). For nomenclature see Figure S3.

Configuration	ΔE / kJ/mol
→→//←←+1	0
←→//→←	+1
→→//→→+1	+2
→→//→←	+3
→→//→←+1	+5
←→//←→	+6
→→//→→	+6
←→//←→+1	+7
→→//←←	+7

3. Relative energies of the AAC reaction

Table S2. Energies of stationary points on the AAC reaction path with respect to the isolated reactants. Model systems of ranks 1-4 are compared.

		1	2	3	4[a]
HSE06-D3	Precomplex	-34	-48	-8	-8
	TS	45	27	71	74
	Product	-368	-380	-348	-342
PBE-TS	Precomplex	-51	-63	-7	-8
	TS	9	-2	56	61
	Product	-345	-349	-307	-301
rPBE-D3	Precomplex	-38	-43	-6	-8
	TS	21	11	49	52
	Product	-332	-334	-307	-303
optB88	Precomplex	-46	-62	-5	-8
	TS	7	-8	49	53
	Product	-332	-340	-299	-294
	Energies in kJ/mol. [a] Surface-accessible structure.				

4. Relative energies of the ACE reaction

Table S3. Energies of stationary points on the ACE reaction path with respect to the isolated reactants. Model systems of ranks 1-4 are compared.

		1	2	3	4[a]
PBE-D3	Precomplex	-38	-35	-22	-19
	TS	25	31	48	50
	Postcomplex	-97	-94	-73	-70
	∑ Products	-68	-66	-13	-10
HSE06-D3	Precomplex	-34	-29	-20	-16
	TS	49	57	71	73
	Postcomplex	-102	-97	-78	-75
	∑ Products	-76	-70	-21	-16
PBE-TS	Precomplex	-42	-39	-24	-20
	TS	24	31	50	53
	Postcomplex	-106	-103	-78	-74
	∑ Products	-76	-74	-18	-13
rPBE-D3	Precomplex	-40	-36	-23	-20
	TS	25	35	51	54
	Postcomplex	-87	-82	-61	-58
	∑ Products	-58	-54	-5	-1
optB88	Precomplex	-45	-45	-26	-24
	TS	14	18	40	42
	Postcomplex	-109	-108	-80	-78
	∑ Products	-77	-77	-18	-15
	Energies in kJ/mol. [a] Surface-accessible structure.				

5. Relative energies of the IEDDA reaction

Table S4. Energies of stationary points on the IEDDA reaction path with respect to the isolated reactants. Model systems of ranks 1-4 are compared.

		1	2	3	4[a]
PBE-D3	Precomplex	-95	-92	-44	-45
	TS	-60	-56	-17	-16
	Product	-148	-143	-110	-110
HSE06-D3	Precomplex	-84	-81	-31	-31
	TS	-33	-33	10	8
	Product	-151	-149	-112	-111
PBE-TS	Precomplex	-112	-109	-52	-51
	TS	-68	-62	-16	-17
	Product	-159	-153	-112	-110
rPBE-D3	Precomplex	-91	-88	-44	-44
	TS	-68	-63	-26	-27
	Product	-156	-152	-120	-119
optB88	Precomplex	-130	-126	-57	-57
	TS	-90	-86	-31	-32
	Product	-176	-169	-120	-120
	Energies in kJ/mol. [a] Surface-accessible structure.				

6. Model error benchmark

Table S5. Reaction energies and barriers (PBE-D3) with their mean absolute errors with respect to rank 1 for the AAC, ACE and IEDDA reactions. Model systems of ranks 1-4 are compared.

	1	2	3	4[a]
ΔE^{o}(AAC)	-297	-292	-304	-297
ΔE^{o}(ACE)	-53	-51	-66	-65
ΔE^{o}(IEDDA)	-59	-59	-51	-51
MAE(^{o})	/	2.3	9.2	6.8
$\Delta E^{\ddagger}$(AAC)	59	57	58	63
$\Delta E^{\ddagger}$(ACE)	35	36	27	26
$\Delta E^{\ddagger}$(IEDDA)	63	66	70	69
MAE(‡)	/	2.3	5.4	6.5
Energies in kJ/mol. [a] Surface-accessible structure.				

Table S6. Reaction energies and barriers (HSE06-D3) with their mean absolute errors with respect to rank 1 for the AAC, ACE and IEDDA reactions. Model systems of ranks 1-4 are compared.

	1	2	3	4[a]
ΔE^{o}(AAC)	-334	-332	-340	-334
ΔE^{o}(ACE)	-67	-67	-81	-80
ΔE^{o}(IEDDA)	-68	-68	-59	-59
MAE(^{o})	/	0.9	10.1	7.6
$\Delta E^{\ddagger}$(AAC)	79	75	78	83
$\Delta E^{\ddagger}$(ACE)	51	49	41	39
$\Delta E^{\ddagger}$(IEDDA)	83	86	91	90
MAE(‡)	/	3.0	5.9	7.3
Energies in kJ/mol. [a] Surface-accessible structure.				

Table S7. Reaction energies and barriers (PBE-TS) with their mean absolute errors with respect to rank 1 for the AAC, ACE and IEDDA reactions. Model systems of ranks 1-4 are compared.				
	1	2	3	4[a]
ΔE^{o}(AAC)	-294	-285	-300	-293
ΔE^{o}(ACE)	-47	-44	-60	-59
ΔE^{o}(IEDDA)	-64	-64	-54	-54
MAE(^{o})	/	4.0	9.8	7.7
$\Delta E^{\ddagger}$(AAC)	60	61	63	69
$\Delta E^{\ddagger}$(ACE)	44	47	35	34
$\Delta E^{\ddagger}$(IEDDA)	66	70	74	73
MAE(‡)	/	2.6	6.3	8.2
Energies in kJ/mol. [a] Surface-accessible structure.				

Table S8. Reaction energies and barriers (rPBE-D3) with their mean absolute errors with respect to rank 1 for the AAC, ACE and IEDDA reactions. Model systems of ranks 1-4 are compared.				
	1	2	3	4[a]
ΔE^{o}(AAC)	-294	-291	-301	-295
ΔE^{o}(ACE)	-65	-64	-76	-75
ΔE^{o}(IEDDA)	-47	-46	-38	-39
MAE(^{o})	/	2.0	8.4	6.3
$\Delta E^{\ddagger}$(AAC)	59	54	55	60
$\Delta E^{\ddagger}$(ACE)	23	25	18	17
$\Delta E^{\ddagger}$(IEDDA)	66	71	74	73
MAE(‡)	/	4.3	5.7	5.2
Energies in kJ/mol. [a] Surface-accessible structure.				

Table S9. Reaction energies and barriers (optB88) with their mean absolute errors with respect to rank 1 for the AAC, ACE and IEDDA reactions. Model systems of ranks 1-4 are compared.				
	1	2	3	4[a]
ΔE^{o}(AAC)	-286	-278	-294	-286
ΔE^{o}(ACE)	-46	-43	-64	-63
ΔE^{o}(IEDDA)	-63	-63	-54	-54
MAE(^{o})	/	3.5	12.1	9.1
$\Delta E^{\ddagger}$(AAC)	53	54	54	61
$\Delta E^{\ddagger}$(ACE)	40	40	26	25
$\Delta E^{\ddagger}$(IEDDA)	59	62	66	66
MAE(‡)	/	1.3	7.5	9.9
Energies in kJ/mol. [a] Surface-accessible structure.				

7. Solvation effects

Table S10. Relative cavitation energies of the ACE reaction path for model system ranks 1-4. The surface tension parameter for H_2O is used.				
	1	2	3	4
Precomplex	-4	-4	-2	-2
TS	-5	-5	-3	-3
Postcomplex	-6	-6	-3	-3
∑ Products	-3	-3	0	0
Energies in kJ/mol.				

Table S11. Stabilization of the IEDDA reaction path by implicit CH_2Cl_2 (ε=8.93). Model system ranks 1-4 are compared. Positive values indicate destabilization.				
	1	2	3	4
Precomplex	24	23	6	7
TS	14	14	-3	-1
Product	19	18	4	5
ΔE^{o}	-5	-5	-1	-1
$\Delta E^{\ddagger}$	-10	-9	-8	-8
Energies in kJ/mol without the cavitation energy E_{cav}.				

Table S12. Stabilization of the AAC reaction path by implicit acetonitrile (ε=36.64). Model system ranks 1-4 are compared. Positive values indicate destabilization.				
	1	2	3	4
Precomplex	13	19	4	4
TS	23	26	11	10
Product	10	10	2	2
ΔE^o	-2	-9	-1	-3
$\Delta E^{\ddagger}$	11	7	7	7
Eenergies in kJ/mol without the cavitation energy E_{cav}.				

8. Structural changes for different model ranks

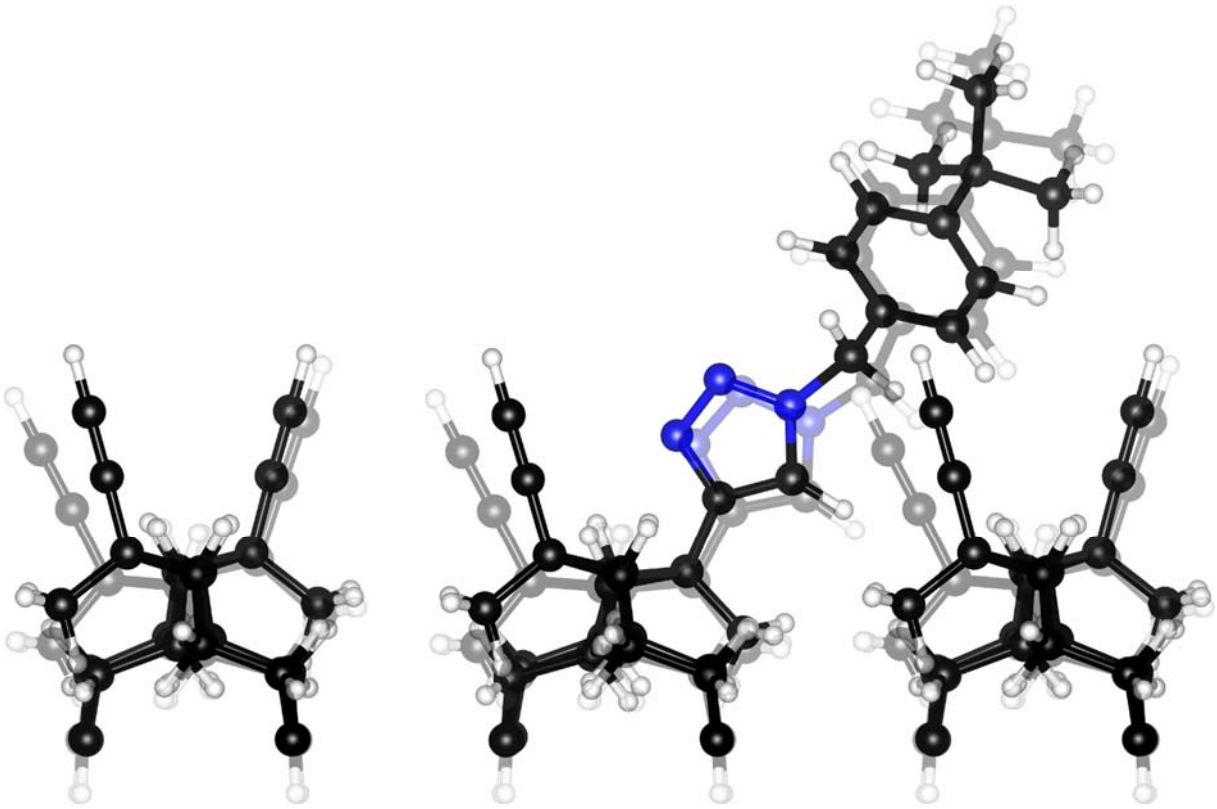

Figure S4. Comparison of the rank 1 (full colors) and rank 2 (faded colors) AAC product structures. Due to the missing steric repulsion between the surface and the first organic layer, the rank 2 structure is more flexible and converges to a different minimum.

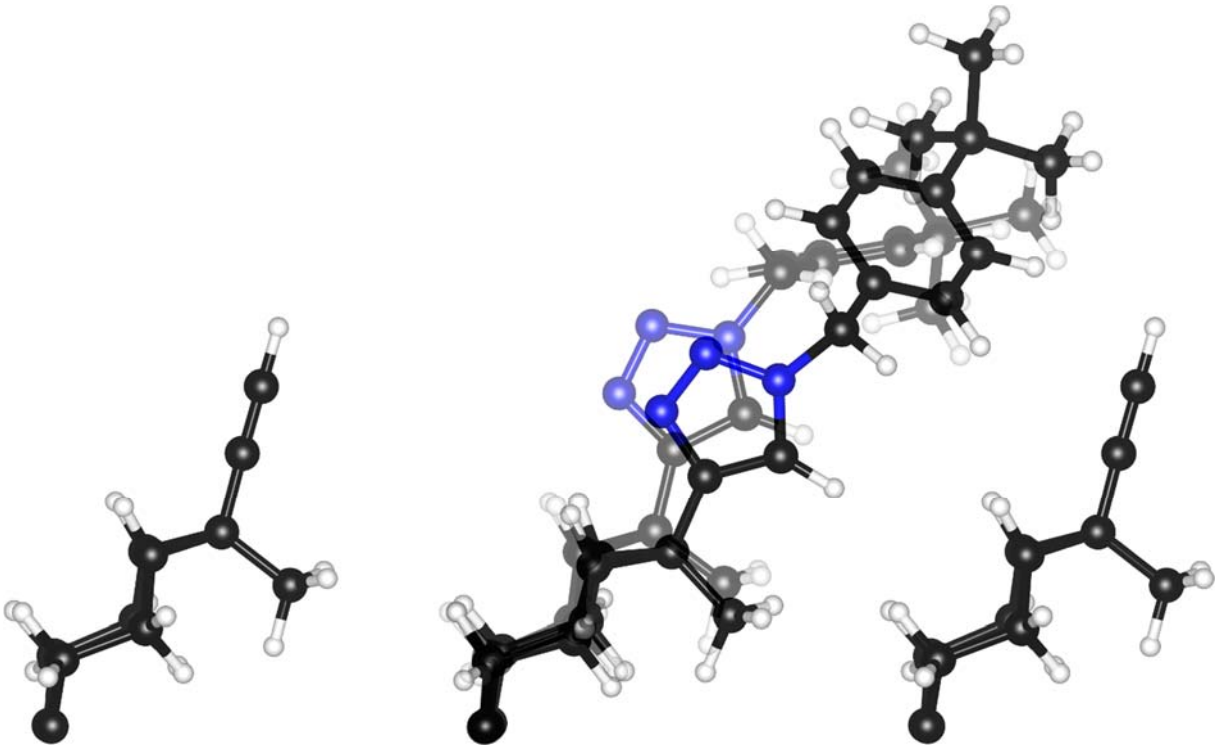

Figure S5. Comparison of the rank 1 (full colors) and rank 3 (faded colors) AAC product structures. Due to the missing steric repulsion within the first organic layer, the rank 3 structure is more flexible and converges to a different minimum.

9. Comparison to cluster model

Table S13. Energies of stationary points on the AAC reaction path with respect to the isolated reactants without dispersion correction. The periodic model system of rank 2 is compared to a cluster calculation.		
kJ/mol	2[a]	2[b]
Precomplex	7	6
TS	85	87
Product	-266	-261
[a] Periodic model. [b] Cluster model.		

10. Coverage dependent adsorption energy

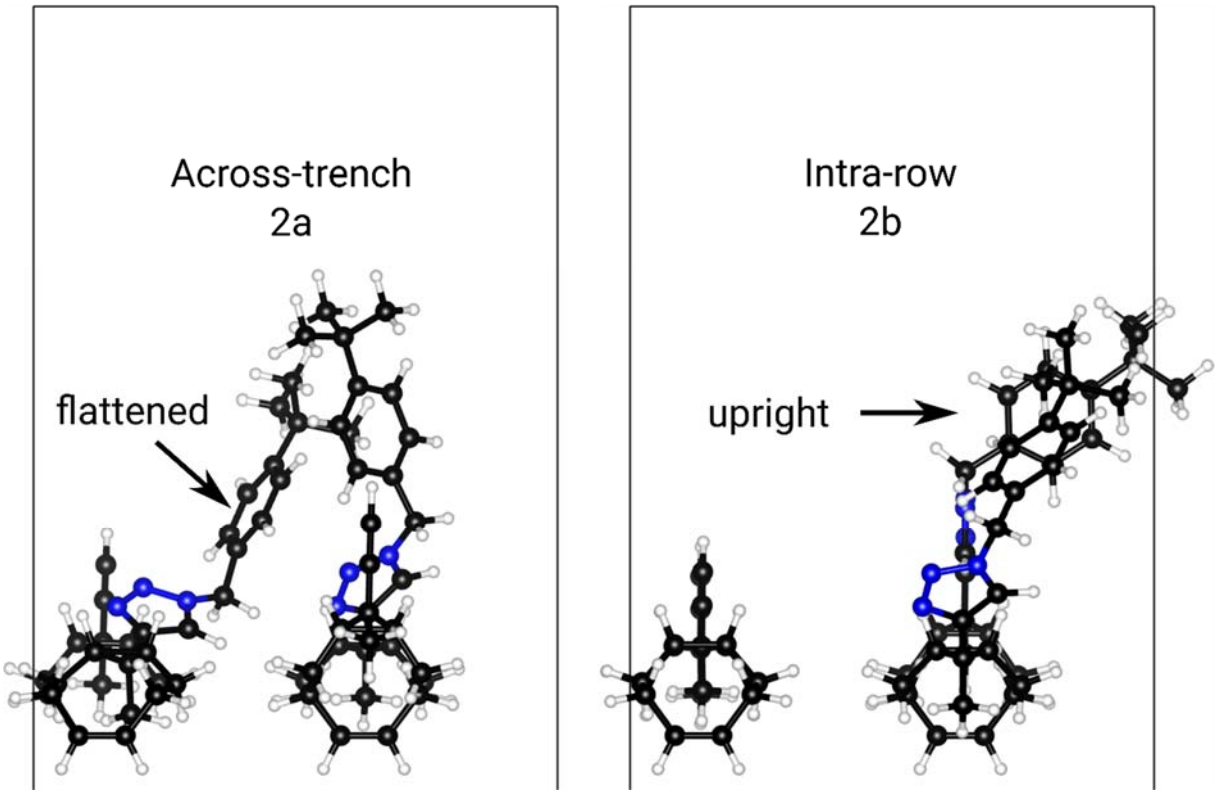

Figure S6. Structural comparison of the across-trench (**2a**) and intra-row (**2b**) adsorption of two azide molecules **2** on a monolayer of CCO **1**. In the former case, one of the molecules flattens onto the surface increasing the dispersion contribution to the adsorption energy.

11. Comparison of rank structures

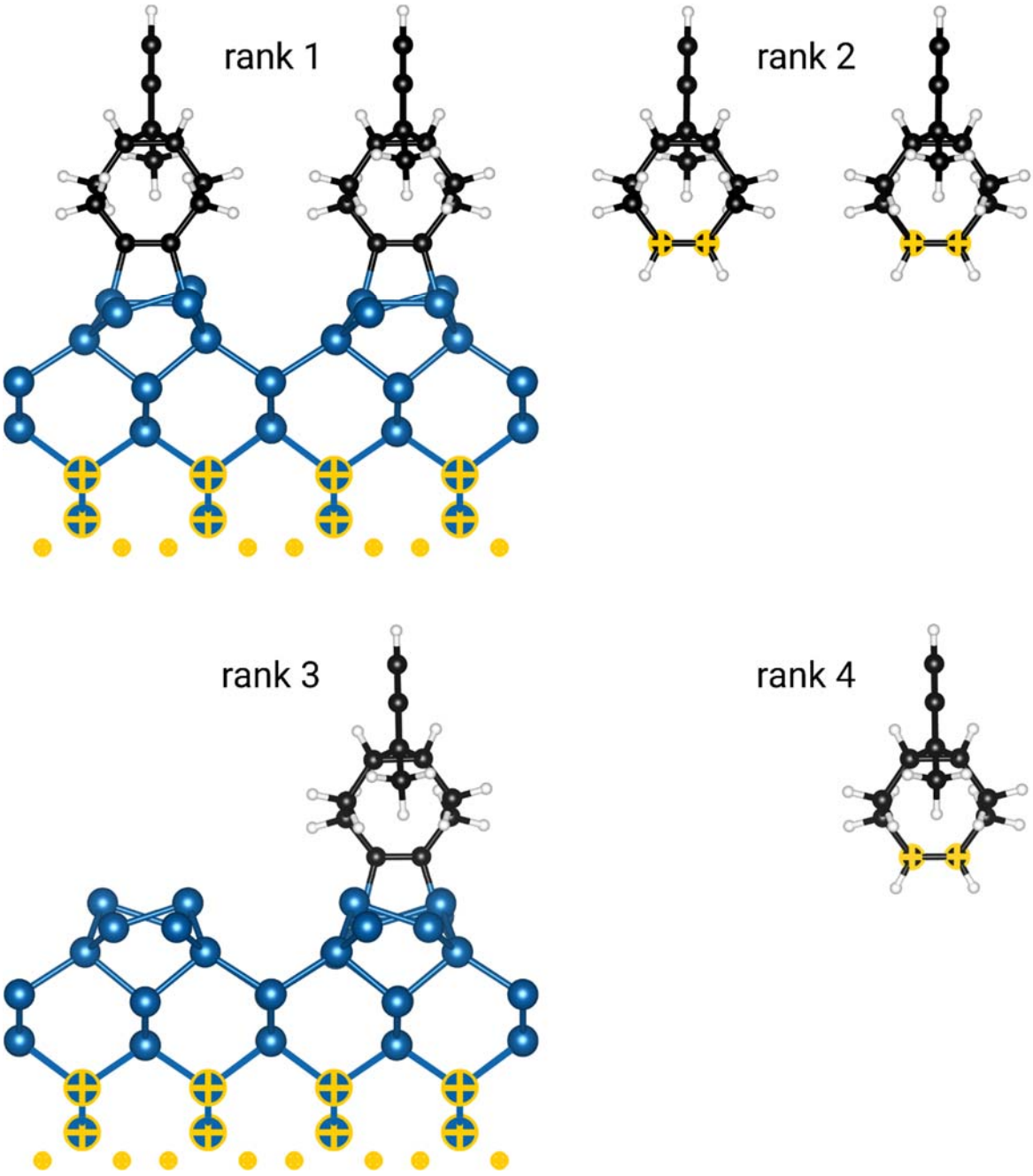

Figure S7. Substrate structures of the AAC reaction at ranks 1-4. Fixed atoms are highlighted in yellow.

12. Calculation timings and memory requirement

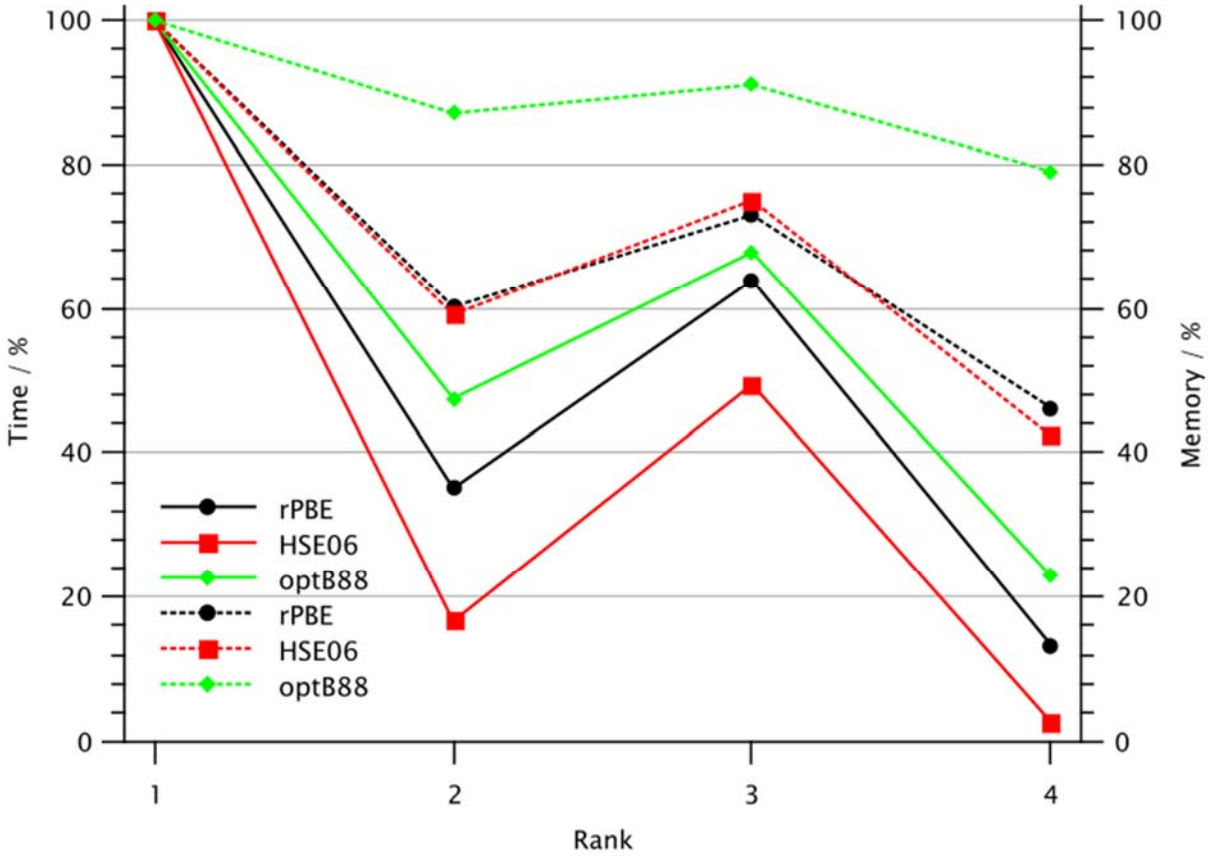

Figure S8. Relative timing (solid lines) and memory (dotted lines) requirements of the AAC reaction for ranks 1-4. Rank 1 is defined as 100% with the other ranks experiencing and reduced time and memory requirements depending on the functional.

Usage of the rank 2 model of AAC results in a reduction of computational time to 17% (HSE06), 36% (rPBE) and 48% (optB88) of the rank 1 value, translating to a speed-up of ca. factor 6,3 and 2, respectively. The rank 3 model yields less speedup and reduces the computational effort by factor 1.5-2. Rank 4 gives as expected the largest speedup of up to a factor of 50. This result corresponds well with the number of atoms present in each system (compare Figure S7). As to be expected, the largest effect is found for HSE06-D3 since hybrid functionals generally scale more strongly than GGAs (here rPBE-D3 and optB88). For the memory requirements, overall a smaller resource reduction is observed, with rPBE-D3 and HSE06-D3 performing similarly. Notably, optB88 shows only a small reduction in memory utilization.

13. Structure and output data repository

Raw data is available at the NOMAD repository.
DOI: https://dx.doi.org/10.17172/NOMAD/2020.12.07-8

14. References

1. Bach, R. D. Ring Strain Energy in the Cyclooctyl System. The Effect of Strain Energy on [3 + 2] Cycloaddition Reactions with Azides. *J. Am. Chem. Soc.* **2009**, *131*, 5233–5243.

THE JOURNAL OF PHYSICAL CHEMISTRY C
A JOURNAL OF THE AMERICAN CHEMICAL SOCIETY

pubs.acs.org/JPCC

Article

Organic Functionalization at the Si(001) Dimer Vacancy Defect—Structure, Bonding, and Reactivity

Published as part of The Journal of Physical Chemistry virtual special issue "Alexander Boldyrev Festschrift".

Jan-Niclas Luy and Ralf Tonner*

Cite This: *J. Phys. Chem. C* 2021, 125, 5635−5646

Read Online

ACCESS | Metrics & More | Article Recommendations | Supporting Information

ABSTRACT: In this density functional theory study, the influence of the bonded dimer vacancy (DV) on the reactivity of the Si(001) surface is investigated. To this end, electronic and structural properties of the defect are analyzed. Band structure calculations reveal a higher-lying valence band which would suggest increased reactivity. However, the opposite is found when organic molecules for interface formation (acetylene, ethylene, and cyclooctyne) are adsorbed at the defect. Significant reaction barriers have to be overcome in order to form bonds with defect atoms, while adsorption on the pristine surface is mostly direct. This suggests the presence of a rather weak Si−Si bond across the defect which must be dissociated before organic adsorbates can react. A rich adsorption and reaction network is found in addition to the structures known from the pristine surface. All three investigated adsorbates show different bonding characteristics. For acetylene and ethylene, the preferred thermodynamic sink is the insertion into the defect, with the latter molecule even dissociating. Bulky cyclooctyne on the other hand avoids reaction with the defect due to steric demands imposed by the small defect cavity. The DV has no effect on the reactivity of neighboring dimers. A combination of defect creation and hydrogen-precoverage could be a promising approach for selective surface functionalization. We thus show the influence of a nonideal surface on organic functionalization and interface build-up reactions for a prototypical interface.

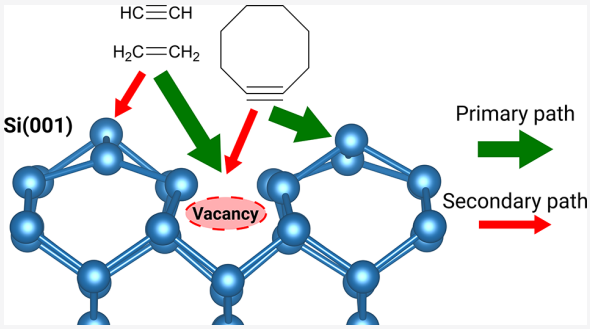

INTRODUCTION

The (001) facet of silicon is one of the most studied surfaces in material science and technology due to its widespread use in electronic devices such as transistors, solar cells, and LEDs. The desired electronic structure signatures defining the properties of the respective device often arise at the interface of silicon with other materials.[1−3] In recent years, particularly organic-silicon interfaces have sparked the interest of researchers due to combining advantages of the mature silicon-based technology with the chemical richness of organic compounds.[4−6]

However, the high reactivity of the pristine Si(001) surface (Figure 1a) makes creating well-defined interfaces challenging.[7] To address this issue, first a contact layer has to be synthesized from selective reactions between surface dimers and suitable organic molecules which saturate reactive dangling bonds. As a promising approach, 1,3-dipolar[8] and [2 + 2][9,10] cycloadditions have been identified (Figure 1e). Cyclooctyne (Figure 1b) has been found to be an excellent platform molecule.[9,10] When the adsorption is done with bifunctional anchor molecules, such as ethynyl−cyclopropyl−cyclooctyne[11] or methyl enolether functionalized cyclooctyne,[12] additional organic layers can be grown on the first layer.[13]

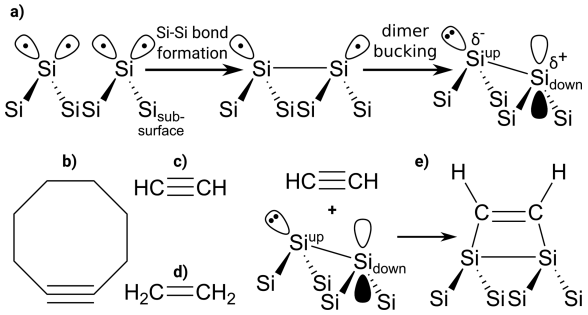
a)
Si-Si bond formation
dimer bucking
Si
Si
Si

Up to now, most of the work on organic thin-layer growth on semiconductor surfaces has focused on pristine substrates while some studies considered step edges.[14,15] This is possible since substrate preparation techniques that suppress defect formation effectively under UHV conditions exist.[16] However, we believe that defects, despite their unfavorable reputation, could actually be used to increase the selectivity of surface reactions and offer a new path to precise patterning.[17,18] As we will show, surface reactivity is altered in the vicinity of defects which results in some molecules bonding preferentially to defect atoms while others tend toward pristine surface sites. This provides a pathway for creating patterns in the organic layer if the defects can be introduced in a controlled manner. Indeed, in a similar spirit, hydrogen-precovered surfaces with distorted dangling bond configurations have been shown to exhibit an increased reactivity in the case of ethylene adsorption on Si(001).[19,20] The main motivation of the present work is therefore to quantify and understand the changes in reactivity of defects with respect to the pristine surface. Furthermore, the investigation of nonideal surfaces will help to create more realistic computational models of organic−inorganic interfaces.

In the past, acetylene and ethylene (Figure 1c,d) have been computationally studied as simple models for cycloaddition reactions of unsaturated hydrocarbons on the pristine Si(001) $c(4 \times 2)$ surface by us and others.[20,21] In the case of ethylene, there exists a π-complex-like precursor bound to a Si_{down} atom preceding covalent attachment in a [2 + 2]-like fashion.[22] For acetylene, adsorption is direct and the π-complex instead serves as a transition state (TS) between two subsurface modes.[23] Notably, experiment indicates an indirect adsorption path via a precursor state[24] which has been discussed before by us[23] and others.[25] Both acetylene and ethylene adsorb preferentially on-top of a single dimer or bridged between two dimers.[26] The already mentioned cyclooctyne (Figure 1b) is the smallest stable cyclic alkyne[27] and contains a ring strain energy (RSE) of about 80 kJ/mol.[13] Reactions involving the triple bond partly release this RSE which increases selectivity and makes catalysts obsolete.[28] Because of this benefit, cyclooctyne and its derivatives are considered promising candidates for layer-by-layer interface building schemes.[29]

Defect-containing surfaces should show a richer adsorption chemistry due to the presence of additional structural motives. In order to focus the scope of this study, we omit defects of higher dimensionality and limit the investigation to the thermodynamically most favorable intrinsic point defect, the bonded dimer vacancy (DV).[30] In comparison to the DV (Figure 2c), single atom vacancies are 94−98 kJ/mol (Figure 2a,b) less stable. This value is in good agreement with earlier results,[31] and experiments showing a high DV concentration of 9% for a surface cleaved at 0.4° and annealed at 800 °C.[32] Moving a whole Si dimer into an ad-position requires just 33 kJ/mol (Figure 2f) per atom which is even less compared to creating an adatom (68 kJ/mol, Figure 2e). This value aligns well with a study in which a strong diffusion of ad-dimers on Si(001) was found.[33] The related twisted dimer vacancy reconstruction (Figure 2d) shows larger bond distances and requires 45 kJ/mol per atom to form. This result agrees with tight binding calculations reported earlier.[34] Additionally, it was proposed that the DV is the energetic sink for bulk vacancies as they slowly diffuse to the surface.[35]

We note in passing that in many scanning tunneling microscopy (STM) studies the DV has also been referred to as "A-defect"[37] while distinguishing it from the double-DV ("B-defect") and dissociatively adsorbed water molecules ("C-defect").[38] However, the identification of different defects has not been unambiguous in the past since water molecules produce similar STM features to missing atom defects in a large range of bias voltages.[39]

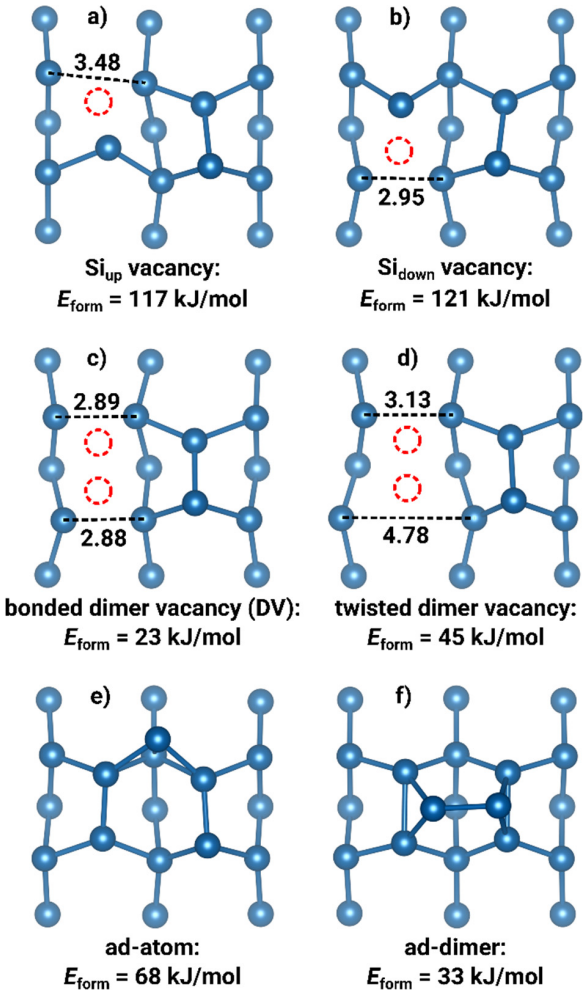

Figure 2. Most common intrinsic point defects of Si(001) as considered in this study. Bond lengths are given in Å. The defect formation energy (E_{form}) is calculated as the difference of the total energy of the pristine slab ($E_{pristine}$) and the defect containing slab (E_{defect}) normalized to the number of defect atoms N (i.e., 2 for the DV) which is added to the cohesive energy E_{coh} of Si in the diamond structure (−553 kJ/mol). $E_{form} = E_{coh} + (E_{defect} - E_{pristine})/N$. Our values agree well with earlier results.[36] Vacancies are indicated by red circles.

The results section is divided into four parts. First, the atomic and electronic structure of the DV is discussed taking bond parameters and formation energies into account. In the second part, the thermodynamic features of molecular adsorption is investigated. Bonding analysis is performed in the third part. Lastly, the kinetic influence of the DV on adsorption is discussed with the help of reaction networks.

METHODS

Density functional theory (DFT) calculations were performed with the Vienna Ab initio Simulation Package (VASP

https://dx.doi.org/10.1021/acs.jpcc.1c00262
J. Phys. Chem. C 2021, 125, 5635−5646

5.4.4).[40−42] The generalized gradient approximation-(GGA-) based exchange-correlation functional proposed by Perdew, Burke, and Ernzerhof (PBE)[43] was used in conjunction with the projector-augmented wave (PAW) method using the "standard" pseudopotentials for all atoms (version PBE5.4).[44] Dispersion effects were treated with the DFT-D3 scheme using the "Becke-Johnson"-type damping function.[45,46] The precision tag was set to accurate and a total energy difference of at most 10^{-5} eV was used for SCF convergence, while setting the plane wave energy cutoff to 400 eV. For structure optimization, the force convergence criterion was 10^{-2} eV/Å. The surface was modeled with a six-layered slab-supercell in periodic boundary conditions. The theoretical lattice parameter (a = 5.418 Å) was determined previously.[9] The bottom side of the slab was saturated with two hydrogen atoms per Si at the silane (SiH_4) bond length (1.480 Å)[47] while the bottom two Si-layers are frozen at their bulk positions. The thickness of the vacuum layer between periodically repeated slabs was at least 13 Å. Electronic levels around the Fermi-energy are smeared out by σ = 0.05 eV with Gaussian functions to accelerate self-consistent field convergence. Momentum space was sampled by a 1 × 2 Γ-centered k-point mesh. This computational setup has yielded accurate results for adsorbates on the pristine surface in the past.[9] Reaction paths have been calculated with the climbing-image nudged elastic band (CI-NEB)[48] method. Transition states found were further optimized with the dimer method.[49] In addition, the influence of spin-polarization on the wave function of the DV was investigated: the SCF procedure was started with a magnetization at the four defect atoms (antiferromagnetic configuration) and the calculation converged to the same values as for the nonpolarized case. We thus present the latter throughout the manuscript.

Crystal orbitals and energy decomposition analysis for extended systems (pEDA)[50] were calculated with ADF-BAND[51] version 2019.301 except in Figure 4 where version 2019.105 was used. Again, the PBE-D3(BJ) functional was used in conjunction with the atom centered TZ2P[52] basis set. Scalar relativistic effects were treated with the zeroth order regular approximation (ZORA).[53] The pEDA method decomposes the bond energy (ΔE_{bond}) between two fragments A and B into well-defined quantities allowing for a chemically meaningful interpretation. The bond energy (ΔE_{bond}), or negative dissociation energy, is the sum of the interaction energy (ΔE_{int}) and a preparation energy (ΔE_{prep}), which is defined as the difference between the isolated fragments and the states found in the final complex. ΔE_{int} can be further divided into an empirical dispersion term (ΔE_{disp}) and an electronic term (ΔE_{elec}). The actual pEDA procedure then decomposes ΔE_{elec} into a quasiclassical electrostatic contribution (ΔE_{elstat}), the Pauli repulsion term (ΔE_{Pauli}) obtained by antisymmetrizing and normalizing the fragment wave functions and finally an orbital interaction (ΔE_{orb}) that results from relaxing the intermediate wave function and includes charge transfer and polarization effects (eq 1).

$$\Delta E_{elec} = \Delta E_{Pauli} + \Delta E_{elstat} + \Delta E_{orb} \quad (1)$$

The orbital term can be further dissected by the Natural Orbitals for Chemical Valence (NOCV) scheme.[54] Here, the NOCVs are constructed as eigenvectors that diagonalize the deformation density matrix in the basis of fragment orbitals. The electron density difference $\Delta\rho_{orb} = \rho_{AB} - \rho^0$ is then expressed by deformation densities $\sum\rho_i$ which aid in visual characterization of the bond. Corresponding eigenvalues ν_i quantify the amount of charge transferred between NOCVs.

Thermodynamic Corrections. Calculation of vibrational modes needed for thermodynamic corrections become prohibitively expensive for large simulation cells. Therefore, we devised a scheme that allows ΔG_{ads} values to be determined approximately by considering only a subsection of the Hessian matrix. In the simplest case, only adsorbate atoms are displaced in the finite-differences method implemented in VASP. Convergence of ΔG_{ads} is then achieved by including ever larger nearest neighbor or next-nearest neighbor spheres in the surface. During calculation of the dynamical matrix, atoms outside of the considered sphere are kept fixed. This approach yields accurate results for the adsorption free energy of acetylene (see Table S1) and is expected to also perform well for larger adsorbates as long as all important Hessian elements are calculated. Benchmarking of this approach, further details and a python script allowing parallel computation can be found d in the Supporting Information.

Convergence of Cell Parameters. To investigate an isolated defect as it would be present on an actual surface, the number of primitive unit cells along directions x and y have to be chosen such that electronic levels are sufficiently localized and artificial interactions with periodic images are avoided. In addition, the structural strain introduced by a defect has to decay within the supercell. Thus, to converge the formation energy (E_{form}) of a DV defect, slabs of different sizes were generated and compared in Table 1. The error (ΔE_{form}) is with

Table 1. Errors in Formation Energy (ΔE_{form}) and Error in Bandgap (ΔE_{Gap}) with Respect to the Largest Cell Investigated in kJ/mol

supercell	no. of layers	ΔE_{form}	ΔE_{gap}
4 × 4	6	18	18
4 × 4	7	14	23
4 × 4	8	12	23
8 × 4	6	7	17
8 × 4	7	3	22
8 × 4	8	<1	22
8 × 8	8	0	21

18 kJ/mol largest for the smallest six-layered slab of a 4 × 4 supercell. The addition of another layer lowers the penalty by 4 kJ/mol while an eighth layer converges it to within 2 kJ/mol. Doubling the size of the slab along rows of surface dimers leading to a 8 × 4 supercell lowers the penalty by 11 kJ/mol regardless of the layer number. Doubling the slab also along the second direction (8 × 8 supercell) has no significant impact on defect formation energies. The band gap converges slightly faster with just one additional layer. Thus, it can be concluded that slabs used for studying defects should contain a larger number of layers and unit cells than for pristine surfaces. All calculations in this study are therefore performed in the 8 × 4 supercell with eight layers where 1/16th of dimers are missing (see Figure S1 in the Supporting Information for a plot of the atomic structure).

RESULTS AND DISCUSSION

Energy of Formation and Atomic Structure of the DV Defect. First, we will discuss the structural changes induced by the DV defect. Removal of a dimer from the pristine surface creates four new dangling bonds at former *subsurface* atoms

https://dx.doi.org/10.1021/acs.jpcc.1c00262
J. Phys. Chem. C 2021, 125, 5635−5646

(see Figure 3c). Thus, the sum of reactive sites should increase by two, making the surface more reactive. However, as we will see, this is not the case. Instead, the defect relaxes into a more favorable configuration by forming single-bonds across the defect. Structural support for this relaxation model is given by a rather short Si−Si distance of 2.88 Å (d(Si−Si) in bulk-like layer = 3.83 Å) as well as noticeable displacement of neighboring atoms from their position on the pristine surface (Figure 3c). The bond is 0.5 Å longer than a Si−Si-bond in the bulk (2.35 Å) due to constraints imparted by the lattice but significantly shorter than the sum of van-der-Waals radii (4.20 Å).[55] To enable the formation of two short Si−Si bonds found in the defect, one dimer adjacent to the DV flips (Figure 3b) thus breaking the buckling periodicity of the $c(4 \times 2)$ reconstruction. The defect formation energies presented in Figure 2 give a lower bound of −46 kJ/mol for the Si−Si bond energy. This is the difference in formation energy of the DV (Figure 2c) compared to the twisted conformer (Figure 2d) which forms just one bond. However, the bond is likely stronger due to the destabilizing contribution of about 30 kJ/mol required for flipping one dimer (in Figure 2d the dimer next to the defect is not flipped).[56] Bonding analysis by EDA gives an interaction energy for the two Si−Si bonds across the DV of ΔE_{int}(elec) = −328 kJ/mol using a cluster model (Table S2), thus approximately 160 kJ/mol per Si−Si bond. The comparison to disilane (ΔE_{int}(elec) = −316 kJ/mol) shows that the Si−Si bond is only half as strong in the DV but can without doubt be called a covalent bond (Figure S2). This is supported by natural bond orbital analysis for periodic systems[57] showing a bond orbital with occupation 1.86 e.

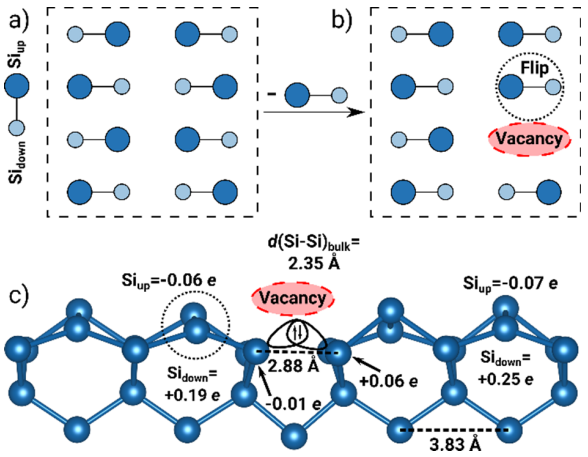

Figure 3. (a) Top view of a pristine 4 × 4 supercell of the Si(001) surface showing only dimers. Si_{down} atoms are represented by small circles, Si_{up} atoms by larger circles. (b) Removal of a dimer results in the formation of a DV (red oval) and the flipping (black circle) of a neighboring dimer. (c) Side view of the bonded DV with structural and electronic properties. Dashed lines: Si−Si distances. Atomic partial charges are given in elementary charge units e.

Electronic Structure of the DV Defect. Next, the electronic structure of the DV (Figure 4) in reciprocal (band structure) and real (crystal orbitals (CO)) space is compared to the pristine surface.

With introduction of the defect, two bands (bold red) are elevated into the former band gap, thus narrowing the gap by

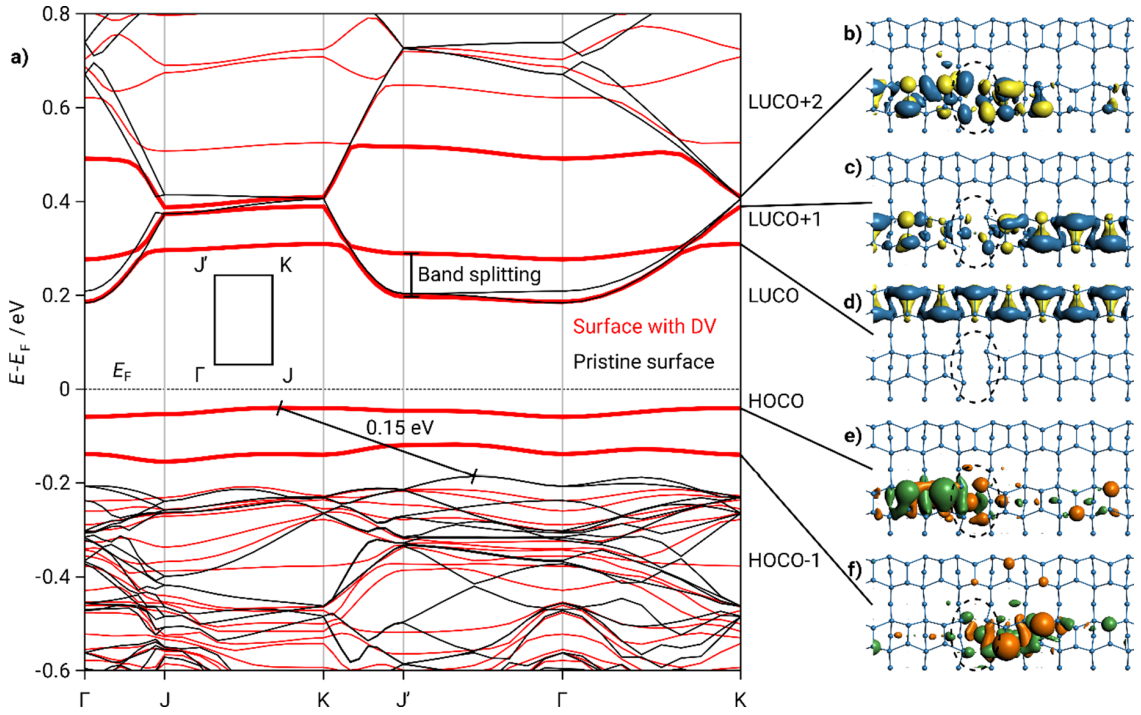

Figure 4. (a) Band structure of the pristine (black) and DV-including (red) 8 × 4 surface supercell. Energies are given with respect to the Fermi energy (E_F) of the pristine surface. The surface bands stemming from the DV are aligned to match the lowest calculated band of pristine surface at the Γ-point. Additional bands introduced by the defect close to the Fermi edge are emphasized in bold, and the reduction of the band gap is indicated by a flat-headed arrow. The position of high-symmetry points in the surface unit mesh is shown as an inset. (b−f) Selected crystal orbital plots at the Γ-point. The position of the defect is indicated with a dashed oval.

https://dx.doi.org/10.1021/acs.jpcc.1c00262
J. Phys. Chem. C 2021, 125, 5635−5646

about 0.15 eV. The valence bands are strongly localized as indicated by the absence of band dispersion and shown by real space plots of the highest occupied COs: HOCO and HOCO-1 at the Γ-point (Figure 4e,f). Conversely, on the pristine surface the HOCO is doubly degenerate and delocalized over the whole cell (Figure S3) as indicated by strong band dispersion. Furthermore, these plots reveal hybridization between defect orbitals and Si_{up} lone pairs with quickly decaying special extent. Degeneracy between both sides of the defect is lifted by breaking the translational symmetry in this supercell model. Thus, an energetic separation of the formerly degenerate HOCO and HOCO-1 is found. Interaction of the DV with the flipped dimer (black circle Figure 3) is slightly less favorable than interaction with alternating dimers, probably due to Si_{up} lone pair repulsion in the HOCO (large green lobes). In the lowest unoccupied bands, hybridization between the DV and empty p-orbitals of Si_{down} atoms is observed (LUCO+1, LUCO+2). As in the occupied bands, this results in slightly reduced dispersion and more localized orbitals compared to the LUCO of the pristine surface. The conduction band minimum is found at the Γ-point. There and at all other high-symmetry points, the presence of the defect causes splitting of formerly degenerate bands. In addition, avoided crossings appear along Brillouin zone paths propagating in the *x*-direction (e.g., Γ-J) as a result of translational symmetry breaking. Therefore, electron mobility along the *x*-direction is expected to be reduced. Notably, there is good qualitative agreement between the band structure of the DV and earlier work on the stepped Si(001) surface.[58]

Because the LUCO+1 shows almost no lobe at the flipped dimer and a lower positive charge at its Si_{down} atom, Lewis-acidity should decrease. This finding is corroborated by periodic natural population analysis[57] which reveals that the four defect atoms carry a partial charge that is opposite to their neighboring dimer atoms (black arrows in Figure 3). The magnitude of the charge (−0.01 to +0.06 *e*) is smaller compared to the Si_{down} atom (up to +0.25 *e*) which should result in decreased electrophilicity. This is indeed the case as shown in the next section.

Reactions with Small Unsaturated Hydrocarbons. The Lewis acidity of the flipped Si_{down} atom can be estimated by calculating its bonding energy with a Lewis donor. Here, we chose ethylene since the system has been intensively analyzed for the pristine surface.[22] With the help of the energy decomposition analysis for extended systems (pEDA), we can quantify the Lewis acidity (Table S3). The interaction energy (which considers the preparation energy to deform the fragments for bonding) is much lower for the flipped dimer (ΔE_{int} = −71 kJ/mol) compared to a dimer on the pristine surface (ΔE_{int} = −113 kJ/mol) leading to a reduction in bonding energy from −82 kJ/mol to −56 kJ/mol. The nature of the bonding is similar—as indicated by the pEDA contributions showing similar trends, but the total bonding energy and thus the Lewis acidity of the flipped dimer is considerably reduced. The Lewis basicity of the Si_{up} atom is hardly changed as shown by the interaction with a Lewis acid (BH_3, Table S3) even though the HOCO energy changes.

Understanding the reactivity at the DV site is a prerequisite for understanding organic functionalization on the surface. Thus, the adsorption of interface building block cyclooctyne and its model molecules acetylene and ethylene are investigated. We find four thermodynamically favorable adsorption modes which are presented in Figure 5. Of those,

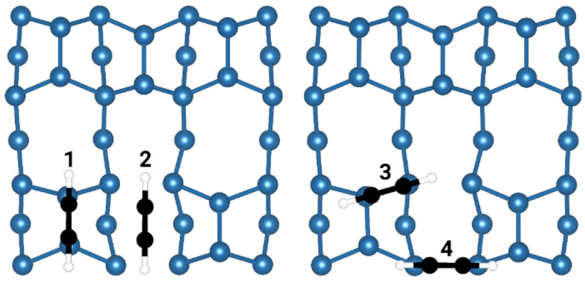

Figure 5. Adsorption modes onto the defect are shown representatively for acetylene: (1) on-top, (2) pedestal, (3) side-on, and (4) bridge. Shown are the first three layers of a Si(001) slab with a DV.

only the "on-top" mode (1) also exists on the pristine surface (a further adsorption mode bridging two dimers is not investigated here since it is less stable at low coverages).[21] Unique to the DV are the modes "pedestal" (2), "side-on" (3) and "bridge" (4). The pedestal mode cures the defect by forming four C−Si bonds, effectively replacing the missing Si dimer. The side-on mode is created by reaction with one dimer and one defect atom. Hence, four adsorbent molecules would be needed to cure the defect. Lastly, the bridge mode connects two opposing defect atoms, requiring two molecules to cure the defect.

Bonding energies of the three molecules are listed in Table 2. Interestingly, the energy in the on-top mode is unchanged with respect to the pristine surface. However, there is large variation in the values of the other modes.

Table 2. Bonding Energies of Acetylene, Ethylene, and Cyclooctyne in Different Adsorption Modes at a DV[a]

mode	acetylene	cyclooctyne	ethylene
on-top (pristine)	−266	−305	−200
on-top	−268	−307	−200
pedestal	−302	−250	−321[b]
side-on	−229	−261	−167
bridge	−281	−273	−203

[a]All energies in kJ/mol computed with PBE-D3(BJ)/PAW. The bonding energy ΔE_{bond} is negative by convention for stable modes and calculated as the difference between isolated reactants and products. [b]The C═C bond dissociates (see Figure 8).

In the case of acetylene, bridge shows only slightly stronger bonding (−281 kJ/mol) than on-top (−268 kJ/mol) while it is weakest for side-on (−229 kJ/mol). The pedestal mode shows the strongest bond with −302 kJ/mol although the carbon−carbon triple bond is reduced to a single bond. These data suggest that a thermodynamic driving force of at least 20 kJ/mol exists in favor of pedestal which is desirable for selective surface functionalization. This beneficial defect property might be used in a combined approach with hydrogen precoverage of Si(001) (Figure S4). Here, the pedestal mode is further stabilized by 15 kJ/mol while the bridge mode is destabilized by 4 kJ/mol and the side-on mode is entirely blocked (Table S4) thus increasing selectivity of surface adsorption at the DV further. In addition, H_2 reacts preferentially with dimer atoms (E_{gap} (on-top) = −166 kJ/mol) over defect atoms (E_{bond} (pedestal) = −95 kJ/mol). Thus, a selective precoverage of the surface by hydrogen excluding the DV site seems possible. It is well-known that hydrogen-coverage of Si(001) is

https://dx.doi.org/10.1021/acs.jpcc.1c00262
J. Phys. Chem. C 2021, 125, 5635−5646

Table 3. pEDA Results for Acetylene and Cyclooctyne in the Pedestal and On-Top Modes. All Energies in kJ/mol at PBE-D3(BJ)/TZ2P Computed at the Γ-Point

	pedestal[a]					on-top[b]					acetylene				
	acetylene		cyclooctyne			acetylene		cyclooctyne			side-on[b]		subsurface[23]		
	kJ/mol	%	kJ/mol	%	ΔΔE	kJ/mol	%	kJ/mol	%	ΔΔE	kJ/mol	%	kJ/mol	%	ΔΔE
ΔE_{int}	−1165		−1079		86	−664		−649		15	−720		−656		−64
ΔE_{int}(disp)[c]	−9	1	−63	6	−54	−10	2	−34	5	−24	−21	3	−22	3	+1
ΔE_{int}(elec)[c]	−1156	99	−1016	94	140	−654	98	−615	95	39	−699	97	−634	97	−65
ΔE_{Pauli}	2966		3121		155	1354		1492		138	1796		1587		209
ΔE_{elstat}[d]	−1649	40	−1754	42	−105	−834	42	−938	45	−104	−1005	40	−912	41	−93
ΔE_{orb}[d]	−2473	60	−2383	58	90	−1176	58	−1169	55	7	−1489	60	−1310	59	−179
ΔE_{prep}	862		825		−37	391		339		−53	487		520		−33
ΔE_{prep}(M)[e]	707		664		−43	365		312		−53	368		364		+4
ΔE_{prep}(S)[e]	156		161		5	27		27		0	119		156		−37
ΔE_{bond}	−303		−255		48	−273		−310		−37	−233		−136		−97
ΔE_{bond}(PAW)[f]	−302		−250		52	−268		−307		−39	−229		−120		−109
d(C−C)/Å	1.632		1.657			1.356		1.367			1.350		1.348		

[a]Fragments are generated from homolytic cleavage at C−Si into neutral quintuplets. [b]Fragments are generated from homolytic cleavage at C−Si into neutral triplets. [c]Percentage values: Relative contributions of dispersion and electronic effects to the interaction energy ΔE_{int}. [d]Percentage values: Relative contributions of the attractive pEDA terms ΔE_{elstat} and ΔE_{orb}. [e]Preparation energies of the molecule (M) and substrate (S) contain structural contributions and electronic excitations. [f]Deviations with respect to the PAW result are due to the basis set and simulation cell setup differences.

temperature-dependent and largely under thermodynamic control[59] pointing toward an experimental way of realizing the theoretically proposed scenario, for example, by finding a temperature window at which H_2 desorbs from the DV but not yet from the plain surface.

For cyclooctyne, two conformers (tilt toward and tilt away from the DV) are found in the on-top mode (only the more stable one is listed in Table 2). While those conformers are separated energetically by just 3 kJ/mol, dispersion-induced bending[9] away from the defect is pronounced and the adsorption height is reduced by 0.262 Å (see Figure S5 for the tilt away-conformer). This might allow a steering effect on adsorption of further cyclooctyne molecules on specific adsorption sites as observed on the pristine surface.[60] While adsorption into the on-top mode is −39 kJ/mol more favorable when compared to acetylene, this trend is less pronounced for side-on (−32 kJ/mol) and even reversed for the bridge (8 kJ/mol) and pedestal (52 kJ/mol) modes. To explain this observation, a detailed bonding analysis by pEDA is performed in the next subsection.

Most trends observed as mentioned for acetylene are also found for ethylene. However, this molecule shows adsorption energies which are 60−80 kJ/mol smaller. The weakest bond is formed in the side-on mode (−167 kJ/mol) followed by on-top (−200 kJ/mol) and bridge (−203 kJ/mol) modes. Again, the pedestal mode (−321 kJ/mol) presents an exception as the former C═C is cleaved in order to form two CH_2 fragments (see Figure 8). The resulting structure is similar to the adsorption of SiH_x molecules at the DV as calculated by tight binding approaches.[61]

Bonding Analysis. To explain the trends in the adsorption energies of Table 2, pEDA calculations are performed as summarized in Table 3. The pEDA is a powerful method that decomposes the interaction energy between two molecular fragments into chemically meaningful quantities such as quasiclassical electrostatic interactions (ΔE_{elstat}), orbital interaction (ΔE_{orb}), and Pauli repulsion (ΔE_{Pauli}). The total bonding energy is obtained by subtracting the preparation energy (deformation, electronic excitation) of the fragments. Further details of the pEDA are found in the methods section.

On-Top. Cyclooctyne and acetylene show almost identical adsorption energies in the on-top mode at the DV and on the pristine surface (Table 4). This observation also holds true for most pEDA terms with the exception of Pauli repulsion which is slightly more positive at the DV. However, this is exactly counterbalanced by a stronger orbital interaction term. We can thus conclude that the dimer neighboring a DV defect shows the same reactivity as on the pristine surface.

Table 4. pEDA Results for Acetylene and Cyclooctyne in the On-Top Mode at the Pristine Surface. All Energies in kJ/mol at PBE-D3(BJ)/TZ2P Computed at the Γ-Point

	on-top (pristine)[9a]			
	acetylene		cyclooctyne	
	kJ/mol	%	kJ/mol	%
ΔE_{int}	−668		−658	
ΔE_{int}(disp)[b]	−12	2	−43	7
ΔE_{int}(elec)[b]	−656	98	−615	93
ΔE_{Pauli}	1323		1468	
ΔE_{elstat}[c]	−828	42	−936	45
ΔE_{orb}[c]	−1152	58	−1148	55
ΔE_{prep}	389		339	
ΔE_{prep}(M)[d]	364		313	
ΔE_{prep}(S)[d]	25		26	
ΔE_{bond}	−279		−319	
ΔE_{bond}(PAW)[e]	−268		−308	

[a]Fragments are generated from homolytic cleavage at C−Si into neutral triplets. [b]Percentage values: Relative contributions of dispersion and electronic effects to the interaction energy ΔE_{int}. [c]Percentage values: Relative contributions of the attractive pEDA terms ΔE_{elstat} and ΔE_{orb}. [d]Preparation energies of the molecule (M) and substrate (S) contain structural contributions and electronic excitations. [e]Deviations with respect to the PAW result are due to the basis set and simulation cell setup differences.

https://dx.doi.org/10.1021/acs.jpcc.1c00262
J. Phys. Chem. C 2021, 125, 5635−5646

The 39 kJ/mol larger bonding energy of cyclooctyne when compared to acetylene can be explained by a release of 53 kJ/mol RSE (manifested through a reduced preparation energy, ΔE_{prep}) together with increased dispersion interaction ($\Delta\Delta E_{int}$(disp) = −24 kJ/mol).

Pedestal. On the pristine surface, pedestal describes a mode that is also referred to as tetra-σ mode. Here, acetylene or cyclooctyne adsorb between two dimers and form four C−Si bonds. This mode is however much less favorable than the DV-*pedestal* and therefore of no relevance for surface adsorption.[9,26] Overall, the main difference of the on-top and pedestal modes is the interaction energy ΔE_{int} which is about twice as large for the latter. This result is expected since four bonds instead of two are formed between molecule and surface. However, ΔE_{int} is offset by excitation of the fragments into quintuplet states which is necessary to form four shared-electron C−Si bonds. Furthermore, the bond distance of the former acetylene C≡C triple bond is even significantly longer than a typical C−C single bond.

The pEDA can also provide an explanation for the reversed trend of bonding energy in the pedestal mode when comparing acetylene and cyclooctyne. The main contribution is given by steric repulsion of the bulkier cyclooctyne in the tight space provided by the DV. As a result, the difference in Pauli repulsion between acetylene and cyclooctyne ($\Delta\Delta E_{Pauli}$) is increased slightly from 138 to 155 kJ/mol and $\Delta\Delta E_{orb}$ rises significantly from 7 to 90 kJ/mol. The orbital interaction energies are reduced by 25−45 kJ/mol compared to acetylene. A smaller, albeit surprising, effect is the reduction of released RSE (−53 to −43 kJ/mol) which can be traced to the eight-membered ring also being strained at the position of the former triple bond. Its bond angles deviate by 7−10° from the ideal tetrahedral angle. This effect is somewhat offset by a larger dispersion attraction as cyclooctyne is positioned closer to the surface (−24 to −54 kJ/mol).

The origin of the large changes in the $\Delta\Delta E_{orb}$ term can be found by further dissecting it with the natural orbitals for chemical valence (NOCV) extension to the pEDA (Figure 6). Visual inspection of the deformation densities for acetylene shows that the four largest contributions of α-spin correspond to electron flow from the adsorbate (red) into the surface. In the β-spin channel, the flow of electrons is reversed (blue). These deformation densities correspond to the four C−Si shared-electron bonds formed from four unpaired electrons per fragment. Using the eigenvalues (ν) to quantify the amount of charge flow in the first four deformation densities, slightly polar (0.125 e) C−Si bonds in favor of C emerge, in line with the electronegativities of the elements. The triple bond is reduced to a single bond. Finally, the difference in ΔE_{orb} between cyclooctyne (Figure 6, values in brackets) and acetylene is revealed to be caused by reduced charge flow into the molecule (β-spin). Here, the associated energy values for cyclooctyne are significantly lowered by about 30 kJ/mol per deformation density.

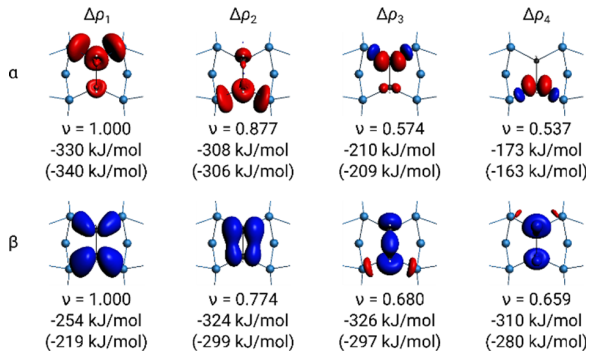

Figure 6. Most significant deformation densities $\Delta\rho_n$, eigenvalues (ν) and energies (total: $\Delta E_{orb}(\alpha)$ = −1161, $\Delta E_{orb}(\beta)$ = −1313) of acetylene in the pedestal mode. Corresponding energy values of cyclooctyne (total: $\Delta E_{orb}(\alpha)$ = −1172, $\Delta E_{orb}(\beta)$ = −1212) are given in brackets: (blue) charge accumulation; (red) charge depletion. A quintuplet fragmentation was generated from the cleavage of four C−Si bonds. Orbitals in the Si-surface are often delocalized resulting in no deformation density being visible at the chosen iso value.

Side-On. The side-on mode shares characteristics with both other modes discussed above due to molecules being attached to one defect atom and one dimer atom. Consequently, the calculated pEDA terms fall in between pedestal and on-top modes. The reason for the relatively small adsorption energy can be found in a ΔE_{int} term that is more comparable to the on-top mode, while the surface preparation energy is more akin to the pedestal mode even though triplet states are used instead of quintuplets. Furthermore, the newly described side-on mode is structurally similar to the subsurface insertion mode (Figure S6) proposed from computations in the past for acetylene on pristine Si(001).[23] Its formation is favored by −97 kJ/mol through a combination of increased electronic interaction and decreased preparation energy for the surface fragment. However, the bonding character is unaltered with electrostatic interaction amounting to roughly 40% in both cases.

Reaction Networks. In the last part of this study, the kinetic accessibility of different adsorption modes is discussed in addition to the already determined thermodynamic driving forces. We show here reaction networks generated from NEB calculations between reactants (precomplexes) and adsorption modes discussed in the previous section. In two cases, this procedure leads to discovery of additional structures: for acetylene another bridge conformer (bridge-*E*) and for ethylene a pedestal variant that is only attached to two defect atoms (pedestal-same). Reaction barriers are calculated as the energy difference between a TS and the previous local minimum (i.e., intermediate). The reaction networks are more complex than on the pristine surface where acetylene adsorbs barrierless into the final state (on-top)[23] while for ethylene and cyclooctyne a short-lived intermediate exists.[11,22,27]

Acetylene. In Figure 7, the reaction network of acetylene is found. Attempts to find the adsorption path (black arrows) into (**1**) did not converge via a single TS. Instead several minima appear on the reaction path corresponding to other already known adsorption modes. This behavior is somewhat expected since partial reduction of the C≡C bond coupled with simultaneous cleavage of two Si−Si bonds at the DV defect site requires a considerable activation energy which can be estimated from the preparation energy (862 kJ/mol). The side-on mode, on the other hand, is directly accessible (green arrows) but further reaction becomes unlikely when thermodynamic corrections are considered. Adsorption free energies ($\Delta\Delta G_{ads}$) are dominated by the loss of translational and rotational entropy of the molecule and are therefore largely independent of adsorption mode. This change is estimated at 69 kJ/mol (pedestal) to 64 kJ/mol (on-top)[9]. Thus, the reaction traversing **TS1** is brought into competition

https://dx.doi.org/10.1021/acs.jpcc.1c00262
J. Phys. Chem. C 2021, 125, 5635−5646

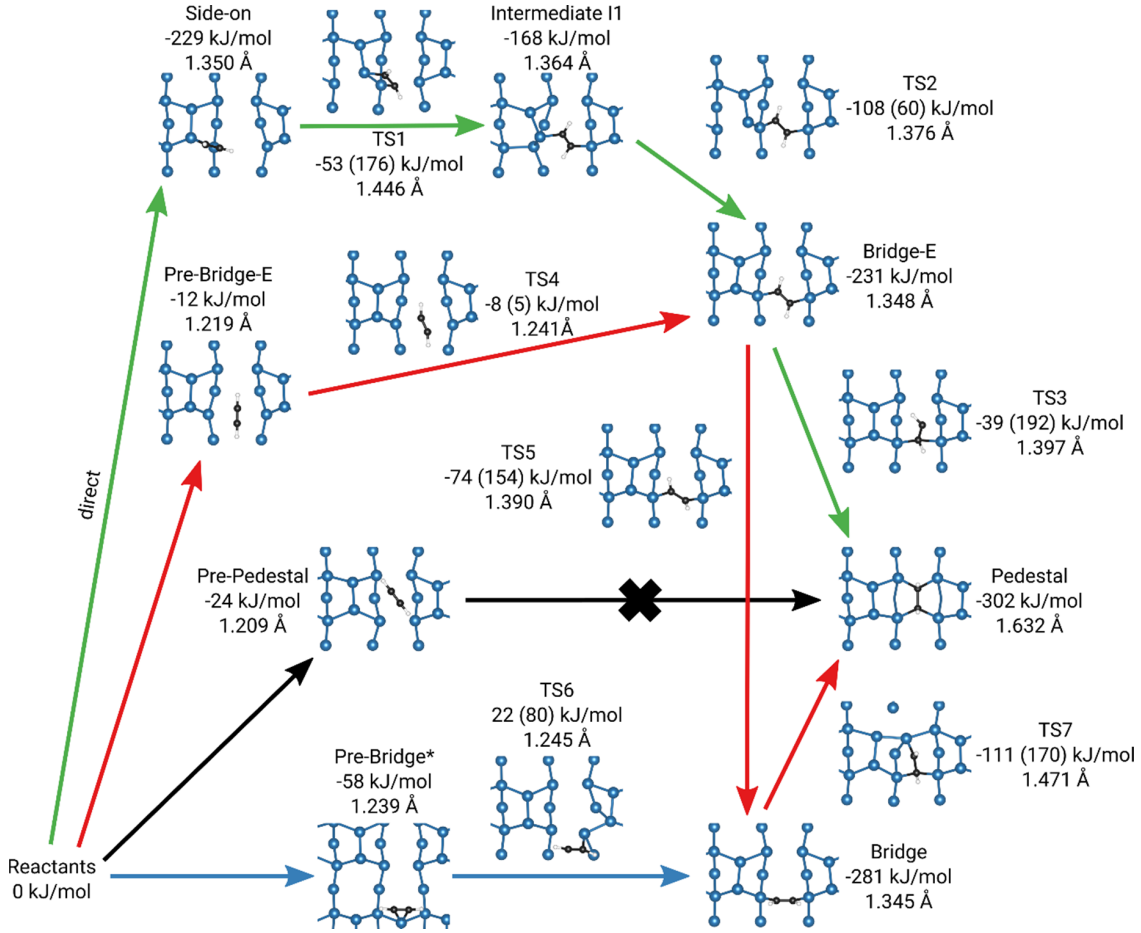

Figure 7. Reaction network of acetylene on the DV-defect. Energies are given relative to the isolated surface and molecule without thermodynamic corrections. Barriers are reported in parentheses and C−C bond lengths in Å. The major reaction path following the lowest transition states is highlighted in red. The pre-bridge structure (∗) is not a stable minimum but a TS between two subsurface modes.[23]

with desorption, and molecules in side-on are kinetically trapped at lower temperatures.

While the bridge mode (blue arrows) is rather stable, its transition state (**TS6**) is 30 kJ/mol higher than that of the bridge-*E* isomer (**TS4**). Furthermore, *E*,*Z*-isomerization is favored (**TS5** = 154 kJ/mol) over the barrier leading to pedestal (**TS3** = 192 kJ/mol). Thus, the path connecting both bridge modes (red arrows) with intermediate **I1** emerges as the minimum energy pathway. The highest barrier in the pathway marked in red (**TS7**) amounts to 170 kJ/mol, which is in the same order of magnitude as other mode-conversion reactions (e.g., **TS1**, **TS3**). In summary, the acetylene + DV reaction network shows that adsorption into side-on is direct, while most other modes have small initial barriers. In contrast, paths between modes as well as into the thermodynamic sink (pedestal) require a larger activation energy.

Cyclooctyne. A reaction network has not been calculated for cyclooctyne. However, based on the analysis for acetylene and the adsorption energies computed (Table 2) some qualitative predictions can be made. Direct adsorption into the pedestal mode remains improbable even for the strained alkyne since the preparation energy is not reduced sufficiently. In all other modes, RSE can be released which is expected to decrease initial adsorption barriers or remove them altogether. However, due to this additional stabilization, barriers between modes will likely be higher than for acetylene.

Ethylene. In the case of ethylene, the reaction mechanism is similar for all pathways leading from the free molecule to the pedestal mode which is also the most stable structure here (Figure 8). Upon initial adsorption and independently of adsorption mode, two new C−Si connections are formed while the C═C bond is reduced to a single bond. Cleavage of the remaining C−C σ-bond is then facilitated by nucleophilic attack of a defect-Si atom. However, distance and angle of attack are generally constrained by the underlying substrate. The resulting high barriers make the final steps toward dissociation rate determining. Similar to acetylene, no direct adsorption of ethylene into the pedestal mode was found (black arrows). Of the initially accessible intermediates, bridge is the most stable with −190 kJ/mol. Further reaction toward the thermodynamic sink (blue arrows) requires overcoming a large barrier of 284 kJ/mol. The corresponding **TS13** is particularly unfavorable due to the occurrence of pentavalent Si. In contrast, the reaction paths running through the side-on (green arrows) and pedestal-same (red arrows) modes have barriers that are about 100 kJ/mol smaller. While a shorter C−C distance makes **TS10** (2.24 Å) more stable than **TS12** (2.40 Å) in absolute terms, all studied rate-determining saddle points have positive energies with respect to the free reactants. When

https://dx.doi.org/10.1021/acs.jpcc.1c00262
J. Phys. Chem. C 2021, 125, 5635−5646

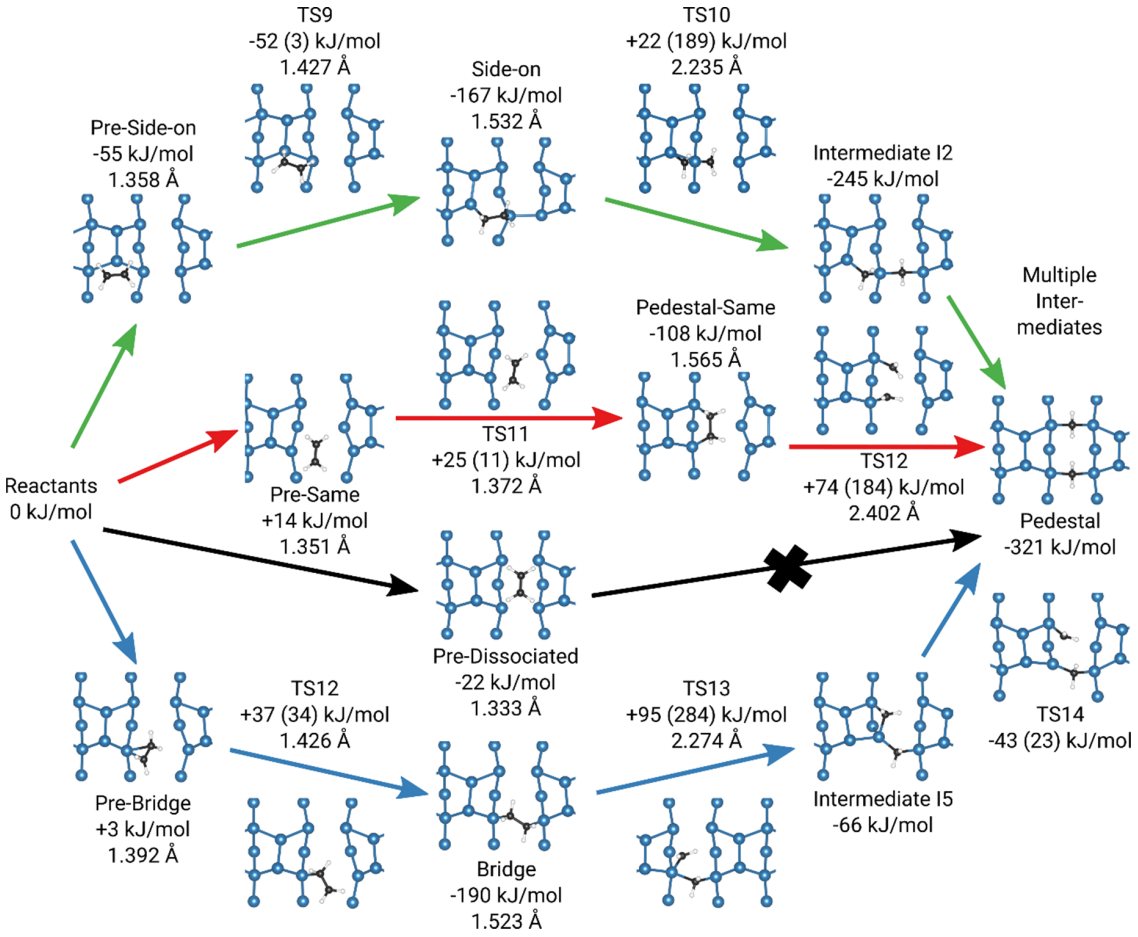

Figure 8. Reaction network of ethylene on the DV-defect. Electronic energies are given relative to the isolated surface and molecule. Barriers are given in parentheses and the central C−C bond length in Å. The reaction path following the lowest transition states is highlighted in red.

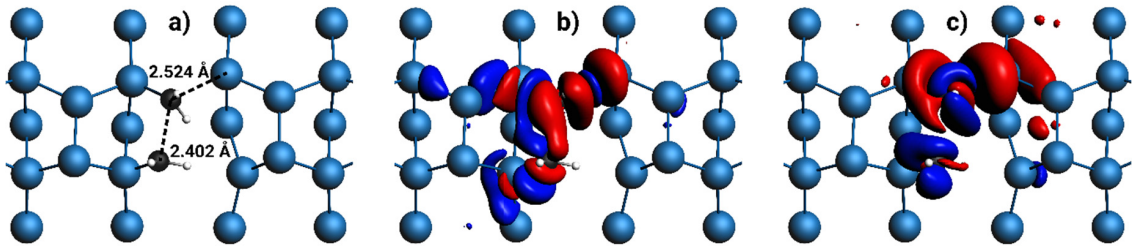

Figure 9. Analysis of **TS12**. (a) TS structure with selected bond lengths. (b) $\Delta\rho(\alpha_3) = -78$ kJ/mol ($\nu = 0.432$, iso = 0.0002): formation of the third C−Si bond. (c) $\Delta\rho(\beta_3) = -83$ kJ/mol ($\nu = 0.446$, iso = 0.0002): donation of density into the former C−C σ^*-bond. Not shown are $\Delta\rho_1$ and $\Delta\rho_2$ as they correspond to the two shared-electron C−Si bonds which are not of interest here.

considering Gibbs energies, TS energies become even more positive by 60 kJ/mol (pedestal-same, on-top)[20] to 63 kJ/mol (pedestal) and therefore desorption of ethylene is kinetically increasingly favored at high temperatures. Since at low temperatures reactions will stop at their respective predissociation intermediates (side-on, pedestal-same, bridge), adjustment to the correct temperature range is critical for dissociating ethylene. However, under ultrahigh vacuum conditions, equilibration between desorption and dissociation is expected to be slow. Therefore, ethylene is inferior to acetylene for saturating all defect atoms via the pedestal mode.

Apart from saturating the defect, the cleavage of C═C double-bonds at semiconductor point defects could potentially have applications in heterogeneous catalysis. Thus, **TS12** situated between the pedestal-same and pedestal modes warrants further investigation.

In a previous study, we found a S_N2-type attack of Si(001) surface-dimer atoms to cleave an ether bond in tetrahydrofuran and diethyl ether.[56] There, an upcoming orbital contribution, as manifested in deformation densities, stabilizes the TS of the nucleophilic attack. For the present case, similar contributions can be found (Figure 9, Table S5). When decomposed by spin, formation of the new Si−C bond (Figure 9b) and weakening of the former C−C bond (Figure 9c) contribute about equally. The resulting barrier of C═C cleavage at the DV (184 kJ/mol) lies between unassisted (377 kJ/mol, experimental

https://dx.doi.org/10.1021/acs.jpcc.1c00262
J. Phys. Chem. C 2021, 125, 5635−5646

enthalpy)[62] and Fe-catalyzed (117 kJ/mol, B3LYP calculation)[63] dissociation energies in molecules. Thus, defects on semiconductor surfaces could play a role for catalytic cleavage of carbon−carbon bonds when questions such as detaching the resulting fragments are solved.

CONCLUSION

We show, in agreement with earlier results, that the bonded dimer vacancy in which defect atoms form new single bonds is the most stable intrinsic point defect on Si(001). However, it is still accompanied by significant structural strain and the appearance of additional occupied bands in the band gap. These bands show low dispersion, suggesting reduced electron mobility with respect to the defect-free case. Reaction networks of unsaturated hydrocarbons, ethylene and acetylene as model adsorbates and cyclooctyne as interface building block, show much richer surface chemistry which is nevertheless limited to the defect itself. Neighboring dimers react in the same way as on the pristine surface. Surprisingly, we find the DV to be less reactive than the Si-dimer on the pristine surface. Barriers are only found toward adsorption modes incorporating defect atoms, such as bridge and pedestal. Those barriers, while small, likely appear as a result of absent dangling bonds. However, adsorption involving dimer atoms (side-on, on-top) is largely direct and can be stepwise transformed into the thermodynamically favored defect modes. Cyclooctyne shows larger steric hindrance in its reaction with the rather small defect cavity. On a more technical note, we show that isolated point defects require larger supercells and thicker slabs.

Thus, the DV exhibits a different reactivity than surrounding surface dimers. This fact might be used by molecules that selectively react with the surface dimers and not the defect. Subsequently deposited molecules which do react with the DV can then be used to introduce different desired functionalities already in the first ad-layer. Furthermore, this analysis of the electronic structure and reactivity of the surface defect can inspire more realistic computational models and thus help develop new approaches for solving challenges encountered in the organic functionalization of semiconductors and interface chemistry.

ASSOCIATED CONTENT

Supporting Information

The Supporting Information is available free of charge at https://pubs.acs.org/doi/10.1021/acs.jpcc.1c00262.

Converged slab-supercell of the dimer vacancy, benchmark of the partial Hessian approach, reconstructing a partial Hessian from fragment calculations, bonding analysis of the defect−Si-Si bond, electronic structure of the flipped dimer, crystal orbitals of the pristine surface, hydrogen precovered surfaces, dispersion induced bending, side-on comparison to sublayer adsorption, pEDA of **TS12**, raw data archive (PDF)

AUTHOR INFORMATION

Corresponding Author

Ralf Tonner − *Fachbereich Chemie, Philipps-Universität Marburg, Marburg D-35032, Germany; Wilhelm-Ostwald-Institut für Physikalische und Theoretische Chemie, Universität Leipzig, Leipzig D-04103, Germany;* orcid.org/0000-0002-6759-8559; Email: ralf.tonner@uni-leipzig.de

Author

Jan-Niclas Luy − *Fachbereich Chemie, Philipps-Universität Marburg, Marburg D-35032, Germany; Wilhelm-Ostwald-Institut für Physikalische und Theoretische Chemie, Universität Leipzig, Leipzig D-04103, Germany*

Complete contact information is available at: https://pubs.acs.org/10.1021/acs.jpcc.1c00262

Funding

This research was funded by Deutsche Forschungsgemeinschaft (DFG) through SFB 1083 (Grant No. 223848855). Computational resources were provided by HLRS Stuttgart, CSC Frankfurt, HRZ Marburg, and RZ Regensburg.

Notes

The authors declare no competing financial interest.

ACKNOWLEDGMENTS

J-N.L. thanks Fabian Pieck for helpful discussions.

REFERENCES

(1) Kumah, D. P.; Ngai, J. H.; Kornblum, L. Epitaxial oxides on semiconductors: From fundamentals to new devices. *Adv. Funct. Mater.* **2020**, *30*, 1901597.

(2) Song, L.; Yu, X.; Yang, D. A review on graphene-silicon Schottky junction interface. *J. Alloys Compd.* **2019**, *806*, 63−70.

(3) Loget, G. Water oxidation with inhomogeneous metal-silicon interfaces. *Curr. Opin. Colloid Interface Sci.* **2019**, *39*, 40−50.

(4) Sundberg, P.; Karppinen, M. Organic and inorganic-organic thin film structures by molecular layer deposition: A review. *Beilstein J. Nanotechnol.* **2014**, *5*, 1104−1136.

(5) Meng, X. An overview of molecular layer deposition for organic and organic-inorganic hybrid materials: Mechanisms, growth characteristics, and promising applications. *J. Mater. Chem. A* **2017**, *5*, 18326−18378.

(6) Zhou, H.; Bent, S. F. Molecular layer deposition of functional thin films for advanced lithographic patterning. *ACS Appl. Mater. Interfaces* **2011**, *3*, 505−511.

(7) Yoshinobu, J. Physical properties and chemical reactivity of the buckled dimer on Si(100). *Prog. Surf. Sci.* **2004**, *77*, 37−70.

(8) Leftwich, T. R.; Teplyakov, A. V. Cycloaddition reactions of phenylazide and benzylazide on a Si(100)-2 × 1 surface. *J. Phys. Chem. C* **2008**, *112*, 4297−4303.

(9) Pecher, L.; Schober, C.; Tonner, R. Chemisorption of a strained but flexible molecule: Cyclooctyne on Si(001). *Chem. - Eur. J.* **2017**, *23*, 5459−5466.

(10) Mette, G.; Dürr, M.; Bartholomäus, R.; Koert, U.; Höfer, U. Real-space adsorption studies of cyclooctyne on Si(001). *Chem. Phys. Lett.* **2013**, *556*, 70−76.

(11) Länger, C.; Heep, J.; Nikodemiak, P.; Bohamud, T.; Kirsten, P.; Höfer, U.; Koert, U.; Dürr, M. Formation of Si/organic interfaces using alkyne-functionalized cyclooctynes- precursor-mediated adsorption of linear alkynes versus direct adsorption of cyclooctyne on Si(001). *J. Phys.: Condens. Matter* **2018**, *31*, 034001.

(12) Glaser, T.; Meinecke, J.; Länger, C.; Luy, J.-N.; Tonner, R.; Koert, U.; Dürr, M. Combined XPS and DFT investigation of the adsorption modes of methyl enol ether functionalized cyclooctyne on Si(001). *ChemPhysChem* **2021**, *22*, 404.

(13) Luy, J.-N.; Molla, M.; Pecher, L.; Tonner, R. Efficient hierarchical models for reactivity of organic layers on semiconductor surfaces. *J. Comput. Chem.* **2021**, DOI: 10.1002/jcc.26503.

(14) Raschke, M. B.; Höfer, U. Influence of steps and defects on the dissociative adsorption of molecular hydrogen on silicon surfaces. *Appl. Phys. B: Lasers Opt.* **1999**, *68*, 649−655.

(15) Mazzone, A. Acetylene adsorption onto Si(100): A study of adsorption dynamics and of surface steps. *Comput. Mater. Sci.* **2006**, *35*, 6−12.
(16) Hata, K.; Kimura, T.; Ozawa, S.; Shigekawa, H. How to fabricate a defect free Si(001) surface. *J. Vac. Sci. Technol., A* **2000**, *18*, 1933−1936.
(17) Oh, S.-C.; Kim, K.-W.; Mamun, A. H.; Lee, H.-J.; Hahn, J. R. Role of coverage and vacancy defect in adsorption and desorption of benzene on Si(001)-2 × n surface. *Bull. Korean Chem. Soc.* **2010**, *31*, 162−167.
(18) Martin, J. A.; Savage, D. E.; Moritz, W.; Lagally, M. G. Structure, stability, and origin of (2×*n*) phases on Si(100). *Phys. Rev. Lett.* **1986**, *56*, 1936−1939.
(19) Mette, G.; Schwalb, C.; Dürr, M.; Höfer, U. Site-selective reactivity of ethylene on clean and hydrogen precovered Si(001). *Chem. Phys. Lett.* **2009**, *483*, 209−213.
(20) Pecher, L.; Mette, G.; Dürr, M.; Tonner, R. Site-specific reactivity of ethylene at distorted dangling-bond configurations on Si(001). *ChemPhysChem* **2017**, *18*, 357−365.
(21) Sorescu, D. C.; Jordan, K. D. Theoretical study of the adsorption of acetylene on the Si(001) surface. *J. Phys. Chem. B* **2000**, *104*, 8259−8267.
(22) Pecher, L.; Tonner, R. Precursor states of organic adsorbates on semiconductor surfaces are chemisorbed and immobile. *ChemPhysChem* **2017**, *18*, 34−38.
(23) Pecher, L.; Tonner, R. Bond insertion at distorted Si(001) subsurface atoms. *Inorganics* **2018**, *6*, 17.
(24) Taylor, P. A.; Wallace, R. M.; Cheng, C. C.; Weinberg, W. H.; Dresser, M. J.; Choyke, W. J.; Yates, J. T. Adsorption and decomposition of acetylene on silicon(100)-(2 × 1). *J. Am. Chem. Soc.* **1992**, *114*, 6754−6760.
(25) Cho, J.-H.; Kleinman, L. Adsorption kinetics of acetylene and ethylene on Si(001). *Phys. Rev. B: Condens. Matter Mater. Phys.* **2004**, *69*, 075303.
(26) Miotto, R.; Ferraz, A. C.; Srivastava, G. P. Acetylene adsorption on the Si(001) surface. *Phys. Rev. B: Condens. Matter Mater. Phys.* **2002**, *65*, 075401.
(27) Pecher, L.; Schmidt, S.; Tonner, R. Modeling the complex adsorption dynamics of large organic molecules: Cyclooctyne on Si(001). *J. Phys. Chem. C* **2017**, *121*, 26840−26850.
(28) Agard, N. J.; Prescher, J. A.; Bertozzi, C. R. A strain-promoted [3 + 2] azide-alkyne cycloaddition for covalent modification of biomolecules in living systems. *J. Am. Chem. Soc.* **2004**, *126*, 15046−15047.
(29) Münster, N.; Nikodemiak, P.; Koert, U. Chemoselective layer-by-layer approach utilizing click reactions with ethynylcyclooctynes and diazides. *Org. Lett.* **2016**, *18*, 4296−4299.
(30) Roberts, N.; Needs, R. J. Total energy calculations of missing dimer reconstructions on the silicon (001) surface. *J. Phys.: Condens. Matter* **1989**, *1*, 3139−3143.
(31) Kirichenko, T. A.; Banerjee, S. K.; Hwang, G. S. Interaction of neutral vacancies and interstitials with the Si(001) surface. *Phys. Rev. B: Condens. Matter Mater. Phys.* **2004**, *70*, 045321.
(32) Wang, J.; Arias, T. A.; Joannopoulos, J. D. Dimer vacancies and dimer-vacancy complexes on the Si(100) surface. *Phys. Rev. B: Condens. Matter Mater. Phys.* **1993**, *47*, 10497−10508.
(33) Fu, C.-C.; Weissmann, M.; Saul, A. Diffusion pathways for Si ad-dimers on Si(001): A high temperature molecular dynamics study. *Surf. Sci.* **2001**, *481*, 97−104.
(34) Owen, J.; Bowler, D.; Goringe, C.; Miki, K.; Briggs, G. Identification of the Si(001) missing dimer defect structure by low bias voltage STM and LDA modelling. *Surf. Sci.* **1995**, *341*, L1042−L1047.
(35) Sueoka, K.; Kamiyama, E.; Spiewak, P.; Vanhellemont, J. Review properties of intrinsic point defects in Si and Ge assessed by density functional theory. *ECS J. Solid State Sci. Technol.* **2016**, *5*, P3176−P3195.
(36) Kirichenko, T. A.; Banerjee, S. K.; Hwang, G. S. Mechanisms of monovacancy annihilation and type-A defect creation on Si(001)-2 × 1. *Surf. Sci.* **2004**, *555*, 187−192.
(37) Hamers, R. J.; Köhler, U. K. Determination of the local electronic structure of atomic sized defects on Si(001) by tunneling spectroscopy. *J. Vac. Sci. Technol., A* **1989**, *7*, 2854−2859.
(38) Yu, S.-Y.; Kim, H.; Koo, J.-Y. Extrinsic nature of point defects on the Si(001) surface: Dissociated water molecules. *Phys. Rev. Lett.* **2008**, *100*, 036107.
(39) Okano, S.; Oshiyama, A. A new alternative model of type-C defects on Si(100) surfaces. *Surf. Sci.* **2004**, *554*, 272−279.
(40) Kresse, G.; Hafner, J. Ab initio molecular dynamics for liquid metals. *Phys. Rev. B: Condens. Matter Mater. Phys.* **1993**, *47*, 558.
(41) Kresse, G.; Furthmüller, J. Efficiency of ab-initio total energy calculations for metals and semiconductors using a plane-wave basis set. *Comput. Mater. Sci.* **1996**, *6*, 15.
(42) Kresse, G.; Furthmüller, J. Efficient iterative schemes for ab initio total-energy calculations using a plane-wave basis set. *Phys. Rev. B: Condens. Matter Mater. Phys.* **1996**, *54*, 11169−11186.
(43) Perdew, J. P.; Burke, K.; Ernzerhof, M. Generalized gradient approximation made simple. *Phys. Rev. Lett.* **1996**, *77*, 3865−3868.
(44) Kresse, G.; Joubert, D. From ultrasoft pseudopotentials to the projector augmented-wave method. *Phys. Rev. B: Condens. Matter Mater. Phys.* **1999**, *59*, 1758−1775.
(45) Grimme, S.; Antony, J.; Ehrlich, S.; Krieg, H. A consistent and accurate ab initio parametrization of density functional dispersion correction (DFT-D) for the 94 elements H-Pu. *J. Chem. Phys.* **2010**, *132*, 154104.
(46) Grimme, S.; Ehrlich, S.; Goerigk, L. Effect of the damping function in dispersion corrected density functional theory. *J. Comput. Chem.* **2011**, *32*, 1456−1465.
(47) Boyd, D. R. J. Infrared spectrum of trideuterosilane and the structure of the silane molecule. *J. Chem. Phys.* **1955**, *23*, 922−926.
(48) Henkelman, G.; Uberuaga, B. P.; Jónsson, H. A climbing image nudged elastic band method for finding saddle points and minimum energy paths. *J. Chem. Phys.* **2000**, *113*, 9901−9904.
(49) Henkelman, G.; Jónsson, H. A dimer method for finding saddle points on high dimensional potential surfaces using only first derivatives. *J. Chem. Phys.* **1999**, *111*, 7010−7022.
(50) Raupach, M.; Tonner, R. A periodic energy decomposition analysis method for the investigation of chemical bonding in extended systems. *J. Chem. Phys.* **2015**, *142*, 194105.
(51) *BAND*, version 2019; SCM, Theoretical Chemistry; Vrije Universiteit: Amsterdam, The Netherlands, 2019.
(52) Van Lenthe, E.; Baerends, E. J. Optimized Slater-type basis sets for the elements 1−118. *J. Comput. Chem.* **2003**, *24*, 1142−1156.
(53) Philipsen, P. H. T.; van Lenthe, E.; Snijders, J. G.; Baerends, E. J. Relativistic calculations on the adsorption of co on the (111) surfaces of Ni, Pd, and Pt within the zeroth-order regular approximation. *Phys. Rev. B: Condens. Matter Mater. Phys.* **1997**, *56*, 13556−13562.
(54) Mitoraj, M. P.; Michalak, A.; Ziegler, T. A Combined Charge and Energy Decomposition Scheme for Bond Analysis. *J. Chem. Theory Comput.* **2009**, *5*, 962−975.
(55) Bondi, A. Van der Waals volumes and radii. *J. Phys. Chem.* **1964**, *68*, 441−451.
(56) Pecher, L.; Laref, S.; Raupach, M.; Tonner, R. Ethers on Si(001): A prime example for the common ground between surface science and molecular organic chemistry. *Angew. Chem., Int. Ed.* **2017**, *56*, 15150−15154.
(57) Dunnington, B. D.; Schmidt, J. R. Generalization of Natural Bond Orbital analysis to periodic Systems: Applications to solids and surfaces via plane-wave density functional theory. *J. Chem. Theory Comput.* **2012**, *8*, 1902−1911.
(58) Okada, H.; Fujimoto, Y.; Endo, K.; Hirose, K.; Mori, Y. Detailed analysis of scanning tunneling microscopy images of the Si(001) reconstructed surface with buckled dimers. *Phys. Rev. B: Condens. Matter Mater. Phys.* **2001**, *63*, 195324.

https://dx.doi.org/10.1021/acs.jpcc.1c00262
J. Phys. Chem. C 2021, 125, 5635−5646

(59) Rosenow, P.; Tonner, R. Extent of hydrogen coverage of Si(001) under chemical vapor deposition conditions from ab initio approaches. *J. Chem. Phys.* **2016**, *144*, 204706.
(60) Pecher, L.; Schmidt, S.; Tonner, R. Dispersion-mediated steering of organic adsorbates on a precovered silicon surface. *Beilstein J. Org. Chem.* **2018**, *14*, 2715−2721.
(61) Zhu, X. Y.; Huang, X. J. SiH_2 adsorption on the single dimer vacancy of the Si(100) surface. *J. Phys.: Condens. Matter* **2006**, *18*, 7045−7050.
(62) Blanksby, S. J.; Ellison, G. B. Bond dissociation energies of organic molecules. *Acc. Chem. Res.* **2003**, *36*, 255−263.
(63) Holthausen, M. C.; Fiedler, A.; Schwarz, H.; Koch, W. How does Fe^+ activate C-C and C-H bonds in ethane? A theoretical investigation using density functional theory. *J. Phys. Chem.* **1996**, *100*, 6236−6242.

https://dx.doi.org/10.1021/acs.jpcc.1c00262
J. Phys. Chem. C 2021, 125, 5635−5646

Organic Functionalization at the Si(001) Dimer Vacancy Defect – Structure, Bonding and Reactivity

Supporting Information

Jan-Niclas Luy[1,2] and Ralf Tonner[1,2]*

[1]Fachbereich Chemie, Philipps-Universität Marburg, Hans-Meerwein-Straße 4, D-35032 Marburg
[2]Wilhelm-Ostwald-Institut für Physikalische und Theoretische Chemie, Universität Leipzig, Linnéstraße 2, D-04103 Leipzig
*Correspondence: ralf.tonner@uni-leipzig.de; Tel.: +49-341-97-36401

Table of contents

1. Converged slab-supercell of the dimer vacancy

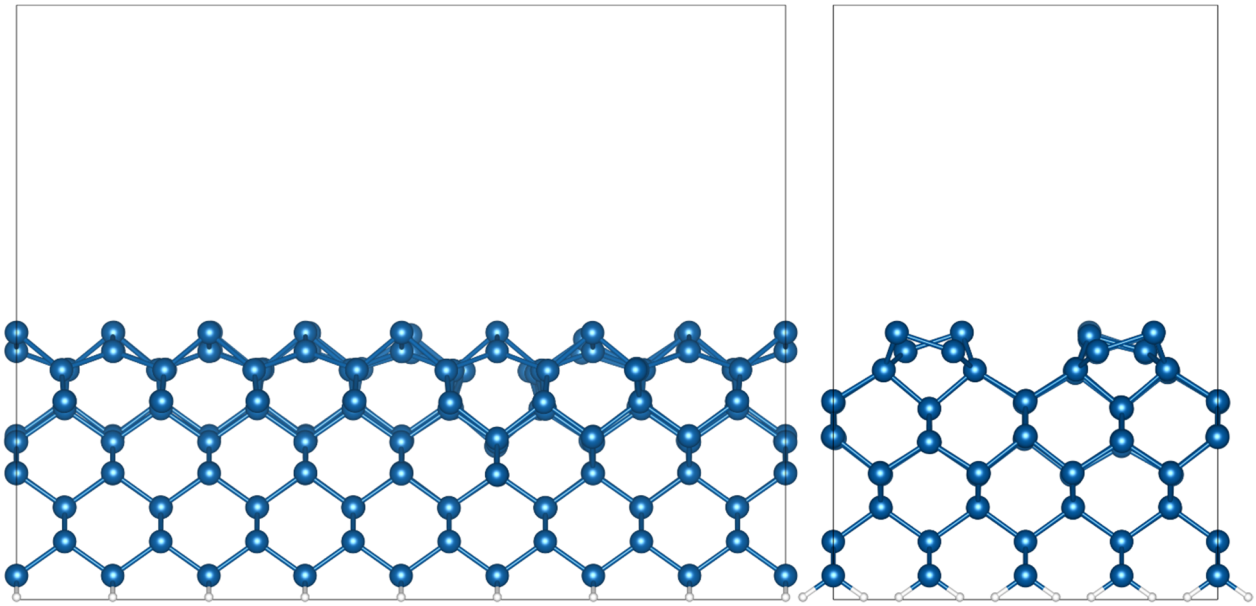

Figure S1. View along *x*- & *y*-axes of the 8×4 supercell with 8 layers including a DV defect.

180

2. Benchmark of the partial Hessian approach

Table S1. Adsorption free energy of acetylene in the *pedestal* mode (8×4 supercell, 8-layer slab). Free energies are generated from a partial Hessian with the finite difference method. While the total electronic energy is calculated for the whole system, only a few atoms are displaced in the finite difference approach. Energies for calculations with fewer reduced atoms are reported relative to the largest one (130 atoms). For a covalently bound adsorbate, all individual energy terms are already well converged for the combined first and second neighbor shells (18 atoms).

Atoms included in the construction of the partial Hessian	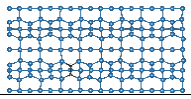	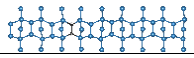			
kJ/mol, 300 K	**130 atoms [a]**	**Δ 58 atoms [b]**	**Δ 18 atoms [c]**	**Δ 8 atoms [d]**	**Δ Molecule only**
ΔE_{ads}	-302	0	0	0	0
ΔE_{ZPE}	17	0	-1	-3	-7
ΔCv_{trans}(0->T)	-4	0	0	0	0
ΔCv_{rot}(0->T)	-3	0	0	0	0
ΔCv_{vib}(0->T)	0	0	0	1	3
$\Delta(Cv->Cp)$	-3	0	0	0	0
ΔH_{ads}	-294	0	-1	-1	-4
ΔTS_{trans}	-45	0	0	0	0
ΔTS_{rot}	-14	0	0	0	0
ΔTS_{vib}	-3	0	0	3	6
$-\Delta TS_{tot}$	61	0	0	-3	-6
ΔG_{ads}	-233	0	-1	-4	-10
ΔG_{ads}- ΔE_{ads}	69	0	-1	-4	-10

[a] Molecule & first four layers.
[b] Molecule & first three layers of the defect-containing Si-dimer row.
[c] Molecule & first and second neighbor shell.
[d] Molecule & first neighbor shell.

In order to calculate thermodynamic corrections from the VASP output, python scripts were written which use the thermochemistry module of ASE 3.17.0.[1] These scripts were published elsewhere.[2]

3. Reconstructing a partial Hessian from fragment calculations

This script allows for a trivial parallelization of the finite difference approach implemented in VASP. In addition, frequency calculations can be restarted.

```
#!/usr/bin/env python3
#ATTENTION constrained atoms MUST be at end of the POSCAR
#OUTCARs have to be renamed starting from OUTCAR1 in the same order of fragmentation
#Atomic masses are not identical to those used in VASP
import os
import sys
import numpy as np
import pickle
import glob
import time
from math import sin, pi, sqrt, log
from ase.utils import basestring
import ase.units as units
from ase.io import write, read
from ase.parallel import rank, paropen
def read_forces(atoms, all=False):
    """Method that reads forces from OUTCAR file.
    If 'all' is switched on, the forces for all ionic steps
    in the OUTCAR file be returned, in other case only the
    forces for the last ionic configuration is returned."""
    file = open(filename, 'r')
    lines = file.readlines()
    file.close()
    n = 0
    if all:
        all_forces = []
    for line in lines:
        if line.rfind('TOTAL-FORCE') > -1:
            forces = []
            for i in range(len(atoms)):
                forces.append(np.array([float(f) for f in
                                        lines[n + 2 + i].split()[3:6]]))
            if all:
                all_forces.append(np.array(forces))
        n += 1
    if all:
        return np.array(all_forces)
    else:
        return np.array(forces)
def read_potim():
    potim = None
    for line in open(filename):
        if line.find('POTIM') != -1:
            potim = float(line.split('=')[1].split()[0].strip())
    return potim
def readc(log=sys.stdout):#Full Hessian
    delta=read_potim()
    atoms=read(filename)
    n = int(g/2)
    natoms=int(n/3)
    rang=range(natoms)
    indices=np.asarray(rang)
    #Hessian computation
    H = np.empty((n, n))
    r = 0
    for a in range(0,n*2,2):
        with open("force" + str(a+1)+".pckl", 'rb') as fm:
            fminus = pickle.load(fm)
            #print(fminus)
        with open("force" + str(a+2)+".pckl", 'rb') as fp:
            fplus = pickle.load(fp)
        H[r] = .5 * (fminus - fplus)[indices].ravel()
        H[r] /= (2*delta)
        r += 1
    H += H.copy().T #Symmetrization
    m = atoms.get_masses()
    im = np.repeat((m[indices])**-0.5, 3)
```

```
    omega2, modes = np.linalg.eigh(im[:, None] * H * im)#mass scaled hessian
    # Conversion factor:
    s = units._hbar * 1e10 / sqrt(units._e * units._amu)
    hnu = s * (omega2*-1).astype(complex)**0.5#Swap sign of eigval. In eV
    #Write results to file
    if isinstance(log, basestring):
        log = paropen(log, 'a')
    write = log.write
    s = 1/units.invcm
    write('---------------------\n')
    write('  #    meV     cm^-1\n')
    write('---------------------\n')
    for n, e in enumerate(hnu):
        if e.imag != 0:
            c = 'i'
            e = e.imag
        else:
            c = ' '
            e = e.real
        write('%3d %6.1f%s  %7.1f%s\n' % (n+1, 1000 * e, c, s * e, c))
    write('---------------------\n')
g = 0 #global counter
files=len(glob.glob('OUTCAR*'))
#Iterate over OUTCARs
for x in range(files):
    filename=('OUTCAR' + str(x+1))
    atoms = read(filename)
    all_forces=read_forces(atoms,all)
    forces=all_forces[1:len(all_forces)]
    dof=len(forces)
    #Output forces to machine readable format
    for i in range(dof):
        force=forces[i]
        pickle_out = paropen("force" + str(g+1)+".pckl","wb")
        pickle.dump(force, pickle_out)
        pickle_out.close()
        #test=open("force" + str(g+1)+".pckl","rb")
        #exa=pickle.load(test)
        #print(exa)
        g += 1
readc(log='frequencies')
#Cleanup
for f in glob.glob('*.pckl'):
    os.remove(f)
```

4. Bonding analysis of the Si-Si bond at DV

Table S2. EDA-NOCV results for the DV compared to disilane in a cluster model (Figure S2). Values for DV represent two Si-Si bonds and thus need to be divided by 2 to be comparable to Disilane.

	DV[d]		**Disilane**[e]	
	kJ/mol	**%**	**kJ/mol**	**%**
ΔE_{int}	-381		-322	
ΔE_{int}(disp)[b]	-55	14	-6	2
ΔE_{int}(elec)[b]	-328	86	-316	98
ΔE_{Pauli}	377		381	
ΔE_{elstat}[c]	-235	33	-348	50
ΔE_{orb}[c]	-470	67	-348	50
	v	***E***	***v***	***E***
NOCV(α1)	0.753	-119	0.461	-162
NOCV(α2)	0.556	-78	0.057	-5
NOCV(α3)	0.107	-10	0.057	-5
NOCV(β1)	0.757	-111	0.461	-162
NOCV(β2)	0.543	-79	0.057	-5
NOCV(β3)	0.105	-10	0.057	-5

[a] All energies in kJ/mol at PBE-D3(BJ)/TZ2P. Fragments are generated from homolytic cleavage at Si-Si into neutral triplets. [b] Percentage values: Relative contributions of dispersion and electronic effects to the interaction energy ΔE_{int}. [c] Percentage values: Relative contributions between the attractive EDA terms ΔE_{elstat} and ΔE_{orb}. [d] Program version: ADF 2017. Values are given for breaking two Si-Si bonds [e] Program version: BAND 2016.

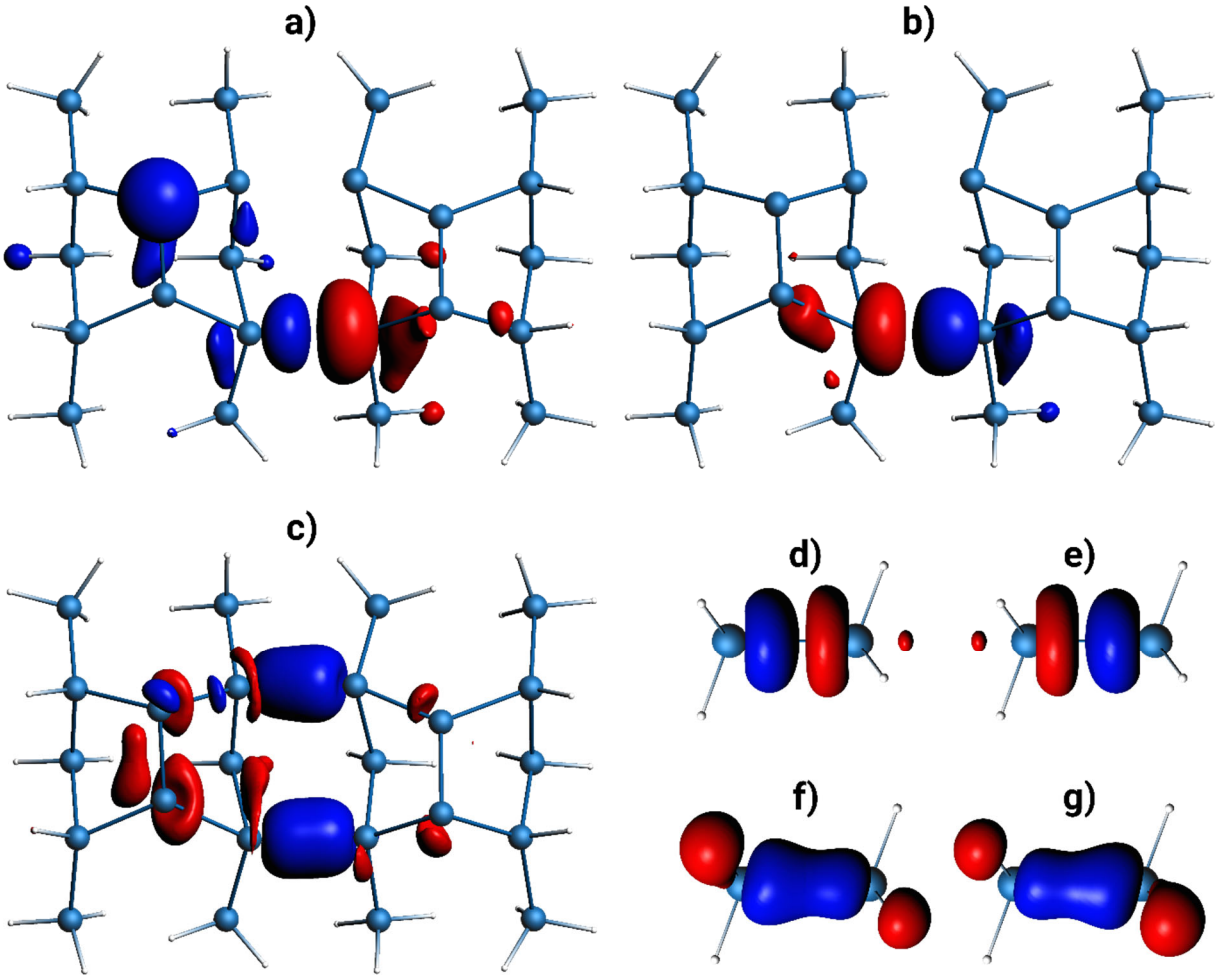

Figure S2. a)-c): Major deformation densities for a cluster model of the DV allowing for cleavage of the Si-Si bond at the defect. Both fragments are in a triplet reference state. Blue: Charge accumulation, red: Charge depletion. a) NOCV-α1 (iso=0.002). b) NOCV-β2 (iso=0.002). Nearly degenerate NOCVs of similar shape also exist at the other bond and are not shown here. c) NOCV-α3 (iso=0.0002). d)/e) NOCV-α1/β1 of disilane (iso=0.002). f)/g) NOCV-α2/β2 of disilane (iso=0.00002).

For shared-electron bonds, EDA-NOCV analysis usually gives two contributions in both spin channels α and β. This is also the case here. Bond strengths can be estimated from the sum of energy contributions for these two channels.
The principal deformation densities of the cluster show two, slightly polarized, shared-e^- σ–Si-Si-bonds of -198 kJ/mol (NOCV(α1) plus NOCV(β2)) and -189 kJ/mol (NOCV(α2) plus NOCV(β1)). Defect atoms bonded to a Si_{down} receive less electrons since some charge is transferred to the neighboring Si_{up}. Comparison to the EDA-NOCV of disilane reveals two visually matching deformation densities of -324 kJ/mol (NOCV(α1) plus NOCV(β1)).

Furthermore, natural bond orbitals[3] are found between the defect atoms in the periodic slab model. The occupation of these orbitals is 1.86 and the bond is polarized approximately 59% to 41% in favor of the atoms connected to a Si_{down} atom.

5. Electronic structure of the flipped dimer

Table S3. Γ-only pEDA comparison of C_2H_4 donor/acceptor complexes on the pristine surface (4×4 cell) and on the flipped dimer (8×4 cell) indicating the Lewis-acid character of the dimer.

	C_2H_4 on flipped dimer		**C_2H_4 on pristine Si(001)[4]**		**BH_3 on flipped dimer**		**BH_3 on pristine Si(001)[5]**	
	kJ/mol	**%**	**kJ/mol**	**%**	**kJ/mol**	**%**	**kJ/mol**	**%**
ΔE_{int}	-71		-113		-179		-170	
ΔE_{int}(disp)[b]	-28	39	-28	25	10	6	-11	6
ΔE_{int}(elec)[b]	-43	61	-85	75	-169	94	-159	94
ΔE_{Pauli}	274		707		405		400	
ΔE_{elstat}[c]	-149	47	-366	46	-170	29	-162	29
ΔE_{orb}[c]	-168	53	-426	54	-403	71	-397	71
ΔE_{prep}[d]	15		31		50		37	
ΔE_{bond}	-56		-82		-129		-133	
ΔE_{bond}(PAW)[e]	-55		-74					

[a] All energies in kJ/mol at PBE-D3(BJ)/TZ2P. Fragments are generated from homolytic cleavage at C-Si into neutral triplets. [b] Percentage values: Relative contributions of dispersion and electronic effects to the interaction energy ΔE_{int}. [c] Percentage values: Relative contributions between the attractive EDA terms ΔE_{elstat} and ΔE_{orb}. [d] Preparation energies contain structural contributions and electronic excitations. [e] Deviations with respect to the PAW result are due basis set and simulation cell set-up differences.

6. Crystal orbitals of the pristine surface

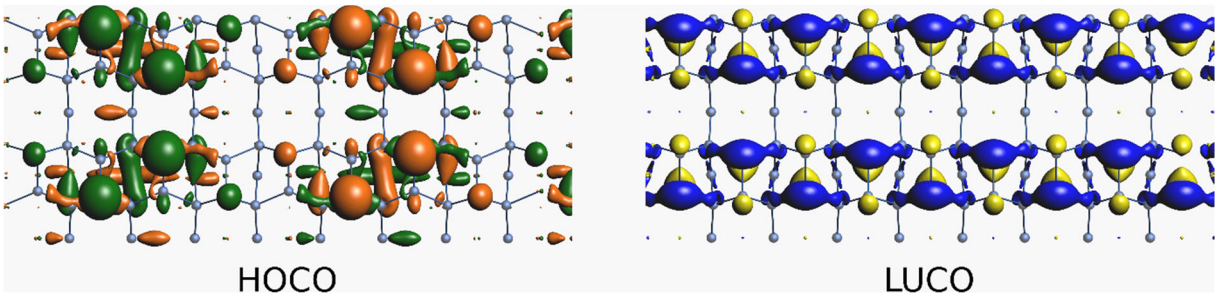

Figure S3. Doubly degenerate HOCO (left) and LUCO (right) of the pristine Si(001) surface in the 8×4 supercell at the Γ-point.

7. Hydrogen-precovered surface

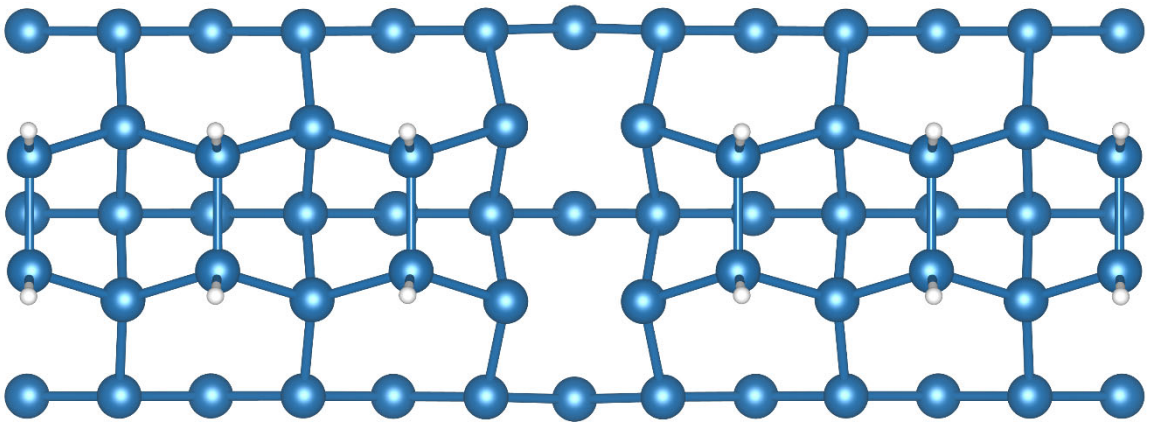

Figure S4. 6. H:Si(001) including DV: Si(001) precovered with hydrogen atoms at every dimer atom.

Table S4. Impact of hydrogen-precoverage on adsorption energies of H_2 and acetylene at the DV.

adsorbate	**adsorption mode**	**ΔE_{ads} (Si(001) with DV)**	**ΔE_{ads} (H:Si(001) with DV)**	**$\Delta\Delta E$**
H_2	*on-top*	-166	blocked	
	pedestal[b]	-95	-104	-9
	bridge	-91	-86	+6
acetylene	*pedestal*	-302	-316	-14
	bridge	-281	-277	+4
	side-on	-229	blocked	

[a] All energies in kJ/mol computed with PBE-D3(BJ)/PAW.
[b] Calculated per H_2. *Pedestal* requires four H atoms in total to be saturated.

8. Dispersion induced bending

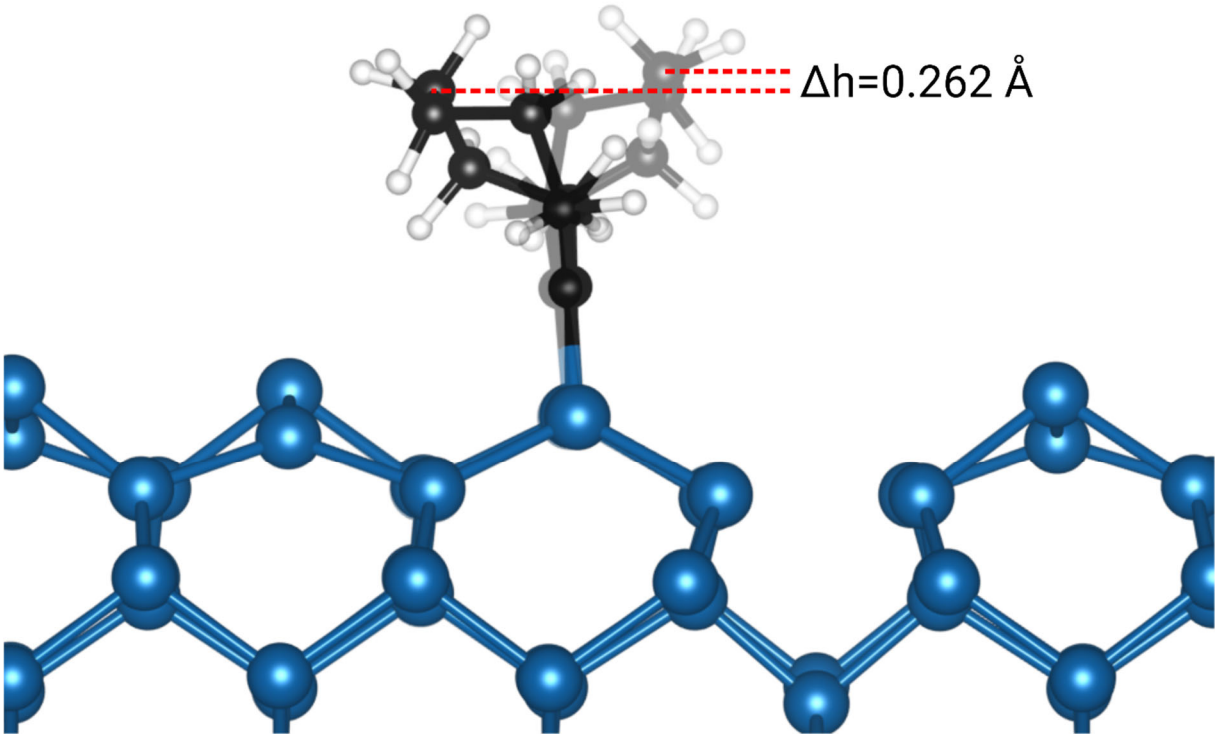

Figure S5. Bending of the cyclooctyne molecule in *on-top* mode towards the defect and away from it.

9. *Side-on* comparison to sublayer adsorption

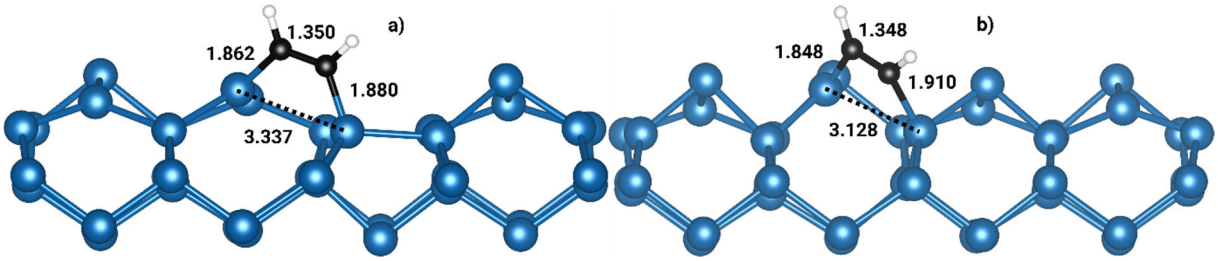

Figure S6. Comparison between acetylene *side-on* adsorption **(a)** and sub-surface insertion **(b)**.

10. pEDA of **TS12**

Table S5. Γ-only pEDA of ethylene at **TS12** in the 8×4 cell.

	TS12	
	kJ/mol	**%**
ΔE_{int}	-753	
ΔE_{int}(disp)[b]	-36	5
ΔE_{int}(elec)[b]	-717	95
ΔE_{Pauli}	2019	
ΔE_{elstat}[c]	-1155	42
ΔE_{orb}[c]	-1581	58
ΔE_{prep}	828	
ΔE_{prep}(M)[d]	728	
ΔE_{prep}(S)[d]	101	
ΔE_{bond}	76	
ΔE_{bond}(PAW)[e]	74	

[a] All energies in kJ/mol at PBE-D3(BJ)/TZ2P. Fragments are generated from homolytic cleavage at C-Si into neutral triplets. [b] Percentage values: Relative contributions of dispersion and electronic effects to the interaction energy ΔE_{int}. [c] Percentage values: Relative contributions between the attractive EDA terms ΔE_{elstat} and ΔE_{orb}. [d] Preparation energies of the molecule (M) and substrate (S) contain structural contributions and electronic excitations. [e] Deviations with respect to the PAW result are due basis set and simulation cell set-up differences.

11. Raw data archives

Raw input and output data may be accessed through the NOMAD archive and Zenodo.

DOI: https://dx.doi.org/10.17172/NOMAD/2021.01.07-1

DOI: https://doi.org/10.5281/zenodo.4536020

12. References

1. Larsen, A. H. et al. The atomic simulation environment-a python library for working with atoms. *J. Phys. Condens. Matter.* **2017**, *29*, 273002.

2. Heep, J.; Luy, J.-N.; Länger, C.; Meinecke, J.; Koert, U.; Tonner, R.; Dürr, M. Adsorption of methyl-substituted benzylazide on Si(001): Reaction channels and final configurations. *J. Phys. Chem. C* **2020**, *124*, 9940–9946.

3. Dunnington, B. D.; Schmidt, J. R. Generalization of Natural Bond Orbital analysis to periodic Systems: Applications to solids and surfaces via plane-wave density functional theory. *J. Chem. Theory Comput.* **2012**, *8*, 1902–1911.

4. Pecher, L.; Tonner, R. Precursor states of organic adsorbates on semiconductor surfaces are chemisorbed and immobile. *ChemPhysChem* **2017**, *18*, 34–38.

5. Raupach, M. Quantenchemische Untersuchungen zur chemischen Bindung an Oberflächen. Dissertation, Philipps Universität Marburg, 2015.

Appendix B

Manuscripts: Organic / Metal

Permissions to reprint full-text publications have been obtained from the right holders where necessary.

Template-controlled on-surface synthesis of a lanthanide supernaphthalocyanine and its open-chain polycyanine counterpart: Copyright (2019) The Authors.

Influence of ring contraction on the electronic structure of nickel tetrapyrrole complexes: corrole versus porphyrin: Copyright (2020) The Authors. Published on behalf of The Electrochemical Society by IOP Publishing Limited.

On-surface formation of a transient corrole radical and aromaticity-driven interfacial electron transfer: Copyright (2020) American Chemical Society.

nature COMMUNICATIONS

ARTICLE

https://doi.org/10.1038/s41467-019-13030-7 OPEN

Template-controlled on-surface synthesis of a lanthanide supernaphthalocyanine and its open-chain polycyanine counterpart

Qitang Fan[1], Jan-Niclas Luy[1], Martin Liebold[1], Katharina Greulich[1], Malte Zugermeier[1], Jörg Sundermeyer[1], Ralf Tonner[1*] & J. Michael Gottfried[1*]

Phthalocyanines possess unique optical and electronic properties and thus are widely used in (opto)electronic devices, coatings, photodynamic therapy, etc. Extension of their π-electron systems could produce molecular materials with red-shifted absorption for a broader range of applications. However, access to expanded phthalocyanine analogues with more than four isoindoline units is challenging due to the limited synthetic possibilities. Here, we report the controlled on-surface synthesis of a gadolinium-supernaphthalocyanine macrocycle and its open-chain counterpart poly(benzodiiminoisoindoline) on a silver surface from a naphthalene dicarbonitrile precursor. Their formation is controlled by the on-surface high-dilution principle and steered by different metal templates, i.e., gadolinium atoms and the bare silver surface, which also act as oligomerization catalysts. By using scanning tunneling microscopy, photoemission spectroscopy, and density functional theory calculations, the chemical structures along with the mechanical and electronic properties of these phthalocyanine analogues with extended π-conjugation are investigated in detail.

[1] Department of Chemistry, Philipps-Universität Marburg, Hans-Meerwein-Straße 4, 35032 Marburg, Germany. *email: tonner@chemie.uni-marburg.de; michael.gottfried@chemie.uni-marburg.de

Porphyrins, the "colors of life," play important roles in many biological processes[1–3]. The planar porphyrin macrocycle consists of four pyrrole subunits linked by methine groups and bears an 18 π-electron-conjugated inner ring system, which shows a strong absorption band in the visible region, the Q-band, corresponding to the π-π* transition[4–6]. This band determines the optical and electronic properties that are relevant for applications in coating, optics, and semiconductor technology[7]. Gaining control over the various physical properties of porphyrinoids thus requires the size-tuning of the π-conjugated chromophore. Extension of the π-electron system results in a bathochromic shift of the Q-band. This extension can be achieved by increasing the number of annulated peripheral benzene rings or the number of pyrrole subunits. The latter approach has inspired the chemistry of expanded porphyrins[6,8–10], in which extended porphyrinoid macrocyles with intriguing physical properties, such as pentaphyrin, hexaphyrin, and heptaphyrin, have been synthesized[11–13]. This approach paves the way towards sophisticated molecular materials, in particular infrared-absorbing chromophores and third-order nonlinear optical materials[14,15], which are interesting for various applications in optoelectronics, optical limiting[16], digital data storage[17], and photodynamic therapy[18–20].

Phthalocyanines (Pcs) are benzo-annulated tetraazaporphyrins, in which the meso-methine units (CH) in porphyrin are replaced by nitrogen. Due to this nitrogen doping, they possess modified properties compared to their porphyrin counterparts. Therefore, changing the number of π-conjugated isoindoline units in Pcs can produce molecular materials with properties that cannot be achieved by the corresponding expanded (or contracted) porphyrins. While the synthesis of contracted boron sub-Pcs with three isoindoline units is well established[21], the development of expanded Pcs is impeded by the limited synthetic possibilities[22–24]. The only known example is uranyl-superphthalocyanine $SPcU(O)_2$[25,26], comprising five isoindoline units, which has been synthesized from phthalonitrile in the presence of large uranium template ions in solution. Apart from this unique case, the reaction of phthalonitriles with other large metal ions such as lanthanide ions typically results in the formation of bis(phthalocyaninato) double-decker complexes rather than five-fold symmetric single-decker super-Pcs[27–29]. Similarly challenging is the synthesis of isoindoline polymers, that is, the open-chain counterparts of Pcs. Typically, Pc macrocycles are the thermodynamically favored products of metal-catalyzed cyclizations of phthalonitriles in solution[30]. Poly(isoindolines) appear as poorly characterized by-products in the synthesis of poly(Pcs) or poly(triazines)[31–34]. Isolation and characterization of well-defined poly(isoindolines) has not been achieved; only isoindoline dimers or trimers have been reported as intermediates in the synthesis of Pcs[35,36]. Related polymers from aliphatic dinitriles have only rarely been reported[37].

In recent years, it has been demonstrated that the co-deposition of *ortho*-dicarbonitriles with metal atoms (manganese[38,39], iron[40]) on surfaces can result in macrocyclization and formation of regular Pcs. Expanding on this approach, we employ differently sized metal templates (iron, gadolinium, and a silver surface) for the synthesis of iron-naphthalocyanine (Fe-NPc), the expanded gadolinium-supernaphthalocyanine (Gd-SNPc), and their unique open-chain counterpart poly(benzodiiminoisoindoline) (here named "polycyanine") from a 5,5,8,8-tetramethyl-5,6,7,8-tetrahydroanthracene-2,3-dicarbonitrile (ADN) building block on a Ag(111) surface (Fig. 1a). The general concept behind this approach is illustrated in

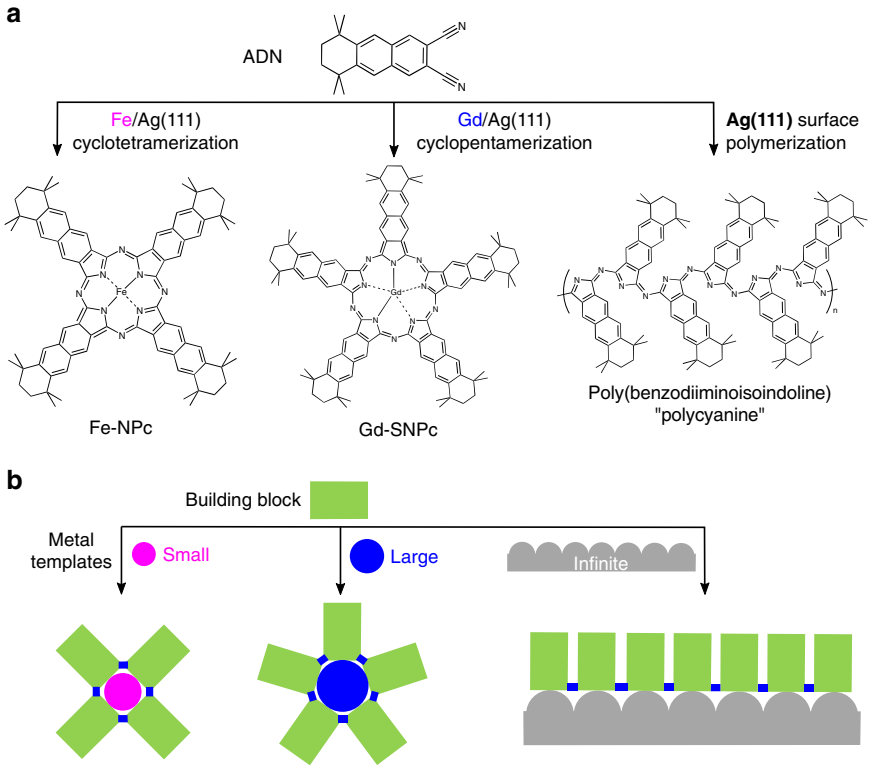

Fig. 1 Reaction scheme and concept. **a** Reactions of the precursor monomer 5,5,8,8-tetramethyl-5,6,7,8-tetrahydroanthracene-2,3-dicarbonitrile (ADN) with different metal templates (Fe, Gd) on Ag(111), resulting in the formation of iron-naphthalocyanine (Fe-NPc) and gadolinium-supernaphthalocyanine (Gd-SNPc). Using the bare Ag(111) surface as a laterally extended template leads to surface-catalyzed polymerization and formation of poly(benzodiiminoisoindoline), here named polycyanine. **b** On-surface template approach: control over the topology of the reaction products is achieved by using differently sized metal templates in 2D confinement

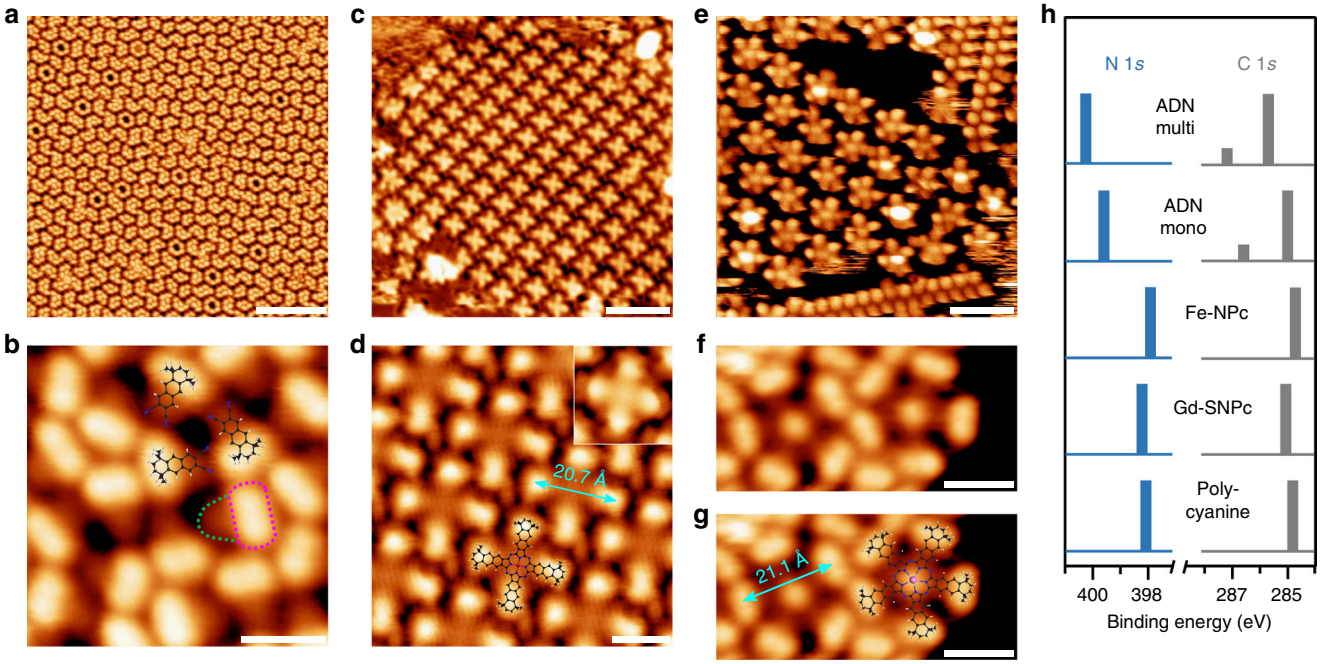

Fig. 2 On-surface synthesis of Fe-NPc and Gd-SNPc. **a** STM image taken after vapor deposition of a monolayer of the precursor ADN onto Ag(111) at 300 K. **c**, **e** STM images taken after subsequent deposition of a low coverage of iron (0.13 ML) and gadolinium (0.06 ML), respectively, on the ADN monolayer followed by annealing to 450 K. **b**, **d**, **f** Magnified views of the samples in **a**, **c**, **e**, respectively. Molecular models of ADN and Fe-NPc are overlaid in **b**, **d**. The inset in **d** shows Fe-NPc imaged with the tunneling parameters $U = 1.2$ V, $I = 0.3$ nA. **g** shows **f** overlaid with a molecular model of Gd-SNPc. Black spheres represent carbon atoms; blue, nitrogen; white, hydrogen; red, iron; pink, gadolinium. Tunneling parameters: **a**, **b**, $U = -3.6$ V, $I = 0.08$ nA; **c**, $U = 1.2$ V, $I = 0.3$ nA; **d**, $U = 1.9$ V, $I = 0.13$ nA; **e**, $U = 0.76$ V, $I = 0.11$ nA; **f**, **g**, $U = -3.6$ V, $I = 0.11$ nA. Scale bars, **a**, 10 nm; **b**, **d**, **f**, **g**, 1.5 nm; **c**, 6 nm; **e**, 4 nm. **h** Binding energies of C 1s (gray) and N 1s (blue) XPS signals for ADN multi- and monolayers, Fe-NPc, Gd-SNPc, and polycyanine chains. The original XP spectra are shown in Supplementary Fig. 1

Fig. 1b: the small (Fe[40]), large (Gd[41–43]), and the infinite (silver surface) templates coordinate different numbers (four, five, and infinite) of building blocks that become eventually covalently connected. The benefits of the on-surface approach are apparent: the two-dimensional (2D) confinement posed by the surface allows only in-plane coordination of ligands with the metal. This results in the formation of the single-decker Gd-SNPc pentamer macrocycle rather than a bis(phthalocyaninato) double-decker complex. The perhaps most surprising advantage of this approach is that it enables the high-yield synthesis of isoindoline polymers, that is, polycyanine chains. The extended $[\text{-C}=\text{N-}]_n$ π-conjugated backbone of the polycyanine chain reported here makes it an intriguing model for an organic semiconducting polymer with an absorption band in the visible range.

Results

On-surface synthesis of Fe-NPc and Gd-SNPc. The scanning tunneling microscope (STM) image in Fig. 2a shows a typical domain of an ADN monolayer (ML) on a Ag(111) surface. The magnified image in Fig. 2b reveals repeated structural motifs with an elongated bright protrusion (magenta dotted contour) and a weak tail (green dotted contour). Considering the chemical structure of ADN, the bright saddle and the weak tail are attributed to the tetramethyl-cyclohexane and the naphthalene dicarbonitrile moieties, respectively, as illustrated by the overlaid molecular models. The assignment to intact ADN is confirmed by the XP spectra taken on precisely the same sample as the STM images. The related X-ray photoelectron spectroscopy (XPS) binding energies (BEs) are summarized in Fig. 2h and the original spectra are shown in the Supplementary Fig. 1. The ML C 1*s* spectrum ("ADN mono") shows a major and a minor component with BEs of 285.0 and 286.6 eV, respectively. Due to a higher electronegativity of nitrogen compared to hydrogen and carbon, the C 1*s* signal of the -C≡N group has a higher BE than that of the tetramethyl-tetrahydroanthracene backbone. Therefore, the major and minor components are related to the carbon atoms in tetramethyl-tetrahydroanthracene and carbonitrile (-C≡N) groups of ADN, respectively. The related N 1*s* spectrum shows a single peak at 399.6 eV, in agreement with the value of 399.5 eV reported for nitrogen in a -C≡N…H hydrogen bonding situation[44].

Vapor deposition of 0.13 ML iron atoms onto this ADN ML at 300 K, followed by annealing to 450 K, results in the formation of an iron-naphthalocyanine species with four tetramethyl-cyclohexane groups (Fe-NPc, Fig. 1a), as indicated by the cross-shaped features in Fig. 2c. The molecular structure has been confirmed by STM and XPS, as will be discussed in the following. First, the C 1*s* signal of the Fe-NPc sample in Fig. 2c shows only one peak at 284.7 eV (Fig. 2g and Supplementary Fig. 1). Compared to the spectrum of intact ADN, the disappearance of the -C≡N-related component supports the transformation from the -C≡N groups in ADN to the pyrrole and aza groups in Fe-NPc. Further evidence is provided by the related N 1*s* signal, which shifts towards lower BE by 1.7 eV upon formation of Fe-NPc. This result is consistent with the expected accumulation of negative charge at the N atoms when the dianionic naphthalocyanine ligand is formed. Based on the N 1*s* and C 1*s* spectra, it can be excluded that these cross-shaped objects are $Fe(ADN)_4$ coordination tetramers (Supplementary Fig. 2d) with four C≡N… Fe bonds, because four free -C≡N groups (along with four intact, but Fe-coordinated -C≡N groups) remain in a $Fe(TCNB)_4$ coordination tetramer. Second, the magnified view of the Fe-NPc layer (Fig. 1d and Supplementary Fig. 2e) reveals that each lobe of the cross-shaped species contains a bright protrusion at the

outer terminal resembling the appearance of the tetramethyl-cyclohexane group shown in Fig. 2b. In addition, the distance between two protrusions on opposite sides of the molecules is 20.7 ± 0.7 Å, in agreement with the expected value of 21.2 ± 0.2 Å (see Supplementary Fig. 2a–c)[45]. Notably, the Fe-NPc complexes in Fig. 2d do not show the Fe centers as protrusions, which is due to the high tip-sample bias of 1.9 V; reducing it to 1.2 V brightens the Fe center and the naphthalene moieties (inset in Fig. 2d).

In the formation of Fe-NPc, the iron atom acts both as a catalyst for the activation of -C≡N and as a template for coordinating the resulting isoindoline units. The small Fe atom has four in-plane coordination sites for -C≡N groups[40] and pyrrole ligands[40], which is consistent with the formation of a tetramer macrocycle. Using a much larger rare-earth metal, gadolinium, which allows for five in-plane coordination sites for -C≡N groups[43–45], enables the on-surface synthesis of the Gd-SNPc pentamer macrocycle, as indicated by the five-lobed pentamer structures in Fig. 2e. The sample in Fig. 2e was prepared by deposition of 0.06 ML Gd onto a complete ML of ADN, followed by annealing to 450 K. The structure of Gd-SNPc is corroborated by the following considerations: Fig. 2f shows the magnified STM image of the pentamer structure in Fig. 2e with high tunneling bias (−3.6 V, identical to that in Fig. 2b). It reveals that the pentamer consists of five axially arranged lobes surrounding a bright protrusion. The contour of each lobe resembles that of the tetramethyl-cyclohexane moiety of intact ADN (Fig. 2b). Therefore, the five lobes and the central bright protrusion are assigned to five tetramethyl-cyclohexane groups and the central Gd atom, respectively, as shown by the overlaid model in Fig. 2g. The distance between the two outermost lobes is 21.1 ± 0.5 Å (Fig. 2g), which agrees well with the expected distance of 21.2 ± 0.5 Å for Gd-SNPc (see Supplementary Fig. 4). Noteworthy, the different appearances of the five lobes of the pentamer structure in Fig. 2e, f arise from the different tunneling conditions. Similar to Fe-NPc (Fig. 2d, inset), imaging Gd-SNPc with a low positive bias of 0.76 V leads to the highlighting of the naphthalene backbone and the Gd metal center, as is illustrated by Fig. 2e. Conversely, a high negative bias (−3.6 V) results in the highlighting of the tetramethyl-cyclohexane moieties and the Gd center, as shown by Fig. 2f and Supplementary Fig. 5a (the latter presents a larger island of Gd-SNPc). Note that STM imaging is more difficult for Gd-SNPc than for Fe-NPc because the former has a five-fold symmetry. Since tiling of an Euclidian plane with regular pentagons is not possible, Gd-SNPc cannot form long-range ordered structures. The residual intermolecular space leads to increased lateral mobility and thus to a fuzzy appearance. The XPS data (Fig. 2h and Supplementary Fig. 1) prove the transformation of the -C≡N groups in ADN to the pyrrole and aza groups in Gd-SNPc with the same arguments as for Fe-NPc.

In order to compare the electronic properties between Fe-NPc and Gd-SNPc, we have calculated their frontier orbitals and the HOMO/LUMO (highest occupied molecular orbital/lowest unoccupied molecular orbital) gaps. The gap of Gd-SNPc is smaller by 0.32 eV than that of Fe-NPc, indicating a red-shifted absorption due to the extended π-conjugation pathway. As shown by Supplementary Figs. 17 and 18, the LUMOs of both Gd-SNPc and Fe-NPc are mixed ligand–metal orbitals. The SOMO of Gd-SNPc is mainly localized at the Gd(II) metal center, whereas the HOMO of Fe-NPc has predominant ligand character. Further details on the electronic structure of the two macrocycles can be found in the Supplementary Discussion.

On-surface synthesis of polycyanine chains. For both macrocycles, the size of the π-conjugated system is determined by the sizes of the metal–atom templates. The further extension of the π-system thus requires even larger templates (Fig. 1b). In the following, we demonstrate that the Ag(111) surface itself acts as a quasi-infinitely extended template for the polymerization of ADN. A prerequisite is a high surface concentration of ADN, because it favors the growth of polymer chains, whereas a low surface concentration favors cyclization, according to the on-surface high-dilution principle[46,47]. Therefore, an ADN multilayer was employed to maximize the concentration at the bottom-most layer on the Ag(111) surface during the reaction. The direct annealing of 5.8 layers of ADN (deposited at 300 K) to 450 K leads to the linear polymerization of ADN into polycyanine chains (Fig. 1a), as shown by the double-row-shaped chain structures in Fig. 3a. The excess ADN molecules desorb. The structure of this polycyanine chain was confirmed by morphological and spectroscopic evidence as discussed below.

Figure 3b displays the magnified view of an isolated polycyanine chain, revealing a repeat unit with features resembling the ADN molecule in Fig. 2b. These repeat units are connected alternatingly at their tails, indicating bonding at the positions of the former -C≡N groups. The periodicity and the width, that is, center–center distances of the bright oval protrusions of the chain, are 8.8 ± 0.5 and 15.1 ± 0.5 Å, respectively. These values agree with the density functional theory (DFT) calculated periodicity (8.6 Å) and width (14.9 Å) of the polycyanine chains adsorbed on Ag(111) (Fig. 3c). We can exclude that the chains represent assemblies of intact ADN molecules connected through coordination or van der Waals bonds, because this would lead to a much larger periodicity. The absence of -C≡N groups in the chains is further confirmed by the C 1*s* and N 1*s* spectra taken on the sample in Fig. 3a (see Fig. 2h and Supplementary Fig. 1). The covalent linking between the chain elements is also supported by lateral manipulation experiments with the STM tip. As shown in Fig. 4, complete chains can be moved across the surface or be reversibly deformed without disintegration, revealing high mechanical stability.

The chains extend along the high-symmetry directions of the substrate and have a periodicity of three times the Ag(111) surface lattice constant, that is, they show point-on-line commensurability with respect to the substrate (Supplementary Fig. 6). The free-standing chain optimized with density functional theory (DFT) on the GGA level including dispersion correction (PBE-D3) shows a lattice mismatch of only 0.4%, underlining the commensurate character (Supplementary Table 2). There is good agreement between the experimental and DFT-simulated STM images (Fig. 3d).

Discussion

Figure 5 shows the calculated electronic band structure of the chain and the related frontier crystal orbitals. Since the GGA approach is known to severely underestimate band gaps, a more reliable value of 2.0 eV is derived from range-separated hybrid density functional computations (HSE06)[48]. The calculated band gap corresponds to a visible-range absorption of ~600 nm. The effective mass of the lowest unoccupied crystal orbital (LUCO) is calculated to be 0.347, indicating that the free-standing polycyanine is a semiconducting polymer[49,50]. The LUCO is delocalized along the $[\text{-C=N-}]_n$ backbone and accordingly shows a large dispersion. Regarding the occupied bands, the two highest occupied crystal orbitals (HOCO, HOCO-1) are rather localized on the benzodiiminoisoindoline units and the N atoms, respectively. The lack of orbital overlap is in line with the low-dispersion nature of these bands. However, HOCO-2 and HOCO-3 show higher dispersion due to the moderate overlap of the non-bonding electron pairs at the nitrogen atoms.

There are two prerequisites for the on-surface formation of polycyanine chains. First, a high surface concentration of ADN

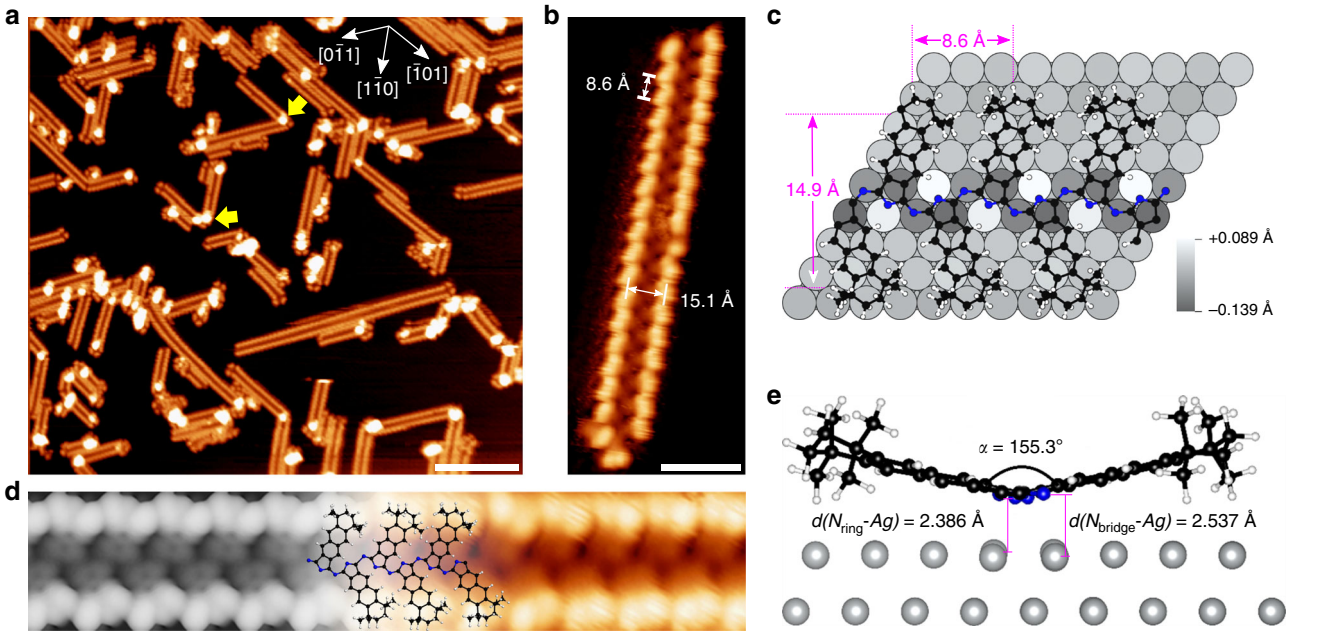

Fig. 3 On-surface synthesis of polycyanine chains. **a** Overview STM image of the polycyanine chains, taken after deposition of 5.8 layers of ADN on Ag(111) at 300 K followed by annealing to 450 K. The white vectors indicate the three high-symmetry directions of the substrate. The yellow arrows indicate protrusions attributed to chain segments that are uplifted for sterical reasons (see Supplementary Fig. 8 for details). **b** Magnified STM image of a single chain observed in the sample of **a**. **c**, **e** Top and side views of the DFT-calculated adsorption model of the polycyanine chain on a Ag(111) slab. The adsorbate-induced vertical displacement of the top-layer Ag atoms is illustrated with a gray scale in **c**. The distances of the N atoms in the pyrrole ring (N_{ring}) and the aza-bridging N atoms (N_{bridge}) with respect to the non-corrugated surface plane as well as the inter-plane angle α between the alternating benzodiiminoisoindoline moieties (see Supplementary Fig. 11 for a definition of α) are shown in **e**. **d** Comparison of the DFT-calculated (left) and experimental (right) STM images of the polycyanine chain on Ag(111). A molecular model of the polycyanine chain is overlaid in the central part. Black spheres represent carbon atoms; blue, nitrogen; white, hydrogen; gray, silver. Tunneling parameters: **a**, $U = -3.6$ V, $I = 0.14$ nA; **b**, $U = 0.20$ V, $I = 0.10$ nA; **d**, $U = 0.55$ V, $I = 0.06$ nA. Scale bars, **a**, 15 nm; **b**, 3 nm

monomers is necessary, because otherwise cyclic tetramer macrocycles are formed (Supplementary Fig. 7). Since ADN partially desorbs at the reaction temperature of 450 K, ensuring a sufficient surface concentration during the reaction requires initial deposition of a multilayer. Second, the non-planar tetramethyl-cyclohexane group in ADN is probably critical for a successful reaction. As shown by the DFT-calculated adsorption model in Fig. 3e, the benzodiiminoisoindoline unit has a tilted adsorption configuration. Surprisingly, the DFT-optimized structure of the free-standing chain shows that this tilt is an intrinsic feature, since a butterfly angle of $\alpha = 140.9°$ (Supplementary Table 2) is calculated, which is close to that of the adsorbed chain (155.3°, Fig. 3e). The tilted conformation optimizes the conjugation between the non-bonding electron pairs at the nitrogen atoms and the π-electron system of the chain (see the Supplementary Figs. 12–16 and the related discussion in the Supplementary Discussion). Without the bulky tetramethyl-cyclohexane unit in the ADN precursor, the chain would be forced to assume a planar adsorption geometry, which is energetically unfavorable. The side groups in the ADN precursor therefore help the chain to maintain its optimal conformation on the surface. The adsorption energy for a unit cell containing two former ADN units is computed to $E_{ads} = -378$ kJ mol^{-1}, which mainly comes from dispersion interactions (Supplementary Fig. 11). Nevertheless, bonding analysis of a model system (Supplementary Fig. 10) with an energy decomposition analysis for extended systems[51] shows that the nitrogen atoms in the pyrrole rings (N_{ring}) show considerable attractive electrostatic and orbital interaction with the surface—an indicator for directional dative bonding (Supplementary Table 1).

Further evidence for the bonding of N_{ring} to the Ag surface is provided by the adsorbate-induced vertical displacements of the top-layer Ag atoms (Fig. 3c). Remarkably, the two sets of nitrogen atoms have opposite effects: the N atoms in the pyrrole rings (N_{ring}) lift up the first-layer Ag atoms, revealing attractive bonding Ag-N_{ring} interactions. In contrast, the aza-bridging N atoms (N_{bridge}) push the Ag atoms into the surface, indicating repulsive interactions. The different bonding behavior of the two N species, which is confirmed by the different Ag-N distances shown in Fig. 3e, reveals an interesting analogy to the cyclic complexes, where only N_{ring} binds to the metal, but not N_{bridge}. This analogy can be taken even further, if the surface-to-chain electron transfer is considered: per unit cell, the chain receives 0.58 electrons (see Supplementary Fig. 10) from the surface, just as the cyclic ligands receive electron density from their metal centers. There is, however, also an important difference: the cyclic ligands receive two electrons from the metal center to establish a Hückel-aromatic 18π electron conjugation path, that is, they are dianions (see Supplementary Fig. 9). In contrast, there is no such requirement regarding the electron count along the open-chain conjugation path. Thus, the chain can remain formally neutral and only fractional electron transfer between surface and molecule occurs.

We have achieved the template-controlled on-surface synthesis of an iron-naphthalocyanine, a gadolinium-supernaphthalocyanine, and a poly(benzodiiminoisoindoline) chain on a silver (111) surface. These syntheses start from an *ortho*-dicarbonitrile monomer (ADN) and employ template effects of iron atoms, gadolinium atoms, and the bare silver (111) surface, respectively. They also take advantage of the on-surface high-dilution principle. The different sizes of the metal templates enable the coordination and covalent linkage of different numbers of ADN monomers. STM and DFT investigations reveal that the intrinsically non-planar, semiconducting poly(benzodiiminoisoindoline) chain is commensurate

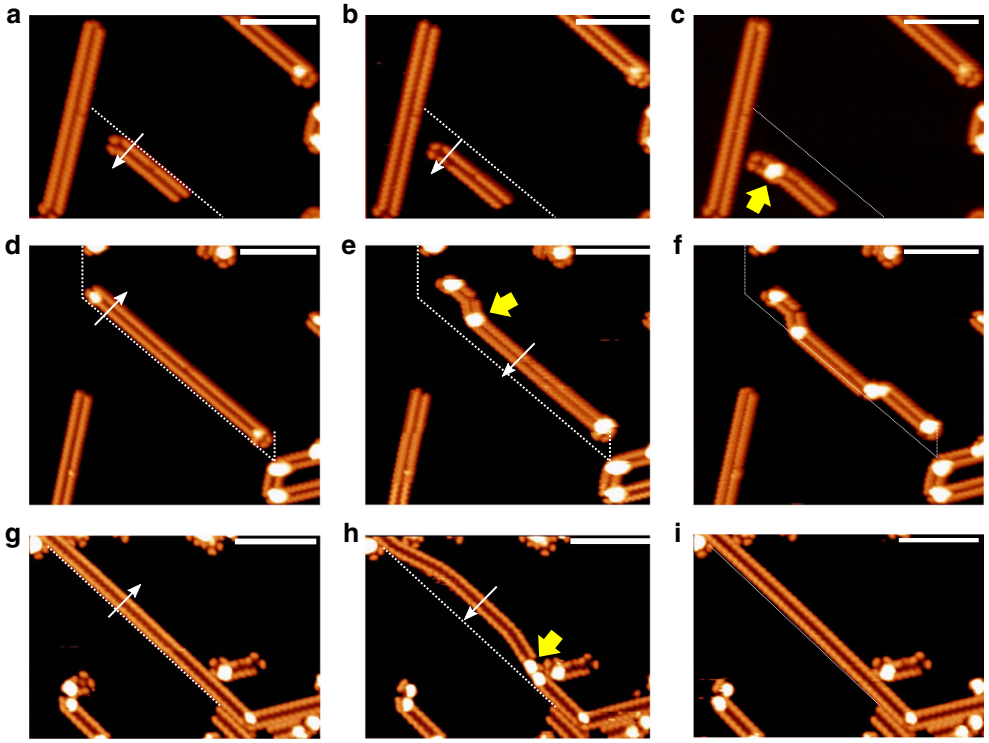

Fig. 4 STM images of lateral manipulation steps of polycyanine chains. The manipulations were performed with the STM tip at the positions and along the directions of the white arrows. The initial locations of the chains are indicated by the dashed lines. **a**, **b** Manipulation of a short isolated chain moves the entire chain across the surface, while retaining its orientation. **b**, **c** Additional manipulation of this chain leads to further displacement and formation of a bent with a bright protrusion (yellow arrow in **c**, which is attributed to an uplifted chain segment (see Supplementary Fig. 8). These protrusions are induced by sterical hindrance and also occur at sharp bends, that is, when a chain changes its orientation, as marked by yellow arrows in Fig. 3a. **d**–**f** Manipulation of a longer chain, resulting in the formation of bends with related protrusions, but no rupture of the chain. **g**–**i** Reversible manipulation of a chain anchored at both ends. The induced protrusions appearing in **h** are reversed by pushing in the opposite direction (see **i**). Tunneling parameters: **a**–**f**, $U = -3.6$ V, $I = 0.09$ nA; **g**–**i**, $U = -3.7$ V, $I = 0.12$ nA. All the scale bars are 10 nm

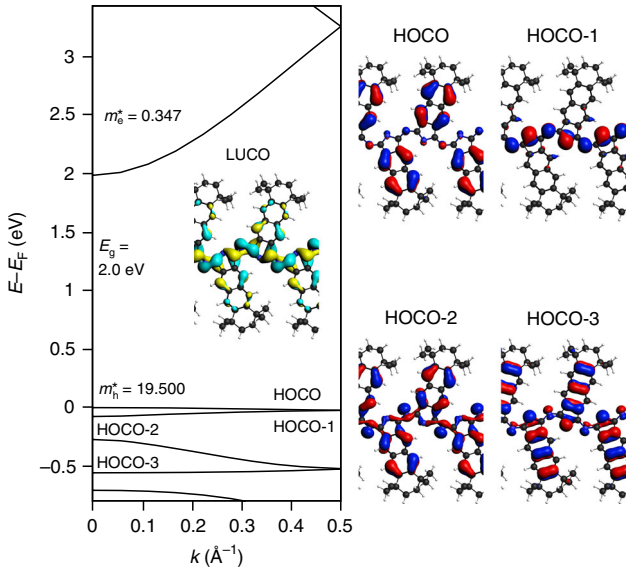

Fig. 5 Band structure and band gap (E_g, HSE06) of polycyanine chains. The crystal orbitals at the Γ-point (LUCO/HOCO: lowest unoccupied / highest occupied crystal orbital) are shown together with effective masses for electron (m_e^*) and hole (m_h^*)

with the Ag surface, shows high mechanical stability and flexibility, and has a small band gap. The extended π-conjugated backbone makes it a potential candidate for applications in optoelectronics. Therefore, the protocols reported in this study may pave the way for the discovery of multifunctional Pc-based molecular materials by control of the size of the π-conjugated system.

Methods

Synthesis. 5,5,8,8-Tetramethyl-5,6,7,8-tetrahydroanthracene-2,3-dicarbonitrile (ADN) was prepared by using a published procedure as described in the Supplementary Discussion. The details of the synthesis and characterization of ADN are also included in the Supplementary Discussion.

STM and XPS. Theory: Density functional theory (DFT) calculations were performed using the GGA-type PBE functional for the structural optimization including a semiempirical dispersion-correction term (DFT-D3). The band structure was derived with the range-separated hybrid functional HSE06. STM simulations used the Tersoff-Hamann approach. Details are found in the Supplementary Discussion.

STM measurements were performed in an ultrahigh vacuum (UHV) system (base pressure 1×10^{-10} mbar) equipped with a SPECS STM Aarhus 150 STM and a photoelectron spectrometer with SPECS Phoibos 150 electron energy analyzer. All bias voltages refer to the sample, and the images were recorded in constant current mode. Moderate filtering (Gaussian smooth, background subtraction) was applied for noise reduction. The Ag(111) single crystals with an alignment of better than 0.1° relative to the nominal orientation were purchased from MaTecK (Germany). Preparation of a clean and well-defined Ag(111) surface was achieved by cycles of bombardment with Ar^+ ions and annealing at 850 K. The ADN precursor was sublimed at 423 K in UHV from homebuilt Knudsen cell evaporators. Fe and Gd were deposited onto the ADN layer with a low flux of 0.04 nm/min, as measured with a quartz crystal microbalance. One monolayer of ADN, Fe, and Gd is defined as 0.047 ADN molecules, 1.31 Fe atoms, and 0.64 Gd atoms per surface Ag atom, respectively.

Data availability

The data supporting the findings of this study are available from the corresponding authors upon request.

Received: 13 April 2019; Accepted: 14 October 2019;
Published online: 06 November 2019

References

1. Kadish, K. M., Smith, K. M. & Guilard, R. *The Porphyrin Handbook* (Academic Press, New York, 2000).
2. Kadish, K. M., Smith, K. M. & Guilard, R. *Handbook of Porphyrin Science* (World Scientific Publishing, Singapore, 2010).
3. Gottfried, J. M. Surface chemistry of porphyrins and phthalocyanines. *Surf. Sci. Rep.* **70**, 259–379 (2015).
4. Kobayashi, N., Nakajima, S., Ogata, H. & Fukuda, T. Synthesis, spectroscopy, and electrochemistry of tetra-tert-butylated tetraazaporphyrins, phthalocyanines, naphthalocyanines, and anthracocyanines, together with molecular orbital calculations. *Chemistry* **10**, 6294–6312 (2004).
5. Sakamoto, K. & Ohno-Okumura, E. Syntheses and functional properties of phthalocyanines. *Materials* **2**, 1127–1179 (2009).
6. Jasat, A. & Dolphin, D. Expanded porphyrins and their heterologs. *Chem. Rev.* **97**, 2267–2340 (1997).
7. Furuyama, T., Ogura, Y., Yoza, K. & Kobayashi, N. Superazaporphyrins: meso-pentaazapentaphyrins and one of their low-symmetry derivatives. *Angew. Chem. Int. Ed.* **51**, 11110–11114 (2012).
8. Sessler, J. L. & Seidel, D. Synthetic expanded porphyrin chemistry. *Angew. Chem. Int. Ed.* **42**, 5134–5175 (2003).
9. Saito, S. & Osuka, A. Expanded porphyrins: Intriguing structures, electronic properties, and reactivities. *Angew. Chem. Int. Ed.* **50**, 4342–4373 (2011).
10. Stepien, M., Sprutta, N. & Latos-Grazynski, L. Figure eights, mobius bands, and more: conformation and aromaticity of porphyrinoids. *Angew. Chem. Int. Ed.* **50**, 4288–4340 (2011).
11. Sessler, J. L., Weghorn, S. J., Hiseada, Y. & Lynch, V. Hexaalkyl terpyrrole: a new building block for the preparation of expanded porphyrins. *Chem. Eur. J.* **1**, 56–67 (1995).
12. Sessler, J. L., Morishima, T. & Lynch, V. Rubyrin, ein neues, expandiertes hexapyrrolporphyrin. *Angew. Chem.* **103**, 1018–1020 (1991).
13. Sessler, J. L., Morishima, T. & Lynch, V. Rubyrin: a new hexapyrrolic expanded porphyrin. *Angew. Chem. Int. Ed.* **30**, 977–980 (1991).
14. de la Torre, G., Vazquez, P., Agullo-Lopez, F. & Torres, T. Phthalocyanines and related compounds: organic targets for nonlinear optical applications. *J. Mater. Chem.* **8**, 1671–1683 (1998).
15. Nalwa, H. S. & Miyata, S. *Nonlinear Optics of Organic Molecules and Polymers* (CRC Press, Boca Raton, 1997).
16. Perry, J. W. et al. Organic optical limiter with a strong nonlinear absorptive response. *Science* **273**, 1533–1536 (1996).
17. Matsuoka, M. *Infrared Absorbing Dyes* (Plenum Press, New York, 1990).
18. Bonnett, R. Photosensitizers of the porphyrin and phthalocyanine series for photodynamic therapy. *Chem. Soc. Rev.* **24**, 19–33 (1995).
19. Sternberg, E. D., Dolphin, D. & Bruckner, C. Porphyrin-based photosensitizers for use in photodynamic therapy. *Tetrahedron* **54**, 4151–4202 (1998).
20. Ali, H. & van Lier, J. E. Metal complexes as photo- and radiosensitizers. *Chem. Rev.* **99**, 2379–2450 (1999).
21. Claessens, C. G., Gonzalez-Rodriguez, D., Rodriguez-Morgade, M. S., Medina, A. & Torres, T. Subphthalocyanines, subporphyrazines, and subporphyrins: Singular nonplanar aromatic systems. *Chem. Rev.* **114**, 2192–2277 (2014).
22. Furuyama, T., Sato, T. & Kobayashi, N. A bottom-up synthesis of antiaromatic expanded phthalocyanines: Pentabenzotriazasmaragdyrins, i.e. Norcorroles of superphthalocyanines. *J. Am. Chem. Soc.* **137**, 13788–13791 (2015).
23. Matsushita, O. et al. Rectangular-shaped expanded phthalocyanines with two central metal atoms. *J. Am. Chem. Soc.* **134**, 3411–3418 (2012).
24. Remiro-Buenamanana, S. et al. Synthesis of meso-substituted subphthalocyanine-subporphyrin hybrids: boron subtribenzodiazaporphyrins. *Angew. Chem. Int. Ed.* **54**, 7510–7514 (2015).
25. Marks, T. J. & Stojakovic, D. R. Large metal ion-centered template reactions. Chemical and spectral studies of the "superphthalocyanine" dioxocyclopentakis(1-iminoisoindolinato)uranium(VI) and its derivatives. *J. Am. Chem. Soc.* **100**, 1695–1705 (1978).
26. Day, V. W., Marks, T. J. & Wachter, W. A. Large metal ion-centered template reactions. Uranyl complex of cyclopentakis(2-iminoisoindoline). *J. Am. Chem. Soc.* **97**, 4519–4527 (1975).
27. Wang, R. et al. Heteroleptic rare earth double-decker complexes with naphthalocyaninato and phthalocyaninato ligands. General synthesis, spectroscopic, and electrochemical characteristics. *Inorg. Chem.* **44**, 2114–2120 (2005).
28. Ng, D. K. P. & Jiang, J. Sandwich-type heteroleptic phthalocyaninato and porphyrinato metal complexes. *Chem. Soc. Rev.* **26**, 433–442 (1997).
29. Pushkarev, V. E., Tomilova, L. G. & Nemykin, V. N. Historic overview and new developments in synthetic methods for preparation of the rare-earth tetrapyrrolic complexes. *Coord. Chem. Rev.* **319**, 110–179 (2016).
30. Liepins, R., Campbell, D. & Walker, C. 1,2-dinitrile polymers. Part 1. Homopolymers and copolymers of fumaronitrile maleonitrile and succinonitrile. *J. Polym. Sci. Polym. Chem.* **6**, 3059–3073 (1968).
31. Wildi, B. S. & Katon, J. E. Synthesis and electrical conductivity measurements on semiconducting organic polymers derived from nitriles. *J. Polym. Sci.* **2**, 4709–4718 (1964).
32. Epstein, A. & Wildi, B. S. Electrical properties of poly-copper phthalocyanine. *J. Chem. Phys.* **32**, 324–329 (1960).
33. Yuan, P. et al. Systematic study on highly efficient thermal synergistic polymerization effect between alicyclic imide moiety and phthalonitrile: Scope, properties and mechanism. *Polymer* **102**, 266–280 (2016).
34. Tsai, Z. H. & Sandman, D. J. Reactions of phthalonitriles with carbohydrates and alkali: phthalocyanine and oligomer formation. *J. Porphyr. Phthalocya.* **5**, 564–568 (2001).
35. Elvidge, J. A. & Linstead, R. P. 975. Heterocyclic imines. Part 1. Imino-derivatives of isoindoline and their reaction with primary bases. *J. Chem. Soc.* **0**, 5000–5007 (1952).
36. Elvidge, J. A. & Linstead, R. P. Conjugated macrocycles. Part 27. The formation of tetrazaporphins from imidines. Tribenzotetrazaporphin. *J. Chem. Soc.* **0**, 3536–3544 (1955).
37. Wöhrle, D. Polymere aus nitrilen. I. Anionische polymerisation von bernsteinsäuredinitril. *Makromol. Chem.* **160**, 83–97 (1972).
38. Koudia, M. & Abel, M. Step-by-step on-surface synthesis: from manganese phthalocyanines to their polymeric form. *Chem. Comm.* **50**, 8565–8567 (2014).
39. Piantek, M. et al. Manganese phthalocyanine derivatives synthesized by on-surface cyclotetramerization. *J. Phys. Chem. C* **118**, 17895–17899 (2014).
40. Kezilebieke, S., Amokrane, A., Abel, M. & Bucher, J. P. Hierarchy of chemical bonding in the synthesis of Fe-phthalocyanine on metal surfaces: a local spectroscopy approach. *J. Phys. Chem. Lett.* **5**, 3175–3182 (2014).
41. Urgel, J. I., Ecija, D., Auwärter, W. & Barth, J. V. Controlled manipulation of gadolinium-coordinated supramolecules by low-temperature scanning tunneling microscopy. *Nano lett.* **14**, 1369–1373 (2014).
42. Chen, Z. et al. Synthesis, characterization, monolayer assembly and 2D lanthanide coordination of a linear terphenyl-di(propiolonitrile) linker on Ag (111). *Beilstein. J. Nanotechnol.* **6**, 327–335 (2015).
43. Ecija, D., Urgel, J. I., Seitsonen, A. P., Auwärter, W. & Barth, J. V. Lanthanide-directed assembly of interfacial coordination architectures-from complex networks to functional nanosystems. *Acc. Chem. Res.* **51**, 365–375 (2018).
44. Muller, K. et al. Cyano-functionalized triarylamines on coinage metal surfaces: Interplay of intermolecular and molecule-substrate interactions. *Chemistry* **22**, 581–589 (2016).
45. Mohn, F., Gross, L., Moll, N. & Meyer, G. Imaging the charge distribution within a single molecule. *Nat. Nanotechnol.* **7**, 227–231 (2012).
46. Fan, Q. et al. On-surface pseudo-high-dilution synthesis of macrocycles: principle and mechanism. *ACS Nano* **11**, 5070–5079 (2017).
47. Krug, C. K. et al. Organometallic ring vs. chain formation beyond kinetic control: steering their equilibrium in two-dimensional confinement. *Chem. Commun.* **54**, 9741–9744 (2018).
48. Garza, A. J. & Scuseria, G. E. Predicting band gaps with hybrid density functionals. *J. Phys. Chem. Lett.* **7**, 4165–4170 (2016).
49. Gutzler, R. Band-structure engineering in conjugated 2D polymers. *Phys. Chem. Chem. Phys.* **18**, 29092–29100 (2016).
50. Hutchison, G. R. et al. Electronic structure of conducting polymers: Limitations of oligomer extrapolation approximations and effects of heteroatoms. *Phys. Rev. B* **68**, 035204 (2003).
51. Raupach, M. & Tonner, R. A periodic energy decomposition analysis method for the investigation of chemical bonding in extended systems. *J. Chem. Phys.* **142**, 194105 (2015).

Acknowledgements

Financial support by the Deutsche Forschungsgemeinschaft (DFG) through projects 223848855 - SFB 1083 and GO1812/2–1 is gratefully acknowledged. Q.F. thanks the Alexander von Humboldt-Foundation for a Research Fellowship for Postdoctoral Researchers. We thank the HRZ Marburg, CSC LOEWE Frankfurt and HLR Stuttgart for computational resources.

Author contributions

J.M.G., Q.F., and J.S. conceived this project. Q.F., K.G., and M.Z. performed the STM/XPS experiments and analysis. M.L. and J.S. performed the multistep synthesis of the organic building block. R.T. and J.-N.L. performed the calculations. J.M.G. and Q.F. co-wrote the draft of this paper. All authors discussed the results and commented on the manuscript.

Competing interests

The authors declare no competing interests.

Additional information

Supplementary information is available for this paper at https://doi.org/10.1038/s41467-019-13030-7.

Correspondence and requests for materials should be addressed to R.T. or J.M.G.

Peer review information *Nature Communications* thanks Dmitrii Perepichka and the other, anonymous, reviewer(s) for their contribution to the peer review of this work. Peer reviewer reports are available.

Reprints and permission information is available at http://www.nature.com/reprints

Publisher's note Springer Nature remains neutral with regard to jurisdictional claims in published maps and institutional affiliations.

Supplementary Information for

Template-Controlled On-Surface Synthesis of a Lanthanide Supernaphthalocyanine and its Open-Chain Polycyanine Counterpart

Fan *et al.*

Supplementary Discussion.

1) X-Ray Photoelectron Spectra

Supplementary Figure 1 shows the C 1*s* and N 1*s* X-ray photoelectron spectra of the different samples studied by STM. Noteworthy, the XPS data where always recorded exactly at the same samples as were used for the STM data shown in the paper and the Supplementary Discussion. This is possible because the used UHV setup contains both a scanning tunneling microscope and an XPS spectrometer connected with a fast transfer system. The deconvolution of the C 1*s* monolayer spectrum of the ADN monolayer shows a major and a minor component with BEs of 285.0 eV and 286.6 eV, respectively. Due to a higher electronegativity of nitrogen compared to hydrogen and carbon, the C 1*s* signal of the -C≡N group has a higher BE than that of the tetramethyl-tetrahydroanthracene backbone. Therefore, the major and minor components are related to the carbon atoms in tetramethyl-tetrahydroanthracene and carbonitrile (-C≡N) groups of ADN, respectively. The N 1*s* spectrum shows a single peak at 399.6 eV, which is a typical value for nitrogen in a -C≡N⋯H hydrogen bonding situation. The C 1*s* XP spectrum of Fe-NPc (sample in Figure 2c) shows only one peak located at 284.7 eV. Comparing to the C 1*s* XP spectrum of intact AND, the disappearance of the minor component (related to -C≡N) with a BE of 286.6 eV supports the transformation from the carbonitrile groups in ADN to the pyrrole and aza groups in Fe-NPc. Further evidence is provided by the related changes of the N 1*s* peak, which shifts towards lower BE by 1.7 eV upon formation of Fe-NPc. This result is consistent with the oxidation of iron to Fe(II) and a related gain of negative charge at the N atoms. Note that the BE (397.9 eV) of N 1*s* here is somewhat lower than that reported for the planar iron-phthalocyanine (398.7 eV) on Ag(111) surface. This is explained by the additional gain of electron density from the Ag(111) surface due to the stronger nitrogen-Ag(111) interaction of Fe-NPc than Fe-Pc. The underlying reason for this effect is the tilted adsorption configuration of the lobes (diiminobenzoisoindoline units) of the Fe-NPc molecule, which make the nitrogen atoms pointing down and position them closer to the Ag(111) surface. In addition, a work function change due to the deposition a slight excess of Fe atoms may play a role. The C 1*s* XPS signal of Gd-SNPc (sample in Figure 2e) consists of a single peak located at a BE of 285.1 eV, similar to that for Fe-NPc (284.7 eV) and thus indicating the transformation of the carbonitrile groups to the pyrrole and aza groups. The corresponding N 1*s* peak appears at a BE of 398.2 eV, which is close to that of Fe-NPc (397.9 eV) and indicates a 1.4 eV shift towards lower BE relative to the -C≡N related N 1*s* peak (399.6 eV). For the polycyanine chains, the absence of -C≡N groups is supported by the C 1*s* and N 1*s* spectra of the sample in Figure 3a. Both spectra show single peaks located at BEs of 284.8 eV and 398.1 eV, respectively, shifted toward lower BE compared to the C 1*s* (286.6 eV) and N 1*s* (399.6 eV) peaks related to the -C≡N group.

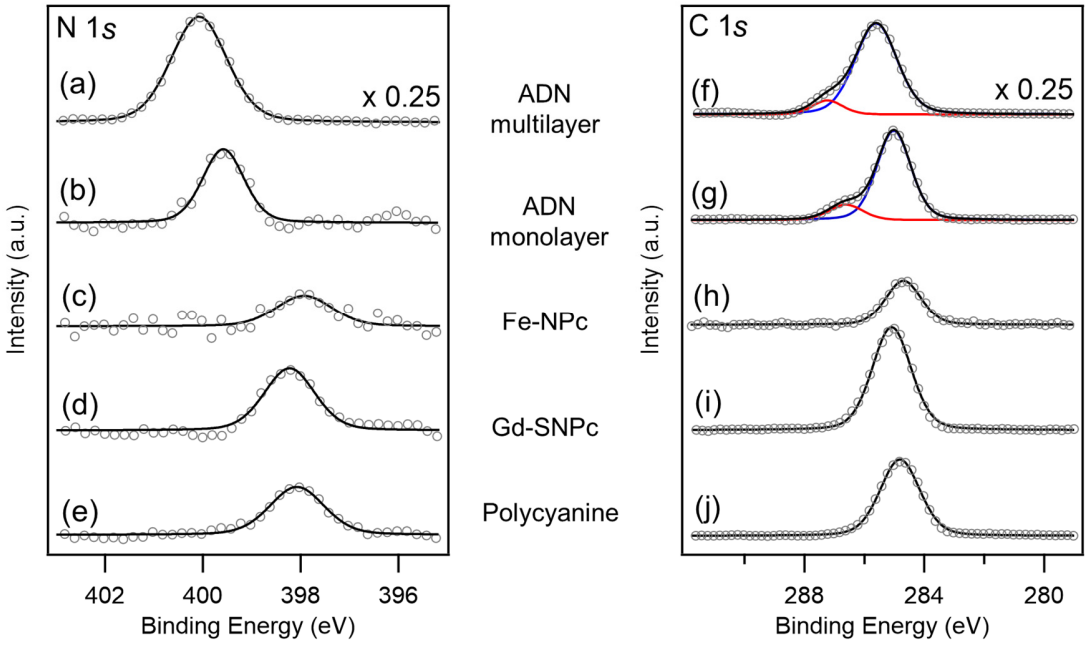

Supplementary Figure 1. N 1*s* and C 1*s* XP spectra of the prepared samples. (a,f) ADN multilayer (5.8 layers), (b,g) ADN monolayer, (c,h) Fe-NPc, (d,i) Gd-SNPc, and (e,j) polycyanine. All spectra were taken at 300 K. The preparation procedure of the corresponding samples can be found in the main text.

2) Structure Confirmation of Fe-NPc by Size Comparison

According to high-resolution AFM images of naphthalocyanine reported previously,[1] the distance (green line, Supplementary Figure 2a) between the centers of two oppositely positioned benzene rings in a naphthalocyanine is measured to be 16.2 ± 0.5 Å as illustrated by Supplementary Figure 2a. The distance (red line, Supplementary Figure 2a) between two adjacent benzene rings is measured to be 2.5 ± 0.5 Å. The corresponding distances of Fe-naphthalocyanine is similar as shown by the Supplementary Figure 2b. Assuming that this distance is close to the distance (red line, Supplementary Figure 2c) between the cyclohexane ring and its adjacent benzene ring, the distance between the centers of two oppositely positioned tetramethyl-cyclohexane units in Fe-NPc is then derived to be 21.2 ± 0.5 Å, as shown by Supplementary Figure 2c. Supplementary Figure 2e-f shows the corresponding experimental distances (20.7 ± 0.5 Å) between the two oppositely positioned tetramethyl-cyclohexane units. This value agrees well with that derived from Supplementary Reference 1. Supplementary Figure 2d illustrates the hypothetical coordination tetramer formed by one Fe atom and four ADN monomers. The chiral vortex arrangement of the four monomer differs completely in appearance from the Fe-NPc with axially arranged four ADN units.

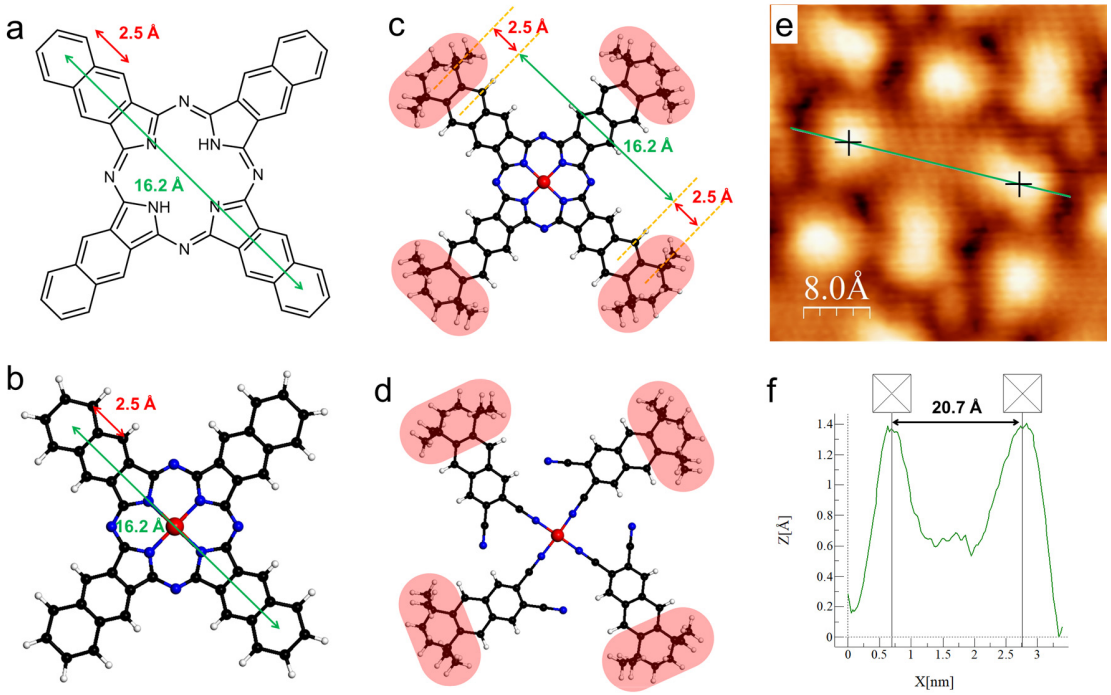

Supplementary Figure 2. Structural analysis of Fe-NPc. (a) Chemical structure of naphthalocyanine labelled with distances derived from its AFM image on NaCl/Cu(111) in ref. 1. The molecular model of (b) Fe-naphthalocyanine with related distances labeled according to the naphthalocyanine, (c) Fe-NPc with distances labeled, and (d) a hypothetical Fe-$(AND)_4$ coordination tetramer. (e) STM image of a single Fe-NPc. Tunneling parameters: U = 1.9 V, I = 0.13 nA. (f) Apparent height profile along the green line in panel (e). The light red ovals in panels (c) and (d) highlight the tetramethyl-cyclohexane moieties, which appear as bright lobes in Fe-NPc and Gd-SNPc. Black spheres represent carbon atoms; blue, nitrogen; white, hydrogen; red, iron.

3) Lateral Distance Uncertainties

The uncertainty of 0.5 Å of the measured distance in Supplementary Figure 2e is derived as show by Supplementary Figure 3 and as discussed in the following. Supplementary Figure 3 shows the apparent height profiles along the green lines overlaid on the STM images. The lobe-to-lobe distances (20.72 Å, 20.45 Å, 20.95 Å, and 20.62 Å) of four cross-shaped species, which are located at different parts of the image, have been measured. Therefore, the average value of these distances is 20.685 Å (≈20.7 Å), and the error bar is derived as 20.95 - 20.685 Å = 0.265 Å (≈0.3 Å). The intrinsic uncertainty from the size of the STM image pixels accounts for another part of the final uncertainty. It is defined as the size of two pixels due to the determination of two peak maxima (2 × 100 Å/512 pixel = 0.4 Å). On this basis, the final maximum uncertainty is estimated to be 0.5 Å. This procedure for the derivation of uncertainties has also been applied to other distance measurements in the main text.

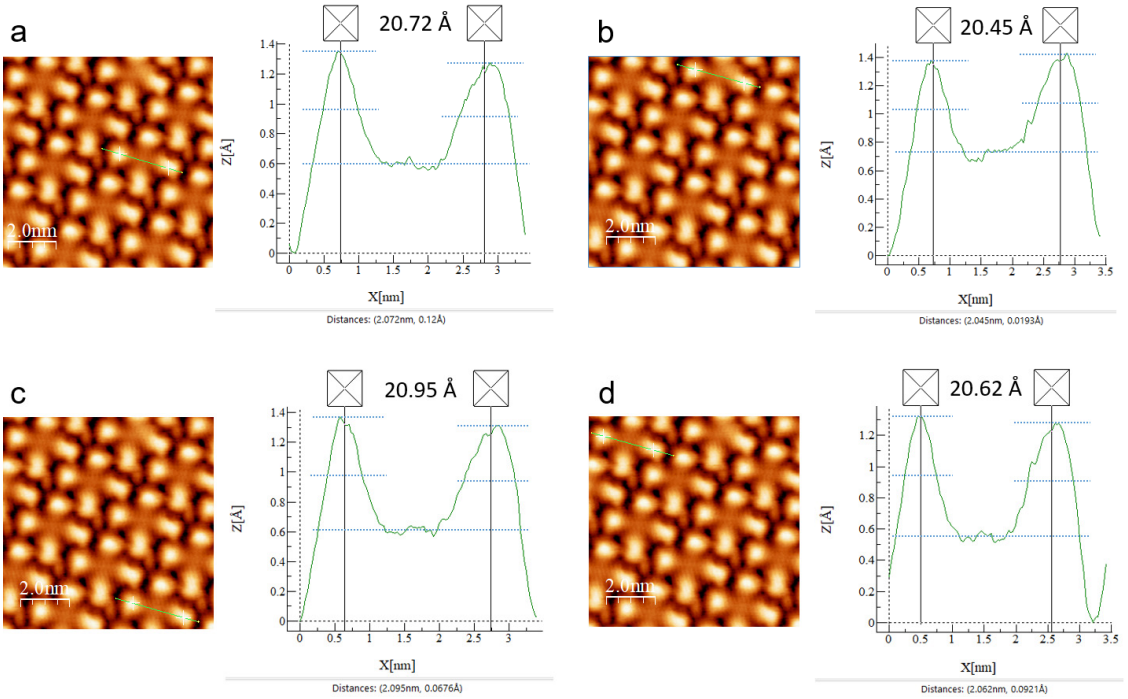

Supplementary Figure 3. Derivation of the uncertainties of the measured lateral distances. (a-d) Apparent height profiles (right part) along the green lines overlaid on different cross-shaped species in the STM images (left part). The three blue dotted lines are given as reference to find the full width at half maximum (FWHM) (the center dotted lines) of the peak. The peak position is defined as the center of the FWHM (black vertical lines).

4) Structure Confirmation of Gd-SNPc by Size Comparison

According to the distance (21.2 ± 0.2 Å, green line, Supplementary Figure 4a) between two opposite tetramethyl-cyclohexane moieties of the Fe-NPc molecule, the distances between the Fe center and the tetramethyl-cyclohexane is derived to be 10.6 ± 0.1 Å. Considering that the N-Gd bond length (2.7 ± 0.5 Å)[2] is about 0.6 Å larger than the N-Fe bond length (2.1 ± 0.5 Å),[3] the distance between Gd and the tetramethyl-cyclohexane moiety in Gd-SNPc is calculated to be 11.2 ± 0.1 Å (Supplementary Figure 4b, red lines). Therefore, the distance between two farthest tetramethyl-cyclohexane moieties in the five-fold symmetric Gd-SNPc molecule is derived to be 21.2 ± 0.1 Å (Supplementary Figure 4b, green line). This agrees well with the experimentally measured distance (21.1 ± 0.7 Å) of two opposite lobes in Gd-SNPc as shown by Supplementary Figure 4c and 4d.

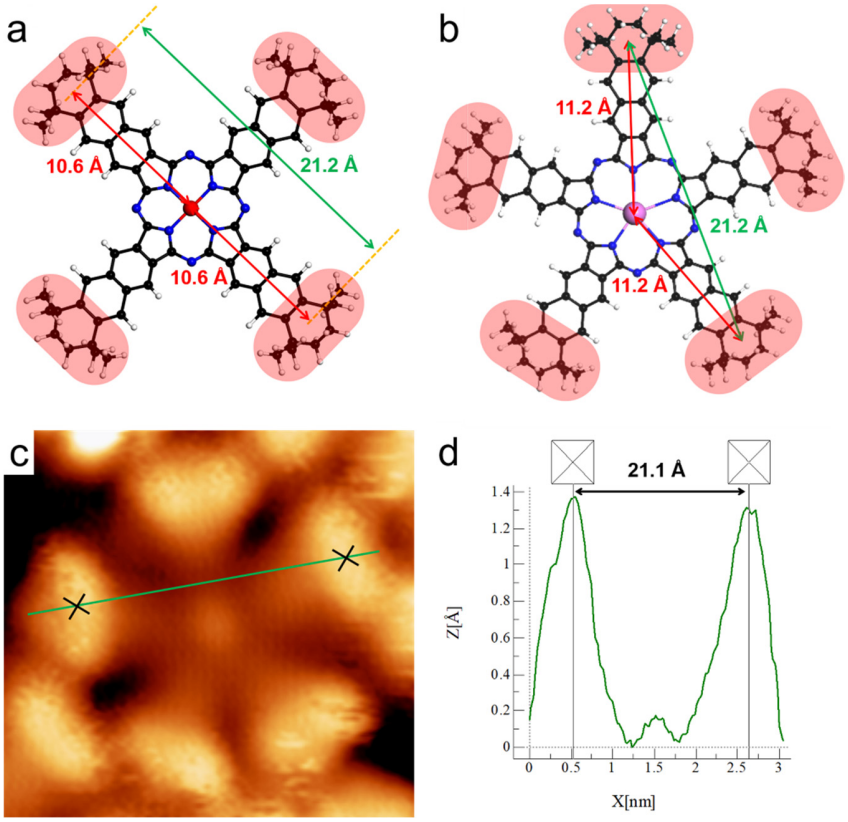

Supplementary Figure 4. Structural analysis of Gd-SNPc. Molecular model of (a) Fe-NPc and (b) SNPc with related distances labeled. The light red ovals in panel (a) and (b) highlight the tetramethyl-cyclohexane moieties, which appear as bright protrusions in Fe-NPc and Gd-SNPc. (c) Magnified STM image of SNPc. Tunneling parameters: U = 1.4 V, I = 0.26 nA. (d) Apparent height profile along the green line in panel (c). Black spheres represent carbon atoms; blue, nitrogen; white, hydrogen; red, iron; pink, gadolinium.

5) Additional High-bias STM Images of Gd-SNPc

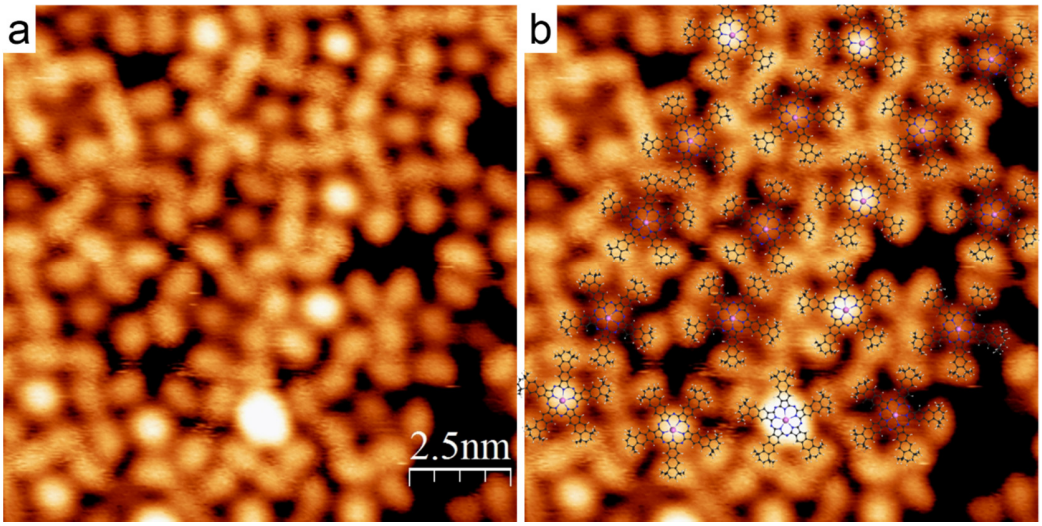

Supplementary Figure 5. STM image of Gd-SNPc assembly recorded with high voltage bias. (a) STM image showing an island of Gd-SNPc with a high tunneling bias. Tunneling parameters: *U* = 3.3 V, *I* = 0.10 nA. (b) STM image from panel (a) overlaid with molecular models. Black spheres represent carbon atoms; blue, nitrogen; white, hydrogen; pink, gadolinium.

6) Orientation of a Polycyanine Chain with Respect to the Ag(111) Surface Lattice

The chains extend along the high-symmetry directions of the substrate and have a periodicity of three times the Ag(111) surface lattice constant, *i.e.*, they are commensurate with respect to the substrate. Direct evidence for this is the high-resolution STM image (Supplementary Figure 6) of a single polycyanine chain with the Ag(111) substrate lattice resolved.

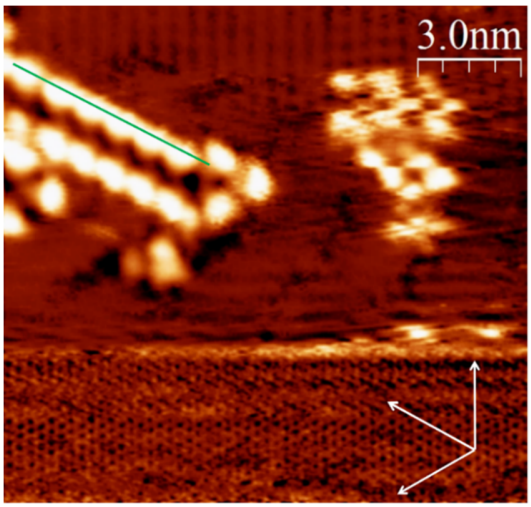

Supplementary Figure 6. STM image of a single polycyanine chain with the Ag(111) surface lattice resolved (in the bottom part). The bottom and top part of the image is recorded with the tunneling parameters *U* = 0.085 V, *I* = 0.17 nA and *U* = 1.3 V, *I* = 0.1 nA, respectively. The extremely low bias in the bottom part enables the resolving of the Ag(111) surface lattice, allowing the identification of the orientation and the periodicity of the polycyanine chain.

7) Coexistence of Polycyanine Chains and Cyclic Tetramers at Low ADN Coverages

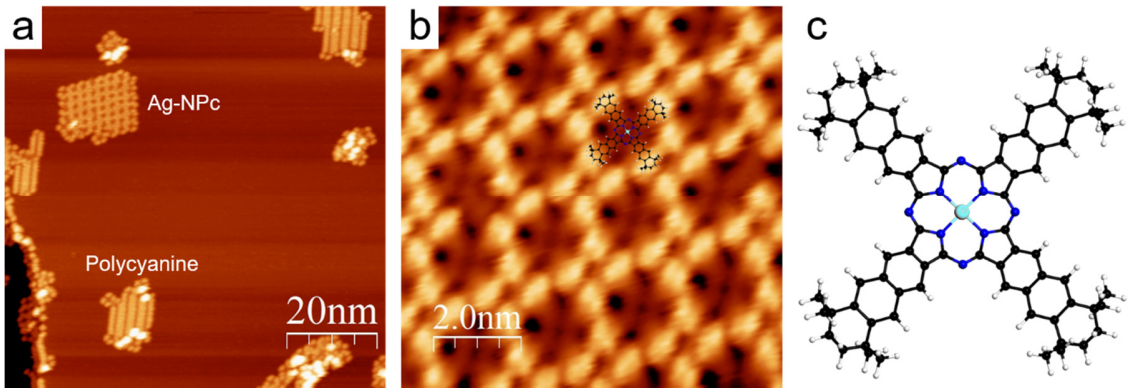

Supplementary Figure 7. STM image showing the coexistence of polycyanine chains and cyclic tetramers. (a) STM image taken after annealing of one monolayer of ADN molecules on Ag(111) to 450 K. The coexistence of polycyanine chains and a cyclic tetramer (tentatively assigned as Ag-NPc) has been observed. (b) Magnified view of the network domain overlaid with the molecular model of hypothetical Ag-NPc. An enlarged image of the molecular structure of the hypothetical Ag-NPc is given in panel (c). Black spheres represent carbon atoms; blue, nitrogen; white, hydrogen; cyan, silver.

8) Conformational Changes Induced by STM Manipulation of the Polycyanine Chains

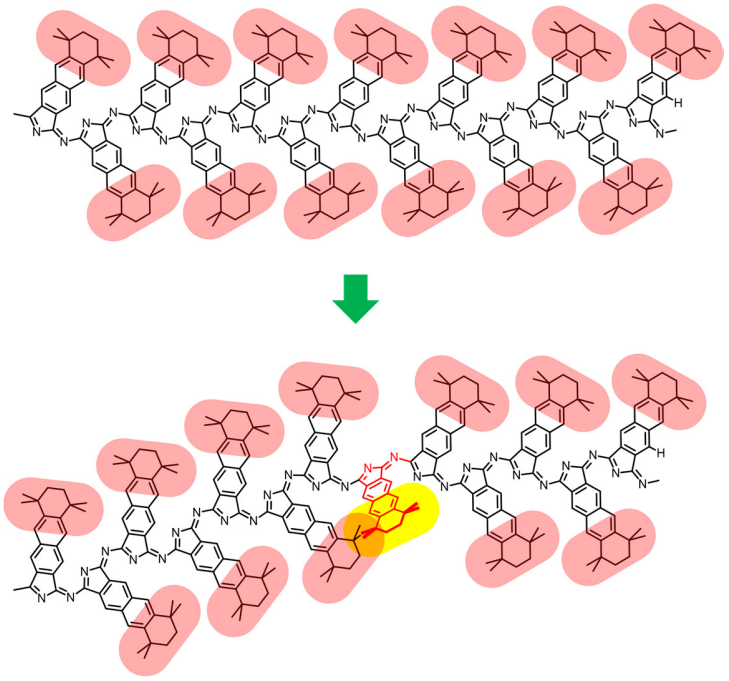

Supplementary Figure 8. Molecular structures of the straight (top) and bent (bottom) polycyanine chains. The bending of a straight polycyanine chain causes the steric repulsion to the benzodiiminoisoindoline units (yellow oval marked) at the corner of a bent chain. This steric repulsion is overcome by the up-lifting of the respective unit.

9) Aromaticity Considerations

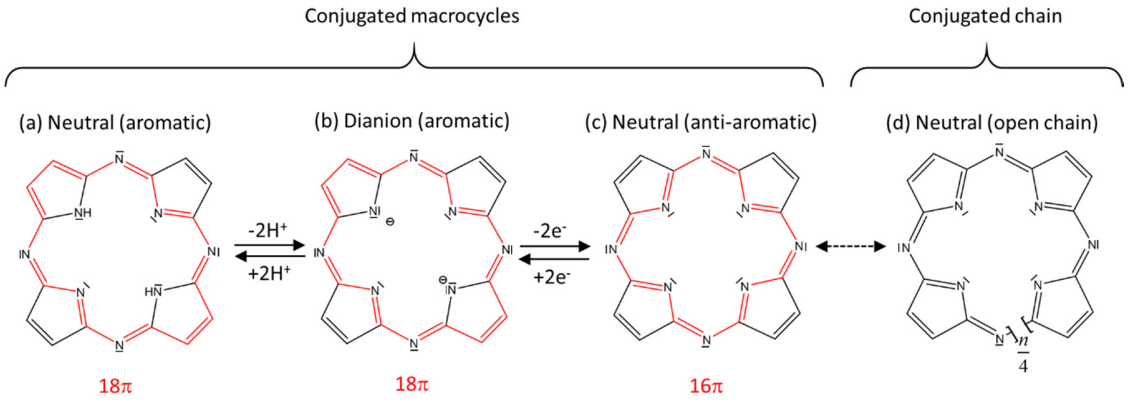

Supplementary Figure 9. Different conjugation pathways in tetraazaporphyrin and its derivatives, compared to the open-chain polymer. (a)-(c) Conjugated tetraazaporphyrin (TAP) macrocycles as models for the phthalocyanine macrocycles. The cyclic systems are stabilized by a Hückel-aromatic 18π electron conjugation path when they contain two NH hydrogens like in the free base (a) or are dianions (b), which occur in metal complexes. If neither condition is fulfilled, an anti-aromatic 16π conjugation path results, as shown in (c). In contrast, conjugation along the open-chain path (d) does not involve aromaticity requirements regarding the electron count. The chain is shown in the quasi-cyclic conformation to illustrate the analogy to the anti-aromatic cyclic system in (c).

10) Bonding Analysis of a Model System with the Periodic Energy Decomposition Analysis (pEDA)

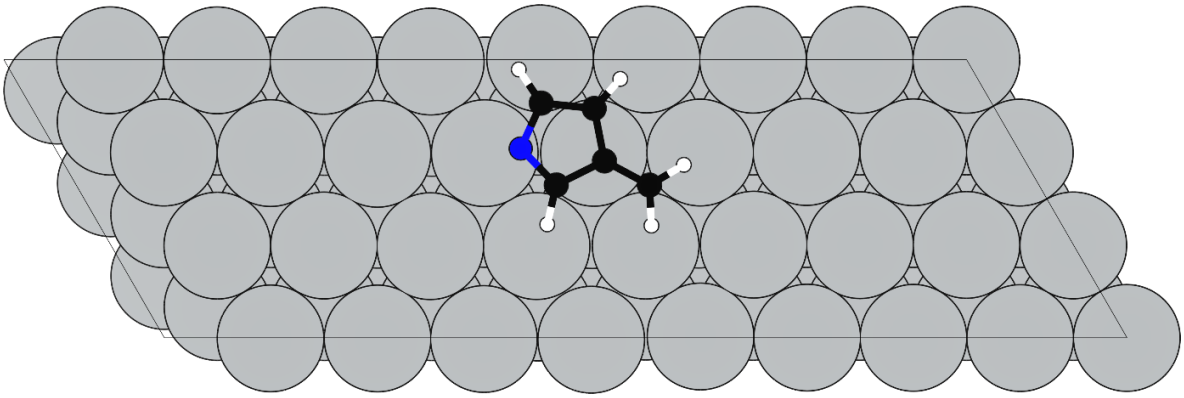

Supplementary Figure 10. Top view of the test system chosen for pEDA. Atoms other than H are frozen in the positions they have in the polycyanine chain.

Supplementary Table 1. pEDA data for the model system (Supplementary Figure 10) with different Monkhorst-Pack type k-meshes (PBE-D3/DZP). Plane wave data for selected energy terms shown for reference. Energies are given in kJ mol^{-1}.

k-mesh	1×1	1×1[a]	3×1	6×2	9×3	6x2[b]
ΔE_{int}	-170	-170	-152	-136	-119	-112
ΔE_{disp}	-89	-89	-89	-89	-89	-89
ΔE_{elec}	-85	-82	-64	-47	-30	-23
ΔE_{Pauli}	483	468	492	489	480	
ΔE_{elstat}	-323	-323	-325	-326	-326	
ΔE_{orb}	-246	-227	-231	-210	-185	

[a] spin-polarized calculation
[b] plane wave calculation with $E_{cut\text{-}off}$ = 400 eV.

Bonding analysis was performed at PBE-D3(BJ)/DZP with different ***k*** space samplings, using pEDA.[4] The pEDA method allows to dissect the interaction energy between two fragments (here: molecule and surface) into well-defined quantities that allow to interpret the bonding in a system in a chemically meaningful way. The interaction energy (ΔE_{int}) is first divided into a dispersion term (ΔE_{disp}) and an electronic term (ΔE_{elec}).

The actual pEDA procedure then decomposes ΔE_{elec} into contributions from Pauli repulsion (ΔE_{Pauli}), electrostatics (ΔE_{elstat}) and orbital interaction (ΔE_{orb}):

$$\Delta E_{elec} = \Delta E_{Pauli} + \Delta E_{elstat} + \Delta E_{orb} \quad (1)$$

This enables a quantitative analysis of the surface-adsorbate bonding.

11) Additional Parameters for the Computed Structure

(a)

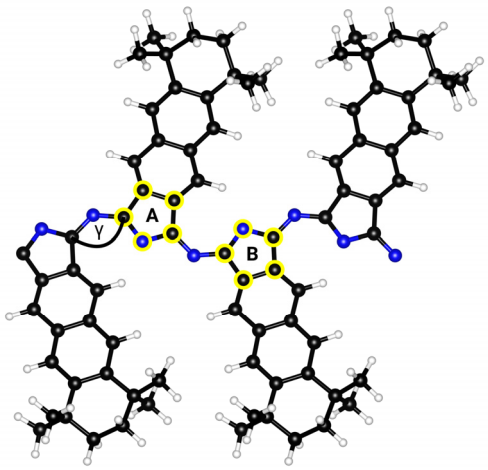

(b)

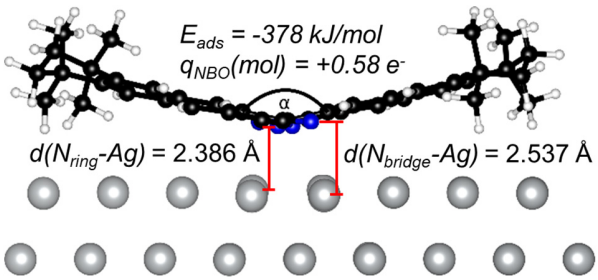

Supplementary Figure 11. Computed structure of polycyanine chains. a) Top view of the chain without the surface. b) Side view of the adsorbed chain with the surface. The charge transfer (q_{NBO}) is calculated with a projection of plane waves[5] onto an atom-centered def2-TZVP basis set.[6] Averaged positions for distance of the N atoms in the ring (N_{ring}) and the aza-bridging N atoms (N_{bridge}) with respect to the non-corrugated surface plane are shown. The adsorption energy term (E_{ads}) is dominated by dispersion interactions (E_{disp} = -412 kJ mol^{-1}) and shows repulsive electronic interactions (E_{elec} = +34 kJ mol^{-1}). The butterfly angle α is defined as an inter-plane angle between the planes spanned by the atoms highlighted in yellow of the two pyrrole rings A and B, respectively.

Supplementary Table 2. Structural parameters of the polycyanine chain free-standing and adsorbed on Ag(111). Definition of angle γ and inter-plane angle α as shown in Supplementary Figure 11, lattice parameter in chain direction.

	Free-standing	Adsorbed
α / °	140.9	155.3
γ / °	130.5	127.2
a / Å[a]	8.67	8.64

[a] the lattice mismatch amounts to 0.4%.

12) Origin of the Unusual Bending Angle of the Polycyanine Chain

The polycyanine chain is not planar, but has an intrinsic bending angle, which is also present in the gas phase calculations. In the following, we will elucidate whether this bending angle is of electronic origin, steric origin, or both. This will be done by using a range of model systems (M1-M8 in Supplementary Figure 12, Supplementary Figures 13 and 14) in which the π-electronic structure and the amount of steric hindrance are systematically varied by substitution or exchange of groups.

Saturation of half of the N atoms in the pyrrole rings (N_{ring}) (M2) reduces bending to 126.62°. The steric repulsion of the N lone pair and –CH in the six-membered "open" ring of M1 is apparently not causing the bending. Instead, it may be of electronic origin. This is indicated by the model system (M3), in which all N atoms in the pyrrole rings (N_{ring}) are saturated. As a result, the bending angle further decreases. Some H-H repulsion prevents an angle of 180°. Removing the H-H repulsion (M4) leads to a perfectly coplanar arrangement. The same is achieved with an all carbon chain (M5). Since isoelectronic substitution does not change the number of π-electrons, another electronic effect must be present. Similarly, saturation of the periphery (M6) only increases the angle to 133.8°. Therefore, the bending effect must be an intrinsic property of the backbone chain. Saturation of the aza-bridging nitrogen (N_{bridge}) (M7) also results in coplanar arrangement. This is also the case for a larger model system based on M7 (Supplementary Figure 13) containing an additional annulated benzene ring in order to include possible steric repulsion (or, alternatively, CH···N hydrogen bonding) effects between hydrogen on this benzene ring and the lone pair on the N atom in the pyrrole ring (N_{ring}). However, this extended model system also shows coplanar arrangement. Therefore, steric repulsion is ultimately ruled out as the cause of bending.

Instead, the conjugation of the N lone pairs with the π-systems of the chain and the periphery, which emerges as a consequence of the specific arrangement of N and C atoms found in the polycyanine chain, remains as the most probable explanation. Furthermore, adding another imine to the periphery (M8) decreases the angle to 106.9°, the most bent structure in this set.

The larger the electron deficiency is in the π-system, the larger is the stabilization by conjugation. For this reason, saturation with H decreases the bending angle, while adding more electron-withdrawing N atoms increases it. Supplementary Figure 15 shows a magnified version of the frontier orbitals HOCO-2 and HOCO-3 of polycyanine from Figure 5. The conjugation of the N-lone pairs with the π-system of the backbone and the periphery is clearly visible.

Even for a very small model system (M9, Supplementary Figure 14), the bending is found. In the case of this model, we use the dihedral angle θ <(N-C-N-C) to describe the bending since a second ring is not available for the definition of α in the same way as done in the original system. For this model system, we can set up a Walsh diagram (Supplementary Figure 16) showing the orbital shape and energies for different dihedral angles θ. In can be clearly seen that upon increasing the dihedral angle from 0° to the structural minimum of 46° the HOMO-3 representing non-bonding electron pair conjugation is strongly stabilized while the conjugation (orbitals HOMO, HOMO-1, HOMO-4) is decreased by a similar but slightly smaller amount. This intrinsic bending thus stems mostly from the increased conjugation of the non-bonding electron pair at nitrogen.

Noteworthy, to achieve more accuracy of the models in Supplementary Figure 12 and Supplementary Figure 13, we reproduced the GGA results with a range-separated hybrid functional (HSE06) and see the same trends (see the comparisons in Supplementary Figure 12 and 13). Higher level optimization for the molecular model system (MP2) did not show significant deviations in the structure.

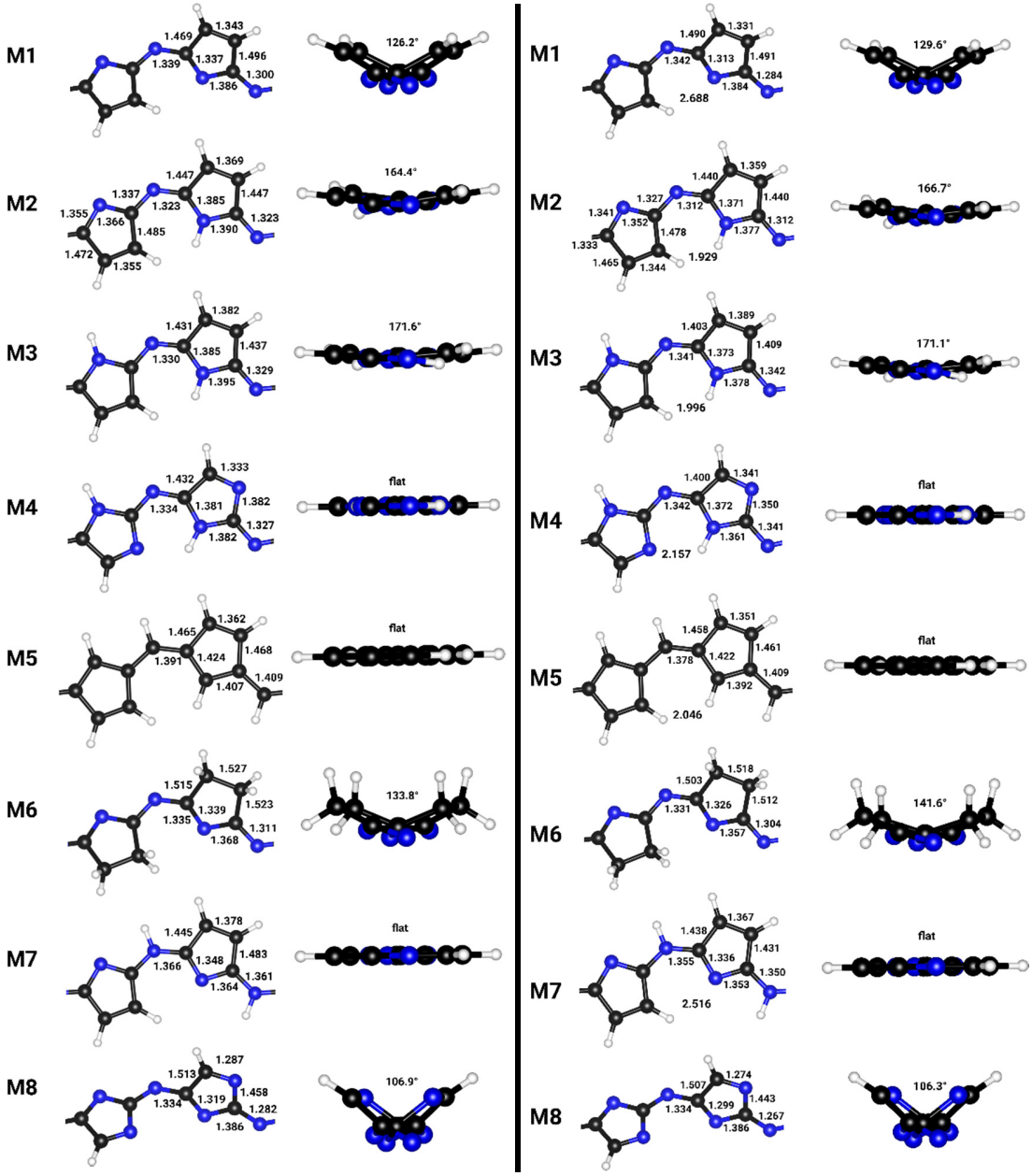

Supplementary Figure 12. Series of model systems for the identification of the origin of the out-of-plane bending (angle defined according to Supplementary Figure 11). (M1) Simplified version of the polycyanine chain. (M2) H saturation of half of the N atoms in the pyrrole rings (N_{ring}). (M3) H saturation of all N_{ring}. (M4) H saturation of all N_{ring} and isoelectronic exchange of a peripheral –CH with N. (M5) Isoelectronic exchange of all N with –CH. (M6) H saturation of the peripheral C=C. (M7) H saturation of all bridging imines (N_{bridge}). (M8) Isoelectronic exchange of a peripheral –CH with N. The calculated models in the left and right columns are obtained by PBE and HSE06 functionals, respectively.

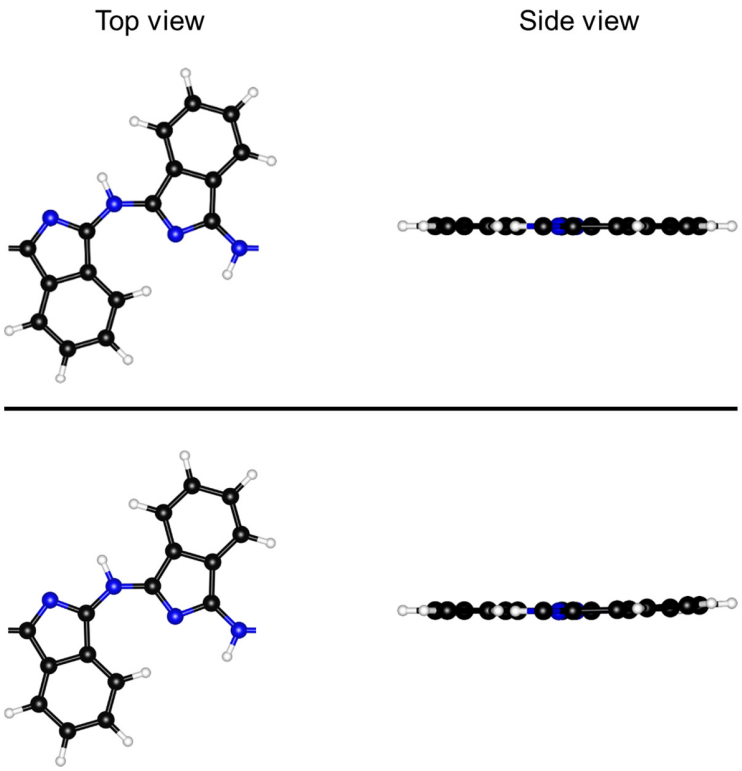

Supplementary Figure 13. A larger model system based on M7, but with an additional annulated benzene ring is planar, excluding steric repulsion (*e.g.* between the H atom at the benzene ring and the lone pair at the N atom in the pyrrole ring) as the cause for the tilted chain. The results at the top and bottom rows are calculated with PBE and HSE06 functionals, respectively.

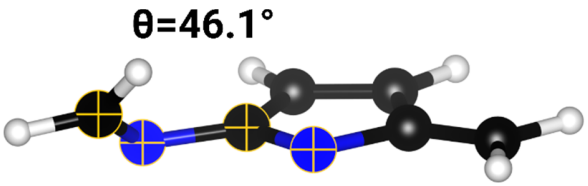

Supplementary Figure 14. A molecular model system (M9) with the same C-N-C-N arrangement as the polycyanine chain shows bending similar to the polymer chain.

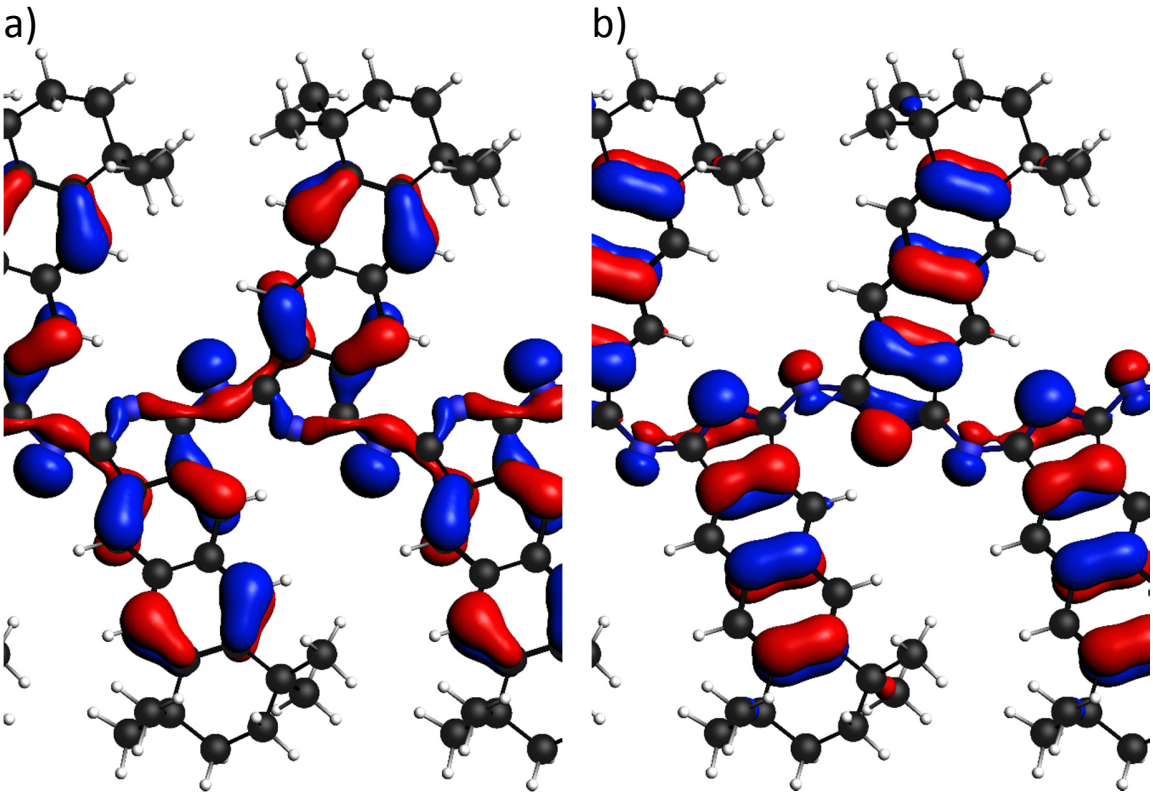

Supplementary Figure 15. Magnified version of the HOCO-2 (**a**) and HOCO-3 (**b**) of the polycyanine from Figure 5 in the main text (isovalue = 0.03). The conjugation of the N-lone pair with the π-system of the backbone (**b**) and the periphery (**a** & **b**) is visible.

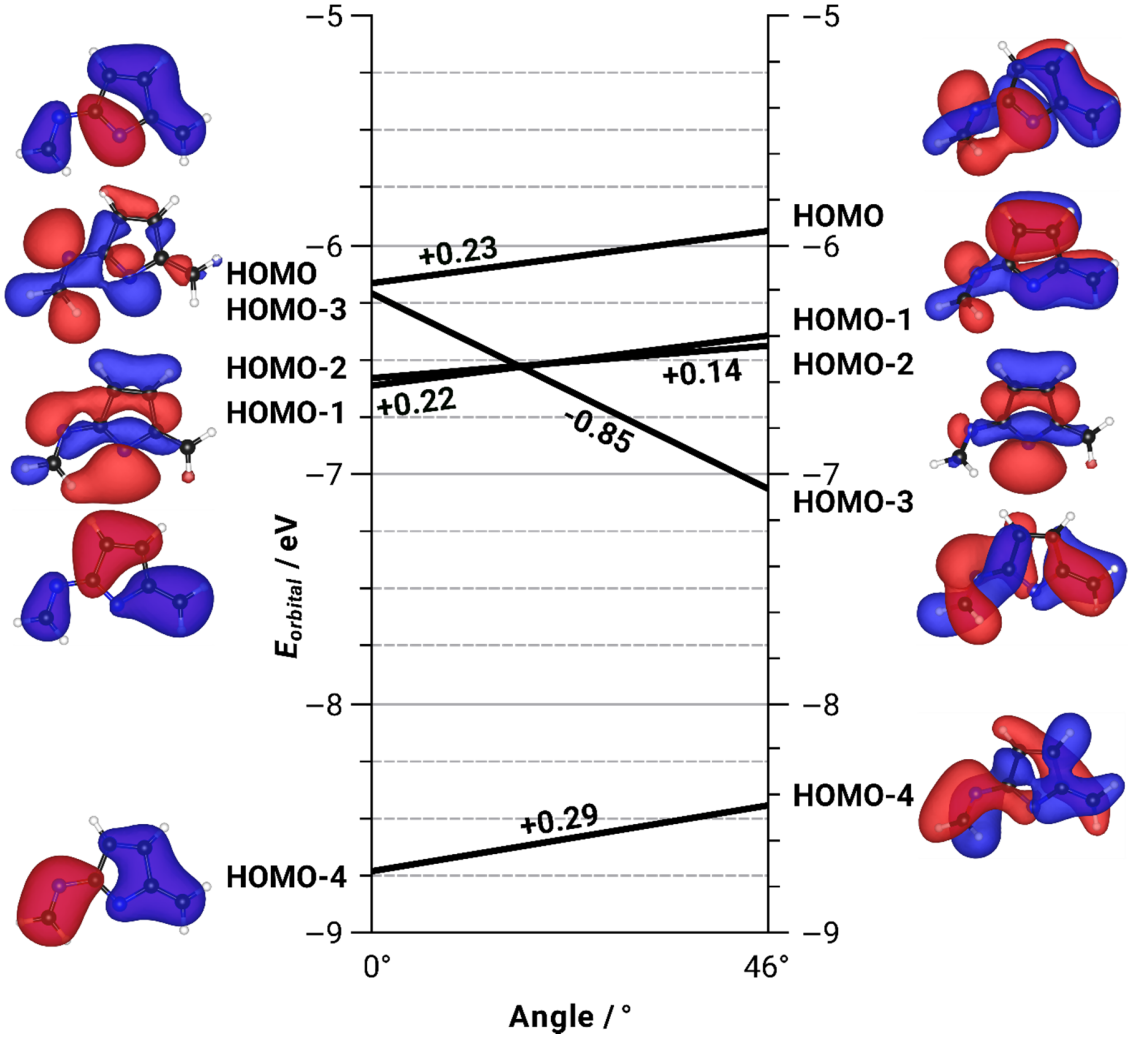

Supplementary Figure 16. Walsh diagram showing the dependence of the canonical Kohn-Sham orbital energies as function of the dihedral angle θ in the model system M9.

13) Electronic Structure of Gd-SNPc and Fe-NPc

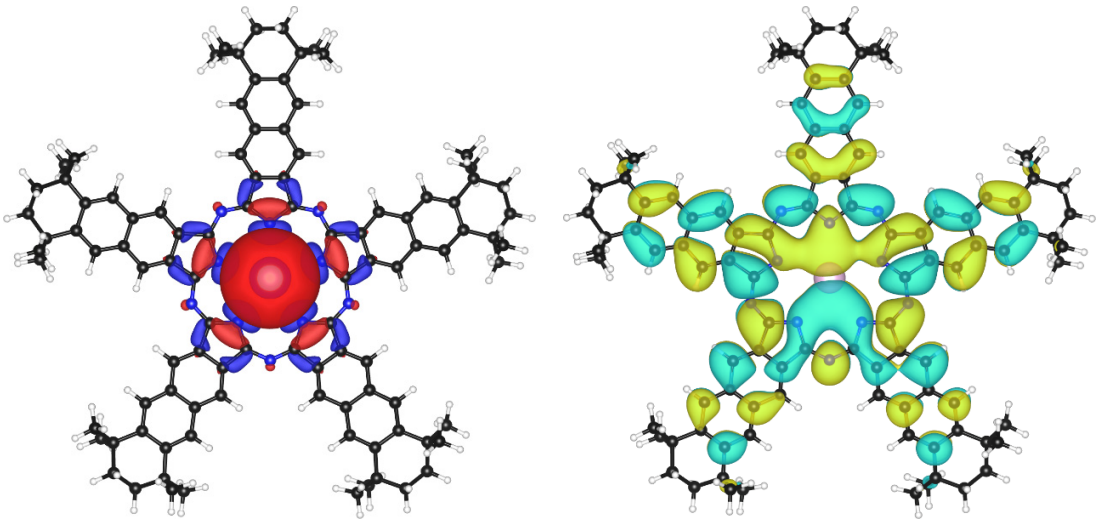

Supplementary Figure 17. Frontier orbitals of Gd-SNPc. Singly-occupied molecular orbital (SOMO, left) and LUMO (right) of the Gd-SNPc as calculated with PBE0. The orbital energy gap amounts to 1.39 eV. Preliminary screening of electronic states with PBE identified eight unpaired electrons as the most favorable state. Seven of the unpaired electrons are located in low-lying 4*f* orbitals, here with α-spin. The eighth unpaired electron, of *β*-spin, is located in the d_{z^2} SOMO which would favor Gd(II) in the gas phase complex (an all-*α* configuration could not be converged). These findings indicate a complex electronic structure for Gd-SNPc which is likely not well reproduced with single-determinant methods. The molecule is nevertheless too large for more accurate wavefunction based multireference methods at the current stage. Additionally, on the surface the electronic state is expected to be different.

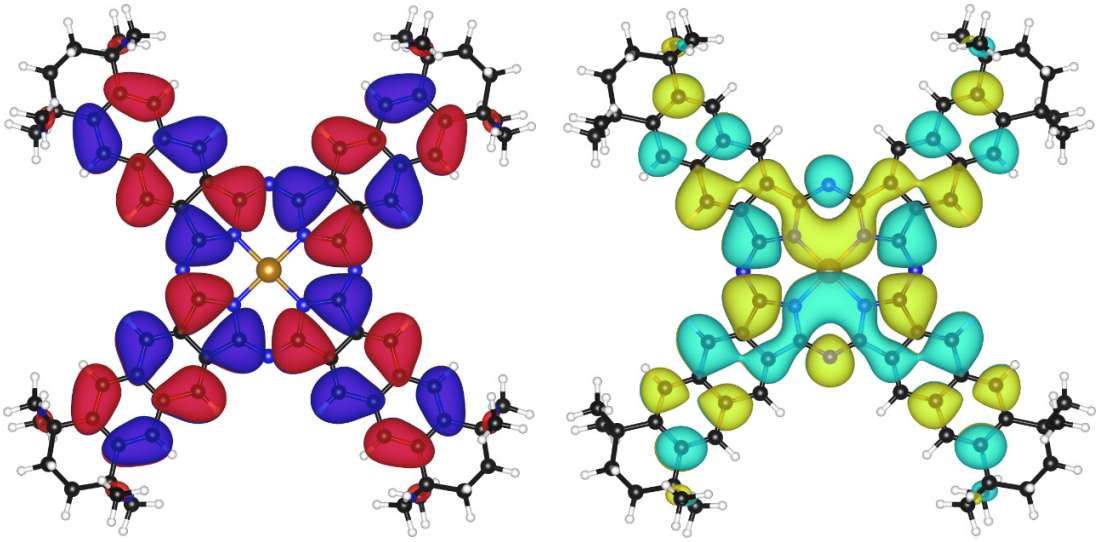

Supplementary Figure 18. Frontier orbitals of Fe-NPc. HOMO (left) and LUMO (right) of the Fe-NPc as calculated with PBE0. The orbital energy gap amounts to 1.71 eV. Of the electronic states investigated, a triplet state was the most favorable in accordance with Fe-PC literature.[7]

14) Optimized Structures in VASP Format

The optimized atomic structures can be found in the NOMAD repositories:
http://dx.doi.org/10.17172/NOMAD/2019.03.18-1
And:
http://dx.doi.org/10.17172/NOMAD/2019.07.01-1

15) ADF/BAND 2017 Input Example

Fragment 1:

```
Accuracy 5
relativistic zora
SCF
Mixing 0.3
Iterations 300
End
Convergence
criterion 1e-6
End
UNITS
  length Angstrom
  angle Degree
END
Atoms C
-0.09450464   -0.64540089   6.00144189
-2.20379164   0.10648111   6.06285689
-0.03599964   0.72955811   6.46990589
-1.34083064   1.18097211   6.51179889
2.11690536   -1.56545189   6.03691489
2.97861936   -2.65075289   6.45969989
-4.35712164   -2.19486689   6.43648289
4.22434036   -0.81019989   5.99716889
End
Atoms N
5.10476136   0.19791011   5.97370089
-1.42231764   -0.98448689   5.73952689
2.89811736   -0.46973389   5.73426389
0.78445436   -1.65376589   5.95038389
End
Atoms H
0.86771436   1.23850211   6.79356789
-1.70970764   2.11766711   6.91097789
-3.45279164   -2.70960989   6.74904089
2.60828736   -3.59945089   6.82687389
End
Lattice
    8.6401377593184261    0.0000000000000000    0.0000000000000000
    4.3200688796592104    7.4825787917669100    0.0000000000000000
End
BasisDefaults
BasisType DZP
Core large
End
XC
LDA LDA
GGA PBE
dispersion Grimme3 BJdamp
END
KSpace
 Grid 3 3
End
skip dos
Dependency basis=1e-8
EndInput
```

Fragment 2:

```
Accuracy 5
```

```
relativistic zora
SCF
Mixing 0.2
Iterations 100
End
Convergence
criterion 1e-6
End
UNITS
  length Angstrom
  angle Degree
END
Atoms Ag
-1.81093864   3.12511111   -3.51784911
1.06910736   3.12511111   -3.51784911
3.94915236   3.12511111   -3.51784911
-4.69098464   -1.86327489   -3.51784911
-1.81093864   -1.86327489   -3.51784911
1.06910736   -1.86327489   -3.51784911
-3.25096164   0.63091711   -3.51784911
-0.37091564   0.63091711   -3.51784911
2.50913036   0.63091711   -3.51784911
-4.69098464   -3.52607089   -1.16630211
-1.81093864   -3.52607089   -1.16630211
1.06910736   -3.52607089   -1.16630211
-3.25096164   -1.03187789   -1.16630211
-0.37091564   -1.03187789   -1.16630211
2.50913036   -1.03187789   -1.16630211
-1.81093864   1.46231511   -1.16630211
1.06910736   1.46231511   -1.16630211
3.94915236   1.46231511   -1.16630211
2.52398236   -2.70599189   1.14001589
-3.20426664   -2.70292489   1.17232689
-0.38249964   -2.70249389   1.16892689
3.95346336   -0.20501789   1.17765489
-1.79878864   -0.22186489   1.19076789
1.10029936   -0.21236889   1.17882189
5.40127736   2.28887911   1.15550789
-0.35609664   2.29087411   1.14698889
2.52441036   2.24692011   1.21120189
-4.63654964   -1.92117789   3.42393889
-1.79183464   -1.88660089   3.62955989
1.07762836   -1.93572189   3.42460589
-3.24477364   0.67610311   3.46137389
-0.31168164   0.66452011   3.45015889
2.53209036   0.60999311   3.68030489
-1.77693964   3.11061711   3.50273689
1.10483336   3.10752911   3.52056289
3.96192936   3.10736811   3.52190589
end
Lattice
    8.6401377593184261    0.0000000000000000    0.0000000000000000
    4.3200688796592104    7.4825787917669100    0.0000000000000000
End
BasisDefaults
BasisType DZP
Core large
End
XC
LDA LDA
GGA PBE
dispersion Grimme3 BJdamp
END
KSpace
 Grid 3 3
End
skip dos
Dependency basis=1e-8
end input
```

PEDA:

```
Accuracy 5
relativistic zora
```

```
SCF
Mixing 0.2
Iterations 200
End
Convergence
criterion 1e-6
End
UNITS
  length Angstrom
  angle Degree
END
fragments f1-mol.runkf
1 1
2 2
3 3
4 4
5 5
6 6
7 7
8 8
9 9
10 10
11 11
12 12
13 13
14 14
15 15
16 16
end
fragments f2-surf.runkf
1 17
2 18
3 19
4 20
5 21
6 22
7 23
8 24
9 25
10 26
11 27
12 28
13 29
14 30
15 31
16 32
17 33
18 34
19 35
20 36
21 37
22 38
23 39
24 40
25 41
26 42
27 43
28 44
29 45
30 46
31 47
32 48
33 49
34 50
35 51
36 52
end
PEDA
Atoms C
-0.09450464   -0.64540089   6.00144189
-2.20379164   0.10648111   6.06285689
-0.03599964   0.72955811   6.46990589
-1.34083064   1.18097211   6.51179889
2.11690536   -1.56545189   6.03691489
2.97861936   -2.65075289   6.45969989
```

```
-4.35712164   -2.19486689   6.43648289
4.22434036   -0.81019989   5.99716889
End
Atoms N
5.10476136   0.19791011   5.97370089
-1.42231764   -0.98448689   5.73952689
2.89811736   -0.46973389   5.73426389
0.78445436   -1.65376589   5.95038389
End
Atoms H
0.86771436   1.23850211   6.79356789
-1.70970764   2.11766711   6.91097789
-3.45279164   -2.70960989   6.74904089
2.60828736   -3.59945089   6.82687389
End
Atoms Ag
-1.81093864   3.12511111   -3.51784911
1.06910736   3.12511111   -3.51784911
3.94915236   3.12511111   -3.51784911
-4.69098464   -1.86327489   -3.51784911
-1.81093864   -1.86327489   -3.51784911
1.06910736   -1.86327489   -3.51784911
-3.25096164   0.63091711   -3.51784911
-0.37091564   0.63091711   -3.51784911
2.50913036   0.63091711   -3.51784911
-4.69098464   -3.52607089   -1.16630211
-1.81093864   -3.52607089   -1.16630211
1.06910736   -3.52607089   -1.16630211
-3.25096164   -1.03187789   -1.16630211
-0.37091564   -1.03187789   -1.16630211
2.50913036   -1.03187789   -1.16630211
-1.81093864   1.46231511   -1.16630211
1.06910736   1.46231511   -1.16630211
3.94915236   1.46231511   -1.16630211
2.52398236   -2.70599189   1.14001589
-3.20426664   -2.70292489   1.17232689
-0.38249964   -2.70249389   1.16892689
3.95346336   -0.20501789   1.17765489
-1.79878864   -0.22186489   1.19076789
1.10029936   -0.21236889   1.17882189
5.40127736   2.28887911   1.15550789
-0.35609664   2.29087411   1.14698889
2.52441036   2.24692011   1.21120189
-4.63654964   -1.92117789   3.42393889
-1.79183464   -1.88660089   3.62955989
1.07762836   -1.93572189   3.42460589
-3.24477364   0.67610311   3.46137389
-0.31168164   0.66452011   3.45015889
2.53209036   0.60999311   3.68030489
-1.77693964   3.11061711   3.50273689
1.10483336   3.10752911   3.52056289
3.96192936   3.10736811   3.52190589
end
Lattice
   8.6401377593184261   0.0000000000000000   0.0000000000000000
   4.3200688796592104   7.4825787917669100   0.0000000000000000
End
BasisDefaults
BasisType DZP
Core large
End
XC
LDA LDA
GGA PBE
dispersion Grimme3 BJdamp
END
KSpace
 Grid 3 3
End
Dependency basis=1e-8
end input
```

16) Synthesis of the ADN Precursor

5,5,8,8-tetramethyl-5,6,7,8-tetrahydroanthracene-2,3-dicarbonitrile (ADN) was prepared in a multistep synthesis *via* 6,7-bis(dibromomethyl)-1,1,4,4-tetramethyltetraline[8] and fumaronitril under reductive coupling conditions:

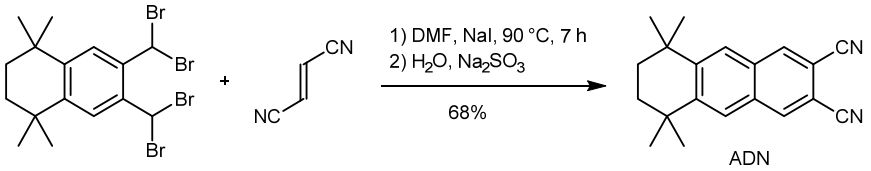

6,7-Bis(dibromomethyl)-1,1,4,4-tetramethyltetraline (10.0 g, 19.0 mmol, 1.0 eq), fumaronitrile (2.63 g, 33.7 mmol, 1.8 eq), and sodium iodide (20.0 g, 134 mmol, 7.1 eq) were dissolved in 20 mL DMF and the solution was stirred at 90 °C for 7 h. After the first 2 h and 4 h, respectively, another two additional portions of fumaronitrile (0.3 g, 3.85 mmol, 0.2 eq each) were added. After 7 h the reaction mixture was cooled down to RT, and 20 mL ice water was added. A brownish precipitate was obtained, which was treated with 50 mL aqueous sodium sulfite solution (10 w%) and isolated by filtration. The product 5,5,8,8-tetramethyl-5,6,7,8-tetrahydroanthracene-2,3-dicarbonitrile (ADN) was purified by column chromatography (silica, toluene) and obtained as brownish powder. Finally, the product was sublimed at 120 °C and 10^{-3} mbar, to obtain ADN as colorless solid.

Yield: 3.75 g, 13.0 mmol, 68%. - R_f (toluene) = 0.30. - **^{1}H NMR** ($CDCl_3$, 300 MHz): δ = 8.24 (s, 2 H, Ar-C*H*-5, *H*-8), 7.89 (s, 2 H, Ar-C*H*-1, *H*-4), 1.80 (s, 4 H, -CH_2), 1.41 (s, 12 H, -CH_3) ppm. - **^{13}C NMR** ($CDCl_3$, 75 MHz): δ = 150.7, 135.6, 131.6, 126.3, 116.4, 108.9, 35.3, 34.6, 32.5 ppm. - **IR** (ATR, 400-4000 cm^{-1}): $\tilde{\nu}$ = 2961 (s) 2925 (s), 2857 (m), 2349 (w), 2326 (w), 2230 (m), 1623 (w), 1460 (vs), 1366 (m), 1205 (w), 1110 (m), 920 (vs), 542 (m), 528 (w), 467 (vs) cm^{-1}. - **MS** (APCI-HRMS(+)): m/z = 311.1523 $[M+Na]^+$, cal. for $C_{20}H_{20}N_2$+Na_1: 311.1519. - **Elemental analysis** ($C_{20}H_{20}N_2$, M = 288.39 g/mol): fnd. (cal.): C 82.50% (82.30%), H 6.97% (6.99%), N 9.53% (9.71%).

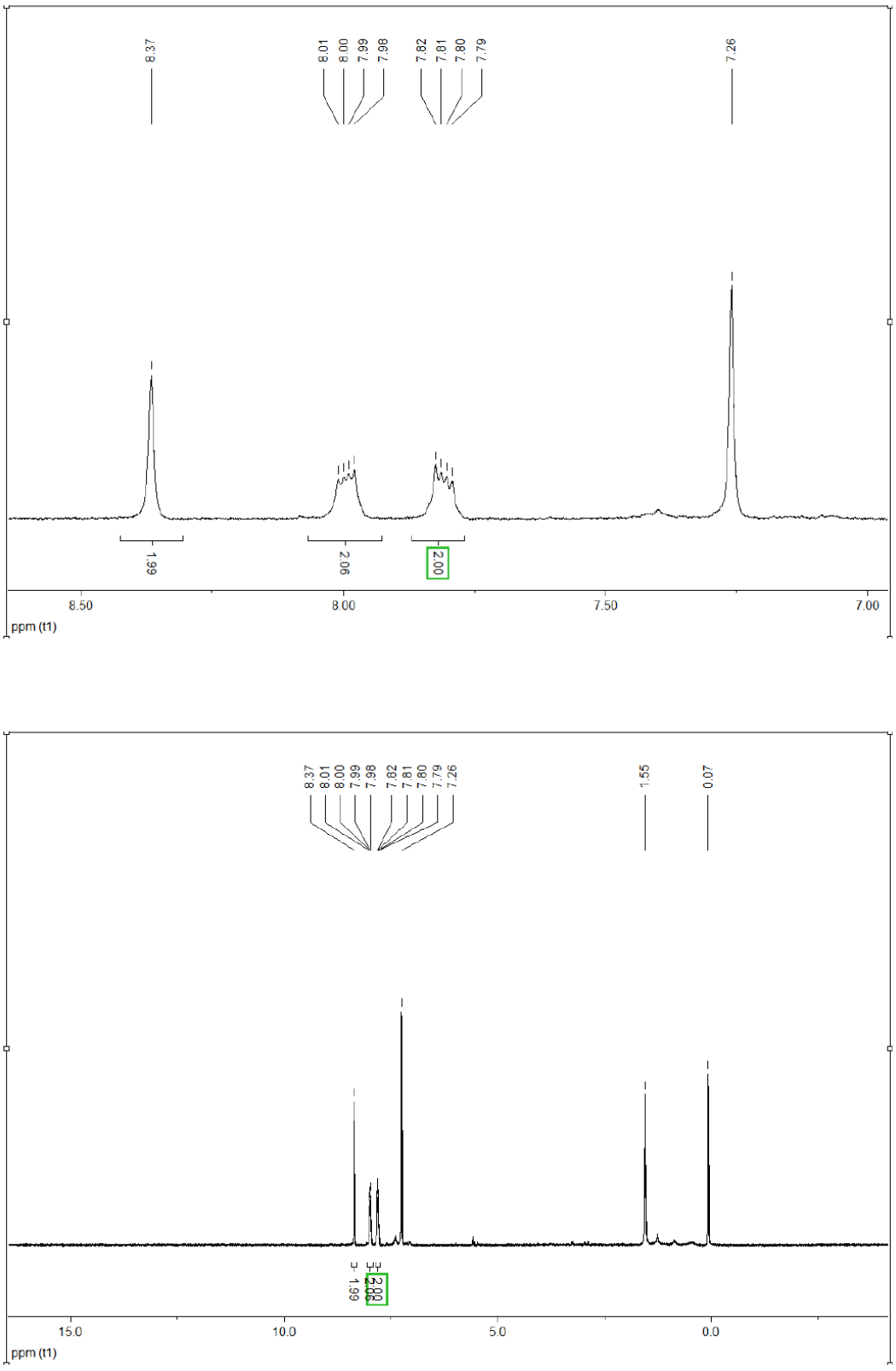

Supplementary Figure 19. 1H NMR of ADN in CDCl3.

Supplementary Methods

1) Details of the DFT Calculations

Density functional theory (DFT) calculations were performed with the Vienna *ab initio* Simulation Package (VASP 5.4.4).[9-12] The generalized gradient approximation-(GGA)-based exchange-correlation functional proposed by Perdew, Burke and Ernzerhof (PBE)[13] was used in conjunction with the projector-augmented wave (PAW) method using the "standard" pseudo potentials for all atoms (version PBE5.4).[14] Dispersion effects were treated with the DFT-D3 scheme using the Becke-Johnson-type damping function.[15, 16] The precision tag was set to accurate, a total energy difference of at most 10^{-5} eV is used for SCF convergence while setting the plane wave energy cutoff to 400 eV. For structure optimization, the force convergence criterion is 10^{-2} eV $Å^{-1}$. The surface was modelled with the slab-supercell approach using periodic boundary conditions (PBC) and a four-layer 3×9 slab to represent the Ag surface of which the two bottom layers were constrained to the bulk structure. The thickness of the vacuum layer between periodically repeated slabs was larger than 13 Å. The lattice parameter (a = 4.073 Å) was determined computationally using the same input parameters and a 10×10 Γ-centered k-point mesh and 4 atoms per unit cell. This approach delivered accurate results in the past.[17] For the surface calculations, a 6×2 Γ-centered k-point mesh was used. The first order Methfessel-Paxton[18] procedure was used to smear out electronic levels by σ = 0.2 eV to accelerate SCF convergence. This level of smearing corresponds to 2321 K of electronic temperature ($\sigma = k_B T$). Energies are then extrapolated to σ = 0.

The corrugation is calculated with respect to the averaged first layer of the relaxed, pristine surface. STM simulations based on the Tersoff-Hamann approximation using the local density of states were carried out with a bias voltage of -2.4 V. The band structure has been computed without consideration of the surface with the PBE and the HSE06[19] functionals.

Electron density plots, crystal orbitals, and periodic energy decomposition analysis (pEDA) (see below) were calculated with the Amsterdam Density Functional (ADF-BAND 17.107).[20-24] Again, the PBE-D3(BJ) functional was used in conjunction with the atom centered DZP[25-27] basis set. The equivalence of plane wave and atom-centered description of crystal orbitals was confirmed by visual inspection.

Supplementary References.

1. Mohn, F., Gross, L., Moll, N. & Meyer, G. Imaging the charge distribution within a single molecule. *Nat. Nanotechnol.* **7**, 227-231 (2012).

2. Konings, M. S. *et al.* Gadolinium complexation by a new diethylenetriaminepentaacetic acid-amide ligand. Amide oxygen coordination. *Inorg. Chem.* **29**, 1488-1491 (1990).

3. König, E. & Watson, K. J. The Fe-N bond lengths, the "ionic radii" of iron (II), and the crystal field parameters (10Dq) in a high-spin and low-spin [FeII-N6] complex. *Chem. Phys. Lett.* **6**, 457-459 (1970).

4. Raupach, M. & Tonner, R. A periodic energy decomposition analysis method for the investigation of chemical bonding in extended systems. *J. Chem. Phys.* **142**, 194105 (2015).

5. Dunnington, B. D. & Schmidt, J. R. Generalization of natural bond orbital analysis to periodic systems: Applications to solids and surfaces *via* plane-wave density functional theory. *J. Chem. Theory Comput.* **8**, 1902-1911 (2012).

6. Weigend, F. & Ahlrichs, R. Balanced basis sets of split valence, triple zeta valence and quadruple zeta valence quality for H to RN: Design and assessment of accuracy. *Phys. Chem. Chem. Phys.* **7**, 3297-3305 (2005).

7. Brena, B. *et al.* Valence-band electronic structure of iron phthalocyanine: An experimental and theoretical photoelectron spectroscopy study. *J. Chem. Phys.* **134**, 074312 (2011).

8. Mikhalenko, S. A. & Lukyanets, E. A. Phthalocyanines and related compounds. Part 2. Synthesis and certain properties of 2, 3-naphthalocyanines. *J. Gen. Chem. USSR* **61**, 905-910 (1991).

9. Kresse, G. & Hafner, J. *Ab initio* molecular dynamics for liquid metals. *Phys. Rev. B* **47**, 558-561 (1993).

10. Kresse, G. & Furthmüller, J. Efficiency of *ab-initio* total energy calculations for metals and semiconductors using a plane-wave basis set. *Comput. Mater. Sci.* **6**, 15-50 (1996).

11. Kresse, G. & Furthmüller, J. Efficient iterative schemes for *ab initio* total-energy calculations using a plane-wave basis set. *Physic. Rev. B* **54**, 11169-11186 (1996).

12. Kresse, G. & Hafner, J. *Ab initio* molecular dynamics for open-shell transition metals. *Phys. Rev. B* **48**, 13115-13118 (1993).

13. Perdew, J. P., Burke, K. & Ernzerhof, M. Generalized gradient approximation made simple. *Phys. Rev. Lett.* **77**, 3865-3868 (1996).

14. Kresse, G. & Joubert, D. From ultrasoft pseudopotentials to the projector augmented-wave method. *Phys. Rev. B* **59**, 1758-1775 (1999).

15. Grimme, S., Antony, J., Ehrlich, S. & Krieg, H. A consistent and accurate *ab initio* parametrization of density functional dispersion correction (DFT-D) for the 94 elements H-Pu. *J. Chem. Phys.* **132**, 154104 (2010).

16. Grimme, S., Ehrlich, S. & Goerigk, L. Effect of the damping function in dispersion corrected density

functional theory. *J. Comput. Chem.* **32**, 1456-1465 (2011).

17. Rosenow, P., Jakob, P. & Tonner, R. Electron–vibron coupling at metal–organic interfaces from theory and experiment. *J. Phys. Chem. Lett.* **7**, 1422-1427 (2016).

18. Methfessel, M. & Paxton, A. T. High-precision sampling for brillouin-zone integration in metals. *Phys. Rev. B* **40**, 3616-3621 (1989).

19. Heyd, J., Scuseria, G. E. & Ernzerhof, M. Hybrid functionals based on a screened coulomb potential. J. *Chem. Phys.* **118**, 8207 (2003).

20. Velde, G. T. & Baerends, E. J. Precise density-functional method for periodic structures. *Phys. Rev. B* **44**, 7888-7903 (1991).

21. Wiesenekker, G. & Baerends, E. J. Quadratic integration over the three-dimensional brillouin-zone. *J. Phys. Condens. Matter* **3**, 6721-6742 (1991).

22. Franchini, M., Philipsen, P. H. T. & Visscher, L. The becke fuzzy cells integration scheme in the amsterdam density functional program suite. *J. Comput. Chem.* **34**, 1819-1827 (2013).

23. Franchini, M., Philipsen, P. H. T., van Lenthe, E. & Visscher, L. Accurate coulomb potentials for periodic and molecular systems through density fitting. *J. Chem. Theory Comput.* **10**, 1994-2004 (2014).

24. BAND2017, SCM, Theoretical Chemistry, Vrije Universiteit, Amsterdam, The Netherlands, http://www.scm.com.

25. Van Lenthe, E. & Baerends, E. J. Optimized slater-type basis sets for the elements 1-118. *J. Comput. Chem.* **24**, 1142-1156 (2003).

26. Chong, D. P., Van Lenthe, E., Van Gisbergen, S. & Baerends, E. J. Even-tempered slater-type orbitals revisited: From hydrogen to krypton. *J. Comput. Chem.* **25**, 1030-1036 (2004).

27. Chong, D. P. Augmenting basis set for time-dependent density functional theory calculation of excitation energies: Slater-type orbitals for hydrogen to krypton. *Mol. Phys.* **103**, 749-761 (2005).

ECS Journal of Solid State Science and Technology, 2020 **9** 061005

Influence of Ring Contraction on the Electronic Structure of Nickel Tetrapyrrole Complexes: Corrole vs Porphyrin

Jan Herritsch,[1] Jan-Niclas Luy,[1] Sebastian Rohlf,[2,3] Manuel Gruber,[2] Benedikt P. Klein,[1] Matthias Kalläne,[2,3] Peter Schweyen,[4] Martin Bröring,[4] Kai Rossnagel,[2,5] Ralf Tonner,[1,a] and J. Michael Gottfried[1,z]

[1]*Fachbereich Chemie, Philipps-Universität Marburg, 35032 Marburg, Germany*
[2]*Institut für Experimentelle und Angewandte Physik, Christian-Albrechts-Universität zu Kiel, 24098 Kiel, Germany*
[3]*Ruprecht-Haensel-Labor, Christian-Albrechts-Universität zu Kiel, 24098 Kiel, Germany*
[4]*Institut für Anorganische und Analytische Chemie, Technische Universität Braunschweig, 38106 Braunschweig, Germany*
[5]*Ruprecht-Haensel-Labor, Deutsches Elektronen-Synchrotron DESY, 22607 Hamburg, Germany*

The influence of the contracted corrole macrocycle, in comparison to the larger porphyrin macrocycle, on the electronic structure of nickel was studied with X-ray and ultraviolet photoelectron spectroscopy (XPS, UPS) and near-edge X-ray absorption fine structure (NEXAFS) spectroscopy. Synthesis and in situ characterization of the Ni complexes of octaethylporphyrin (NiOEP) and hexaethyldimethylcorrole (NiHEDMC) were performed in ultra-high vacuum. XPS and NEXAFS spectra reveal a +2 oxidation state and a low-spin d^8 electron configuration of Ni in both complexes, despite the formal trianionic nature of the corrole ligand. UPS, in combination with density functional theory (DFT) calculations, support the electronic structure of a Ni(II) corrole with a π-radical character of the ligand. The NEXAFS spectra also reveal differences in the valence electronic structure, which are attributed to the size mismatch between the small Ni(II) center and the larger central cavity of NiOEP. Analysis of the gas-phase structures shows that the Ni−N bonds in NiOEP are 4%–6% longer than those in NiHEDMC, even when NiOEP adopts a ruffled conformation. The individual interactions that constitute the Ni−ligand bond are altogether stronger in the corrole complex, according to bonding analysis within the energy decomposition analysis and the natural orbitals for chemical valence theory (EDA-NOCV).

 [DOI: 10.1149/2162-8777/ab9e18]

Manuscript received May 31, 2020. Published July 8, 2020. *This paper is part of the JSS Focus Issue on Porphyrins, Phthalocyanines, and Supramolecular Assemblies in Honor of Karl M. Kadish.*

Supplementary material for this article is available online

Nickel complexes of porphyrins and related tetrapyrrolic macrocycles play a prominent role in nature as the active centers of enzymes,[1] such as the cofactor F430 found in methanogenic archaea, and occur as biomarkers in sediments.[2,3] Their coordination chemistry[4–7] is of broad scientific and technological interest, especially in connection with potential applications as molecular sensors and switches.[8–10] The porphyrin ligand provides a square-planar coordination environment for the central nickel ion, which normally has a low-spin d^8 electron configuration. However, nickel porphyrin complexes tend to undergo out-of-plane distortion leading to ruffled conformations that were observed in crystal structures and in solution for different porphyrin ligands.[11–18] This tendency for distortion can be explained by the size mismatch between the small nickel(II) center and the larger central cavity of the ligand macrocycle. The ruffled conformation leads to an effective contraction of the macrocycle and thus to a more favorable coordination geometry for the small low-spin Ni(II) cation.[14,19] Additional axial coordination used to manipulate the spin state of the nickel center can be accompanied by a change of the conformation of the porphyrin.[20]

A contracted coordination environment for the central nickel(II) cation can also be achieved through modification of the ligand skeletal structure, i.e., by replacing the porphyrin by the related corrole.[21–24] The corrole contains one carbon atom less in the macrocycle and thus can be described as a ring-contracted porphyrin (Fig. 1a). Its molecular structure with a missing methine (=CH−) bridge leads to a modified electronic structure. In accordance with the rules of aromaticity, corroles comprise three NH-groups and therefore are formally trianionic ligands.[22] Their smaller ring with the contracted cavity provides a tighter coordination environment,[23] making corroles promising ligands for the stabilization of small metal ions in high oxidation states.[25]

In contrast to nickel porphyrin complexes, nickel corrole complexes have received only little attention in the past, despite their interesting electronic structure.[23] In the early days of corrole research, nickel corroles were synthesized and described as paramagnetic, non-aromatic compounds.[26–29] However, at that time the exact structure of nickel corroles was unclear. The structure was assumed as a peculiar, not fully conjugated macrocycle with an additional hydrogen atom at one of the *meso*-methine bridges.[26,27] This sp^3 center would interrupt the conjugation path along the macrocycles and thus destroy the aromatic character. An alternative description of the ground-state of nickel corroles as a nickel(II) d^8 central atom with a π-radical ligand system did not follow until much later and was supported by electron paramagnetic resonance (EPR) spectroscopy and crystallographic structure analysis.[30] This interpretation was later confirmed by DFT calculations.[23,31,32]

In the present paper, a nickel corrole complex is—to our knowledge—for the first time characterized by X-ray photoelectron spectroscopy (XPS) and near-edge X-ray absorption fine structure (NEXAFS) spectroscopy under ultra-high vacuum (UHV) conditions. By this approach, the oxidation state of the central atom is verified and the corrole complex is compared to a related nickel porphyrin to reveal changes in the electronic structure induced by a porphyrinoid ring contraction.

Until now, most studies of nickel corrole complexes have been performed with octaalkyl substituted ligands. Therefore, the 2,3,8,12,17,18-hexaethyl-7-13-dimethylcorrole (H_3HEDMC) ligand provides a good starting point for the investigation of nickel corroles under UHV conditions. 2,3,7,8,12,13,17,18-octaethylporphyrin (H_2OEP) was used as the porphyrin reference system. The studied complexes were obtained by direct metalation achieved by physical vapor deposition (PVD) of nickel onto thin films of H_3HEDMC and H_2OEP, respectively, in UHV. This previously established method[33–41] for the

[a]Present address: Institut für Physikalische und Theoretische Chemie, Universität Regensburg, 93053 Regensburg, Germany.
[z]E-mail: michael.gottfried@chemie.uni-marburg.de

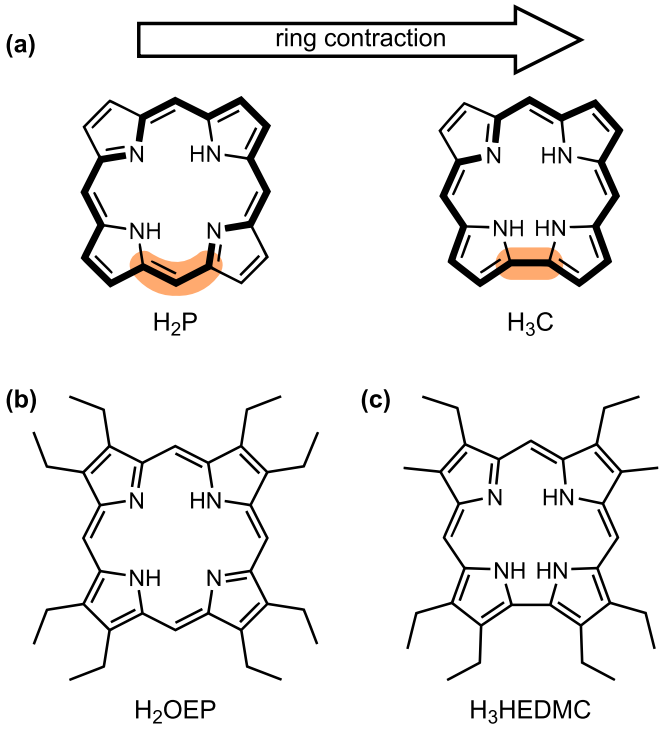

Figure 1. Molecular structures of (a) the free-base porphine and corrole macrocycles, (b) 2,3,7,8,12,13,17,18-octaethylporphyrin (H_2OEP) and (c) 2,3,8,12,17,18-hexaethyl-7-13-dimethylcorrole (H_3HEDMC). The structural difference regarding the methine bridge is highlighted and the aromatic 18π electron delocalization pathway is shown by bold lines.

preparation of transition-metal tetrapyrrole complexes has the formidable advantage of providing exceptionally clean UHV conditions during the metalation and immediately following in situ spectroscopic characterization of the complexes. As a result, influences of oxidation or other reactions with ambient gases are avoided, which is especially important when surface spectroscopic techniques such as XPS are employed. The thin films of the free corrole and porphyrin bases were also prepared in UHV by PVD of the respective molecules onto a Ag (111) single crystal surface. This in situ metalation was previously successfully applied for the metalation of H_2OEP and H_3HEDMC with iron.[34] The direct metalation with nickel was established for different tetrapyrrole ligand systems and provides the basis for our study.[40,42–44] Here, we apply conditions of Ni deficiency (i.e., an excess of ligand molecules) to minimize the amount of remaining unreacted Ni. The limited diffusion and reaction depth of transition metal atoms in the molecular thin films ensures that only the topmost layers of the thin films are metalated.[45] The complexes are therefore electronically decoupled from the Ag surface by layers of pristine, unmetalated molecules.[46]

Using XPS, UPS, NEXAFS, and DFT calculations, we show that NiOEP and NiHEDMC both exhibit a nickel(II) central atom in a low-spin d^8 electron configuration. Hence, our results support the description of the corrole ligand in NiHEDMC as a π-radical. With DFT, we analyze differences in the geometric and electronic structures between the corrole and porphyrin complexes. By using the energy decomposition analysis combined with the natural orbitals for chemical valence theory (EDA-NOCV), we characterize the individual bonding interactions between ligand and central atom.

Experimental and Computational Details

H_3HEDMC was prepared according to the reported procedure.[34] H_2OEP (purity > 98%, J&K Scientific Ltd) and its nickel complex NiOEP (purity > 95%, Por-Lab, Porphyrin Laboratories GmbH) were purchased from commercial sources. All experiments were performed in UHV with a base pressure below 10^{-9} mbar. Note that the UHV conditions ensure that the oxygen and water partial pressures during the preparation and characterization are at least 10^6 times lower than under typical glove box conditions. The Ag (111) single crystal used as substrate was cleaned by repeated cycles of Ar^+ ion bombardment (0.5 keV) followed by annealing (800 K). Surface cleanliness was checked prior to the experiments by XPS. H_3HEDMC, H_2OEP and NiOEP were vapor-deposited onto the Ag(111) surface from a Knudsen cell evaporator held at 195, 220 and 250 °C, respectively. The flux was monitored at the sample position using a quartz crystal microbalance and the thickness of the resulting thin films was in the range of 10 monolayers. Metalation was performed by vapor deposition of nickel onto the organic multilayers using electron beam evaporators (FOCUS EFM-3/4). Substoichiometric amounts of Ni were used to avoid or minimize the presence of unreacted Ni(0), as was subsequently confirmed by spectroscopy. During the preparation, the Ag sample was kept at room temperature. For XPS, a monochromated Al K_α X-ray source (1486.7 eV) and a SPECS Phoibos 150 electron energy analyzer equipped with an MCD-9 multichanneltron detector were used. A linear background was subtracted from the Ni 2p spectra. Valence photoemission spectra (UPS) were measured with the same analyzer and a gas-discharge UV source providing He-I radiation (21.2 eV). Near-edge X-ray absorption fine structure (NEXAFS) spectroscopy was performed at the ASPHERE experimental station at the beamline P04[47] of PETRA III (DESY, Hamburg). Several spectra were collected in total electron yield mode and averaged to improve the signal-to-noise ratio. In case of the Ni L-edge, a spectrum of the pristine Ag(111) surface was used for a background correction. In this procedure, the background spectrum was interpolated by a smoothing spline; afterwards, the measured spectra were divided by the spline function.

Structural optimization was carried out with Gaussian09 C.01[48] using the PBE functional[49] and the def2-TZVPP[50] basis set as a part of the density functional theory (DFT) calculations. The "tight" convergence criteria were applied in this regard. Densities of states (DOS) were calculated using the PBE0[51] hybrid functional. Atomic contributions of molecular orbitals were obtained based on the Mulliken population analysis using GaussSum 3.0.[52] For simulations of NEXAFS spectra, the Slater transition potential method[53,54] implemented in the Amsterdam Density Functional (ADF) program package[55] version 2016.106 and the PBE[49] functional were used. Hence, the structures were reoptimized (gridsize m4) including the D3BJ dispersion correction[56] with the def2-TZVPP[50] basis set using Turbomole 7.1. For the simulation itself, the TZ2P[57] basis set was used for all elements except Ni to which the larger, even-tempered ET-QZ3P-3DIFFUSE[58] basis set was supplied for a more detailed description of the core electronic structure. To reproduce the shape of the spectrum, a Gaussian broadening (FWHM = 0.8 eV) was applied on the calculated transitions. The binding situation was further analyzed with the help of the energy decomposition analysis[59–61] (EDA) in combination with the natural orbitals for chemical valence theory[62] (EDA-NOCV) using ADF version 2018.105 and the PBE[49] functional in combination with the TZ2P[57] basis set.

Results and Discussion

Information about the oxidation state of nickel in its complexes was obtained from the position and shape of the Ni 2p XPS signals shown in Fig. 2. To confirm the feasibility of the in situ metalation method,[33–46] we use a film of directly vapor-deposited NiOEP as a reference, because NiOEP is readily available and its stability is well established.[63] The Ni 2p XPS signal of this NiOEP layer is shown in Fig. 2a. The spectra in Figs. 2b and 2c correspond to films of H_2OEP and H_3HEDMC after their partial metalation with vapor-deposited Ni, resulting in the formation of NiOEP and NiHEDMC, respectively. The fraction of metalated molecules was approximately 10%, as was estimated from the N 1s XP spectra presented in Fig. S1 (available online at stacks.iop.org/JSS/9/061005/mmedia) of the

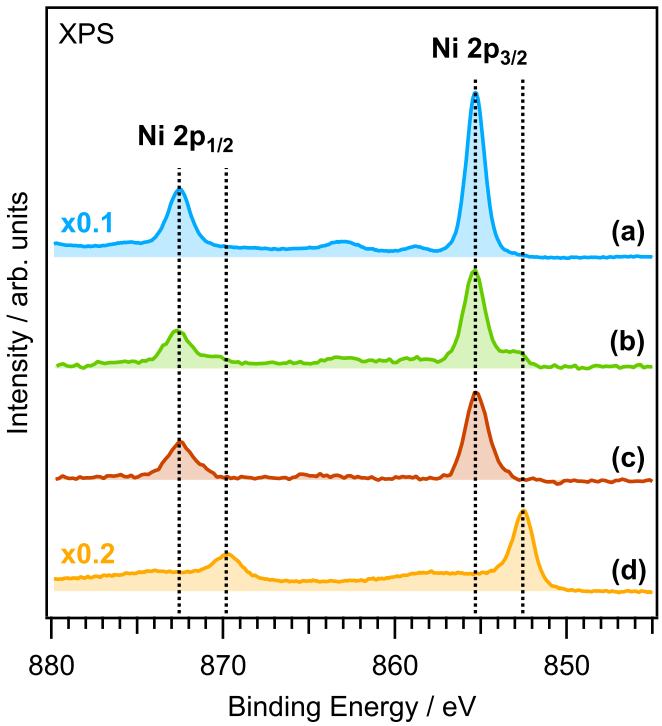

Figure 2. Ni 2p XP spectra of (a) a NiOEP film (reference) and (b), (c) partially Ni metalated films of H_2OEP and H_3HEDMC, resulting in the in situ formation of (b) NiOEP and (c) NiHEDMC. The films have a thickness of 10 monolayers. (d) Ni 2p XP spectrum of Ni directly deposited onto a pristine Ag(111) surface as reference for Ni(0).

supplementary material. Since the XPS signals in the Ni 2p region are element-specific, the unmetalated molecules do not contribute to the spectra and thus do not disturb. The spectrum in Fig. 2d corresponds to Ni directly vapor-deposited onto the clean Ag(111) surface. It serves as a reference for nickel in the zero oxidation state, Ni(0).

Besides some satellite structure, the XP spectrum of the reference NiOEP film (Fig. 2a) shows a narrow Ni $2p_{3/2}$ signal at a binding energy (BE) of 855.3 eV and a Ni $2p_{1/2}$ signal at 872.5 eV. The spectrum has the typical shape and features previously reported for nickel(II) porphyrins.[64,65] The Ni 2p spectrum of the sample prepared by vapor deposition of Ni onto the H_2OEP film (Fig. 2b) is very similar to the NiOEP reference spectrum, indicating successful in situ metalation and formation of NiOEP. The additional shoulders visible at the at low-BE side of the Ni $2p_{3/2}$ and Ni $2p_{1/2}$ signals in Fig. 2b are attributed to small amounts of residual unreacted Ni(0). (Note that these shoulders are shifted towards higher BEs, compared to the Ni(0) reference spectrum in Fig. 2d, due to a less effective core-hole screening in the organic film.)

The spectrum of the partially metalated H_3HEDMC film in Fig. 2c is very similar to the spectrum of NiOEP. In particular, the NiHEDMC spectrum shows a narrow Ni $2p_{3/2}$ signal at 855.2 eV and Ni $2p_{1/2}$ signal at 872.5 eV. These BEs are almost identical to those found for NiOEP. It can therefore be concluded that the Ni ions in NiOEP and NiHEDMC have very similar oxidation states and partial charges. In addition, both spectra lack multiplicity in the Ni 2p region apart from the spin–orbit splitting. Therefore, they support earlier reports[30] that the central nickel atom in corrole complexes is best described as a divalent cation in a low-spin d^8 electron configuration.[66] As a consequence of the formally trianionic nature of the corrole ligand and a divalent central atom, the ligand must bear an unpaired electron. Hence, the studied complex NiHEDMC can be described by the molecular formula shown in Fig. 3b with a delocalized π-radical. This feature represents an important difference between nickel complexes of porphyrin and corrole. Our DFT calculations of the gas-phase structure of NiHEDMC are consistent with these experimental findings. The spin density shows that the unpaired electron is mainly located in a ligand orbital (Fig. 3c). Due to a minor mixing of the singly occupied molecular orbital (SOMO) of the ligand with a d_π orbital of the central metal atom, a small part of the spin-density remains located at the metal center.

Before we turn to the electronic structure in more detail, we briefly discuss the molecular geometry to obtain insight into the structural consequences of the corrole ring contraction. We have analyzed the calculated gas-phase structures of NiOEP and NiHEDMC along with the structures of complexes of the parent ligands, nickel(II) porphine (NiP) and nickel(II) corrole (NiC). In this way, influences of the ring contraction and the peripheral alkyl substituents can be identified and discriminated. In the case of NiOEP, two different minimum-energy structures with almost equal energies were obtained; one is a planar conformer and the other has a strongly out-of-plane distorted ruffled macrocycle. While the ruffled conformer is lower in energy and discussed here in detail, the planar conformer is described in the supplementary material. The cavity size of the macrocycle filled by the nickel ion can be estimated by the lengths of the Ni−N bonds. For NiOEP and NiP, the Ni−N bond lengths are very similar with 1.955 Å and 1.957 Å, respectively (see also Table SI). In comparison, the corrole ligands leave less space for the central nickel atom; the bond lengths range from 1.842 Å to 1.878 Å (see Table SI). (The variation of the bond lengths in the case of the corroles is due to their lower symmetry, compared to the porphyrins.) Unlike corroles, the porphyrin systems undergo substantial out-of-plane distortion to compensate the size mismatch between cavity and central atom. This is a common behavior of porphyrin complexes and was previously reported.[67] The deformation manifests in a so-called ruffling of the macrocycle. In the course of this, the *meso* carbon atoms (i.e., the methine bridges) are displaced alternately above and below the mean plane of the molecule.[16] The distinct ruffling deformation of NiOEP and NiP, compared to the almost planar form of the corrole systems, can be seen in Fig. 4. According to the optimized gas-phase structures, the

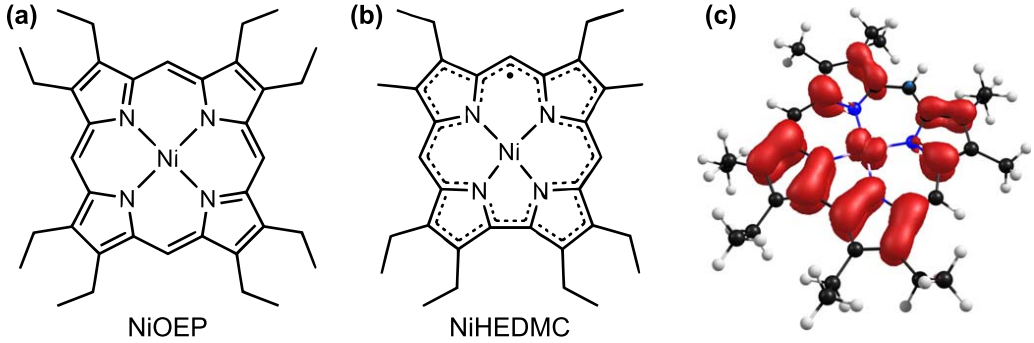

Figure 3. Molecular formulas of the nickel(II) complexes (a) NiOEP and (b) NiHEDMC (as delocalized π-radical). This formulation is consistent with the spin-density (iso surface value = 0.0015) obtained from DFT calculations (PBE/def2-TZVPP) as shown in (c).

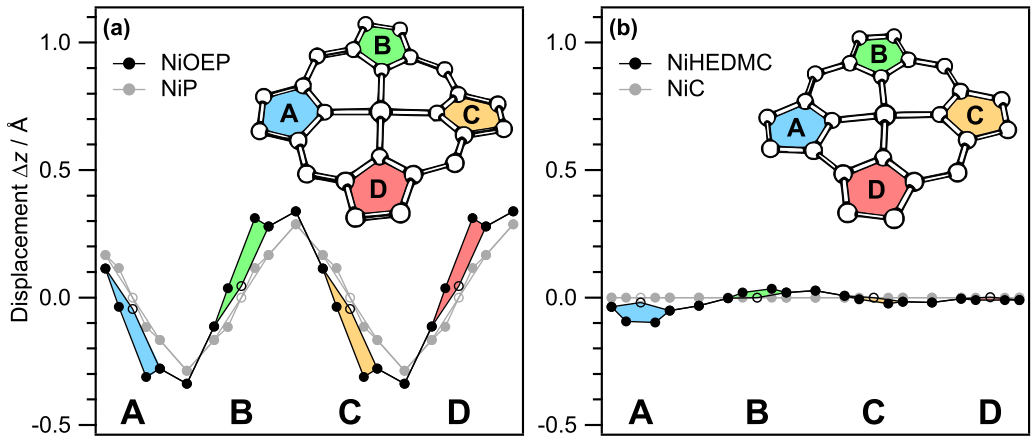

Figure 4. Out-of-plane displacement Δz in Å of the different atoms for (a) NiOEP and NiP and (b) NiC and NiHEDMC. Optimized gas-phase structures (PBE/def2-TZVPP) of NiOEP and NiHEDMC are shown with numbering of the individual pyrrole units (A, B, C, D). Hydrogen atoms and alkyl substituents are omitted for clarity. Δz is given as deviations from the mean plane defined by the average displacement of all atoms.

alkyl substituents have only little impact on the deformation. In conclusion, even when the OEP ligand adopts a strongly ruffled conformation, its cavity remains larger compared to the HEDMC ligand, as indicated by the Ni−N bond lengths.

In the following, we analyze the effects of the ring contraction on the electronic structure. The valence electronic structure in the occupied range was probed using UPS. In Fig. 5, we compare the UP spectra of the nickel complexes with those of the free ligands. This approach allows us to pinpoint the changes in the valence region of the two different ligands upon metalation. To obtain films with higher fractions of the metal complexes while still avoiding unreacted Ni(0), a different layer-by-layer metalation procedure was applied, as described in the supplementary material. Fig. 5 shows valence spectra of H_2OEP and NiOEP (Fig. 5a) and of H_3HEDMC and NiHEDMC (Fig. 5e). In addition, the corresponding difference spectra (nickel complex minus free-base ligand) are presented (Figs. 5b, 5f). For comparison of the experimental spectra

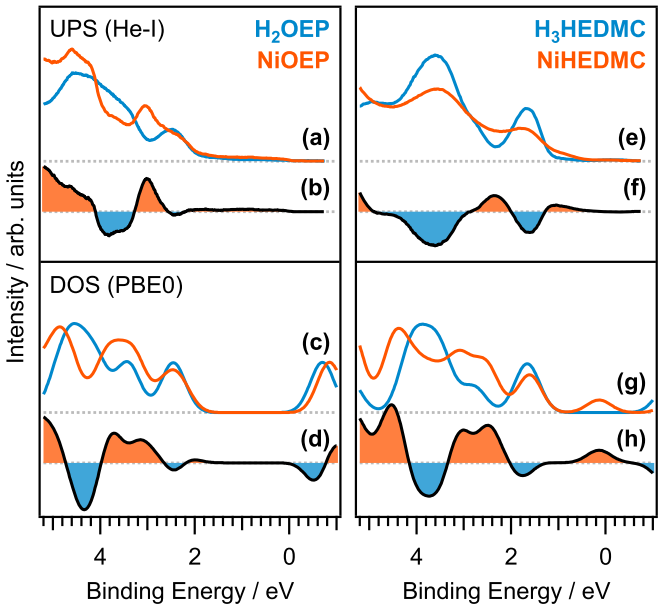

Figure 5. Experimental and calculated valence spectra of the free ligands (blue lines) and the corresponding nickel complexes (orange lines). Experimental photoelectron spectra of (a) H_2OEP and NiOEP, (e) H_3HEDMC and NiHEDMC. (b), (f) Difference spectra (Ni complex minus free ligand). (c), (g) Corresponding calculated DOS (PBE0/def2-TZVPP) and (d), (h) differences in the same color code. For the open shell system NiHEDMC, the two spin channels are summed up. The calculated DOS is aligned to the experimental HOMO energy.

with DFT results, Gaussian broadening (FWHM = 0.6 eV) was applied to the calculated molecular orbital eigenvalues. Because the latter are referenced to the vacuum energy level, which cannot be measured experimentally, the calculated eigenvalues were aligned to the experimental BE of the highest occupied molecular orbital (HOMO). The density of states (DOS) obtained in this way (Figs. 5c, 5g) agrees reasonably well with the experimental spectra considering the limitations of the used method (which includes the initial-state approximation and neglects influences of cross section effects). Looking at the highest occupied states, distinct differences between the experimental spectra of the porphyrin and corrole derivatives upon metalation can be seen. Upon formation of NiOEP, the BE range around 2.3 eV shows almost no changes, while the corrole ligand system shows a peak around 1.6 eV that decreases significantly upon metalation. This peak can be attributed to the HOMO and the SOMO of H_3HEDMC and NiHEDMC, respectively. The decreased peak intensity is a further indication that the metalation product NiHEDMC is a π-radical with one singly occupied ligand orbital. Besides these differences, changes in the electronic structure below the highest occupied states are visible in both ligand systems.

Figure 6 shows the calculated total DOS for both complexes along with the projected densities of states of the nickel atoms (Ni-PDOS). All energies are given as BE and thus aligned to the experimental HOMO energy. Comparison between the total DOS and the Ni-PDOS allows to distinguish between contributions from the ligand and the metal center. Typically, the valence region of porphyrins comprises two sets of mostly degenerate ligand orbitals representing the frontier orbitals.[68] This structure also appears in NiOEP (Fig. 6a), which has two occupied ligand orbitals (with BEs of +2.6 eV and +2.3 eV) and two degenerate unoccupied orbitals (−0.9 eV), resulting in a HOMO-LUMO gap of 3.2 eV. The valence region of NiHEDMC differs from this structure. Here, a singly occupied molecular orbital (SOMO) appears at +1.6 eV. The corresponding singly unoccupied molecular orbital with opposite spin (SUMO) is found at +0.1 eV resulting in a small SOMO −SUMO separation of 1.5 eV. Despite a general shift of the orbital energies to lower BE in case of NiHEDMC, the electronic structure is similar in both complexes; especially the electronic structure of the central atom is similar in both complexes. However, one important feature is the decisive difference for the nickel electronic structure in the unoccupied states. NiOEP has an unoccupied orbital at −1.9 eV BE with a high nickel 3d atomic orbital character. This orbital can be described as a σ^* state formed by the antibonding combination of the nickel $3d_{x2-y2}$ atomic orbital and a ligand orbital. In contrast to this, the corresponding antibonding σ^* orbital of NiHEDMC has a BE of −3.3 eV. The stronger destabilization of the antibonding state in the corrole complex may result from a better

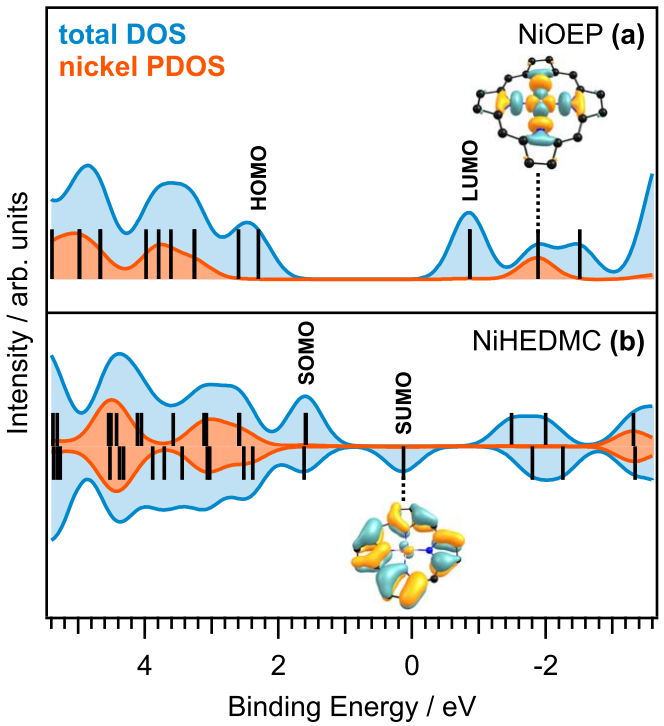

Figure 6. Calculated total DOS (PBE/def2-TZVPP, blue), Ni-PDOS (orange) plotted against the BE for (a) NiOEP and (b) NiHEDMC. The black bars indicate the negative energies of the corresponding orbital eigenvalues. Gaussian broadening (FWHM = 0.6 eV) was applied to the calculated molecular orbital eigenvalues and the Ni atomic orbital contributions to obtain the blue and orange curves, respectively. The DOS and the negative orbital eigenvalues are aligned to the experimental HOMO energy. Visualizations (iso surface value = 0.03) are shown for selected orbitals. Hydrogen atoms and alkyl substituents are omitted for clarity.

overlap of the Ni $3d_{x2-y2}$ atomic orbital with the ligand orbital due to the reduced Ni−N bond length.

NEXAFS spectroscopy provides information about the unoccupied valence states and, thus, was used to verify the calculated electronic structure. Figure 7 shows Ni L-edge absorption spectra of (a) NiOEP and (b) NiHEDMC as well as (c) a Ni(0) reference. In the case of NiOEP, the main transitions appear at 853.4 eV (L_3) and 870.3 eV (L_2), which can be assigned to the transitions from the Ni $2p_{3/2}$ and Ni $2p_{1/2}$ core levels, respectively, to the aforementioned σ^* bond type molecular orbital. The spectrum of NiHEDMC has a similar shape with main transitions at 854.0 eV and 870.9 eV, i.e., the spectrum is shifted to higher photon energies by 0.6 eV relative to the spectrum of NiOEP.

According to a recent NEXAFS study of a nickel porphyrin based molecular spin-state switch,[20] the Ni L-edge of the nickel low-spin d^8 state is characterized by only one main transition, while the corresponding high-spin state shows a double peak structure.[20] Thus, our NEXAFS spectra clearly indicate that nickel has a low-spin d^8 electron configuration in both complexes. The experimental results are corroborated by DFT calculations for the parent molecules NiP and NiC (Figs. 7d, 7e). With the used method (see the computational details), the spin–orbit splitting of the core level is not included within the calculations. Therefore, the simulation does not show separate L_3- and L_2-edges. The calculation supports the assignment of the main transition peak (see visualized orbital in Figs. 7d, 7e). The absolute energy values, the overall shape and the trend are well described by the used method: NiP exhibits a significantly lower excitation energy for the main transition than NiC. Apart from that, all other transitions have only minor contributions to the simulated spectra for both complexes.

These findings clearly support the +2 oxidation state with a low-spin d^8 configuration for the central nickel atom in both complexes.

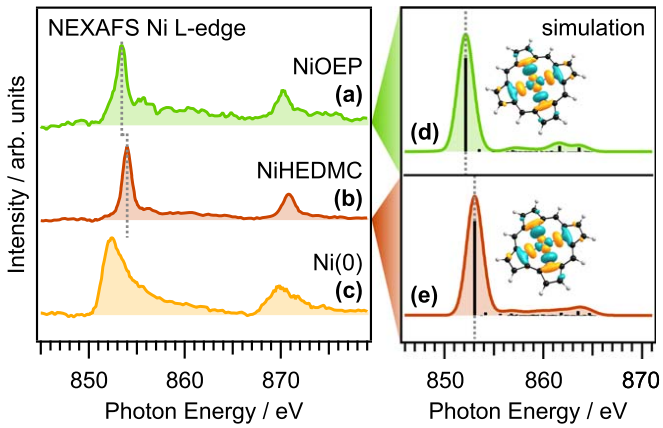

Figure 7. Ni L-edge NEXAFS spectra of (a) NiOEP, (b) NiHEDMC, and (c) Ni on Ag(111). The Ni complexes were prepared by partial in situ metalation of films of the ligands. (d), (e) Simulated spectra of the complexes of the parent macrocycles NiP and NiC. The main transition peak can be assigned to an excitation into the visualized unoccupied orbital (iso surface value = 0.03). The solid lines in the simulation indicate the discrete transition energies.

This means that the stable nickel(II) state forces the corrole ligand to be formally oxidized bearing a π-radical character. Although the former aromatic system of the ligand is lost upon metalation, the reduced aromatic stabilization appears to be compensated by the increased stability of the central atom. As a result of the unpaired electron, nickel corroles are expected to be reduced easily, forming anionic species, in which the aromatic character is reestablished. Nevertheless, an oxidation of the central atom is rather not expected. In contrast to this, reduction of the central atom in nickel porphyrins is known from literature, e.g., in solution[69–71] or in the adsorbed state due to charge transfer from Cu(110) or Cu(100) surfaces to nickel(II) tetraphenylporphyrin.[72,73] Our results show how the reactivity (i.e., ligand vs central atom reduction) can be controlled by varying the ligand structure.

To quantify the different contributions to the chemical bond between the central atom and the ligand, we performed an in-depth bonding analysis. This analysis provides further insight into the influence of the porphyrinoid ring contraction on the nickel−ligand bond. In the framework of an energy decomposition analysis (EDA),[60] the complexes are divided into two fragments along the bond(s) under investigation. This enables the decomposition of the interaction between these fragments in different energy terms. Therefore, the complexes of the parent macrocycles NiP and NiC are divided into two fragments that are as close to the electronic structure the fragments have in the complex as possible. A similar procedure has previously been applied to five- and six-coordinate high-spin iron(III) porphyrin complexes.[74] Here, we omit the peripheral substituents and use the parent molecules NiP (D_{2h}) and NiC (C_{2v}) instead of the experimentally studied substituted systems, because their higher symmetry enables a clearer designation of bonding character to the interactions. In the chosen approach, the complexes were split into a nickel(II) fragment and the corresponding dianionic ligand fragment. In the case of the corrole, the dianionic ligand fragment is a radical bearing an unpaired electron. Table I gives an overview of the individual energy terms obtained within the EDA. Note that negative energies indicate stabilizing interactions, while positive energies indicate repulsive interactions. A detailed description and analysis of these energy terms is given in the supplementary material. Briefly, our findings reveal that the overall Ni-ligand bond is stronger in NiC than in NiP. (In the following, all energies are given in kJ mol^{-1}.) As can be seen in Table I, the overall bonding energy ΔE_{bond} of NiC (−3378) is more negative than that of NiP (−3315). This difference is largely due to an increased interaction energy ΔE_{int}, which comprises attractive (electrostatic ΔE_{elstat} and orbital ΔE_{orb}) and repulsive contributions

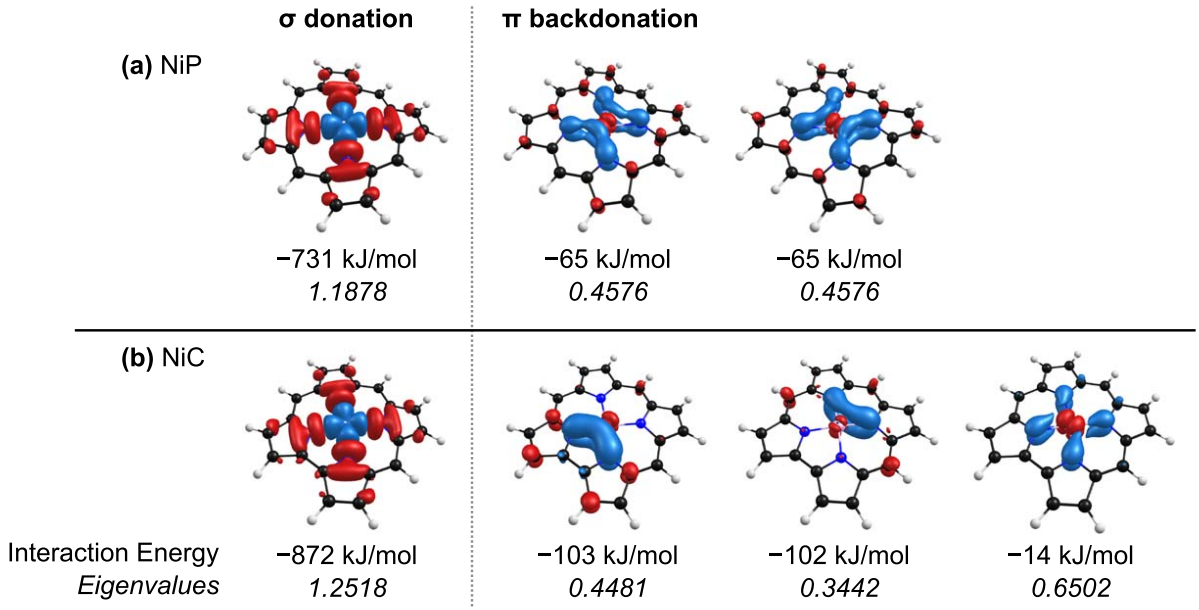

Figure 8. Selected NOCV deformation densities $\Delta\rho_i$ (iso surface value = 0.03) for (a) NiP and (b) NiC. Blue regions show charge accumulation and red regions charge depletion.

Table I. Results of the energy decomposition analysis (EDA) for the nickel complexes of the parent macrocycles NiP and NiC. Energies in kJ mol^{-1}; bond length d in Å.

	NiP (D_{2h})		NiC (C_{2v})	
ΔE_{int}	−3701		−3798	
ΔE_{Pauli}	+720		+1071	
ΔE_{elstat} [a]	−2727	(62%)	−2946	(61%)
ΔE_{orb} [a]	−1694	(38%)	−1923	(39%)
$\Delta E(\sigma$ donation) [b]	−1055	(62%)	−1203	(61%)
$\Delta E(\pi$ backdonation) [b]	−130	(8%)	−219	(11%)
ΔE(polarization) [b]	−273	(16%)	−233	(12%)
ΔE(rest) [b]	−237	(14%)	−308	(16%)
ΔE_{prep}	+386		+421	
ΔE_{deform} [c]	+70	(18%)	+59	(14%)
ΔE_{exc} [c]	+316	(82%)	+362	(86%)
ΔE_{bond}	−3315		−3378	
d(Ni−N)	1.957		1.842, 1.872	

a) Values in parentheses give the percentage contribution to the total attractive interactions $\Delta E_{elstat} + \Delta E_{orb}$. b) Values in parentheses give the percentage contribution to the orbital interactions ΔE_{orb}. c) Values in parentheses give the percentage contribution to the preparation energy ΔE_{prep}.

(Pauli repulsion ΔE_{Pauli}). The Pauli repulsion is stronger in NiC than in NiP (+1071 vs +720), but this is overcompensated by the stronger electrostatic (−2946 vs −2727) and orbital (−1923 vs −1694) attraction in the corrole complex. As a result, NiC has the more negative interaction energy (−3798 vs −3701). The stronger Pauli repulsion and the more attractive ΔE_{elstat} as well as the increased ΔE_{orb} in the case of NiC can be attributed to the shorter Ni−N bond distances and, thus, can be seen as a direct consequence of the smaller corrole cavity. A further partitioning of the orbital interactions in contributions of individual symmetry terms is given in the supplementary material.

The combination of the EDA with the natural orbital for chemical valence theory (EDA-NOCV)[62] enables further partitioning and interpretation of the orbital interaction ΔE_{orb}. ΔE_{orb} is divided into contributions of pairwise interactions between an orbital of the central atom and a ligand orbital of corresponding symmetry, referred to as deformation densities $\Delta\rho_i$. The deformation densities for each interaction can be visualized, which allows a classification of the interactions in categories by visual inspection. The EDA-NOCV also provides, as quantitative results, the corresponding energies ΔE_i for each interaction and the eigenvalues v_i that give an indication on the amount of charge flow in number of electrons. For a more detailed description of the method, the reader is referred to the supplementary material and the literature.[60,62]

Figure 8 shows selected deformation densities, which represent the most tangible interactions. For all of these, σ donation and π backdonations, the interactions are stronger in the corrole complex than in the porphyrin complex. The larger amount of charge that is redistributed by the formation of the Ni−N bond indicates a stronger bond to the central atom in nickel corroles. This is in line with the increased overall ΔE_{orb} term for the corrole complex. The nature of this bond influences the electronic structure of the nickel center, making the porphyrinoid ring contraction a viable way of tuning the properties of the central atom without changing its formal oxidation state.

Conclusions

The influence of ring contraction on the electronic structure of nickel tetrapyrrole complexes was studied by comparing the nickel corrole NiHEDMC with the nickel porphyrin NiOEP using XPS, UPS, and NEXAFS measurements, in combination with DFT calculations. The Ni 2p XP and Ni L-edge NEXAFS spectra support previous findings that both complexes contain low-spin d^8 Ni(II) cations. In the case of NiHEDMC, the combination of a trianionic ligand with the divalent central atom leads to a ligand π-radical, as was confirmed by computations. The calculated SOMO-related spin density is mainly located on the ligand. UPS shows that the HOMO intensity of the free corrole ligand decreases upon metalation with Ni, supporting the radical character of the corrole ligand in NiHEDMC. The valence spectra are in line with the calculated DOS. The Ni-PDOS supports the Ni d^8 electron configuration with one unoccupied Ni 3d type valence orbital, which can be described as the antibonding combination of a ligand orbital with the Ni $3d_{x2-y2}$ forming a Ni−N σ* state. The corresponding state has a much higher energy in NiHEDMC than in NiOEP, in agreement with the NEXAFS data. The Ni L-edges of both complexes have a similar shape with one narrow main feature, which can be assigned to the transition from the Ni 2p level to the aforementioned Ni−N σ* state. In-depth bonding analysis by the EDA-NOCV theory reveals

that Ni-corrole and Ni-porphyrin bonds show the same bonding character. However, the Ni-corrole bond shows larger interaction energy terms throughout, resulting in a higher overall bonding energy. The stronger Ni-N interactions in the corrole are attributed to its shorter Ni−N bonds. Calculations of the gas-phase structures reveal a ruffled porphyrin core in NiOEP, while the corrole core in NiHEDMC is almost planar. The reason for the ruffling of NiOEP lies in the size mismatch between the small Ni(II) cation and the large cavity of the porphyrin. Even with the effective contraction of the porphyrin ligand due to the ruffling, the Ni−N distance in NiOEP is larger than the Ni-N distances in NiHEDMC. Our results show that a seemingly small change of the ligand skeletal structure can lead to substantial changes of the electronic structure and the metal-ligand interaction, even when the formal oxidation number of the metal center remains unchanged.

Acknowledgments

Financial support by the Deutsche Forschungsgemeinschaft (DFG) through the SFB 1083 (223848855-SFB 1083) is gratefully acknowledged. We thank DESY (Hamburg, Germany), a member of the Helmholtz Association HGF, for the provision of experimental facilities. Parts of this research were carried out at PETRA III. Funding for the photoemission spectroscopy instrument ASPHERE at beamline P04 (Contracts 05KS7FK2, 05K10FK1, 05K12FK1, and 05K13FK1 with Kiel University; 05KS7WW1 and 05K10WW2 with Würzburg University) by the Federal Ministry of Education and Research (BMBF) is gratefully acknowledged. We thank HRZ Marburg, Goethe-CSC Frankfurt and HLRS Stuttgart for computational resources.

ORCID

Kai Rossnagel https://orcid.org/0000-0001-5107-0090
Ralf Tonner https://orcid.org/0000-0002-6759-8559
J. Michael Gottfried https://orcid.org/0000-0001-5579-2568

References

1. S. W. Ragsdale, *J. Biol. Chem.*, **284**, 18571 (2009).
2. R. A. Ware and J. Wei, *J. Catal.*, **93**, 100 (1985).
3. P. Schaeffer, R. Ocampo, H. J. Callot, and P. Albrecht, *Nature*, **364**, 133 (1993).
4. W. S. Caughey, R. M. Deal, B. D. McLees, and J. O. Alben, *J. Am. Chem. Soc.*, **84**, 1735 (1962).
5. D. Kim, C. Kirmaier, and D. Holten, *Chem. Phys.*, **75**, 305 (1983).
6. D. Kim and D. Holten, *Chem. Phys. Lett.*, **98**, 584 (1983).
7. L. X. Chen, W. J. H. Jäger, G. Jennings, D. J. Gosztola, A. Munkholm, and J. P. Hessler, *Science*, **292**, 262 (2001).
8. S. Thies, C. Bornholdt, F. Köhler, F. D. Sönnichsen, C. Näther, F. Tuczek, and R. Herges, *Chem. Eur. J.*, **16**, 10074 (2010).
9. M. K. Peters and R. Herges, *Inorg. Chem.*, **57**, 3177 (2018).
10. A. G. Martynov, E. A. Safonova, A. Y. Tsivadze, and Y. G. Gorbunova, *Coordin. Chem. Rev.*, **387**, 325 (2019).
11. E. F. Meyer, *Acta Crystall., B*, **28**, 2162 (1972).
12. R. G. Alden, B. A. Crawford, R. Doolen, M. R. Ondrias, and J. A. Shelnutt, *J. Am. Chem. Soc.*, **111**, 2070 (1989).
13. X. Y. Li, R. S. Czernuszewicz, J. R. Kincaid, and T. G. Spiro, *J. Am. Chem. Soc.*, **111**, 7012 (1989).
14. J. A. Shelnutt, C. J. Medforth, M. D. Berber, K. M. Barkigia, and K. M. Smith, *J. Am. Chem. Soc.*, **113**, 4077 (1991).
15. K. K. Anderson, J. D. Hobbs, L. Luo, K. D. Stanley, J. M. E. Quirke, and J. A. Shelnutt, *J. Am. Chem. Soc.*, **115**, 12346 (1993).
16. W. Jentzen et al., *J. Am. Chem. Soc.*, **117**, 11085 (1995).
17. C. M. Drain et al., *J. Am. Chem. Soc.*, **120**, 3781 (1998).
18. J. S. Evans and R. L. Musselman, *Inorg. Chem.*, **43**, 5613 (2004).
19. J. L. Hoard, *Ann. N. Y. Acad. Sci.*, **206**, 18 (1973).
20. A. Köbke et al., *Nat. Nanotechnol.*, **15**, 18 (2020).
21. S. Nardis, D. Monti, and R. Paolesse, *Mini-Rev. Org. Chem.*, **2**, 355 (2005).
22. J. H. Palmer, *Struct. Bond.*, **142**, 49 (2012).
23. A. Ghosh, *Chem. Rev.*, **117**, 3798 (2017).
24. S. Nardis, F. Mandoj, M. Stefanelli, and R. Paolesse, *Coordin. Chem. Rev.*, **388**, 360 (2019).
25. I. Aviv and Z. Gross, *Chem. Commun.*, 1987 (2007).
26. A. W. Johnson and I. T. Kay, *J. Chem. Soc.*, 1620 (1965).
27. R. Grigg, A. W. Johnson, and G. Shelton, *Chem. Commun.*, 1151 (1968).
28. R. Grigg, A. W. Johnson, and G. Shelton, *Liebigs Ann. Chem.*, **746**, 32 (1971).
29. Y. Murakami, Y. Matsuda, K. Sakata, S. Yamada, Y. Tanaka, and Y. Aoyama, *Bull. Chem. Soc. Jpn.*, **54**, 163 (1981).
30. S. Will, J. Lex, E. Vogel, H. Schmickler, J. P. Gisselbrecht, C. Haubtmann, M. Bernard, and M. Gross, *Angew. Chem. Int. Ed.*, **36**, 357 (1997).
31. A. Ghosh, T. Wondimagegn, and A. B. J. Parusel, *J. Am. Chem. Soc.*, **122**, 5100 (2000).
32. B. van Oort, E. Tangen, and A. Ghosh, *Eur. J. Inorg. Chem.*, 2442 (2004).
33. T. E. Shubina, H. Marbach, K. Flechtner, A. Kretschmann, N. Jux, F. Buchner, H. P. Steinruck, T. Clark, and J. M. Gottfried, *J. Am. Chem. Soc.*, **129**, 9476 (2007).
34. M. Schmid et al., *J. Phys. Chem. C*, **122**, 10392 (2018).
35. K. Diller, A. C. Papageorgiou, F. Klappenberger, F. Allegretti, J. V. Barth, and W. Auwärter, *Chem. Soc. Rev.*, **45**, 1629 (2016).
36. H. Marbach, *Acc. Chem. Res.*, **48**, 2649 (2015).
37. J. M. Gottfried, *Surf. Sci. Rep.*, **70**, 259 (2015).
38. J. M. Gottfried, K. Flechtner, A. Kretschmann, T. Lukasczyk, and H. P. Steinrück, *J. Am. Chem. Soc.*, **128**, 5644 (2006).
39. Y. Bai, F. Buchner, M. T. Wendahl, I. Kellner, A. Bayer, H. P. Steinrück, H. Marbach, and J. M. Gottfried, *J. Phys. Chem. C*, **112**, 6087 (2008).
40. C. C. Wang, Q. T. Fan, S. W. Hu, H. X. Ju, X. F. Feng, Y. Han, H. B. Pan, J. F. Zhu, and J. M. Gottfried, *Chem. Commun.*, **50**, 8291 (2014).
41. T. Lukasczyk, K. Flechtner, L. R. Merte, N. Jux, F. Maier, J. M. Gottfried, and H. P. Steinruck, *J. Phys. Chem. C*, **111**, 3090 (2007).
42. M. Chen, X. F. Feng, L. Zhang, H. X. Ju, Q. Xu, J. F. Zhu, J. M. Gottfried, K. Ibrahim, H. J. Qian, and J. O. Wang, *J. Phys. Chem. C*, **114**, 9908 (2010).
43. A. Goldoni, C. A. Pignedoli, G. Di Santo, C. Castellarin-Cudia, E. Magnano, F. Bondino, A. Verdini, and D. Passerone, *ACS Nano*, **6**, 10800 (2012).
44. S. Ditze, M. Röckert, F. Buchner, E. Zillner, M. Stark, H. P. Steinrück, and H. Marbach, *Nanotechnology*, **24**, 115305 (2013).
45. M. Schmid, S. R. Kachel, B. P. Klein, N. Bock, P. Müller, R. Riedel, N. Hampp, and J. M. Gottfried, *J. Phys. Condens. Matter*, **31**, 094002 (2019).
46. M. Chen, H. Zhou, B. P. Klein, M. Zugermeier, C. K. Krug, H. J. Drescher, M. Gorgoi, M. Schmid, and J. M. Gottfried, *Phys. Chem. Chem. Phys.*, **18**, 30643 (2016).
47. J. Viefhaus, F. Scholz, S. Deinert, L. Glaser, M. Ilchen, J. Seltmann, P. Walter, and F. Siewert, *Nucl. Instrum. Meth. A*, **710**, 151 (2013).
48. J. R. M. J. Frisch et al., *Gaussian 09 Revision C.01* (Gaussian Inc, Wallingford CT) (2009).
49. J. P. Perdew, K. Burke, and M. Ernzerhof, *Phys. Rev. Lett.*, **77**, 3865 (1996).
50. F. Weigend and R. Ahlrichs, *Phys. Chem. Chem. Phys.*, **7**, 3297 (2005).
51. C. Adamo and V. Barone, *J. Chem. Phys.*, **110**, 6158 (1999).
52. N. M. O'Boyle, A. L. Tenderholt, and K. M. Langner, *J. Comput. Chem.*, **29**, 839 (2008).
53. R. De Francesco, M. Stener, and G. Fronzoni, *J. Phys. Chem. A*, **116**, 2885 (2012).
54. G. Fronzoni, G. Balducci, R. De Francesco, M. Romeo, and M. Stener, *J. Phys. Chem. C*, **116**, 18910 (2012).
55. G. te Velde, F. M. Bickelhaupt, E. J. Baerends, C. Fonseca Guerra, S. J. A. van Gisbergen, J. G. Snijders, and T. Ziegler, *J. Comput. Chem.*, **22**, 931 (2001).
56. S. Grimme, S. Ehrlich, and L. Goerigk, *J. Comput. Chem.*, **32**, 1456 (2011).
57. E. van Lenthe and E. J. Baerends, *J. Comput. Chem.*, **24**, 1142 (2003).
58. D. P. Chong, E. van Lenthe, S. van Gisbergen, and E. J. Baerends, *J. Comput. Chem.*, **25**, 1030 (2004).
59. T. Ziegler and A. Rauk, *Theoret. Chim. Acta*, **46**, 1 (1977).
60. L. Zhao, M. von Hopffgarten, D. M. Andrada, and G. Frenking, *WIREs Comput Mol Sci*, **8**, e1345 (2018).
61. F. M. Bickelhaupt and E. J. Baerends, *Kohn–Sham Density Functional Theory: Predicting and Understanding Chemistry* (Wiley-VCH, Inc, New York) (2000).
62. P. M. Mitoraj, A. Michalak, and T. Ziegler, *J. Chem. Theory Comput.*, **5**, 962 (2009).
63. L. Scudiero, D. E. Barlow, and K. W. Hipps, *J. Phys. Chem. B*, **106**, 996 (2002).
64. P. S. Johnson, J. M. Garcia-Lastra, C. K. Kennedy, N. J. Jersett, I. Boukahil, F. J. Himpsel, and P. L. Cook, *J. Chem. Phys.*, **140**, 114706 (2014).
65. S. A. Krasnikov, A. B. Preobrajenski, N. N. Sergeeva, M. M. Brzhezinskaya, M. A. Nesterov, A. A. Cafolla, M. O. Senge, and A. S. Vinogradov, *Chem. Phys.*, **332**, 318 (2007).
66. G. I. Svirskiy, N. N. Sergeeva, S. A. Krasnikov, N. A. Vinogradov, Y. N. Sergeeva, A. A. Cafolla, A. B. Preobrajenski, and A. S. Vinogradov, *Phys. Solid State*, **59**, 368 (2017).
67. J. Conradie and A. Ghosh, *ACS Omega*, **2**, 6708 (2017).
68. M. Gouterman, G. H. Wagnière, and L. C. Snyder, *J. Mol. Spectrosc.*, **11**, 108 (1963).
69. D. Lexa, M. Momenteau, J. Mispelter, and J. M. Savéant, *Inorg. Chem.*, **28**, 30 (1989).
70. G. S. Nahor, P. Neta, P. Hambright, L. R. Robinson, and A. Harriman, *J. Phys. Chem.*, **94**, 6659 (1990).
71. Y. Z. Han, H. Y. Fang, H. Z. Jing, H. L. Sun, H. T. Lei, W. Z. Lai, and R. Cao, *Angew. Chem. Int. Ed.*, **55**, 5457 (2016).
72. G. Zamborlini et al., *Nat. Commun.*, **8**, 335 (2017).
73. G. Zamborlini, M. Jugovac, A. Cossaro, A. Verdini, L. Floreano, D. Luftner, P. Puschnig, V. Feyer, and C. M. Schneider, *Chem. Commun.*, **54**, 13423 (2018).
74. R.-J. Cheng, P.-Y. Chen, T. Lovell, T. Liu, L. Noodleman, and D. A. Case, *J. Am. Chem. Soc.*, **125**, 6774 (2003).

Supplementary Material

Influence of Ring Contraction on the Electronic Structure of Nickel Tetrapyrrole Complexes: Corrole versus Porphyrin

Jan Herritsch[1], Jan-Niclas Luy[1], Sebastian Rohlf[2,3], Manuel Gruber[2], Benedikt P. Klein[1], Matthias Kalläne[2,3], Peter Schweyen[4], Martin Bröring[4], Kai Rossnagel[2,5], Ralf Tonner[1§], J. Michael Gottfried[1]*

[1]*Fachbereich Chemie, Philipps-Universität Marburg, Hans-Meerwein-Straße 4, 35032 Marburg, Germany, michael.gottfried@chemie.uni-marburg.de*

[2]*Institut für Experimentelle und Angewandte Physik, Christian-Albrechts-Universität zu Kiel, Olshausenstraße 40, 24098 Kiel, Germany*

[3]*Ruprecht-Haensel-Labor, Christian-Albrechts-Universität zu Kiel, Olshausenstraße 40, 24098 Kiel, Germany*

[4]*Institut für Anorganische und Analytische Chemie, Technische Universität Braunschweig, Hagenring 30, 38106 Braunschweig, Germany*

[5]*Ruprecht-Haensel-Labor, Deutsches Elektronen-Synchrotron DESY, Notkestraße 85, 22607 Hamburg, Germany*

[§]*Present address: Institut für Physikalische und Theoretische Chemie, Universität Regensburg, Universitätsstraße 31, 93053 Regensburg, Germany*

Table of Contents

1 Sample Preparation

1.1 Top-layer Metalation

For X-ray photoelectron spectroscopy (XPS) and near-edge X-ray absorption fine structure (NEXAFS) spectroscopy the molecules were investigated in a vapor-deposited thin film of about 10 monolayer thickness on a Ag(111) single crystal. The studied complexes NiOEP and NiHEDMC were prepared by the metalation with post-deposited nickel on a layer of the free ligand H_2OEP and H_3HEDMC, respectively. Here, a particular challenge is to avoid nickel cluster formation by unreacted metal atoms and at the same time to maintain a high degree of metalation. As the diffusion of vapor-deposited transition-metal atoms in porphyrin thin films is limited to 1.0-1.5 nm at room temperature, only the topmost layers can be metalated.[1,2] The metalation is monitored in the N 1s spectrum in which the chemically different nitrogen atoms can be distinguished (Figure S1). The pyrrolic (−NH−) signal at a binding energy (BE) of 399.8 eV and the iminic (−N=) signal at a BE of 397.7 eV labeled in blue belong to the unreacted free-base ligand.[3] The deposition of nickel yields a third signal labeled in orange at a BE of 398.8 eV representing four chemically equivalent nitrogen atoms bound to the central atom in the final complex.[3] The comparison of a fully metalated layer of directly deposited NiOEP in Figure S1(a) with the prepared samples of (b) NiOEP and (c) NiHEDMC indicates a successful reaction. The fraction of metalated molecules can be determined from the ratio of the fitted peak areas and is estimated to 10%.

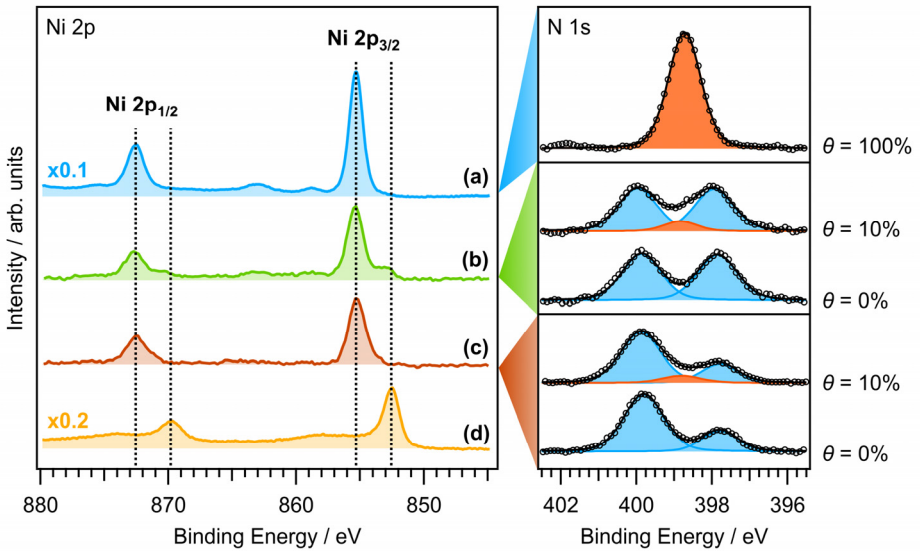

Figure S1. (left) Ni 2p region of (a) a NiOEP multilayer, a partially metalated multilayer of (b) H_2OEP and (c) H_3HEDMC as well as (d) nickel(0) deposited on pristine Ag(111) for comparison. (right) Corresponding N 1s spectra showing the free ligand multilayer (each bottom graph) and the partially metalated multilayer (each top graph). The degree of metalation θ can be estimated by the ratio of the peak areas of the free ligand (blue) and the metal complex (orange).

1.2 Layer-by-layer Metalation

Probing the molecular orbitals in the valence region by ultraviolet photoelectron spectroscopy (UPS) requires a higher degree of metalation as the unreacted molecules underneath also contribute to the spectrum. Therefore, a layer-by-layer procedure was used for the NiHEDMC sample. First, a very thin layer of the free ligand was deposited onto the sample. Afterwards this layer was metalated by deposition of nickel. These steps were repeated until a layer of 3-4 nm thickness was reached. Figure S2 shows the Ni $2p_{3/2}$ and the corresponding N 1s region of (a) the "conventionally" prepared sample and (b) the sample prepared by the layer-by-layer deposition and metalation. According to the Ni $2p_{3/2}$ spectra we avoided formation of a significant amount of nickel clusters for both preparation methods. The layer-by-layer procedure yields a significant higher degree of metalation (27 %) in comparison to that obtained using the top-layer metalation (10 %). The corresponding NiOEP samples for UPS measurements were prepared by direct deposition of the metalated complex.

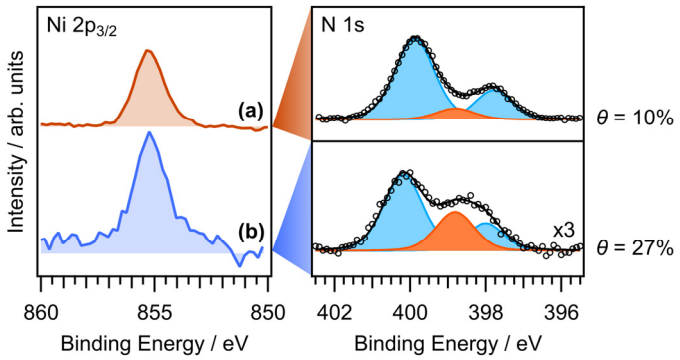

Figure S2. Ni $2p_{3/2}$ and N 1s spectra of (a) a NiHEDMC sample prepared with the "conventional" procedure compared with (b) a NiHEDMC sample prepared by layer-by-layer deposition and metalation.

2 Discussion of the Calculated Gas Phase Structures

2.1 Planar Conformer of NiOEP

Besides the ruffled conformer a planar structure for NiOEP was found as a minimum on the potential energy surface. This conformer is almost equal in energy (ΔE = +1.2 kJ/mol) in comparison to the ruffled conformer. Table S1 gives the Ni−N bond lengths for all investigated conformers. The planar NiOEP conformer has an increased bond length compared to the ruffled conformer. However, even by adopting the ruffled conformation and, thus, decreasing the Ni−N distance the bond length is much larger than in the corrole complexes. According to our calculations, we were not able to find a planar conformer of the parent NiP complex as a minimum on the potential energy surface.

Table S1. Comparison of the Ni−N bond lengths in Å of different optimized ground state structures of gas phase calculations.

#	NiOEP (ruffled)	NiOEP (planar)	NiP (D_{2h})	NiHEDMC	NiC (C_{2v})
1	1.955	1.970	1.957	1.878	1.872
2	1.955	1.970	1.957	1.877	1.872
3	1.955	1.970	1.957	1.842	1.842
4	1.955	1.970	1.957	1.842	1.842

3 Energy Decomposition Analysis

3.1 Used Partitioning Scheme

The energy decomposition analysis (EDA)[4-6] was used for the metal ligand bonding analysis. In the course of this, the corresponding bond is broken and the studied complex is split into two fragments A and B. The bond energy ΔE_{bond} is defined as the difference between the energy of the final complex E_{AB} and the fragments E_A^0 and E_B^0. In other words, ΔE_{bond} is the negative dissociation energy D. It is further divided in the preparation energy ΔE_{prep} and the interaction energy ΔE_{int}.

$$\Delta E_{bond} = -D = E_{AB} - (E_A^0 + E_B^0) \quad (1)$$

$$\Delta E_{bond} = \Delta E_{prep} + \Delta E_{int}$$

The preparation energy ΔE_{prep} consists of structural deformation ΔE_{deform} and electronic excitation ΔE_{exc} and is, thus, the amount of energy needed to bring the fragments from their ground state into the actual state in the final complex. The energy difference between the fragments in their final state (E_A and E_B) and their ground state (E_A^0 and E_B^0) gives ΔE_{prep}.

$$\Delta E_{prep} = (E_A + E_B) - (E_A^0 + E_B^0) \quad (2)$$

$$\Delta E_{prep} = \Delta E_{deform} + \Delta E_{exc}$$

The interaction energy ΔE_{int} represents the energy difference of the fragments in their final state and the assembled complex. Furthermore, we can divide the interactions into Pauli repulsion ΔE_{Pauli} and attractive electrostatic ΔE_{elstat} as well as orbital interactions ΔE_{orb}.

$$\Delta E_{int} = E_{AB} - (E_A + E_B) \quad (3)$$

$$\Delta E_{int} = \Delta E_{Pauli} + \Delta E_{elstat} + \Delta E_{orb}$$

3.2 Preparation Energy

The preparation energy ΔE_{prep} consists of the deformation energy ΔE_{deform} required to distort the ligand geometry from its ground state to the structure present in the final complex and of the excitation energy ΔE_{exc} needed to bring the fragments to their final electronic state. ΔE_{deform} is larger in case of NiP (+70 kJ/mol) in contrast to NiC (+59 kJ/mol). This can be attributed to the fact that the central atom is too small for the porphyrin ligand forcing the ligand to adapt a more unfavorable structure. The excitation energy ΔE_{exc} needed to bring the fragments to their final electronic state is, however, larger in case of NiC (+362 kJ/mol) than for NiP (+316 kJ/mol) since an additional excitation of the corrole dianion needs to be taken into account. The excitation of the nickel fragment from five degenerated 3d orbitals [Ni $3(d_{xy})^{1.6}(d_{xz})^{1.6}(d_{yz})^{1.6}(d_{z2})^{1.6}(d_{x2-y2})^{1.6}$] into the Ni $3(d_{xy})^2(d_{xz})^2(d_{yz})^2(d_{z2})^2(d_{x2-y2})^0$ state contributes with +316 kJ/mol to this term in each case.

Thus, the overall preparation energy ΔE_{prep} is smaller in case of NiP (+386 kJ/mol) in contrast to NiC (+421 kJ/mol).

Table S2. The preparation energy ΔE_{prep} is divided into the deformation energy ΔE_{deform} and the excitation energy ΔE_{exc}. Energies in kJ/mol; values in parentheses give the percentage contribution to ΔE_{prep}.

	NiP (D_{2h})	NiC (C_{2v})
ΔE_{prep}	+386	+421
ΔE_{deform}	+70 (18 %)	+59 (14 %)
ΔE_{exc}	+316 (82 %)	+362 (86 %)

3.3 Natural Orbitals for Chemical Valence

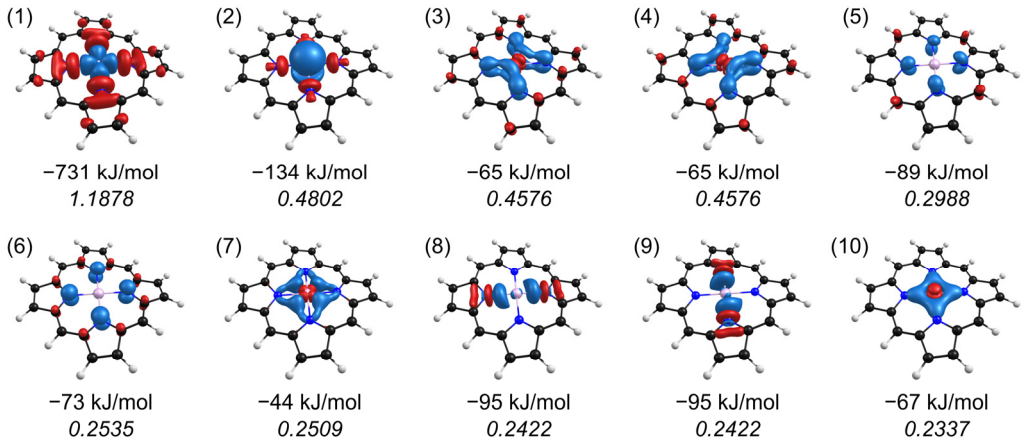

Figure S3. NOCV Deformation densities (with eigenvalue $v_i \geq 0.2$) for NiP (top, iso surface = 0.0016) and corresponding energies and eigenvalues (italic numbers). Blue regions show electron accumulation and red regions electron depletion.

Table S3. Results of NOCV analysis for individual deformation densities n and classification of the individual energy terms into categories such as σ donation or π backdonation. Energy values ΔE(n) in kJ/mol, values in parentheses give the percentage contribution to the total orbital interaction.

	NiP (D_{2h})		
ΔE_{orb}	−1694		
σ donation			
ΔE(1)	−731	(43 %)	ligand → Ni $3d_{x2-y2}$
ΔE(2)	−134	(8 %)	ligand → N 4s Ni $3d_{z2}$ → N 4s
ΔE(8)	−95	(6 %)	ligand → Ni $4p_x$
ΔE(9)	−95	(6 %)	ligand → Ni $4p_y$
π backdonation			
ΔE(3)	−65	(4 %)	Ni $3d_{xz}$ → ligand
ΔE(4)	−65	(4 %)	Ni $3d_{yz}$ → ligand
charge rearrangement			
ΔE(10)	−67	(4 %)	Ni $3d_{z2}$ → N 4s ligand → N 4s
ΔE(5)	−89	(5 %)	
ΔE(6)	−73	(4 %)	
ΔE(7)	−44	(3 %)	
not assigned			
ΔE(rest)	−237	(14 %)	

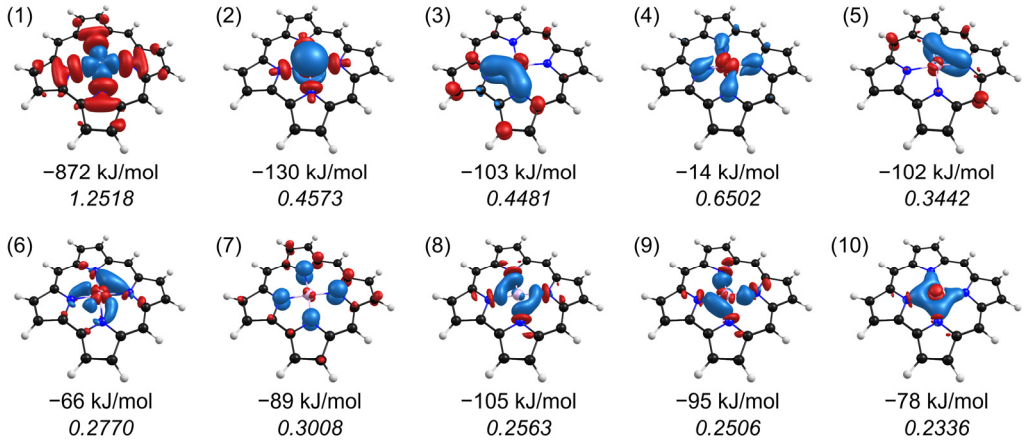

Figure S4. NOCV Deformation densities (with eigenvalue $v_i \geq 0.2$) for NiC (top, iso surface = 0.0016) and corresponding energies and eigenvalues (italic numbers). Blue regions show electron accumulation and red regions electron depletion.

Table S4. Results of NOCV analysis for individual deformation densities n and classification of the individual energy terms into categories such as σ donation or π backdonation. Energy values ΔE(n) in kJ/mol, values in parentheses give the percentage contribution to the total orbital interaction.

	NiC (C_{2v})		
ΔE_{orb}	−1923		
σ donation			
ΔE(1)	−872	(45 %)	ligand → Ni $3d_{x2-y2}$
ΔE(2)	−131	(7 %)	ligand → N 4s Ni $3d_{z2}$ → N 4s
ΔE(8)	−105	(5 %)	Ligand → Ni $4p_x$
ΔE(9)	−95	(5 %)	Ligand → Ni $4p_y$
π backdonation			
ΔE(3)	−14	(1 %)	Ni $3d_{xz}$ → ligand
ΔE(4)	−103	(5 %)	Ni $3d_{yz}$ → ligand
ΔE(5)	−102	(5 %)	Ni $3d_{yz}$ → ligand
charge rearrangement			
ΔE(10)	−78	(4 %)	Ni $3d_{z2}$ → N 4s ligand → N 4s
ΔE(7)	−89	(5 %)	
ΔE(6)	−66	(3 %)	
not assigned			
ΔE(rest)	−308	(14 %)	

4 Structural Parameters

4.1 Optimized Gas Phase Structure of NiP

Table S5. Cartesian coordinates of optimized gas phase structure (PBE/def2-TZVPP) of NiP in Å. Total energy = −2495.75392898 H.

	x	y	z
Ni	-0.000007	-0.000007	-0.000063
N	-0.000016	1.957478	0.004546
N	1.957478	-0.000016	0.004766
N	-0.000003	-1.957487	-0.004599
N	-1.957486	-0.000003	-0.004819
C	2.396904	-2.398309	0.287426
C	2.398338	2.398306	-0.275388
C	-2.398341	2.396938	0.286877
C	-2.396888	-2.396921	-0.298911
C	-1.080882	-2.800789	-0.176298
C	1.080891	-2.801598	0.163012
C	2.800770	-1.081718	0.171267
C	2.801610	1.081699	-0.157366
C	-2.800769	-1.080902	-0.176493
C	-2.801616	1.080910	0.162570
C	-1.081737	2.800790	0.170824
C	1.081718	2.801591	-0.157561
C	-0.670805	-4.179072	-0.127171
C	0.670832	-4.179629	0.107230
C	4.179056	-0.671390	0.124376
C	4.179635	0.671373	-0.103457
C	0.671388	4.179623	-0.103849
C	-0.671406	4.179071	0.123804
C	-4.179057	-0.670820	-0.127568
C	-4.179640	0.670847	0.106666
H	-1.344902	-5.023564	-0.241152
H	1.344940	-5.024660	0.217080
H	5.023534	-1.346039	0.235148
H	5.024673	1.346025	-0.209857
H	1.346054	5.024648	-0.210262
H	-1.346070	5.023561	0.234388
H	-5.023536	-1.344930	-0.241567
H	-5.024684	1.344969	0.216332
H	3.161534	-3.163575	0.415311
H	3.163621	3.163574	-0.399292
H	-3.163623	3.161583	0.414577
H	-3.161511	-3.161560	-0.430531

4.2 Optimized Gas Phase Structure of NiOEP (ruffled conformer)

Tables S6. Cartesian coordinates of optimized gas phase structure (PBE/def2-TZVPP) of NiOEP (ruffled conformer) in Å. Total energy = −3124.11515062 H.

	x	y	z
Ni	0.000001	-0.000003	0.000019
N	1.904889	0.435955	-0.045106
N	-0.435958	1.904886	0.045126
N	-1.904888	-0.435962	-0.045108
N	0.435958	-1.904892	0.045141
C	2.850977	-1.801544	-0.338112
C	-2.491372	-1.674109	0.113890
C	2.958227	-0.424726	-0.278961
C	-0.424722	-2.958230	0.278997
C	1.674105	-2.491376	-0.113858
C	0.285596	-4.220729	0.312322
C	1.598709	-3.930337	0.035786
C	-0.333857	-5.554744	0.597562
C	2.762088	-4.870869	-0.054430
C	-0.592908	-5.807596	2.093216
C	3.557094	-5.004297	1.256093
C	-1.801540	-2.850980	0.338147
C	-3.930333	-1.598711	-0.035748
C	2.491372	1.674103	0.113888
C	0.424721	2.958225	0.278978
C	-1.674105	2.491368	-0.113880
C	-2.958225	0.424717	-0.278974
C	4.220726	0.285593	-0.312286
C	-4.220724	-0.285601	-0.312296
C	-4.870867	-2.762090	0.054475
C	3.930333	1.598707	-0.035757
C	1.801539	2.850976	0.338134
C	-0.285598	4.220724	0.312293
C	-1.598708	3.930331	0.035746
C	-2.850976	1.801534	-0.338134
C	5.554742	-0.333860	-0.597525
C	-5.554739	0.333850	-0.597544
C	-5.004293	-3.557103	-1.256042
C	4.870865	2.762088	0.054450
C	0.333852	5.554741	0.597531
C	-2.762086	4.870863	-0.054488
C	5.807593	-0.592915	-2.093179
C	-5.807588	0.592889	-2.093200
C	5.004292	3.557085	-1.256077
C	0.592892	5.807603	2.093185
C	-3.557100	5.004303	1.256028
H	0.323199	-6.346784	0.206609

H	3.441291	-4.547059	-0.859296
H	-1.266239	-5.047668	2.513161
H	3.955463	-4.032695	1.579215
H	-1.282795	-5.653678	0.045576
H	2.397165	-5.865212	-0.355640
H	-1.049306	-6.794987	2.252462
H	2.918513	-5.383565	2.065697
H	0.344078	-5.768621	2.665723
H	4.401576	-5.697769	1.134930
H	-2.378894	-3.761369	0.490484
H	3.761367	-2.378897	-0.490448
H	-4.547056	-3.441288	0.859345
H	-5.865209	-2.397165	0.355684
H	2.378892	3.761368	0.490462
H	-3.761365	2.378886	-0.490476
H	6.346782	0.323198	-0.206574
H	5.653676	-1.282796	-0.045537
H	-6.346780	-0.323203	-0.206586
H	-5.653672	1.282793	-0.045565
H	-4.032691	-3.955474	-1.579162
H	-5.383562	-2.918527	-2.065651
H	-5.697765	-4.401585	-1.134874
H	4.547053	3.441296	0.859312
H	5.865207	2.397167	0.355664
H	-0.323201	6.346779	0.206567
H	1.282795	5.653671	0.045551
H	-3.441284	4.547045	-0.859355
H	-2.397160	5.865202	-0.355706
H	5.047666	-1.266248	-2.513121
H	6.794985	-1.049314	-2.252424
H	5.768617	0.344069	-2.665689
H	-5.047658	1.266215	-2.513149
H	-6.794978	1.049287	-2.252452
H	-5.768613	-0.344102	-2.665699
H	4.032689	3.955450	-1.579203
H	5.383562	2.918500	-2.065677
H	5.697762	4.401570	-1.134919
H	1.266219	5.047678	2.513141
H	1.049290	6.794996	2.252428
H	-0.344099	5.768633	2.665685
H	-3.955471	4.032705	1.579157
H	-2.918525	5.383580	2.065633
H	-4.401581	5.697774	1.134852

4.3 Optimized Gas Phase Structure of NiOEP (planar conformer)

Tables S7. Cartesian coordinates of optimized gas phase structure (PBE/def2-TZVPP) of NiOEP (planar conformer) in Å. Total energy = -3124.11470086 H.

	x	y	z
Ni	0.010383000	-0.001347000	-0.000228000
N	1.442323000	1.351495000	-0.013712000
N	1.363584000	-1.432972000	-0.011468000
N	-1.421569000	-1.354150000	0.012934000
N	-1.342829000	1.430246000	0.011341000
C	-0.085647000	-3.408072000	0.001633000
C	3.417362000	-0.097382000	-0.054942000
C	0.106326000	3.405372000	-0.009000000
C	-3.396470000	0.094693000	0.061570000
C	-2.785739000	-1.143026000	0.037564000
C	-1.287039000	-2.728255000	0.003373000
C	1.152183000	-2.797179000	-0.001695000
C	2.737635000	-1.298715000	-0.036487000
C	-2.716800000	1.296030000	0.040744000
C	-1.131470000	2.794427000	-0.002202000
C	1.307743000	2.725619000	-0.008448000
C	2.806551000	1.140349000	-0.034454000
C	-3.518091000	-2.392616000	0.035003000
C	-2.575745000	-3.389303000	0.011653000
C	2.401532000	-3.529760000	-0.012365000
C	3.398374000	-2.587610000	-0.037849000
C	3.538864000	2.389945000	-0.033712000
C	2.596453000	3.386686000	-0.016102000
C	-3.377537000	2.584938000	0.041614000
C	-2.380781000	3.527012000	0.010496000
C	2.531305000	-5.022227000	0.026626000
C	2.409281000	-5.617867000	1.440263000
C	4.881610000	-2.802595000	-0.036274000
C	5.524296000	-2.696776000	1.357696000
C	5.031897000	2.519490000	-0.020429000
C	5.654140000	2.375783000	1.379623000
C	2.810961000	4.869501000	0.018014000
C	2.711299000	5.479587000	1.427140000
C	-2.510645000	5.019386000	-0.031527000
C	-2.391087000	5.611993000	-1.446647000
C	-4.860772000	2.799970000	0.044433000
C	-5.507579000	2.694252000	-1.347629000
C	-5.011161000	-2.522096000	0.025159000
C	-5.636838000	-2.375858000	-1.373096000
C	-2.790295000	-4.872008000	-0.026552000
C	-2.690927000	-5.478275000	-1.437351000
H	-0.116828000	-4.496216000	0.002791000

H	4.505209000	-0.128501000	-0.082087000
H	0.137418000	4.493516000	-0.013053000
H	-4.484238000	0.125796000	0.091848000
H	1.772143000	-5.481992000	-0.626521000
H	3.504926000	-5.308493000	-0.400452000
H	1.439933000	-5.368245000	1.893068000
H	3.192507000	-5.222260000	2.101483000
H	2.504451000	-6.712831000	1.415709000
H	5.098761000	-3.797059000	-0.456209000
H	5.365376000	-2.080784000	-0.713832000
H	5.099502000	-3.442585000	2.043582000
H	5.351255000	-1.706394000	1.801107000
H	6.609827000	-2.862133000	1.303803000
H	5.479047000	1.770829000	-0.694011000
H	5.310215000	3.499719000	-0.437616000
H	5.412880000	1.399450000	1.822009000
H	5.271689000	3.148685000	2.060488000
H	6.748506000	2.470859000	1.335776000
H	3.803254000	5.096647000	-0.401558000
H	2.085443000	5.368724000	-0.644391000
H	3.461286000	5.040038000	2.098992000
H	1.723607000	5.294442000	1.871391000
H	2.875087000	6.566291000	1.397612000
H	-3.483537000	5.306534000	0.396602000
H	-1.750355000	5.480590000	0.619308000
H	-3.175264000	5.214691000	-2.105712000
H	-1.422418000	5.361696000	-1.900533000
H	-2.486554000	6.706977000	-1.424317000
H	-5.342529000	2.078157000	0.723399000
H	-5.076671000	3.794412000	0.465094000
H	-5.335749000	1.703929000	-1.791654000
H	-5.084931000	3.440186000	-2.034710000
H	-6.592968000	2.859480000	-1.290505000
H	-5.288515000	-3.503045000	0.441319000
H	-5.456599000	-1.774630000	0.701183000
H	-5.256268000	-3.147657000	-2.056262000
H	-5.396463000	-1.398797000	-1.814358000
H	-6.731115000	-2.470778000	-1.326698000
H	-2.064643000	-5.373078000	0.634333000
H	-3.782513000	-5.100254000	0.392567000
H	-1.703322000	-5.292003000	-1.881315000
H	-3.441010000	-5.036861000	-2.107869000
H	-2.854779000	-6.565042000	-1.410723000

4.4 Optimized Gas Phase Structure of NiC

Tables S8. Cartesian coordinates of optimized gas phase structure (PBE/def2-TZVPP) of NiC in Å. Total energy = −2457.06957687 H

	x	y	z
Ni	0.011283	-0.000046	0.000576
N	1.269275	-1.385864	0.000347
N	-1.377844	-1.210293	-0.000719
N	-1.376071	1.212283	0.000253
N	1.271740	1.384101	0.000215
C	2.632044	-1.233701	0.000074
C	3.255196	-2.540916	-0.000437
C	2.255207	-3.469655	0.000082
C	0.999784	-2.756610	0.000137
C	3.287680	-0.002574	-0.000202
C	-0.263739	-3.332270	0.000166
C	-1.440411	-2.560282	-0.000114
C	-2.839441	-2.942235	-0.000394
C	-3.595178	-1.788018	-0.000107
C	-2.675518	-0.694854	-0.000454
C	-3.592611	1.793709	-0.000318
C	-2.834943	2.946556	-0.000244
C	-1.436572	2.562154	0.000129
C	-0.258604	3.332528	0.000353
C	1.004250	2.755538	0.000359
C	2.260915	3.466175	-0.000200
C	3.259395	2.535780	-0.000776
C	2.633939	1.229731	-0.000247
C	-2.674765	0.699026	-0.000308
H	4.328518	-2.711621	-0.000863
H	2.345959	-4.552513	0.000245
H	4.376981	-0.003076	-0.000623
H	-0.336588	-4.418863	0.000320
H	-3.204788	-3.965800	0.000270
H	-4.678072	-1.710181	0.000505
H	-4.675620	1.717860	-0.000483
H	-3.198512	3.970795	-0.000368
H	-0.329812	4.419216	0.000682
H	2.353490	4.548893	-0.000197
H	4.333040	2.704493	-0.001260

4.5 Optimized Gas Phase Structure of NiHEDMC

Tables S9. Cartesian coordinates of optimized gas phase structure (PBE/def2-TZVPP) of NiHEDMC in Å. Total energy = −3006.89087382 H.

	x	y	z
N	-0.022758	-0.001248	-0.045230
N	-1.411987	0.782049	-1.035074
N	-0.882049	-1.630313	-0.010920
N	1.216948	-0.945867	0.936780
N	1.013135	1.562878	0.032852
C	-1.467427	2.077721	-1.471740
C	-2.713962	2.301651	-2.195748
C	-3.401515	1.112084	-2.181467
C	-2.584341	0.156450	-1.455707
C	-0.467564	3.022531	-1.245392
C	-2.907750	-1.170144	-1.218133
C	-2.062834	-2.046137	-0.511563
C	-2.241528	-3.446971	-0.171885
C	-1.126278	-3.850075	0.553460
C	-0.266727	-2.695718	0.662493
C	2.039793	-2.794886	2.036017
C	2.931884	-1.743134	2.198907
C	2.390837	-0.592035	1.497874
C	2.910094	0.707570	1.356062
C	2.250222	1.707670	0.658692
C	2.724611	3.066675	0.470323
C	1.770306	3.728257	-0.264366
C	0.702230	2.770940	-0.529934
C	0.953186	-2.292523	1.227746
C	-0.895885	-5.235725	1.084479
C	-0.440614	-6.245276	0.017161
C	-3.436991	-4.262824	-0.556073
C	-3.469833	-4.670241	-2.040814
C	-3.133358	3.611717	-2.787820
C	-3.741929	4.581412	-1.759046
C	1.759025	5.160553	-0.700831
C	0.973836	6.083415	0.248050
C	4.207891	-1.732456	2.983340
C	4.046522	-1.158830	4.403030
C	2.232371	-4.171881	2.601507
C	2.879369	-5.159629	1.617530
C	-4.735652	0.800527	-2.778030
H	-0.612152	4.022574	-1.651293
H	-3.858775	-1.543466	-1.595303
H	3.870994	0.944168	1.811019
H	-0.159508	-5.208945	1.895935
H	-1.829016	-5.602967	1.542374

H	0.467928	-5.900577	-0.494869
H	-1.214193	-6.388642	-0.749222
H	-0.227350	-7.224767	0.468755
H	-3.478473	-5.167818	0.069111
H	-4.353139	-3.692830	-0.325932
H	-2.594992	-5.280575	-2.302966
H	-3.461967	-3.789143	-2.696645
H	-4.373921	-5.253922	-2.265319
H	-2.267679	4.092670	-3.271747
H	-3.864336	3.431876	-3.590934
H	-3.032194	4.794411	-0.948005
H	-4.644222	4.151087	-1.303048
H	-4.018242	5.534696	-2.231764
H	2.794157	5.525611	-0.784685
H	1.332007	5.234082	-1.713870
H	1.415197	6.076837	1.254263
H	-0.070537	5.756065	0.343875
H	0.975696	7.119561	-0.119411
H	4.613640	-2.753145	3.047573
H	4.963891	-1.142231	2.440106
H	3.335628	-1.757842	4.988908
H	3.663286	-0.129694	4.372792
H	5.008250	-1.150607	4.935531
H	2.866302	-4.097057	3.498086
H	1.272703	-4.572321	2.958466
H	3.879745	-4.813492	1.322336
H	2.283433	-5.258813	0.701237
H	2.982046	-6.157514	2.067608
H	-4.678427	-0.043569	-3.482687
H	-5.471549	0.524570	-2.006470

5 References

1. M. Schmid, S. R. Kachel, B. P. Klein, N. Bock, P. Müller, R. Riedel, N. Hampp and J. M. Gottfried, *J. Phys. Condens. Matter*, **31**, 094002 (2019).
2. M. Chen, H. Zhou, B. P. Klein, M. Zugermeier, C. K. Krug, H. J. Drescher, M. Gorgoi, M. Schmid and J. M. Gottfried, *Phys. Chem. Chem. Phys.*, **18**, 30643 (2016).
3. J. M. Gottfried, *Surf. Sci. Rep.*, **70**, 259 (2015).
4. F. M. Bickelhaupt and E. J. Baerends, *Kohn-Sham Density Functional Theory: Predicting and Understanding Chemistry*, Wiley-VCH, Inc., New York (2000).
5. T. Ziegler and A. Rauk, *Theoret Chim Acta*, **46**, 1 (1977).
6. L. Zhao, M. von Hopffgarten, D. M. Andrada and G. Frenking, *WIREs Computational Molecular Science*, **8**, e1345 (2018).

THE JOURNAL OF PHYSICAL CHEMISTRY C

pubs.acs.org/JPCC Article

On-Surface Formation of a Transient Corrole Radical and Aromaticity-Driven Interfacial Electron Transfer

Malte Zugermeier, Jan Herritsch, Jan-Niclas Luy, Min Chen, Benedikt P. Klein, Falk Niefind, Peter Schweyen, Martin Bröring, Martin Schmid, Ralf Tonner,* and J. Michael Gottfried*

Cite This: *J. Phys. Chem. C* 2020, 124, 13825−13836 Read Online

ACCESS | Metrics & More | Article Recommendations | Supporting Information

ABSTRACT: Corroles on metal surfaces show substantial reactivity and aromaticity-driven interfacial electron transfer of their transient σ/π-radicals. These effects are much more pronounced than for the closely related porphyrins, as has been demonstrated by using an octaalkylcorrole (2,3,8,12,17,18-hexaethyl-7,13-dimethylcorrole, 3H-HEDMC) and its singly N−H dehydrogenated product 2H-HEDMC on a Ag(111) surface through a combination of experimental and theoretical methods. 3H-HEDMC assumes a nonplanar adsorption geometry caused by intramolecular steric repulsion between the three N−H hydrogen atoms. One of the N−H bonds is tilted far out of the molecular plane and points toward the surface. This N−H bond undergoes surface-catalyzed and entropy-driven homolytic scission already below 230 K, resulting in the formation of planar, strain-relieved 2H-HEDMC as a formal π-radical with a 17π-electron conjugation path. The experimental N−H bond scission barrier of 74 kJ/mol agrees well with theory. 2H-HEDMC engages in transfer of electron density from the surface to the molecule. The additional electron density quenches the radical spin and leads to aromatic stabilization because it influences the electronic structure toward an aromatic 18π-electron conjugation path. Our study demonstrates that aromaticity considerations are useful to rationalize and predict interfacial electron transfer effects, which play an important role in organic electronics, electrocatalysis, and sensors.

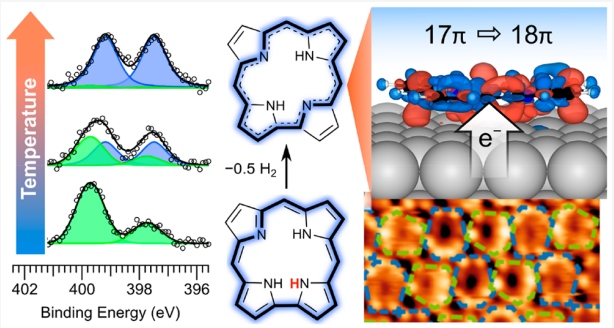

INTRODUCTION

Corroles are cyclic tetrapyrroles and structurally closely related to porphyrins and phthalocyanines,[1] which find numerous technological applications.[2] Metal complexes of porphyrins also play prominent roles in living organisms as the active centers of enzymes, whereas phthalocyanines are industrially used as pigments, catalysts, and organic semiconductors.[2,3] Like phthalocyanines, corroles do not occur in nature. However, corrin as a partially hydrogenated corrole is the core of vitamin B_{12}.[4] Because many applications of tetrapyrroles involve interface related aspects, the interface chemistry of tetrapyrroles has found substantial scientific interest during the past years.[3,5,6] In particular, coordination reactions with metal surfaces and adsorbed metal atoms have been studied intensively.[3,7−9] Another central aspect of porphyrins and their relatives is aromaticity.[10−12] Here, we combine these two aspects and demonstrate aromaticity-driven interfacial electron transfer at the corrole/metal interface. Interfacial charge transfer effects play a prominent role in the context of charge injection in organic electronic devices.[13−15]

Unlike porphyrins, corroles contain only three methine bridges and one direct pyrrole−pyrrole link (Figure 1a,b). Free-base corroles also possess one iminic (−N=) and three pyrrolic (−NH−) nitrogen atoms; i.e., they are tribasic acids, whereas porphyrins are dibasic acids (Figure 1b).[16] As a result, corroles form neutral complexes with trivalent metal ions. The contracted corrole macrocycle provides a tighter coordination environment for the metal ion compared to porphyrins, resulting in an additional stabilization of higher oxidation states.[16,17] Until recently, corroles have found much less attention in research and technology than porphyrins and phthalocyanines, partly because their more difficult synthesis resulted in limited availability.[16,18] Recently, however, numerous applications of corroles have been explored,[19] especially in (electro)catalysis,[19−29] as sensitizers in solar cells,[30] as sensors,[31−33] for hydrogen storage in metal−organic frameworks,[34] and for pharmaceutical applications.[35−37]

Although many of these applications involve surfaces and interfaces, the interface chemistry of corroles has rarely been

Received: May 18, 2020
Revised: May 22, 2020
Published: May 22, 2020

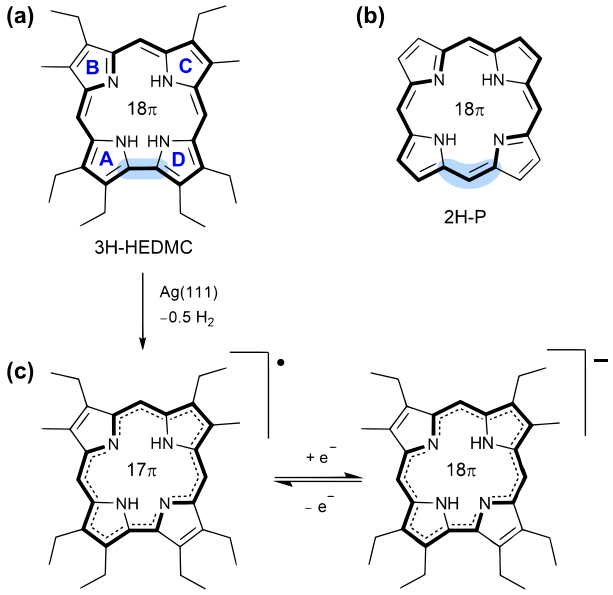

Figure 1. Structure and interfacial reactivity of a corrole. (a) 2,3,8,12,17,18-Hexaethyl-7,13-dimethylcorrole (3H-HEDMC) and (b) porphine (2H-P). The individual pyrrole units in the corrole are labeled with blue capital letters. (c) Surface reaction of 3H-HEDMC on Ag(111) resulting in the formation of a radical species and the loss of the 18π-electron system. Because of charge transfer from the surface to the adsorbate, the aromatic 18π-electron system in the negatively charged 2H-HEDMC is retained. Main delocalization pathways are highlighted and can be compared with the structure of a porphine (b).

addressed. Besides few publications with focus on transition-metal corroles[38−42] or corrole dimers,[43,44] there is only a small number of studies of free-base corroles on metal surfaces. All of these studies were performed with tris(pentafluorophenyl)-corrole.[45−48] The pentafluorophenyl substituents exert a strong electron-withdrawing effect and thereby influence the electronic structure of the corrole macrocycle. In addition, their substantial steric demand leads to a nonplanar distorted adsorption geometry with a relatively large adsorption height,[46,48] which reduces the electronic coupling between the corrole macrocycle and the surface. Around and above room temperature, the tris(pentafluorophenyl)corrole undergoes complex reactive processes including N−H and C−F bond dissociation, resulting in cyclization reactions at the periphery.[46]

To avoid substituent-induced molecular distortion and peripheral reactions on the surface, we used an octaalkylcorrole (3H-HEDMC) as shown in Figure 1a. Similar as in the well-studied octaethylporphyrins,[49−51] the alkyl substituents in β-positions of the pyrrole units are more flexible and point away from the surface in the adsorbed state without causing deformation of the macrocycle. In addition, they have a very moderate electron-donating effect and are chemically more inert than the fluorinated substituents. With this model system, we show that 3H-HEDMC is highly reactive toward the Ag(111) surface and that the first N−H bond dissociation starts already below 230 K. The product, 2H-HEDMC (Figure 1c), is a formal 17π-electron radical that experiences electron transfer from the surface, which is explained by aromaticity considerations using the concept of the nucleus-independent chemical shift (NICS).[52] In addition, the peculiar monolayer adsorption structure of 3H-HEDMC is clarified.

METHODS

The experiments were performed in a two-chamber ultrahigh-vacuum setup (base pressure in the low 10^{-10} mbar range), equipped with a gas-discharge UV source, a monochromated Al Kα X-ray source (1486.7 eV), three-grid low-energy electron diffraction (LEED) optics (SPECS ErLEED 1000A), a SPECS Phoibos 150 electron energy analyzer, and a preparation chamber. The Ag(111) sample was prepared by repeated cycles of Ar^+ ion bombardment (500 eV) and annealing (800 K). Surface cleanliness and long-range order were confirmed by X-ray photoelectron spectroscopy (XPS) and LEED, respectively. 2,3,8,12,17,18-Hexaethyl-7,13-dimethylcorrole (3H-HEDMC, Figure 1c) was vapor-deposited

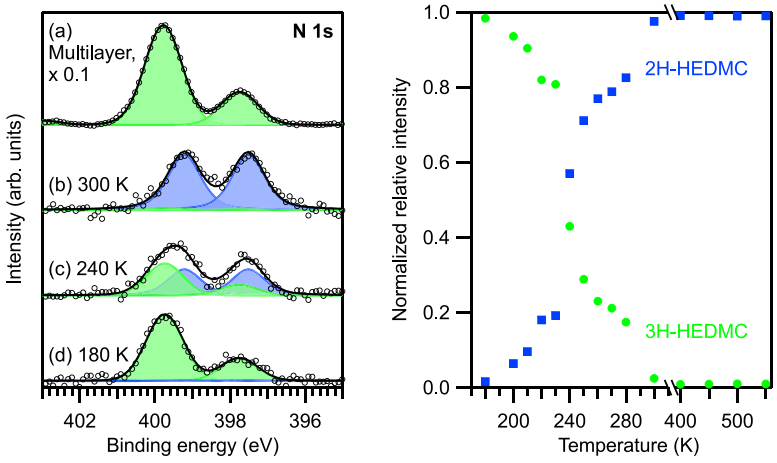

Figure 2. N 1s XP spectra of 3H-HEDMC and its dehydrogenation product 2H-HEDMC on Ag(111). (a) Multilayer at 300 K; (b−d) monolayer at increasing temperatures between 180 and 300 K as indicated. The fits are superpositions of a 3:1 component (3H-HEDMC, green lines) and a 2:2 component (2H-HEDMC, blue lines). The black line is the sum of both components. The experimental data are represented by open circles. Detailed N 1s XPS temperature series in the range 180−650 K are shown in Figure S2. The resulting relative intensities of 3H-HEDMC and 2H-HEDMC are shown in (e), with 2H-HEDMC and 3H-HEDMC represented by blue squares and green dots, respectively.

https://dx.doi.org/10.1021/acs.jpcc.0c04451
J. Phys. Chem. C 2020, 124, 13825−13836

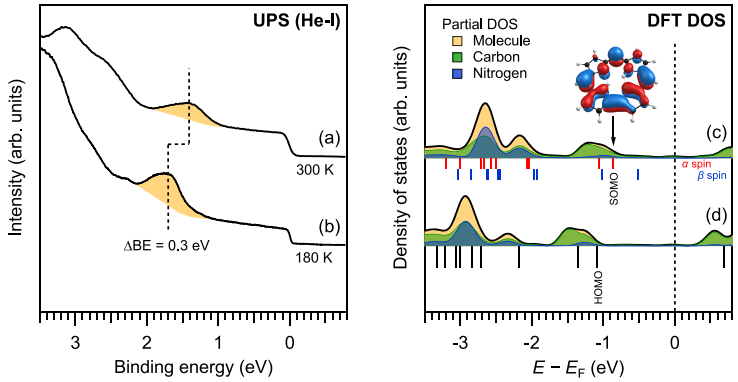

Figure 3. UP spectra (He I, 21.22 eV, normal emission) of a monolayer of 3H-HEDMC and 2H-HEDMC on Ag(111). (a) 2H-HEDMC monolayer at 300 K. (b) 3H-HEDMC monolayer at 180 K. DFT calculations of the partial DOS for the adsorbed (c) 2H-C and (d) 3H-C subdivided into different atomic contributions. The vertical lines below the DOS indicate the energy eigenvalues of the gas phase molecules. The figure also shows the shape of the SOMO of the gas phase 2H-C (isosurface value = 0.03).

onto the Ag(111) surface by using a home-built Knudsen cell evaporator. Sample annealing temperatures were held for 3 min, if not indicated otherwise. 3H-HEDMC was synthesized from the respective didesoxybiladiene by oxidative ring closure according to the literature.[41] The term *monolayer* is used for a complete monomolecular layer that uniformly covers the surface. In contrast, the unit *ML* refers to the number of objects (atoms or molecules) per Ag surface atom. According to this definition, a complete monolayer of 3H-HEDMC corresponds to 0.047 ML, as determined by STM. Details on the computational methods can be found in the Supporting Information.

RESULTS AND DISCUSSION

Surface Reactivity. X-ray photoelectron (XP) spectra of free-base tetrapyrroles typically show two components in the N 1s spectral region: one around 400 eV and another around 398 eV for nitrogen in pyrrolic (−NH−) and iminic bonding situations (−N=), respectively. Corroles contain three −NH− groups and one −N= group, according to the molecular structure shown in Figure 1b. Therefore, the two N 1s peaks should have a 3:1 intensity ratio. This ratio is indeed found in the N 1s spectrum of a 3H-HEDMC multilayer at 300 K. As shown in Figure 2a, this spectrum consists of a larger −NH− related component at 399.8 eV and a smaller −N= related component at 397.8 eV, indicating that 3H-HEDMC can be vapor deposited intact and without loss of a −NH− hydrogen during the evaporation.

However, deposition of one monolayer of 3H-HEDMC onto a Ag(111) surface kept at 300 K results in deviations from the expected 3:1 stoichiometry: The two N 1s components in Figure 2b have the same intensity, indicating the presence of two −NH− and two −N== groups (2:2 stoichiometry). Evidently, one of the −NH− groups undergoes dehydrogenation, resulting in the formation of 2H-HEDMC. Because this process does not occur in the multilayer at 300 K, it must be induced by the interaction with the Ag(111) surface. This is further confirmed by the observation that the N−H bond dissociation does not occur on Au(111), even after heating the monolayer to 500 K (see Figure S1 in the Supporting Information).

To suppress the surface-induced dehydrogenation, 3H-HEDMC was deposited onto a Ag(111) surface kept at 180 K during deposition. As can be seen in Figure 2d, the N 1s spectrum now shows the 3:1 intensity ratio of the intact 3H-HEDMC molecule. Increasing the sample temperature shortly (for 3 min) to 240 K results in a partially reacted monolayer with 57% of 2H-HEDMC, indicating that the partial −NH− dehydrogenation sets in well below room temperature (Figure 2c). Figure 2e shows the fractions of 3H-HEDMC and 2H-HEDMC as a function of temperature, as derived from the detailed XPS temperature series in Figure S2. Obviously, the dehydrogenation reaction starts already below 200 K. The data in Figure S2 also show that the remaining two −NH− groups are very stable, and further −NH− dehydrogenation does not occur until 600 K, which is the onset temperature for unspecific decomposition. The temperature dependence above 300 K is therefore very similar to that of octaalkylporphyrins and tetraphenylporphyrins on Ag(111).[53] From the temperature-dependent intensities in Figure 2e, the activation barrier for the dissociation of the first N−H bond is derived by using a pre-exponential factor of 10^{13} s^{-1} (see details in the Supporting Information).[54] The resulting value of 74 kJ/mol agrees well with the theoretical value of 76 kJ/mol reported below. In a previous study using 5,10,15-tris(pentafluorophenyl)corrole on Ag(111), the first N−H dissociation was reported at a much higher temperature of 330 K.[47] The increased surface reactivity of 3H-HEDMC is attributed to its smaller adsorption height due to the absence of the sterically demanding pentafluorophenyl substitutents.

Additional insight into the bonding situation of the pristine and reacted corrole species is obtained from the XPS peak positions and chemical shifts. Comparison of the N 1s spectra of intact 3H-HEDMC in the multilayer and the monolayer at 180 K indicates that the 3H-HEDMC monolayer is not substantially affected by the interaction with the surface: The spectra show the same peak separation of 2.0 eV and only a small shift of 0.1 eV to lower binding in the monolayer. The peak separation is also almost identical with that of octaethylporphyrin (2H-OEP) in multilayers (2.0−2.1 eV)[50,55] and monolayers on Ag(111) (2.0 eV).[50,56] In contrast, the reacted 2H-HEDMC monolayer at 300 K shows a reduced peak separation of 1.7 eV, and the whole spectrum is shifted toward lower binding energy (BE) by 0.6 eV for the −NH− peak. The low-BE shift indicates either charge transfer from the surface to the N atoms of the molecule, or increased final-state

https://dx.doi.org/10.1021/acs.jpcc.0c04451
J. Phys. Chem. C 2020, 124, 13825−13836

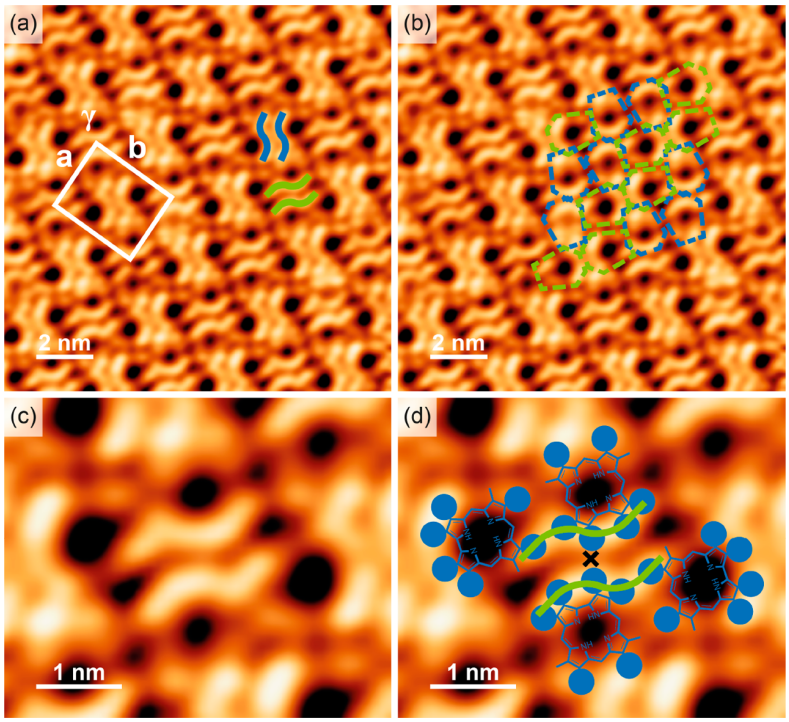

Figure 4. STM topographs of a 2H-HEDMC monolayer on Ag(111) prepared at 300 K. (a) Overview image of the monolayer structure with overlaid unit cell (25.8 ± 0.2 Å × 33.1 ± 0.2 Å, 90 ± 2°) containing four molecules. Representatives for the two enantiomeric double-wave motifs are marked by blue and green curves. (b) STM image from (a) with overlaid contours indicating the four different azimuthal orientations with relative angles of (multiples of) 90°. (c) High-resolution image of a single double-wave motif. (d) Structural model with four corrole molecules contributing to a single double-wave motif from (c). The ethyl substituents are represented by blue discs. The cross represents the position of the C_2 rotational axis. Tunneling conditions: −1.54 V, −0.89 nA, and 160 K.

screening, or a combination of both. Both effects point toward an increased interaction with the surface. The corresponding C 1s signal (see Figure S3) shifts in the same direction, but by only 0.2 eV, indicating that the N atoms interact more strongly with the surface than the rest of the molecule.

The reduced N 1s peak separation found for the 2H-HEDMC monolayer, compared to a 2H-OEP monolayer, indicates fundamental differences in the chemical states of 2H-HEDMC and 2H-OEP, despite their close structural similarities. In view of previous work with triarylcorroles in solution[57] and on a Ag(111) surface,[47] we propose (and later prove) that adsorbed 2H-HEDMC has the character of a π-radical that interacts with a metal surface. Previous DFT calculations on the mono-N-dehydrogenated tris(pentafluorophenyl)corrole show that the singly occupied molecular orbital (SOMO) of the free corrole radical extends over large parts of the molecule including the nitrogen atoms.[47] The lack of significant spin-induced broadening of our N 1s signals suggests that the spin is quenched by the surface interaction, most likely by electron transfer to the corresponding singly unoccupied orbital (SUMO),[15] which then also causes the low-binding-energy shift of 2H-HEDMC compared to 3H-HEDMC (Figure 1). Support for this hypothesis will be provided below.

Valence Electronic Structure and Work Function Change. Valence-level photoelectron spectra reveal more details of the electronic structure of the adsorbed corrole species. Figure 3b shows an UV photoelectron spectrum of a 3H-HEDMC monolayer on Ag(111) prepared at 180 K to prevent N−H dissociation. The most pronounced feature is a peak at 1.7 eV below the Fermi energy (E_F). In the spectrum of 2H-HEDMC at 300 K (Figure 3a), this peak appears at 1.4 eV; i.e., it is shifted by 0.3 eV toward lower BE. Within the initial-state approximation, the spectra can be compared to the calculated density of states (DOS) of adsorbed 2H-corrole (2H-C) and 3H-corrole (3H-C) as well as energy eigenvalues of the gas phase molecules as shown in Figures 3c and 3d. In general, the density functional used in this study underestimates the HOMO−LUMO gap, which means that the occupied orbitals appear at higher BEs in the calculation;[58] this is also seen here. Apart from that, the shape of the spectra is correctly reproduced by the partial DOS of the molecule. Thus, the valence states can be assigned to the two nearly degenerate frontier orbitals of corrole. These are typical characteristics of porphyrinoid systems.[17] The shift of these states upon N−H dissociation can also be observed in the partial DOS of the molecule. Moreover, the calculations show that the SOMO of 2H-HEDMC in the gas phase lies below E_F, indicating that a charge transfer from the surface to the corresponding SUMO should be possible, and thus the spin should be quenched due to surface interactions. A spin-polarized calculation shows the same DOS for 2H-C for both spins (see Figure S7).

UV photoelectron spectroscopy also provides access to the work function (WF) φ (see details in the Supporting Information). Knowledge of φ is important because adsorbate−substrate interactions and especially charge transfer typically result in WF changes $\Delta\varphi$. The unreacted monolayer of 3H-HEDMC reduces the WF of the Ag(111) surface by $\Delta\varphi$ = −0.92 eV, whereas the 2H-HEDMC monolayer induces a

https://dx.doi.org/10.1021/acs.jpcc.0c04451
J. Phys. Chem. C 2020, 124, 13825−13836

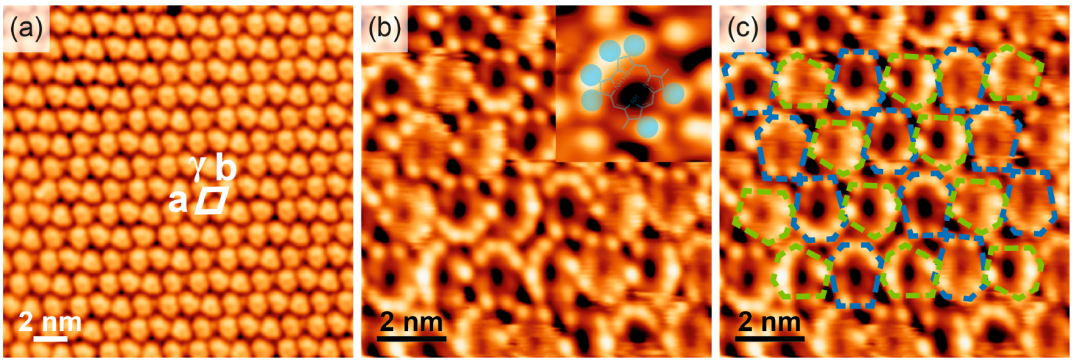

Figure 5. STM topographs of intact 3H-HEDMC on Ag(111) at 150 K. (a) Overview STM image of the monolayer structure with overlaid unit cell (14.3 ± 0.1 Å × 13.0 ± 0.2 Å, 108 ± 2°). (b) High-resolution image with submolecular details. The inset shows a single molecule with a superimposed molecular model of 3H-HEDMC in which the ethyl groups are shown as filled circles. (c) STM image from (b) with overlaid contours highlighting the four different azimuthal orientations. The colors represent molecules with the four adjacent ethyl groups oriented either toward top/bottom (blue) or left/right (green). Tunneling conditions: (a) −1.68 V and −1.22 nA; (b, c) −1.20 V and −1.76 nA.

slightly lower WF reduction of $\Delta\varphi = -0.86$ eV. This trend is corroborated by DFT calculations (see Table S9). If surface-to-molecule electron transfer occurs, the WF change is the balance of two competing effects. First, adsorption on metals is typically accompanied by the pillow (or pushback) effect. This effect is caused by Pauli repulsion between electrons in the molecule and those in the metal. It reduces the WF because the surface dipole is decreased due to the electron density of the molecule pushing back the excess charge at the surface of a metal substrate.[59] Previously, it has been demonstrated[60] that a stronger and shorter surface chemical bond leads to an increased pushback and thus to a more negative WF change. This increased pushback often even overcompensates the WF increase from a concomitant surface-to-molecule electron transfer, which represents the second major contribution to the WF change. The overcompensation has been demonstrated for example for the isomers naphthalene and azulene on Cu(111). Azulene, which forms the stronger bond, lowers the WF by −1.07 eV compared to −0.73 eV for naphthalene (both at 1 ML), even though only azulene receives electron density from the surface (0.49 e^- per molecule). The pushback-related negative WF change here clearly outweighs the positive WF change due to the electron transfer.[60] Because 2H-HEDMC forms a stronger and shorter bond to the Ag(111) surface than 3H-HEDMC (see below), it is expected to cause a more negative WF change than 3H-HEDMC, especially if only the pushback is considered. However, the experiment shows the opposite result: 2H-HEDMC causes a less negative WF change. This finding can be explained by substantial electron transfer from the surface to the 2H-HEDMC molecule. In this case, the WF increase due to this electron transfer apparently even overcompensates the WF decrease due to the increased Pauli pushback of 2H-HEDMC.

Therefore, valence photoemission spectra and WF changes are in agreement with the transfer of electron density from the surface to 2H-HEDMC. Before this finding is further analyzed, we will turn our attention to the structures of the adsorbate phases.

Adsorbate Structure. The 2H-HEDMC molecules formed upon room temperature deposition of 3H-HEDMC on Ag(111) arrange in an ordered monolayer phase with a characteristic chiral double-wave motif, which occurs in both enantiomeric forms (Figure 4a). The two enantiomers are rotated by 90° and assemble in an alternating pattern with a 25.8 ± 0.2 Å × 33.1 ± 0.2 Å, 90 ± 2° unit cell (Figure 4a,b). To understand the molecular arrangement, it is helpful to compare with 2H-OEP, which has eight peripheral ethyl groups, while 2H-HEDMC has six. Scanning tunneling microscopy (STM) images of 2H-OEP on Ag(111) and Au(111) show that the ethyl groups are imaged as bright protrusions under a wide range of tunneling conditions.[49,51] It is therefore likely that the double-wave features are related to the ethyl groups of 2H-HEDMC. The six ethyl groups in the corrole can be divided into two sets: one set of adjacent four groups on one side of the molecule and another set of two groups on the other side. These two sets are separated by the two methyl groups. A closer inspection of the double-wave motif reveals that each wave contains contributions from two neighboring molecules (Figure 4c,d): a set of four ethyl groups from one molecule and a single ethyl group, of a set of two, from a neighboring molecule. The second wave in the double-wave motif is formed in the same way, but with ethyl groups from another two molecules. Therefore, four neighboring molecules contribute to every double-wave feature. The molecules in this structure occur in four different azimuthal orientations with relative angles of (multiples of) 90°. The driving force for the formation of this structure is proposed to be the attractive van der Waals interaction between the ethyl groups of neighboring molecules.

To study the monolayer structure of 3H-HEDMC, the molecules were deposited at a sample temperature of 180 K and imaged at 150 K. The overview STM image in Figure 5a shows an oblique lattice with an average primitive unit cell of 14.3 ± 0.1 Å × 13.0 ± 0.2 Å, 108 ± 2°. The individual ethyl groups are resolved in Figure 5b. At first sight, the structure appears to be disordered with respect to the azimuthal rotational angles, which can be determined by using the positions of the individually resolved ethyl groups (see also inset in Figure 5b). In Figure 5c, these azimuthal orientations are indicated by the shapes of the overlaid dashed contours. They reveal that the molecules assume only four azimuthal orientations, just like in the case of 2H-HEDMC. While the arrangement is not fully periodic, it has a certain degree of order: the molecules are arranged in two types of rows, distinguished by blue and green contours. In Figure 5c, the sets of four ethyl groups point to the left or to the right in the green rows, while they have a top/bottom orientation in the blue rows. To compare the molecular densities of 3H-HEDMC and

https://dx.doi.org/10.1021/acs.jpcc.0c04451
J. Phys. Chem. C 2020, 124, 13825−13836

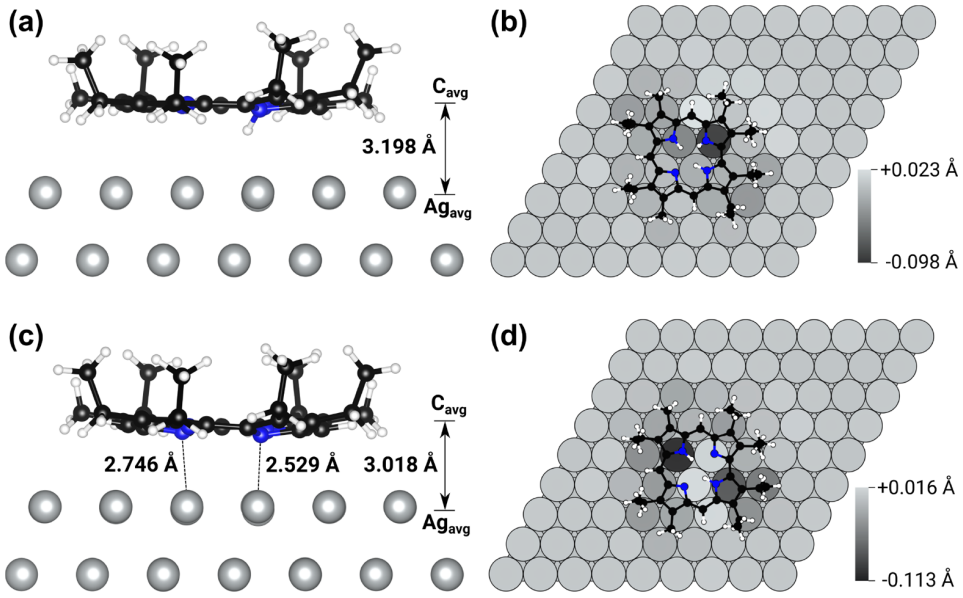

Figure 6. Adsorption geometries of (a, b) 3H-HEDMC and (c, d) 2H-HEDMC on Ag(111) in side and top view. C_{avg} and Ag_{avg} indicate the average heights of the C atoms in the corrole ring and the Ag atoms in the topmost silver layer, respectively. (b) and (d) show the vertical displacements of the Ag atoms in the topmost surface layer compared to the relaxed pristine surface without molecule. Positive values (lighter gray) mean a displacement toward the molecule. For a discussion of other adsorption conformations, see Table S8.

2H-HEDMC in the monolayers, the unit-cell areas were calculated: The unit cell of the double-wave motif at 300 K (Figure 4a) covers 854 Å^2 and contains four 2H-HEDMC molecules, while the area of the primitive unit cell in the rotationally disordered phase of intact 3H-HEDMC at 150 K (Figure 5a) is 177 Å^2 with one 3H-HEDMC molecule. The ratio of the areas is 4.8 and thus deviates from the ratio of the numbers of molecules in the unit cell, which is 4. This shows that the ordered phase in Figure 4 has a lower packing density than the rotationally disordered phase in Figure 5. Such effects can occur in the case of directional bonding, which is energetically favorable but requires more space. A well-known example is water, which has a lower density in the crystalline phase (ice) than in the partially disordered liquid phase. The directionality is here likely a result of the arrangement of the ethyl substituents at the periphery of the molecule, which allow maximization of the intermolecular van der Waals interactions only for a highly ordered, but spatially slightly more demanding structure.

Density Functional Theory (DFT) Calculations. The results of a computational investigation of structure and reactivity of parent (3H-C) and alkyl-substituted (3H-HEDMC) corroles will now be presented in a two-step approach: First, the optimized gas-phase structures—hereafter termed free corroles—are discussed, followed by an analysis of the reactivity and electronic structure on the metal surface. This enables us to discuss the effects of backbone substitution and to reveal the influence of the surface on the properties of the corroles. We present only the main structural features here; more details on computed gas phase and adsorption structures are found in the Supporting Information (Figures S4−S6 and Tables S1−S8). As a side note, corroles form two tautomers, which are close in energy (ΔE(3H-HEDMC) = 4 kJ/mol); the most stable tautomer has been used for the computations. The optimized structures of gas-phase 3H-C and 3H-HEDMC reveal a nonplanar structure with large displacement angles of the N−H hydrogen atoms relative to the plane formed by the pyrrolic nitrogen atoms. The largest angles are found for N_D−H (i.e., the N−H bond in ring D), which is displaced by −43.8° (3H-C) and −45.8° (3H-HEDMC), in line with previous findings for 3H-C[61] (see Table S4 for more details). The displaced H atom bonded to N_D is thus the most likely candidate for the on-surface dehydrogenation reaction. Bond lengths and angles (Tables S4−S6) are very similar for 3H-C and 3H-HEDMC, which confirms that the unusual structure is an inherent feature of the corrole macrocycle and not related to the alkyl substitution. These findings agree with crystallographic data for other substituted corroles.[16]

Adsorption Geometries and Bond Energies. For free 3H-HEDMC, the most stable conformation shows the ethyl groups at C2 and C17 pointing to a different hemisphere than the other alkyl groups. On the Ag(111) surface, this conformation is less stable by 16 kJ/mol compared to the conformation where all alkyl groups point away from the surface (Table S8). This adsorption structure is in line with previous results for 2H-OEP on Ag(111).[49] The out-of-plane displacement of the N_D−H bond is even more pronounced after adsorption, with dihedral angles of −50.4° for 3H-C and −49.6° for 3H-HEDMC. It is energetically slightly preferable for this H atom to point toward the surface (Table S8). The adsorption energy is large (E_{ads}(3H-C) = −267 kJ/mol, E_{ads}(3H-HEDMC) = −403 kJ/mol) and given solely by attractive dispersion interaction, while the electronic interaction energy is even repulsive (Tables S1 and S8). Because directional covalent interactions are not important in comparison to isotropic van der Waals interactions, this also explains why different adsorption sites (bridge, hollow, and on-top) show very similar adsorption energies (see Figures S4, S5 and Tables S1, S2 in the Supporting Information).

The proximity of the N_D−H bond to the surface is expected to facilitate its dissociation, resulting in the singly N−H dehydrogenated corroles 2H-C and 2H-HEDMC. Dissociation

https://dx.doi.org/10.1021/acs.jpcc.0c04451
J. Phys. Chem. C 2020, 124, 13825−13836

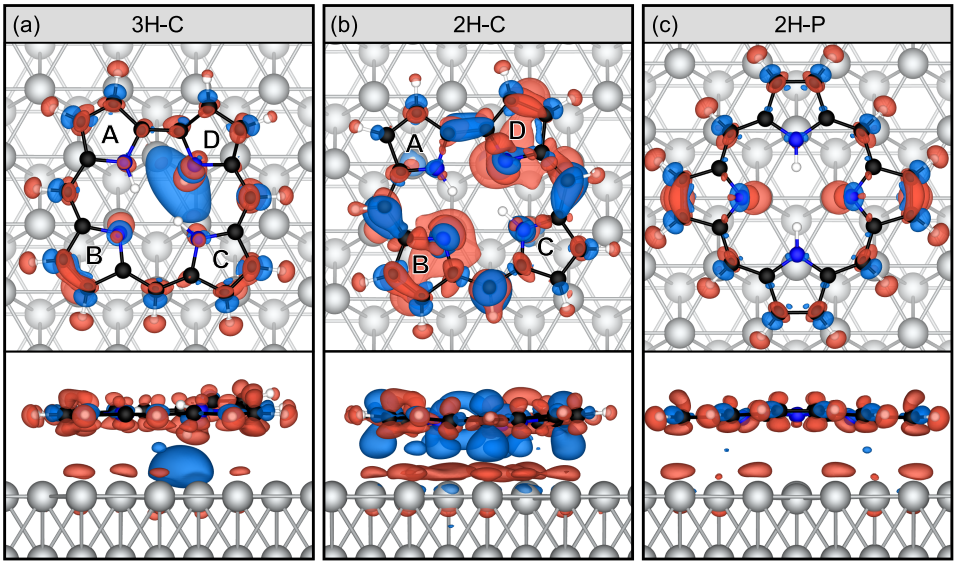

Figure 7. Charge density difference plots with an isosurface value of 0.001 e/Å^3 of (a) 3H-C, (b) 2H-C, and (c) 2H-P on Ag(111). The colors denote charge accumulation (blue) and depletion (red) with respect to the state before adsorption.

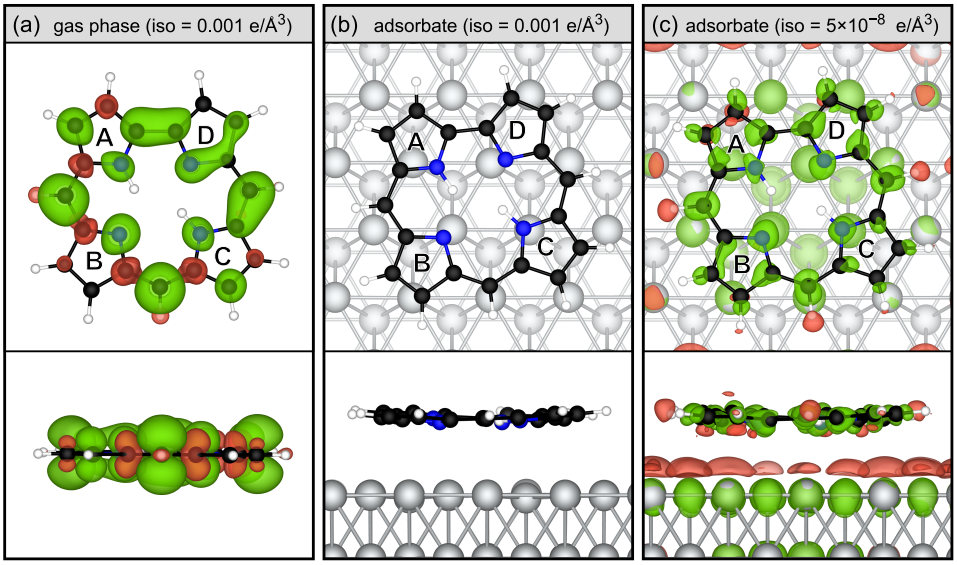

Figure 8. Spin densities (isosurface value = 0.001e/Å^3) of (a) gas-phase 2H-C and (b) 2H-C on Ag(111), indicating that the spin at the molecule is almost completely quenched in the adsorbed state. (c) Residual delocalized spin density of adsorbed 2H-C visible with an extremely low isosurface value of 5 × 10^{-8}e/Å^3. Green and red regions represent excess of α- or β-spin, respectively.

of the N_D−H bond relieves the steric stress in the macrocycle, and thus a planar structure results (Table S4). The adsorption heights of 2H-C and 2H-HEDMC are reduced by ∼0.2 Å in comparison to 3H-C and 3H-HEDMC (Figure 6). The adsorption energies are increased to −337 kJ/mol (2H-C) and −457 kJ/mol (2H-HEDMC), which is not only due to increased dispersion attractions (resulting from the smaller adsorption heights) but also due to attractive electronic interactions (Table S2). This is a first indication for a covalent bonding interaction of 2H-HEDMC with the Ag(111) surface. For a more detailed discussion of the electronic structure, we now focus on the unsubstituted model corroles 3H-C and 2H-C.

Interfacial Electron Transfer. The charge density difference plots in Figure 7 visualize the influence of the Ag(111) surface on the charge density distribution of the adsorbed species. For the unreacted 3H-C (Figure 7a), the most pronounced feature is an accumulation of negative charge (blue) just below the pyrrolic hydrogen atom of ring D (N_D−H), which points toward the surface and is slightly elongated by 1.4 pm. Much larger effects are found for 2H-C, i.e., after dissociation of the N_D−H bond: As shown in Figure 7b, the molecule receives negative charge (blue color) from the surface. The spatial distribution of this negative charge resembles the shape of the SOMO of the gas-phase molecule (cf. Figure 3). This result confirms the experimentally observed

https://dx.doi.org/10.1021/acs.jpcc.0c04451
J. Phys. Chem. C 2020, 124, 13825−13836

charge transfer from the surface to the molecule and reveals that the charge goes mainly into the SUMO related to the former SOMO. For comparison, the structurally closely related porphine (2H-P, Figure 7c) shows much less adsorption-induced charge redistribution.

The total charge flow between surface and molecule can be quantified by Hirshfeld partitioning. The adsorbed 3H-C receives a very small negative charge of $-0.08e$. In contrast, 2H-C accumulates a much higher negative charge of $-0.43e$, confirming considerable transfer of electron density from the surface to the adsorbate. The value for 2H-P is smaller ($-0.16e$) and in good agreement with previous work ($-0.19e$).[62]

Radical Character of Free and Adsorbed 2H-C. The DFT calculations confirm the radical character of 2H-C in the gas phase. Figure 8a shows the spatial distribution of the spin density ($\rho(\alpha\text{-spin}) - \rho(\beta\text{-spin})$), which is delocalized and resembles the shape of the SOMO, in line with previous work.[57] The delocalization of the unpaired electron in a π-orbital may seem surprising because the dissociation of the N_D−H bond should lead to a σ-radical localized at N_D. There are two factors that may be responsible for the formation of a π-radical instead of a σ-radical at N_D: First, the N_D−H bond is strongly displaced and therefore overlaps with the π-electron system, facilitating hyperconjugation of the N_D−H bond in 3H-C (Figure S9) and subsequent delocalization of the unpaired electron in 2H-C. Second, electronegativity and resonance stabilization (or delocalization) of the radical electron may play an important role. The transformation from a σ-radical localized at N_D to a π-orbital means that the delocalized former HOMO donates one electron into the semioccupied nonbonding σ-orbital at N_D, resulting in an electron pair (and an additional charge) at the more electronegative N_D and a corresponding hole in the former HOMO, turning it into a SOMO with a delocalized radical electron.

The spin density in the SOMO/SUMO is strongly affected by the interaction with the surface. Figures 8b and 8c show the spin density for the adsorbed 2H-C at different isosurface values. When the same isosurface value as in Figure 8a is used ($0.001e/Å^3$), the remaining spin density is so small that it appears invisible (Figure 8b), indicating that the charge transfer from the surface into the SOMO-related SUMO of the molecule almost completely quenches the spin. Only at an extremely low isosurface value of $5 \times 10^{-8} e/Å^3$, the weak residual spin density with a highly delocalized spatial distribution becomes visible (Figure 8c).

Aromaticity and Driving Force for the Interfacial Electron Transfer. The driving force for the unusually large charge transfer from the surface to 2H-C can be rationalized with the concepts of electron delocalization and aromaticity. According to the Hückel molecular orbital (HMO) theory, an aromatic conjugated system is energetically more stable than its antiaromatic counterpart.[63] A versatile approach to quantify aromaticity in a spatially resolved fashion is the nucleus-independent chemical shift (NICS).[52,64] This method is based on the computed aromatic ring current induced by a (hypothetical) external magnetic field perpendicular to the plane of the aromatic system. Here, we calculated NICS(0) values for the centers of the pyrrole units, the inner cross, and between two pyrrole units (Figure 9). Negative values (diatropic ring current, red circles) indicate aromaticity, while antiaromaticity is characterized by positive values

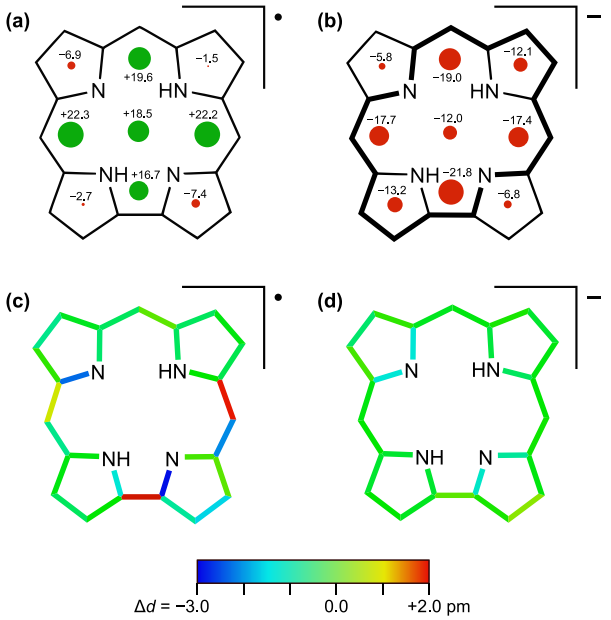

Figure 9. Spatially resolved aromaticity of (a) 2H-C radical and (b) 2H-C$^-$ anion as estimated by the NICS(0) method. Positive NICS values (antiaromaticity) are represented by green circles, and negative NICS values (aromaticity) are represented by red circles. The 2H-C radical (a) has mainly antiaromatic character, while the 2H-C$^-$ anion (b) is aromatic. Note that the two cross-conjugated pyrrole rings outside the conjugation path (upper left, bottom right) are not affected by the charge transfer and show almost the same NICS values in both species. Calculated NICS(1) values at 1 Å above the ring plane qualitatively give the same result (see Figure S11). (c, d) Color-coded bond length difference ($\Delta d = d_{gas} - d_{ads}$) between the adsorbate structure of 2H-C and (c) the gas-phase 2H-C radical and (d) the gas-phase 2H-C$^-$ anion. The comparison shows that the adsorbed 2H-C structurally resembles the aromatic 2H-C$^-$ anion, indicating that the adsorbed state is characterized by aromatic stabilization.

(paratropic ring current, green circles). To investigate the influence of the electron transfer on the aromaticity of 2H-C, the NICS(0) values were calculated for the radical 2H-C gas phase structure (Figure 9a) and for the negatively charged 2H-C monoanion as a simple approximation of the negatively charged molecule in its adsorbed state (Figure 9b).

According to these calculations, the internal cross structure inside the macrocycle of the radical 2H-C species (Figure 9a) has a distinct antiaromatic character, while the four pyrrole units show small negative NICS values indicating weakly aromatic to nonaromatic character. This result indicates that electron delocalization over the whole π-electron system destabilizes the 2H-C radical (even though a σ-radical localized at N_D is apparently even less stable, as mentioned above). Moreover, the four pyrrole units can be interpreted as four separated delocalized systems.

In contrast, the 2H-C monoanion (Figure 9b) shows a pronounced aromatic character inside the internal cross and the two pyrrole units containing the amine −NH− functions. These findings also confirm that the main delocalization pathway (highlighted by bold lines in Figure 9b) encloses the inner cross and two pyrrole units. For 2H-HEDMC, similar results were obtained, indicating that there is no significant

https://dx.doi.org/10.1021/acs.jpcc.0c04451
J. Phys. Chem. C 2020, 124, 13825−13836

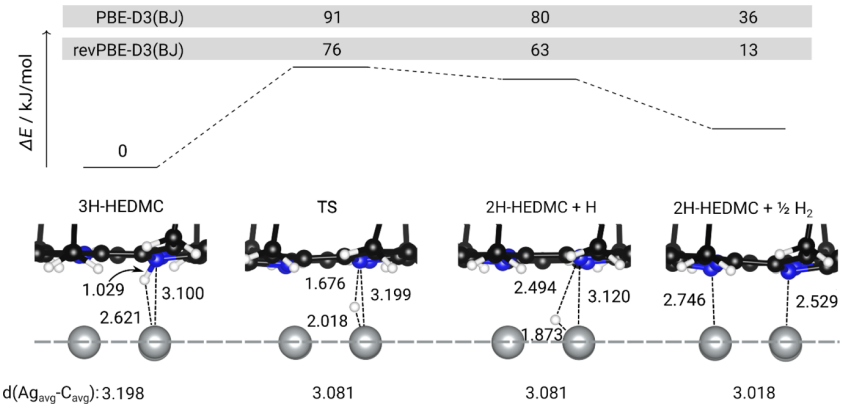

Figure 10. Reaction energy profile of the dissociation of the N_D−H bond of 3H-HEDMC and subsequent desorption of H_2. Energies in kJ/mol and distances in Å.

influence of the peripheral alkyl groups on the aromaticity (see Figure S9).

Another criterion for aromaticity is based on the bond length alternation, which is typically lowest in the case of aromatic conjugation (cf. the HOMA method).[65,66] For example, the two adjacent C−C bonds in the methine bridge between rings A and B in the antiaromatic 17π radical differ in length by 0.018 Å, while they have the same lengths in the three 18π systems: the 3H-corrole, the 2H-corrole anion, and the adsorbed 2H-corrole. Further bond length values are shown in Figure S12. For comparison of the two gas-phase species, the 2H-corrole radical and the anion, with the adsorbed 2H-corrole, the bond lengths differences are shown by the colored code in Figure 9c,d. As can be seen, the adsorbed state closely resembles the gas-phase anion, indicating that adsorption results in a similar aromaticity state as is reached by the additional electron in the 18π anion. This suggests that the charge transfer from the surface to the adsorbed 2H-HEDMC can be described as aromaticity driven; by accepting electron density from the metal surface, the molecule gains aromatic character and thus aromatic stabilization.

Energetics of the N_D−H Bond Dissociation. Next, we estimate the barrier for the N_D−H dissociation in adsorbed 3H-HEDMC. In the minimum-energy structure (Figure 6a,b), the six ethyl groups of 3H-HEDMC are bent away from the surface and therefore have only a negligible influence on the adsorption geometry of the macrocycle (Table S1). This contrasts previous findings for triphenylcorrole and tris(pentafluorophenyl)corrole:[38,39,45−47] In the adsorbed state, these molecules experience complex distortion resulting from the steric repulsion between the peripheral phenyl groups and the corrole macrocycle. In the adsorbed, intact 3H-HEDMC molecule, the N_D−H bond shows an out-of-plane displacement by −49.6°, very similar to the value obtained for 3H-C and the free 3H-HEDMC (Table S4). The distance of the N_D−H hydrogen to the surface is 2.202 Å, whereas the other two N−H hydrogen atoms have much larger distances of 3.181 and 3.189 Å. The Ag atom directly below the N_D−H hydrogen is pushed into the surface by 0.1 Å.

To estimate the energy difference between 3H-HEDMC and 2H-HEDMC in the adsorbed state as well as the energy barrier for the N−H dissociation, a nudged elastic band calculation of the dissociation path was performed for the N_D−H hydrogen atom (Figure S12) because this H atom shows by far the largest out-of-plane displacement. The initial guess of the transition state has been further refined by using the more accurate dimer method (see the Methods section in the Supporting Information). The results of different exchange-correlation functionals (Table S10) with varying treatment of the crucial dispersion interactions for the reaction barrier can be compared to the experimental barrier of 74 kJ/mol (see above). The best agreement is found for the revPBE functional in combination with the DFT-D3 dispersion correction scheme, which provides a barrier height of 76 kJ/mol. The revPBE functional does not suffer from the spurious exchange binding observed for PBE and is thus most suitable for the combination with the DFT-D3 dispersion correction as observed before.[67]

The final state, consisting of an adsorbed 2H-HEDMC and an adsorbed hydrogen atom, lies 63 kJ/mol above the initial state, making this reaction step endothermic. As the H atom moves toward a hollow site on the Ag(111) surface, the corrole macrocycle gradually flattens, again underlining that the ring distortion is caused by steric repulsion between the three N−H hydrogen atoms in 3H-HEDMC.

Because hydrogen atoms on Ag(111) recombine and desorb as H_2 already at 185 K,[68] i.e., below the experimental reaction temperature, calculation of the total reaction energy must include the following contribution ΔE for the formation and desorption of H_2:

$$\Delta E = E(\text{2H-HEDMC} + \text{H})_{\text{ads}} - E(\text{2H-HEDMC})_{\text{ads}} - \frac{1}{2}E(\text{H}_2)_{\text{gas}} \quad (1)$$

Diffusion of the transferred H atom from underneath the molecule results in a relaxation of the adsorbate. Its bond to the surface is dominated by coordination of iminic N to surface atoms (see Figure 10) and results in a structure that is 39 kJ/mol more stable. Subsequent recombination of the hydrogen atoms and their desorption as H_2 results in a further energy gain of 11 kJ/mol. Therefore, the total dehydrogenation reaction requires only 63 − 50 = 13 kJ/mol, which is still endothermic. However, the reaction is exergonic, i.e., has a negative Gibbs energy ΔG, because of the large entropy gain of the desorbing H_2 in ultrahigh vacuum.[69] For an estimate of ΔG, we consider only the gain of translational entropy of the formed H_2 because this is by far the largest contribution. At 200 K and a H_2 residual gas pressure of 10^{-10} mbar, the entropic part $T\Delta S$ of ΔG is 67 kJ/mol, according to the

https://dx.doi.org/10.1021/acs.jpcc.0c04451
J. Phys. Chem. C 2020, 124, 13825−13836

Sackur–Tetrode equation.[70] For ΔG we therefore obtain a negative value of 13 − 67 = −54 kJ/mol; i.e., the reaction is thermodynamically favored at 200 K, in agreement with the experimental observations. With increasing temperature, ΔG becomes even more negative (e.g., −96 kJ/mol at 300 K).

CONCLUSIONS

The interaction of the corrole 3H-HEDMC and its dehydrogenation product 2H-HEDMC with a Ag(111) surface was studied to understand aromaticity-related electron-transfer effects at a metal/organic interface. Multilayers of 3H-HEDMC are stable at room temperature, whereas a surface-catalyzed loss of one pyrrolic N–H atom occurs in the monolayer. Variable-temperature XPS reveals that the N–H bond dissociation starts already at 200 K and has a barrier of only 74 kJ/mol, in line with the theoretical prediction. Considerations of energy and entropy effects reveal that the N–H dissociation is partially driven by the entropy gain of the released hydrogen. The dehydrogenation product, 2H-HEDMC, is formally a π-radical with a 17π-electron conjugation path. In the adsorbed state, its spin is quenched due to surface interactions, as revealed by XPS, UPS, and DFT. The latter shows a substantial charge transfer (−0.43e) from the surface to the SUMO of the π-radical. The driving force for the electron transfer is related to the aromaticity of the macrocycle. By accepting electron density from the surface, the corrole radical can increase the aromatic character of its π-electron system, as was confirmed by model calculations of the nucleus-independent chemical shift (NICS) and bond-length considerations. 2H-HEDMC forms an ordered monolayer structure in which the molecules are alternatingly rotated by multiples of 90°. Monolayers of 3H-HEDMC are stable only below 200 K, where they show translational long-range order but partial rotational disorder. 3H-HEDMC assumes a nonplanar adsorption geometry, which is caused by the steric repulsion between the three N–H hydrogens. Especially the N–H hydrogen of pyrrole ring D is substantially displaced and points toward the surface. After dissociation of this N_D–H bond, the out-of-plane distortion is relieved, and the remaining 2H-HEDMC assumes a nearly flat conformation, similar to adsorbed 2H-porphine. The out-of-plane distortion occurs similarly in the octaalkylcorrole (3H-HEDMC) and the unsubstituted corrole macrocycle (3H-C), revealing that it is an inherent property of the adsorbed corrole. Our analysis of a prototypical corrole/metal interface reveals substantial differences to similar porphyrin/metal interfaces. The steric overcrowding by the presence of three N–H hydrogen atoms and the shorter conjugation path lead to increased on-surface reactivity and electron transfer. Our study also demonstrates that aromaticity considerations are useful to rationalize interfacial electron-transfer effects between metals and π-conjugated organic molecules.

ASSOCIATED CONTENT

Supporting Information

The Supporting Information is available free of charge at https://pubs.acs.org/doi/10.1021/acs.jpcc.0c04451.

Computational methods, additional N 1s and C 1s XPS data, estimation of the activation barrier, work function data, supplementary computational investigations (PDF)

AUTHOR INFORMATION

Corresponding Authors

Ralf Tonner − *Fachbereich Chemie, Philipps-Universität Marburg, 35032 Marburg, Germany*; orcid.org/0000-0002-6759-8559; Email: ralf.tonner@chemie.uni-regensburg.de

J. Michael Gottfried − *Fachbereich Chemie, Philipps-Universität Marburg, 35032 Marburg, Germany*; orcid.org/0000-0001-5579-2568; Email: michael.gottfried@chemie.uni-marburg.de

Authors

Malte Zugermeier − *Fachbereich Chemie, Philipps-Universität Marburg, 35032 Marburg, Germany*

Jan Herritsch − *Fachbereich Chemie, Philipps-Universität Marburg, 35032 Marburg, Germany*

Jan-Niclas Luy − *Fachbereich Chemie, Philipps-Universität Marburg, 35032 Marburg, Germany*

Min Chen − *Fachbereich Chemie, Philipps-Universität Marburg, 35032 Marburg, Germany*

Benedikt P. Klein − *Fachbereich Chemie, Philipps-Universität Marburg, 35032 Marburg, Germany*; orcid.org/0000-0002-6205-8879

Falk Niefind − *Fachbereich Chemie, Philipps-Universität Marburg, 35032 Marburg, Germany*

Peter Schweyen − *Institut für Anorganische und Analytische Chemie, Technische Universität Braunschweig, 38106 Braunschweig, Germany*

Martin Bröring − *Institut für Anorganische und Analytische Chemie, Technische Universität Braunschweig, 38106 Braunschweig, Germany*

Martin Schmid − *Fachbereich Chemie, Philipps-Universität Marburg, 35032 Marburg, Germany*

Complete contact information is available at: https://pubs.acs.org/10.1021/acs.jpcc.0c04451

Author Contributions

M.Z. and J.H. contributed equally to this work.

Notes

The authors declare no competing financial interest.

ACKNOWLEDGMENTS

Financial support by the Deutsche Forschungsgemeinschaft (DFG) through 223848855-SFB 1083 "Structure and Dynamics of Internal Interfaces" is gratefully acknowledged. M.S. thanks the Stiftung Stipendien-Fonds der Chemischen Industrie for funding. We thank Dr. Phil Rosenow for assistance in the computations and the HLR Stuttgart, LOEWE-CSC Frankfurt, and HRZ Marburg for providing computational resources.

REFERENCES

(1) Nardis, S.; Mandoj, F.; Stefanelli, M.; Paolesse, R. Metal complexes of corrole. *Coord. Chem. Rev.* **2019**, *388*, 360–405.
(2) Kadish, K. M.; Smith, K. M.; Guilard, R. *Handbook of Porphyrin Science*; Singapore, 2010.
(3) Gottfried, J. M. Surface Chemistry of Porphyrins and Phthalocyanines. *Surf. Sci. Rep.* **2015**, *70*, 259–379.
(4) Banerjee, R.; Ragsdale, S. W. The many faces of vitamin B-12: Catalysis by cobalamin-dependent enzymes. *Annu. Rev. Biochem.* **2003**, *72*, 209–247.
(5) Auwärter, W.; Ecija, D.; Klappenberger, F.; Barth, J. V. Porphyrins at interfaces. *Nat. Chem.* **2015**, *7* (2), 105–120.

(6) Yokoyama, T.; Yokoyama, S.; Kamikado, T.; Okuno, Y.; Mashiko, S. Selective assembly on a surface of supramolecular aggregates with controlled size and shape. *Nature* **2001**, *413* (6856), 619−621.
(7) Diller, K.; Papageorgiou, A. C.; Klappenberger, F.; Allegretti, F.; Barth, J. V.; Auwärter, W. In vacuo interfacial tetrapyrrole metallation. *Chem. Soc. Rev.* **2016**, *45*, 1629−1656.
(8) Marbach, H. Surface-Mediated in Situ Metalation of Porphyrins at the Solid−Vacuum Interface. *Acc. Chem. Res.* **2015**, *48* (9), 2649−2658.
(9) Chen, M.; Zhou, H.; Klein, B. P.; Zugermeier, M.; Krug, C. K.; Drescher, H. J.; Gorgoi, M.; Schmid, M.; Gottfried, J. M. Formation of an interphase layer during deposition of cobalt onto tetraphenylporphyrin: a hard X-ray photoelectron spectroscopy (HAXPES) study. *Phys. Chem. Chem. Phys.* **2016**, *18* (44), 30643−30651.
(10) Peeks, M. D.; Claridge, T. D. W.; Anderson, H. L. Aromatic and antiaromatic ring currents in a molecular nanoring. *Nature* **2017**, *541*, 200.
(11) Yoon, Z. S.; Osuka, A.; Kim, D. Möbius aromaticity and antiaromaticity in expanded porphyrins. *Nat. Chem.* **2009**, *1*, 113.
(12) Stępień, M.; Sprutta, N.; Latos-Grażyński, L. Figure Eights, Möbius Bands, and More: Conformation and Aromaticity of Porphyrinoids. *Angew. Chem., Int. Ed.* **2011**, *50* (19), 4288−4340.
(13) Scott, J. C. Metal−organic interface and charge injection in organic electronic devices. *J. Vac. Sci. Technol., A* **2003**, *21* (3), 521−531.
(14) Gao, Y.; Shao, Y.; Yan, L.; Li, H.; Su, Y.; Meng, H.; Wang, X. Efficient Charge Injection in Organic Field-Effect Transistors Enabled by Low-Temperature Atomic Layer Deposition of Ultrathin VOx Interlayer. *Adv. Funct. Mater.* **2016**, *26* (25), 4456−4463.
(15) Hollerer, M.; Lüftner, D.; Hurdax, P.; Ules, T.; Soubatch, S.; Tautz, F. S.; Koller, G.; Puschnig, P.; Sterrer, M.; Ramsey, M. G. Charge Transfer and Orbital Level Alignment at Inorganic/Organic Interfaces: The Role of Dielectric Interlayers. *ACS Nano* **2017**, *11*, 6252−6260.
(16) Aviv-Harel, I.; Gross, Z. Aura of Corroles. *Chem. - Eur. J.* **2009**, *15* (34), 8382−8394.
(17) Ghosh, A. Electronic Structure of Corrole Derivatives: Insights from Molecular Structures, Spectroscopy, Electrochemistry, and Quantum Chemical Calculations. *Chem. Rev.* **2017**, *117* (4), 3798−3881.
(18) Orłowski, R.; Gryko, D.; Gryko, D. T. Synthesis of Corroles and Their Heteroanalogs. *Chem. Rev.* **2017**, *117* (4), 3102−3137.
(19) Aviv, I.; Gross, Z. Corrole-based applications. *Chem. Commun.* **2007**, *20*, 1987−1999.
(20) Schoefberger, W.; Faschinger, F.; Chattopadhyay, S.; Bhakta, S.; Mondal, B.; Elemans, J. A. A. W.; Muellegger, S.; Tebi, S.; Koch, R.; Klappenberger, F.; et al. A Bifunctional Electrocatalyst for Oxygen Evolution and Oxygen Reduction Reactions in Water. *Angew. Chem., Int. Ed.* **2016**, *55* (7), 2350−2355.
(21) Zou, H.; Wang, H.; Mei, G.; Liu, H.; Chang, C.-K. Catalytic Application of Iron Corrole Complexes in Organic Synthesis. *Prog. Chem.* **2015**, *27* (6), 666−674.
(22) Wang, Z.; Lei, H.; Cao, R.; Zhang, M. Cobalt Corrole on Carbon Nanotube as a Synergistic Catalyst for Oxygen Reduction Reaction in Acid Media. *Electrochim. Acta* **2015**, *171*, 81−88.
(23) Robert, C.; Ohkawara, T.; Nozaki, K. Manganese-Corrole Complexes as Versatile Catalysts for the Ring-Opening Homo- and Co-Polymerization of Epoxide. *Chem. - Eur. J.* **2014**, *20* (16), 4789−4795.
(24) Huang, H. C.; Shown, I.; Chang, S. T.; Hsu, H. C.; Du, H. Y.; Kuo, M. C.; Wong, K. T.; Wang, S. F.; Wang, C. H.; Chen, L. C.; et al. Pyrolyzed Cobalt Corrole as a Potential Non-Precious Catalyst for Fuel Cells. *Adv. Funct. Mater.* **2012**, *22* (16), 3500−3508.
(25) Aviv, I.; Gross, Z. Iron(III) corroles and porphyrins as superior catalysts for the reactions of diazoacetates with nitrogen- or sulfur-containing nucleophilic substrates: Synthetic uses and mechanistic insights. *Chem. - Eur. J.* **2008**, *14* (13), 3995−4005.
(26) Kadish, K. M.; Fremond, L.; Burdet, F.; Barbe, J. M.; Gros, C. P.; Guilard, R. Cobalt(IV) corroles as catalysts for the electro reduction of O-2: Reactions of heterobimetallic dyads containing a face-to-face linked Fe(III) or Mn(III) porphyrin. *J. Inorg. Biochem.* **2006**, *100* (4), 858−868.
(27) Kadish, K. M.; Fremond, L.; Ou, Z. P.; Shao, J. G.; Shi, C. N.; Anson, F. C.; Burdet, F.; Gros, C. P.; Barbe, J. M.; Guilard, R. Cobalt(III) corroles as electrocatalysts for the reduction of dioxygen: Reactivity of a monocorrole, biscorroles, and porphyrin-corrole dyads. *J. Am. Chem. Soc.* **2005**, *127* (15), 5625−5631.
(28) Kadish, K. M.; Fremond, L.; Shen, J.; Chen, P.; Ohkubo, K.; Fukuzumi, S.; El Ojaimi, M.; Gros, C. P.; Barbe, J.-M.; Guilard, R. Catalytic Activity of Biscobalt Porphyrin-Corrole Dyads Toward the Reduction of Dioxygen. *Inorg. Chem.* **2009**, *48* (6), 2571−2582.
(29) Kadish, K. M.; Shen, J.; Fremond, L.; Chen, P.; El Ojaimi, M.; Chkounda, M.; Gros, C. P.; Barbe, J.-M.; Ohkubo, K.; Fukuzumi, S.; Guilard, R. Clarification of the oxidation state of cobalt corroles in heterogeneous and homogeneous catalytic reduction of dioxygen. *Inorg. Chem.* **2008**, *47* (15), 6726−6737.
(30) Sudhakar, K.; Giribabu, L.; Salvatori, P.; De Angelis, F. Triphenylamine-functionalized corrole sensitizers for solar-cell applications. *Phys. Status Solidi A* **2015**, *212* (1), 194−202.
(31) Tortora, L.; Pomarico, G.; Nardis, S.; Martinelli, E.; Catini, A.; D'Amico, A.; Di Natale, C.; Paolesse, R. Supramolecular sensing mechanism of corrole thin films. *Sens. Actuators, B* **2013**, *187*, 72−77.
(32) Barbe, J. M.; Canard, G.; Brandes, S.; Jerome, F.; Dubois, G.; Guilard, R. Metallocorroles as sensing components for gas sensors: remarkable affinity and selectivity of cobalt(III) corroles for CO vs. O-2 and N-2. *Dalton Trans.* **2004**, *8*, 1208−1214.
(33) Nulens, W.; Grabowska, I.; Ngo, T. H.; Maes, W.; Dehaen, W.; Radecka, H.; Radecki, J. Determination of the surface acidity of a free-base corrole in a self-assembled monolayer. *J. Inclusion Phenom. Mol. Recognit. Chem.* **2011**, *71* (3−4), 499−505.
(34) Stergiannakos, T.; Tylianakis, E.; Klontzas, E.; Trikalitis, P. N.; Froudakis, G. E. Hydrogen Storage in Novel Li-Doped Corrole Metal-Organic Frameworks. *J. Phys. Chem. C* **2012**, *116* (15), 8359−8363.
(35) Haber, A.; Mahammed, A.; Fuhrman, B.; Volkova, N.; Coleman, R.; Hayek, T.; Aviram, M.; Gross, Z. Amphiphilic/bipolar metallocorroles that catalyze the decomposition of reactive oxygen and nitrogen species, rescue lipoproteins from oxidative damage, and attenuate atherosclerosis in mice. *Angew. Chem., Int. Ed.* **2008**, *47* (41), 7896−7900.
(36) Lim, P.; Mahammed, A.; Okun, Z.; Saltsman, I.; Gross, Z.; Gray, H. B.; Termini, J. Differential Cytostatic and Cytotoxic Action of Metallocorroles against Human Cancer Cells: Potential Platforms for Anticancer Drug Development. *Chem. Res. Toxicol.* **2012**, *25* (2), 400−409.
(37) Hwang, J. Y.; Lubow, D. J.; Chu, D.; Sims, J.; Alonso-Valenteen, F.; Gray, H. B.; Gross, Z.; Farkas, D. L.; Medina-Kauwe, L. K. Photoexcitation of tumor-targeted corroles induces singlet oxygen-mediated augmentation of cytotoxicity. *J. Controlled Release* **2012**, *163* (3), 368−373.
(38) Kuck, S.; Hoffmann, G.; Bröring, M.; Fechtel, M.; Funk, M.; Wiesendanger, R. "Naked" Iron-5,10,15-triphenylcorrole on Cu(111): Observation of Chirality on a Surface and Manipulation of Multiple Conformational States by STM. *J. Am. Chem. Soc.* **2008**, *130* (43), 14072−14073.
(39) Kuck, S.; Prostak, M.; Funk, M.; Bröring, M.; Hoffmann, G.; Wiesendanger, R. Disposition of the axial ligand in the physical vapor deposition of organometallic complexes. *J. Vac. Sci. Technol., A* **2010**, *28* (4), 795−798.
(40) Wu, F.; Liu, J.; Mishra, P.; Komeda, T.; Mack, J.; Chang, Y.; Kobayashi, N.; Shen, Z. Modulation of the molecular spintronic properties of adsorbed copper corroles. *Nat. Commun.* **2015**, *6*, 7547.
(41) Schmid, M.; Zugermeier, M.; Herritsch, J.; Klein, B. P.; Krug, C. K.; Ruppenthal, L.; Müller, P.; Kothe, M.; Schweyen, P.; Bröring, M.; et al. On-Surface Synthesis and Characterization of an Iron Corrole. *J. Phys. Chem. C* **2018**, *122* (19), 10392−10399.

https://dx.doi.org/10.1021/acs.jpcc.0c04451
J. Phys. Chem. C 2020, 124, 13825−13836

(42) Paszkiewicz, M.; Biktagirov, T.; Aldahhak, H.; Allegretti, F.; Rauls, E.; Schofberger, W.; Schmidt, W. G.; Barth, J. V.; Gerstmann, U.; Klappenberger, F. Unraveling the Oxidation and Spin State of Mn-Corrole through X-ray Spectroscopy and Quantum Chemical Analysis. *J. Phys. Chem. Lett.* **2018**, *9* (22), 6412−6420.
(43) Miao, X. R.; Gao, A. M.; Li, Z. M.; Hiroto, S.; Shinokubo, H.; Osuka, A.; Deng, W. L. First self-assembly study of large pi-conjugated corrole dimers on solid substrates. *Appl. Surf. Sci.* **2009**, *255* (11), 5885−5890.
(44) Miao, X. R.; Gao, A. M.; Hiroto, S.; Shinokubo, H.; Osuka, A.; Xin, H. L.; Deng, W. L. Adsorption characteristic of self-assembled corrole dimers on HOPG. *Surf. Interface Anal.* **2009**, *41* (3), 225−230.
(45) Rashidi, M.; Muellegger, S.; Roithner, M.; Schoefberger, W.; Koch, R. Spectroscopic Scanning Tunneling Microscopy Studies of Single Surface-Supported Free-Base Corroles. *J. Am. Chem. Soc.* **2012**, *134* (1), 91−94.
(46) Tebi, S.; Aldahhak, H.; Serrano, G.; Schöfberger, W.; Rauls, E.; Schmidt, W. G.; Koch, R.; Müllegger, S. Manipulation resolves non-trivial structure of corrole monolayer on Ag(111). *Nanotechnology* **2016**, *27* (2), 025704.
(47) Tebi, S.; Paszkiewicz, M.; Aldahhak, H.; Allegretti, F.; Gonglach, S.; Haas, M.; Waser, M.; Deimel, P. S.; Aguilar, P. C.; Zhang, Y.-Q.; et al. On-Surface Site-Selective Cyclization of Corrole Radicals. *ACS Nano* **2017**, *11* (3), 3383−3391.
(48) Aldahhak, H.; Paszkiewicz, M.; Allegretti, F.; Duncan, D. A.; Tebi, S.; Deimel, P. S.; Aguilar, P. C.; Zhang, Y. Q.; Papageorgiou, A. C.; Koch, R.; et al. X-ray Spectroscopy of Thin Film Free-Base Corroles: A Combined Theoretical and Experimental Characterization. *J. Phys. Chem. C* **2017**, *121* (4), 2192−2200.
(49) Bai, Y.; Buchner, F.; Kellner, I.; Schmid, M.; Vollnhals, F.; Steinrück, H. P.; Marbach, H.; Gottfried, J. M. Adsorption of cobalt (II) octaethylporphyrin and 2H-octaethylporphyrin on Ag(111): new insight into the surface coordinative bond. *New J. Phys.* **2009**, *11*, 125004.
(50) Borghetti, P.; Di Santo, G.; Castellarin-Cudia, C.; Fanetti, M.; Sangaletti, L.; Magnano, E.; Bondino, F.; Goldoni, A. Adsorption geometry, conformation, and electronic structure of 2H-octaethylporphyrin on Ag(111) and Fe metalation in ultra high vacuum. *J. Chem. Phys.* **2013**, *138* (14), 144702.
(51) Heinrich, B. W.; Ahmadi, G.; Muller, V. L.; Braun, L.; Pascual, J. I.; Franke, K. J. Change of the Magnetic Coupling of a Metal-Organic Complex with the Substrate by a Stepwise Ligand Reaction. *Nano Lett.* **2013**, *13* (10), 4840−4843.
(52) Schleyer, P. v. R.; Maerker, C.; Dransfeld, A.; Jiao, H.; van Eikema Hommes, N. J. R. Nucleus-independent chemical shifts: A simple and efficient aromaticity probe. *J. Am. Chem. Soc.* **1996**, *118* (26), 6317−6318.
(53) Bai, Y. Photoelectron Spectroscopic Investigations of Porphyrins and Phthalocyanines on Ag(111) and Au(111): Adsorption and Reactivity. Ph.D. Thesis, Friedrich-Alexander Universität Erlangen-Nürnberg, Erlangen, 2010.
(54) Campbell, C. T.; Arnadottir, L.; Sellers, J. R. V. Kinetic Prefactors of Reactions on Solid. *Z. Phys. Chem.* **2013**, *227*, 1435.
(55) Bai, Y.; Sekita, M.; Schmid, M.; Bischof, T.; Steinrück, H.-P.; Gottfried, J. M. Interfacial coordination interactions studied on cobalt octaethylporphyrin and cobalt tetraphenylporphyrin monolayers on Au(111). *Phys. Chem. Chem. Phys.* **2010**, *12* (17), 4336−4344.
(56) Buchner, F.; Xiao, J.; Zillner, E.; Chen, M.; Röckert, M.; Ditze, S.; Stark, M.; Steinrück, H.-P.; Gottfried, J. M.; Marbach, H. Diffusion, Rotation, and Surface Chemical Bond of Individual 2H-Tetraphenylporphyrin Molecules on Cu(111). *J. Phys. Chem. C* **2011**, *115* (49), 24172−24177.
(57) Schweyen, P.; Brandhorst, K.; Wicht, R.; Wolfram, B.; Bröring, M. The Corrole Radical. *Angew. Chem., Int. Ed.* **2015**, *54* (28), 8213−8216.
(58) Kronik, L.; Kummel, S. Gas-Phase Valence-Electron Photoemission Spectroscopy Using Density Functional Theory. In *First Principles Approaches to Spectroscopic Properties of Complex Materials*; DiValentin, C., Botti, S., Cococcioni, M., Eds.; Springer-Verlag: Berlin, 2014; Vol. *347*, pp 137−191.
(59) Vázquez, H.; Dappe, Y. J.; Ortega, J.; Flores, F. Energy level alignment at metal/organic semiconductor interfaces: "Pillow" effect, induced density of interface states, and charge neutrality level. *J. Chem. Phys.* **2007**, *126* (14), 144703.
(60) Klein, B. P.; van der Heijden, N. J.; Kachel, S. R.; Franke, M.; Krug, C. K.; Greulich, K. K.; Ruppenthal, L.; Müller, P.; Rosenow, P.; Parhizkar, S.; et al. Molecular Topology and the Surface Chemical Bond: Alternant Versus Nonalternant Aromatic Systems as Functional Structural Elements. *Phys. Rev. X* **2019**, *9*, 011030.
(61) Capar, J.; Conradie, J.; Beavers, C. M.; Ghosh, A. Molecular Structures of Free-Base Corroles: Nonplanarity, Chirality, and Enantiomerization. *J. Phys. Chem. A* **2015**, *119* (14), 3452−3457.
(62) Müller, M.; Diller, K.; Maurer, R. J.; Reuter, K. Interfacial charge rearrangement and intermolecular interactions: Density-functional theory study of free-base porphine adsorbed on Ag(111) and Cu(111). *J. Chem. Phys.* **2016**, *144* (2), 024701.
(63) Hückel, E. *Grundzüge der Theorie ungesättigter und aromatischer Verbindungen*; Verlag Chemie: Berlin, 1938.
(64) Di Giovannantonio, M.; Eimre, K.; Yakutovich, A. V.; Chen, Q.; Mishra, S.; Urgel, J. I.; Pignedoli, C. A.; Ruffieux, P.; Müllen, K.; Narita, A.; et al. On-surface synthesis of antiaromatic and open-shell indeno[2,1-b]fluorene polymers and their lateral fusion into porous ribbons. *J. Am. Chem. Soc.* **2019**, *141* (31), 12346−12354.
(65) Krygowski, T. M. Crystallographic studies of inter- and intramolecular interactions reflected in aromatic character of.pi.-electron systems. *J. Chem. Inf. Model.* **1993**, *33* (1), 70−78.
(66) Cyrañski, M. K.; Krygowski, T. M.; Wisiorowski, M.; van Eikema Hommes, N. J. R.; Schleyer, P. v. R. Global and Local Aromaticity in Porphyrins: An Analysis Based on Molecular Geometries and Nucleus-Independent Chemical Shifts. *Angew. Chem., Int. Ed.* **1998**, *37* (1−2), 177−180.
(67) Moellmann, J.; Ehrlich, S.; Tonner, R.; Grimme, S. A DFT-D study of structural and energetic properties of TiO_2 modifications. *J. Phys.: Condens. Matter* **2012**, *24* (42), 424206.
(68) Lee, G.; Sprunger, P. T.; Okada, M.; Poker, D. B.; Zehner, D. M.; Plummer, E. W. Chemisorption of hydrogen on the Ag(111) surface. *J. Vac. Sci. Technol., A* **1994**, *12* (4), 2119−2123.
(69) Björk, J. Kinetic and Thermodynamic Considerations in On-Surface Synthesis. In *On-Surface Synthesis II*; de Oteyza, D. G., Rogero, C., Eds.; Springer: 2018; pp 19−34.
(70) Paños, F. J.; Pérez, E. Sackur−Tetrode equation in the lab. *Eur. J. Phys.* **2015**, *36* (5), 055033.

https://dx.doi.org/10.1021/acs.jpcc.0c04451
J. Phys. Chem. C 2020, 124, 13825−13836

Supporting Information for

On-Surface Formation of a Transient Corrole Radical and Aromaticity-Driven Interfacial Electron Transfer

Malte Zugermeier[a‡], Jan Herritsch[a‡], Jan-Niclas Luy[a], Min Chen[a], Benedikt P. Klein[a], Falk Niefind[a], Peter Schweyen[b], Martin Bröring[b], Martin Schmid[a], Ralf Tonner*[a§], J. Michael Gottfried*[a]

[a] *Philipps-Universität Marburg, Fachbereich Chemie, Hans-Meerwein-Str. 4, 35032 Marburg, Germany*
michael.gottfried@chemie.uni-marburg.de
ralf.tonner@chemie.uni-regensburg.de

[b] *Technische Universität Braunschweig, Institut für Anorganische und Analytische Chemie, Hagenring 30, 38106 Braunschweig, Germany*

‡ These authors contributed equally.

§Present address: Universität Regensburg, Institut für Physikalische und Theoretische Chemie, Universitätsstraße 31, 93053 Regensburg, Germany

1. Computational methods

Density functional theory (DFT) calculations were performed with the Vienna Ab initio Simulation Package (using version VASP 5.3.5 if not otherwise stated below).[1-3] The generalized gradient approximation-(GGA-)based exchange-correlation functional proposed by Perdew, Burke and Ernzerhof (PBE)[4] is used in conjunction with the projector-augmented wave (PAW) method using the "standard" pseudo potentials for all atoms (version PBE5.2).[5] Dispersion effects were treated with the DFT-D3 scheme using the Becke-Johnson-type damping function.[6-7] The precision tag was set to accurate, a total energy difference of at most 10^{-5} eV is used for SCF convergence while setting the plane wave energy cutoff to 400 eV. For structure optimization, the force convergence criterion is 10^{-2} eV/Å.

The surface was modelled with the slab-supercell approach using periodic boundary conditions (PBC) and a four-layer slab to represent the Ag surface of which the two bottom layers were constrained to the bulk structure. The lattice parameter (a = 4.073 Å) was determined computationally using the same input parameters and a 10×10 Γ-centered k-point mesh and 4 atoms per unit cell. This approach delivered accurate results in the past.[8] The thickness of the vacuum layer between periodically repeated slabs was larger than 13 Å, ensuring an error of less than 1 meV/atom for the given system. A non-orthogonal 6×6 unit cell was used for the unsubstituted species, while surface-adsorbate complexes of the alkyl substituted corroles were based on an 8×8 unit cell. This is close to the single-adsorbate limit with a remaining adsorbate-adsorbate interaction of less than 3.4 meV for substituted corroles.

To keep computational demand feasible, a 2×2 Γ-centered k-point mesh was used for the slab calculations. This results in an error in total energies of 1.2 meV/atom compared to next larger mesh (3×3). The first order Methfessel-Paxton procedure[9] is utilized to smear out electronic levels by $\sigma = 0.2$ eV to accelerate SCF convergence. This level of smearing corresponds to 2321 K of electronic temperature ($\sigma = k_B T$). Energies are then extrapolated to $\sigma = 0$.

Partial charges of the thus optimized adsorbate structures were calculated using the Amsterdam Density Functional (ADF) package with module BAND version 17.108[10-14] using the Hirshfeld partitioning scheme. Here, the PBE method including the DFT-D3 dispersion correction and Becke-Johnson-type damping was used as well as an atom-centered TZ2P[15-17] basis set.

A reaction path has been calculated with the climbing-image nudged elastic band (CI-NEB)[18] method at a convergence threshold of 10^{-1} eV/Å. The transition state found has been re-optimized with the DIMER method[19] with a convergence criterion of 10^{-2} eV/Å using VASP 5.4.4 and pseudo potential version PBE5.4.

Gas phase calculations were performed with Gaussian09, C.01[20] using the PBE[4] functional and the def2-TZVPP[21] basis set and compared to results from VASP 5.4.4 of the free molecules in a sufficiently large unit cell. As a criterion for aromaticity, we used the nucleus-independent chemical shift (NICS) method, which calculates the aromatic ring current induced by an external magnetic field that is perpendicular to the plane of the π-electron system.[22] This approach was applied to the optimized gas phase structures using gauge-independent atomic orbital (GIAO) basis functions.[23-27]

We discuss adsorbate/substrate bonding energies E_{ads} based on total energy differences according to $E_{ads} = E_{sac} - E_{surf} - E_{adsorbate}$, where $E_{adsorbate}$ is the energy of one adsorbate molecule in a large simulation box with periodic boundary conditions and E_{surf} is the energy of the clean surface and E_{sac} the energy of the surface-adsorbate complex. Note that negative values for E_{ads} thus indicate a stable adsorption structure. Electronic (E_{elec}) and dispersive (E_{disp}) contributions to the total bonding energy E_{ads} are derived from the PBE and the DFT-D3 contributions to the energy, respectively.

2. N 1s and C 1s XP spectra of one monolayer 3H-HEDMC on Au(111)

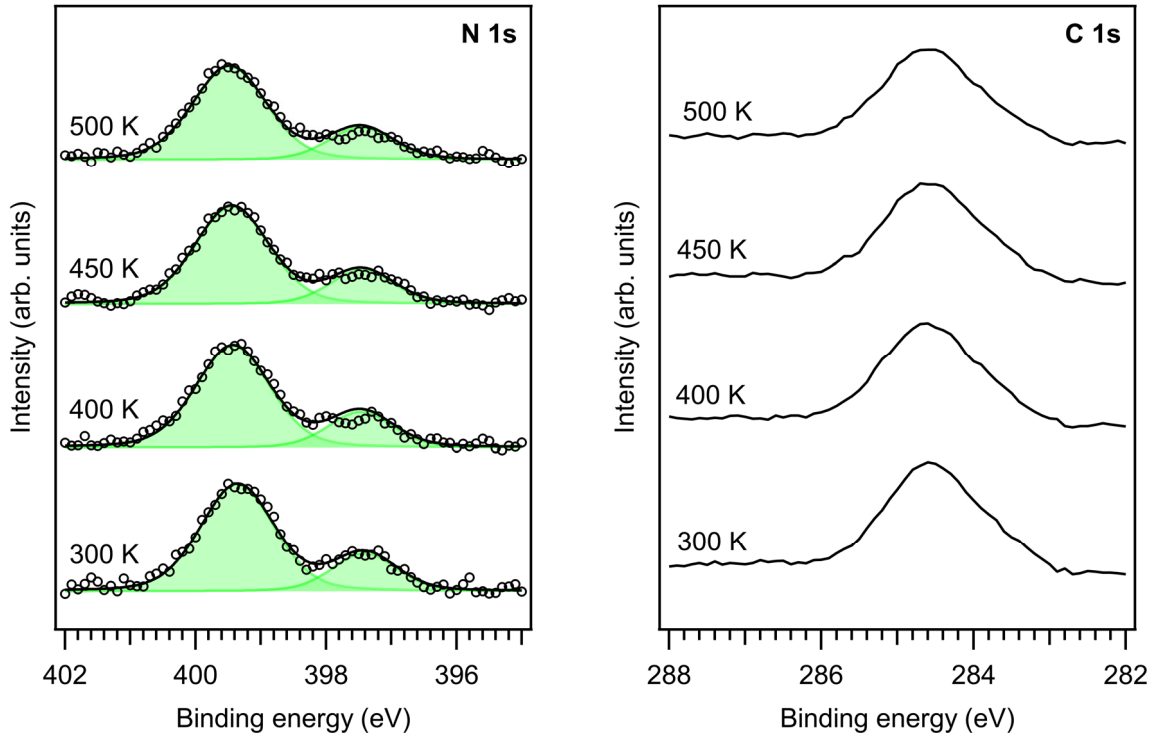

Figure S1. X-ray photoelectron spectra of (a) the N 1s and (b) the C 1s region of one monolayer 3H-HEDMC adsorbed on Au(111) at 300 K and after heating to different temperatures up to 500 K. The intact molecule bears three pyrrolic (−NH−) and two iminic (−N=) nitrogen atoms. Therefore, the nitrogen signal can be described by two components in a 3:1 ratio. Even at high temperatures neither the N 1s nor C 1s spectra show any significant changes, indicating that the N−H bonds do not dissociate.

3. Supplementary X-ray photoelectron Spectra on Ag(111) and N_D-H dissociation barrier

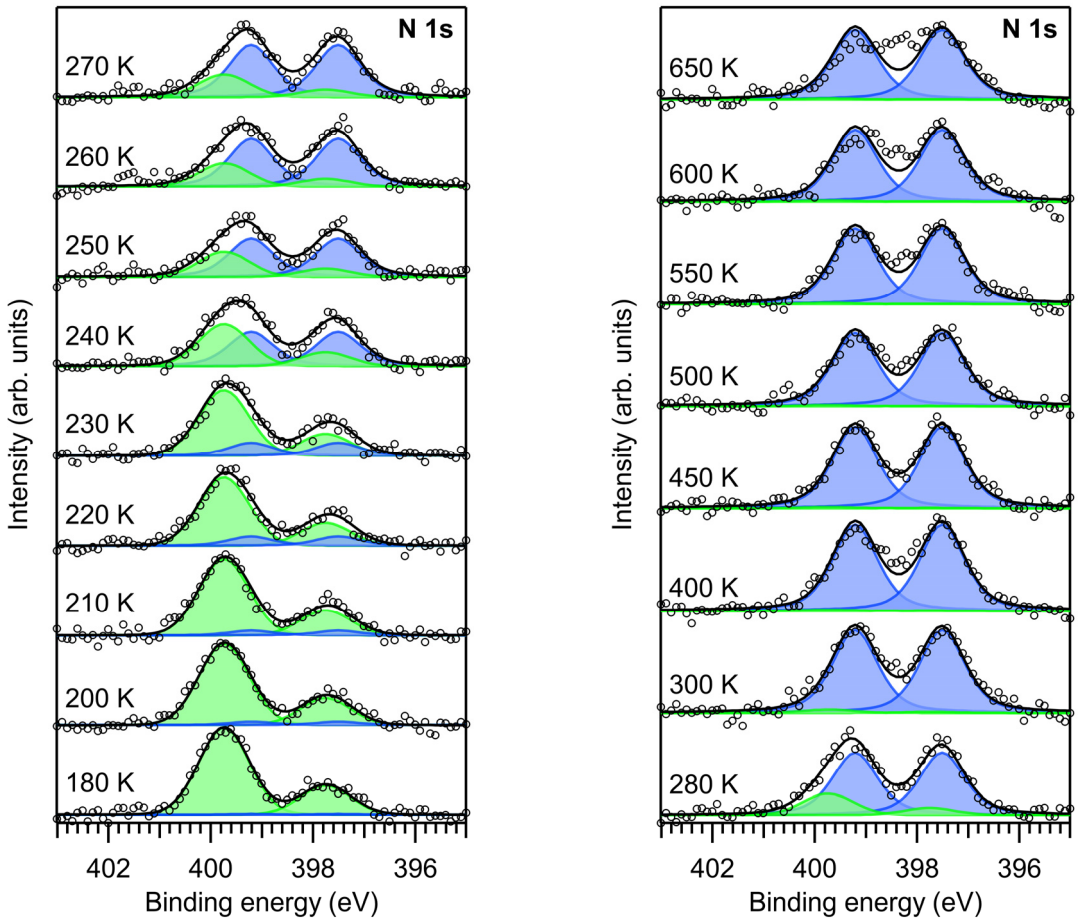

Figure S2. N 1s X-ray photoelectron spectra of one monolayer of 3H-HEDMC on Ag(111) in the temperature range 180 K - 650 K. The fits are superpositions of a 3:1 component (3H-HEDMC, green lines) and a 2:2 component (2H-HEDMC, blue lines). The black line is the sum of both components. The experimental data are represented by open circles. The data show that dissociation of the first N-H bond starts above 200 K and is nearly complete at room temperature (300 K). Further changes in the N 1s spectra occur only at much higher temperatures (≥ 500 K).

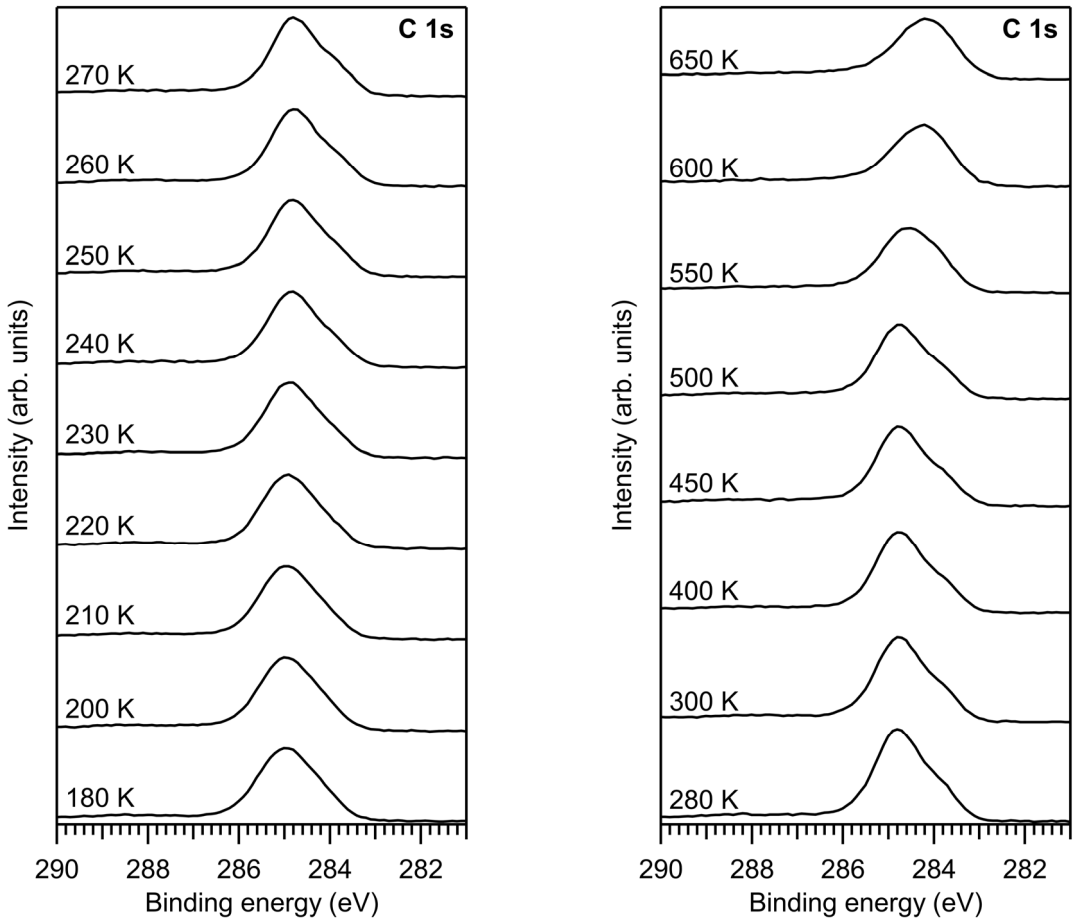

Figure S3. C 1s X-ray photoelectron spectra of one monolayer of 3H-HEDMC on Ag(111) in the temperature range 180 K - 650 K, corresponding to the N 1s spectra in Figure S1.

Estimation of the activation barrier for the reaction from 3H-HEDMC to 2H-HEDMC

Assume first-order reaction kinetics:

$$A = A_0 \cdot e^{-k_1 \tau}$$

$$k_1 = -\frac{1}{\tau} \cdot \ln\frac{A}{A_0} = \nu \cdot e^{-E^{\ddagger}/RT}$$

$$-\frac{1}{\tau\nu} \cdot \ln\frac{A}{A_0} = e^{-E^{\ddagger}/RT}$$

$$E^{\ddagger} = -\mathrm{RT} \cdot \ln\left(-\frac{1}{\tau\nu} \cdot \ln\frac{A}{A_0}\right)$$

A… concentration

A_0… initial concentration

k_1… rate constant

τ … annealing time

$E^{\ddagger}$… activation energy

T… temperature

ν … prefactor

Calculation for three different temperatures and averaging of the results:

$$\mathrm{R} = 8.3144598 \ \frac{\mathrm{J}}{\mathrm{mol \cdot K}}$$

$\tau = 180$ s (annealing time)

$\nu = 10^{13}\ \mathrm{s}^{-1}$ (estimated)[28-29]

T (K)	A_0	A	$E^{\ddagger}$ (kJ/mol)
230	0.81967	0.80795	75.28
240	0.80795	0.42968	71.01
250	0.42968	0.28857	74.93
			$\bar{E}^{\ddagger} = \mathbf{73.74}$

4. Supplementary computational investigations

4.1 Adsorption sites and energies of 3H-C on Ag(111)

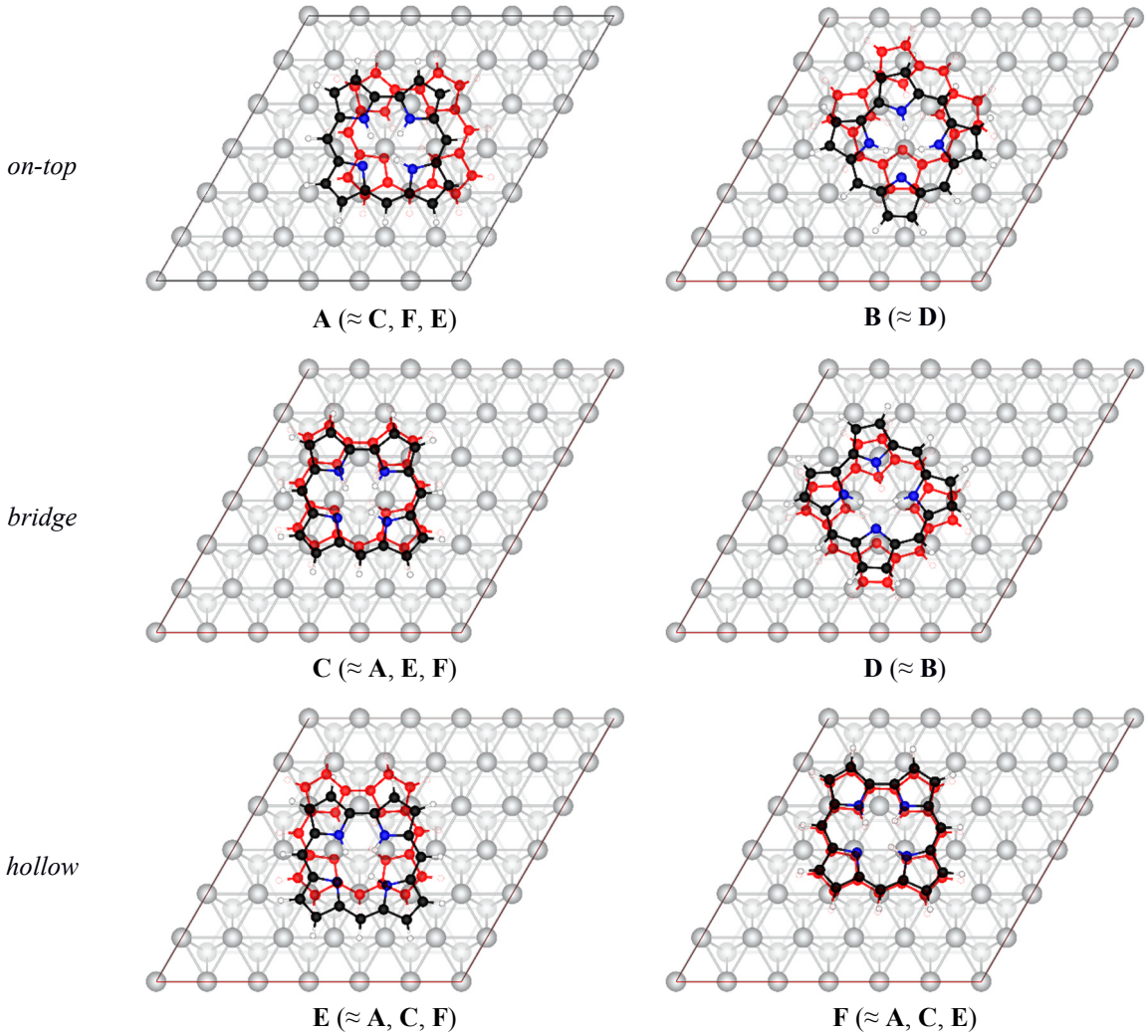

Figure S4. Starting geometries (black) and optimized structures (red) for 3H-C on different sites on the Ag(111) surface. Denotation of the different sites (*on-top*, *bridge*, *hollow*) refers to the position of the empty coordination site in the ring.

Table S1. Electronic (E_{elec}) and dispersive (E_{disp}) contributions to the total adsorption energy (E_{ads}) in kJ mol^{-1} of 3H-C on different sites on Ag(111).

	A	**B**	**C**	**D**	**E**	**F**
E_{ads}	−249	−249	−249	−249	−249	−250
E_{elec}	+17	+15	+16	+17	+17	+17
E_{disp}	−266	−264	−265	−266	−266	−267

The energy difference between different adsorption sites is negligible. Adsorption is dominated by dispersion. **Site F** has been used for further investigations.

4.2 Adsorption sites and energies of 2H-C on Ag(111)

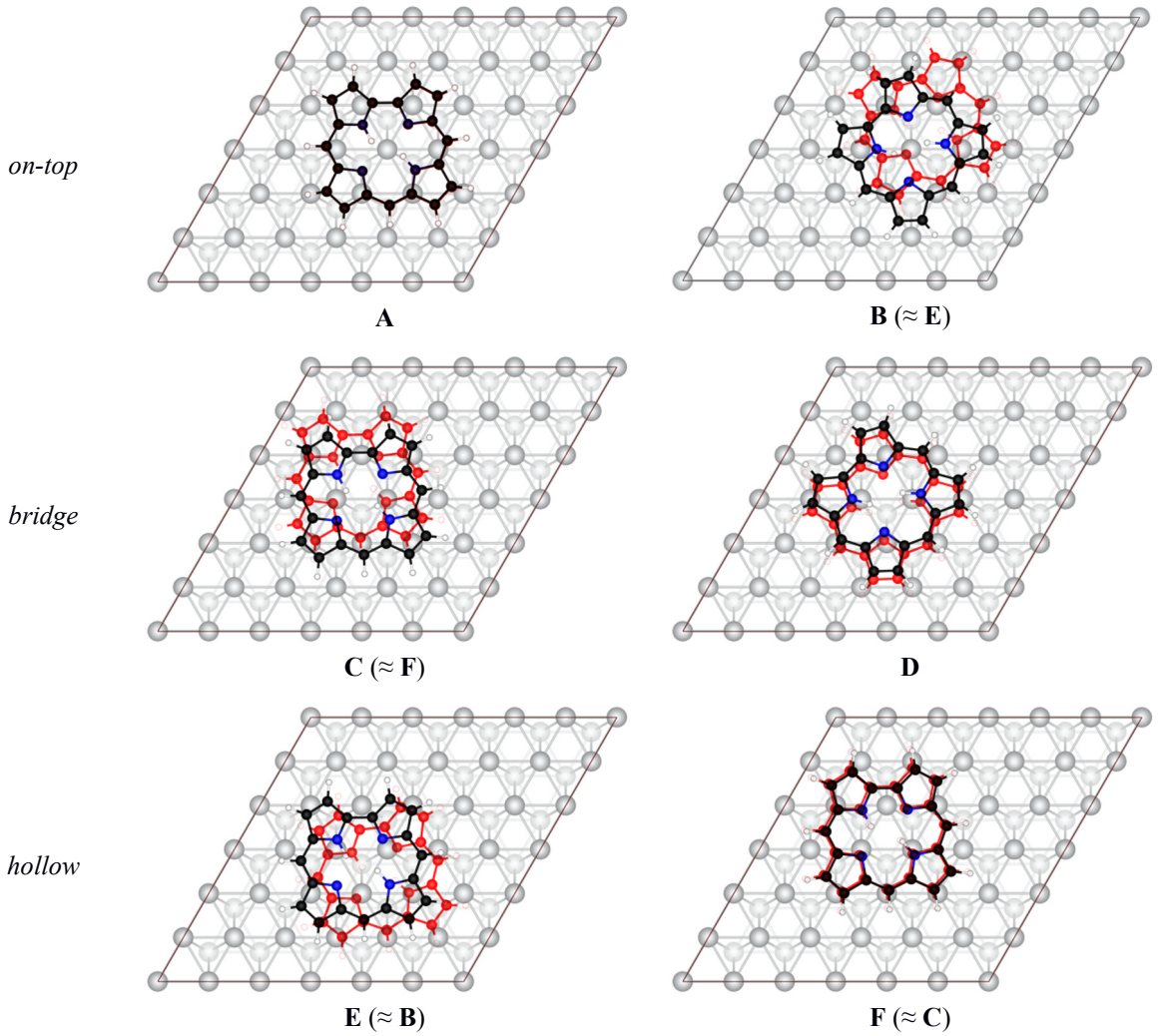

Figure S5. Starting geometries (black) and optimized structures (red) for 2H-C on different sites on the Ag(111) surface. Denotation of the different sites (*on-top*, *bridge*, *hollow*) refers to the position of the empty coordination site in the ring.

Table S2. Electronic (E_{elec}) and dispersive (E_{disp}) contributions to the total adsorption energy (E_{ads}) in kJ mol^{-1} of 2H-C on different sites on Ag(111).

	A	**B**	**C**	**D**	**E**	**F**
E_{ads}	−304	−330	−336	−328	−337	−335
E_{elec}	−12	−34	−37	−32	−38	−38
E_{disp}	−292	−296	−299	−296	−299	−297

The energy difference between different adsorption sites is small. Adsorption is dominated by dispersion. **Site E** has been used for further investigations.

4.3 Adsorption sites and energies of 2H-P on Ag(111)

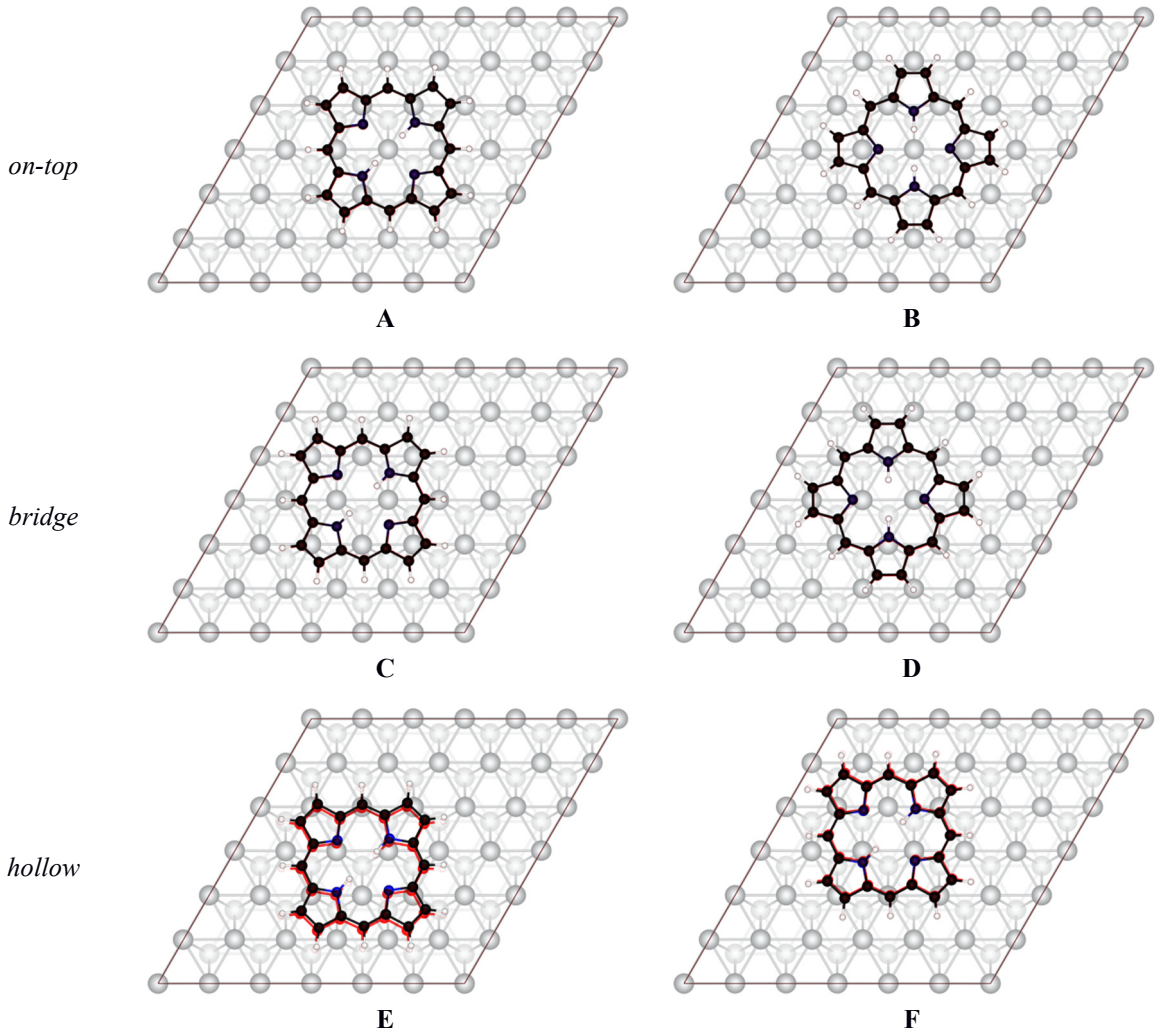

Figure S6. Start geometries and optimized structures (red overlay) for 2H-P on different sites on the Ag(111) surface. Denotation of the different sites (*on-top*, *bridge*, *hollow*) refers to the position of the empty coordination site in the ring.

Table S3. Electronic (E_{elec}) and dispersive (E_{disp}) contributions to the total adsorption energy (E_{ads}) in kJ mol^{-1} of 2H-P on different sites on Ag(111).

	A	**B**	**C**	**D**	**E**	**F**
E_{ads}	−243	−243	−246	−261	−253	−253
E_{elec}	+28	+29	+27	+36	+20	+25
E_{disp}	−271	−272	−273	−297	−273	−278

The energy difference between different adsorption sites is small. Adsorption is dominated by dispersion. **Site D** has been used for further investigations.

5. Deformation of the corrole macrocycle in the gas phase and adsorbed on Ag(111)

The corrole ring shows characteristic deformation. Details of the structural distortion and the changes upon adsorption are summarized here.

5.1 Displacement angles of the N-H hydrogen atoms

Table S4. Displacement angles (in degrees) of the N-H hydrogen atoms relative to the plane formed by the pyrrolic nitrogen atoms, in the gas phase (gas) and the adsorbed state (ads), for the corrole macrocycles 3H-C, 2H-C and 3H-HEDMC, 2H-HEDMC. Negative angles in the adsorbed molecules indicate displacement towards the surface. The values for the most distorted N_D-H bond are highlighted in bold.

	method	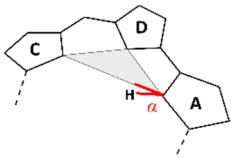	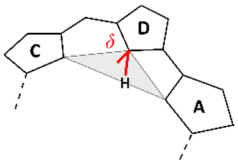	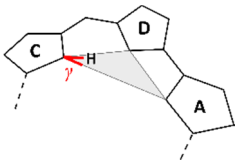
3H-C (gas)	PBE/def2-TZVPP[a]	−0.5	**−43.8**	+20.6
3H-C (gas)	PBE-D3/PAW[a]	−0.6	**−43.7**	+20.2
3H-C (ads)	PBE-D3/PAW	+0.8	**−50.4**	+13.7
2H-C (ads)	PBE-D3/PAW	−0.7	**--**	−0.9
3H-HEDMC (gas)	PBE-D3/PAW	+3.7	**−45.8**	+17.1
3H-HEDMC (ads)	PBE-D3/PAW	+3.6	**−49.6**	+7.7
2H-HEDMC (ads)	PBE-D3/PAW	−3.4	**--**	−4.2

[a] Computations with Gaussian-type local and extended plane wave basis sets do not show marked differences.

5.2. Dihedral angles between the pyrrole rings

Table S5. Dihedral angles (in degrees) between the pyrrole rings for 3H-C (gas phase and adsorbate) and for 2H-C (adsorbate) as well as for 3H-HEDMC (gas phase and adsorbate) and for 2H-HEDMC (adsorbate). "Gas phase" refers to the optimized gas phase structure; "adsorbate" to the molecular structure in the surface-adsorbate complex.

	method	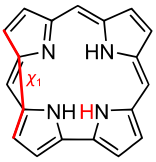	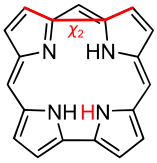	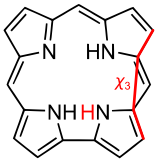	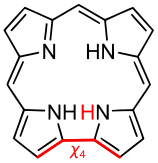
3H-C (gas phase)	BP86-D/TZP[a]	20.3[a]	7.3[a]	56.1[a]	21.5[a]
	PBE/def2-TZVPP	19.4	7.0	53.4	20.3
	PBE-D3/PAW	19.3	7.0	53.5	20.5
3H-C (adsorbate)	PBE-D3/PAW	3.7	7.8	38.8	17.0
2H-C (adsorbate)[b]	PBE-D3/PAW	4.5	2.4	8.4	4.9
3H-HEDMC (gas phase)	PBE-D3/PAW	4.5	2.9	48.6	28.2
3H-HEDMC (adsorbate)	PBE-D3/PAW	2.8	0.4	22.8	16.9
2H-HEDMC (adsorbate)[b]	PBE-D3/PAW	12.0	3.7	13.2	14.9

[a] J. Capar, J. Conradie, C. M. Beavers, A. Ghosh, *J. Phys. Chem. A* **2015**, *119*, 3453−3457.
[b] The H atom that is released by the first N-H dissociation is marked in red.

5.3. Additional structural parameters

Table S6. Additional bonding parameters of 3H-C and 3H-HEDMC (gas phase and adsorbate) as well as 2H-C and 2H-HEDMC (adsorbate). "Gas phase" refers to the optimized gas phase structure; "adsorbate" to the molecular structure in the surface-adsorbate complex.

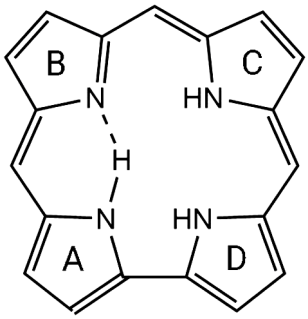

	N_A-H	N_A-H--N_B	N_A-Ag	N_B-Ag	N_C-Ag	N_D-Ag	C_{avg}-Ag_{avg}[a]
3H-C (gas phase)	1.046	1.733	-	-	-	-	-
3H-C (adsorbate)	1.040	1.760	3.393	3.079	3.254	3.412	3.143
2H-C (adsorbate)	1.034	1.801	3.075	2.723	2.878	2.765	2.910
3H-HEDMC (gas phase)	1.040	1.780	-	-	-	-	-
3H-HEDMC (adsorbate)	1.034	1.827	3.258	3.271	3.121	3.100	3.198
3H-HEDMC (adsorbate, flipped)[b]	1.034	1.810	3.320	3.153	3.136	3.433	3.225
3H-HEDMC TS (adsorbate)	1.030	1.887	2.842	2.746	3.115	3.199	3.081
2H-HEDMC + H (adsorbate)	1.029	1.876	3.168	3.045	2.953	3.120	3.081
2H-HEDMC (adsorbate)	1.027	1.880	3.110	2.746	2.826	2.529	3.018

[a] Cartesian z-positions of C atoms of the corrole backbone and Ag atoms of the first surface layer have been averaged.

[b] See Table S8.

5.4. Tautomers

Table S7. Adsorption energies of tautomers of 3H-C.

	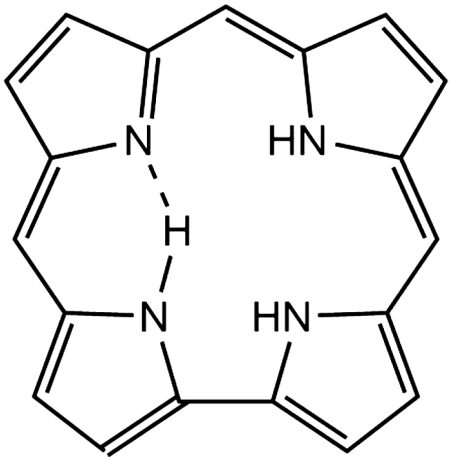	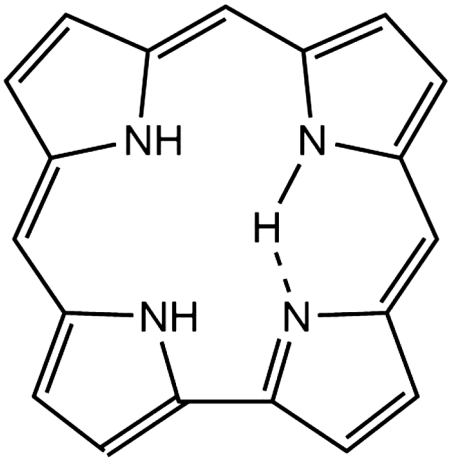
	3H-C	3H-C tautomer
E_{ads}	-249	-245
E_{elec}	15	16
E_{disp}	-264	-262

5.5. Adsorption energies for different conformers of 3H-HEDMC

Table S8. Adsorption energy E_{ads} in kJ mol^{-1} of 3H-HEDMC in different conformations on Ag(111).

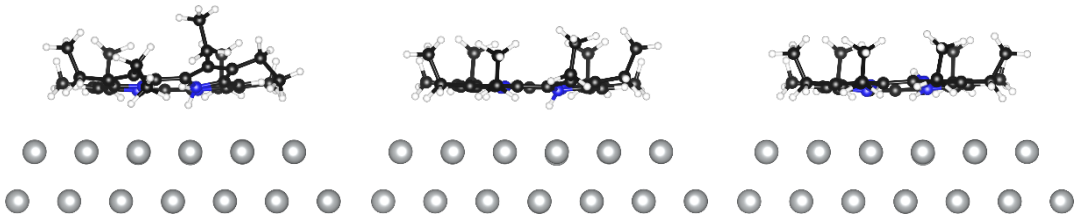

	gas phase[a]	side up[b]	flipped[c]
E_{ads}	-357	-373	-370
E_{elec}	34	36	34
E_{disp}	-391	-409	-403

[a] Adsorption in gas-phase optimized geometry. Ethyl groups point to different ring hemispheres. Acidic H atom (i.e., atom on N_D-H bond that undergoes dissociation) points towards the surface.

[b] All ethyl groups point away from the surface. Acidic H atom points towards the surface.

[c] All ethyl groups and the acidic H atom point away from the surface.

6. Partial density of states of 2H-C on Ag(111): Spin-polarized and non-spin-polarized calculations

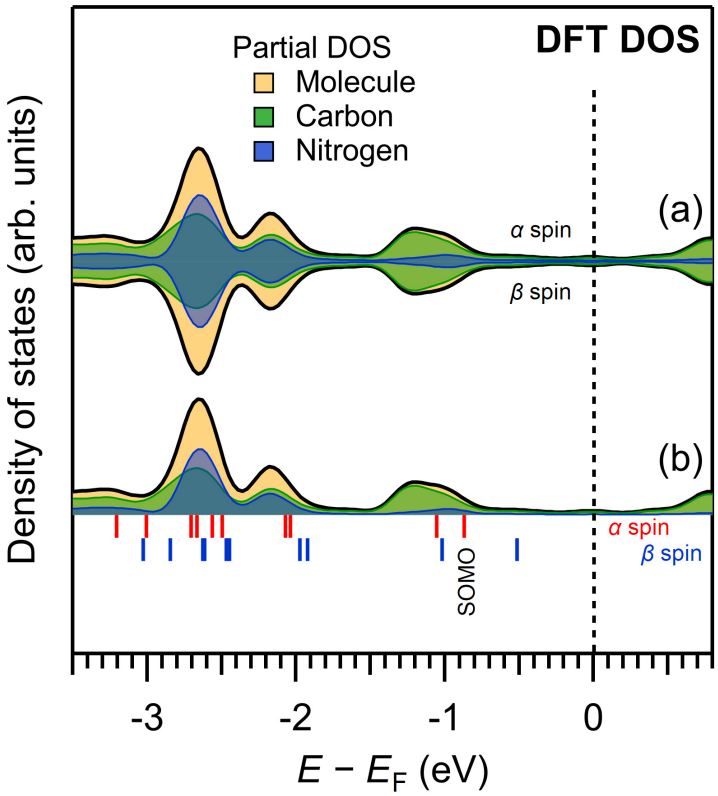

Figure S7. Calculated partial density of states (partial DOS) of 2H-C on Ag(111) from (a) a spin-polarized calculation. Both spins are characterized by the same density of states and are following the results from (b) a non-spin-polarized calculation. Contributions from the adsorbate (molecule) and atom types (carbon, nitrogen) to the total DOS are shown.

7. Determination of the work function changes

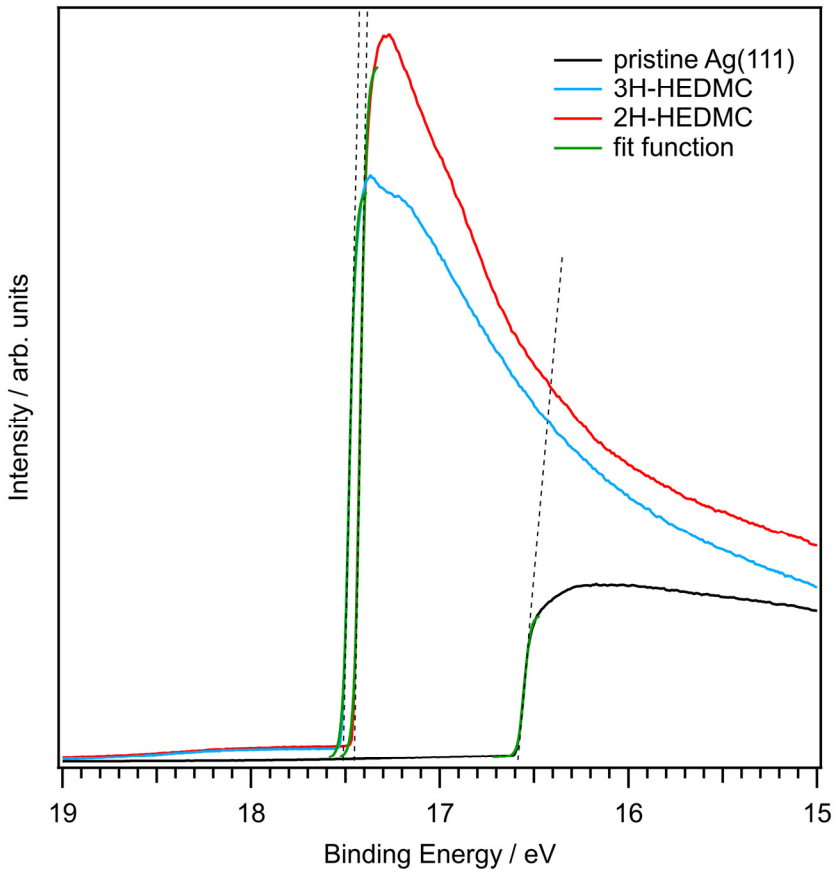

Figure S8. Work function changes obtained from the secondary-electron cut-off edges of He-I UV photoelectron spectra, taken with a sample bias of −5.00 V. To determine the exact values, a sigmoid function was fitted to the corresponding cut-off edge. In this way, a line could be constructed which intersects the inflection point with the same slope. The intersection of the energy axis of this tangent $E_{\text{cut-off}}$ was then used to determine the work function by the following equation: $\varphi = E_{\text{cut-off}} - h\nu$.

Table S9. Experimentally determined work function changes in eV compared with DFT for the unsubstituted molecules 3H-C and 2H-C results.

	Experiment		**DFT**	
	φ	$\Delta\varphi$	φ	$\Delta\varphi$
pristine Ag(111)	4.61	0	4.27	0
3H-HEDMC	3.69	−0.92	3.77	−0.50
2H-HEDMC	3.75	−0.86	3.98	−0.29

8. Proposed hyperconjugation effects in 3H-C, 2H-C radical, and 2H-C anion

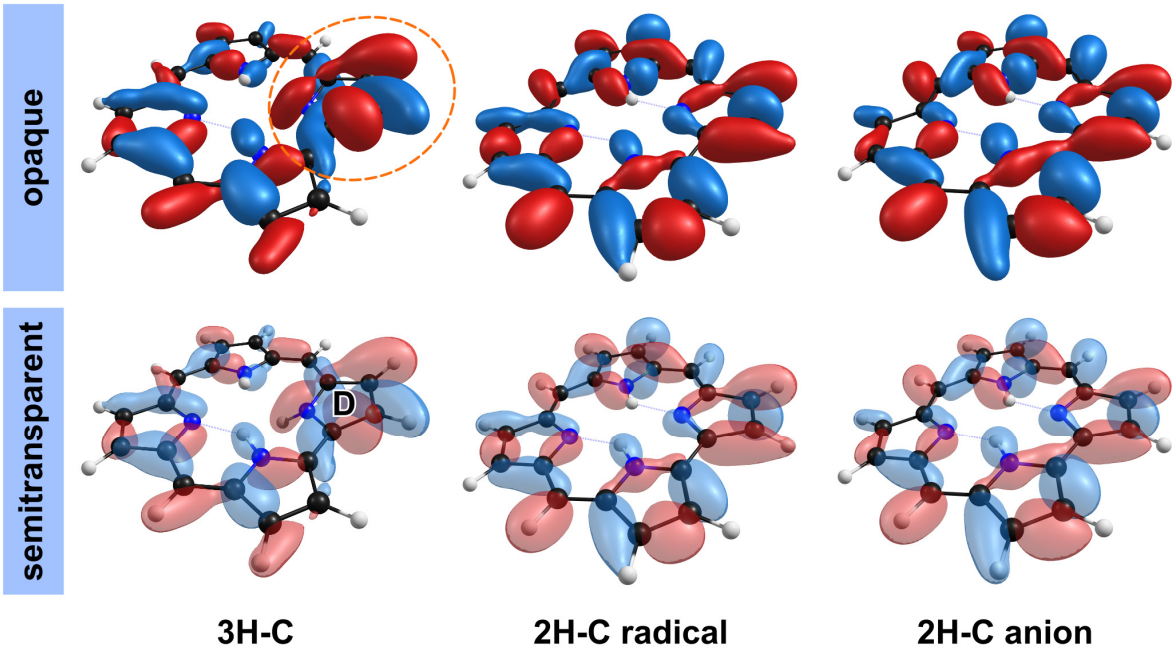

Figure S9. Visualized molecular orbital (opaque and semitransparent styles, iso-value = 0.03) for 3H-C (E = −9.89 eV), 2H-C radical (E_{alpha} = −9.95 eV, E_{beta} = −9.93 eV) and 2H-C anion (E = −6.35 eV). In case of 3H-C the orbital shows a distinct mixing (highlighted with orange circle) at the pyrrole unit D of the σ N_D-H bond and the delocalized π-electron system. This can be interpreted as a consequence of hyperconjugation. This phenomenon cannot be seen for the planar 2H-C radical or anion.

9. NICS(0) values for 2H-HEDMC radical compared with the monoanion

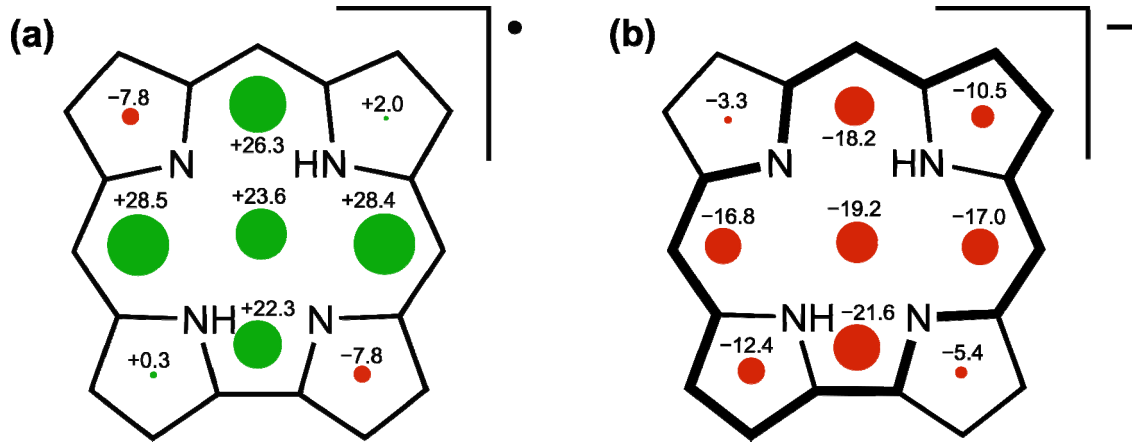

Figure S10. Anti-aromatic behavior of (a) the 2H-HEDMC radical compared with (b) the aromatic corrole monoanion. The extent of aromaticity is estimated by the NICS(0) method. Negative values show aromaticity and positive values represent anti-aromaticity. The resulting main delocalization path in the monoanion is highlighted by bold lines. The alkyl substituents have been included in the calculation but are not shown for the sake of clarity.

10. NICS(1) values for 2H-C radical compared with the monoanion

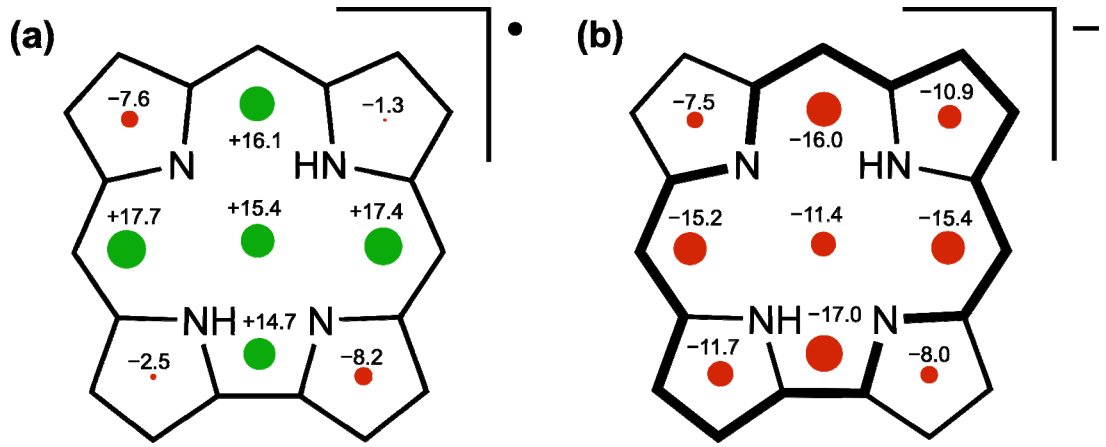

Figure S11. Corresponding NICS(1) values at 1 Å above the ring plane for (a) radicalic and (b) negatively charged 2H-C. The NICS(1) values give qualitatively the same results than the corresponding in-plane NICS(0) values.

11. Bond length of 3H-C, radical and negatively charged 2H-C

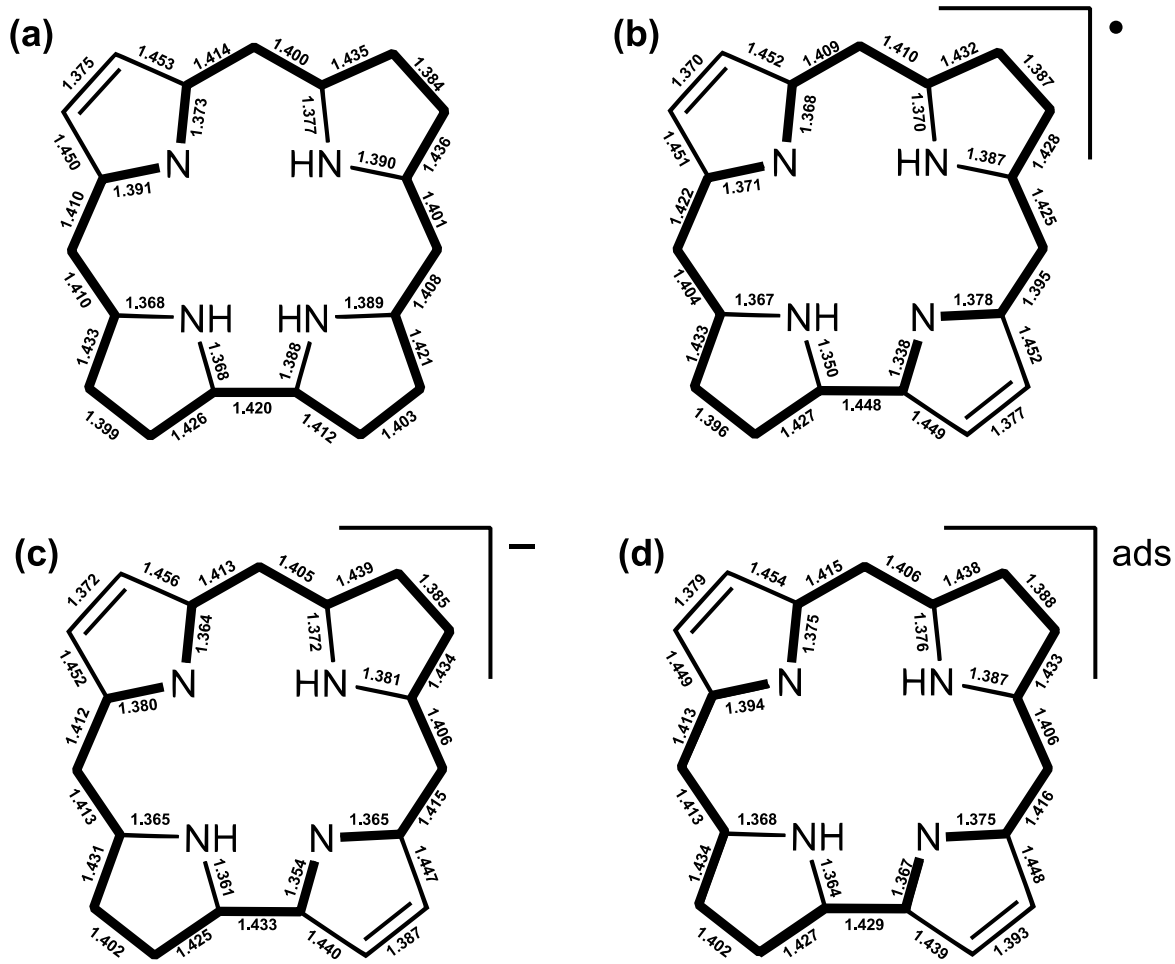

Figure S12. Calculated bond length in Å of (a) molecular 3H-C, (b) radical and (c) negatively charged 2H-C compared to (d) the adsorbate structure. Localized double bonds are shown and proposed main delocalization pathways are highlighted.

12. Reaction path for H-transfer reaction and density functional test for barrier height

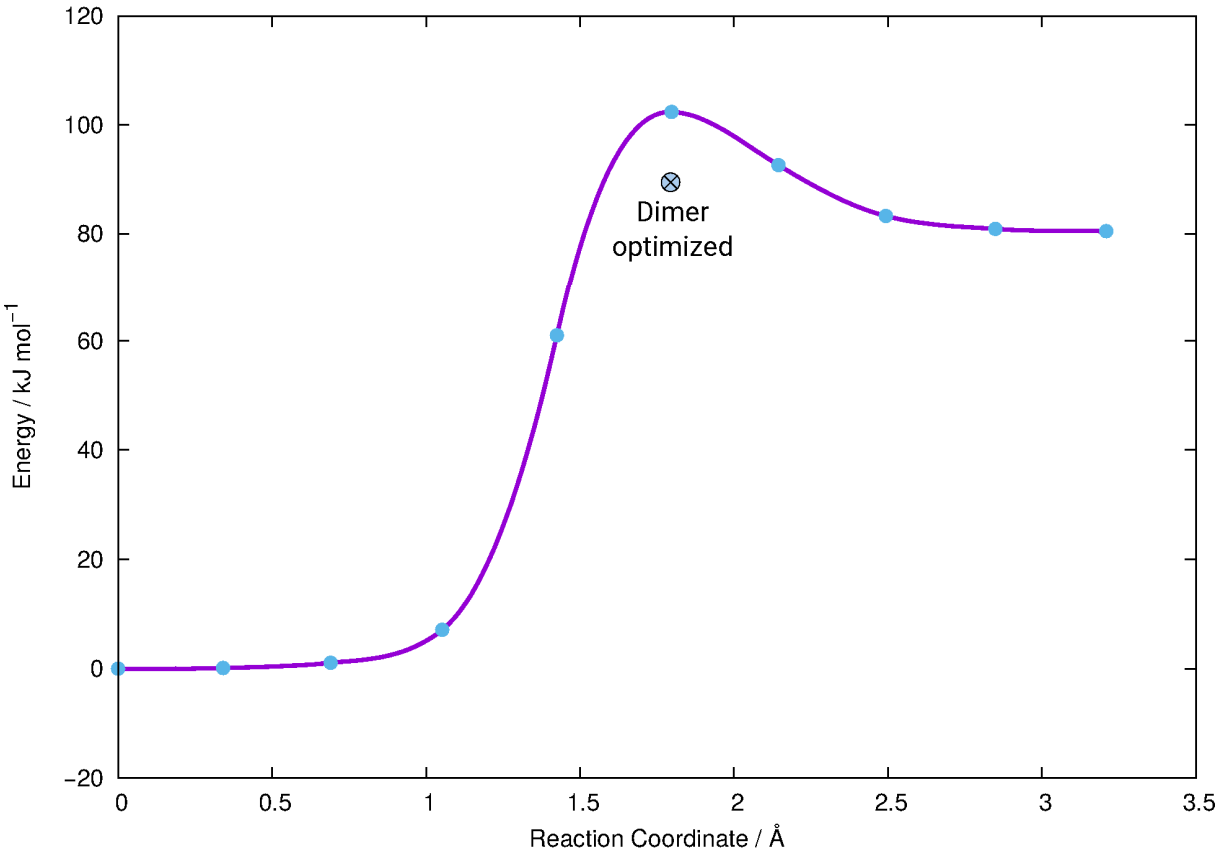

Figure S13. Path resulting from climbing-image nudge-elastic-band (CI-NEB) calculation of the reaction 3H-HEDMC → 2H-HEDMC + H at the Ag(111) surface (forces converged to 10^{-1} eV/Å). The transition state has been re-optimized with the dimer method (force convergence of 10^{-2} eV/Å).

Table S10. Barrier height $\Delta E^{\ddagger}$ for the H-transfer reaction shown in Figure S11 with different density functionals based on PBE-D3 structures.

Functional	**Type**	**$\Delta E^{\ddagger}$ / kJ mol^{-1}**
PBE-D3	GGA	91
revPBE-D3	GGA	76
PBE-vdW^{surf}[a]	GGA	85
PBE0-D3[b]	global hybrid	99[c]
HSE06-D3[d]	range-separated hybrid	102
optB88[e]	vdW-DF	102

[a] V.G. Ruiz, W. Liu and A. Tkatchenko, Phys. Rev. B, **2016**, *93*, 035118.
[b] M. Ernzerhof, G.E. Scuseria, J. Chem. Phys., **1999**, *110*, 5029.
[c] SCF cycle converged to 1.9*10^{-5} eV.
[d] J. Heyd, G.E. Scuseria, and M. Ernzerhof, J. Chem. Phys., **2006**, *124*, 219906.
[e] J. Klimeš, D.R. Bowler, and A. Michaelides, J. Phys.: Condens. Matter, **2010**, *22*, 022201.

13. Optimized atomic structures

The optimized atomic structures can be found in the NOMAD repository:

http://dx.doi.org/10.17172/NOMAD/2019.08.16-3

References

1. Kresse, G.; Hafner, J., Ab-initio molecular dynamics for liquid metals. *Phys. Rev. B* **1993,** *47* (1), 558-561.
2. Kresse, G.; Furthmuller, J., Efficiency of ab-initio total energy calculations for metals and semiconductors using a plane-wave basis set. *Comp. Mater. Sci.* **1996,** *6* (1), 15-50.
3. Kresse, G.; Furthmüller, J., Efficient iterative schemes for ab initio total-energy calculations using a plane-wave basis set. *Phys. Rev. B* **1996,** *54* (16), 11169-11186.
4. Perdew, J. P.; Burke, K.; Ernzerhof, M., Generalized gradient approximation made simple. *Phys. Rev. Lett.* **1996,** *77* (18), 3865-3868.
5. Kresse, G.; Joubert, D., From ultrasoft pseudopotentials to the projector augmented-wave method. *Phys. Rev. B* **1999,** *59* (3), 1758-1775.
6. Grimme, S.; Antony, J.; Ehrlich, S.; Krieg, H., A consistent and accurate ab initio parametrization of density functional dispersion correction (DFT-D) for the 94 elements H-Pu. *J. Chem. Phys.* **2010,** *132* (15), 154104.
7. Grimme, S.; Ehrlich, S.; Goerigk, L., Effect of the Damping Function in Dispersion Corrected Density Functional Theory. *J. Comp. Chem.* **2011,** *32* (7), 1456-1465.
8. Rosenow, P.; Jakob, P.; Tonner, R., Electron-Vibron Coupling at Metal-Organic Interfaces from Theory and Experiment. *Journal of Physical Chemistry Letters* **2016,** *7* (8), 1422-1427.
9. Methfessel, M.; Paxton, A. T., High-precision sampling for Brillouin-zone integration in metals. *Phys. Rev. B* **1989,** *40* (6), 3616-3621.
10. Velde, G. T.; Baerends, E. J., Precise density-functional method for periodic structures. *Phys. Rev. B* **1991,** *44* (15), 7888-7903.
11. Wiesenekker, G.; Baerends, E. J., Quadratic integration over the 3-dimensional Brillouin zone. *J. Phys. Condens. Matter* **1991,** *3* (35), 6721-6742.
12. Franchini, M.; Philipsen, P. H. T.; Visscher, L., The Becke Fuzzy Cells Integration Scheme in the Amsterdam Density Functional Program Suite. *J. Comp. Chem.* **2013,** *34* (21), 1819-1827.
13. Franchini, M.; Philipsen, P. H. T.; van Lenthe, E.; Visscher, L., Accurate Coulomb Potentials for Periodic and Molecular Systems through Density Fitting. *J. Chem. Theory Comput.* **2014,** *10* (5), 1994-2004.
14. BAND2017 SCM, T. C., Vrije Universiteit, Amsterdam, The Netherlands, http://www.scm.com.
15. Van Lenthe, E.; Baerends, E. J., Optimized slater-type basis sets for the elements 1-118. *Journal of Computational Chemistry* **2003,** *24* (9), 1142-1156.
16. Chong, D. P.; Van Lenthe, E.; Van Gisbergen, S.; Baerends, E. J., Even-tempered slater-type orbitals revisited: From hydrogen to krypton. *J. Comp. Chem.* **2004,** *25* (8), 1030-1036.
17. Chong, D. P., Augmenting basis set for time-dependent density functional theory calculation of excitation energies: Slater-type orbitals for hydrogen to krypton. *Molecular Physics* **2005,** *103* (6-8), 749-761.
18. Henkelman, G.; Uberuaga, B. P.; Jonsson, H., A climbing image nudged elastic band method for finding saddle points and minimum energy paths. *J. Chem. Phys.* **2000,** *113* (22), 9901-9904.
19. Henkelman, G.; Jonsson, H., A dimer method for finding saddle points on high dimensional potential surfaces using only first derivatives. *J. Chem. Phys.* **1999,** *111* (15), 7010-7022.
20. Frisch, M. J.; Trucks, G. W.; Schlegel, H. B.; Scuseria, G. E.; Robb, M. A.; Cheeseman, J. R.; Scalmani, G.; Barone, V.; Mennucci, B.; Petersson, G. A.; Nakatsuji, H.; Caricato, M.; Li, X.; Hratchian, H. P.; Izmaylov, A. F.; Bloino, J.; Zheng, G.; Sonnenberg, J. L.; Hada, M.; Ehara, M.; Toyota, K.; Fukuda, R.; Hasegawa, J.; Ishida, M.; Nakajima, T.; Honda, Y.; Kitao, O.; Nakai, H.; Vreven, T.; J. A. Montgomery, J.; Peralta, J. E.; Ogliaro, F.; Bearpark, M.; Heyd, J. J.; Brothers, E.; Kudin, K. N.; Staroverov, V. N.; Kobayashi, R.; Normand, J.; Raghavachari, K.; Rendell, A.; Burant, J. C.; Iyengar, S. S.; Tomasi, J.; Cossi, M.; Rega, N.; Millam, J. M.; Klene, M.; Knox, J. E.; Cross, J. B.; Bakken, V.; Adamo, C.; Jaramillo, J.; Gomperts, R.; Stratmann, R. E.; Yazyev, O.; Austin, A. J.; Cammi, R.; Pomelli, C.; Ochterski, J. W.; Martin, R. L.; Morokuma, K.; Zakrzewski, V. G.; Voth, G. A.; Salvador, P.; Dannenberg, J. J.; Dapprich, S.; Daniels, A. D.; Farkas, Ö.; Foresman, J. B.; Ortiz, J. V.; Cioslowski, J.; Fox, D. J., Gaussian 09 (Gaussian, Inc., Wallingford CT). **2009**.

21. Weigend, F.; Ahlrichs, R., Balanced basis sets of split valence, triple zeta valence and quadruple zeta valence quality for H to Rn: Design and assessment of accuracy. *Phys. Chem. Chem. Phys.* **2005,** *7* (18), 3297-3305.
22. Schleyer, P. V.; Maerker, C.; Dransfeld, A.; Jiao, H. J.; Hommes, N., Nucleus-independent chemical shifts: A simple and efficient aromaticity probe. *J. Am. Chem. Soc.* **1996,** *118* (26), 6317-6318.
23. London, F., The quantic theory of inter-atomic currents in aromatic combinations. *J. Phys. Radium* **1937,** *8*, 397-409.
24. McWeeny, R., Perturbation theory for Fock-Dirac density matrix. *Phys. Rev.* **1962,** *126* (3), 1028.
25. Ditchfield, R., Self-consistent perturbation theory of dieamagnetism. 1. Gauge-invariant LCAO method for NMR chemical shifts. *Molec. Phys.* **1974,** *27* (4), 789-807.
26. Wolinski, K.; Hinton, J. F.; Pulay, P., Efficient implementation of the gauge-independent atomic method for NMR chemical shift calculations. *J. Am. Chem. Soc.* **1990,** *112* (23), 8251-8260.
27. Cheeseman, J. R.; Trucks, G. W.; Keith, T. A.; Frisch, M. J., A comparison of models for calculating nuclear magnetic resonance shielding tensors. *J. Chem. Phys.* **1996,** *104* (14), 5497-5509.
28. Campbell, C. T.; Árnadóttir, L.; Sellers, J. R. V., Kinetic Prefactors of Reactions on Solid Surfaces. *Z. Phys. Chem.* **2013**, *227*, 1435.
29. Campbell, C. T.; Sun, Y. K.; Weinberg, W. H., Trends in preexponential factors and activation energies in dehydrogenation and dissociation of adsorbed species. *Chem. Phys. Lett.* **1991,** *179* (1), 53-57.

Appendix C

Miscellaneous

C.1 BAND Parser for the NOMAD Repository

The Novel Materials Discovery (NOMAD) repository [128] is an effort by members of the computational materials science community to make research data shareable and reproducible. Furthermore, the raw data produced by different program packages is parsed into a common data format to facilitate analysis with e.g. machine learning approaches. The uploaded data is kept accessible for at least ten years in order to comply with the requirements of many funding agencies. Following the principles of good scientific practice, raw input and output files generated for this dissertation have been uploaded to the NOMAD archive. For the BAND program no parser had been available prior to this work and was subsequently written by the author during a visit in Berlin. The source code (Python) is given below.

```
#   Copyright 2019 Jan-Niclas Luy
#   Licensed under the Apache License, Version 2.0 (the "License");
#   you may not use this file except in compliance with the License.
#   You may obtain a copy of the License at
#     http://www.apache.org/licenses/LICENSE-2.0
#   Unless required by applicable law or agreed to in writing, software
#   distributed under the License is distributed on an "AS IS" BASIS,
#   WITHOUT WARRANTIES OR CONDITIONS OF ANY KIND, either express or implied.
#   See the License for the specific language governing permissions and
#   limitations under the License.
import sys
import numpy as np
from ase.io import read as ase_read
from scipy.constants import physical_constants as pc
from nomadcore.simple_parser import SimpleMatcher
from nomadcore.baseclasses import ParserInterface, MainHierarchicalParser
from nomad.parsing import LocalBackend
"""
A basic BAND parser.
"""
class BANDParser(ParserInterface):
    def get_metainfo_filename(self):
        return 'band.nomadmetainfo.json'
    def get_parser_info(self):
        return {
            'name': 'band_parser',
            'version': '1.0.0'
        }
```

```
    def setup_version(self):
        self.setup_main_parser(None)
    def setup_main_parser(self, _):
        self.main_parser = MainParser(self.parser_context)
class MainParser(MainHierarchicalParser):
    def __init__(self, parser_context, *args, **kwargs):
        super().__init__(parser_context, *args, **kwargs)
        self.lattice_vectors = []
        self.lattice_vectors_opt = []
        self.atom_labels = []
        self.atom_positions = []
        self.atom_labels_opt = []
        self.atom_positions_opt = []
        self.configuration_periodic_dimensions = []
        self.XC_functional_name = []
        self.LDA_functional_name = []
        self.GGA_functional_name = []
        self.meta_GGA_functional_name = []
        self.dos_values = []
        self.dos_energies = []
        #self.system_index = None
        self.root_matcher = SimpleMatcher(
            name='root',
            startReStr=r'B A N D',
            weak=True,
            sections=['section_run', 'section_method', 'section_sampling_method'],
            subMatchers=[
                SimpleMatcher(
                    startReStr=r'       \*  (?P<sampling_method>GEOMETRY OPTIMIZATION)  \*'
                ),
                SimpleMatcher(
                    startReStr=r' \*   Amsterdam Density Functional  \(ADF\)\s*\d*\s*\*.*',
                    subMatchers=[
                        SimpleMatcher(startReStr=r'\s\*\s{47}r(?P<program_version>\d+).*'),
                    ],
                    endReStr=r'\s\*{2}.*'),
                SimpleMatcher(
                    startReStr=r'Geometry.*',
                    sections=['section_system'],
                    subMatchers=[
                        SimpleMatcher(
                            startReStr=r'  Index Symbol       x \(bohr\)       y \(bohr\)       z \(bohr\)
                                .*',
                            subMatchers=[
                                SimpleMatcher(startReStr=r'\s*\d+\s+([A-Z][a-z]?)\s+([+-]?\d+\.\d+)\s*([+-]?\
                                    d+\.\d+)\s*([+-]?\d+\.\d+)\s*', repeats=True, startReAction=self.
                                    save_atoms)
                            ],
                            endReStr=r'\s*'
                        ),
                        SimpleMatcher(
                            startReStr=r'Lattice vectors \(bohr\).*',
                            subMatchers=[
                                SimpleMatcher(startReStr=r'\s*\d+\s+(\d+\.\d+)\s*(\d+\.\d+)\s*(\d+\.\d+)\s*',
                                    repeats=True, startReAction=self.save_lattice)
                            ],
                            endReStr=r'\s*'
                        )
                    ]
                ),
                SimpleMatcher(startReStr=r'Total System Charge            (?P<total_charge>\d+)\.\d+.*',
                ),
                SimpleMatcher(
                     startReStr=r'Band Engine Input.*',
                     subMatchers=[
                         SimpleMatcher(
                             startReStr=r'((?i) \s*Basis)',
                             subMatchers=[
                                 SimpleMatcher(startReStr=r'((?i)\s*Type\s*(?P<basis_set>[a-z,A-Z]*).*)', )
                             ],
                             endReStr=r'((?i) \s*End)'
```

```
                        )
                    ],
                    endReStr=r' Using the following basis set files:'
                ),
                SimpleMatcher(
                    startReStr=r' DENSITY FUNCTIONAL POTENTIAL \(scf\)',
                    subMatchers=[
                        SimpleMatcher(startReStr=r'    LDA:                                ([a-z,A-Z]*).*',
                            startReAction=self.save_lda
                        ),
                        SimpleMatcher(startReStr=r'    Gradient Corrections:               ([a-z,A-Z]*)c\s*([a
                            -z,A-Z]*)x.*', startReAction=self.save_functional
                        ),
                        SimpleMatcher(startReStr=r'    Meta-GGA:                           ([a-z,A-Z]*).*',
                            startReAction=self.save_meta_gga
                        )
                    ],
                    endReStr=r' DENSITY FUNCTIONAL ENERGY \(post-scf\)'
                ),
                SimpleMatcher(
                    startReStr=r' R U N    C O N F I G.*', repeats=True,
                    sections=['section_single_configuration_calculation'],
                    subMatchers=[
                            SimpleMatcher(
                                startReStr=r' G E O M E T R Y    I N    X - Y - Z    F O R M A T.*',
                                sections=['section_system'],
                                subMatchers=[
                                    SimpleMatcher(startReStr=r'\s*([A-Z][a-z]?)\s*([+-]?\d+\.\d+)\s*([+-]?\d
                                        +\.\d+)\s*([+-]?\d+\.\d+)\s*', repeats=True, startReAction=self.
                                        save_atoms
                                    ),
                                    SimpleMatcher(startReStr=r'\s*VEC\d+\s+([+-]?\d+\.\d+)\s*([+-]?\d+\.\d+)\
                                        s*([+-]?\d+\.\d+)\s*', repeats=True, startReAction=self.
                                        save_lattice_opt
                                    )
                                ],
                                endReStr=r'   Total nr. of atoms'
                            ),
                            SimpleMatcher(startReStr=r' Final bond energy \([a-zA-Z]*\)\s*(?P<
                                energy_total__hartree>-\d+\.\d+).*'
                            ),
                            SimpleMatcher(
                                sections=['section_dos'],
                                startReStr=r' TOTALDOS.*',
                                subMatchers=[
                                    SimpleMatcher(startReStr=r' NSPIN,NE= 2.*',
                                        subMatchers=[
                                            SimpleMatcher(
                                                startReStr=r'\s*([+-]?\d+\.\d+E[+-]?\d+)\s*([+-]?\d+\.\d+E
                                                    [+-]?\d+)\s*([+-]?\d+\.\d+E[+-]?\d+).*', repeats=True,
                                                    startReAction=self.save_dos_2)
                                        ]
                                    ),
                                    SimpleMatcher(startReStr=r' NSPIN,NE= 1.*',
                                        subMatchers=[
                                            SimpleMatcher(
                                                startReStr=r'\s*([+-]?\d+\.\d+E[+-]?\d+)\s*([+-]?\d+\.\d+E
                                                    [+-]?\d+).*', repeats=True, startReAction=self.
                                                    save_dos_1)
                                        ]
                                    )
                                ],
                                endReStr=r' ENDINPUT.*',
                            )
                    ]
                ),
            ]
        )
    def save_dos_2(self, _, groups):
        self.dos_values.append([float(groups[1]), float(groups[2])])
        self.dos_energies.append(float(groups[0]))
    def save_dos_1(self, _, groups):
        self.dos_values.append([float(groups[1])])
```

```
157 |         self.dos_energies.append(float(groups[0]))
158 |     def save_atoms(self, _, groups):
159 |         self.atom_positions.append([float(groups[1]), float(groups[2]), float(groups[3])])
160 |         self.atom_labels.append(groups[0])
161 |     def save_atoms_opt(self, _, groups):
162 |         self.atom_positions_opt.append([float(groups[1]), float(groups[2]), float(groups[3])])
163 |         self.atom_labels_opt.append(groups[0])
164 |     def save_lattice(self, _, groups):
165 |         self.lattice_vectors.append([float(groups[0]), float(groups[1]), float(groups[2])])
166 |     def save_lattice_opt(self, _, groups):
167 |         self.lattice_vectors_opt.append([float(groups[0]), float(groups[1]), float(groups[2])])
168 |     def save_lda(self, _, groups):
169 |         self.LDA_functional_name.append(groups[0])
170 |     def save_meta_gga(self, _, groups):
171 |         self.meta_GGA_functional_name.append(groups[0])
172 |     def save_functional(self, _, groups):
173 |         if groups != None:
174 |             self.GGA_functional_name.append([groups[0], groups[1]])
175 |     def onClose_section_system(self, backend, index, *args, **kwargs):
176 |         self.system_index = index
177 |         backend.addArrayValues('atom_labels', np.array(self.atom_labels))
178 |         backend.addArrayValues('atom_positions', np.array(self.atom_positions)*pc['Bohr radius'][0])
179 |         if self.configuration_periodic_dimensions != []:
180 |             backend.addArrayValues('configuration_periodic_dimensions', np.array(self.
                      configuration_periodic_dimensions))
181 |             for _ in range(0, len(self.lattice_vectors)):
182 |                 self.configuration_periodic_dimensions.append(True)
183 |             for _ in range(len(self.lattice_vectors),3):
184 |                 self.configuration_periodic_dimensions.append(False)
185 |         for _ in range(len(self.lattice_vectors),3):
186 |             self.lattice_vectors.append([0,0,0])
187 |         if self.lattice_vectors != []:
188 |             backend.addArrayValues('lattice_vectors', np.array(self.lattice_vectors)*pc['Bohr radius'][0])
189 |     def onClose_section_dos(self, backend, *args, **kwargs):
190 |         backend.addArrayValues('dos_values', np.array(self.dos_values))
191 |         backend.addArrayValues('dos_energies', np.array(self.dos_energies)*pc['Hartree energy'][0])
192 |     def onClose_section_method(self, backend, *args, **kwargs):
193 |         backend.addValue('electronic_structure_method', 'DFT')
194 |         if self.GGA_functional_name != []:
195 |             backend.openNonOverlappingSection('section_XC_functionals')
196 |             backend.addValue('XC_functional_name', 'GGA_X_' + self.GGA_functional_name[0][1])
197 |             backend.closeNonOverlappingSection('section_XC_functionals')
198 |             backend.openNonOverlappingSection('section_XC_functionals')
199 |             backend.addValue('XC_functional_name', 'GGA_C_' + self.GGA_functional_name[0][0])
200 |             backend.closeNonOverlappingSection('section_XC_functionals')
201 |         if self.meta_GGA_functional_name != []:
202 |             backend.openNonOverlappingSection('section_XC_functionals')
203 |             backend.addValue('XC_functional_name', 'MGGA_XC_' + self.meta_GGA_functional_name[0])
204 |             backend.closeNonOverlappingSection('section_XC_functionals')
205 |         if self.LDA_functional_name != [] and self.GGA_functional_name == []:
206 |             backend.openNonOverlappingSection('section_XC_functionals')
207 |             backend.addValue('XC_functional_name', 'LDA_XC_' + self.LDA_functional_name[0])
208 |             backend.closeNonOverlappingSection('section_XC_functionals')
209 |     def onClose_section_run(self, backend, *args, **kwargs):
210 |         backend.addValue('program_name', 'BAND')
211 |         backend.addValue('program_basis_set_type', 'Slater')
212 |     def onClose_section_single_configuration_calculation(self, backend, *args, **kwargs):
213 |         backend.addValue('single_configuration_calculation_to_system_ref', self.system_index)
214 |         backend.addValue('single_configuration_to_calculation_method_ref', 0)
215 | if __name__ == "__main__":
216 |     parser = BANDParser(backend=LocalBackend)
217 |     parser.parse(sys.argv[1])
```

C.2 Raw Data Archive

The raw data necessary to reproduce the results of this dissertation are available for download at digital archives. Each entry is assigned a permanent DOI (digital object identifier).

Adsorption of methyl-substituted benzylazide on Si(001): reaction channels and final configurations:
https://dx.doi.org/10.17172/NOMAD/2019.12.12-1
https://dx.doi.org/10.17172/NOMAD/2020.04.03-1

Combined XPS and DFT investigation of the adsorption modes of methyl enol ether functionalized cyclooctyne on Si(001):
https://dx.doi.org/10.17172/NOMAD/2020.11.24-1

Click chemistry in ultra-high vacuum - tetrazine coupling with methyl enol ether covalently linked to Si(001):
https://dx.doi.org/10.17172/NOMAD/2020.11.19-1

Complementary base lowers the barrier in SuFEx click chemistry for primary amine nucleophiles:
https://dx.doi.org/10.17172/NOMAD/2020.08.05-1

Efficient hierarchical models for reactivity of organic layers on semiconductor surfaces:
https://dx.doi.org/10.17172/NOMAD/2020.12.07-8

Organic functionalization at the Si(001) dimer vacancy defect – structure, bonding and reactivity:
https://dx.doi.org/10.17172/NOMAD/2021.01.07-1
https://doi.org/10.5281/zenodo.4536020

Template-controlled on-surface synthesis of a lanthanide supernaphthalocyanine and its open-chain polycyanine counterpart:
http://dx.doi.org/10.17172/NOMAD/2019.03.18-1
http://dx.doi.org/10.17172/NOMAD/2019.07.01-1

On-surface formation of a transient corrole radical and aromaticity-driven interfacial electron transfer:
http://dx.doi.org/10.17172/NOMAD/2019.08.16-3